Fourth International Conference on Cryocrystals and Quantum Crystals (CC 2002). Preface

Fiz. Nizk. Temp. **29**, 939–940 (September–October 2003)

The conference on Cryocrystals and Quantum Crystals, CC 2002, was a continuation of a series of conferences started in 1995 in Almaty, Kazakstan by Prof. Andrei Drobyschev. The original intent of the conference was to provide a platform for scientists from the former Soviet Union and the countries of Eastern Europe to meet and exchange information with their Western colleagues, and, in particular, to make it possible for the younger investigators to become acquainted directly with the most recent research and results in their respective fields from elsewhere in the world. With nearly a hundred participants, the conference was a resounding success, and it was therefore decided to organize a second, similar conference two years later, this time chaired by Prof. Andrzei Jeżowski in Polanica-Zdroj, Poland. [DOI: 10.1063/1.1614171]

The scientists present there voiced their preference for holding a third conference in 1999 in Germany, and suggested that, in particular, Munich or the surrounding Bavarian region, with their central location and easy accessibility from east or west, would provide a suitable venue. Severe funding difficulties, however, made it impossible to hold the conference as planned, but fortunately Prof. Jeżowski once again came to the rescue and was able to obtain sufficient funding to organize the conference for 2000, again in Poland, only this time in the attractive Karkonosze Mountains region, in Szklarska Poremba.

For the next conference of the series, CC 2002, we finally managed to obtain some funding from the German funding agency, Deutsche Forschungsgemeinschaft, so that with additional support from the Fonds der Chemischen Industrie as well as some funds from several industrial sponsors we could go ahead. Let me note that when I say we, I am adhering to the practice common in the academic world, where if a professor says we did this or that, he (or she) actually means that his students and coworkers did it. This fully applies in the present case, and I would at this point like to express my gratitude to my coworkers who took care of most of the difficult and time-consuming tasks and chores necessarily involved in organizing a conference.

At this point, we would like to express our gratitude to a number of our colleagues and friends invited as participants or speakers at the conference, who have, in view of the very tight financial situation, agreed to come on their own money, without any support from the conference organizers. I am also very pleased to acknowledge the help of the two organizers of the previous conferences of this series, who provided me with the lists and addresses of former participants, agreed to participate in the CC 2002 conference, and were always generous with their help and advice. Finally, our sincere thanks go also to the members of the organizing committee and the international advisory committee for their assistance, advice, and countless helpful suggestions.

The Conference was held in the Kardinal-Döpfner-Haus in Freising. Several of my colleagues have asked me, why on Earth did we organize it in some small dump they had never heard of, rather than in Munich. Actually, if one looks back into history, one can easily find a time when there was no Munich at all, while Freising already existed as a prosperous bishop's seat and an important commercial crossroads. The Marienkirche church adjoining the conference site and located on a hill called Domberg, and another church, Stephanskirche on the nearby Weihenstephaner hill, had both been built already by the beginning of the 8th Century. Freising at that time also boasted the only bridge over the river Isar in this area, and was an important crossroads long before Munich was ever first mentioned or appears on any map.

Only several hundred years later, an insignificant Benedictine monastery was built some twenty miles south of Freising. The monks living there and the Duke of Bavaria viewed with some displeasure the generous income which Freising and its bishop collected from the numerous business travelers moving along the important east–west salt road and crossing the bridge in Freising. In 1158, the monks and the Duke, who was perhaps appropriately called Henry the Lion, decided on a three-step plan to remedy this situation. First they constructed their own bridge near their monastery. Then they burned down the bridge in Freising. In the third, and perhaps most important step, they had the whole procedure sanctioned by the Emperor, Henry Barbarossa, and in fact the day this happened, June 14, 1158, is considered the date of the founding of Munich. Considering the methods employed in founding the place, one might even come to the conclusion that holding the Cryocrystal meeting in Freising rather than Munich was the wiser choice.

In addition to now being distinguished for hosting this conference dealing with low-temperature solids, Freising is also well known in the area of liquids. Besides its long history and ancient churches, Freising also boasts presumably the oldest continuously operating brewery, the Weihenstephaner Kloster Brauerai, which got its license to brew beer in 1040, long before Munich came into existence. Initially, the brewery belonged to the monastery, but since beer in Bavaria is a rather precious commodity, the worldly authorities did not particularly like seeing all the profits go to the Church and its monks. In the 19th Century the brewery was therefore ''secularized,'' as a sign at its entrance proudly states, and is now operated by the state for the enjoyment of

all, as many participants of the conference who visited the adjoining Biergarten may have experienced themselves.

However, the major reason for organizing the conference obviously was science, rather than just enjoyment of the relaxed Bavarian lifestyle, and this is the topic to which we would now briefly like to turn.

In all more than one hundred scientists from at least sixteen different countries took part in the conference, presenting more than thirty oral presentations as well as numerous posters in the evening poster sessions.

True to the original goals of the conferences, nearly half of the participants came from countries of the former Soviet Union and Eastern Europe, with young scientists and graduate students being strongly represented.

In view of these goals, the decision was also made to publish the proceedings of CC 2002 in *Fizika Nizkikh Temperatur* (*Low Temperature Physics*), a journal based in Kharkov, Ukraine, rather than in a Western commercial journal as had been done for the previous conferences of the series.

In spite of the name, which would suggest a relatively narrow, tightly focused conference, its topical coverage, as in the previous conferences of the series, was relatively broad. Strongly represented again were studies of spectroscopy and dynamics of cryocrystals and low-temperature matrices. As in the previous conferences, a number of talks also dealt with the interesting topic of the spectroscopy and behavior of condensed systems at ultrahigh pressures. Also strongly represented were presentations dealing with quantum solids, condensed systems in which the amplitudes of the zero-point motions are not negligible compared with the interatomic distances and quantum effects become increasingly important; in particular, the isotopes of hydrogen and helium fall into this category. Besides three-dimensional solids, a session was included dealing mainly with surfaces, monolayers, and two-dimensional systems. One session dealt with the thermodynamics of low-temperature systems, and new to this conference were presentations dealing with fast dynamics on the femtosecond time scale, as well as several studies of biological systems at low temperature, including, among other topics, relaxation of proteins at ultralow temperatures.

Obviously, the most important ingredient of any conference is its participants, and the main factor deciding the success of a conference is the quality of the science presented there. I personally found most of the presentations at the conference excellent, and in my opinion the CC 2002 was from that point of view a resounding success. We are therefore deeply indebted to all of the participants, whether authors of oral presentations, session chairmen, contributors to the poster sessions, or just those taking part in the ample discussions. We sincerely hope that everyone had an enjoyable time in Freising and are looking forward to seeing you all at the next conference, presumably in the year 2004.

Vladimir E. Bondybey
Elena V. Savchenko

HIGH-PRESSURE STUDIES

Ortho-para conversion in the solid hydrogens at high pressures

M. A. Strzhemechny*

B. Verkin Institute for Low Temperature Physics and Engineering of the National Academy of Sciences of Ukraine, 47 Lenin Ave., Kharkov 61103, Ukraine; Geophysical Laboratory and Center for High-Pressure Research, Carnegie Institution of Washington, 5251 Broad Branch Road NW, Washington DC 20015, USA

R. J. Hemley

Geophysical Laboratory and Center for High-Pressure Research, Carnegie Institution of Washington, 5251 Broad Branch Road NW, Washington DC 20015, USA

Fiz. Nizk. Temp. **29**, 941–946 (September–October 2003)

At low pressures the ortho-para conversion in H_2 and D_2 is a slow process governed by the magnetic dipole interaction of the nuclear magnetic moments, phonons being the main energy sink. As the pressure is raised to a few GPa and the Debye temperature increases substantially, the conversion energy finds itself in an area where phonon states are depleted and conversion slows down. The recent Raman and NMR experiments showed that the conversion rate in H_2, after an initial slowdown predicted by theory, increases immensely. As to solid D_2, the conversion rates have apparently not yet been directly measured under pressure. In order to explain the anomaly observed in H_2, we have suggested a new conversion mechanism, in which the basic conversion-producing interaction only initiates conversion, whereas the energy is removed by rotational excitations via the stronger electric quadrupole–quadrupole interaction. Estimated conversion rates are in good qualitative agreement with available experimental observations. Here we extend the theory to solid D_2, taking into account the differences between H_2 and D_2 in the molecular and solid-state parameters. The new libron-mediated channel is predicted to result in conversion rates for D_2 under pressure that are an order of magnitude larger than at $P=0$. © *2003 American Institute of Physics.* [DOI: 10.1063/1.1614172]

1. INTRODUCTION

The requirements of quantum mechanics for a homonuclear hydrogen species (H_2, D_2, T_2) rigidly link the rotational momentum J and the total nuclear spin I of the molecule.[1,3–9] The states with even I values have even J values and vice versa. The states with the parity of the largest possible I value are called ortho while the states with the other parity are para. Thus in H_2 the states with $I=1$ (and, hence, odd J) are para; in D_2 the states with $I=2$ (and, hence, with $I=0$ too and with even J) are ortho, while those with $I=1$ (and odd J) are para. Since the energy difference between the $J=1$ and $J=0$ rotational levels is about 170 K for H_2 and 85 K for D_2, only these two states are actually occupied in the solid phase at low temperatures. Transitions between states of different parity (J or I), termed ortho-para conversion, are strictly forbidden in a single molecule. The presence of magnetic fields produced by other molecules results in observable conversion rates. At low pressures and low temperatures the conversion process has a low probability, especially in solid deuterium (for conversion rates in H_2 and D_2 at ambient pressure see Ref. 2). The main conversion-promoting mechanism both in H_2 and D_2 is the magnetic dipole interaction $\mathcal{H}_{ss}$ between nonzero nuclear spins of two $J=1$ molecules, one of which goes from the $J=1$ to the $J=0$ state, dissipating the energy into one or two phonons.

With the advent of the modern diamond anvil cell techniques, pressure has become an instrument that is able to drastically change the interplay between different energies in many physical phenomena, one of which is conversion in the hydrogens. The conversion rate in solid H_2 increases slightly with pressure, reaches a maximum, then goes down (as predicted by the low-pressure conversion theory[3,4]). But as the pressure is raised above ≈ 2.5 GPa the conversion rate unexpectedly curves upward (see Fig. 1), reaching values a few orders of magnitude higher than those observed at moderate pressures (see the detailed discussion and relevant references in Ref. 5). This conversion enhancement in pressurized H_2 was first studied in sufficient detail by Raman scattering[6] and then by NMR;[7] indirectly it has been corroborated by Raman scattering in the $Ar(H_2)_2$ stoichiometric compound.[8]

Three factors control the conversion process. The first is the interaction that initiates a conversion event. The second is the agent that carries away the conversion energy E_c released during this event. The third is the pathway by which the energy goes from the kinetic rotational form to that determined by the energy sink excitations.

The shape of the density of phonon states does not suffer crucial changes[9] under pressure; the width of the phonon energy distribution expands very fast with compression; the energy E_c (to be dissipated into phonons) decreases with compression. Due to the combination of these facts, even at

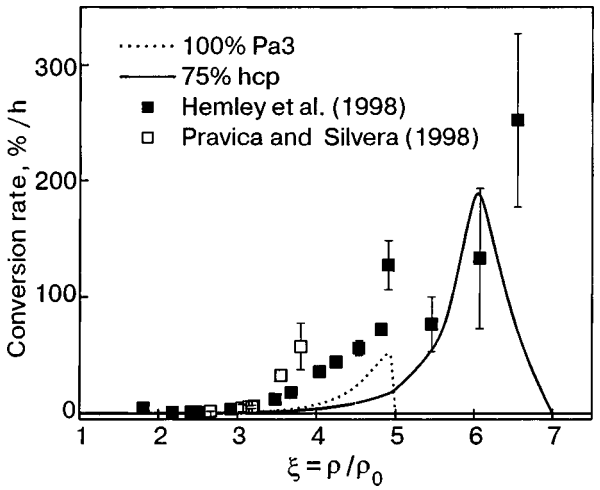

FIG. 1. Measured conversion rates in H_2 versus density. The points are from Refs. 6 (■) and 7 (□). Rate data for low and moderate pressures are not shown. The curves are semi-quantitative evaluations[10] for 100% and 75% ortho fractions.

relatively moderate pressures the value of E_c finds itself in an energy domain where the density of phonon states is extremely low, rendering the conversion less and less probable. Therefore, all else equal, phonons cannot be the agent for efficient removal of the conversion energy at high pressures. It is clear that one has to look for some other type(s) of excitation. The most obvious candidate is rotational excitations. Quite simple considerations[10] show that pressure-related changes in the rotational spectrum of mixed ortho-para H_2 crystals open up the possibility of dissipating the conversion energy into the rotational energy bath. Below we discuss the new conversion mechanism in some detail.

At low pressures, the conversion mechanisms in solid D_2 are known.[11] The ambient-condition conversion rates are known to high accuracy at low temperatures in the solid (cf. Ref. 2) and the calculated conversion constants[11,12] are in good agreement with experiment. Although a certain conversion enhancement in pressurized D_2 was reported by Cui *et al.*,[13] apparently no systematic conversion rate measurements have been made in D_2 at elevated pressures.

The authors know only of one Raman scattering measurement that can give an estimate of the conversion rate K in solid D_2 at a pressure of 17 GPa.[14] The corresponding evaluation, using the known relationship[15] modified for D_2, and assuming an exponential variation of the $J=1$ fraction in time (see subsequent Sections), gives $K \approx 8\times10^{-3}$ h^{-1}, which is substantially faster than at zero pressure ($K=5.6\times10^{-4}$ h^{-1}).[16] The main aim of this work is to show that considerations similar to those for dense H_2 are applicable for the conversion in D_2 at high pressures and that a conversion acceleration should be expected at sufficiently high pressures. The theoretical predictions for conversion rates in solid D_2 at high pressures should stimulate further experimental study.

In the next Section we analyze the deuterium molecular parameters and the interactions relevant to the issue of conversion in solid D_2 at high densities (comparing them with those in solid H_2) with an eye toward ascertaining the most efficient mechanisms operative at high pressures. We then present (Sec. 3) the current understanding of the reasons behind the pressure-related conversion acceleration in H_2. Section 4 deals with a qualitative evaluation of the conversion rates in solid D_2 at high pressures for a few of the most promising mechanisms.

TABLE I. The molecular and nuclear parameters of the deuterium and hydrogen molecules; $\mu_n = 5.05038(36)\times10^{-24}$ erg/G is the nuclear magneton; the Q unit for quadrupole moment times electron charge is 1.3449×10^{-26} c.g.s. e.s.u.

Property (units)	D_2	H_2
μ (in μ_n)	0.8574073 [17]	2.79245(2) [18]
μ_{rot}/J (in μ_n)	0.44288(52) [19]	0.88291(7)* [20]
Q_N (10^{-27}cm^{-2})	2.738(16) [22]	–
Q (Q units)	0.48529 [23]	0.47702 [23]
$E(J=1)$ (cm^{-1})	59.7804 [24]	118.495 [25]
$E(J=2)$ (cm^{-1})	179.065 [24]	354.39 [25]

*Consistency of the relationship $\mu_{rot}(J=2)\approx2\mu_{rot}(J=1)$ was shown by Ramsey.[21]

2. MOLECULAR PARAMETERS AND INTERACTIONS

In Table I we compile the values of the quantities that are relevant to the conversion in H_2 and D_2.

There are three basic interactions that can change the parity of the total nuclear spin of a D_2 or H_2 molecule that is to undergo conversion:[11]

(A) Interaction of the magnetic nuclear moment of the chosen molecule with the nonzero nuclear spin of a neighbor molecule.

(B) Interaction of the same chosen nuclear magnetic moment with the effective magnetic moment of the $J=1$ state of a proper neighbor.

(C) Interaction of the nuclear electrical quadrupole moment of the chosen molecule (nonzero for $I\geqslant1$) with the electric field gradient due to the quadrupole moment of the $J=1$ rotational state of a proper neighbor.

Interaction (A) is operative not only when the conversion-promoting neighbor has $I=1$, i.e., is in the $J=1$ state (case A1) but also when $I=2$, i.e., when the promoter is in a state with $J=0$ (case A2). The former interaction (A1) is a direct analog of the corresponding interaction in H_2, whereas the latter (A2) is inherent only in D_2. Both terms can be written in the same form:

$$\mathcal{H}_{ss} = -4\sqrt{6}\mu^2 \sum_{\sigma,\sigma'=\pm1} (\{\mathbf{S}_\sigma \otimes \mathbf{S}_{\sigma'}\}_2 \cdot \mathbf{C}_2(\mathbf{n}_{\sigma\sigma'}))R^{-3}_{\sigma\sigma'}. \tag{1}$$

Here μ the nuclear magnetic moment of the deuteron (proton); $\mathbf{R}_{\sigma\sigma'} = \mathbf{R}_0 + (d/2)(\mathbf{w}'\sigma' - \mathbf{w}\sigma) = R_{\sigma\sigma'}\mathbf{n}_{\sigma\sigma'}$; $\mathbf{R}_0$ is the radius vector between the two molecular centers; σ and σ' refer to the respective deuterons (protons) in the primed and unprimed molecules, respectively; $\mathbf{S}_\sigma$ is the nuclear spin operator of deuteron (proton) σ; d is the interatomic distance in the molecule; $\mathbf{w}$ and $\mathbf{w}'$ are the unit vectors along the respective molecular axes; $\{\mathbf{A}\otimes\mathbf{B}\}_N$ and $(\mathbf{A}_N\cdot\mathbf{B}_M)$ denote,

respectively, the direct and scalar products[26] of two irreducible tensors (in the latter case, of the same rank).

Interaction (B) is another direct analog of the respective interaction in solid H_2, with the difference that the effective value of $\mu_{\rm rot}$ in D_2 is appreciably larger than in H_2 (see Table I).

Interaction (C) can be represented by the following Hamiltonian:

$$\mathcal{H}_q = 3\sqrt{70}e^2 Q Q_N \sum_i (\{\mathbf{C}_2(\mathbf{S}_i)\otimes\mathbf{C}_2(\mathbf{w}')\}_4\cdot\mathbf{C}_4(\mathbf{n}_i))R_i^{-5}. \tag{2}$$

Here Q is the quadrupole moment of the deuterium molecule in the $J=1$ state; Q_N is the nuclear quadrupole moment of the deuteron; $\mathbf{R}_i = R_i\mathbf{n}_i$ is the distance between deuteron i in the chosen molecule and the center of the conversion-promoting para neighbor; the other notation is as in Eq. (1).

Since the orientational interactions play an important role at high pressures, the above two Hamiltonians should be complemented by the electric quadrupole–quadrupole (EQQ) interaction energy

$$\mathcal{H}_{EQQ} = \sqrt{\frac{35}{2}}(eQ)^2 \sum_{ij} (\{\mathbf{C}_2(\mathbf{w}_i)\otimes\mathbf{C}_2(\mathbf{w}_j)\}_4\cdot\mathbf{C}_4(\mathbf{n}_{ij}))R_{ij}^{-5}, \tag{3}$$

where i and j enumerate lattice sites occupied by $J=1$ molecules.

The macroscopic equations for the $J=1$ fraction x are different for the two hydrogen isotopes under consideration. In H_2, both operative conversion-promoting interactions result in a second-order reaction equation

$$\frac{dx}{dt} = Kx^2 \quad \text{for hydrogen,} \tag{4}$$

where the conversion parameter K can depend on compression and, generally, on x. At low pressures, K is virtually a constant K_0, and Eq. (4) has the solution (x_0 being the ortho fraction at $t=0$): $1/x = K_0 t$. In D_2, both $J=1$ and $J=0$ contribute to the conversion probability as promoters, so that the respective equation for the $J=1$ fraction is

$$\frac{dx}{dt} = -kx^2 - k'x(1-x) \quad \text{for deuterium.} \tag{5}$$

At zero pressure the values of k and k' are very close, so that, effectively, Eq. (5) yields an exponential-decay dependence $x(t)\propto\exp(-kt)$.

3. CONVERSION IN SOLID H_2 AT HIGH PRESSURE

We briefly summarize the main causes that lead to the dramatic acceleration of conversion in solid H_2 at high pressures. As was shown above, phonons cease to be an efficient sink of conversion energy at comparatively moderate pressures. The main idea for a consistent explanation of the pressure-related conversion enhancement was to consider orientational (rotational) degrees of freedom. There are a few problems to be solved for a successful implementation of that idea: (i) the particular conversion channel (energy path, type of conversion event, sink excitations); (ii) the shape of the rotational energy spectrum in such a highly random system as an orientationally disordered ortho-para mixture; and (iii) the compression-induced variation of the said spectrum.

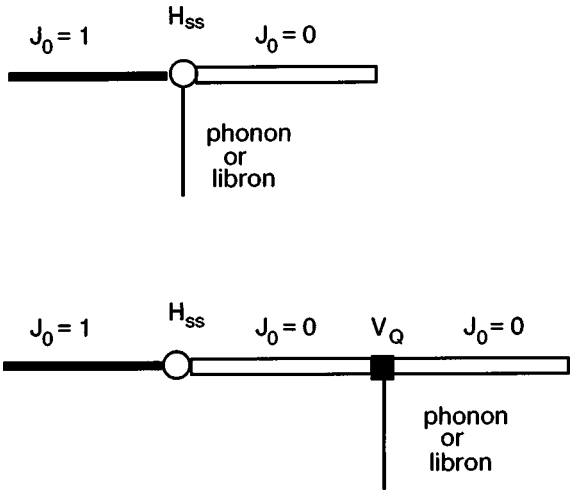

FIG. 2. Vertices for the direct (standard) pathway and a pathway with an intermediate state. For standard channels (upper diagram), $\mathcal{H}_{ss}$ starts conversion and produces sink excitations. In channels with intermediate states, $\mathcal{H}_{ss}$ only starts conversion whereas excitations are created through the stronger EQQ interaction.

The path mainly responsible for this acceleration[10] is as follows (Fig. 2). The Hamiltonian $\mathcal{H}_{ss}$ starts conversion, producing a nonequilibrium intermediate state, from which the system goes to equilibrium through the stronger EQQ interaction and emits a rotational excitation. This path becomes efficient only at a sufficiently high pressure.[5]

Proceeding from the available experimental evidence, we argue[5,27] that, given a large enough $J=1$ concentration, the rotational spectrum of a mixed crystal basically resembles that of an orientationally ordered state: a low-energy maximum containing local ground states and a maximum at higher energies that corresponds to local but collectivized excited rotational states.

Evolution of the rotational spectrum with compression is schematically represented in Fig. 3. Because of the normalization employed the plot is valid both for H_2 or D_2. Though being directly applicable to a 100% $J=1$ orientationally ordered solid, the reasoning of the preceding paragraph makes the plot qualitatively valid for sufficiently high $J=1$ concentrations even in the disordered state. A very important feature is the pressure-related decrease in the conversion energy due to the growing strength of the negative molecular-field offset.

Calculation of the conversion rate at high pressure in analytical form is impossible; using semi-quantitative evaluations,[10] we obtained results (the curves in Fig. 1) that are consistent with the experimental findings. It was later shown[5] that other channels, though bringing about considerable changes (mostly at moderate pressures), do not contribute appreciably to the pressure-related conversion enhancement. The new theory predicts a few effects, some of which find confirmation in the available experimental results. Un-

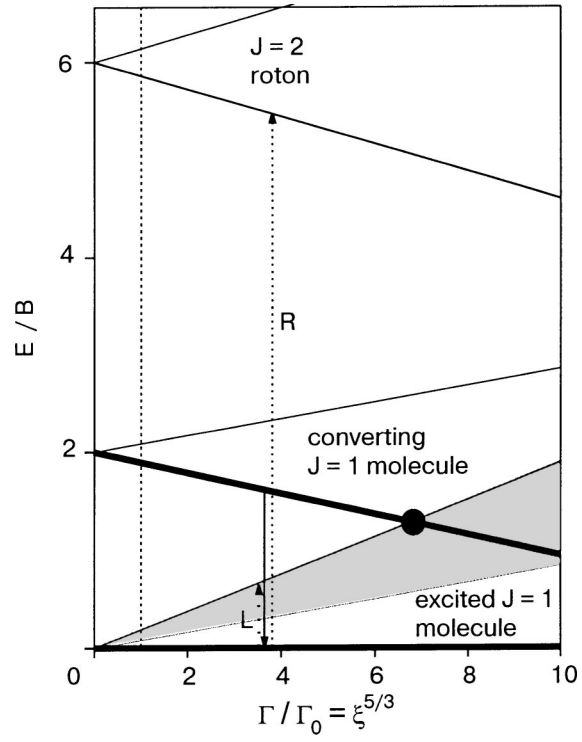

FIG. 3. Energy scheme (applicable both for H_2 and D_2) for conversion transitions involving $J=1$ and $J=2$ excitations with varying EQQ interaction. The $J=2$ roton (arrow R) is too energetic to take up the conversion energy. The energy floor is the state in which the chosen molecule has converted and all other $J=1$ molecules are in their local rotational ground states. During conversion the chosen molecule starts from a state with the energy to be released (solid down-pointing arrow). Another ortho molecule can now be excited to the libron band (shaded region) to take up the energy (shown as a broken up-pointing arrow L). At a critical Γ value (large circle) the energy span of the excited molecule is wide enough to accommodate the entire conversion energy.

like at low pressures, the conversion rate K should be a strong function of the running $J=1$ fraction x. Analysis of the x versus time curves[5,6] for sufficiently high pressures shows (Fig. 4) that, indeed, the conversion rate decreases considerably in time (or with decreasing $J=1$ fraction).

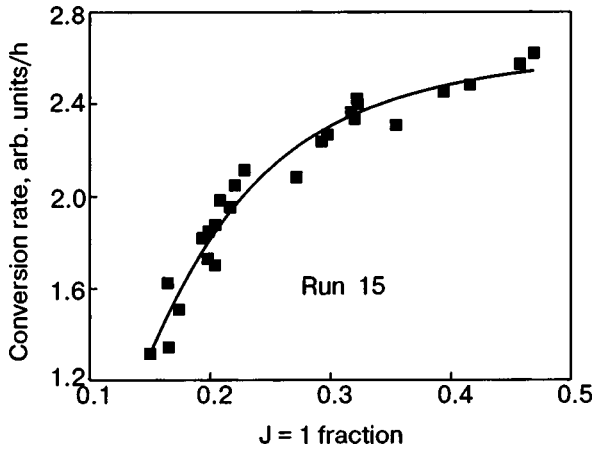

FIG. 4. The conversion rate K in H_2 as a function of the running $J=1$ fraction for a pressure of 47.7 GPa, as reconstructed from Raman scattering measurements.[6] The drop in K is more than twofold.

4. CONVERSION IN SOLID D_2 AT HIGH PRESSURE

Turning now to the efficiency of various conversion channels in solid deuterium at high pressures, we can make use of some of the formulas derived for the case of H_2 (Ref. 5) by allowing for the differences in the molecular parameters. All of the standard channels (i.e., those without an intermediate state) are phonon-assisted and are therefore inefficient at high pressures.

The idea of the intermediate state with subsequent participation of the EQQ interaction is productive for D_2 as well. Without going into detailed calculations for channels with intermediate state, which will be published elsewhere, we give a quantitative description of what can be expected for conversion rates in compressed D_2. Interaction A1 (cf. Sec. 2) will yield the same result as for H_2 but only for the conversion parameter k in Eq. (5), viz. (cf. Ref. 10),

$$k_{A1} \propto \frac{\xi^{13/3}}{[E_c(\xi)]^2} g_0(\varepsilon). \tag{6}$$

Here $\xi=\rho/\rho_0$ is the crystal density ratio reduced to the $P=0$ value; E_c is the conversion energy as a function of ξ (see Fig. 3), and $g_0(\varepsilon)$ is the density of rotational (libronlike) states. The contribution of interaction A2 to the conversion parameter k' is similar in analytical form to Eq. (6). Interaction B gives a contribution to k of the same form as in Eq. (6). Finally, interaction C also contributes to k but, originating from the energy with a different dependence on the separation R [compare Eqs. (1) and (2)], has a different form as a function of compression ξ:

$$k_C \propto \frac{\xi^{19/3}}{[E_c(\xi)]^2} g_0(\varepsilon). \tag{7}$$

As was mentioned above, at zero pressure the constants k and k' are virtually the same, that is, $k_{A1}+k_B+k_C \approx k'_{A2}$. As the pressure is increased to the level at which the channels with intermediate state become efficient, this match will be lifted and the time dependence of the $J=1$ concentration will cease to be exponential.

As was explained above, Fig. 3 is plotted in reduced variables such that it is valid both for H_2 and D_2. However, when replotted in absolute values ($J=1$ energies, pressures, compressions) it will look different for the two isotopes. It should also be noted that Fig. 3 is rigorously applicable only for pure $J=1$ solids; lower values of x necessitate recalculation, for example, of the position of the critical point (the solid circle in Fig. 3) at which rotational excitations come into play. The quantities we need for rescaling to absolute values are the volume dependence of the Debye frequency[28] and the equation of state (EOS). Fortunately, at high pressures the equations of state for H_2 and D_2 are almost the same;[29] the differences are appreciable only at rather low pressures. The corresponding estimations give the following critical pressure values. For pure para ($J=1$) deuterium the indirect channel will become efficient at a pressure of 1.5 GPa and cease to operate around 4.8 GPa; for normal (33% para) deuterium these two pressure values are 14 GPa and 32 GPa. We note that the working range for normal D_2 extends

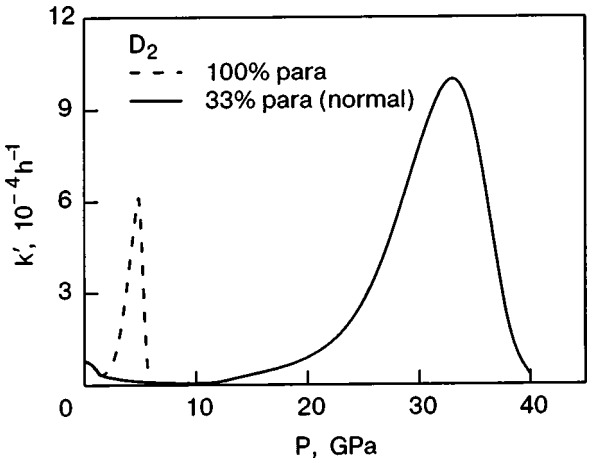

FIG. 5. The conversion parameter k' in D_2 as a function of pressure, as predicted in this report.

beyond the critical pressure (28 GPa)[30] at which D_2 transforms to the broken-symmetry phase (BSP). This means that at these pressures the amount of the admixed $J=2$ state should be appreciable. As can be seen from Table I, the effective magnetic moment of this state is large enough to change noticeably the strength of the total conversion-initiating interaction. This problem requires a special consideration, preferably with the structure of the BSP known.

Since the zero-pressure conversion energy is less than the deuterium Debye temperature, the principal conversion mechanism at $P=0$ is a one-phonon mechanism (unlike in H_2). Therefore, the phonon-mediated conversion rate as a function of pressure will have no distinct maximum at low pressures but will start to decrease on initial compression, and at a comparatively low pressure (if the para fraction is high) will start building up but to lower final values as compared to H_2. A schematic representation of this dependence is shown in Fig. 5.

This work was supported by the CRDF (Grant UP2-2445-KH-02) and NSF/DMR. The authors thank A. F. Goncharov for providing his unpublished results. M.A.S. also thanks Irina Legchenkova for technical assistance.

*E-mail: strzhemechny@ilt.kharkov.ua

[1] J. Van Kranendonk, *Solid Hydrogen*, Plenum, New York (1983).
[2] V. G. Manzhelii and M. A. Strzhemechny, ''Quantum molecular crystals,'' in *Physics of Cryocrystals*, V. G. Manzhelii, Yu. A. Freiman, M. L. Klein, and A. A. Maradudin (eds.), AIP Publishers, Woodbury, NY (1997).
[3] K. Motizuki and T. Nagamiya, J. Phys. Soc. Jpn. **11**, 93 (1956).
[4] A. J. Berlinsky and W. N. Hardy, Phys. Rev. B **8**, 5013 (1973).
[5] M. A. Strzhemechny, R. J. Hemley, H. K. Mao, A. F. Goncharov, and J. H. Eggert, Phys. Rev. B **66**, 014103 (2002).
[6] R. J. Hemley, A. F. Goncharov, H. K. Mao, E. Karmon, and J. H. Eggert, J. Low Temp. Phys. **110**, 75 (1998).
[7] M. G. Pravica and I. F. Silvera, Phys. Rev. Lett. **81**, 4180 (1998).
[8] F. Grazzi and L. Ulivi, Europhys. Lett. **52**, 564 (2000).
[9] S. B. Feodosyev, I. A. Gospodarev, M. A. Strzhemechny, and R. J. Hemley, Physica B **300**, 186 (2001).
[10] M. A. Strzhemechny and R. J. Hemley, Phys. Rev. Lett. **85**, 5595 (2000).
[11] K. Motizuki, J. Phys. Soc. Jpn. **12**, 163 (1957).
[12] M. A. Strzhemechny and O. I. Tokar, Fiz. Nizk. Temp. **11**, 813 (1985) [Sov. J. Low Temp. Phys. **11**, 446 (1985)].
[13] L. Cui, N. H. Chen, and I. F. Silvera, Phys. Rev. B **51**, 14987 (1995).
[14] A. F. Goncharov, private communication.
[15] I. F. Silvera, Rev. Mod. Phys. **52**, 393 (1980).
[16] Yu. Ya. Milenko and R. M. Sibileva, Fiz. Nizk. Temp. **1**, 796 (1975) [Sov. J. Low Temp. Phys. **1**, 382 (1975)].
[17] N. F. Ramsey, *Molecular Beams*, Clarendon Press, Oxford (1956).
[18] F. Bloch and C. D. Jeffries, Phys. Rev. **80**, 305 (1950).
[19] G. G. Barnes, P. J. Bray, and N. F. Ramsey, Phys. Rev. **94**, 893 (1954).
[20] N. J. Harrick and N. F. Ramsey, Phys. Rev. **88**, 228 (1952).
[21] N. F. Ramsey, Phys. Rev. **58**, 226 (1940).
[22] H. G. Kolsky, T. E. Phipps, N. F. Ramsey, and H. B. Silsbee, Phys. Rev. **87**, 395 (1952).
[23] G. Karl and J. D. Poll, J. Chem. Phys. **46**, 2944 (1967).
[24] A. R. W. McKellar and T. Oka, Can. J. Phys. **56**, 1315 (1978).
[25] A. P. Stoicheff, Can. J. Phys. **35**, 730 (1957).
[26] D. A. Varshalovitch, A. N. Moskalev, and V. K. Khersonskii, *Theory of Angular Momentum*, World Scientific, Singapore (1988).
[27] M. A. Strzhemechny, in *Proceedings of the NATO Advanced Research Workshop, Frontiers of High Pressure Research II: Application of High Pressure to Low-Dimensional Novel Electronic Materials, Pingree Park, Colorado, USA, June 10–15, 2001*, edited by H. D. Hochheimer, B. Kuchta, P. K. Dorhout, and J. L. Yarger, Vol. 48 of NATO Series II, Kluwer Academic (2001), p. 235.
[28] R. J. Hemley, J. H. Eggert, and H. K. Mao, Phys. Rev. B **48**, 5779 (1993).
[29] P. Loubeyre, R. LeToullec, D. Hausermann, M. Hanfland, R. J. Hemley, H. K. Mao, and L. W. Finger, Nature (London) **383**, 702 (1996).
[30] I. F. Silvera and R. J. Wijngaarden, Phys. Rev. Lett. **47**, 39 (1981).

This article was published in English in the original Russian journal. Reproduced here with stylistic changes by AIP.

Structures and optical properties of solid hydrogen at ultrahigh pressures

H. Nagara*

Division of Materials Physics, Graduate School of Engineering Science, Osaka University, Toyonaka, Osaka 560-8531, Japan
Fiz. Nizk. Temp. **29**, 947–950 (September–October 2003)

The electronic energy bands in structures whose primitive cell contains up to four molecules are studied with full optimization of the structures on the basis of GGA and LDA band calculations. Above 250 GPa, the eventual optimal structure obtained by the GGA or the LDA calculation is $Cmca$, which is a layered structure with the molecular bonds lying in planes and which has a metallic band structure with no band gaps. The metallic property of the band structure remains unchanged even if the molecular bonds in the plane of the $Cmca$ are inclined so that the atoms in the molecule lie out of the plane. The electronic bands of the $Cmca$ structure and those of some other candidate structures are discussed in the light of recent experimental results. Effects of the occupation of electronic states on the predicted optimal structures are also studied. © *2003 American Institute of Physics.*
[DOI: 10.1063/1.1614173]

1. INTRODUCTION

Recent experimental studies of compressed hydrogen have revealed nonmetallic behavior at pressures higher than $\sim$300 GPa.[1,2] They report the possibility of metallization by the closure of the direct electronic band gaps at even higher pressures. The result contradicts many theoretical studies based on first-principles band calculations, which predict the closure of indirect band gaps at lower pressures in energetically favorable structures,[3–5] and call into question the ability of band calculations to predict the structures of compressed hydrogen.

In spite of the well-known shortcoming of the band calculation based on the local density approximation (LDA) or its modification with the gradient correction (GGA), that is, underestimation of the electronic band gaps, recent first-principles band calculations have achieved much success in predicting the structures and properties of solids at ambient as well as at high pressures. In the study of compressed hydrogen it is not yet clear whether this shortcoming might hamper the prediction of the structures and mislead one into false structures, since there is a lack of experimental data available on the structure above 100 GPa.

In order to check this point at some levels, we have carried out some preliminary calculations and re-examined the structures which have been predicted to be most probable at high pressures, paying attention to the occupation of the electronic bands by the electrons. We perform full optimization of the structures above 250 GPa in the GGA and the LDA and study the changes of the electronic bands for structures which appear in the course of the optimization. We compare the results with a new type of calculation[6] which is expected to overcome the shortcoming and discuss the band structures in the light of very recent optical measurements.[1]

2. NEW RESTRICTIONS IMPOSED ON THE STRUCTURES

The results of the optical experiment[1] impose new restrictions on the structures from 150 GPa to at least 320 GPa. The first important point to be mentioned is that the softening of the vibron frequency seems to occur continuously with increasing pressure. No jump of the frequency nor change of the slope has been observed, which means no drastic changes of the structure. If the structure changes at all, it should be accompanied by a very small change of the vibron frequency. The second point is that the experiment reveals the features characteristic of a direct band gap, which means the top of the valence band and the bottom of the conduction band are located at the same place in the Brillouin zone.

Earlier experimental papers have reported the vibron frequencies and optical properties at pressures over 250 GPa and have presented estimates of the pressure of direct-gap closure based on the optical data.[7,8] The recent optical measurements show the pressures and the character of the optical absorption more clearly. These new results impose important restrictions on the structures of solid hydrogen above the well-known 150 GPa transition. Bearing these points in mind, we examine again some of the structures which have been studied theoretically so far.

3. CALCULATIONS AND RESULTS

The structures which can be transformed continuously among them are the $Pca2_1$, $Cmc2_1$, $Cmca$, and $Pbca$ family, which is shown in Fig. 1. Starting from one of these structures, the others are obtained by a continuous change of the molecular centers and the molecular orientation.

At pressures lower than 200 GPa, the candidates for the most probable structure are $Cmc2_1$ and $Pca2_1$, with hcp molecular centers, or slight modifications of them.[3,4]

However, according to theoretical calculations[3–5] the struture becomes unstable at pressures higher than about 200 GPa. Those calculations were done using methods based on the LDA or the GGA, which have the shortcoming of underestimating the band gaps, resulting in the closure of indirect band gaps at around 200 GPa. Optimization of the structure is a delicate problem, and the shortcoming might mislead us into false optimal structures because of the false occupation of the states by the electrons whose energy is in the vicinity of the Fermi level. To investigate the effect of the electron

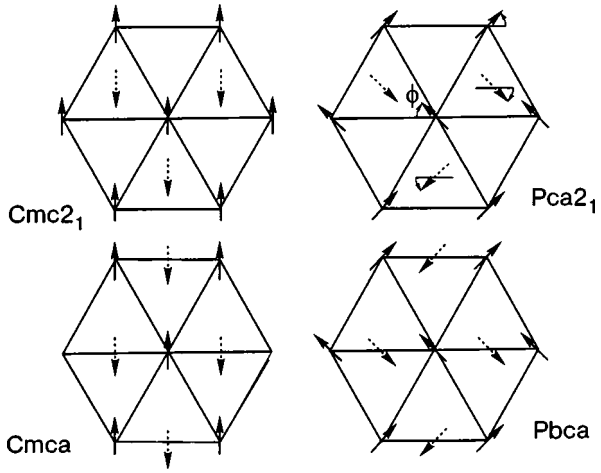

FIG. 1. The $Pca2_1$, $Cmc2_1$, $Pbca$, and $Cmca$ structures. Arrows show the directions of molecular axes whose direction cosines with the z axes are positive. These structures can be transformed into one another by a continuous change of the molecular centers and orientations.

occupation, we performed the calculations with restrictions on the electron occupation.

We carried out band calculations using the plane-wave basis functions with an energy cutoff of 40 hartree and a pseudo-potential for the ionic potential. Throughout our calculations, we used the packaged codes ABINIT[9] and PHI98PP.[10]

3.1. Preliminary calculations under restricted and unrestricted electronic occupation

To study the effect of the false occupation on the optimal structures, we performed following preliminary calculations. First we show an example in which the restricted electron occupation and the unrestricted one give different conclusions in the comparison of total energies.

We compare the energies of the $Cmc2_1$ and the $Pca2_1$ structures with molecular centers fixed at the hcp sites and with c/a fixed at the ideal hcp value (see Fig. 1). We used a unit cell containing 4 molecules for both structures. In the first calculation, we performed the usual calculations in which the electrons occupy the states with energies lower than the Fermi energy. And in the second one, we restricted the occupation of the electronic states to the lowest 4 branches at each **k** point, which simulates the insulator type of the electronic occupation of the bands. Up to $r_s=1.25$, which corresponds to a pressure around 430 GPa, the lowest 4 branches of the electronic energy states in the $Cmc2_1$ and $Pca2_1$ structures seem to be well separated from the 5th branch. Here r_s is the density parameter, which is defined as the radius, in units of the Bohr radius, of a sphere whose volume is equal to the volume per electron.

Comparing the energies of these two structures, we find that $Cmc2_1$ is of lower energy than $Pca2_1$ in the case of the first calculation. On the other hand, in the case of the second calculation, $Pca2_1$ becomes lower.

3.2. Full optimization of the structures

Above example shows the possibility that the false occupation of the electronic states might affect the optimal structures at each pressure. The change of the occupation occurs when the indirect band gaps disappear. Starting from some arrangements of the atomic positions, we then performed full optimization of the structures. As a starting arrangement we take the $Pca2_1$ structure with an orthorhombic unit cell containing 4 molecules. We set the molecular centers at ideal hcp lattice sites and at several points between that of the ideal hcp site and the molecular center of the $Pbca$ structure (see Fig. 1). The optimization was been done at constant volumes, at $r_s=1.40$, 1.35, 1.30, and 1.25, which correspond to pressures of around 200, 270, 330, and 430 GPa, respectively. The pressures are estimated from the volume dependence of the total energy obtained in our calculations. The LDA calculations show smoother convergence than the GGA ones, which include a calculation of the density gradient. In the optimization of the structures, some runs did not converge to any meaningful structures. This is probably due to some problems in the optimization codes.

All of the structures to which the calculations converged and which were obtained as optimal ones in our runs are of the $Cmca$ type for $r_s \leqslant 1.35$. We note here that the compression seems to be nearly isotropic above 200 GPa ($r_s \leqslant 1.40$). Although the molecular centers move from the ideal hcp sites to that of the $Cmca$, the orthorhombic unit cell is compressed isotropically. At the highest density, $r_s=1.25$, the ratio c/a of the orthorhombic lattice decreased about 3% and b/a (the distance between layers) increased about 3%, with the molecular bonds tilted about 76° from the z axes and with a bond length of $1.41a_0$. They did not show any molecular dissociation at the densities studied. These results are same as those obtained from the usual calculations with no restriction of the band occupation for both the GGA and LDA.

4. CHANGES OF THE ELECTRONIC BAND STRUCTURE

We study then the changes in the electronic band structures for those structures studied in the optimization process. The $Cmc2_1$ structure is also a layered structure with molecular bonds lying in the planes. The $Cmc2_1$ space group holds for any position of the molecular center between the hcp site and the molecular center of the $Cmca$ structure. When the molecular bond is inclined in a certain way in the $Cmc2_1$ structure and two atoms of the molecule lie off the plane, the structure becomes $Pca2_1$. For the extreme case of the $Pca2_1$ structure in which the molecular center is moved to that of the $Cmca$ structure, the space group becomes $Pbca$.

To compare the band structures we take a nonprimitive unit cell containing 4 molecules for all structures studied. All of the structures except for the $Cmca$ have a band structure in which the lowest 4 branches are well separated from higher ones up to the highest densities, $r_s=1.25$. The indirect band gaps, however, close at much lower densities. The gaps becomes wider when the molecules in the $Cmc2_1$ are tilted toward the $Pca2_1$ structure.

For $Cmca$ the band structure is completely different from the others, having no band gaps. The lowest 4 branch touches the higher ones at some points on the Σ, Δ, and c lines. The nature of the touching is line-type.[3] Figure 2 shows the band structure for $Cmca$ with the nonprimitive unit cell. Even when the molecular bonds are tilted towards the $Pbca$ structure, the metallic band character still remains

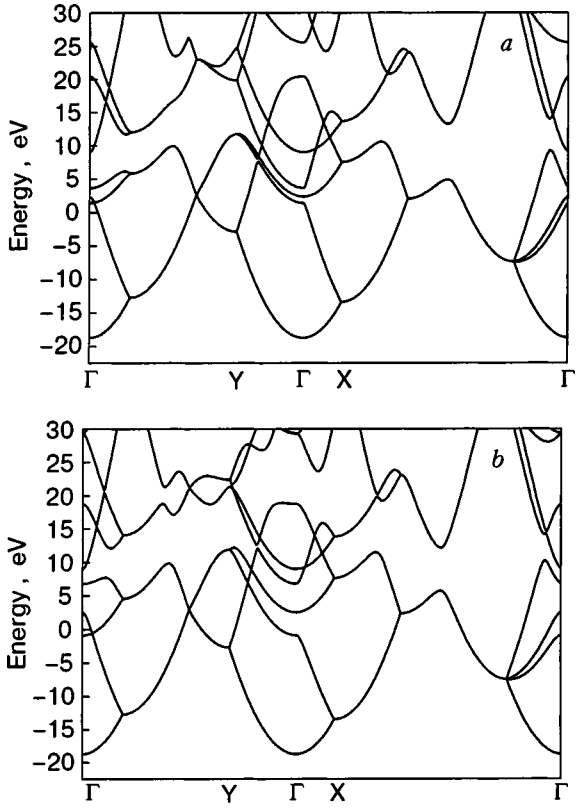

FIG. 2. The electronic band structures for the $Cmca$ (a) and the $Pbca$ (b) structures at $r_s=1.25$. To compare the changes in the energy bands, we used a nonprimitive unit cell containing 4 molecules for the $Cmca$ structure, whose primitive cell contains 2 molecules.

unchanged, although changes of the distances between the branches are observed at several points in the Brillouin zone. In Fig. 2 we compare the band structure of the $Cmca$ structure with that of the $Pbca$ at $r_s=1.25$.

It should be noted that the touching of the branches is due to the symmetry properties of the structure, independent of the approximation (GGA or LDA) used in the calculations. The distances between branches depend on the approximation.

5. DISCUSSION AND SUMMARY

We discuss these results in the light of the recent optical measurements. Although the $Cmca$ structure is energetically most favorable, it may be excluded because of the metallic character of the band structure. The large fluctuation of the molecular orientation remaining in the $Cmca$ structure[11] might change the electronic bands. The metallic character of the electronic bands of the $Pbca$ structure, however, may offer some negative insight into the changes of the band structure due to the fluctuation, although the movement from the $Cmca$ to the $Pbca$ is coherent. The possible fluctuation of the molecular center leaving the positions of the $Cmca$ toward those of the $Cmc2_1$, however, might lift the metallic character of the electronic bands. If the energetically favorable $Cmca$ structure is ruled out, there will remain two possibilities. One is that there are some other structures which we have overlooked in our study. An example is a structure of larger unit cell.[4] The second possibility is the case that all of the present GGA and LDA based calculations fail to predict energetically favorable structures of compressed hydrogen. In that case, the structure might remain one which is close to the $Cmc2_1$ or $Pca2_1$ structure up to at least 320 GPa. The possibility of the second case has been reported recently in a new type of calculation[6] which is designed to overcome the shortcoming of the GGA and the LDA, although the optimization of the structures has not been carried out by that type of calculations owing mainly to the demands on machine resources.

We mention here the low-lying librational and phonon modes observed in Raman experiments.[12] The $Pca2_1$ structure has 9 optical phonons and 8 librational modes which are Raman active, the $Cmc2_1$ structure has 3 optical phonons and 4 such librational modes, while the $Cmca$ structure has only 4 librational modes with no Raman active optical phonons.

Finally, we mention that the metallization, which is predicted to occur at $\sim$450 GPa by extrapolation of the absorption edge to higher pressure, might happen at some lower pressures where the metallization is due to the closure of indirect band gaps.[8]

We have studied the optimal structures and the electronic bands in those energetically favorable structures. The new results of the optical measurements have raised new problems in the theoretical study of compressed hydrogen.

This work was supported by Grant-in-Aid for COE Research (10CE2004) of the Ministry of Education, Culture, Sports, Science and Technology of Japan.

*E-mail: nagara@mp.es.osaka-u.ac.jp

[1] P. Loubeyre, F. Occelli, and R. LeToullec, Nature (London) **416**, 613 (2002).
[2] C. Narayana, H. Luo, J. Orloff, and A. L. Ruoff, Nature (London) **393**, 46 (1998).
[3] K. Nagao, T. Takezawa, and H. Nagara, Phys. Rev. B **59**, 13741 (1999).
[4] J. Kohanoff, S. Scandolo, S. Gironcoli, and E. Tosatti, Phys. Rev. Lett. **83**, 4097 (1999).
[5] K. A. Jonson and N. W. Ashkroft, Nature (London) **403**, 632 (2000).
[6] M. Stadele and R. M. Martin, Phys. Rev. Lett. **84**, 6070 (2000).
[7] H. K. Mao and R. J. Hemly, Science **244**, 1462 (1989).
[8] M. Hanfland, R. J. Hemly, and H. K. Mao, Phys. Rev. B **43**, 8767 (1991).
[9] The ABINIT code is a common project of the Université Catholique de Louvain, Corning Incorporated, and other contributors; URL http:// www.abinit.org.
[10] M. Fuchs and M. Scheffler, Comput. Phys. Commun. **119**, 67 (1999), URL http:// www.fhi-berlin.mpg.de/th/fhi98vd/fhi98PP/index. html.
[11] H. Kitamura, S. Tsuneyuki, T. Ogitsu, and T. Miyake, Nature (London) **404**, 259 (2000).
[12] A. F. Goncharov, R. J. Hemly, H. K. Mao, and J. Shu, Phys. Rev. Lett. **80**, 101 (1998).

This article was published in English in the original Russian journal. Reproduced here with stylistic changes by AIP.

Influence of vibrational anharmonicity and vacancies on the thermodynamic properties of rare gas crystals

A. I. Karasevskii*

Institute for Metal Physics of the National Academy of Science of Ukraine, 36 Vernadsky Blvd., Kiev 03142, Ukraine

W. B. Holzapfel

Department Physik, Universität Paderborn, D-33095 Paderborn, Germany
Fiz. Nizk. Temp. **29**, 951–956 (September–October 2003)

A statistical method is used to calculate thermodynamic properties of Ar, Kr and Xe (isobaric and isochoric heat capacity, bulk modulus, thermal expansion coefficient, interatomic distances, Grüneisen parameter), and good agreement with experimental values is observed. It is shown that at high temperature, slightly above the melting point of the rare gas crystals, an instability of the crystalline state occurs. As the temperature approaches this instability, the isobaric heat capacity and the thermal expansion coefficient show strong increases similar to the experimentally observed anomalies. © *2003 American Institute of Physics.*
[DOI: 10.1063/1.1614174]

1. INTRODUCTION

Many thermodynamic quantities of solids show some peculiar features at high temperature just before melting. Usually this behavior is attributed to effects from both vibrational anharmonicity and thermal defects (vacancies) occurring in an appreciable concentration in rare gas crystals (RGCs) in this temperature range.[1] A phenomenological approach taking into account anharmonic contributions to the crystal free energy[2] gives good agreement between the observed and calculated values for many thermodynamic properties of the rare gas crystals[2] and some fcc metals (Cu, Ag, Au).[3] However, the role of vacancies and the distinctive features of the anharmonic contributions to the thermodynamics of these substances are not yet well understood. These problems are not easily handled in the framework of self-consistent phonon (SCP) theory,[4–6] widely used for numerical investigation of crystal thermodynamics. In the present study we therefore evaluate the thermodynamic characteristics of both perfect RGCs and RGCs with vacancies within the framework of a statistical theory for crystals,[7] whereby a crystal is represented as an ordered ensemble of particles whose spatial distributions are described by a binary distribution function. Recently this method has been applied successfully for investigating the equations of state and thermodynamic properties of rare-gas solids under pressure.[8] In Sec. 2 the main results of this statistical theory[7] are outlined, and the internal energy, the heat capacities, the bulk modulus, the Grüneisen parameter, and the thermal expansion are calculated for perfect crystals of Ar, Kr, and Xe with contributions from anharmonicity. In Sec. 3 the vacancy contribution to the thermodynamic behavior of the RGC is added.

2. STATISTICAL THEORY OF SIMPLE PERFECT CRYSTALS

The effective nearest-neighbor interaction energy for atoms located at the sites R_i and R_j in a crystal is reasonably approximated by the Morse potential

$$u(r_{ij})=A[\exp(-2\alpha(r_{ij}-R_0))-2\exp(-\alpha(r_{ij}-R_0))], \tag{1}$$

where $r_{ij}=|\mathbf{R}_i-\mathbf{R}_j+\mathbf{q}_i-\mathbf{q}_j|$ is the distance between atoms, and A, α, and R_0 are the potential parameters. The values for these parameters listed in Table I were determined previously[7] in such a way that the internal energy, the lattice parameter, and the bulk modulus of the RGS at zero temperature and zero pressure fitted the observed values within the framework of the statistical model.[7] The determination of the total free energy of the crystals starts from the Gibbs–Bogoliubov functional, which in the present case includes a term for the cubic anharmonicity of the atomic vibrations, $\Delta F_3(\tau,c)$, determined in second-order perturbation theory:[9]

$$F_T=F_0+\langle U-U_0\rangle+\Delta F_3(\tau,c) \tag{2}$$

whereby

$$\frac{F_0}{NA}=\tau\sum_j\int\ln\left[2\sinh\left(\frac{c\Lambda}{2\tau}\tilde{\omega}_j(\mathbf{K})\right)\right]d\mathbf{K} \tag{3}$$

and

$$\frac{U_0}{NA}=\frac{c\Lambda}{4}\sum_j\int\tilde{\omega}_j(\mathbf{K})\coth\left[\frac{c\Lambda}{2\tau}\tilde{\omega}_j(\mathbf{K})\right]d\mathbf{K} \tag{4}$$

are the free energy and the average potential energy of a harmonic crystal, respectively. The integration in (3) and (4)

TABLE I. Morse potential parameters for RGCs.[7,8]

	α, Å^{-1}	A, K	R_0, Å	Λ
Ne	2.05	52.98	3.04	0.4357
Ar	1.62	170.76	3.71	0.1360
Kr	1.52	249.08	3.97	0.0767
Xe	1.38	332.04	4.32	0.0457

runs over the unit cell volume of the reciprocal lattice, and K represents reduced components of the wave vector, varying from 0 to 1.[7]

The average potential energy of the interatomic interaction is calculated by the use of a binary distribution functions for the atomic displacements[7] and is given within the present approximation by

$$\langle u\rangle=\frac{\langle U\rangle}{AN}=\exp\left(-2b+\frac{q(\zeta)}{\gamma^*}\right)-2\exp\left(-b+\frac{q(\zeta)}{4\gamma^*}\right), \tag{5}$$

whereby

$$\gamma^*(\tau)=\frac{c}{\Lambda}\sum_j\int\tilde{\omega}_j(\mathbf{K})\tanh\left[\frac{c\Lambda}{2\tau}\tilde{\omega}_j(\mathbf{K})\right]e_{ij}(\mathbf{K})^2 d\mathbf{K} \tag{6}$$

is a parameter representing both thermal and quantum broadening of the atomic motion around the lattice sites,

$$\zeta(\tau)=-\frac{c}{\Lambda\gamma^*}\sum_j\int\tilde{\omega}_j(\mathbf{K})\tanh\left[\frac{c\Lambda}{2\tau}\tilde{\omega}_j(\mathbf{K})\right]e_{ij}(\mathbf{K})^2 \times\cos(2\pi K_x R)d\mathbf{K}, \tag{7}$$

is a parameter taking into account correlations between displacements of neighboring atoms, and $q(\zeta)$ is a correlation factor, which represents the contribution of the interatomic correlation to the energy of the interatomic interactions. One may notice[7] that $q(\zeta)$ changes only slowly with temperature, from $q_0\approx 187$ at $T=0$ K to $q\approx 2$ at high temperature, where it coincides with the value for completely uncorrelated atomic states. The $\tilde{\omega}_j(\mathbf{K})$ are the reduced frequencies determined by the dynamical matrix of the harmonic crystal, i.e., they depend only on the lattice structure and are related to the real phonon frequency by

$$\omega_j(\mathbf{K})=c\frac{A\Lambda}{\hbar}\tilde{\omega}_j(\mathbf{K}). \tag{8}$$

In terms of these variables, the crystal free energy (2) depends only on two parameters:

I) the reduced temperature $\tau=T/A$ and

II) the de Boer parameter

$$\Lambda=\frac{\hbar\alpha}{\sqrt{MA}} \tag{9}$$

which represents the strength of quantum effects (M is the atomic mass). The normalized lattice expansion

$$b(\tau)=\alpha(R(\tau)-R_0), \tag{10}$$

depends on the parameters α and R_0 of the interatomic potential and on the temperature-dependent nearest-neighbor distance R. The dimensionless quasi-elastic bond parameter

$$c=\sqrt{\frac{\beta_1}{\alpha^2 A}}, \tag{11}$$

includes an effective force constant β_1 for nearest-neighbor atoms, and minimization of the crystal free energy (2) results in temperature-dependent equilibrium values for b and c, denoted b_0 and c_0. This variational approach is computationally simpler than the SCP approach and gives a number of results that are not easily obtained within the SCP model.

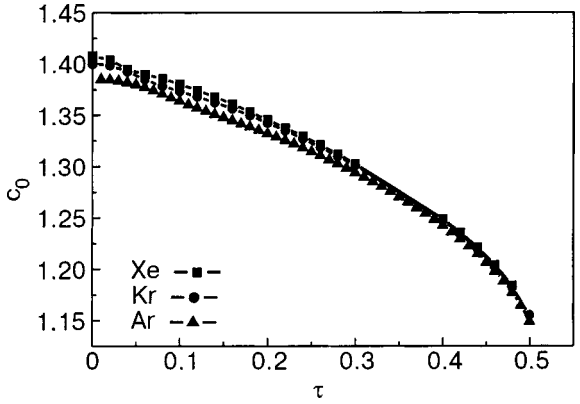

FIG. 1. Normalized temperature dependence of the quasi-elastic bond parameters of Ar, Kr and Xe at ambient pressure.

Equations (3)–(8) allow calculation of the equilibrium values for the crystal free energy (2) and for b_0 and c_0 at any temperature. Results calculated for the RGS by this procedure are illustrated in Figs. 1–6.

Figure 1 shows the effect of the reduced temperature on the quasi-elastic bond parameter c_0 for Ar, Kr, and Xe at zero pressure. The differences in c_0 for different crystals at low temperature are primarily caused by differences in the de Boer parameters for these elements. At a critical temperature τ_c close to the melting temperature, the minimum of the crystal free energy with respect to the quasi-elastic bond parameter c disappears due to an increase in the anharmonicity of the atomic vibrations. These temperatures are illustrated in the Figs. 2–6, respectively, as the upper ends of the calculated curves for the temperature dependences of the interatomic distance $R(T)$, the heat capacities C_P and C_V, the bulk modulus K_T, and the Grüneisen parameters γ_G for Ar, Kr, and Xe at zero pressure. One may notice that the temperature dependence of the effective quasi-elastic bond parameter increases rapidly as the temperature approaches the instability point τ_c. This manifests itself also in a strong nonlinear increase of C_P and of the thermal expansion coefficient α_V and the Grüneisen parameter γ_G near the melting point (Figs. 2, 4, and 6).

In the limits of low ($\tau\ll c_0\Lambda$) and high ($\tau\gg c_0\Lambda$) temperatures one can obtain simple analytical expressions for (2)–(7).[7] For a better understanding of the peculiarities in the high-temperature behavior of the RGCs and the related solid state instability, let us consider the classical limit ($\Lambda\to 0$) in the expression for the free energy (2):

$$\frac{F_T}{AN}=\frac{\tau}{3}+3\tau\log\left[\frac{c\Lambda}{\tau}\right]+6\left[\exp\left(-2b+\frac{\tau}{c^2}\right)-2\exp\left(-b+\frac{\tau}{4c^2}\right)\right]-\frac{a_3}{c^6}\left[\exp\left(-2b+\frac{\tau}{c^2}\right)-\frac{1}{4}\exp\left(-b+\frac{\tau}{4c^2}\right)\right]^2\tau^2. \tag{12}$$

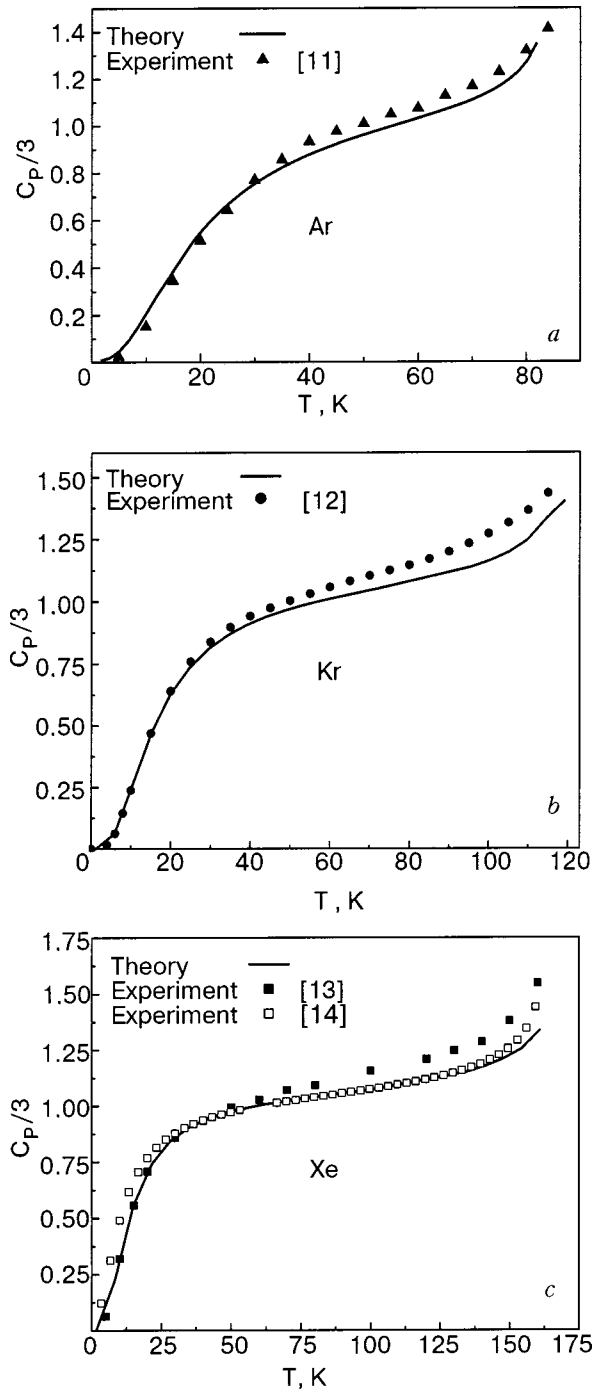

FIG. 2. Temperature dependence of the (normalized) isobaric heat capacity C_P for Ar, Kr, and Xe at ambient pressure and experimental data points from the literature.

The last term in (12) takes into account the contribution due to the cubic anharmonicity in the atomic vibrations at high temperature ($\tau \gg c_0\Lambda$), with $a_3 \approx 1.5$ for crystals with an fcc lattice.

Minimization of (12) with respect to c and b gives the equilibrium values b_0 and c_0:

$$c_0 \approx \left(1+\sqrt{1-\frac{\tau}{\tau_c}}\right)^{1/2}, \tag{13}$$

$$b_0 \approx \frac{3\tau}{4c_0^2}. \tag{14}$$

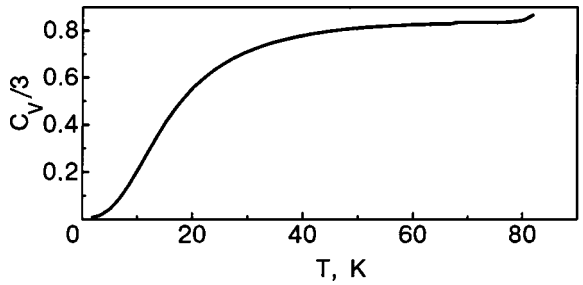

FIG. 3. Calculated (normalized) isochoric heat capacity for Ar at ambient pressure.

The value of the critical temperature τ_c is determined by cubic anharmonicity:

$$\tau_c \approx \frac{1}{(1+9a_3/16)}. \tag{15}$$

The internal energy and the isobaric heat capacity of the crystal at zero pressure and high temperature ($\tau \gg c_0\Lambda$) are given (in normalized form) by

$$E \approx -6+3\tau+\frac{3\tau^2}{4c_0^4}, \tag{16}$$

$$\frac{C_P}{3} \approx 1+\frac{\tau}{2c_0^4}+\frac{\tau^2}{4\tau_c c_0^6\sqrt{1-\tau/\tau_c}}. \tag{17}$$

For the bulk modulus K_T and the thermal volume expansion coefficient α_V at $\tau \gg c_0\Lambda$ one obtains

$$K_T \approx \frac{4\sqrt{2}}{3}\frac{A\alpha^3\exp\left(-\dfrac{\tau}{2c_0^2}\right)}{(\alpha R_0+b_0)} \times\left[1-\frac{9\exp\left(-\dfrac{\tau}{2c_0^2}\right)\tau}{2c_0^4\left[1+\dfrac{7}{2}\exp\left(-\dfrac{\tau}{2c_0^2}\right)\dfrac{\tau}{c_0^4}\right]}\right] \tag{18}$$

and

$$\alpha_V \approx \frac{9}{4c_0^2A(\alpha R_0+b_0)}\left[1+\frac{\tau}{2c_0^2\tau_c\sqrt{1-\dfrac{\tau}{\tau_c}}}\right]. \tag{19}$$

Minor contributions from terms $\approx a_3\tau^2$ are neglected in Eqs. (17)–(19), which obviously represent very well the qualitative behavior of the RGCs at high temperature. The relations (13)–(19) show that the main internal parameter governing the thermodynamic behavior of a simple crystal at high temperature is the effective quasi-elastic bond parameter $c_0(\tau)$, which depends parametrically on the reduced critical temperature τ_c also. From the linear relation between the sound velocities u_{jk} and the quasi-elastic bond parameter

$$c_0(\tau) = \left(\frac{m}{A\alpha^2}\right)^{1/2}\frac{u_{j\mathbf{k}}}{\kappa_{j\mathbf{k}}R(\tau)}, \tag{20}$$

with the coefficients $\kappa_{j\mathbf{k}}$ depending on the polarization j and on the $\mathbf{k}$ vectors of the sound waves, one obtains for the commonly used (acoustic) Debye temperature

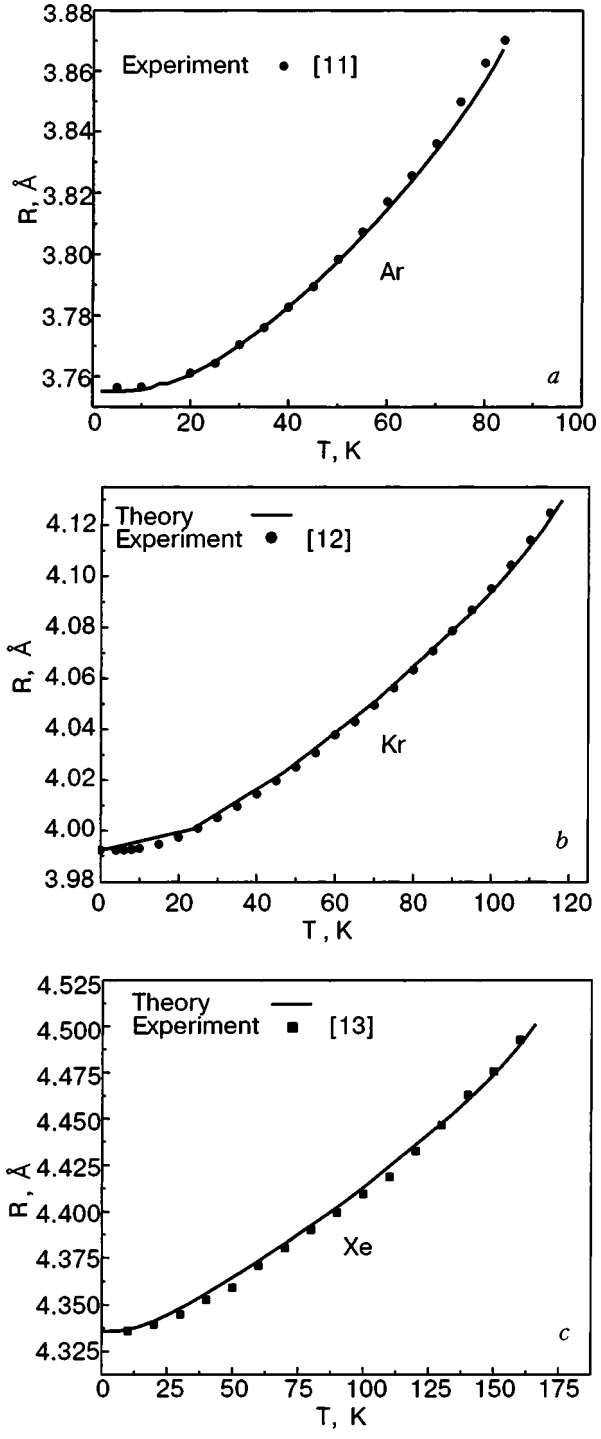

FIG. 4. Calculated temperature dependence of the nearest-neighbor distance in solid Ar and Xe at ambient pressure and in solid Kr at zero pressure, and experimental data points from the literature (Ref. number in square brackets).

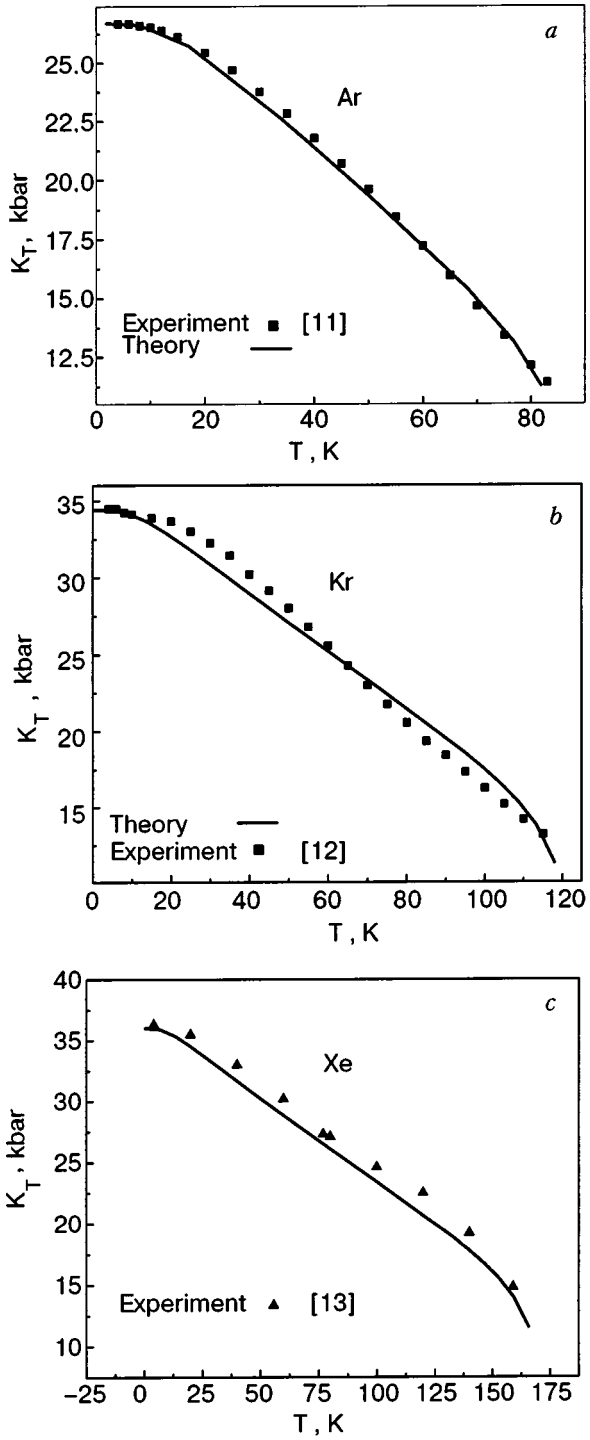

FIG. 5. Calculated temperature dependence of the isothermal bulk modulus for Ar (*a*), Kr (*b*), and Xe at ambient pressure (*c*), and experimental data points from the literature (Ref. number in square brackets).

$$\Theta_D = (6\sqrt{2}\pi^2)^{1/3}\langle \kappa_{j\mathbf{k}} \rangle > AAc_0(\tau) \tag{21}$$

whereby $\langle \kappa_{j\mathbf{k}} \rangle \approx 0.677$ for the fcc lattice. This direct relation between the (acoustic) Debye temperature and the quasielastic bond parameter indicates that the temperature and volume dependence of $c_0(\tau)$ can be used in the determination of all the thermodynamic properties of these crystals in the same way as the Debye temperature in the commonly applied Debye model, although in the present case the temperature dependence of $c_0(\tau)$ also includes anharmonic contributions, which are not included in the commonly used quasiharmonic Debye approach.

3. CONTRIBUTIONS OF VACANCIES TO THE THERMODYNAMIC PROPERTIES

Vacancy contributions to thermodynamic properties of crystals are determined primarily by their equilibrium concentrations

$$n_v = \exp(-g_v/T), \tag{22}$$

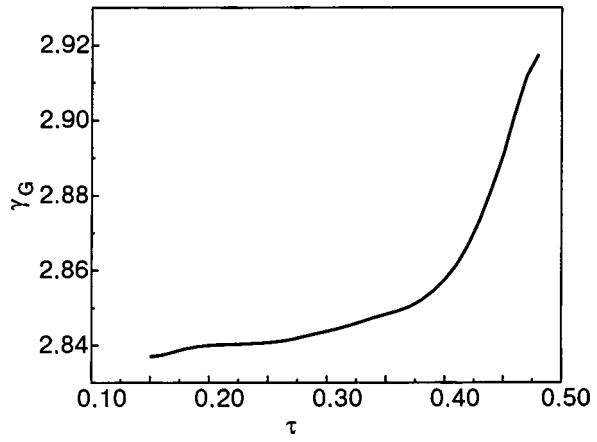

FIG. 6. Calculated temperature dependence of the thermal Grüneisen parameter for Ar at ambient pressure.

where $g_v = h_v - Ts_v$ is the excess Gibbs energy associated with the vacancies, and $h_v = \varepsilon_v + Pv_v$ and s_v are the corresponding enthalpy and entropy, respectively.

The broken bonds result in local deformations around the vacant sites and in changes of the quasi-elastic bond parameters for the surrounding atoms. The total contribution to the Gibbs energy of vacancy formation is then represented by[14]

$$g_v = -2.33A\tau + 3.77A. \tag{23}$$

The vacancy contribution to the isobaric heat capacity (at zero pressure) of a simple crystal is given within this approximation by

$$C_{\text{vac}} = \left[\frac{h_{\text{vac}}}{T}\right]^2 \exp(-g_v/T). \tag{24}$$

As can be seen from (24), the largest contribution of the vacancies to the heat capacity of the crystal should be seen at the highest temperatures. In the present cases $C_{\text{vac}}/3 \ll 1$, i.e., the contribution of vacancies to the total heat capacity of the crystal remains small compared with the lattice contributions even at the highest temperatures.

The change of the crystal volume under pressure depends on both the lattice compression and the decrease in the number of vacancies:

$$\frac{dV}{dP} = -\frac{1}{K_T^0}V + v_v\frac{dn_{\text{vac}}}{dP}, \tag{25}$$

where K_T^0 is the bulk modulus of a perfect crystal. The pressure dependence of the number of vacancies is determined by the enthalpy of vacancy formation $h_v = \varepsilon_v + Pv_v$. In this case the effective bulk modulus of the crystal with defects can be written as

$$K_T = \frac{K_T^0}{1 + \dfrac{\alpha^3 v_v}{\tau} n_{\text{vac}} K_T^0}. \tag{26}$$

An estimate of the contributions in (26) shows that the denominator is close to 1 at any temperature, i.e., contributions from vacancies to the bulk modulus of the RGCs are very small and can be safely neglected.

In the literature[15] similar conclusions can be found with respect to the thermodynamic contribution of the vacancies in the case of copper.

This research was supported in parts by an award from the Deutscher Akademischer Austauschdienst (DAAD) to A.I.K.

*E-mail: akaras@imp.kiev.ua

[1] D. L. Losee and R. O. Simmons, Phys. Rev. **172**, 934 (1968).
[2] W. B. Holzapfel, M. Hartwing, and G. Reiss, J. Low Temp. Phys. **122**, 401 (2001).
[3] W. B. Holzapfel, High Press. Res. **16**, 81 (1998).
[4] N. Boccara and G. Sarma, Physics (Long Island City, N.Y.) **1**, 219 (1965).
[5] T. R. Koehler, Phys. Rev. Lett. **17**, 89 (1966).
[6] H. Horner, Z. Phys. **205**, 72 (1967).
[7] A. I. Karasevskii and V. V. Lubashenko, Phys. Rev. B **66**, 054302 (2002).
[8] A. I. Karasevskii and W. B. Holzapfel, Phys. Rev. B **67**, 224301 (2003).
[9] V. V. Goldman, G. K. Horton, and M. L. Klein, Phys. Rev. Lett. **21**, 1527 (1968).
[10] O. G. Peterson, D. N. Batchelder, and R. O. Simmons, Phys. Rev. **150**, 703 (1966).
[11] D. L. Losee and R. O. Simmons, Phys. Rev. **172**, 944 (1968).
[12] P. Korpiun and E. Luscher, *Rare Gas Solids*, Vol. 2, Academic Press, London (1977), p. 729.
[13] P. Korpiun and H. J. Coufal, Phys. Status Solidi A **10**, 187 (1971).
[14] S. Sh. Soulayman, J. V. Zanchetta, and J. C. Giuntini, J. Chem. Phys. **102**, 7641 (1995).
[15] D. Acoccella, G. K. Horton, and E. R. Cowley, Phys. Rev. B **61**, 8753 (2000).

This article was published in English in the original Russian journal. Reproduced here with stylistic changes by AIP.

PHYSICS IN QUANTUM CRYSTALS

Equilibrium helium film in the thick-film limit

J. Klier, F. Schletterer, and P. Leiderer

Department of Physics, University of Konstanz, Konstanz D-78457, Germany

V. Shikin*

Institute of Solid State Physics of the Russian Academy of Sciences, Chernogolovka 142432, Moscow District, Russia

Fiz. Nizk. Temp. **29**, 957–960 (September–October 2003)

There are still some open questions about how the thickness of a liquid or solid quantum film, such as liquid helium or solid hydrogen, develops in certain limits. One of these is the thick-film limit, i.e., the crossover from the thick film to the bulk. We have performed measurements in this range using the surface plasmon resonance technique and an evaporated Ag film deposited on a glass substrate. The thickness of the adsorbed helium film is varied by changing the distance h of the bulk reservoir to the surface of the substrate. In the limiting case when $h \to 0$ the film thickness approaches about 100 nm, following the van der Waals law in the retarded regime. The film thickness and its dependence on h is determined precisely and modeled theoretically. The behavior of the equilibrium film thickness is discussed in detail. The agreement between theory and experiment is very good. © *2003 American Institute of Physics.* [DOI: 10.1063/1.1614175]

INTRODUCTION

The thickness of a liquid film grown under complete wetting conditions on a horizontal substrate is an important parameter for many areas of condensed matter physics, especially for surface science studies. This film thickness, under thermodynamic equilibrium conditions (i.e., in coexistence with its saturated vapor pressure), is very dependent on the distance of the bulk liquid level to the surface of the substrate; see Fig. 1. The existing description of thick adsorbed films[1,2] generally deals with van der Waals forces. In the case when retardation plays a role the dependence of the film thickness d is

$$d \propto h^{-1/4}. \tag{1}$$

However, the singularity in definition (1) when $h \to 0$ is not physical, i.e., d would go to infinity although the bulk level is just at the height of the substrate (see Fig. 2). This shows that this limiting case has to be described more accurately; see below.

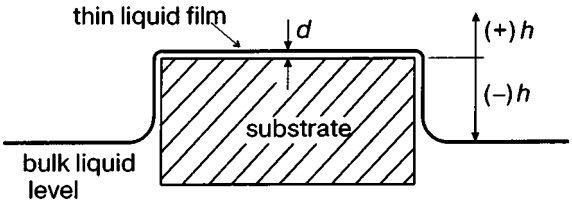

FIG. 1. The thickness d of a thin liquid film completely wetting a horizontal substrate and being in coexistence with its saturated vapor pressure, i.e., in the presence of bulk liquid. The distance between the substrate and the bulk liquid level is h.

There are some alternative interpretations to the van der Waals dependence of $d(h)$. One of them can be formulated as the meniscus problem. It is well known that the vertical substrate walls can lift some amount of the liquid above the bulk level due to the competition between the Laplace force and gravity,[3] a scenario known as suspended films. The same mechanism could, in principle, be responsible for the creation of a macroscopically thick liquid film when $h \to 0$ without the participation of van der Waals forces (see Figs. 3 and 4).

In addition to the theoretical discussion we have performed precise measurements of the thickness of a liquid helium film on a silver substrate using the surface plasmon

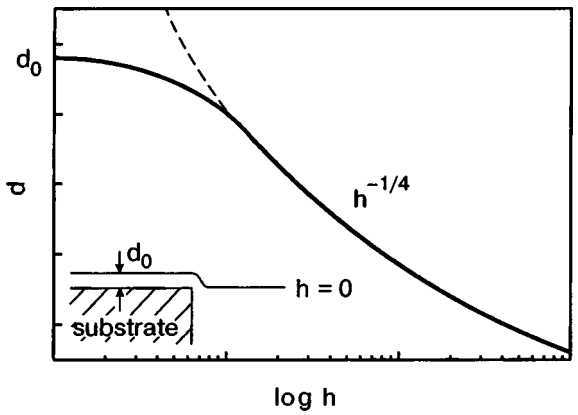

FIG. 2. The dependence of $d(h)$ in the van der Waals approximation (qualitatively), considering Eqs. (4) and (5) on a semilog scale. The dashed line indicates the behavior of $d(h)$ if it is described only by Eq. (1). The inset illustrates the limiting case when $h=0$, and so the thickness of the adsorbed film is d_0.

technique.[4] The experimental dependence of $d(h)$ for $h\to 0$ follows the corrected van der Waals scenario.

THEORETICAL DESCRIPTION

1. First we will consider the general van der Waals scenario for the behavior of $d(h)$. If the substrate on which a helium film is adsorbed is perfect (i.e., ideally flat), then the definition of the thickness d of this film in the van der Waals approximation is given by

$$\left(\frac{k_w}{d}\right)^4 = d-h. \tag{2}$$

Here k_w is the van der Waals constant including retardation. For the definition of h see Fig. 1. Typical values of k_w are of the order of $10^{-6}\mathrm{cm}^{5/4}$ (Ref. 5).

Under the conditions $h>0$ the solution of Eq. (2) with respect to d is possible provided $h\leqslant d$. So we get

$$d\simeq h+\left(\frac{k_w}{h}\right)^4, \quad \text{for} \quad h\gg\left(\frac{k_w}{h}\right)^4. \tag{3}$$

At the special point $h=0$, i.e., when the bulk level is at the height of the substrate, we have

$$\left(\frac{k_w}{d_0}\right)^4 = d_0, \quad \text{or} \quad d_0=k_w^{4/5}. \tag{4}$$

For the bulk helium level below the substrate, i.e., when $h<0$, we get

$$\left(\frac{k_w}{d}\right)^4 = -h, \quad \text{for} \quad h<0. \tag{5}$$

The predicted behavior of $d(h)$ in the van der Waals approximation is presented in Fig. 2.

2. The lift of the thin liquid film by the bulk meniscus is estimated using the geometry shown in Fig. 3.

The calculations, as in Ref. 3, show that

$$h_{\mathrm{menis}}=a(1-\sin\Theta)^{1/2} \quad \text{with} \quad a^2=\frac{2\sigma_{lv}}{\rho g}. \tag{6}$$

Here ρ is the liquid density, g is the acceleration due to gravity, σ_{lv} is the liquid helium surface tension, and a is the capillary length. It becomes evident that for the limiting case $\Theta\to\pi/2$ one has $h_{\mathrm{menis}}\ll a$. Therefore, lifting of the liquid by the meniscus in the case of an ideal wetted horizontal substrate is ineffective.

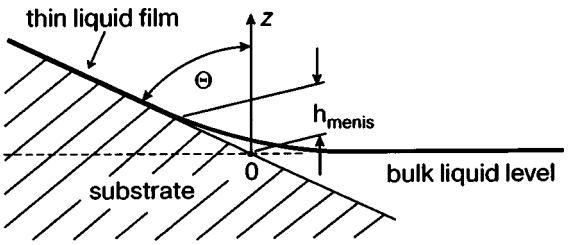

FIG. 3. A tilted substrate, with tilt angle Θ, which is partially immersed in bulk liquid. The upper part of the substrate, i.e., for $h>0$, is covered by a thin liquid film. However, just above the value $h=0$ the liquid film is lifted by the meniscus forming between the substrate wall and the bulk liquid level. The height h_{menis} up to which the film is governed by the meniscus, is described by Eq. (6).

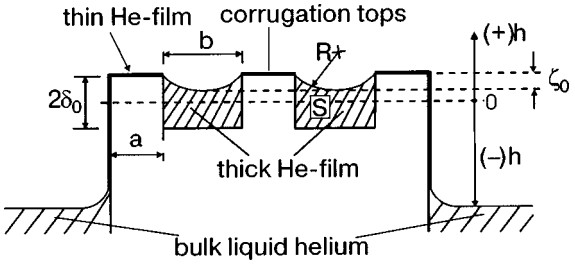

FIG. 4. A schematic sketch of a corrugated surface where, due to the meniscus effect, a suspended thick liquid helium film can be formed. The symbols are explained in the text.

3. However, if the solid substrate is not flat (which is usually the case), then there is another channel for a substrate $d(h)$ dependence. This arises also from the meniscus effect.[3] Now we will formulate this dependence for a corrugated perturbation of the surface of the solid substrate; see Fig. 4. In this case we have

$$\langle d(h)\rangle = \frac{S(h)}{a+b}+\frac{a}{a+b}\tilde{d}(h), \tag{7}$$

where

$$S=2\delta_0 b-\frac{1}{2}[lR-b(R-\zeta_0)] \tag{8}$$

and

$$l=\sqrt{b^2+\frac{16}{3}\zeta_0}, \quad \zeta_0=R-\sqrt{R^2-\frac{b^2}{4}}, \quad R(h)=\frac{2\sigma_{lv}}{\rho g h}. \tag{9}$$

Here $\tilde{d}(h)$ represents the van der Waals contribution to $\langle d\rangle$, from Eq. (5).

Under the condition $R(h)\gg b$ the value $S(h)$ from Eq. (8) is insennsitive to h, and so the dependence $d(h)$ can be presented as

$$\langle d(h)\rangle \simeq d_{\mathrm{cor}}+\tilde{d}(h)\frac{a}{a+b},$$

$$\text{with} \quad d_{\mathrm{cor}}\simeq\frac{2\delta_0 b}{a+b}, \tag{10}$$

with the asymptotic behavior of $\tilde{d}(h)$ as

$$\left[\frac{k_w}{\tilde{d}(0)}\right]^4 \simeq \delta_0+\tilde{d}(0) \quad \text{for} \quad h\to 0, \tag{11}$$

$$\left[\frac{k_w}{\tilde{d}(h)}\right]^4 \simeq h \quad \text{for} \quad h\gg\tilde{d}(0)+\delta_0. \tag{12}$$

One can see that the meniscus effect $S(h)$ in $\langle d(h)\rangle$ can be dominant if $\delta_0\gg d_0$, where d_0 is from Eq. (4). It can also be sensitive to h if the Laplace radius $R(h)$ is comparable to the corrugation parameter b. In the opposite limit, Eq. (10), the presence of roughness of the solid substrate (more precisely, a solid corrugation) leads to a shift of the film thickness in the dependence $\langle d(h)\rangle$.

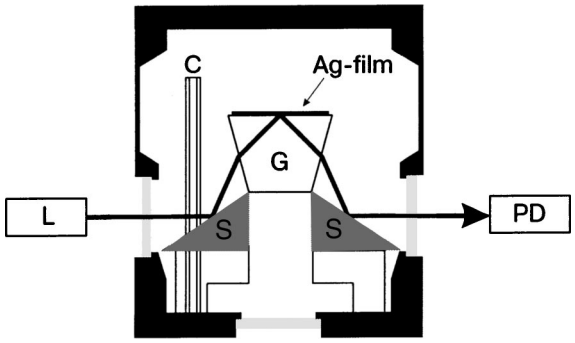

FIG. 5. Sketch of the experimental cell. An incoming light beam from a monochromatic source L is reflected from a mirror S towards the face of a glass prism G. From there the reflected light is detected by a sensitive photodiode P. The adsorbed helium is measured on top of a thin, 40-nm-thick Ag film evaporated onto the glass prism. The bulk helium level (not shown) is measured via a cylindrical capacitor C standing vertically inside the cell. Temperature equilibrium is checked both by a thermometer mounted on the prism surface and via the vapor pressure measured with a high-resolution pressure gauge outside the cryostat.

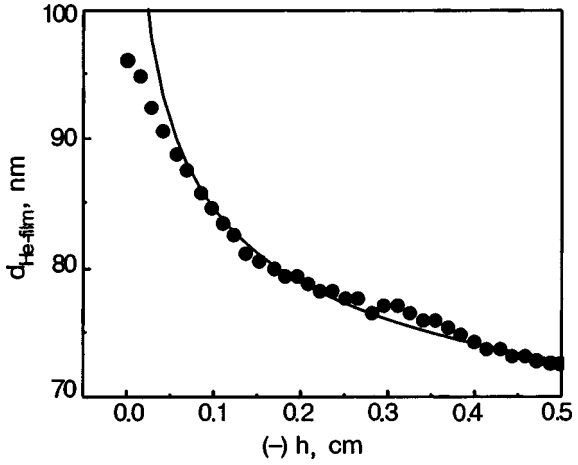

FIG. 6. The thickness d of the adsorbed helium film as a function of the varying bulk helium level h. Here h is already very small and so the dependence of d follows the $h^{-1/4}$ law (solid line) for $h \geq 0.06$ cm; see text. For smaller values of h, i.e., $h < 0.1$ cm, the film thickness deviates from this law.

EXPERIMENTAL VERIFICATION

In order to check the above predictions for the limiting case when $h \to 0$ we have performed preliminary measurements of the thickness of a growing ^{4}He film. As the experimental technique we used a surface plasmon (SP) resonance setup which allows for a resolution of the helium film thickness of about 1 Å; see Ref. 4. The surface plasmons are excited at the interface between a thin quench-condensed Ag film deposited on a glass prism and the adsorbed helium film by means of a monochromatic light source; see Fig. 5. The light beam is reflected at the prism, and the reflected light is measured with a very sensitive photodiode (for a more detailed description of such a setup see Ref. 6). Under resonance conditions, i.e., when the angle of incidence corresponds to the surface plasmon resonance angle, little or no light is detected. By maintaining this resonance condition with the aid of a feedback loop, the thickness of the adsorbed helium film can be measured.

The thickness of the helium film is determined as function of the bulk helium level. This bulk level is changed in small steps by slowly condensing in helium gas from a known volume. It turns out that the relaxation times to achieve a stable bulk level is of the order of hours. The experiment is performed at 1.4 K, i.e., when the helium is superfluid. The height of the bulk level is measured with a cylindrical capacitor (see Fig. 5), which gives a resolution of about 50 μm. This height measurement is cross-checked by the total volume of gas added to the cell and a precise check of the cell volume and the inside geometry after the experiment.

In Fig. 6 we show the growth of the helium film starting from a bulk level of $(-)h = 0.5$ cm below the surface of the substrate. At this point the thickness d of the helium film is about 73 nm. As the bulk level is raised the film thickness grows, showing a $h^{-1/4}$ dependence as described by Eqs. (10)–(12). Within these results we can fit our experimental data. When fitting the data in the interval $0.1 \text{ cm} < (-)h < 0.3$ cm, using Eq. (10), the agreement is quite good, see Fig. 7, and the parameter d_{cor} can be obtained. It turns out that $d_{\text{cor}} \approx 49$ nm, and so (if we assume that $a \approx b$) we get $\delta_0 \simeq d_{\text{cor}} = 49$ nm.

We interpret this observation as being due to the circumstance that the surface must be very rough but without Gaussian peaks, and so there is bulk condensation between some roughness peaks which adds to the measured film thickness. That our surface was indeed quite rough was seen in the measured SP resonance curves, which showed a large resonance width, much wider than for an ideal smooth Ag film. However, once the adsorbed helium film is thicker than the height of the roughness peaks its influence is screened, and so a further growth in film thickness should show the ideal behavior, seen in the data for $h \to 0$. The influence of substrate roughness in the film thickness of adsorbed films will be investigated and presented elsewhere.

When h drops below 0.1 cm the measured data deviate from the above law; see Fig. 6. Eventually the film thickness levels off at around 100 nm; see Fig. 7. Using Eq. (11) and

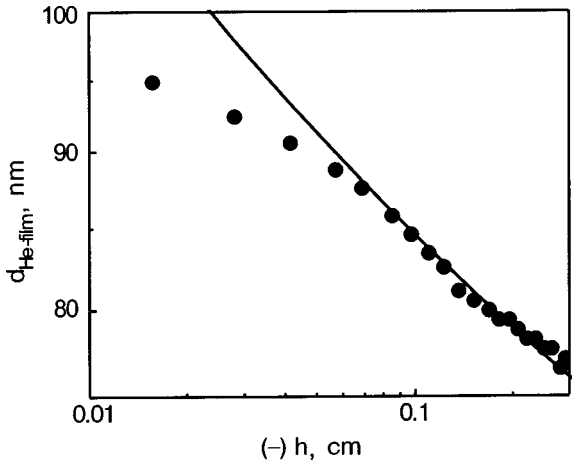

FIG. 7. The same data points of d plotted against h as in Fig. 6, however now on a semilog scale. The deviation from the expected $h^{-1/4}$ behavior (solid line) for small values of h is clearly seen. The thickness of the helium film approaches a final value of around 100 nm. This is the predicted behavior shown in Fig. 2 and described by Eqs. (4) and (5).

$k_w \approx 6.4\times 10^{-7}$ cm$^{5/4}$, one gets $\tilde{d}(0)\approx 102$ nm. From Eq. (10) we get $d(0)\simeq d_{\rm cor}+0.5\tilde{d}(0)=100$ nm, which corresponds well to the experimental value for $h\to 0$.

CONCLUSIONS

We have investigated the growing of an adsorbed liquid film d on a substrate as function of the distance h between the bulk liquid level and the substrate surface, which is above the bulk level. The calculations of the thickness of such a film are given for the thick-film limit, i.e., when $h\to 0$ and under retardation conditions, on ideal smooth surfaces. These predictions are confirmed by measurements of a liquid helium film adsorbed to a silver surface. Both the thickness of the helium film and the change in the bulk helium level are measured with high resolution in the range 70 nm$<d<$100 nm for 0.5 cm$>(-)h>0$. Experiments to study the crossover from the retarded to the non-retarded regime are currently running. The influence of substrate roughness on adsorbed quantum films is also under investigation, both theoretically and experimentally.

This work was supported by the DFG-Schwerpunkt ''Wetting and Structure Formation at Interfaces'' under Kl 1186/1.

*E-mail: shikin@issp.ac.ru

[1] H. B. G. Casimir and D. Polder, Phys. Rev. **73**, 360 (1948).
[2] L. W. Bruch, M. W. Cole, and E. Zaremba, *Physical Adsorption: Forces and Phenomena*, Clarendon Press, Oxford (1997), and references therein.
[3] L. D. Landau and E. M. Lifshitz, *Hydrodynamics*, Akademie Verlag, Berlin (1991).
[4] D. Reinelt, J. Klier, and P. Leiderer, J. Low Temp. Phys. **113**, 805 (1998).
[5] E. Y. Andrei, Phys. Rev. Lett. **52**, 1449 (1984).
[6] V. Iov, J. Klier, and P. Leiderer, J. Low Temp. Phys. **126**, 367 (2002).

This article was published in English in the original Russian journal. Reproduced here with stylistic changes by AIP.

Translational–rotational interaction in the dynamics and thermodynamics of a 2D atomic crystal with a molecular impurity

T. N. Antsygina, M. I. Poltavskaya, and K. A. Chishko*

B. Verkin Institute for Low Temperature Physics and Engineering of the National Academy of Sciences of Ukraine, 47 Lenin Ave., Kharkov 61103, Ukraine

Fiz. Nizk. Temp. **29**, 961–966 (September–October 2003)

The interaction between the rotational degrees of freedom of a diatomic molecular impurity and the phonon excitations of a two-dimensional atomic matrix commensurate with a substrate is investigated theoretically. It is shown that the translational–rotational interaction changes the form of the rotational kinetic energy operator as compared to the corresponding expression for a free rotator, and also renormalizes the parameters of the crystal field without altering in its initial form. The contribution of the impurity rotational degrees of freedom to the low-temperature heat capacity for a dilute solution of diatomic molecules in an atomic two-dimensional matrix is calculated. The possibility of experimental observation of the predicted effects is discussed. [DOI: 10.1063/1.1614176]

1. INTRODUCTION

Two-dimensional (2D) cryocrystals on substrates of different kinds are of great theoretical and experimental interest due to the wide variety of physical phenomena (in thermodynamics, excitation spectra, and magnetism) they demonstrate. For 2D monoatomic crystals containing molecular impurities the interaction between rotational degrees of freedom and matrix phonon excitations, the so-called translational–rotational interaction (TRI),[1] is an important factor controlling the dynamics of the impurity molecules. Since an impurity in a 2D solution moves in a low-symmetry potential, its dynamics appears to be substantially more complex than that in a 3D system.[2] This can appreciably affect all physical characteristics, in particular, the low-temperature heat capacity, and also can lead to some effects not found in the 3D case. Theoretically, the problem of the TRI in 2D cryosolutions has not been sufficiently studied.

The aim of the present paper is to investigate theoretically the effect of the phonon excitations on the rotational dynamics of a diatomic impurity in a 2D close-packed atomic matrix and on the impurity heat capacity at low temperatures.

2. HAMILTONIAN

Let us consider a diatomic homonuclear substitutional impurity with mass M and internuclear distance $2d$ in a two-dimensional close-packed monoatomic matrix (the coordination number in the layer $z_1=6$) placed on a rigid substrate. The matrix and the substrate structures are supposed to be commensurate, so that a monolayer atom has z_2 nearest neighbors in the substrate. The substrate forms either a triangular ($z_2=3$) or honeycomb ($z_2=6$) lattice. For definiteness we assume that the impurity is located at the origin, the OZ axis is chosen normal to the layer and is directed from the substrate, and the OX and OY axes are oriented in the matrix plane. We restrict consideration to the case of an isotopic impurity.

Assuming that the displacement $\mathbf{u_f}$ of the impurity center of inertia from its equilibrium position is small in comparison with the distances to the nearest neighbors both in the layer, R_1, and in the substrate, R_2, and taking into account the smallness of d/R_i $(i=1,2)$, we can write the total Hamiltonian of the system as

$$H=-B\Delta_{\theta,\varphi}+H_{\rm ph}+H_c+H_{\rm int}, \tag{1}$$

where the first term is the kinetic energy of the impurity molecule, $B=\hbar^2/(2I)$ is the rotational constant of the molecule, $I=Md^2$ is its moment of inertia, $\Delta_{\theta,\varphi}$ is the angular part of the Laplacian, θ and φ are the azimuthal and polar angles specifying the orientation of the molecular axis.

The Hamiltonian $H_{\rm ph}$ of the phonon subsystem has the form

$$H_{\rm ph}=\frac{1}{2}\sum_{\nu}\left(\frac{|\pi_\nu|^2}{m}+m\Omega_\nu^2\left|\xi_\nu\right|^2\right)+\frac{\varepsilon}{2MN}\sum_{\nu,\nu'}(\mathbf{e}_\nu,\mathbf{e}_{\nu'})\pi_\nu\pi_{\nu'}^*,$$

where $\mathbf{e}_\nu$ and Ω_ν are the unit polarization vectors and frequencies, respectively, of the phonon excitions of a pure monolayer, $\nu=(\mathbf{k},\alpha)$, $\mathbf{k}$ is a two-dimensional wave vector, $\alpha=l,t,z$; l,t specify the longitudinal and transverse modes polarized in the layer plane (in-plane modes), and z is the index for the mode polarized normal to the layer (out-of-plane mode), ξ_ν are coefficients in a series expansion of $\mathbf{u_f}$ in the unit polarization vectors $\mathbf{e}_\nu$, $\pi_\nu=-i\hbar\partial/\partial\xi_\nu$, m is the mass of a matrix atom, $\varepsilon=(m-M)/m$ is the mass defect, and N is the number of sites in the layer. For a pure crystal in the commensurate regime all the phonon spectrum branches have gaps: equal to Δ for the in-plane modes and to Δ_z for the out-of-plane mode with $\Delta_z>\Delta$. As a rule, the z mode is practically dispersionless.[3] Explicit forms of Ω_ν for the system under consideration can be found in Refs. 3 and 4.

With an accuracy to $(d/R_i)^4$ the crystal field H_c has the form

$$H_c=-\frac{G_0}{2}w_z^2+\frac{1}{2}[G_1w_z^4+\Delta_{z_23}G_2w_yw_z(w_y^2-3w_x^2)]. \tag{2}$$

Here $\mathbf{w}=(\sin\theta\cos\varphi, \sin\theta\sin\varphi, \cos\theta)$, Δ_{ij} is the Kronecker delta,

$$G_0=d^2\left\{\sum_{i=1,2,} z_i\mathcal{M}_i-z_2(1-b^2)\right.$$
$$\left.\times[3\mathcal{M}_2+d^2(5b^2-2)P_2]\right\},$$
$$G_1=\frac{d^4}{2}\left[\sum_{i=1,2} z_iP_i+\frac{5}{3}z_2(1-b^2)(1-7b^2)P_2\right],$$
$$G_2=\frac{4d^4}{3}z_2b^3\sqrt{1-b^2}P_2,$$
$$\mathcal{M}_i=A_i+\frac{d^2}{8}R_i\frac{d}{dR_i}\left(\frac{1}{R_i}\frac{dA_i}{dR_i}\right),$$
$$P_i=\frac{1}{8}R_i\frac{d}{dR_i}\left(R_i^3\frac{d}{dR_i}\frac{A_i}{R_i^4}\right),$$
$$A_i=R_i\frac{d}{dR_i}\left(\frac{1}{R_i}\frac{dV_i}{dR_i}\right),$$

the parameter b is equal to $R_1/(\sqrt{3}R_2)$ and $R_1/(3R_2)$ for substrates with triangular and honeycomb lattices, respectively; V_i are atom-atom potentials describing interactions between the impurity and matrix atoms ($i=1$) and between the impurity and substrate atoms ($i=2$).

The first two terms in (2) are determined by both the matrix and the substrate, whereas the last term with a lower symmetry (of group S_6) is associated only with the crystal field of the substrate. The analysis of $G_{0,1}$ shows that the substrate field makes the impurity lie in the layer, while the matrix field tends to orient it perpendicular to the substrate. Thus, the equilibrium position of the impurity is determined by a competition between the two factors.

The interaction between the phonon subsystem and the rotational degrees of freedom of the impurity is described by the following Hamiltonian:[5,6]

$$H_{\rm int}=-\frac{d^2}{2\sqrt{N}}\sum_\nu (f_\nu^*\xi_\nu+\text{c.c.}),\quad f_\nu=\Gamma_\nu^{\alpha\beta}Q_{\alpha\beta}+C_\nu. \tag{3}$$

Here $Q_{\alpha,\beta}=w_\alpha w_\beta-\Delta_{\alpha\beta}/3$ is the dimensionless quadrupole moment of the impurity molecule,

$$\Gamma_\nu^{\alpha\beta}=s^{\alpha\beta\gamma}(\mathbf{k})\mathrm{e}_\nu^\gamma+2h^\alpha(\mathbf{k})\mathrm{e}_\nu^\beta,$$
$$C_\nu=\frac{1}{3}[s^{\alpha\alpha\gamma}(\mathbf{k})+5h^\gamma(\mathbf{k})]\mathrm{e}_\nu^\gamma,$$
$$s^{\alpha\beta\gamma}(\mathbf{k})=\mathcal{K}_1\sum_{\vec\delta}\delta^\alpha\delta^\beta\delta^\gamma\exp(ik\cdot\vec\delta R_1)$$
$$+\mathcal{K}_2\sum_{\vec\Delta}\Delta^\alpha\Delta^\beta\Delta^\gamma, \tag{4}$$
$$h^\alpha(\mathbf{k})=\kappa_1\sum_{\vec\delta}\delta^\alpha\exp(ik\cdot\vec\delta R_1)+\kappa_2\sum_{\vec\Delta}\Delta^\alpha,$$

$$\mathcal{K}_i=R_i^2\frac{d}{dR_i}\frac{A_i}{R_i^2},\quad \kappa_i=\frac{A_i}{R_i},$$

$\vec\delta$ and $\vec\Delta$ are unit vectors directed to the nearest neighbors in the layer and in the substrate.

3. IMPURITY DYNAMICS

Let us consider the effect of interaction between the rotational degrees of freedom of the impurity and the matrix phonon excitations on the character of the molecule motion. To do this we use the functional integration method.[7] Within an insignificant normalizing factor the partition function Z of the system under study has the following form:

$$Z=\int D[\xi(\tau)]D[\mathbf{w}(\tau)]\exp(S/\hbar), \tag{5}$$

where S is the total action

$$S=\int_0^{\hbar/T}d\tau L(\tau),\quad L=L_{\rm ph}+L_{\rm rot}+L_{\rm int}+L_c,$$
$$L_{\rm ph}=-\frac{m}{2}\sum_\nu\left[\left|\dot\xi_\nu\right|^2+\Omega_\nu^2\left|\xi_\nu\right|^2-\frac{\varepsilon}{N}\sum_{\nu'}(\mathbf{e}_\nu,\mathbf{e}_{\nu'})\dot\xi_\nu\dot\xi_{\nu'}^*\right],$$
$$L_{\rm rot}=-\frac{I}{2}\left(\frac{\partial\mathbf{w}}{\partial\tau}\right)^2=-\frac{I}{2}(\dot\theta^2+\dot\varphi^2\sin^2\theta),$$
$$L_{\rm int}+L_c=-(H_{\rm int}+H_c),$$

τ is the imaginary time, and the Boltzmann constant $k_B=1$. The dots denote differentiation with respect to τ.

After integration over the phonon variables, the partition function (5) takes the form of the product $Z=Z_{\rm ph}Z_1$. The factor $Z_{\rm ph}$ is the phonon partition function of the 2D crystal, and Z_1 corresponds to the rotational motion of the molecule with regard to the influence of the phonon subsystem on it. For real systems rotational levels of a molecular impurity are, as a rule, low-energy, and, hence, specific effects caused by rotational excitations make themselves evident at extremely low temperatures. Besides, due to the presence of an isotopic impurity, local $\omega_{\rm loc}$ and quasi-local frequencies appear in the phonon spectrum.[8] For the light impurity ($\varepsilon>0$) the local levels lie above the top edge of the continuous spectrum, whereas for the heavy impurity ($\varepsilon<0$) these levels are situated below its bottom edge, i.e., in the gap. Our interest here is in the temperature range $T\leqslant\hbar\Delta,\ \hbar\omega_{\rm loc}$.

Within the present approximation the TRI gives rise to additional terms of order $(d/R_i)^4$ in the crystal field:

$$H_c\to\tilde H_c=H_c+\Delta H_c,$$
$$\Delta H_c=-\frac{d^4}{2mN}\sum_\nu\frac{|f_\nu|^2}{\Omega_\nu^2}, \tag{6}$$

and also in the kinetic energy operator:

$$H_{\rm rot}\to\tilde H_{\rm rot}=H_{\rm rot}+\Delta H_{\rm rot},$$
$$\Delta H_{\rm rot}=\frac{d^4}{2m}\left\{\frac{1}{N}\sum_\nu\frac{|\dot f_\nu|^2}{\Omega_\nu^4}-\varepsilon\left|\frac{1}{N}\sum_\nu\frac{\dot f_\nu\mathbf{e}_\nu}{\Omega_\nu^2}\right|^2\right\}. \tag{7}$$

To analyze Eqs. (6) and (7) it is necessary to calculate sums (4) over the nearest neighbors in the layer. For lattices

with large enough coordination numbers, an effective way of calculation is to replace the summation by integration over the unit circle.[3,4] Such a replacement is quite justified since the corrections (6), (7) are integral characteristics (obtained by summation over **k** in the Brillouin zone).

The interaction between the impurity rotational degrees of freedom and phonons does not modify the general form of the crystal field (2), but renormalizes its coefficients:

$$G_i \to \tilde{G}_i = G_i + \Delta G_i, \quad \Delta G_i = \Delta G_i^L + \Delta G_i^S, \quad i = 0,1,2,$$

where the indices L and S specify contributions caused mainly by the impurity interaction with the matrix atoms and substrate atoms, respectively:

$$\Delta G_0^L = -\frac{z_1^2 d^4}{6m}(A_1 + 3B_1 + C_1),$$

$$\Delta G_1^L = -\frac{z_1^2 d^4}{4m}(A_1 + B_1),$$

$$\Delta G_0^S = \frac{z_2^2 d^4}{2m}[(2K_0^2 - K_2^2\Delta_{z_2,3})s_\perp^{(1)} - K_0 K_1 s_z^{(0)}],$$

$$\Delta G_1^S = \frac{z_2^2 d^4}{4m}[(4K_0^2 - K_2^2\Delta_{z_2,3})s_\perp^{(1)} - K_1^2 s_z^{(1)}],$$

$$\Delta G_2^S = -\frac{z_2^2 d^4}{m} K_0 K_2 s_\perp^{(1)}.$$

Here

$$A_m = \frac{1}{N}\sum_{\mathbf{k}} \frac{\alpha_1^2}{\Omega_l^{2m}},$$

$$B_m = \frac{1}{8N}\sum_{\mathbf{K}} \left[\frac{(\alpha_2 - \alpha_3)^2}{\Omega_l^{2m}} + \frac{(\alpha_2 + \alpha_3)^2}{\Omega_t^{2m}}\right],$$

$$\mathcal{C}_m = \frac{1}{N}\sum_{\mathbf{k}} \frac{\alpha_1(3\alpha_2 - \alpha_1)}{\Omega_l^{2m}}, \quad \alpha_1 = (\mathcal{K}_1 + 2\kappa_1)J_1(kR_1),$$

$$\alpha_2 = (\mathcal{K}_1 + 4\kappa_1)J_1(kR_1),$$

$$\alpha_3 = \mathcal{K}_1 J_3(kR_1), \quad K_0 = \sqrt{1-b^2}(b^2\mathcal{K}_2 + 2\kappa_2),$$

$$K_1 = \sqrt{1-b^2}[(3b^2-2)\mathcal{K}_2 - 4\kappa_2], \quad K_2 = \frac{b^3}{2}\mathcal{K}_2,$$

$$s_\perp^{(m)} = \frac{1}{2N}\sum_{\mathbf{k},\alpha=l,t} \frac{1}{\Omega_\alpha^{2m}}, \quad s_z^{(m)} = \frac{1}{N}\sum_{\mathbf{k}} \frac{1}{\Omega_z^{2m}},$$

where $J_n(x)$ is the Bessel function. By symmetry reasoning the impurity interaction with the neighbors in the layer results only in a renormalization of the coefficients G_0 and G_1 in (2). It can be shown that for short-range potentials the values ΔG_0^L and ΔG_1^L are negative, whereas ΔG_0^S is positive.

The contributions to the crystal field both from the monolayer and from the substrate decrease in amplitude due to the TRI. Such a result is physically quite clear. The rotational motion is mainly affected by high-frequency phonons creating maximal deformations in the first coordination sphere around the impurity. The situation considered is close to the known problem on the motion of a particle in a rapidly oscillating field, where after averaging over oscillations the depth of the initial potential well effectively decreases.[9]

The situation is rather different for the kinetic energy. The TRI results in a substantial change in the form of $H_{\rm rot}$. After appropriate transformations the effective kinetic energy (7) can be represented as a generalized quadratic form of the angular velocity components $\dot{w}_i$ with coefficients dependent on the molecular orientation:

$$\Delta H_{\rm rot} = \frac{1}{2}(\Delta I_\perp \dot{\mathbf{w}}_\perp^2 + \Delta I_z \dot{w}_z^2 + \Delta_{z_2,3}\Delta I_{ij}\dot{w}_i\dot{w}_j),$$

$$\dot{\mathbf{w}} = (w_x, w_y, 0). \tag{8}$$

The additives $\Delta I_{\perp,z}$ to the impurity moment of intertia are

$$\Delta I_{\perp,z} = \Delta I_{\perp,z}^L + \Delta I_{\perp,z}^S,$$

$$\Delta I_\perp^L = z_1^2 \frac{d^4}{m} B_2 w_\perp^2,$$

$$\Delta I_z^L = z_1^2 \frac{d^4}{m} A_2 w_z^2,$$

$$\Delta I_\perp^S = \frac{z_2^2 d^4}{m}\zeta_\perp(K_0^2 w_z^2 + \Delta_{z_2,3}K_2^2 w_\perp^2),$$

$$\Delta I_z^S = \frac{z_2^2 d^4}{m}[K_0^2\zeta_\perp(1 - 3w_z^2) + K_1^2\zeta_z w_z^2],$$

where

$$\zeta_{\perp,z} = s_{\perp,z}^{(2)} - \varepsilon(s_{\perp,z}^{(1)})^2.$$

Besides, for substrates with a triangular lattice ($z_2 = 3$) there are also terms in (8) which are nondiagonal with respect to $\dot{w}_i\dot{w}_j$, with

$$\Delta I_{ij} = -\frac{z_2^2 d^4}{m}\zeta_\perp K_0 K_2 \begin{pmatrix} 2w_y w_z & 2w_x w_z & 2w_x w_y \\ 2w_x w_z & -2w_y w_z & w_x^2 - w_y^2 \\ 2w_x w_y & w_x^2 - w_y^2 & 0 \end{pmatrix}.$$

By virtue of the positive definiteness of form (8), the coefficients $\Delta I_{\perp,z} > 0$. As a result, the TRI leads to an increase in the impurity principal moments of inertia, that is, the molecule becomes effectively heavier.

We have calculated the renormalized parameters for a number of atomic–molecular systems, using for both the impurity–matrix and impurity–substrate interactions the Lennard-Jones model with the parameters corresponding to the gaseous phase.[10] It was found that at real values of d/R_i the maximal relative change in the moment of inertia is about 30%, and the renormalization of the crystal field amplitude may be as much as 50–60%. Certainly, the estimations are quite rough because the Lennard-Jones potential is known to be extremely sensitive to the choice of its parameters, and the real values of these parameters for a 2D system can differ significantly from those in the gaseous phase.[3] Nevertheless, it is clear that the properties of the system under consideration can be substantially affected by the TRI, so that the renormalization effects due to the TRI should be properly taken into account when discussing physical phenomena in real systems.

4. ROTATIONAL HEAT CAPACITY

Now we consider the rotational heat capacity of a dilute solution of diatomic molecules in a 2D atomic matrix. We restrict ourselves to the case of strong binding, when the molecules make small librations near their equilibrium positions normal to the layer plane. The impurity contribution to the free energy (per impurity molecule) from the rotational degrees of freedom and the molecular in-plane translational motion has the form

$$\Delta\mathcal{F}=\frac{\hbar}{\pi}\lim_{\delta\to 0}\int_0^\infty d\omega\coth\frac{\hbar\omega}{2T}\arctan\left(\frac{P(\omega,\delta)}{R(\omega)}\right).$$

Here

$$P(\omega,\delta)=2\omega\delta[1-\varepsilon\rho(\omega)(2\omega^2-\omega_0^2)]-\mu(\omega)[\varepsilon\omega^2(\omega^2-\omega_0^2)+a],$$

$$R(\omega)=(\omega^2-\omega_0^2)[1-\varepsilon\omega^2\rho(\omega)]-a\rho(\omega),$$

$$\rho(\omega)+i\mu(\omega)=\frac{1}{2N}\sum_{\mathbf{k},\alpha=l,t}\frac{1}{(\omega+i\delta)^2-\Omega_\alpha^2(\mathbf{k})},$$

ω_0 is the libratoinal frequency of the rotator with unnormalized parameters (in the absence of TRI), and $a=2z_2^2d^4K_0^2B/(m\hbar)$ is a parameter describing the TRI intensity.

For most real systems the librational frequency ω_0 is small as compared to the top edge $\Omega_{\max}$ of the continuous spectrum of the pure 2D crystal, so that ω_0 is either in the gap ($\omega_0<\Delta$) or in the continuous spectrum near its bottom. On the other hand, the smaller the value of ω_0 and the lower the temperature, the easier it is to extract the rotational part from the total heat capacity, which also contains contributions from translational excitations (from both the continuous spectrum and the local and quasi-local states). Hereafter we consider the case of small ω_0.

We start with $\omega_0<\Delta$. For a light impurity ($\varepsilon>0$) the local and quasilocal translational levels are close to $\Omega_{\max}$, and their influence on the low-temperature thermodynamics is negligible. Thus the main contribution to the thermodynamic functions is from the rotational degrees of freedom. The rotational free energy and the heat capacity (per particle) have the form:

$$\Delta\mathcal{F}_{\rm rot}=2T\ln\left(2\sinh\frac{\hbar\tilde\omega_0}{2T}\right),$$

$$\Delta C=2\left(\frac{\hbar\tilde\omega_0}{2T}\sinh^{-1}\frac{\hbar\tilde\omega_0}{2T}\right)^2, \qquad (9)$$

$$\tilde\omega_0^2=\omega_0^2[1-a\zeta_1]-as_\perp^{(1)},$$

where $\tilde\omega_0$ is the librational frequency renormalized due to the TRI. The result (9) corresponds to the heat capacity of a two-dimensional Einstein oscillator with the frequency $\tilde\omega_0$. As it should, renormalization of the parameters of the rotator motion leads to an effective decrease of ω_0 and, hence, to an increase of the relative contribution from the rotational degrees of freedom to the low-temperature heat capacity.

In the case of a heavy impurity ($\varepsilon<0$) the local level falls within the gap ($\omega_{\rm loc}<\Delta$), and the contribution from $\omega_{\rm loc}$ to the thermodynamic functions can be comparable to that from the rotational degrees of freedom. Thus the main contribution to the free energy and heat capacity from the impurity subsystem consists of two terms of the form (9) with frequencies $\tilde\omega_0$ and $\tilde\omega_{\rm loc}$, which are determined as the two least roots of the equation $R(\omega)=0$. Namely,

$$\tilde\omega_0^2=\omega_0^2[1-af(\omega_0,\omega_{\rm loc})]-as_\perp^{(1)},$$

$$\tilde\omega_{\rm loc}^2=\omega_{\rm loc}^2[1+af(\omega_0,\omega_{\rm loc})],$$

$$f(\omega_0,\omega_{\rm loc})=\frac{s_\perp^{(1)}+\omega_{\rm loc}^2s_\perp^{(2)}}{\omega_{\rm loc}^2-\omega_0^2}.$$

If the spacing between the frequencies $\omega_{\rm loc}$ and ω_0 is large in comparison with the TRI intensity, $a\ll(\omega_{\rm loc}^2-\omega_0^2)^2$, the excitations under consideration can be classified as librational and local excitations with renormalized frequencies. In the opposite case, when $a\gg(\omega_{\rm loc}^2-\omega_0^2)^2$, "mixing" of the frequencies occurs, and, as a result, molecular librations and local oscillations are no longer well-defined eigenstates.

The situation is more complicated when the librational frequency lie inside the continuous phonon spectrum near its bottom ($\omega_0>\Delta$).[2,11] Since $\omega_{\rm loc}<\Delta$ for a heavy impurity, the contribution to the thermodynamic functions from the local excitations prevails over the contribution from the rotational degrees of freedom. Thus the solutions with light impurities ($\varepsilon>0$) are of main interest here. In this case the rotational free energy can be written as

$$\Delta\mathcal{F}=\frac{2T}{\pi}\int_\Delta^{\Omega_{\max}}d\omega\ln 2\sinh\left(\frac{\hbar\omega}{2T}\right)\frac{\gamma_0}{(\omega-\tilde\omega_0)^2+\gamma_0^2}, \qquad (10)$$

where $\gamma_0=-a\mu(\tilde\omega_0)/(2\tilde\omega_0)$ is the Lorentzian peak halfwidth and $\tilde\omega_0$ is the same as in Eq. (9). It should be noted that the validity of Eq. (10) is restricted to the condition $\omega_0-\Delta\gg\gamma_0$ (i.e., ω_0 is not too close to the bottom of the continuous spectrum). Taking into account smallness of γ_0, the rotational heat capacity can be represented approximately in the form (9). Thus the rotational heat capacity at low temperatures has an exponential form:

$$\Delta C=2\left(\frac{\hbar\tilde\omega_0}{T}\right)^2\exp\left(-\frac{\hbar\tilde\omega_0}{T}\right), \qquad (11)$$

unlike three-dimensional systems, where a power-type dependence obtains.[2] Such a result is due to the gap in the phonon spectrum of a 2D monoatomic crystal commensurate with the substrate.[3,12] In this connection we recall that the matrix heat capacity is also of exponential form:[3,12]

$$C_{\rm ph}\sim\frac{\hbar\Delta}{T}\exp\left(-\frac{\hbar\Delta}{T}\right),$$

but its temperature dependence idffers from Eq. (11) in the pre-exponential factor. This circumstance can be useful when extracting the rotational part from a measured total heat capacity, particularly if ω_0 and Δ are close in magnitude.

5. CONCLUSION

The most pronounced effect resulting from the interaction between translational and rotational degrees of freedom consists in the radical change of the inertial properties of the impurity molecule. This manifests itself in the change in the form of the rotational kinetic energy operator as compared to

the corresponding expression for the free rotator. The inertia tensor components become functions of molecular orientation, and the molecule, in terms of rotational motion, transforms into a ''parametric rotor'' whose effective kinetic energy is represented as a generalized quadratic form of the angular velocity components with a symmetry corresponding to the external crystal field. For example, if the substrate atoms form a honeycomb structure, then within the present approximation the tensor of inertia remains diagonal, while for substrates with triangular lattices it has also off-diagonal components.

The TRI also results in a renormalization of the crystal field parameters. However, although the corresponding corrections are rather large, the potential form determined by the symmetry of the system remains unchanged.

We would like to note that the dynamics of a diatomic impurity in a 2D monoatomic matrix on a substrate is more complicated than in a 3D matrix of cubic symmetry.[2,5] Indeed, due to the high symmetry of the surroundings in 3D systems, TRI leads only to an increase in the molecular moment of inertia without changing the form of the kinetic energy operator.

In view of possible experiments on the rotational heat capacity of 2D solid solutions of diatomic molecules in monoatomic matrices on commensurate substrates, the 2D solutions with light impurities are expected to be preferable, because at low temperatures the contribution from the rotational degrees of freedom dominates over the contribution from the local translational excitations. Being richer from the theoretical standpoint, the systems with heavy impurities are more complicated for experimental research due to the problem of correct separation of the contributions from the local and rotational excitations.

*E-mail: chishko@ilt.kharkov.ua

[1] R. M. Lynden-Bell and K. H. Michel, Rev. Mod. Phys. **66**, 721 (1994).
[2] T. N. Antsygina and V. A. Slusarev, Teor. Mat. Fiz. **77**, 234 (1988) (in Russian).
[3] T. N. Antsygina, I. I. Poltavsky, M. I. Poltavskaya, and K. A. Chishko, Fiz. Nizk. Temp. **28**, 621 (2002) [Low Temp. Phys. **28**, 442 (2002)].
[4] T. N. Antsygina, K. A. Chishko, and I. I. Poltavsky, J. Low Temp. Phys. **126**, 15 (2002).
[5] T. N. Antsygina, K. A. Chishko, and V. A. Slusarev, Phys. Rev. B **55**, 3548 (1997).
[6] T. N. Antsygina, M. I. Poltavskaya, and K. A. Chishko, Phys. Solid State **44**, 1268 (2002).
[7] R. P. Feynman and A. R. Hibbs, *Quantum Mechanics and Path Integrals*, McGraw-Hill, New York (1965).
[8] I. M. Lifshits and A. M. Kosevich, Rep. Prog. Phys. **29**, 217 (1966).
[9] L. D. Landau and E. M. Lifshitz, *Mechanics*, 2nd ed., Pergamon Press, Oxford (1969), Nauka, Moscow (1965).
[10] V. G. Manzhelii and Yu. A. Freiman (Eds.), *Physics of Cryocrystals*, AIP Press, New York (1996).
[11] Yu. Kagan and Ya. Iosilevskiĭ, Zh. Éksp. Teor. Fiz. **45**, 819 (1963) [Sov. Phys. JETP **18**, 562 (1964)].
[12] J. G. Dash, Fiz. Nizk. Temp. **1**, 839 (1975) [Low Temp. Phys. **1**, 401 (1975)].

This article was published in English in the original Russian journal. Reproduced here with stylistic changes by AIP.

Conductivity of a 2D electron crystal over liquid helium in the region of coupled electron–ripplon resonances

V. Syvokon* and Y. Kovdrya

B. Verkin Institute for Low Temperature Physics and Engineering of the National Academy of Sciences of Ukraine, 47 Lenin Ave., Kharkov 61103, Ukraine

Fiz. Nizk. Temp. **29**, 967–969 (September–October 2003)

The spectrum of the coupled electron–ripplon oscillations of a 2D electron crystal over liquid helium is studies as a function of the holding electric field at a temperature much lower than the temperature of melting. An analysis of the spectrum near the main resonance (0,1) allowed finding both the real and imaginary components of the crystal conductivity. The imaginary part of the conductivity is shown to be in good agreement with theoretical estimates. At the same time, additional theoretical and experimental studies are necessary to clear up the possible reasons for energy losses in the electron crystal. © *2003 American Institute of Physics.*
[DOI: 10.1063/1.1614177]

The ordered electron system over the liquid helium surface—the electron or Wigner crystal (EC)—is of interest from two interconnected aspects: first, in relation to the interaction of the 2D solid with the surface of liquid helium and the properties of the helium surface, and, second, in relation to the properties of the 2D solid itself, including the features of 2D crystal melting.

As a result of crystallization the coupled electron–ripplon oscillations which are due to the interaction between plasma modes of the electron system and capillary waves can be excited in the EC.[1,2] Many aspects of the coupled oscillations are well studied. The resonance frequencies of such oscillations, calculated within the self-consistent theory,[3] agree rather well with the experimental data.[4] The resonances in EC are a reliable tool for studing the surface properties of liquid helium. The method of resonances in EC was employed to measure of the surface tension coefficients in ^{3}He–^{4}He mixtures.[5]

However, important features of the interaction of the EC with the helium surface have not been adequately studied. In particular, it is not very clear what process is responsible for the energy losses in the EC. The movement of the EC along the helium surface was studied theoretically for uniform[6] and nonuniform[7] electric fields along the surface (leading fields). The energy loss of from the EC was supposed to be a result of attenuation of the capillary waves. It follows from the experimental data[8] on the attenuation of the coupled electron–ripplon oscillations that the losses are at least two order of magnitude higher than the result predicted by the capillary wave attenuation in a comparable frequency range.

The aim of present work is study the attenuation of the coupled oscillations in the EC. Measurements are performed at various values of the holding electric field, which is one of the essential parameters of the electron–surface interaction. An electron crystal with a surface density of 6.4×10^8 cm^{-2} (the melting at temperature $T=0.56$ K) was studied at a temperature of 83 mK. The holding field was varied from $E_\perp = 640$ V/cm, corresponding to complete screening of the holding potential by the surface electrons, to $E_\perp = 1180$ V/cm.

For the measurements an experimental cell of Corbino geometry was employed. It consisted of a horizontally placed plane capacitor with plates of 2.7 cm diameter and gap of 0.2 cm. The helium surface with the electrons over it was placed approximately in the middle of the gap. The cell was adjusted at $T \sim 1.5$ K so as to obtain a uniform thickness of the helium layer above the bottom capacitor plate. The accuracy of the adjustment was better than 20 μm. The positive electric potential was applied to the bottom plate to form the holding field. The upper capacitor plate consisted of ring measuring electrodes. The ac voltage was applied to the input (exciting) electrode. The voltage caused an ac electric field in the electron layer plane and electron density variations. The variations spread out along the layer and induced a current in the output electrode. The relation between the voltage at the input electrode and current in the output electrode reflects the properties (complex conductivity σ) of the electron layer. To estimate σ from the output–input relation the solution of Maxwell's equations for the cell was used. The solution, the experimental cell, and the measurement procedure were described in detail in Ref. 9.

The experiment started from the placing of electrons on the helium surface at $T \sim 1.5$ K until complete screening of the holding potential was reached. After that the cell was cooled down to $T = 83$ mK. During the cooling the crystallization in the electron layer was observed, and the crystallization temperature was used to determine the electron density.

A voltage with an amplitude of 1 mV and a frequency in the range 1–20 MHz was applied to the input electrode, and the current induced in the output electrode was measured. In the range 1–20 MHz the resonance features in the EC were observed. The value chosen for the exciting amplitude, 1 mV, was a compromise between the necessity of having a suitable signal- to-noise ratio and of remaining in the linear measurement mode in which there is no dependence of the EC properties on the input signal. The frequency and relative amplitude of main resonance (0,1) were measured at input amplitudes of 0.3, 0.5, 1, and 2 mV and led to the conclusion that the 1 mV amplitude corresponds rather to the linear

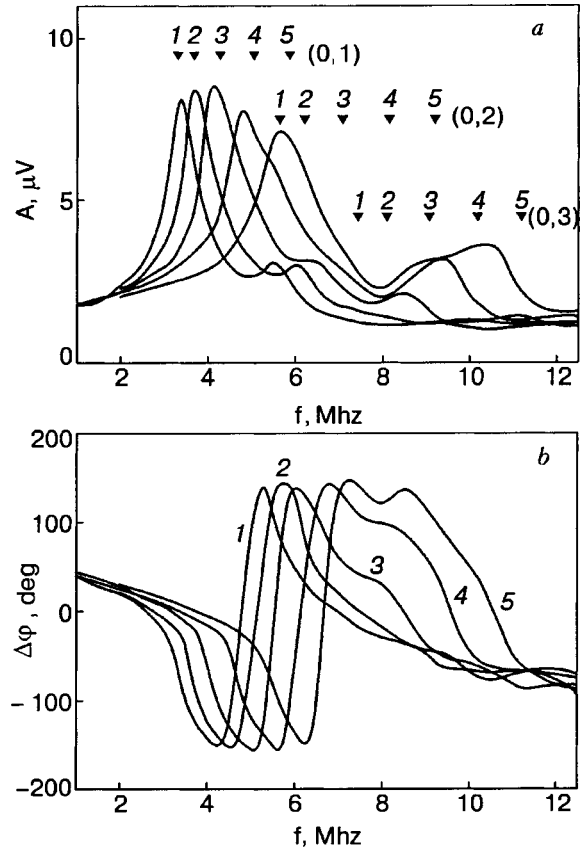

FIG. 1. Amplitude (*a*) and phase shift (*b*) of the response of an electron crystal with a surface density of 6.4×10^{-8} cm^{-2} at temperature $T=83$ mK versus the frequency of the ac exciting voltage for values of the holding field $E_\perp$, V/cm: 1150 (*1*); 1000 (*2*); 850 (*3*); 705 (*4*); 590 (*5*). The triangles correspond to the calculated frequencies of the resonant modes (0,1), (0,2), (0,3).

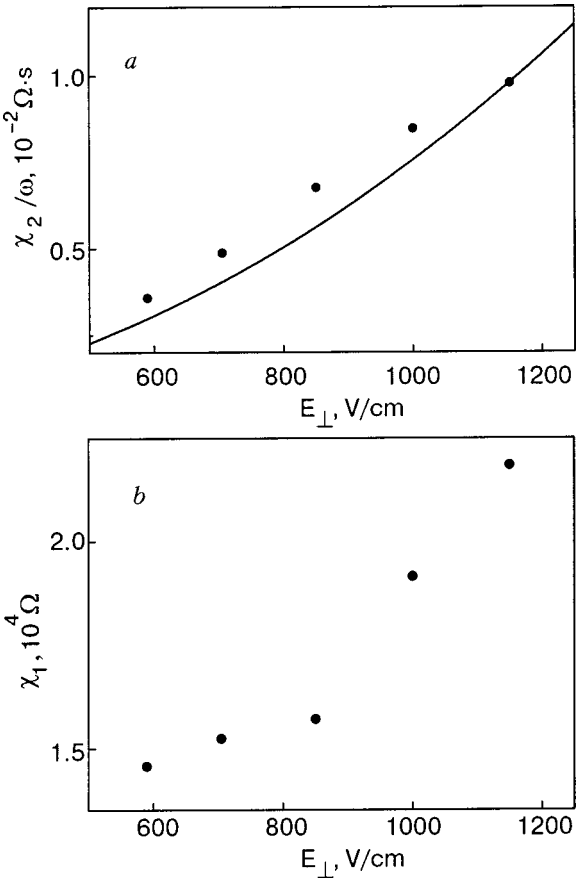

FIG. 2. Holding-field dependences of the inverse conductivity of the electron crystal measured at the resonance frequency: imaginary part (*a*) and real part (*b*). The solid line panel *a* corresponds to the theory (see text).

mode border, although there was no noticeable difference between the frequencies and relative amplitude of the (0,1) mode at the 0.3, 0.5, and 1 mV signal levels.

The primary experimental data are shown in Fig. 1. Figure 1*a* illustrates the frequency dependence of the induced current amplitude at the various holding fields. Here $f=\omega/2\pi$. On the vertical axis the voltage on the input resistance of the measuring circuit pre-amplifier is plotted. Figure 1*b* shows the phase shift between the input and output signals. As one can see in Fig. 1*a*, the response of the cell to the exciting signal has the main resonance and a few less pronounced resonances. It is also seen that as $E_\perp$ increases, the resonances other than the main are suppressed. The modes (0,1), (0,2), and (0,3) calculated according to he theory[9] are shown as triangles. The experimental frequencies of the mode (0,1) are in good accordance with the theoretical ones at all $E_\perp$. There is good enough accordance for the mode (0,2) at $E_\perp=1060$ V and $E_\perp=1180$ V. The distinctive features at frequencies around 8–11 MHz at the lowest $E_\perp$ can be interpreted as the modes (0,2) and (0,3) shifted noticeably to the lower frequency range. Probably such a shift could be a result of nonlinearities in the EC response.

The experimental values of the frequency $f_{\rm res}$ and the width $\Delta f_{\rm res}$ of the resonance (0,1) allow one to calculate the real and imaginary parts of σ, using the solution of Maxwell's equations for the cell.[9] The solution consists of two expressions reflecting relation between measured values of G_1 and G_2 in the expression for the output current J and components of the inverse conductivity of the electron layer $\chi_1=\mathrm{Re}\,\sigma_{\rm eff}^{-1}$ and $\chi_2=\mathrm{Im}\,\sigma_{\rm eff}^{-1}$:

$$J=(G_1+i\omega G_2)V_0e^{i\omega t}, \tag{1}$$

where V_0 is the exciting voltage amplitude.

Components of the inverse conductivity of the electron layer χ_1 and χ_2 can be calculated not only from $f_{\rm res}$ and $\Delta f_{\rm res}$ but from any pair of linearly independent functions of χ_1 and χ_2 which are capable of being measured.

In this paper for the calculation of χ_1 and χ_2 we used the amplitude and phase shift of the induced current at a fixed frequency. The most convenient for the calculations are the measurements at the resonance frequency because of the highest signal-to-noise ratio and suppressed influence of errors, especially systematic errors of measurement. However, the probability of nonlinear processes in the EC is present at the resonance because the leading electric field can reach high values. The problem of the influence of the leading fields needs a special analysis and is not discussed in the present report.

One can express the relation between χ_1 and χ_2 and the components of Z_1 calculated in Ref. 6:

$$\chi_1=\frac{m\omega}{ne^2}\,\mathrm{Im}\,Z_1,\quad \chi_2=-\frac{m\omega}{ne^2}\,\mathrm{Re}\,Z_1. \tag{2}$$

Although the experimental conditions and the theoretical model are not the same, the theory is rather general and is supposed to reflect adequately the main features of our experiment. Without rewriting the complete expression,[6] let us note that at low enough frequencies ($\omega < \omega_1$, where ω_1 is the lowest capillary wave mode) we have $\mathrm{Re}\, Z_1 \sim C_1$ and $\mathrm{Im}\, Z_1 \sim C_1 \gamma/\omega$, where C_1 is the electron–ripplon interaction coefficient, which depends on the electron density, temperature, holding electric field, etc., and γ is the capillary wave attenuation coefficient. It is clear that $\chi_2/\omega \sim \mathrm{Re}\, Z_1$ and $\chi_1 \sim \mathrm{Im}\, Z_1$. In Figure 2 the holding field dependences of χ_2/ω and χ_1 are shown. The solid line in Fig. 2*a* is the theoretical prediction for the dependence. The theoretical calculations do not contain any fitting or scale coefficient and lead to a good consistency with the experiment.

The real part of the inverse conductivity χ_1 increases with increasing $E_\perp$ approximately as $E_\perp^2$ (Fig. 2*b*). That is in accordance with the theory[6] inasmuch as $C_1 \sim E_\perp^2$, but the value of χ_1 is much higher than the theoretical estimations in which capillary wave attenuation was considered as the main mechanism for dissipation. The reason for the high dissipation observed remains unclear.

The change of the resonance spectrum with increasing $E_\perp$ probably (Fig. 1*a*) reflects the appearance of nonlinearity in the crystal response to the leading field, and it is quite possible that the interaction of ripplons with structural defects in the EC can play an essential role in energy losses in the crystal. In this connection additional studies of the influence of the leading field on the processes in ECs over liquid helium are highly desirable.

We would like to thank V. Dotsenko for help in the experiments.

*E-mail: sivokon@ilt.kharkov.ua

[1] C. C. Grimes and G. Adams, Phys. Rev. Lett. **42**, 795 (1979).
[2] D. S. Fisher, B. I. Galperin, and P. M. Platzman, Phys. Rev. Lett. **42**, 798 (1979).
[3] Yu. P. Monarkha and V. B. Shikin, Fiz. Nizk. Temp., **9**, 913 (1983) [Sov. J. Low Temp. Phys. **9**, 471 (1983)].
[4] V. E. Sivokon, V. V. Dotsenko, Yu. Z. Kovdrya, and V. N. Grigor'ev, Fiz. Nizk. Temp., **22**, 1107 (1996) [Low Temp. Phys. **22**, 845 (1996)].
[5] G. Deville, Phys. Rev. Lett. **72**, 135 (1988).
[6] Yu. P. Monarkha, Fiz. Nizk. Temp., **6**, 685 (1980) [Low Temp. Phys. **6**, 331 (1980)].
[7] Yu. P. Monarkha, Fiz. Nizk. Temp., **7**, 692 (1981) [Sov. J. Low Temp. Phys. **7**, 338 (1981)].
[8] V. V. Dotsenko, V. E. Sivokon, Yu. Z. Kovdrya, and V. N. Grigor'ev, Fiz. Nizk. Temp., **23**, 1028 (1997) [Sov. J. Low Temp. Phys. **22**, 772 (1997)].
[9] V. E. Sivokon, V. V. Dotsenko, S. S. Sokolov, Yu. Z. Kovdrya, and V. N. Grigor'ev, Fiz. Nizk. Temp., **22**, 715 (1996) [Low Temp. Phys. **22**, 549 (1996)].

This article was published in English in the original Russian journal. Reproduced here with stylistic changes by AIP.

Influence of the concentration of H_2-D_2 mixtures on their triple-point dewetting behavior

S. Tibus,* M. Sohaili, J. Klier, and P. Leiderer

Department of Physics, University of Konstanz, Konstanz D-78457, Germany
Fiz. Nizk. Temp. **29**, 970–974 (September–October 2003)

Triple-point dewetting of pure gases like hydrogen and deuterium on solid substrates is a well-known phenomenon. This property persists even for the mixed system of H_2 and D_2. There exists an effective triple-point temperature $T_3^{(\mathrm{mix})}$, between the T_3 of pure H_2 and that of pure D_2, which depends on the species concentrations. We present new investigations for a wide range of H_2-D_2 concentrations measured under different thermodynamic conditions. This allows us to map out $T_3^{(\mathrm{mix})}$ as function of concentration, which can be different in the melting or solidifying direction. Furthermore, it turns out that the time the system needs to reach an equilibrium state can be very long and depends on concentration. This is not observed for the pure H_2 and D_2 systems. Sometimes the relaxation times are so extremely long that significant hysteresis occurs during ramping of the temperature, even if this is done very slowly on a scale of hours. This behavior can be understood on the basis of mixing and demixing processes. Possible differences in the species concentrations in the gas, liquid, and especially solid phase of the system are discussed. A preliminary phase diagram of the H_2-D_2 system is established. © *2003 American Institute of Physics.* [DOI: 10.1063/1.1614178]

1. INTRODUCTION

Wetting of solid substrates exposed to a gas in thermodynamic equilibrium is an ubiquitous phenomenon with both fundamental aspects[1,2] and important applications.[3–5] Microscopically the wetting of a substrate by a liquid film is caused by a strong substrate–particle attraction mediated by van der Waals forces. At present an almost complete microscopic understanding of wetting on a well-defined solid substrate is available.[1,2,6] The main prediction of all these studies, for given thermodynamic parameters such as temperature and pressure, is that the thickness of the liquid film is a function of the substrate–particle and interparticle interactions. In other words, if the van der Waals force between substrate–adsorbate becomes stronger than the interparticle interaction, then complete wetting of the substrate, i.e., diverging of the thickness of the liquid layer at the coexistence line is expected. Dewetting will occur if the attraction is weak. In the latter case the growing of the liquid film will become energetically unfavorable, and dewetting will take place by forming droplets on a very thin (a few atomic layers) liquid film on the substrate. In the solid phase, however, even in the case of strong substrate–adsorbate interaction dewetting occurs due to the lateral stress induced by substrate roughness.[7,8] This leads to the T_3 dewetting as observed in our systems.

In this work, we have investigated the wetting–dewetting of both pure and binary system of H_2 and D_2 on a gold substrate. The use of D_2 as the impurity component in an H_2-D_2 dilute mixture was motivated by both its similar structure to H_2 and its different physical properties from H_2. Moreover, D_2 is a slightly weaker wetting agent in the solid phase than H_2 (Ref. 9) and has a relatively small zero-point motion (negligible in comparison with H_2; Ref. 10). Therefore the interaction between molecules and substrate atoms will be different for H_2 and D_2. Regarding substrate roughness our experiments are in a range where the difference between the two isotopes (in their pure form) is negligible. We discuss how the concentration of D_2 modifies the effective triple point of the two-component system.

2. EXPERIMENTAL PROCEDURE

All the experiments presented here were performed by utilizing surface plasmon spectroscopy, which allows one to determine the layer thickness of an adsorbed medium with

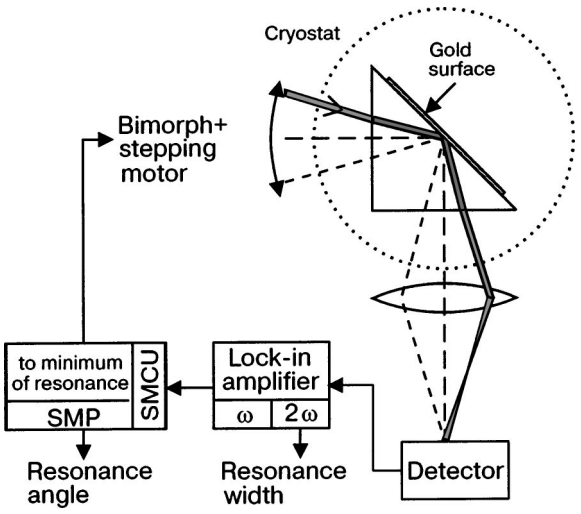

FIG. 1. Experimental setup: Surface plasmon resonance is enhanced at the interface of a gold substrate and an adsorbed medium. The angle of the incident light is modulated by means of a bimorph. Via a lock-in amplifier the intensity signal is coupled back to a stepping motor control unit (SMCU) so that the angle of minimum intensity (i.e., resonance) is maintained. From the shift in angle relative to the bare gold surface the thickness of an adsorbed film can be determined.

high resolution (up to a few tenths of a monolayer). The substrate in our measurements was a gold film (45 nm thick) evaporated onto the base of a glass prism. The experimental setup is shown in Fig. 1; more details can be found in Ref. 11. However, the signal processing was improved in comparison to the previous experiments, and it therefore resulted in more-precise measurements giving results with improved accuracy. The system was fully computer controlled, so that parameters like the temperature, for example, could be swept up and down in time very slowly in small steps. This was done several times to check for reproducibility of the measured data. The height and width of the ramping steps, as will be discussed in the results, were chosen, firstly, according to the normal relaxation of the system under investigation and, secondly, to fulfill the equilibrium thermodynamic conditions during the experiment.

3. RESULTS

Presented here are the results of wetting–dewetting measurements of both pure H_2 and D_2 as well as mixtures of both isotopes. As typical examples for the mixed systems we discuss 10% and 50% D_2 samples (these numbers are the mole-percents of D_2 in the mixture of H_2 and D_2). The samples were prepared as follows: after an adsorption isotherm of H_2 was taken at 16 K, the temperature was raised to 19 K, an adsorption isotherm of D_2 was followed in order to reach a certain concentration ratio. Afterwards, a ramping of the temperature in the range of 10 to 20 K was done. The T_3 dewetting of pure H_2 and D_2 and the effective triple-point wetting–dewetting of the mixture of them are plotted in Fig. 2. It is observed that for each mixed system the cooling and warming curves reveal a large hysteresis, which is not found for the pure H_2 and D_2 temperature runs. The hysteresis is found to be solid and stable.

The triple-point temperatures for pure H_2 and D_2 are 13.85 and 18.55 K, respectively. These temperatures, which indicate the onset of dewetting, show no significant hysteresis within an accuracy of 50 mK.

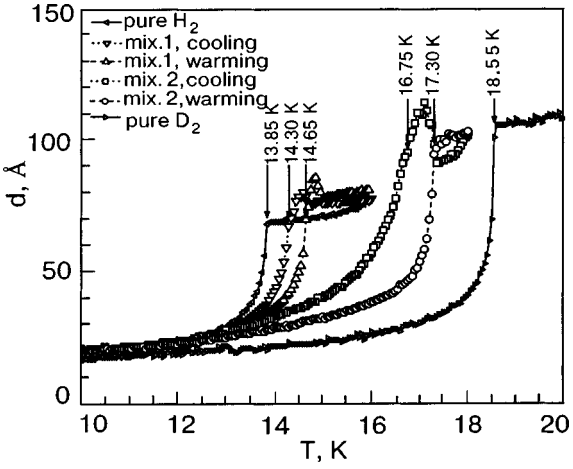

FIG. 2. The dewetting curves (film thickness d against temperature) of pure H_2 ($\lhd$), pure D_2 ($\rhd$), and on cooling ($\bigtriangledown$) and warming ($\bigtriangleup$) of a 10%-doped mixture (mix. 1), and cooling ($\square$) and warming ($\bigcirc$) of a 50%-doped mixture (mix. 2). For pure systems the cooling and warming curves trace the same path. Arrows show the positions together with the values of the wetting transition, i.e., the effective T_3.

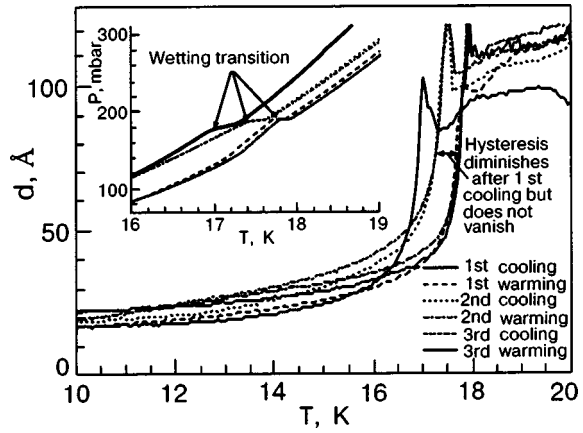

FIG. 3. The dynamics of an equimolar mixture of H_2-D_2 is shown by monitoring the film thickness d over temperature. The temperature scans are done three times. The big hysteresis during the first cooling and warming is attributed to incomplete mixing. The inset shows the associated vapor pressure curves.

For the 10%-doped system, the dewetting (cooling) and wetting (warming) temperatures are 14.30 and 14.65 K, respectively. For the 50%-doped system the dewetting and wetting temperatures are 16.75 and 17.30 K, respectively. In order to examine the genuineness of the hysteresis, another 50% mixture of H_2-D_2 was prepared, but this time at room temperature. Thereafter the adsorption isotherm of the mixture was taken at 20 K. Furthermore three complete cycles, i.e., cooling from 20 K to 10 K and return with steps of 25 mK/min and a resolved time of 2 min between two successive steps, were done. Figure 3 summarizes the results. A hysteresis of essentially the same width exists even when the measurements are done at lower ramping speeds, e.g., 10 mK/min. We should mention that during the first scan the hysteresis appeared in a more pronounced way, as shown in Fig. 3.

In the inset of Fig. 3 the associated vapor pressure curves are plotted. It shows that the slope of each curve levels off somewhere in the middle of the curve and rises again. The effective triple points of wetting and dewetting occur exactly at the point of the lower kink for both the cooling and warming curves. In order to understand this be-

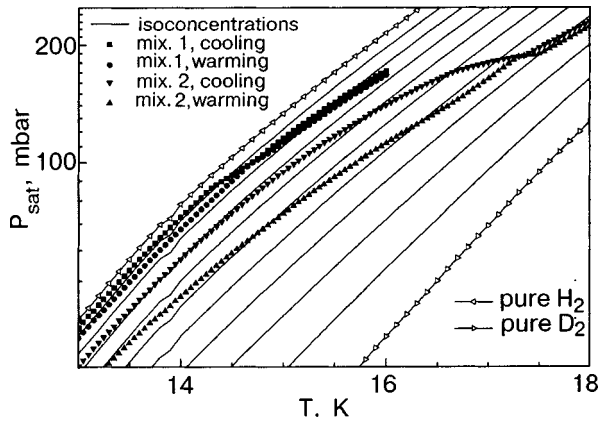

FIG. 4. The corresponding vapor pressure curves of Fig. 2. The solid lines are calculated vapor pressure curves (Eq. (1)) for different concentrations of D_2. Pure H_2 and D_2 pressure curves are also plotted.

havior, in Fig. 4 we have redrawn the supplementary vapor pressure curves of Fig. 2. The solid curves lying between the vapor pressure curves of pure H_2 and D_2 are calculated pressure curves of H_2-D_2 binary systems with different concentrations of D_2, derived from the partial pressure law

$$P_{\text{total}}(T)=C_{D_2}P_{D_2}(T)+(1-C_{D_2})P_{H_2}(T), \tag{1}$$

where C_{D_2} is the D_2 concentration in the mixture and $P_{D_2}(T)$ and $P_{H_2}(T)$ are the pressure of H_2 and D_2 at the given temperature T, respectively. Having obtained these values, one can calculate the total pressure of the mixture under the assumption that the concentrations of the species remain constant in the solid, liquid, and gas phases. It is known that this condition does not hold even for an ideal binary mixture, and the data plotted in Fig. 4 illustrate this deviation.

The data demonstrate that the concentration of D_2 in the liquid phase increases as the temperature rises and vice versa. Furthermore, the size of the hysteresis and the deviations from the predicted standard curves depend on the concentration of the D_2 phase in the mixture. The size of the hysteresis is largest for concentrations around 50% and diminishes with increasing fraction of either species.

Using Eq. (1), one can extract the D_2 concentration in the liquid phase from the measured vapor pressure curves of the pure H_2 and D_2 and their mixture. Thus we have

$$C_{D_2}=\frac{P_{\text{mix}}(T)-P_{H_2}(T)}{P_{D_2}(T)-P_{H_2}(T)}, \tag{2}$$

where $P_{\text{mix}}(T)$ is the vapor pressure of the mixture at a given temperature. Figure 5 displays the evolution of the D_2 concentration in the liquid phase of the two previously introduced sets of mixtures (see Figs. 2 and 4). The solid line, which is extended between the triple-point temperatures of the pure H_2 and D_2, is a fit to the transition line obtained from Fig. 6. The small dips in the curves, near 13.85 K, occur precisely at the position of the T_3 of pure H_2. The concentration of D_2 in the liquid phase increases gradually as the temperature rises and vice versa. The noticeable effect is a steep increase (decrease) of the D_2 concentration along the transition line during warming (cooling) of the system. In

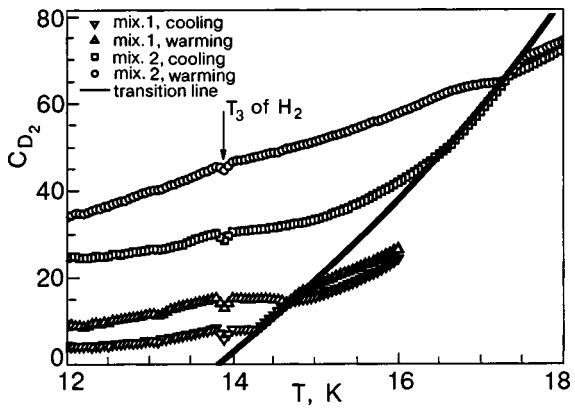

FIG. 5. The rising (falling) of the D_2 concentration in the liquid phase (Eq. (2)) during warming (cooling) for the two mixtures, as presented in Fig. 2. Along the transition line the rise is rather steep, which in turn is a sign of wetting (dewetting) when warming (cooling).

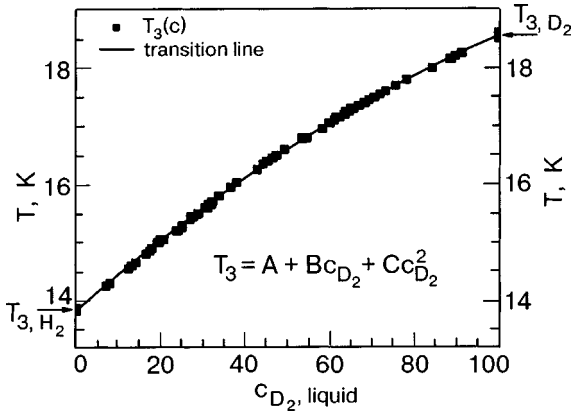

FIG. 6. The experimental data on the effective triple points of all the investigated mixtures and for pure H_2 and D_2. The solid curve is a fit to the data, with $A=13.83$ (which is the T_3 of H_2), $B=6.366\times10^{-2}$, and $C=-1.646\times10^{-4}$.

summary, in Fig. 6 the effective triple points of all the investigations are plotted against the D_2 concentration in the liquid phase. The curve fitted to the data shows that the behavior of the wetting–dewetting temperature against the liquid concentration of D_2 is not linear. (It should be pointed out that the effective T_3 values on both heating and cooling, $T_3^{(\text{up})}$ and $T_3^{(\text{down})}$, lie on this curve.)

The observed behavior can be interpreted by taking into account the temperature-dependent differences in concentration in the gaseous, liquid, and solid phases inside the sample cell. Let us consider, e.g., a mixture with a nominal D_2 concentration of 50%: i) When we start at a *high* temperature at gas–liquid coexistence, a thick liquid wetting film will be present on the substrate, as is observed in our measurement. As the temperature is lowered and the *liquidus* curve of the mixture is reached (at $\approx$17 K in this case[12]), a solid will start to form at the bottom of the sample cell, with a concentration distinctly higher than 50% (given by the *solidus* curve at that temperature). As T is decreased further, the D_2 concentration in the remaining liquid—both at the bottom of the cell, and on the surface where we measure the film thickness—drops, until eventually all of the bulk liquid has crystallized. At that point ($T_3^{(\text{down})}$) the drop in film thickness, characteristic of T_3 dewetting, starts to take place. ii) For a run starting at a *low* temperature, on the other hand, the bulk solid has—due to homogenization at $T>12$ K (Ref. 12)—a homogeneous concentration of about 50% throughout the whole sample. Upon increasing T the first bulk liquid will appear in the cell when the solidus curve is met ($\approx$15.5 K in this case). However, only at higher temperature will the thickness of our film, when in coexistence with bulk liquid of the right concentration, have reached its ''complete wetting value'' of about 100 Å, identifying T_3(up). Since $T_3^{(\text{down})}$ and $T_3^{(\text{up})}$ do not coincide, due to the paths in the phase diagram as described, a hysteresis results, as is in fact observed.

4. CONCLUSIONS

In summary we have shown that mixtures of the simple van der Waals adsorbates of hydrogen isotopes are well suited for investigations of the wetting behavior of binary systems. In pure H_2 and D_2 the adsorbed films display the

phenomenon of triple-point wetting (i.e., dewetting sets in rapidly as the temperature is decreased below T_3), and we have studied how this behavior is affected when, instead of a one-component system, a mixture of H_2 and D_2 is used (where, strictly speaking, a triple point does not exist). It is found that the feature typical for triple-point wetting—the rapid drop in film thickness below T_3—persists, but the characteristic onset temperature is different for cooling and for heating, in contrast to pure systems. We attribute this hysteretic behavior to the different concentrations of the hydrogen isotopes in the solid, liquid and gas phases, respectively. Our results suggest that the method applied here does not only yield insight into the wetting behavior of mixed systems, but a further analysis of the data should also provide detailed information on the phase diagram of H_2-D_2 mixtures.

This work is supported by the Deutsche Forschungsgemeinschaft under Grant Le 315/20 within the Priority Program ''Wetting and Structure Formation at Interfaces.''

*E-mail: Stefan.Tibus@uni-konstaz.de

[1] S. Dietrich, in *Phase Transitions and Critical Phenomena*, Vol. 12, edited by C. Domb and J. Lebowitz, Academic Press, London (1988).
[2] R. Evan, in *Liquids at Interfaces*, in *Proceeding of the Les Houches Summer School, Session XLVII*, edited by J. Charvolin, J. F. Joanny, and J. Zinn-Justin, Elsevier, Amsterdam (1990).
[3] H. Gau *et al.*, Science **283**, 46 (1999).
[4] K. Kargupta and A. Sharma, Phys. Rev. Lett. **86**, 4536 (2001).
[5] J. Bico, C. Marzolin, D. Quéré *et al.*, Europhys. Lett. **47**, 220 (1999).
[6] S. Dietrich and M. Schick, Phys. Rev. B **33**, 4952 (1986).
[7] F. T. Gittes and M. Schick, Phys. Rev. B **30**, 209 (1984).
[8] A. Esztermann, M. Heni, and H. Löwen, Phys. Rev. Lett. **88**, 055702 (2002).
[9] G. Mistura, H. C. Lee, and M. H. W. Chan, J. Low Temp. Phys. **96**, 221 (1994).
[10] D. L. Demin, N. N. Grafov, V. G. Grebinnik, V. I. Pryanichnikov, A. I. Rudenko, S. A. Yukhimchuk, and V. G. Zinov, J. Low Temp. Phys. **120**, 45 (2000).
[11] M. Sohaili, J. Klier, and P. Leiderer, J. Low Temp. Phys. **122**, 249 (2001).
[12] M. A. Strzhemechny, A. I. Prokhvatilov, G. N. Shcherbakov, and N. N. Galtsov, J. Low Temp. Phys. **115**, 109 (1999).

This article was published in English in the original Russian journal. Reproduced with stylistic changes by AIP.

Helium adsorbed on carbon nanotube bundles: one-dimensional and/or two-dimensional solids?

T. Wilson and O. E. Vilches*

Department of Physics, University of Washington, Seattle WA 98195-1560, USA
Fiz. Nizk. Temp. **29**, 975–979 (September–October 2003)

Heat capacity measurements of ^{4}He adsorbed on closed-end single-wall carbon nanotube bundles in the temperature range 1.5 K$<T<$6 K are reported. Heats of adsorption Q_{st} calculated from isotherms measured on the same calorimeter cell are included. We correlate Q_{st} features with features of the helium heat capacity. We discuss possible interpretations of the current data. © *2003 American Institute of Physics.* [DOI: 10.1063/1.1614179]

Single-layer helium films physisorbed on exfoliated graphite have been studied in great detail, both experimentally and theoretically, for a long time.[1–5] These films provided, for the first time, realizations of several phases of matter in reduced dimensionality: two-dimensional (2D) gases and fluids,[6–8] commensurate (CS)[9,10] and incommensurate (ICS) solids,[11–13] as well as the phase transitions between them as a function of temperature and coverage.

A new carbon material discovered in the last decade is carbon nanotubes.[14,15] In the form of bundles or ropes, they have a rather large surface area per gram of material, which makes them suitable for physisorption studies using somewhat conventional techniques. Although many types of carbon nanotubes exist, considerable theoretical[16–27] and some experimental[28–36] work has been done on the adsorption of many rare gas atoms and simple molecules deposited on closed-end single-wall carbon nanotube (SWNT) bundles. The attraction of the SWNT bundles is that on the interstitial channels between three nanotubes and on the grooves between two nanotubes on the outside surface of a bundle, one-dimensional (1D) chains of atoms/molecules can be adsorbed. These chains may be in the form of 1D gases and fluids if mobile[17,21,26,27] and perhaps may exist as commensurate and/or incommensurate solids.[37] Further adsorption on the outside surface of the bundles should lead to their coating with a monolayer that physically resembles adsorption on graphite, perhaps with different properties due to the curvature of the graphene surfaces, finite size, and confinement between grooves of the bundle.[37] A crossover from 1D to 2D or 3D properties is then possible, given that one can start with 1D chains that eventually, as a function of coverage and/or temperature, interact with each other in 2D and 3D space.

In this article we report on initial studies of the heat capacity of ^{4}He on SWNT bundles as a function of temperature and volume of gas adsorbed (coverage); these measurements are complemented by a few volumetric adsorption isotherms on the same bundles. Two previous somewhat indirect measurements of the heat capacity of ^{4}He on SWNT bundles have appeared.[38,39] In both cases, the prime intent of the measurement was to obtain the heat capacity of the nanotubes; ^{4}He was used as an exchange gas to cool the bundles and/or the calorimeter and inner parts of the cryostat. The ''nuisance'' ^{4}He heat capacity had to be subtracted from the total. In Ref. 39 though, the ^{4}He excess heat capacity at an estimated 80% of monolayer completion was fitted by an expression of the form $C_{film}=\alpha T+\beta T^2$. In our measurements, performed over a wide range of ^{4}He coverages, we find heat capacities with the same temperature dependence, but with α and β being coverage dependent.

A theoretical study of ^{4}He by Miller and Krostcheck[26] using density functional theory predicts that at temperatures above $T=0$ K the 1D ^{4}He is a gas/fluid, a result in agreement with expectations that in 1D there is no liquid–vapor critical point at finite temperature. At $T=0$ K these authors find coexistence between a very low-density liquid (linear density $\lambda=0.036$ Å^{-1}) and a zero-density gas. Compression of this liquid leads to solidification at about $\lambda\approx 0.2$ Å^{-1}. Studies by Gordillo *et al.*[21] and Stan *et al.*[17] on 1D ^{4}He deposited on the grooves of nanotube bundles support these results. Those studies, though, used smoothed potentials with no atomic structure for the nanotubes. Including the atomic structure of the nanotubes may lead to the formation of novel commensurate structures.[37] A unique structure found for adsorption of heavier rare gases on SWNT bundles is a ''three-line phase,'' predicted theoretically (see review by Calbi *et al.*[16]) and deduced from Ar adsorption experiments by Talapatra and Migone.[33] This phase is formed after filling of the outside grooves with 1D lines of atoms. The most favorable next place to add atoms is by forming three lines of atoms anchored at the grooves. Completion of the three-line phase should occur at a total coverage of about three times the amount of helium needed to form one compact line on the grooves.

Our experiments have searched for the 1D gas/fluid phase, the three-line phase, and the eventual crossover to 2D adsorption on a graphitelike surface (the exterior of the bundles between the grooves). In the following paragraphs we describe our experimental methods, the results obtained, and how the results relate to expectations.

The adsorption/heat capacity cell used in these measurements was made by pressing 100 mg of HiPco™ nanotube bundles[40] between two very thin-wall copper foils, soldering the edges, and adding a 1/16″ diameter thin-wall stainless steel capillary to serve as support, thermal link, and gas dosing line.

The cell was connected to a room-temperature gas dosing system. The cell was thermally connected via the fill line

to a brass plate, which in turn was thermally connected to a pumped liquid ^{4}He evaporator. The temperature of the intermediate plate could be regulated between 1.1 and 16 K; a brass shield thermally attached to the brass plate served to isolate the adsorption/heat-capacity cell from the 4.2 K walls of the vacuum can. The cell had a thermometer and heater attached to opposite sides.

We started every set of measurements by pumping our adsorption cell at room temperature to the 10^{-7} Torr range. For adsorption isotherm measurements we kept the cell at the desired constant temperature; for each point we dosed helium in and waited for pressure equilibration, sometimes many hours. For the heat-capacity measurements we dosed He at a temperature high enough that the equilibrium vapor pressure was in the 10^{-2} Torr range for annealing purposes. We used the ac calorimetry method. After a frequency/amplitude scan of the T_{ac} oscillations, we chose to work at the highest possible frequency, which was 1 Hz. We were extremely careful to keep the pressure in the cell to less than 10 Torr while doing the isotherms to prevent blowing it into the vacuum can. For essentially all but one heat-capacity measurement the pressure in the cell while doing the calorimetric measurements was always below 10^{-4} Torr, the smallest pressure we can measure, and no desorption heat capacity was observed.

While the adsorption isotherms on this cell show the same general features as the ones we obtained in an extensive study using other SWNT bundles made in Montpellier, France,[41] the calculated isosteric heats, $Q_{st}/k_B = -\partial(\ln P)/\partial(1/T)$, at very low coverages appear to be substantially higher than in our earlier work; compare Figs. 1a and 1b. In particular, the extrapolated zero-coverage Q_{st}/k_B for this sample is about 400 K or more, Fig. 1a, while for the Montpellier SWNT bundles we used in Ref. 36 the highest

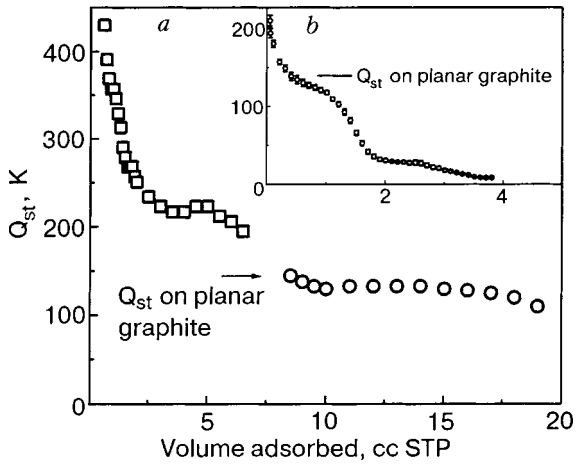

FIG. 1. *a*) Isosteric heat of adsorption of ^{4}He on HiPco™ SWNT bundles,[40] obtained from four isotherms on the heat-capacity cell at $T=14$ and 16 K ($0<V_{ads}<7$ cc STP) and 9 and 11 K (8 cc STP$<V_{ads}<$11 cc STP). *b*) Isosteric heat of adsorption of ^{4}He on Montpellier SWNT bundles,[41] from extensive set of adsorption isotherms between 2.1 and 14 K, as reported in Ref. 36. Note the agreement in the isosteric heats between both SWNT samples at the graphitelike plateau, but the differences at low coverages both in Q_{st}/k_B and in the volume adsorbed compared to that needed for completion of the plateau. Full monolayer coverage of the bundles, though, is not achieved until about 1.6 cc STP in *b* and about 24 cc STP (from heat capacity) in *a*.

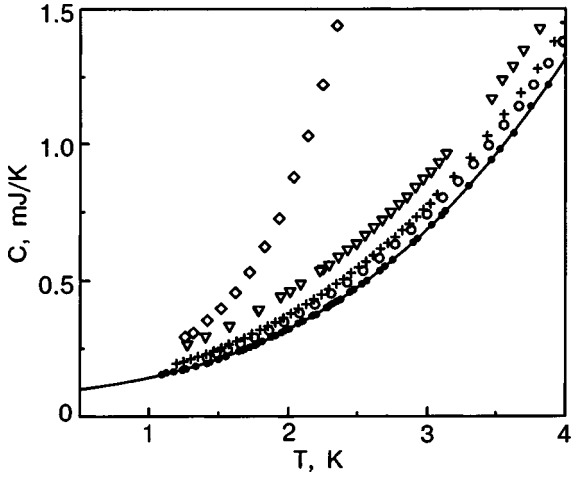

FIG. 2. Total measured heat capacity between 1.2 and 4 K: empty cell (●), 3.2 cc STP (○), 6.3 cc STP (+), 15.8 cc STP (▽), 31.1 cc STP (◇). The solid line is the fit to the background used for obtaining the heat capacity of the films.

Q_{st} was approximately 240 K. This difference, in part, may come from different pumping times of the sample cells before the experiment (cleaning higher-binding sites before the experiments), but it may be entirely due to the different characteristics of the SWNT bundles[40,41]. We observe also that the fraction of gas adsorbed before reaching the graphitelike adsorption plateau is also larger (referred to coating the bundles with a full monolayer) for this cell than for the one used in the previous work.

For the calorimetric measurements we measured first the empty cell heat capacity and assumed it to be constant. We then added (occasionally removed) controlled amounts of helium to (from) the cell and measured it again. The film heat capacity is the difference between each measurement and a polynomial fit to the background. Results for the total heat capacity for the empty cell (fitted solid line) and for the cell plus four films are shown in Fig. 2. The difference heat capacity for three of these films plus three other films is shown in Fig. 3a. Although we have measured several more coverages than shown, the ones of Fig. 3a are representative of the different regions of the Q_{st}/k_B versus amount of gas adsorbed graph, Fig. 1a. The film at 31.1 cc STP in Fig. 2 clearly demonstrates desorption in its exponential temperature dependence, confirmed by the measurable increasing vapor pressure. It is not included in the discussion.

We begin our discussion of the results by emphasizing that none of the measured specific heats is constant with temperature, not even at the lowest coverage we have measured (about 0.75 cc STP). The scatter in the film heat capacity at lower coverages is very high; improvements will require a modification of our experimental setup. Thus we do not find a 1D (at the lowest coverage) or 2D (when graphitelike adsorption starts), almost ideal gas regime as observed for both helium isotopes on graphite (2D) over the lower-density half of the first adsorbed layer. On the contrary, all the heat capacities measured increase steadily with temperature, albeit with some significant variations in their temperature dependence. Furthermore, all the measured heat capacities appear to be too small for what one would expect for 1D or 2D solids with Debye temperatures comparable to those

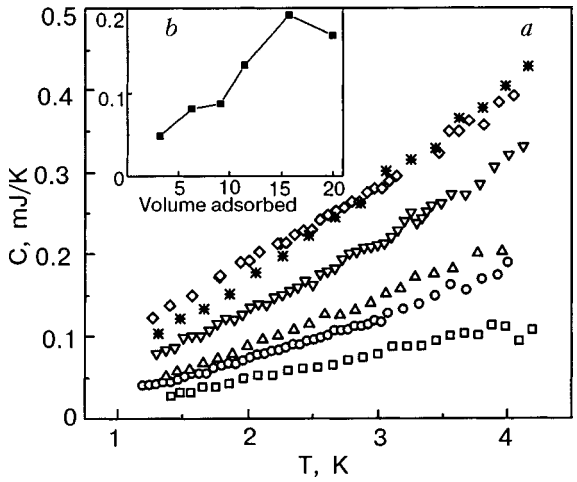

FIG. 3. *a*) Heat capacity of ^{4}He adsorbed/SWNT bundles: 3.2 cc STP (□), 6.3 cc STP (○), 9.1 cc STP (△), 11.5 cc STP (▽), 15.8 cc STP (◇), and 20.1 cc STP (∗). *b*) The total heat capacity versus volume adsorbed at 2 K. Note the two well-separated regimes, below and above 9 to 10 cc STP, corresponding to features in Q_{st}/k_B in Fig. 1a.

for ^{4}He in 2D or 3D for similar interatomic spacings. This may be due to a portion of the SWNT bundles not being in good thermal contact with the outside wall of the calorimeter cell, although it could be due too to some intrinsic property of this new type of helium films.

The very high binding energy at very low coverage ($Q_{st}/k_B \approx 450$ K at $V_{ads} \approx 0$) likely leads to very localized atoms and possibly very small specific heats. With moderate increases in coverage the heat capacity increases rapidly, correlated with the rapid decrease in Q_{st}/k_B. Figure 3b shows a heat capacity isotherm at 2 K for this set of data. By about 3 cc STP adsorbed the growth in heat capacity slows down. This slowing down corresponds to the slight rise in Q_{st} in Fig. 1a. By about 9 to 10 cc STP adsorbed the heat capacity suddenly starts to rise again. This feature corresponds very well with starting adsorption on a surface with Q_{st} comparable to that of ^{4}He on graphite; Fig. 1a. Increases in heat capacity with coverage stop at 16 to 17 cc STP adsorbed; from then on the total heat capacity decreases with increasing coverage, much like it does for both helium isotopes on graphite when 2D incommensurate solids (ICS) form. On graphite, these 2D ICS exist at densities above 0.079 Å^{-2}. Nevertheless, a direct comparison with He/graphite, as assumed in Ref. 39, cannot be made. For the lowest 2D solid density melting occurs at $T=1$ K; the melting temperature increases rather uniformly with increasing coverage. At temperatures above melting the specific heat becomes constant and near $0.9k_B$ per atom, a signal of a compressed 2D almost classical gas/fluid. For our system of He/SWNT bundles there is no observation of melting and no observation of a constant specific heat.

One possible scenario for different film/SWNT bundles regimes is the following. First, adsorption occurs in the outside grooves of the bundles in the form of very localized linear chains of helium atoms. Heterogeneous and uniform sites are occupied, and at about 3 cc STP all possible linear chains have been formed. This regime is now followed by adsorption on lines parallel and next to the atoms in the linear (groove) phase, similar to the case for Ar/SWNT bundles.[16,33] The maximum capacity of this phase is reached then, for our cell, at 9 to 10 cc STP. The increase we observe in Q_{st} at ≈ 4 cc STP could be associated with the latent heat of condensation of this phase. On a third adsorption stage, the space between the three-lines begins to be filled. This is adsorption on a bare, graphitelike curved surface, but in narrow strips between the anchored three lines of atoms. These strips could be rather long compared to their width. Simple geometric estimates using the density of helium on graphite indicate that up to 4 or 5 compressed lines of ^{4}He could be formed at full density in spaces between adjacent grooves on the ''flat'' facets of bundles, and that 7 to 9 compressed lines could be formed on ''corner tubes'' between facets of the bundles. It is remarkable that for 37-nanotube ideal bundles (they have 18 outside grooves) the total additive coverages measured in lines of atoms, for the 1D groove phase, three-line phase, and graphitelike adsorption will be in the ratio 18:54:138 at completion of the solid monolayer on a SWNT bundle, or 39% of adsorbed atoms would be in the three-lines-per-groove phase. Looking at Fig. 1a and the heat capacity measurements, we judge that completion of a first layer of atoms in our cell occurs at about 24 cc STP. If completion of the three-line phase is at 10 cc STP, experimentally the number of atoms in that phase is 42% of a monolayer, remarkably close to the geometric estimate with no absorption on interstitial channels.

In conclusion, we have measured adsorption isotherms and the heat capacity of ^{4}He adsorbed on SWNT bundles using the same cell for both measurements. We have been able to correlate features of the isosteric heat with those of the heat capacity. We have not found a 1D or 2D gas phase formed by the adsorbed atoms, but rather we observe a temperature dependence of the heat capacity that can be fitted to an expression of the form $C \approx \alpha T + \beta T^2$, with both coefficients being coverage dependent. We are continuing our experiments to obtain a complete description of the evolution of this 1D/2D system.

This research was supported by the USA NSF, Grants 986767 and 0115663. We acknowledge very useful discussions with M.W. Cole, M. Kostov, R. B. Hallock, K. Johnson, A. D. Migone, J. G. Dash, D. Cobden, J. Rehr, and M. den Nijs. Discussions with K. Chishko, L. Firlej, and B. Kuchta at the CC 2002 conference and their providing us with some of their data prior to publication have been extremely valuable.

*E-mail: vilches@phys.washington.edu

[1] J. G. Dash, *Films on Solid Surfaces*, Academic Press, New York (1975).
[2] H. Godfrin and H. J. Lauter, in *Progress in Low Temperature Physics*, Vol. XIV, edited by W. P. Halperin, North-Holland, Amsterdam (1995), p. 213.
[3] L. W. Bruch, M. W. Cole, and E. Zaremba, *Physical Adsorption: Forces and Phenomena*, Clarendon Press, Oxford (1997).
[4] M. E. Pierce and E. Manousakis, Phys. Rev. B **62**, 5228 (2000).
[5] T. N. Antsygina, I. I. Poltavsky, M. I. Poltavskaya, and K. A. Chishko, Fiz. Nizk. Temp. **28**, 621 (2002) [Low Temp. Phys. **28**, 442 (2002)].
[6] M. Bretz, J. G. Dash, D. C. Hickernell, E. O. McLean, and O. E. Vilches, Phys. Rev. A **8**, 1589 (1973); **9**, 2814 (1974).
[7] R. E. Ecke, Q. S. Shu, T. S. Sullivan, and O. E. Vilches, Phys. Rev. B **31**, 448 (1985).
[8] D. S. Greywall and P. A. Busch, Phys. Rev. Lett. **67**, 3535 (1991).
[9] M. Bretz, Phys. Rev. Lett. **38**, 501 (1997).

[10] M. J. Tejwani, O. Ferreira, and O. E. Vilches, Phys. Rev. Lett. **44**, 152 (1980).
[11] R. L. Elgin and D. L. Goodstein, Phys. Rev. A **9**, 2657 (1974).
[12] S. V. Hering, S. W. Van Sciver, and O. E. Vilches, J. Low Temp. Phys. **25**, 789 (1976).
[13] D. S. Greywall, Phys. Rev. B **47**, 309 (1993).
[14] S. Iijima, Nature (London) **354**, 56 (1991); S. Iijima and T. Ichihashi, *ibid.* **363**, 603 (1993).
[15] B. Y. Yacobson and R. E. Smalley, Scientific American **85**, 324 (1997).
[16] M. M. Calbi, M. W. Cole, S. M. Gatica, M. J. Bojan, and G. Stan, Rev. Mod. Phys. **73**, 857 (2001).
[17] G. Stan, V. H. Crespi, M. W. Cole, and M. Boninsegni, J. Low Temp. Phys. **113**, 447 (1998).
[18] Q. Wang, S. R. Challa, S. S. Scholl, and J. K. Johnson, Phys. Rev. Lett. **82**, 956 (1999).
[19] S. M. Gatica, M. W. Cole, G. Stan, J. M. Hartman, and V. H. Crespi, Phys. Rev. B **62**, 9989 (2000).
[20] K. A. Williams and P. C. Eklund, Chem. Phys. Lett. **320**, 352 (2000).
[21] M. C. Gordillo, J. Boronat, and J. Casulleras, Phys. Rev. Lett. **85**, 2348 (2000); Phys. Rev. B **61**, R878 (2000); *ibid.* **65**, 014503 (2002).
[22] M. W. Cole, V. H. Crespi, G. Stan, C. Ebner, J. M. Hartman, S. Moroni, and M. Boninsegni, Phys. Rev. Lett. **84**, 3883 (2000).
[23] M. Boninsegni, S-Y. Lee, and V. H. Crespi, Phys. Rev. Lett. **86**, 3360 (2001).
[24] M. K. Kostov *et al.*, J. Chem. Phys. **116**, 1720 (2002).
[25] M. M. Calbi and M. W. Cole, Phys. Rev. B **66**, 115413 (2002).
[26] E. Krotscheck and M. D. Miller, Phys. Rev. B **60**, 13038 (1999).
[27] A. Siber, Phys. Rev. B **66**, 205406 (2002).
[28] W. Teizer, R. B. Hallock, E. Dujardin, and T. W. Ebbesen, Phys. Rev. Lett. **82**, 5305 (1999); **84**, 184(E) (2000).
[29] S. Talapatra, A. Z. Zambano, S. E. Weber, and A. D. Migone, Phys. Rev. Lett. **85**, 138 (2000).
[30] S. E. Weber, S. Talapatra, C. Journet, A. Zambano, and A. D. Migone, Phys. Rev. B **61**, 13150 (2000).
[31] M. Muris *et al.*, Langmuir **16**, 7019 (2000).
[32] M. Muris, N. Dupont-Pavlovsky, M. Bienfait, and P. Zeppenfed, Surf. Sci. **492**, 67 (2000).
[33] S. Talapatra and A. D. Migone, Phys. Rev. Lett. **87**, 206106 (2001).
[34] Y. H. Kahng, R. B. Hallock, E. Dujardin, and T. W. Ebbesen, J. Low Temp. Phys. **126**, 223 (2002).
[35] T. Wilson, A. Tyburski, M. R. DePies, O. E. Vilches, D. Becquet, and M. Bienfait, J. Low Temp. Phys. **126**, 403 (2002).
[36] T. Wilson and O. E. Vilches, accepted for publication in Physica B (April 2003).
[37] L. Firlej and B. Kuchta have modeled numerically the adsorption of He on a single carbon nanotube and a bundle of three nanotubes, observing the formation of a commensurate phase (private communication).
[38] J. Hone, B. Battlogg, Z. Benes, A. T. Johnson, and J. E. Fischer, Science **289**, 1730 (2002).
[39] J. C. Lasjounias, K. Biljakovic, Z. Benes, J. E. Fischer, and P. Monceau, Phys. Rev. B **65**, 113409 (2002).
[40] HiPcoTM SWNT bundles, prepared by laser ablation using Fe as catalyst, can be purchased from Carbon Nanotechnologies. Our particular sample had 98% bundles. The diameter of the individual nanotubes is stated as about 1 nm.
[41] We thank Prof. Michel Bienfait from CRMC2 and Luminy, Marseille, France, for giving us a sample of SWNT bundles fabricated in Montpellier, France, see C. Journet *et al.*, Nature (London) **388**, 756 (1997). These bundles were made by the electric-arc method using Ni–Y as catalyst and are not purified. The diameter of these nanotubes is about 1.3 nm, with 1.7 nm between adjacent nanotubes in the bundles.

This article was published in English in the original Russian journal. Reproduced here with stylistic changes by AIP.

Orientational ordering in monolayers of ortho–para hydrogen

V. B. Kokshenev*

Departamento de Física, Universidade Federal de Minas Gerais, Caixa Postal 702, Belo Horizonte 30123-970, Minas Gerais, Brazil

N. S. Sullivan

Physics Department, University of Florida, PO Box 118400, Gainesville, FL 32611-8400, USA
Fiz. Nizk. Temp. **29**, 980–984 (September–October 2003)

We discuss orientational ordering in monolayers of solid hydrogen in view of recent experimental findings in NMR studies of $(\text{ortho})_c-(\text{para})_{1-c}$-hydrogen mixtures on a boron nitride substrate. Analysis of the temperature–concentration behavior for the observed NMR frequency splitting is given on the basis of a two-dimensional $(J=1)_c-(J=0)_{1-c}$-rotor model with the quadrupolar coupling constant $\Gamma_0=(0.50\pm 0.03)$ K and the crystalline field amplitude $V_0=(0.70\pm 0.10)$ K derived from experiment. The two distinct pararotational short-range ordered structures are described in terms of the local alignment and orientation of the polar principal axis and are shown to be due to the interplay between the positive and negative crystalline fields. It is shown that the local structures observed below the 2D site-percolation threshold $c_p=0.72$ are rather different from the ferromagnetic-type para–rotational ordering suggested earlier by Harris and Berlinsky. [DOI: 10.1063/1.1614181]

1. INTRODUCTION

Careful studies at low temperatures of the thick films (from 2 to 12 monolayers)[1,2] and monolayers[2,3] of ortho–para hydrogen on boron nitride (BN) substrates revealed new short-range frozen structures at low ortho-H_2 concentrations. Besides the analog of the known[4–13] quadrupolar glass (QG) phase that emerges[2] in monolayers below the concentration $c_p=0.72$, which is apparently close to the site-percolation threshold[14] in the honeycomb lattice, uncommon pararotational (PR) phases, denoted PR-A and PR-B, have been discovered.[2,3] They are demarcated by a crossover temperature $T_x^{(\exp)}(c)$ at which the NMR frequency splitting passes through zero (see 2D diagram in Fig. 1). Distinct from of the $Pa3$ structure known in bulk hydrogen, the herringbone (HB) and pinwheel (PW) 2D long-range ordered structures have been the subject of scientific interest since 1979, when Harris and Berlinsky made their famous mean-field theory predictions.[15] Meanwhile, thorough experimental studies on grafoil[16,17] and BN[2,3] substrates have registered only the PW orientational order at sufficiently high concentrations, i.e., above the percolation limit c_p.

Analysis is given within the scope of the site-disordered microscopic 2D $(J=1)_c-(J=0)_{1-c}$-rotor model, which is introduced on the basis of the 3D-rotor analog developed earlier[18–21] for an in-depth study of the QG phase. We will give a microscopic explanation of the observed temperature–concentration behavior for the orientational local-order parameters related to the NMR line shapes. We will show that the PR-A and PR-B short-range correlated structures are due to the interplay of the frustrated o-H^2-molecular exchange interaction with the molecule–substrate interaction.

2. MICROSCOPIC DESCRIPTION

Description of the orientational degrees of freedom of the site-disordered ortho–para-hydrogen system with pure electrostatic quadrupole–quadrupole (EQQ) intermolecular interactions has been discussed extensively within the context of the 3D QG problem.[6,8,12,18] In general, the thermodynamic rotational states of a given ortho molecule located at a site i are characterized by a second-rank local tensor that has only five independent components: the three principal local axes (given by vector $\mathbf{L}_i$), and the alignment $\sigma_i\langle(1-3\hat{J}_{zi}^2/2)\rangle_T$ and the eccentricity $\eta_i=\langle\hat{J}_{xi}^2-\hat{J}_{yi}^2\rangle_T$ defined with respect to the $\mathbf{L}_i$ axes. (Here $\hat{J}_{\alpha i}$ stands for the angular-operator rotational moment of a given ortho-molecule located[8] at site i, and $\langle\ldots\rangle_T$ refers to a thermodynamic average at temperature T.) A thermodynamic description, given in terms of the local molecular fields $\varepsilon_{\sigma i}$ and $\varepsilon_{\eta i}$ conjugate to the local order parameters and extended by the crystalline field h_i can be introduced[18,19] on the basis of the fundamental local-order-parameter equations, namely

$$\sigma_i=1-\frac{3\cosh(\sqrt{3}\varepsilon_{\eta i}/2T)}{2\cosh(\sqrt{3}\varepsilon_{\eta i}/2T)+\exp[3(\varepsilon_{\sigma i}+h_i)/2T]}; \quad (1)$$

$$\eta_i=\frac{3\sinh(\sqrt{3}\varepsilon_{\eta i}/2T)}{2\cosh(\sqrt{3}\varepsilon_{\eta i}/2T)+\exp[3(\varepsilon_{\sigma i}+h_i)/2T]}. \quad (2)$$

These equations follow from the conditions of local equilibrium[10] and they are shown[19] to be consistent with the density-matrix representation.[7] In what follows, we restrict our consideration to a reduced set of local order parameters $\{\mathbf{L}_i,\sigma_i\}$ with $\eta\equiv 0$ which corresponds to the so-called "powder approximation" common[5] in NMR theory applications. This description ignores the local field $\varepsilon_{\eta i}$, conjugate

to the local eccentricity η_i, and Eqs. (1) and (2) (where $\varepsilon_{\sigma i}=\varepsilon_i$ and $\varepsilon_{\eta i}=0$) are therefore reduced to

$$\frac{1-\sigma_i}{1+2\sigma_i}=\exp\left[-\frac{3}{2}\frac{(\varepsilon_i+h_i)}{T}\right]$$

$$\text{with}\quad \varepsilon_i=-\sum_{j\neq i}^{z} J_{ij}\sigma_j c_j. \tag{3}$$

Here the effective exchange interaction J_{ij} and the crystalline field h_i are given by

$$J_{ij}=-\frac{3}{2}\Gamma_0 P_{20}(L_{zi})P_{20}(L_{zj})\quad\text{and}\quad h_i=\frac{2}{3}V_0 P_{20}(L_{zi}). \tag{4}$$

This reduced mean-field description formally follows from the truncated 2D Hamiltonian given for N quantum rotors with z neighbors placed in the plane, namely

$$\hat{H}_N=-\sum_{i=1}^{N}\sum_{j\neq i}^{z} J_{ij}\hat{\sigma}_i\hat{\sigma}_j c_i c_j-\sum_{i=1}^{N} h_i\hat{\sigma}_i c_i$$

$$\text{with}\quad \hat{\sigma}_i=1-\frac{3}{2}\hat{J}_{zi}^2. \tag{5}$$

Here c_i is a random occupation number whose mean, given by the configurational average, is the concentration: $c=\langle c_i\rangle_c$; $\hat{J}_{zi}$ is a z projection of the angular momentum operator in the local principal coordinate system. In turn, Γ_0 stands for the EQQ coupling constant and V_0 is the crystal-field amplitude; $P_{20}(L_{zi})=(3\cos^2\Theta_i-1)/2$, where Θ_i is the polar angle of the principal molecular axis $\mathbf{L}_j$.

In bulk hcp solid ortho–para-hydrogen the coupling constant Γ_0 and the amplitude V_0 are well established theoretically; such is not the case for commensurate $\sqrt{3}\times\sqrt{3}$ solid monolayers. The magnitudes of $\Gamma_0=6Q^2/(25R_0^5)$ (Q is the molecular electrostatic quadrupole moment and R_0 is the nearest-neighbor molecular separation) calculated for graphite and BN substrates are 0.534 K[15] and 0.470 K,[2] respectively. The approximate estimates for the crystal-field amplitude $|V_0^{(\exp)}|\approx 0.6$–$0.8$ K for grafoil[22] and $|V_0^{(\exp)}|\approx 0.6$ K for BN[17] were derived from the observed NMR line shapes. As is seen from Fig. 1, the experimentally established position of the order–disorder boundary is consistent for the cases of grafoil[16] and BN[2] substrates (shown by crosses and triangles, respectively, in Fig. 1). On the other hand, the PW–PR boundary (bounded by points *a* and *b* in the inset of Fig. 1) exists only for positive crystalline fields. These yield the following fundamental model parameters

$$\Gamma_0=(0.50\pm 0.03)\ \text{K}\quad\text{and}\quad V_0=(0.70\pm 0.10)\ \text{K} \tag{6}$$

which are needed to specify our estimates based on the 2D $(J=1)_c$–$(J=0)_{1-c}$-rotor model given in Eqs. (3)–(6).

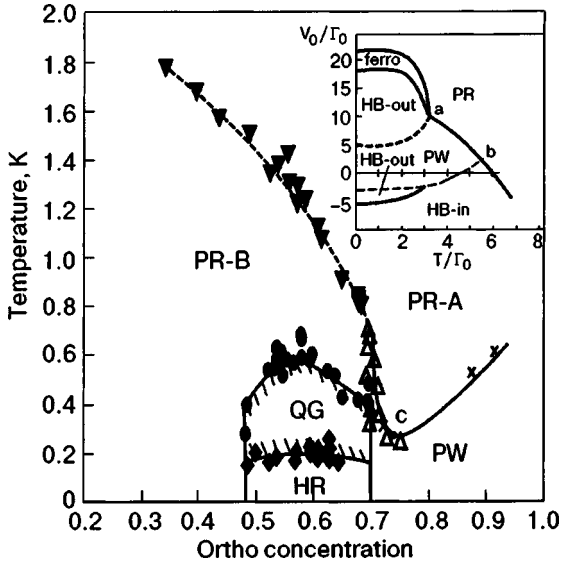

FIG. 1. Phase diagram for site-disordered monolayers of ortho–para-hydrogen $(o\text{-H}^2)_c(p\text{-H}^2)_{1-c}$ mixtures. The symbols refer to observed changes in the NMR line shapes reported in the literature: *crosses* for hydrogen monolayers on graphite, Ref. 16; *open triangles* for commensurate hydrogen monolayers on BN, Ref. 2. The solid symbols refer to NMR studies of Ref. 2: *solid circles*, transitions to the quadrupolar glass (QG) state; *diamonds*, transitions to the hindered rotor (HR) state. The *inverted triangles* refer to the vanishing of the small splitting of the NMR lines in the pararotational state. Inset: theoretical phase diagram from Fig. 2 of Ref. 15; *a* and *b* are the tricritical points,[15] and *c* is the minimum in the observed PR–PW transition temperatures.

3. MACROSCOPIC DESCRIPTION

The phase diagram for the pure $J=1$ rotor system on a 2D triangle solid lattice was scaled by Harris and Berlinsky[15] in terms of the EQQ coupling constant Γ_0 and the crystal-field amplitude V_0 of both signs (see insert in Fig. 1). The PR phase was postulated as a single ferromagnetic-type structure that can be given as $\{\Theta_i=0,\sigma_i=\sigma_0\}$. Moreover, one can see that the equation for the PR alignment σ_0 obtained by minimization of the relevant free energy (see Eq. (17) in Ref. 15) is equivalent to Eqs. (2)–(6) with the adopted parameter set $z=6$, $\varepsilon_i=\varepsilon_0=-9\Gamma_0\sigma_0$, $J_{ij}=-3\Gamma_0/2$, and $h_i=h_0=2V_0/3$, which corresponds to a ferrorotational-type (FR type) local structure given by $\Theta_i=\Theta_j=0$ and $\sigma=\sigma_0$.

A description for the long-range orientationally disordered, but locally correlated PR-A phase is introduced through the short-range order parameter $\sigma_A(c,t)=\langle\sigma_i(T)\rangle_c^{(PRA)}$, where a configurational average is limited by the PR-A temperature–concentration region shown in Fig. 1. Application of this average procedure to both the sides of Eq. (4) can be presented in the following form, namely

PRA:

$$\frac{1-\sigma_A}{1+2\sigma_A}=\exp\left[-\frac{V_0}{T}-\frac{3}{2}\left(\frac{\varepsilon_{1A}+\delta\varepsilon_{1A}}{T}\right)+\frac{9}{8}\left(\frac{\varepsilon_{2A}}{T}\right)^2\right]. \tag{7}$$

Unlike the case of the QG, we assume here that fluctuations of the local alignment (or the quadrupolarization) are small. The same assumption is made for the crystalline field given by the mean $h_{1A}=2V_0/3$. The local fluctuations of the molecular field are introduced through the mean $\varepsilon_{1A}=J_{1A}zc^{5/2}\sigma_A$ (with $J_{1A}=-3\gamma_{1A}\Gamma_0/2$ and with $z=6$) and the variance $\varepsilon_{2A}^2=3J_{2A}^4zc(1-c)(1-\sigma_A^2)/8T^2$ and are estimated[1)] within the Gaussian distribution justified in Ref. 19). Taking the Zeeman-field local polarization effects18 into account by the mean $\delta\varepsilon_{1A}=-J_{2A}^2zc\sigma_A(1-\sigma_A^2)/T$, we have analyzed[2)] the concentration behavior of the observed[22] NMR frequency splitting given in Fig. 8 of Ref. 2 for T

$=0.65$ K and $T=0.546$ K. Analysis is given with the help of Eqs. (2)–(6) where the polar–principal-axis correlation parameters γ_{1A} and γ_{2A}, namely,

$$\gamma_{1A}=\langle P_{20}(L_{zi})P_{20}(L_{zj})\rangle_c^{(PRA)}$$

$$\text{and}\quad \gamma_{2A}=\sqrt{\langle P_{20}^2(L_{zi})P_{20}^2(L_{zi})\rangle_c^{(PRA)}} \tag{8}$$

are treated as fitting parameters. In the particular cases of the FR type ($\Theta_i=\Theta_j=0$) and AFR type ($\Theta_i=0,\Theta_j=\pi/2$) locally correlated structures are characterized by $\gamma_1=\gamma_2=1$ and $\gamma_1=-\gamma_2=-1/2$, respectively. For the PR-A phase we have derived[23] $\gamma_{1A}^{(\exp)}=-1/3$ and $\gamma_{2A}^{(\exp)}\approx 0.75$. This local structure is in a way similar to that in the PW phase modified by orientations of in-plane rotors which show out-of-plane orientations.

As is seen from Fig. 1, the long-range disordered PR-B phase is stable at low temperatures ($T<V_0$) and low concentrations ($c<c_p$), where the site-dilution effects are expected to be more pronounced than in the PR-A phase. The short-range orientational arrangement results from the interplay between the random EQQ coupling and the random negative crystalline fields. Adopting for the latter a Gaussian distribution, and taking into account its variance h_{2B} (with the mean $h_{1B}=2V_0/3$) one finds, after elaboration of the configurational average in Eq. (3), the effective amplitude of the crystalline field can be introduced as

$$V(c,T)=V_0\left(1-\frac{T_x^{(\exp)}(c)}{T}\right)\quad \text{for}\quad T\approx T_x^{(\exp)}(c). \tag{9}$$

Here $T_x^{(\exp)}(c)$ is a crossover temperature between the PR-A and the PR-B structures, corresponding to a reconstruction of the local order from $\sigma_A^{(\exp)}(c,T)>0$ to $\sigma_B^{(\exp)}(c,T)<0$ (shown by the dashed line in Fig. 1).

The explicit form in Eq. (9) follows from $h_{2B}=(\langle\Delta h_i^2\rangle_c^{(PRB)})^{1/2}=2(2V_0T_x)^{1/2}/3$, where T_x is approximated by the observed PRA–PRB boundary. An analysis of the observed PR-B quadrupolarization σ_B is given through the averaged Eq. (9), namely,

PR-B:

$$\ln\left(\frac{1-\sigma_B}{1+2\sigma_B}\right)+\frac{V_0}{T}\left(1-\frac{T_x^{(\exp)}(c)}{T}\right)$$
$$-9\left(\frac{\gamma_{2B}\Gamma_0}{T}\right)^2 c\sigma_B(1-\sigma_B^2)=0. \tag{10}$$

Treating the PR-B phase as a precursor of the 2D QG phase, in Eq. (10) we have omitted all molecular-field local ordering effects. As in the QG case, we have therefore adopted $\langle\varepsilon_i\rangle_c^{(PRB)}=\delta\varepsilon_{1B}$, employed in Eq. (7) for the PR-A phase. Analysis of the available experimental data for $c=0.44$ (with $T_x^{(\exp)}=1.64$ K; see Fig. 12 of Ref. 2) on the temperature dependence of the short-range orientational order parameter in PR-B, given with the help of Eq. (5), results[23] in, approximately, $\gamma_{1B}=0$, $\gamma_{2B}=1$, which in a way is characteristic for the QG local order.

The observed order parameters $\sigma_A^{(\exp)}$ and $\sigma_B^{(\exp)}$ vanish at a certain crossover temperature $T_x(c)$ associated with the PRA–PRB boundary $T_x^{(\exp)}(c)$ (shown by the dashed line in Fig. 1). For concentrationsc $c\leqslant c_p$ this boundary can be therefore deduced from the conditions $\sigma_A(c,T_x)=\sigma_B(c,T_x)$

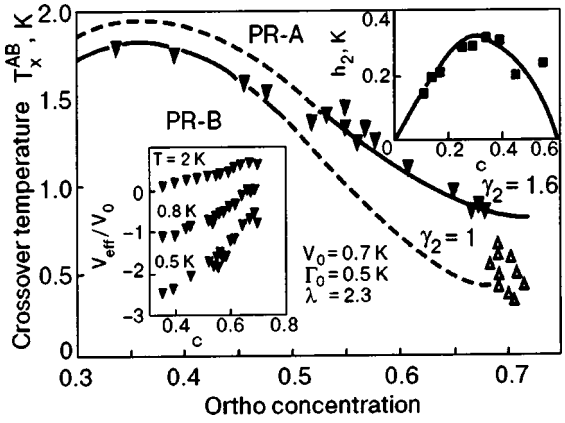

FIG. 2. Pararotational A–B crossover temperature against concentration. The symbols refer to the experimental points represented in Fig. 1: *solid inverted triangles*, vanishing of NMR doublet, Ref. 2; *open triangles*, onset of PW state in the anomalous upturn region of the phase transition boundary, Ref. 2. The *lines* designate solutions of Eq. (6) for an adjustable parameter $\lambda=2.3$. Other parameters shown include the fitting parameter γ_2. Inset: left; concentration dependence of the effective crystalline field at distinct temperatures derived from experiment[2] using Eq. (9); right, the variance of the crystalline field in bulk ortho–para-H_2 (*squares*, from the inset in Fig. 5 of Ref. 20).

$=0$. To satisfy the boundary observation conditions, the interplay between the fluctuating crystalline and Zeeman-type molecular fields for $T_0<T\leqslant T_x$ is made implicit in the form $8V_0(T-T_0)-9\varepsilon_2^2(c,T)=0$, where $T_0=9h_2^2/8V_0$ plays the role of T_x when the competing fluctuations the EQQ field are ignored. The variance h_2 was studied[20] in detail for the 3D disordered PR phase in $o-p$-H_2 systems for temperatures $0.80\ \text{K}<T\ll 4.9$ K. As is seen from the right insert in Fig. 2, unlike the mean of the crystal-field $h_1^{(3D)}$, its variance depends strongly on the overall concentration, i.e., $h_2^{(3D)}\sim c(c_M-c)$ and disappears at the highest concentration for the 3D QG state, $c_M=0.55$ (for the 3D phase diagram see Fig. 2 in Ref. 19). In the 2D case c_M is very close to the threshold concentration c_p. Therefore, we adopt $V_2\sim c(c_p-c)$, which reduces the aforegiven boundary observation condition to the following cubic equation:

$$T_x^3-T_0(c)T_x^2-\left(\frac{3}{2}\gamma_2\Gamma_0\right)^4\frac{c(1-c)}{2V_0}=0 \tag{11}$$

$$\text{with}\quad T_0=8V_0\left[\lambda\frac{c}{c_p}\left(1-\frac{c}{c_p}\right)\right]^2.$$

Treating λ as an adjustable parameter characterizing the scale of the crystal-field fluctuations, we analyze in Fig. 2 the physical solution T_x of Eq. (11) by comparing it with the observed PRA–PRB boundary. Taking into account the above analysis for the PR-B and PR-A phases, we adopt $\gamma_2=1$ as a typical value. As is seen from Fig. 2, the idea that the disordered PRB phase is constructed from mostly disordered ''in-plane'' rotors is corroborated by experimental observations.[2] On the other hand, our consideration of the reduced orientational degrees of freedom fails to give quantitative descriptions above $c=0.45$. The unphysical value $\gamma_2>1$ deduced from experimental data in Fig. 2 signals the existence of ignored local order parameters (e.g., $q_\sigma\neq\sigma^2$),

which (similar to the case of the 3D QG given in Eq. (6) of Ref. 18) can play an appreciable role near the crossover temperature. A complete analysis should be given beyond the ''powder approximation'' and based on the fundamental order-parameter Eqs. (1), (2) given for both the local alignment and the eccentricity.

4. CONCLUSIONS

We have discussed the short-range orientationally correlated structures discovered[2,3] in monolayers of $(o\text{-}H_2)_c$–$(p\text{-}H_2)_{1-c}$ on a BN substrate. Analysis of the temperature–concentration behavior for the observed NMR line shapes, related to the short-range order parameter $\sigma(c,T)$, is given on the basis of the 2D $(J=1)_c$-$(J=0)_{1-c}$-rotor model, for which a 3D analog was employed earlier[18,19] for the QG problem. In the current study the focus is on the nearest-neighbor correlated structures observed by NMR spectroscopy in the orientationally disordered phases (shown in Fig. 1). In spite of the fact that fundamental order-parameter equations are consistent with the corresponding Eq. (17) in Ref. 15, the observed PR-A and PR-B structures are ''antiferromagnetic'' rather than ''ferromagnetic,'' as was suggested in Ref. 15 for a unique PR phase. This conclusion follows from our analysis of the observed[2,3] macroscopic quadrupolarizations $\sigma_A(c,t)$ and $\sigma_B(c,T)$ adjusted through the polar-axis correlation parameters given in Eq. (8). We have shown that the short-range correlated PR-A phase is driven by positive crystalline fields, for which thermal and spatial fluctuations overwhelm those of the short-range EQQ interactions. With decreasing temperature, the interplay between the EQQ coupling and the crystalline fields, which are both sensitive to the site-dilution and thermal-fluctuation effects, results in the PRA-PRB boundary $T_x^{(\exp)}(c)$, along which both the quadrupolarizations are zero (see the analysis in Fig. 2). The low-temperature PR phase, denominated as the PR-B phase, is driven by the negative crystalline field given near the boundary $T_x^{(\exp)}$ by Eq. (9). As in the case of the QG phase (see Fig. 4 of Ref. 19), this phase is expected to be richer than the PR-A phase, and more order parameters are therefore needed to give a complete description of the observed $\sigma_B^{(\exp)}(c,T)$. Unfortunately, the necessary experimental data (on $\Delta q_B=\langle\sigma_i^2(T)-\eta_i^2(T)\rangle_c^{(PRB)}$ are not available at the present time.

The authors acknowledge financial support by the CNPq (V.B.K.) and by the NSF-DMR-98 (N.S.S.).

*E-mail: valery@fisica.ufmg.br

[1)] One can show that for the Gaussian average $\langle\exp(\pm ax)\rangle_G=\exp[\pm ax_1-(ax_2)^2/2]$ is true for a random value x with mean x_1 and variance x_2.

[2)] The observable quadrupolarization is introduced by the relation $|\sigma^{(\exp)}(c,T)|=\nu(c,T)/3d$, where ν is the NMR frequency splitting and $d=57.67$ kHz.

[1] K. Kim and N. S. Sullivan, Phys. Rev. B **57**, 12595 (1998).
[2] K. Kim and N. S. Sullivan, J. Low Temp. Phys. **114**, 173 (1999).
[3] K. Kim and N. S. Sullivan, Phys. Rev. B **55**, R664 (1997).
[4] N. S. Sullivan, C. E. Edwards, Y. Lin, and D. Zhou, Phys. Rev. B **17**, 5016 (1978).
[5] A. B. Harris and H. Meyer, Can. J. Phys. **63**, 3 (1985).
[6] V. B. Kokshenev, Solid State Commun. **55**, 143 (1985).
[7] Y. Lin and N. S. Sullivan, Mol. Cryst. Liq. Cryst. **142**, 141 (1987).
[8] V. B. Kokshenev and A. A. Litvin, Fiz. Nizk. Temp. **13**, 339 (1987) [Sov. J. Low Temp. Phys. **13**, 195 (1987)].
[9] U. T. Hchli, K. Knorr, and A. Loidl, Adv. Phys. **39**, 405 (1990).
[10] V. B. Kokshenev, Phys. Status Solidi B **164**, 83 (1991).
[11] K. Binder and J. D. Reger, Adv. Phys. **41**, 547 (1992).
[12] K. Walasek, Phys. Rev. B **46**, 14480 (1992); Phys. Rev. **51**, 9314 (1995).
[13] V. B. Kokshenev and N. S. Sulivan, J. Low Temp. Phys. **122**, 413 (2001).
[14] M. B. Isichenko, Rev. Mod. Phys. **64**, 961 (1992).
[15] A. B. Harris and A. J. Berlinsky, Can. J. Phys. **57**, 1852 (1979).
[16] P. R. Kubik and W. N. Hardy, Phys. Rev. Lett. **41**, 257 (1978).
[17] P. R. Kubik, W. N. Hardy, and H. Glattli, Can. J. Phys. **63**, 605 (1985).
[18] V. B. Kokshenev, Phys. Rev. B **53**, 2191 (1996).
[19] V. B. Kokshenev, J. Low Temp. Phys. **104**, 1 (1996).
[20] V. B. Kokshenev, J. Low Temp. Phys. **104**, 25 (1996).
[21] V. B. Kokshenev, J. Low Temp. Phys. **111**, 489 (1998).
[22] K. Kim, *NMR Studies of Thin Films of Solid Hydrogen*, Ph.D. Dissertation, University of Florida (1999), unpublished.
[23] N. S. Sulivan and V. B. Kokshenev, New J. Phys. **5**, 35.1 (2003); URL: stacks.iop.org/1367-263/5/35.

This article was published in English in the original Russian journal. Reproduced here with stylistic changes by AIP.

A study on diffusion of H atoms in solid parahydrogen

M. Fushitani* and T. Momose**

Division of Chemistry, Graduate School of Science, Kyoto University, Kyoto 606-8502, Japan
Fiz. Nizk. Temp. **29**, 985–988 (September–October 2003)

Diffusion of hydrogen atoms in solid parahydrogen was investigated using high-resolution infrared spectroscopy. Hydrogen atoms were produced as by-products of a photoinduced reaction of nitric oxides embedded in solid parahydrogen. The diffusion of the hydrogen atoms is mainly terminated by the reaction $H+NO\rightarrow HNO$. The diffusion rate determined from the increase of the intensity of rotation–vibration transitions of HNO molecules was found to be two orders of magnitude larger than that determined by the self-recombination reaction of $H+H\rightarrow H_2$ in pure parahydrogen crystals. © *2003 American Institute of Physics.* [DOI: 10.1063/1.1614182]

INTRODUCTION

Diffusion of hydrogen atoms in solid hydrogen has attracted much attention as an object of research,[1–9] because the diffusion is believed to proceed through the exchange reaction between an H atom and a hydrogen molecule,

$$H+H_2\rightarrow H_2+H, \tag{1}$$

via quantum tunneling.[1,2] Since the activation energy of the reaction (1) in solid hydrogen is about 103 K,[3] quantum tunneling is the only possible mechanism at liquid He temperatures for the diffusion of H atoms to take place through this reaction (1).

The diffusion of H atoms in solid parahydrogen produced by x-ray or γ-ray irradiation has been extensively studied using ESR spectroscopy. The diffusion of H atoms is terminated by the self-recombination reaction

$$H+H\rightarrow H_2, \tag{2}$$

and thus the decay of the ESR signal of H atoms has been described well by second-order kinetics,[3–5]

$$\frac{d[H]_t}{dt}=k_{H-H}[H]_t^2, \tag{3}$$

where $[H]_t$ is the concentration of H atoms at time t. Since the diffusion rate of H atoms in solid hydrogen is much slower than the recombination rate of the reaction (2), the rate constant k_{H-H} in Eq. (3) has been considered to be the diffusion rate of the reaction (1). It was found that the rate k_{H-H} depends not only on temperature[3,6] and pressure[5] but also on the concentration of impurities such as orthohydrogen[1,4] and deuterium molecules.[2,7] The concentration dependence has been explained by the local distortion of the lattice due to the difference in the $H-H_2$ and H–impurity interactions.[4] The local distortion induced by the different interactions leads to a decrease of the quantum diffusion rate due to the energy difference between the initial and final states.[4] Since the interaction between a hydrogen atom and an isotopic impurity such as D_2 and HD is stronger than the interaction between a hydrogen atom and an orthohydrogen molecule, the existence of these isotopic impurities makes the diffusion rate slower than that where only orthohydrogen impurities are present.[2,7]

In this paper we report on our recent study of the diffusion of H atoms in solid parahydrogen. Hydrogen atoms were produced as by-products of the photolysis of NO molecules in solid parahydrogen. We found that the diffusion is terminated mainly by the reaction between an H atom and an NO molecule,

$$H+NO\rightarrow HNO. \tag{4}$$

Since the reaction (4) must be a diffusion-controlled reaction, the diffusion rate of H atoms in solid parahydrogen is obtained from the temporal change of the intensity of rotation–vibration transitions of HNO.

EXPERIMENTS

Parahydrogen crystals containing small amounts of NO molecules were prepared employing the same method described in Ref. 10. Briefly, pure parahydrogen gas prepared through low-temperature catalysis with ferric oxides was premixed with 10 ppm NO gas at room temperature. Nitric oxide (Sumitomo Seika, 99.999%) was used without further purification. The premixed gas was introduced into a sample cell kept at 8.4 K to grow a transparent parahydrogen crystal. The cell was made of copper, whose ends were sealed with BaF_2 optical windows for infrared spectroscopy.

An ArF excimer laser (193 nm, 2 mJ/pulse, 40 Hz) was used for the photolysis of NO in solid parahydrogen. Spectral measurements were carried out at 5.2 K using a Fourier-transform infrared (FTIR) spectrometer (Bruker IFS 120HR) combined with a liquid N_2-cooled MCT detector and a globar source. The globar light was turned on during the whole experiment.

RESULTS OF PHOTOLYSIS

Figure 1 shows FTIR spectra in the spectral regions 3800–3710, 2720–2680, 1890–1860 and 990–950 cm^{-1} before UV irradiation (a), just after the UV (193 nm) irradiation for 20 minutes (b), and 155 minutes after the UV irradiation (c). After the UV irradiation, the sample was constantly kept at 5.2 K in darkness, except for the weak light of the globar source of the FTIR spectrometer. The peaks in the region 1890–1860 cm^{-1} are assigned to the rotation–vibration transitions of NO molecules isolated in

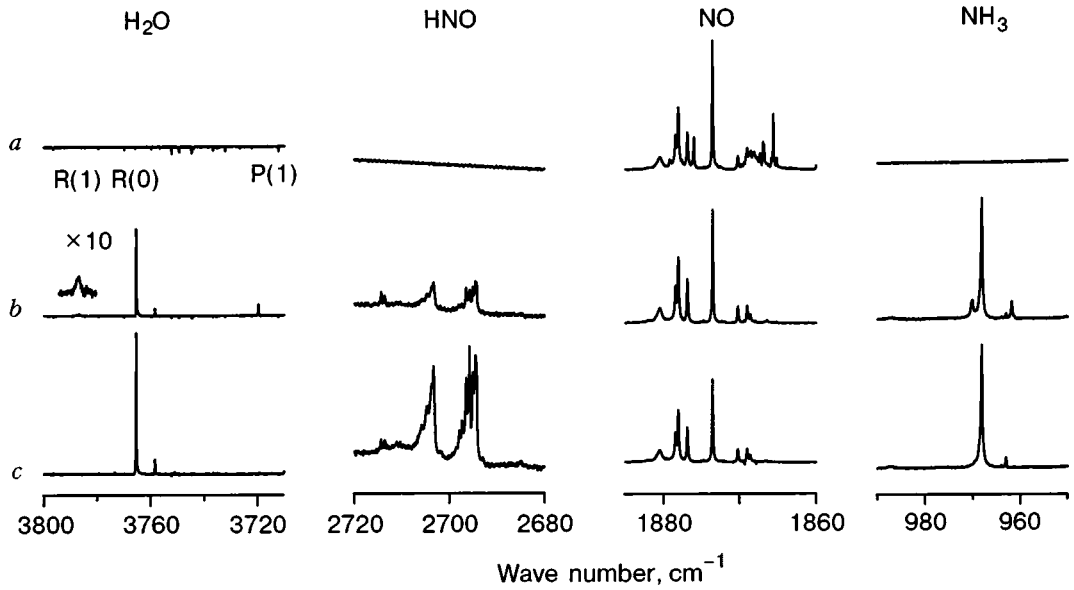

FIG. 1. FTIR spectra of H_2O, HNO, NO, and NH_3 in solid parahydrogen at 5.2 K: before UV irradiation (*a*); just after UV (193 nm) irradiation for 20 min (*b*); after 155 min in the dark (*c*).

solid parahydrogen. The corresponding absorption in the Ar matrix has been observed[11] at 1873 cm^{-1}. After the 193-nm irradiation, the absorption of NO decreased while new absorption appeared in the spectral regions of 3800–3710, 2720–2680 and 990–950 cm^{-1}, as seen in Fig. 1*b*. The peaks at 3787.1, 3765.5, and 3719.9 cm^{-1} in the region of 3800–3710 cm^{-1} are assigned to the $R(1)$, $R(0)$, and $P(1)$ transitions, respectively, of the ν_3 asymmetric vibration of H_2O molecules isolated in solid parahydrogen.[12,13] The spectrum at 990–950 cm^{-1} is identical to that for the ν_2 bending vibrational transition which we have observed previously[14] for NH_3 molecules isolated in solid parahydrogen. The spectral change from Fig. 1*a* to Fig. 1*b* clearly indicates that H_2O and NH_3 molecules were produced by the 193-nm excitation of NO molecules in solid parahydrogen.

It should be noted that one photon of 193-nm radiation is not enough to dissociate an NO molecule into N and O atoms in the gas phase, since the dissociation energy of NO molecules (6.50 eV)[15] is slightly higher than the photon energy of 193 nm (=6.42 eV). In condensed phases, however, the formation of N(^4S) atoms by 193-nm photolysis of NO molecules has been observed in solid Ar[16] and in solid hydrogen,[17] although the mechanism of the photodissociation of NO molecules in the condensed phases is yet to be explained clearly. In any case, we surmise that NH_3 molecules in the present system must be produced by the reaction between the photodissociated N atoms and hydrogen molecules as follows:

$$NO + h\nu(193\ \text{nm}) \rightarrow N + O, \tag{5}$$

$$N + 2H_2 \rightarrow NH_3 + H. \tag{6}$$

As to the O atoms produced in the reaction (5), they immediately reacted with hydrogen molecules to form H_2O via the OH radical thus:

$$O + H_2 \rightarrow OH + H, \tag{7}$$

$$OH + H_2 \rightarrow (H_3O) \rightarrow H_2O + H. \tag{8}$$

The mechanism of formation of the H_2O molecules will be discussed in more detail in a separate paper.[18] In any case, it is important to know here that H atoms were produced as by-products of the above reactions.

It is seen in Fig. 1*c* that the absorption of NO that survived from the UV photolysis further decreased after the sample was kept in darkness at 5.2 K, while new absorption appeared simultaneously in the spectral regions 2720–2680 cm^{-1}. The new absorption can be attributed to HNO molecules, as the H–N stretching vibrational transition of HNO in solid Ar has been observed[11] at 2717 cm^{-1}. Thus, the spectral change from Fig. 1*b* to Fig. 1*c* indicates that HNO molecules were produced in darkness in the UV-irradiated solid parahydrogen.

The formation of HNO is not a result of the reaction $H_2 + NO \rightarrow HNO + H$, since the reaction is endothermic by 239.6 kJ/mol ($\approx$30 000 K)[19] and thus does not proceed at low temperatures. In fact, no trace of the formation of HNO molecules was observed in crystals that had not been irradiated and were kept in darkness for several hours after the crystal growth. Thus, the production of HNO must be the result of a reaction between an H atom produced by the reactions (6)–(8) and an NO molecule surviving the UV photolysis, as shown in reaction (4). The reaction (4) is known to be exothermic to a degree of -196.3 kJ/mol.[19]

ANALYSIS

Since NO molecules are immobile in solid parahydrogen at 5 K, the reaction (4) must be a result of the diffusion of H atoms in solid parahydrogen. A migrated H atom that encounters an NO molecule forms an HNO molecule through the reaction (4). Since this reaction (4) proceeds without any barrier,[20] the rate of HNO formation corresponds to the diffusion rate of H atoms in solid parahydrogen.

The NHO formation rate must be described in terms of second-order kinetics thus:

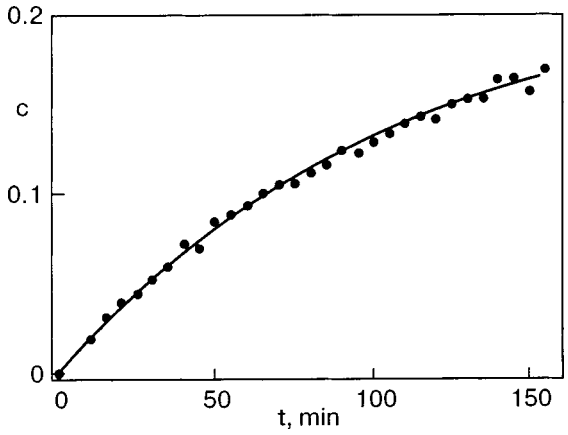

FIG. 2. Time evolution of the mole fraction of HNO in darkness. The solid curve represents the theoretical curve fitted with Eq. (11).

$$\frac{d[\mathrm{HNO}]_t}{dt} = k_{\mathrm{H-NO}}[\mathrm{H}]_t[\mathrm{NO}]_t, \tag{9}$$

where $[\mathrm{X}]_t$ is the concentration of molecule X at time t. The reaction rate $k_{\mathrm{H-NO}}$ in Eq. (9) is considered to be the diffusion rate of H atoms in solid hydrogen. For convenience, we define the mole fraction of the concentration of HNO molecules at time t as

$$c(t) = \frac{[\mathrm{HNO}]_t}{[\mathrm{HNO}]_t + [\mathrm{NO}]_t}. \tag{10}$$

By integrating Eq. (9) with respect to time t, the solution of Eq. (9) in terms of the mole fraction is found to be

$$c(t) = \frac{[\mathrm{H}]_0 \exp\{k_{\mathrm{H-NO}}([\mathrm{NO}]_0 - [\mathrm{H}]_0)t\} - [\mathrm{H}]_0}{[\mathrm{NO}]_0 \exp\{k_{\mathrm{H-NO}}([\mathrm{NO}]_0 - [\mathrm{H}]_0)t\} - [\mathrm{H}]_0}, \tag{11}$$

where $[\mathrm{X}]_0$ is the initial concentration of molecule X.

The mole fraction $c(t)$ can be obtained from the observed integrated intensities of HNO and NO molecules as

$$c(t) = \frac{I[\mathrm{HNO}]_t}{I[\mathrm{HNO}]_t + AI[\mathrm{NO}]_t}, \tag{12}$$

where $I[\mathrm{X}]_t$ is the integrated intensity of molecule X. The constant A in Eq. (12) is the ratio of the transition intensity of the H–N stretching vibration of HNO to that of the fundamental vibration of NO. In the present study, we have estimated the constant A from the condition that the sum $[\mathrm{HNO}]_t + [\mathrm{NO}]_t$ is constant at any time.

Figure 2 shows the temporal behavior of the mole fraction $c(t)$ of HNO molecules after the photolysis. The time when the UV laser was turned off was taken as the initial time, that is, $t=0$. Although some HNO molecules were produced during the photolysis, we ignored them in Fig. 2; the initial mole fraction $c(0)$ was set to zero in Fig. 2. The solid curve in Fig. 2 represents the curve fitted with Eq. (11). The best-fit parameters were $k_{\mathrm{H-NO}} = 6.22 \times 10^{-25}$ m^3/(atoms $\cdot$min) and $[\mathrm{H}]_0 = 3.95 \times 10^{21}$ atoms/m^3. Here, the initial concentration of NO was fixed to $[\mathrm{NO}]_0 = 1.99 \times 10^{22}$ molecules/m^3 which was calculated from the integrated intensity of NO assuming that the transition intensity of NO in solid parahydrogen is identical to the transition intensity (4.38×10^{-20} m/molecule) of NO in the gas phase.[21] The initial concentration of H atoms determined by the fitting is in good agreement with the calculated value $[\mathrm{H}]_0 = 2.26 \times 10^{22}$ atoms/m^3, assuming that $[\mathrm{H}]_0 = [\mathrm{NH_3}]_0 + 2[\mathrm{H_2O}]_0$ and using the transition intensity (2.55×10^{-19} m/molecule) of the ν_2 bending mode of NH_3 and the intensity (8.27×10^{-20} m/molecule) of the ν_3 asymmetric mode of H_2O in the gas phase.[21]

The rate constant $k_{\mathrm{H-NO}}$ in the reaction (4) is considered to be a diffusion rate of H atoms in the present system. It should be noted that the rate $k_{\mathrm{H-NO}} = 6.22 \times 10^{-25}$ m^3/(atoms$\cdot$min) determined above is two orders of magnitude larger than the rate $k_{\mathrm{H-H}} = 5.0 \times 10^{-27}$ m^3/(atoms$\cdot$min) reported previously for the rate of the self-recombination reaction (2) of H atoms in solid parahydrogen.[4] If both $k_{\mathrm{H-NO}}$ and $k_{\mathrm{H-H}}$ correspond to the diffusion rate of H atoms in solid parahydrogen, the rate $k_{\mathrm{H-NO}}$ must be one-half the rate $k_{\mathrm{H-H}}$. The discrepancy between the experimentally determined values of these two rates, however, is obvious.

Part of the reason for the discrepancy may be due to the difference in the condition of the crystal, such as the concentration of orthohydrogen molecules and/or vacancies or defects. Another explanation could be due to the difference in the interactions between H and NO, and between the two H atoms. Since NO molecules have a permanent electric dipole moment, the attractive interaction between an H atom and an NO molecule must be stronger than the interaction between two H atoms. By employing the classical intermolecular interaction theory,[22] the interaction between H and NO is estimated to be roughly 200 times stronger than the interaction between two H atoms. The stronger interaction between an H atom and an NO molecule may accelerate the diffusion of H atoms in solid parahydrogen containing NO molecules compared with the diffusion in a crystal without NO molecules in it. In any case, the discrepancy is so obvious that further experiments may be needed to understand the rate obtained in this study.

This study was partially supported by a Grant-in-Aid for Scientific Research of the Ministry of Education, Science, Culture, and Sports of Japan.

*Present address: Institut für Experimentalphysik, Freie Universität Berlin, Germany
**E-mail: momose@kuchem.kyoto-u.ac.jp

[1] T. Kumada, S. Mori, T. Nagasaka, J. Kumagai, and T. Miyazaki, J. Low Temp. Phys. **122**, 265 (2001).
[2] T. Miyazaki, K.-P. Lee, K. Fueki, and A. Takeuchi, J. Phys. Chem. **88**, 4959 (1984).
[3] A. V. Ivliev, A. Ya. Katunin, I. I. Lukashevich, V. V. Sklyarevskii, V. V. Suraev, V. V. Filippov, N. I. Filippov, and V. A. Shevtsov, JETP Lett. **36**, 472 (1982).
[4] T. Kumada, M. Sakakibara, T. Nagasaka, H. Fukuta, J. Kumagai, and T. Miyazaki, J. Chem. Phys. **116**, 1109 (2002).
[5] V. Shevtsov, T. Kumada, Y. Aratono, and T. Miyazaki, Chem. Phys. Lett. **319**, 535 (2000).
[6] A. Ya. Katunin, I. I. Lukashevich, S. T. Orozmamatov, V. V. Sklyarevskii, V. V. Suraev, V. V. Filippov, N. I. Filippov, and V. A. Shevtsov, JETP Lett. **34**, 357 (1981).
[7] H. Tsuruta, T. Miyazaki, K. Fueki, and N. Azuma, J. Phys. Chem. **87**, 5422 (1983).
[8] A. V. Ivliev, A. S. Iskovskikh, A. Ya. Katunin, I. I. Lukashevich, V. V. Sklyarevskii, V. V. Suraev, V. V. Filippov, N. I. Filippov, and V. A. Shevtsov, JETP Lett. **38**, 379 (1983).
[9] T. Miyazaki, H. Tsuruta, and K. Fueki, J. Phys. Chem. **87**, 1611 (1983).

[10] T. Momose and T. Shida, Bull. Chem. Soc. Jpn. **71**, 1 (1998).
[11] M. E. Jacox and D. E. Milligan, J. Mol. Spectrosc. **48**, 536 (1973).
[12] M. Fushitani, T. Shida, T. Momose, and M. Räsänen, J. Phys. Chem. A **104**, 3635 (2000).
[13] M. E. Fajardo and S. Tam, J. Chem. Phys. **115**, 6807 (2001).
[14] H. Hoshina, M. Fushitani, N. Sogoshi, and T. Momose, to be published.
[15] K. P. Huber and G. Herzberg, *Molecular Spectra and Molecular Structure IV. Constants of Diatomic Molecules*, Van Nostrand, New York (1979).
[16] J. Eloranta, K. Vaskonen, H. Häkänen, T. Kiljunen, and H. Kunttu, J. Chem. Phys. **109**, 7784 (1998).
[17] T. Kumada, manuscript in preparation.
[18] M. Fushitani, Y. Miyamoto, Z. Shimizu, and T. Momose, manuscript in preparation.
[19] *80th CRC Handbook of Chemistry and Physics*, edited by D. R. Lide, CRC, Boca Raton (1999).
[20] S. P. Walch and C. M. Rohlfing, J. Chem. Phys. **91**, 2939 (1989).
[21] K. N. Rao (Ed.), *Molecular Spectroscopy: Modern Research*, Vol. 2, Academic Press, New York (1976).
[22] A. D. Buckingham, Adv. Chem. Phys. **12**, 107 (1967).

This article was published in English in the original Russian journal. Reproduced here with stylistic changes by AIP.

Excess thermal resistivity in N_2–CO solid solution at low carbon monoxide concentration

P. Stachowiak,* V. V. Sumarokov, J. Mucha, and A. Jeżowski

Institute for Low Temperatures and Structure Research, Polish Academy of Sciences, P.O. Box 1410, Wroclaw 50-950, Poland

Fiz. Nizk. Temp. **29**, 989–991 (September–October 2003)

The results of measurements of the thermal conductivity of pure and carbon-monoxide-doped nitrogen crystals in the temperature range 1.2–26 K are presented for samples containing up to 0.7% CO molecules. It follows from a preliminary analysis that the interaction of phonons with an admixture molecule having the same mass as the host molecule is relatively weak and depends weakly on the admixture concentration within the investigated range of carbon monoxide concentrations in the nitrogen crystal. © *2003 American Institute of Physics.* [DOI: 10.1063/1.1614183]

INTRODUCTION

Crystals of nitrogen and carbon monoxide belong to the same group of the simplest molecular solids. Both of them at low temperatures have a crystallographic structure featuring cubic symmetry with four molecules in the unit cell, with molecules axes oriented along spatial diagonals of the cubic cell. Because of the displacement of the center of mass relative to the center of interaction of the CO molecule, the CO crystal belongs to the $P2_13$ space group, while N_2 belongs to $Pa3$ (Ref. 1).

Crystalline carbon monoxide forms homogeneous solutions with nitrogen at any concentration and the molecules mutually replace one another in the lattice sites.[2] The solid solution of N_2 with CO is a unique system for thermal conductivity investigation due to the equality of the masses of the nitrogen and carbon monoxide molecules. In the previous thermal conductivity admixture-effect investigations the guest atom (or molecule) possessed a mass different from that of the host; see, e.g., Refs. 3 and 4. Therefore, the effect that was observed and analyzed was regarded as an ''isotopic'' phenomenon—phonons in the investigated crystals were ''scattered by the mass difference.'' In CO:N_2 crystals the situation is different. With no mass defect one can observe phonon scattering on the different force constants and the related deformation of the lattice around the admixture molecule. In the case of nitrogen crystals doped with carbon monoxide, the deformation of the lattice is even stronger due to abovementioned displacement of the centers of mass and interaction of the CO admixture molecule.

The purpose of the experiment whose preliminary results are being presented here is the investigation of phonon scattering on difference of the force constants for the interactions between the molecules forming the crystal and the related lattice deformation around a foreign molecule embedded in the crystal.

EXPERIMENTAL

To investigate the same-mass-impurity effect in solidified nitrogen, measurements of the temperature dependence of the thermal conductivity coefficient $\kappa(T)$ were made for several samples containing intentionally introduced carbon monoxide molecules at different concentrations. The measurements were made in a ^{4}He setup which we designed ourselves and is described in Ref. 5. The measurements were made by a steady-state flow method in the temperature range 1.2–26 K. The samples were grown and measured in a glass ampoule of inner diameter 6.7 mm and length 67 mm. Two calibrated germanium thermometers were attached (spaced 37 mm apart) to the ampoule for the purpose of determining the value and gradient of the temperature. The nuclei of the crystal were obtained from the liquid phase, the main part being grown directly from gaseous phase. The growth rate of the crystal, of about 1 mm/h, was assured by a drift of the temperature of the ampoule base (about -0.3 K/h). When the crystal fully filled the ampoule, the sample was annealed for 12 h in a temperature gradient of 0.4 K/cm at a temperature slightly below the triple point of the mixture of gases used to obtain the sample. Then the sample was cooled to the temperature of liquid helium, the cooling rate for both β and α phases being 1 K/h. Passage through the phase transition region was realized for a time period of 16 h, while a temperature gradient of about 0.3 K/cm caused the phase interface to move with a velocity of about 0.5 cm/h. The samples cooled down to liquid-helium temperature appeared to be transparent, without notable cracks and voids.

The gases used in the experiment had the natural isotopic composition with impurities not exceeding 0.003% (mostly oxygen). The random error of the thermal conductivity measurements did not exceed 7%. The systematic error, which resulted mostly from inaccuracy of the geometry specification, did not exceed 5%.

RESULTS AND DISCUSSION

The results of the measurements—the temperature dependence of the thermal conductivity coefficient for the pure nitrogen crystal and for samples of N_2 containing 0.2, 0.25, 0.3, 0.5 and 0.7% CO—are plotted in Fig. 1. The dependences display the behavior typical of a dielectric crystal: initially the thermal conductivity increases with increasing temperature, and then, after reaching a maximum value, decreases exponentially. The samples containing additional phonon scattering centers—carbon monoxide admixture molecules—show at low temperatures a thermal conductivity

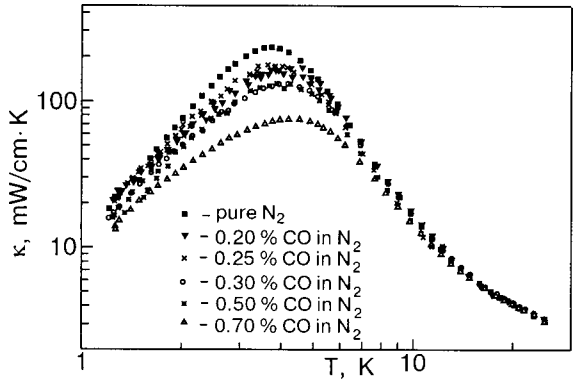

FIG. 1. Thermal conductivity of pure and carbon-monoxide-doped solid nitrogen versus temperature.

lower than that of pure nitrogen, following the expectation. For temperatures above the maxima, where phonon–phonon scattering in U-processes begin to dominate the thermal conductivity, the data points of all samples tend to the same curve.

For preliminary analysis of the data, the dependence of the reduced excess thermal resistivity ΔW^* on the concentration c of the CO admixture molecules was obtained:

$$\Delta W^*(c)=[\kappa_{\text{doped}}^{-1}(c)-\kappa_{\text{pure}}^{-1}]/c|_{T=\text{const}}.$$

In the formula, κ_{pure} and $\kappa_{\text{doped}}(c)$ stand for the thermal conductivity coefficients at a fixed temperature for the pure nitrogen crystal and the N_2:CO sample, respectively. The $\Delta W^*(c)$ curve obtained by smoothing the data for the temperature 2.5 K is shown in Fig. 2.

The dependence of reduced excess thermal conductivity on impurity concentration can be interpreted in the framework of the ''most-significant phonons'' approximation. In this approximation one assumes that for steady state flow at any temperature there exists a frequency $\omega\sim T$ such that a group of phonons of frequencies from the range $(\omega-\Delta\omega,\omega+\Delta\omega)$, where $\Delta\omega/\omega\ll 1$, carries the greatest part of the heat flux being transported in the sample. In the most-significant-phonons approximation, the contributions to the total thermal resistivity W of a sample from phonons scattered in separate mechanisms are additive. Therefore, the excess thermal resistivity $\Delta W^*(c)$ depicted in Fig. 2 can be regarded as the component related to the scattering of phonons on CO molecules. From Fig. 2 one can see that the excess resistance per molecule of the admixture hardly depends on the carbon monoxide concentration. Only a slight tendency (but still within the experimental error) toward an increase of $\Delta W^*(c)$ is observed. It could mean that for concentrations of carbon monoxide molecules in nitrogen crystal not exceeding 0.7% one is observing an interaction that leads to weakening of the phonon scattering on the carbon monoxide molecules with increasing concentration of the admixture.

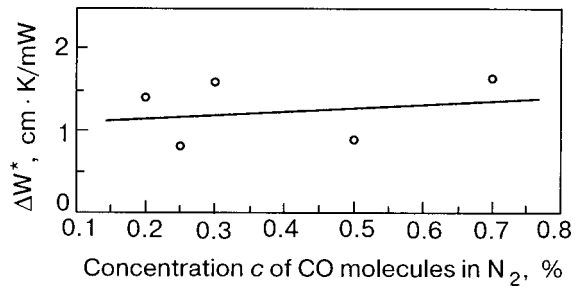

FIG. 2. Admixture effect in the N_2–CO system at 2.5 K. The solid line is a plot of the function $\Delta W^*=1.07+0.398c$.

It also should be noticed that in the N_2:CO crystal the excess thermal resistivity per unit concentration is a small number compared to that obtained for impurities having a different mass than the host; see, e.g., Ref. 6. This confirms the results of earlier theoretical investigations which have shown that the scattering of phonons on point defects with different force constants and on the deformations of the lattice around foreign impurities is less effective then the scattering resulting from a mass difference between the host and admixture molecules.[7] This also explains the earlier success of the approach in which foreign impurities in dielectric crystals are regarded as pure isotopic admixtures, e.g., in Ref. 4.

In summary, the thermal conductivity of pure and carbon-monoxide-doped nitrogen crystals has been measured in the temperature range 1.2–26 K for samples containing 0.2, 0.25, 0.3, 0.5 and 0.7% CO molecules. A simple analysis has shown that the scattering of phonons on admixture molecules possessing the same mass as the host molecule is relatively weak compared to the scattering on a molecule having a different mass. It has also been found that the interaction depends rather weakly on the admixture concentration within the investigated range of carbon monoxide concentrations in the nitrogen crystal.

*E-mail: p_stach@int.pan.wroc.pl

[1] Yu. A. Freiman and V. G. Manzhelii (Eds.), *Physics of Cryocrystals*, AIP, New York (1996).
[2] V. G. Manzhelii, A. I. Prokhvatilov, I. Ya. Minchina, and L. D. Yantsevich, *Handbook of Binary Solutions of Cryocrystals*, Begell House, New York (1996).
[3] J. E. Clemans, Phys. Rev. B **15**, 1072 (1977).
[4] F. C. Baumann and R. O. Pohl, Phys. Rev. **163**, 843 (1967).
[5] A. Jeżowski and P. Stachowiak, Cryogenics **32**, 601 (1992).
[6] Yu. A. Freiman, A. Jeżowski, P. Stachowiak, V. V. Sumarokov, and J. Mucha, Fiz. Niz. Temp. **22**, 194 (1996) [Low Temp. Phys. **22**, 148 (1996)].
[7] J. A. Krumhansl and J. A. D. Matthew, Phys. Rev. **140**, A 1812 (1965).

This article was published in English in the original Russian journal. Reproduced here with stylistic changes by AIP.

ELECTRONICALLY INDUCED PHENOMENA

Tunneling dynamics in cryocrystals: localization and delocalization

V. G. Storchak*

Russian Research Centre "Kurchatov Institute," 46 Kurchatov Sq., Moscow 123182, Russia
Fiz. Nizk. Temp. **29**, 992–1000 (September–October 2003)

The phenomenon of quantum diffusion of muonium in cryocrystals with rotational degrees of freedom is discussed. The quantum tunneling dynamics and electron transport are considered with the effects of disorder taken into account. © *2003 American Institute of Physics.*
[DOI: 10.1063/1.1614184]

1. INTRODUCTION

A vast number of kinetic processes in chemistry and biology, nuclear and solid state physics, disordered systems and liquids, etc. have to do with mass and charge transport, i.e., potential-barrier-limited dynamics of neutral particles (typically atoms) and charged particles (typically electrons or electronic complexes). At low temperatures there is no other way for a particle to overcome a potential barrier than by quantum tunneling through it. This phenomenon is called quantum diffusion (QD). The concept of quantum diffusion is introduced for diffusing particles which are heavy compared with the electron. On the other hand, a quantum-mechanical evaluation suggests that the tunneling probability is crucially enhanced for light particles. Therefore, in the context of QD the role of the positive muon (μ^+) is of particular interest because of its intermediate mass (about 200 times more than that of the electron, but about an order of magnitude less than that of the proton). Being a complete chemical analog of the proton, μ^+ captures an electron and forms the light hydrogen isotope known as muonium (Mu $=\mu^+ + e^-$). This happens in insulators and semiconductors, while in metals we deal with the ''bare'' muon. Because of the unique mass of the muon one can hardly mention any other example where quantum diffusion has been observed in such a wide temperature range as for μ^+ and Mu.[1] The other reason for the success of the quantum diffusion study using muons is the sensitivity of the muon spin relaxation (μSR) techniques (see, e.g., Ref. 2) to μ^+ and Mu dynamics.

The basic issue in nonclassical transport is whether a wavelike or particlelike description is appropriate, i.e., whether the tunneling is coherent or incoherent. This depends on whether the interaction with the environment is such as to lead to spatial localization of the wave function or to bandlike (Bloch wave) motion. One of the possible channels for localization of a particle is through its interaction with lattice excitations (phonons, librons, magnons, etc.). In a dissipative environment[3] the lattice excitations can be represented as a bath of harmonic oscillators; interaction with this environment causes a crossover from coherent quantum tunneling to incoherent hopping dynamics, when the particle ''dressed'' with the lattice excitations can be effectively thought of as a polaron.

At low temperatures, the environmental excitations are frozen out. In this case, conventional understanding suggests that the only possible channel for particle localization is the introduction of crystal disorder, which thus may dramatically change the transport properties of a solid. A well-known example is the spatial localization of electron states near the Fermi level in a disordered metallic system, which leads to a transition to a dielectric state (the Anderson transition).[4] The concept of Anderson localization suggests that the wave function of a particle in a random potential may change qualitatively if the randomness becomes large enough. Coherent tunneling of a particle is possible only between levels with the same energy (e.g., between equivalent sites); in the case of strong randomness, states with the same energy may be too distant (spatially separated) for tunneling to be effective.

Although the concept of localization by disorder has been introduced primarily in order to describe the electronic transport properties of condensed matter, it may also be applied to the quantum dynamics of heavier particles, whether charged or neutral.[5,1] Recent experimental results for positive muons as well as for muonium atoms clearly indicated that interaction with crystal excitations and crystal disorder dramatically changes the nature of tunneling dynamics for particles ~ 200 times heavier than the electron.

In this lecture we discuss recent studies on both quantum tunneling dynamics and electron transport in cryocrystals using μ^+SR techniques and paying particular attention to processes of particle localization and delocalization.

2. QUANTUM DIFFUSION VIA μ^+SR

Under-the-barrier tunneling dynamics of particles in crystalline lattice is a pure quantum-mechanical phenomenon which has no analog in classical physics. Typically, tunneling occurs between two or more potential wells which would be degenerate in a pure system. In this case the quantum-mechanical coherence between the particle's states in different wells manifests itself (the well-known example is the Bloch wave propagation of electrons in crystalline solids). The basic concept introduced to describe this phenomenon is that of a band motion (coherent tunneling) of a particle, with a bandwidth Δ determined by the amplitude of the particle's resonance transitions between the potential minima.[6,7] Particle dynamics in perfect crystal at $T=0$ presents the sim-

plest case of a band motion. The standard expression for the tunneling amplitude between the two nearest wells is given in the semiclassical approximation as (see, e.g., Ref. 8; $\hbar=1$)

$$\Delta = 2Z\nu_0 e^{-S_0}. \tag{1}$$

Here we assume that for the particle with mass $m \gg m_e$, where m_e is the electron mass, zero-point vibrations (ZPV) around local minima of the crystal potential are small as compared with the interwell separation a (or lattice constant, if there is only one minimum in the unit cell). This condition implies that tunneling splitting of the lowest levels in each well is much less than the ZVP frequency $\omega_0 = 2\pi\nu_0$, and the lowest states are well separated from the rest of the particle spectrum. The tunneling action $S_0 = \int_{\mathbf{r}_1}^{\mathbf{r}_2} p\,\mathrm{d}x$ is given by the integral along the optimal path connecting turning points $\mathbf{r}_1$ and $\mathbf{r}_2$ on different sides of the barrier; Z is the coordination number. Typically in solids $S_0 \gg 1$, which in fact is already satisfied when the barrier height U_B is only few times larger than the ZPV energy.[1] Therefore even for particles of intermediate mass like muons or muonium atoms the bandwidth turns out to be exponentially small. Nevertheless, at $T=0$ in a perfect crystal any particle is completely delocalized.

At $T\neq 0$, however, tunneling occurs against the background of the coupling with the excitations of the medium. Since Δ is so small, the interaction of the particle with environmental excitations may easily destroy the coherence and lead to particle localization. The basic characteristic of the particle interactions with the medium excitations is the frequency Ω of phase correlations damping at neighboring equivalent positions of the particle. Even at low temperatures Ω could be as large as Δ; the temperature rise results in an exponential decrease of the coherent tunneling transition.[5,1]

Here one has to distinguish different frequency regimes: those modes which have frequencies significantly larger than Δ will follow the motion of the particle adiabatically and can at best renormalize Δ; while those of frequencies of order of Δ or less can extract energy from the system during the tunneling process. The latter effect is known as dissipation in quantum tunneling,[3,9] which causes strong particle localization. Destruction of bandlike propagation and eventual localization of the muonium atom in molecular crystals of solid methanes[10] and solid nitrogen[11] due to coupling to molecular rotations at low temperatures are typical examples of this kind of effect: interaction with low-frequency rotational modes causes a crossover from coherent quantum tunneling to incoherent hopping dynamics at low temperatures.

Since Δ is small with respect to all other energy parameters in a solid, quantum dynamics is extremely sensitive to crystal imperfections. Therefore, localization of the particle often takes place at a relatively low defect concentration.

Until very recently studies of Mu diffusion have focussed on nearly perfect crystals, in which bandlike motion of Mu persists at low temperatures. Crystalline defects have been treated mainly as local traps[12] with trapping radii of the order of the lattice constant a. The justification for such an approach was that the characteristic energy of the crystalline distortion, $U(a)$, is usually much less than the characteristic energy of lattice vibrations, Θ. Unfortunately, since it does not take the particle bandwidth Δ into consideration, this comparison turns out to be irrelevant to the problem of particle dynamics, for which the crucial consideration is that Δ is usually several orders of magnitude less than $U(a)$. For example, a typical Mu bandwidth in insulators is of the order of $\Delta \sim 0.01-0.1$ K,[1] whereas $U(a)$ could be as large as 10 K. In metals the mismatch is even more drastic: typical values [$U(a) \sim 10^3$ *K* versus $\Delta \sim 10^{-4}$ K] differ by about seven orders of magnitude. Under these circumstances, the influence of crystalline defects extends over distances much larger than a. If the ''disturbed'' regions around defects overlap sufficiently, complete particle localization can result.

In this lecture we concentrate our attention on Mu quantum diffusion phenomena in cryocrystals with rotational degrees of freedom. A more general review of muon and muonium diffusion in a variety of materials may be found elsewhere.[1]

2.1. Destruction of bandlike propagation in orientationally ordered crystals: the two-phonon quantum diffusion regime

Studies of the diffusion of hydrogen atoms[15] and μ^+ in metals and of Mu diffusion in insulators and semiconductors[1] have convincingly shown the quantum-mechanical character of the phenomenon, most clearly seen at low temperatures, where the particle hop rate τ_c^{-1} increases with decreasing temperature T according to the power law $\tau_c^{-1} \propto T^{-\alpha}$, thus manifesting the onset of the coherent process. In metals, coupling to conduction electrons is the dominant scattering mechanism[16] and causes $\alpha < 1$. In insulators, where phonon scattering processes prevail, α is predicted[5,6] to be 7 or 9 at low temperatures where the absorption of single phonons shifts the energy of the diffusing particle too much for tunneling to occur and so two-phonon diagrams (which can leave the energy almost unchanged) are expected to dominate. Surprisingly, the experimental results on Mu diffusion in ionic insulators[17] indicate that α is generally close to 3; this ''universal'' power-law behavior with $\alpha \sim 3$ prompted the authors of Ref. 18 to conclude that muonium diffusion is governed by one-phonon scattering. On the other hand, in Ref. 19 it was shown that $\alpha \sim 3$ can also be obtained from two-phonon scattering processes if the actual phonon spectrum of the ionic crystal is taken into account; unfortunately, that procedure requires the introduction of adjustable parameters. This basic problem of the validity of the former or the latter remained open until recent results on Mu quantum diffusion in solid nitrogen,[11] methanes,[10] and carbon dioxide[20] presented direct experimental evidence of the dominance of the two-phonon scattering mechanism in insulators at low temperatures.

In the harmonic approximation, the transport properties of a neutral particle in a simple crystalline insulator (e.g., a monatomic or ionic crystal) depend only on the phonon modes of the lattice. For crystals composed of molecules, two additional contributions enter from the internal vibrational and rotational degrees of freedom of the molecules. Internal vibrations of molecules scarcely change the particle dynamics because of their extremely high frequencies. Molecular rotation, however, is a different matter. Two extremes are possible: the molecules may rotate almost freely in the

crystal, or the rotational motion may be severely restricted and hence transformed into torsional excitations (librons). Since typical rotational frequencies are still much higher than the particle bandwidth, in the first extreme the energy levels in different unit cells are degenerate and therefore the particle dynamics remains unperturbed. In the second extreme, the anisotropic interaction between molecules (which causes orientational ordering in the first place) changes the crystalline potential so that this degeneracy is lifted. As far as the particle dynamics is concerned, this splitting of the energy levels of adjacent sites acts as an effective disorder, creating a bias ξ. To demonstrate this, a suitable molecular lattice should be found where (a) this disorder is essentially weak and short-range and (b) both extremes can be reached in the accessible temperature range. The simplest molecular solids are the cryocrystals formed by the small, light-weight molecules, namely solid H_2, D_2, CH_4, CD_4, N_2, N_2O, CO_2, etc. In solid N_2O and CO_2 the anisotropic part of the intermolecular interaction is so strong that the lattice keeps its orientational order in the entire solid phase. In solid para-H_2 and ortho-D_2, by contrast, this interaction is so weak that orientational order cannot be reached even at the lowest temperatures. Here we discuss our study of muonium dynamics in solid nitrogen and methanes (CH_4 and CD_4) which undergo orientational ordering in the solid phase. In solid N_2 this transition takes place at $T=35.6$ K, in CH_4—at $T=20.4$ K, while in solid CD_4 partial orientational ordering occurs at $T=27$ K with a further transition to complete molecular ordering at $T=22.1$ K. These crystals show similar nonmonotonic temperature dependences of the muonium relaxation rate T_2^{-1}. Figure 1 presents the temperature dependence of the muonium hop rate τ_c^{-1} in solid nitrogen. For temperatures $T \ll \Theta$ (the Debye temperature) quantum diffusion is believed[5] to be governed by two-phonon processes, for which τ_c^{-1} is given by

$$\tau_c^{-1} \sim \frac{\tilde{\Delta}_0^2 \Omega(T)}{\Omega^2(T)+\xi^2}, \tag{2}$$

where $\tilde{\Delta}_0$ is the renormalized bandwidth for Mu diffusion and ξ is the typical difference between energy levels of the particle at adjacent tunneling sites due to static disorder.

The main feature of Eq. (2) is the minimum of $\tau_c(T)$ at $\xi \sim \Omega(T)$.

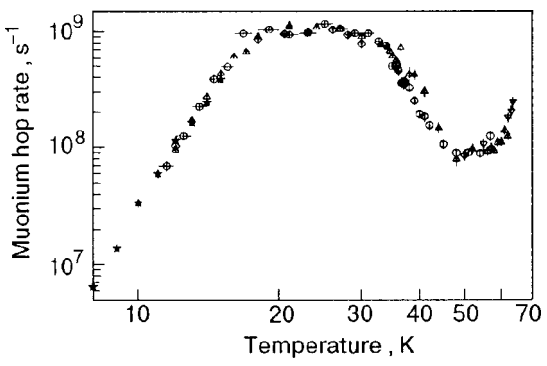

FIG. 1. Temperature dependence of the muonium hop rate in ultrahigh-purity solid N_2. Stars correspond to the combined longitudinal field measurements; circles, triangles, diamonds and inverted triangles correspond to transverse field measurements in different samples.

Note that

$$\tau_c^{-1} \propto \frac{\tilde{\Delta}_0^2}{\Omega(T)} \quad \text{for} \quad \xi < \Omega, \tag{3}$$

$$\text{whereas} \quad \tau_c^{-1} \propto \frac{\tilde{\Delta}_0^2 \Omega(T)}{\xi^2} \quad \text{for} \quad \xi \gg \Omega \tag{4}$$

giving the opposite temperature dependence, so that Mu atoms are localized as $T \to 0$. In the $T \to 0$ limit only acoustic phonons are important, and

$$\Omega(T) \propto T^{7(+2)}. \tag{5}$$

The two additional powers of T appear only in the case of muonium tunneling between absolutely equivalent sites.

In the temperature range $30\ \text{K} < T < 50$ K, the measured Mu hop rate in solid nitrogen exhibits an empirical temperature dependence $\tau_c^{-1} \propto T^{-\alpha}$ with $\alpha = 7.3(2)$; since, from Eq. (3), $\tau_c^{-1} \propto \Omega^{-1}(T)$, we have $\Omega(T) \propto T^7$, as expected [Eq. (5)]. This is the first experimental confirmation of the T^{-7} dependence of τ_c^{-1} predicted by the two-phonon theory of quantum diffusion.[5]

Below about 30 K the Mu hop rate levels off, due to band motion with an estimated[11] renormalized bandwidth of $\tilde{\Delta}_0 \sim 10^{-2}$ K.[11] Similar experiments in solid methanes give the following values for the muonium bandwidth: about 3×10^{-2} K in CH_4 and about 10^{-3} K in CD_4. These values for the Mu bandwidth in solid nitrogen and methanes should be compared with the bandwidth $\Delta \sim 10^{-4}$ K obtained for the quantum diffusion of ^{3}He atoms in ^{4}He crystals:[21] the qualitative similarity of these results suggests a common dynamical behavior for light particles in insulators, as opposed to metals, where different scattering mechanisms lead to quite different impurity dynamics.

Muonium motion in solid nitrogen slows down again below about 20 K, probably due to the orientational ordering of N_2 molecules. For $T < 18$ K the data in Fig. 1 obey

$$\tau_c^{-1} = \tau_0^{-1} \left(\frac{T}{\Theta} \right)^{\alpha}, \tag{6}$$

with $\Theta = 83$ K, $\tau_0^{-1} = 3.6(8) \times 10^{13}$ s^{-1} and $\alpha = 6.7(1)$.

The change in the temperature dependence of the Mu hop rate from a T^7 to a T^{-7} law reflects a crossover from Eq. (3) to Eq. (4). Muonium diffusion in solid methane isotopes and solid carbon dioxide exhibits similar temperature dependences of τ_c^{-1} (Refs. 10 and 20). In all four crystals, at low temperatures a gradual Mu localization takes place which reflects a suppression of band motion by static disorder introduced by orientational ordering.

2.2. Coherent quantum diffusion of the muonium atom in a highly disordered material: orientational glass

To date most of our knowledge on tunneling dynamics of particles in solids comes from the extensive studies of crystalline or nearly crystalline materials. However, in reality, the crystalline state is the exception rather than the rule. Disorder exists in varying degrees, ranging from a few impurities in an otherwise perfect crystalline host to the strongly disordered limit of alloys or glassy structures. All the studies on muon and muonium localization so far have been focused on

crystals with weak disorder.[1] In this Section we present experimental studies of muonium tunneling dynamics under conditions of strong disorder in orientational glasses.[22,23]

The term ''orientational glasses'' usually refers to randomly diluted (or randomly mixed) molecular crystals. Molecular crystals without such randomness in their chemical constitution undergo an order–disorder phase transition from the ''plastic crystal'' phase at high temperatures, where the multipole moments associated with the molecules can rotate more or less freely, to a phase with a long-range orientational order at lower temperature (e.g., N_2, ortho-H_2, CH_4, CD_4, etc.). This order gets severely disturbed by dilution of the material with atomic species which have no multipole moment (e.g., Ar in N_2, Kr in CH_4, para-H_2 in ortho-H_2, etc.); strong enough dilution leads to a new type of phase wherein the multipole moments are frozen into random directions. These glass phases are believed to result from the combined effect of the frustration of the highly anisotropic interactions between the molecules (e.g., electrostatic multipole–multipole) and the disorder introduced by the random substitution of molecular multipoles by noninteracting shperical atoms or molecules.[22] The frustration in these systems arises from the geometrical impossibility of realizing the minimum possible energy configuration for all pairs of neighboring molecular quadrupoles in close 3D lattices, and disorder simply comes from the replacement of multipole-bearing molecules by noninteracting diluents such as Kr in the CH_4–Kr system.

Although orientational glasses have many common features with structural glasses (like amorphous SiO_2) and spin glasses (like CuMn) there is an important difference even in the qualitative description of these glass systems. Unlike the canonical spin glasses such as CuMn alloys, for which the frustration and the disorder go hand-in-hand, the orientational glasses belong to a new class of systems characterized by independent effects of both frustration and disorder. The interaction between two molecules responsible for the orientational ordering (the short-range highly anisotropic electric quadrupole–quadrupole or octopole–octopole interaction) is explicitly known. This fact allows one to extract the influence of disorder, which can be easily varied (or even switched on and off) by changing the temperature and/or composition, allowing a detailed investigation of the effects of strong disorder on quantum tunneling of muonium atoms.

Since the early heat-capacity measurements[24] it has been known that the specific-heat anomalies in CH_4 at the orientational transition vanish if a sufficient amount of Kr is added to CH_4. It has been established by heat-capacity, NMR,[25] and dielectric techniques[26] that as the Kr concentration increases, the temperature of the orientational transition gradually decreases. Above a critical concentration (about 25%) an ordered phase never forms. Instead, as the temperature goes down the dynamical orientational disorder eventually freezes into a static pattern of randomly oriented octupoles, the orientational glass.

Figure 2 shows the temperature dependences of the muonium hop rate in pure CH_4 and $CH_4+25\%$ Kr, extracted in the regime of dynamical averaging using the values of δ obtained from the low-temperature values of T_2^{-1} (Ref. 10). The plateaus in $\tau_c^{-1}(T)$ (around 45–55 K in pure CH_4 and 50–60 K in the mixture) manifest the onset of muonium band motion.[1,5] The bandwidth $\tilde{\Delta}\sim 10^{-2}$ K determined in the $CH_4+25\%$ Kr mixture turns out to be remarkably high: it is only slightly less than the value in pure CH_4 ($\tilde{\Delta}\sim 3\times 10^{-2}$ K), about the same as that in pure solid nitrogen,[11] and an order of magnitude higher than in pure solid CD_4 ($\tilde{\Delta}\sim 10^{-3}$ K).[10] The addition of 16% Kr to CH_4 does not change the bandwidth for Mu tunneling dynamics. This fact suggests that substitution of 2 nearest neighbors out of 12 does not destroy the coherence in the Mu band regime. This is a remarkable feature never observed in quantum diffusion studies so far: the presence of impurities in a crystal even at the level of 10^{-3} is typically enough to destroy the coherent tunneling regime.[1,5] Although the addition of 25% Kr to CH_4 does change the muonium bandwidth, in the temperature range between 50 and 60 K the Mu atom still exhibits coherent tunneling, which means that substitution of 3 nearest neighbors out of 12 still does not destroy the coherence. The question why does such a high concentration of foreign atoms fails to destroy coherence in the muonium dynamics still remains open.

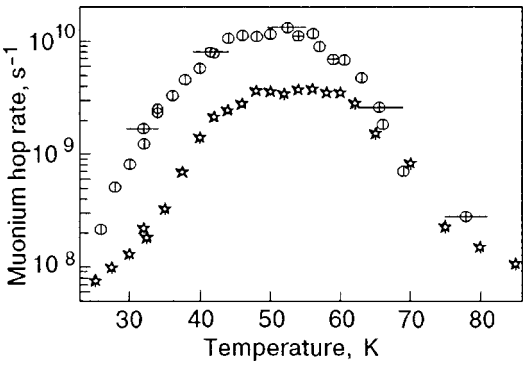

FIG. 2. Temperature dependence of the muonium hop rate in pure solid methane (circles) and solid mixture of $CH_4+25\%$ Kr (stars).

3. ELECTRON TRANSPORT VIA μ^+SR

Ionization of matter by high-energy charged particle radiation inevitably produces excess electrons and thus may cause electrical breakdown even in wide-gap insulating materials subjected to high electric field. These materials are used in a large number of applications ranging from power generation equipment to microelectronic devices. It is therefore important to understand the transport mechanisms of radiolysis electrons in insulators.

In condensed matter, the transport of a charged particle depends upon the adiabaticity of its interaction with excitations of the environment. For particles slow enough that electronic excitations are prohibited, the general picture depends critically on the interplay of two characteristic times. The first represents the typical time that a charged particle spends interacting with a given atom or molecule: $\tau_i=a/v$, where a is the lattice constant and v is the velocity of the charged particle. The other characteristic time is ω^{-1}, where $\hbar\omega$ is the characteristic phonon energy. Fast particles ($\omega\tau_i \ll 1$) retain their ''bare'' identity in moving through the medium, whereas charge carriers moving so slowly that $\omega\tau_i > 1$ are followed ''instantaneously'' by phonon modes and

are best thought of as a polaron[27] whose mobility is drastically decreased. This crossover from the fast ($\omega\tau_i<1$) to the slow ($\omega_i\tau>1$) regime thus leads to a dramatic change in the charge transport properties.

In different insulators, electron transport is determined by qualitatively different interactions of electrons with the medium. Measurements on Ar, Kr, and Xe crystals[28,29] show clearly that electron mobilities in these solids are comparable to those found in wide-band semiconductors ($b_e \sim 10^3$ cm^2 s^{-1} V^{-1}), which has encouraged different authors to apply the well-known Shockley theory.[30] An approximation in which the free charge carriers are completely delocalized and the electron–phonon interaction is treated as a perturbation gave an adequate description of the observed electron transport.

The rather low electron mobilities ($b_e \sim 10^{-2}$–10^{-3} cm^2 s^{-1} V^{-1}) found in the diatomic solids of N_2, CO, and O_2 (Ref. 31) suggest that a fundamentally different mechanism of electron transport occurs in these materials. Localization of excess electrons with the formation of a small polaron[27] due to strong interactions with excitations of the medium has been proposed to explain such low values of the drift mobility.

Measurements of the electron mobility by a time-of-flight (TOF) technique represent a very direct approach to the study of charge transport properties in solids. It should be noted, however, that in such experiments the path length between electrodes is macroscopic ($\sim 10^{-2}$–10^{-1} cm), making the results highly susceptible to spurious TOF changes if electrons interact with crystalline defects such as impurities, strains, and microcracks. The muon spin rotation technique avoids these difficulties inherent to the traditional TOF technique because the distances involved are much shorter ($\sim 10^{-6}$–10^{-4} cm).

In μSR experiments each incoming several-MeV μ^+ leaves behind an ionization track of liberated electrons and ions. Although this circumstance has been disregarded in a great majority of experimental and theoretical studies of condensed matter by μ^+SR techniques, the liberation of electrons by muon radiolysis is far from a negligible effect—in fact, in some insulators and semiconductors it may determine much of the subsequent behavior of the system. Recent μ^+SR, experiments in liquid helium,[32] solid nitrogen,[33–36] and liquid[37] and solid[29,38] neon and argon have shown that the spatial distribution of the ionization track products is highly anisotropic with respect to the final position of the muon: the μ^+ thermalizes well ''downstream'' from the end of its track. Some of the excess electrons generated in this track turn out to be mobile enough to reach the thermalized muon and form the hydrogenlike muonium (Mu$\equiv\mu^+e^-$) atom.

The phenomenon of delayed muonium formation (DMF) described above is crucially dependent on the electron interaction with the environment through its influence on electron mobility. Thus DMF forms the basis of a new technique[34] for measurements of the electron mobility b_e in insulators[36–38] and semiconductors[39–41] on a microscopic scale: b_e can be estimated whenever one can measure both the characteristic time for Mu atom formation and the characteristic distance between the stopped muon and its ''last'' radiolysis electron.

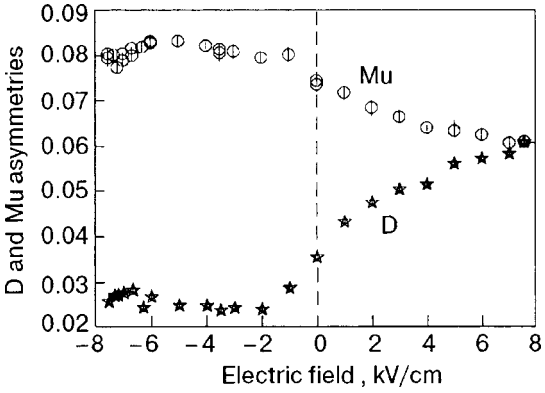

FIG. 3. Electric field dependence of the muonium (Mu, circles) and diamagnetic (D, stars) amplitudes in α-N_2 at $T=20$ K.

In this Section we consider several examples where μ^+SR techniques allow one to determine whether an excess electron in a cryocrystal becomes a polaron or occupies the conduction band (in other words, whether electron is localized or delocalized).

3.1. Electron delocalization in solid α-nitrogen

Both muonium (Mu) and diamagnetic (D) signals are evident in solid N_2 at all temperatures.[33] We found a strong correlation between the muonium amplitude and the electron mobility in solid nitrogen: both have similar temperature dependences. The straightforward implication is that Mu formation in s-N_2 is at least partially due to convergence of the μ^+ and a radiolysis electron. Since positive charges have been found[31] to be immobile in s-N_2, the e^- must move to the μ^+.

Rather strong evidence in support of this picture comes from the electric field dependences of the diamagnetic and Mu amplitudes (Fig. 3). A positive sign for E signifies that the electric field is applied in the same direction as the initial muon momentum. The results show that, on average, muons thermalize downstream from the last radiolysis electrons of the muon's ionization track; in this case a positive E will pull the μ^+ and e^- apart, giving rise to an increased D amplitude, whereas a negative E will push the μ^+ and e^- together. The characteristic muon–electron distance R in solid α-N_2 was estimated[34,35] from these measurements to be about 5×10^{-6}. Analogous measurements in β-N_2 at $T=59$ K reveled a much weaker electric-field dependence, giving an estimate of the characteristic μ^+–e^- distance of about half that in α-N_2 (Ref. 36). The characteristic time τ for e^- transport to the μ^+ can be determined by measurement of the magnetic field dependence of the Mu amplitude. Assuming that the muonium formation process is governed by a first-order kinetic equation $dn_{\rm Mu}(t)=-dn_\mu(t)=\lambda n_\mu(t)$, where $\lambda\equiv1/\tau$ is the characteristic formation rate, the muonium amplitude has been shown to be

$$A_{\rm Mu}\propto\frac{\lambda}{\sqrt{\lambda^2+\omega_{\rm Mu}^2}}. \tag{7}$$

For a weak local electric field E the electron mobility be is independent of E, and the charge drift velocity v is given by

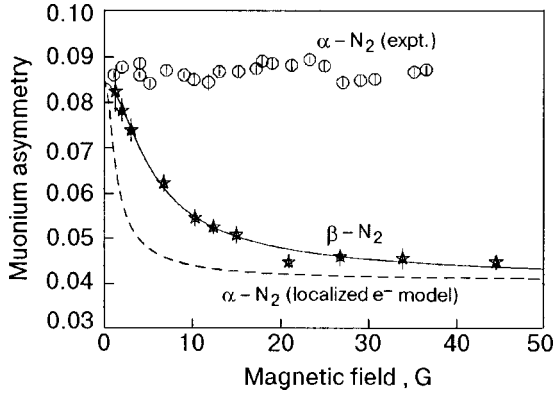

FIG. 4. Magnetic field dependence of the muonium amplitudes in α-N_2 at $T=20$ K (circles) and in β-N_2 at $T=59$ K (stars). The smooth curves represent numerical calculations in the framework of a localized electron model (see text).

$$v = b_e E. \tag{8}$$

In the absence of an applied field, the electric field at a distance r from the muon is $E=e/\epsilon r^2$, which can be integrated to give an expression for the Mu formation time:

$$\tau = \frac{R^3 \epsilon}{3 e b_e}. \tag{9}$$

Very near the muon, E is large and b_e is no longer constant; however, Eq. (9) turns out to be a good approximation anyway because τ is determined mainly by slow motion at large distances in low electric fields. Expressions (7) and (9) allow one to estimate the electron mobility b_e.

Figure 4 shows the magnetic field dependence of A_{Mu} in α-N_2 (circles) and in β-N_2 (stars). In β-N_2 the estimate of the electron mobility from μ^+SR measurements using Eqs. (7) and (9) gives a value of the same order of magnitude as that extracted by the time-of-flight technique. The dashed curve shows numerical calculations according to Eqs. (7) and (9) with the values of electron mobility determined from TOF measurements[31] in α-N_2. The experiment, however, show that A_{Mu} is field independent (i.e., $\lambda \gg \omega_{\mathrm{Mu}}$), which means that the Mu formation time is much shorter than expected from TOF measurements. Using Eq. (7) one can estimate a lower limit for the electron mobility in α-N_2: $b_e > 100\ \mathrm{cm^2\,s^{-1}\,V^{-1}}$—a value more than 10^5 times higher than the electron mobility in β-N_2. The discrepancy between TOF and μ^+SR results in α-N_2 is probably due to cracking of the crystal at the α–β transition of s-N_2. The TOF technique,[31] which relies on electron drift over the macroscopic distances between electrodes, is inevitably sensitive to crystal imperfections. We claim that the μ^+SR technique, which involves microscopic characteristic distances, avoids these difficulties. Such a high electron mobility suggests that the electron transport mechanism in α-N_2 is fundamentally different from that in β-N_2. Probably the localization of electrons does not occur in α-N_2, and Shockley's delocalized approximation[30] can be applied. A possible mechanism for electron localization in β-N_2 may be interactions with the rotational modes of the N_2 molecules—a scattering mechanism that is absent in α-N_2 due to the orientational ordering of the molecules.

3.2. Electron localization in orientational glass

Most of our understanding of electron transport in solids is modeled on nearly perfect crystalline materials, but even in this limit disorder plays a crucial role.[42] The most familiar phenomenon governing electron transport in disordered metals is "Anderson localization:"[4] the introduction of sufficiently strong disorder into a metallic system causes spatial localization of electron states near the Fermi level and thus drives a transition to an insulating state. In metals, however, electron–electron interactions dramatically modify the density of states at the Fermi level, leading to the formation of a Coulomb pseudogap.[43] To observe the effects of disorder on electron transport without the complications of electron–electron interactions, one must therefore study electron dynamics in a disordered insulating host.[44]

Orientational glasses formed by random mixtures of molecular and atomic species[22] offer a unique opportunity for such studies. One of the best-studied orientational glass systems is the N_2–Ar mixture.[45] Pure N_2 has two low-pressure crystalline forms, the hexagonal close-packed (hcp) high-temperature phase and the cubic $Pa3$ (fcc) low-temperature phase. Despite intrinsic geometrical frustration, pure N_2 undergoes a first-order phase transition to the long-range periodic orientationally ordered α phase below $T_{\alpha\beta}=35.6$ K; the high-temperature β phase is orientationally disordered.

Solid $(N_2)_{1-x}Ar_x$ is obtained by simply cooling liquid mixtures, as nitrogen and argon are completely miscible. As the Ar concentration x is increased, the hcp-to-fcc transition temperature decreases. Above the critical Ar concentration $x_c \sim 0.23$ the hcp lattice appears to be stable down to $T=0$.

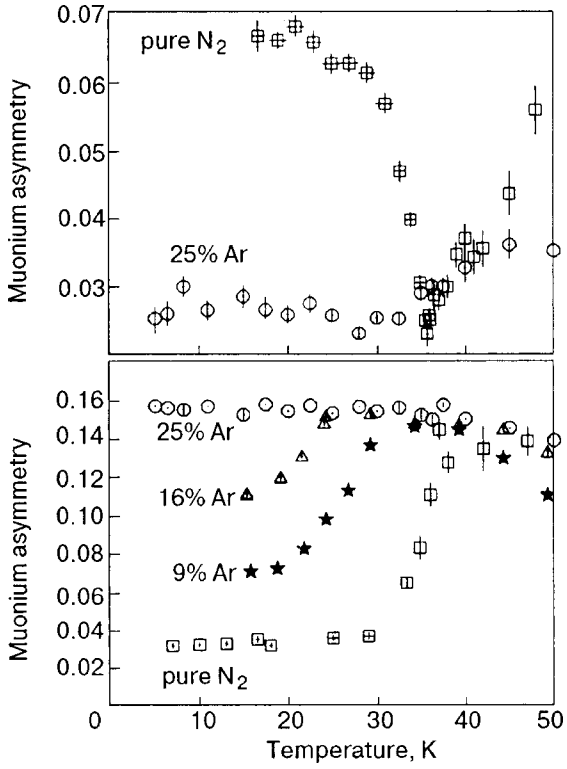

FIG. 5. Temperature dependence of the muonium (top, $H\sim 5$ G) and diamagnetic (bottom, $H\sim 100$ G) signal amplitudes in pure solid nitrogen (squares) and solid $(N_2)_{1-x}Ar_x$ (circles: $x=0.25$; triangles: $x=0.16$; stars: $x=0.09$).

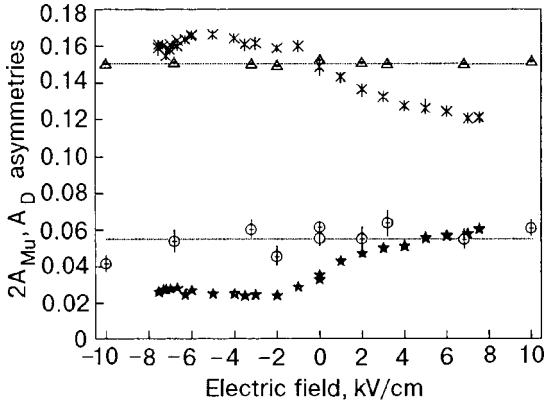

FIG. 6. Electric field dependence of $2A_{\mathrm{Mu}}$ and A_D in pure solid nitrogen (crosses and stars, respectively) and in solid 75% N_2 + 25% Ar (circles and triangles, respectively) in a transverse magnetic field $H=36$ G at $T=20$ K. The muonium amplitudes are doubled to compensate for the 50% depolarization of Mu by hyperfine oscillations.[2]

The dynamical orientational disorder of the high-T phase eventually freezes into a static pattern of randomly oriented N_2 molecules, the orientational glass.[45]

Being a mixture of insulators, the N_2–Ar system has a very large energy gap ($\sim$10 eV), so that even at high temperature the ambient density of free electronic states is exponentially low. Experimental study of electron transport in this system therefore requires that the empty conduction band be ''injected'' with free carriers, ideally in low enough concentrations that electron–electron interactions can be safely ignored. The ionization of molecules and/or atoms by high-energy charged particles (e.g., positive muons) offers just such a source of free carriers.

Figure 5 depicts the temperature dependences of the asymmetries (amplitudes) of the various signals in solid $(N_2)_{1-x}Ar_x$ for $x=0$, 0.09, 0.16, and 0.25. At high temperature (above about 40 K), all the mixtures have roughly the same Mu and μ_D asymmetries as pure N_2. At low temperatures, however, adding argon causes dramatic changes. In pure N_2 below about 30 K there is a large Mu signal and a small μ_D signal, indicating efficient DMF; as Ar is added there is a progressively larger μ_D signal, indicating reduced DMF, until at $x=0.25$ there is only a small Mu signal. In solid N_2 muonium formation has been shown[34,36] to proceed via two channels: the thermal DMF process outlined above, and the epithermal prompt process which takes place prior to the μ^+ thermalization and is therefore independent of temperature, electron mobility, etc. The small, temperature-independent Mu amplitude in the $x=0.25$ sample (see Fig. 5) is the same as the prompt Mu amplitude in pure solid nitrogen,[36] suggesting a complete absence of DMF in the orientational glass.

The hypothesis that Mu formation in the $x=0.25$ mixture is essentially all via the prompt channel at 20 K is further supported by the observation that A_{Mu} and A_D do not depend on an externally applied electric field for that sample, as shown in Fig. 6. Both amplitudes show significant electric field dependence in pure N_2 at 20 K, from which the characteristic muon–electron distance R is estimated to be about 50 nm;[34,36] about the same value of R is found in solid Ar, which exhibits almost 100% DMF.[38] The absence of DMF at this length scale at low temperature in the $x=0.25$ mixture suggests that electrons are localized in an orientational glass.[44]

4. CONCLUSIONS

Recent studies on both quantum diffusion of muonium atoms and electron transport in condensed matter have demonstrated the considerable power of muon spin relaxation techniques for determination of the quantum state of these particles. The dynamics of neutral and charged particles is basically governed by different mechanisms of localization and delocalization.

This work was supported by the INTAS Foundation, the Royal Society of London, NSF, and NATO.

*E-mail: storchak@dnus.polyn.kiae.su

[1] V. G. Storchak and N. V. Prokof'ev, Rev. Mod. Phys. **70**, 929 (1998).
[2] A. Schenck, *Muon Spin Rotation: Principles and Applications in Solid State Physics*, Adam Hilger, Bristol (1986); S. F. J. Cox, J. Phys. C **20**, 3187 (1987); J. H. Brewer, ''Muon spin rotation/relaxation/resonance,'' in *Encyclopedia of Applied Physics*, edited by G. L. Trigg, VCH, New York (1995).
[3] A. O. Caldeira and A. J. Leggett, Phys. Rev. Lett. **46**, 211 (1981); Ann. Phys. (N.Y.) **149**, 374 (1983).
[4] P. W. Anderson, Phys. Rev. **109**, 1492 (1958).
[5] Yu. M. Kagan and N. V. Prokof'ev, ''Quantum tunneling diffusion in solids,'' in *Quantum Tunneling in Condensed Media*, edited by A. J. Leggett and Yu. M. Kagan, North-Holland (1992), p. 37.
[6] A. F. Andreev and I. M. Lifshitz, Zh. Eksp. Teor. Fiz. **56**, 2057 (1969) [Sov. Phys. JETP **29**, 1107 (1969)].
[7] R. A. Guyer and L. I. Zane, Phys. Rev. **188**, 445 (1969).
[8] L. D. Landau and E. M. Lifshitz, *Quantum Mechanics. Non-Relativistic Theory*, 3rd ed., Pergamon Press, Oxford (1977), Nauka, Moscow (1974).
[9] A. J. Leggett *et al.*, Rev. Mod. Phys. **59**, 1 (1987).
[10] V. G. Storchak *et al.*, Phys. Rev. Lett. **82**, 2729 (1999).
[11] V. G. Storchak, J. H. Brewer, W. N. Hardy, S. R. Kreitman, and G. D. Morris, Phys. Rev. Lett. **72**, 3056 (1994).
[12] R. Kadono, in *Perspectives in Meson Science*, edited by T. Yamazaki, K. Nakai, and K. Nagamine, North-Holland, Amsterdam (1992), p. 113.
[13] S. F. J. Cox and D. S. Sivia, Hyperfine Interact. **87**, 971 (1994).
[14] C. P. Slichter, *Principles of Magnetic Resonance*, Springer-Verlag, Berlin (1980).
[15] D. Steinbinder *et al.*, Europhys. Lett. **6**, 535 (1988).
[16] J. Kondo, Physica B **125**, 279 (1984); **126**, 377 (1984); K. Yamada, Prog. Theor. Phys. **72**, 195 (1984).
[17] R. Kadono, Hyperfine Interact. **64**, 615 (1990).
[18] P. C. E. Stamp and C. Zhang, Phys. Rev. Lett. **66**, 1902 (1991).
[19] Yu. M. Kagan and N. V. Prokof'ev, Phys. Lett. A **150**, 320 (1990).
[20] D. G. Eshchenko, V. G. Storchak, J. H. Brewer, S. P. Cottrell, S. F. Y. Cox, E. Karlsson, and Waeppling, Fiz. Nizk. Temp. **27**, 1153 (2001) [Low Temp. Phys. **27**, 854 (2001)].
[21] M. G. Richards *et al.*, J. Low Temp. Phys. **24**, 1 (1976); V. A. Mikheev, B. N. Esel'son, V. N. Grigor'ev, and N. P. Mikihn, Fiz. Nizk. Temp. **3**, 387 (1977) [Sov. J. Low Temp. Phys. , 3 (1977)].
[22] U. T. Hochli, K. Knorr, and A. Loidl, Adv. Phys. **39**, 405 (1990).
[23] K. Binder and J. D. Reger, Adv. Phys. **41**, 547 (1992).
[24] A. Eucken and H. Veith, Z. Phys. Chem. Abt. B **34**, 275 (1936).
[25] P. Calvani *et al.*, Phys. Lett. A **86**, 490 (1981).
[26] R. Bohmer and A. Loidl, Z. Phys. B: Condens. Matter **80**, 139 (1990).
[27] T. Holstein, Ann. Phys. (N.Y.) **8**, 343 (1959).
[28] L. S. Miller, S. Howe, and W. E. Spear, Phys. Rev. **166**, 871 (1968).
[29] D. G. Eshchenko, V. G. Storchak, J. H. Brewer *et al.*, Phys. Rev. B **66**, 035105 (2002).
[30] W. Shockley, Bell Syst. Tech. J. **30**, 900 (1951).
[31] R. J. Loveland, P. L. Le Comber, and W. E. Spear, Phys. Rev. B **6**, 3121 (1972).
[32] E. Krasnoperov, E. Meilikhov, R. Abela, D. Herlach, E. Morenzoni, F. Gydax, A. Schenck, and D. G. Eshchenko, Phys. Rev. Lett. **69**, 1560 (1992).

[33] V. Storchak, J. H. Brewer, and G. D. Morris, Phys. Lett. A **193**, 199 (1994).
[34] V. Storchak, J. H. Brewer, and G. D. Morris, Phys. Rev. Lett. **75**, 2384 (1995).
[35] V. Storchak, J. H. Brewer, and G. D. Morris, Philos. Mag. **72**, 241 (1995).
[36] V. Storchak, J. H. Brewer, G. D. Morris, D. J. Arseneau, and M. Senba, Phys. Rev. B **59**, 10559 (1999).
[37] V. Storchak, J. H. Brewer, and G. D. Morris, Phys. Rev. Lett. **76**, 2969 (1996).
[38] V. Storchak, J. H. Brewer, and D. G. Eshchenko, Appl. Magn. Reson. **13**, 15 (1997).
[39] V. G. Storchak *et al.*, Phys. Rev. Lett. **78**, 2835 (1997).
[40] D. G. Eshchenko, V. G. Storchak, and G. D. Morris, Phys. Lett. A **264**, 226 (1999).
[41] D. G. Eshchenko, V. G. Storchak, J. H. Brewer, and R. L. Lichti, Phys. Rev. Lett. (in press).
[42] N. F. Mott and E. A. Davis, *Electron Processes in Non-Crystalline Materials*, Clarendon Press, Oxford (1979).
[43] N. F. Mott, *Metal–Insulator Transitions*, Taylor and Francis, London (1974).
[44] V. G. Storchak, D. G. Eshchenko, J. H. Brewer, G. D. Morris, S. P. Cottrell, and S. F. J. Cox, Phys. Rev. Lett. **85**, 166 (2000).
[45] J. A. Hamida, E. B. Genio, and N. S. Sullivan, J. Low Temp. Phys. **103**, 49 (1996).

This article was published in English in the original Russian journal. Reproduced here with stylistic changes by AIP.

Exciton relaxation in KBr and CaF_2 at low temperature: molecular dynamics study

K. S. Song*

Department of Physics, University of Ottawa, Ottawa, Canada
Fiz. Nizk. Temp. **29**, 1001–1006 (September–October 2003)

The results of a molecular-dynamics simulation of exciton relaxation in several ionic crystals at low temperature are reported. Both the lowest energy spin triplet and some of the low lying hole excited states are allowed to relax for the purpose of studying the radiation defect formation channels. The previously used semi-classical program has been modified to implement the solution of Newton's equations with a 0.48 fs time step. The relaxation of an exciton localized on a single site (as Br^0+e or F^0+e, respectively) is studied at 10 K in KBr and in CaF_2. In KBr the triplet self-trapped exciton leads to separated Frenkel pair in about 1–2 ps, followed by slow oscillation of the hole center along the (110) axis. The defect pair created is separated by about 10 Å (third-nearest neighbor). In CaF_2, the relaxation reaches the geometry of the nearest Frenkel pair, with the hole center oriented along a (111) axis in about 0.3 ps at 10 K. However, at 80 K the system can undergo further relaxation into slightly more distant defect pairs. When the hole is excited to higher levels, the molecular bond of the hole center undergoes violent oscillations. In KBr, the hole center is found to form in the second-nearest-neighbor position within about 0.5 ps. The species formed are, however, different from the well-known primary radiation defects. A similar process is also observed in CaF_2. [DOI: 10.1063/1.1614185]

1. INTRODUCTION

In the ionic halides under study in this paper the top valence band originates from the halogen p orbital and is narrow (about 1 eV). The conduction bands are broad and originate from several excited orbitals of both ions. The hole is quickly self-trapped in the form of a molecular ion X_2^- and is stable at low temperature. When an exciton is created, it is also self-trapped. The nature of the self-trapped exciton (STE) in these ionic halides has been of great interest in part because of its role in the radiation defect creation process.[1] The low-temperature dynamic F-center production is now understood to be the result of strong axial relaxation of the STE in alkali halides with the NaCl structure. This has been demonstrated by both static calculations of the STE structure as well as by recent molecular-dynamics (MD) studies. As for the alkaline earth fluorides (AEF), the early magnetic resonance data clearly showed that the STE itself is a close $F-H$ pair,[2] with the hole center oriented along a (111) axis.

There has been an ongoing debate about the possible role of the hole excitation in the defect process. Experiments have indicated that in the AEF stable Frenkel pairs (well separated pairs) are created when the STE is excited in the hole absorption band.[3] A recent paper[4] suggested a similar process leading to even faster creation of Frenkel pairs in NaCl-type crystals than by the dynamic channel.

In this paper we present results recently obtained on the possible channels of defect creation as a result of exciton relaxation in ionic halides of two different lattice structures: KBr and CaF_2. We first compare the relaxation of the lowest-energy spin triplet STE state in the two materials and discuss the similarities and differences. The dynamic relaxation of the triplet STE in KBr and NaBr at 10 K has recently been published.[5] In this work, a system of a hole and excited electron is allowed to relax for about 3 ps. The main results obtained are as follows. The localization of an excited electron at an anion site drives the relaxation process, resulting in the fast formation of an interstitial–vacancy pair in the anion sublattice (respectively known as the H center and the F center). The spin triplet STE in KBr leads to a spatially separated Frenkel defect pair in about 1–2 ps, followed by slow oscillation of the hole center along the (110) axis. The defect pair created is separated by about 10 Å (third-nearest neighbor.). In CaF_2, the situation is qualitatively different due to the different lattice structure and the coordination of atoms. The relaxation reaches the geometry of the nearest Frenkel defect pair, with the hole center oriented along a (111) axis in about 0.3 ps at 10 K and 0.2 ps at 80 K. However, at 80 K the system can undergo further relaxation into a slightly more distant defect pair, reoriented by about 70°.

We then present results of relaxation when the exciton is in one of the low-lying hole excited states. In particular, when the hole is excited to a higher level, violent oscillations of the molecule bond of the hole center appear. In KBr, it is found that a set of three defects is formed: an F center at an anion vacancy, a V_k center (occupying two adjacent anion sites) at the second-nearest-neighbor site from the anion vacancy, and an I center (an interstitial Br ion close to the F center). Depending on the rate of energy dissipation employed in the MD simulation this process takes place very fast, within about 0.5 ps. The species formed are therefore different from the well-known primary radiation defects (a pair of Frenkel defects). A similar process takes place in CaF_2 resulting in the creation of the three defects mentioned above. These results are compared with experimental data.

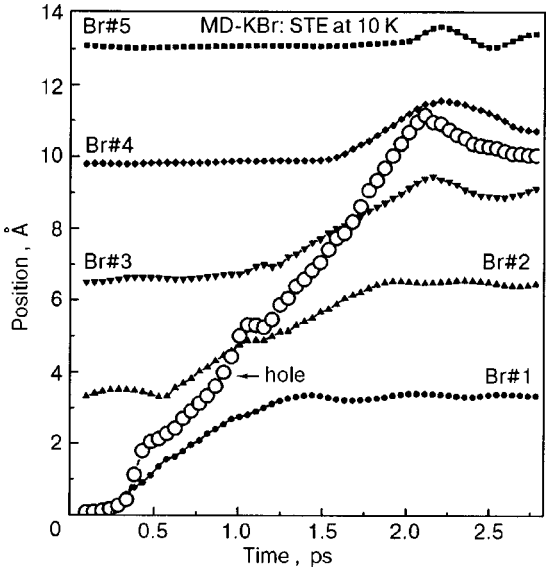

FIG. 1. MD results of exciton relaxation in KBr (at 10 K), with the hole in the lowest-energy σ_u MO. The positions of the five Br atoms and the hole charge distribution (the x coordinates on the (110) plane in Å) as functions of time are shown.

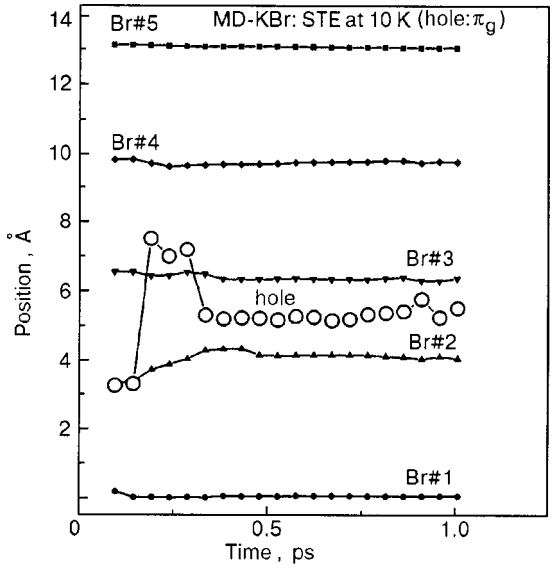

FIG. 2. MD results of exciton relaxation, with the hole in the π_g MO. The dissipation used: 0.75/3.

2. METHOD

The method is based on a semi-classical approach of excited defect study in insulating crystals,[6] which has recently been modified for MD simulation.[5] The details are given in Refs. 5 and 6. At the beginning the perfect lattice in the ground state is equilibrated at the specified temperature. In the present work the number of atoms included in the MD simulation varies between about 110 and 180, depending on the system studied. This cluster is embedded in an infinite lattice. The role of hole excited states in the exciton relaxation is examined by keeping the hole in several molecular obitals (MO): σ_u (...222221), π_g [(...222212) and (...222122)], and π_u [(...221222) and (...212222)]. The σ_u MO is the bonding, the π_g MO a nonbonding, and the π_u MO an antibonding state. An excess electronic energy of about 1–2 eV becomes available when the hole is in an antibonding MO. To prevent an excessive temperature rise associated with the small size of the MD cluster, a fixed rate of kinetic energy dissipation is implemented in the program. We found it reasonable to reduce the kinetic energy of all atoms by a factor of 0.85 every 5 time steps (designated as 0.85/5) for the lowest triplet STE state and by 0.55/3 for the excited hole states. As will be shown below, the rate does not have an influence on the final range of the defect pair separation, but will have an influence on the time scale of onset of the final relaxation product.

3. RESULTS

3.1. STE relaxation in KBr

As a reference we present in Fig. 1 the relaxation of the triplet STE at 10 K obtained previously.[5] A Frenkel-type free exciton (a Br^0 with an electron in a diffuse orbital around it in an otherwise perfect lattice) is allowed to relax. The time evolution of the x coordinate of the five Br atoms as well as the position (the x coordinate) of the center of gravity of the hole charge are shown. The main points are: the Br atom nearest to the electron at (000) moves off-center well before the hole center (the Br molecule ion) forms; the hole center continues to move ahead, jumping from the first- to the second- and then to the third-nearest-neighbor position in about 2 ps. What is noteworthy is that even before a well-formed hole center is established, the electron seems to be in an F-centerlike state within about 0.5 ps. In fact, it is the transformation of the excited electron into an F center that drives the entire process of off-center relaxation.

We present here two hole excited states: (...212), which is a π_g state, and (...21222), a π_u state. The time evolution of the relaxation of the Br atoms is shown for the π_g state in Fig. 2. It is obtained with 0.75/3. The hole is kept in the π_g MO throughout the time shown. The main point is that initially the hole jumps around until it fixes between the Br atoms at (110) and (220). The bond forms at around 0.5 ps. With faster dissipation 0.55/3 the hole center forms at the same geometry, but more slowly, after about 1.5 ps, and remains there for the duration of our study. The hole center thus formed is, however, more like a V_k center (a Br_2^- occupying two anion sites) than an H center (a Br_2^- occupying one anion site).

With the π_u state we observe a similar result. A stable hole center forms at around 0.4 ps independent of the dissipation rate. Although the hole center forms quite early at the second-nearest-neighbor position from the electron localized at an anion vacancy, there is no further diffusion toward a more distant position in any of our studies. It should be noted that the created hole center is an H center in the case of the lowest energy STE, but is a V_k center when the hole is in an excited state. As a result of this difference, the Br atom originally at (000) lingers around the F center and therefore becomes an I center (interstitial anion), instead of moving to the next site (110) as it does in Fig. 1. Figure 3 illustrates the difference of the two types of relaxation in a more schematic way.

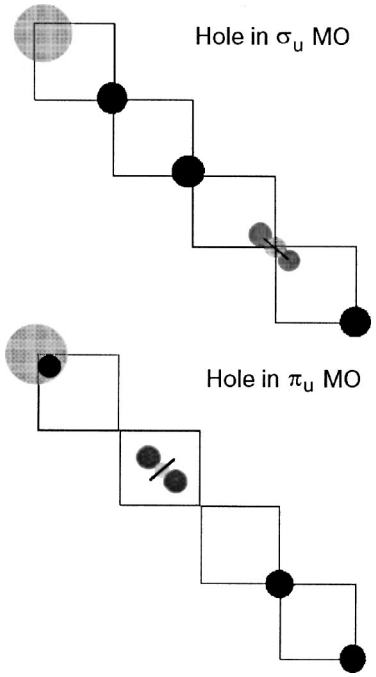

FIG. 3. A schematic diagram showing the end products of exciton relaxation. With the hole in the σ_u MO, an H center is created at the fourth anion site. With the hole kept at an excited π_g MO, a V_k center is formed by the second and third Br atoms. The solid circles are Br atoms along the (110) axis. The dumbbell suggests a hole center shared between two Br atoms. The larger gray circle represents the excited electron, the F center.

3.2. STE relaxation in CaF_2

The situation in the fluorites is different from that in the halides with the NaCl structure because of the differenc in the lattice structure. The self-trapped hole is of the molecular form, F_2^-, as in the NaCl lattice. However, it is oriented along a (100) axis. In 1975 it was determined from an optically detected ESR study[2] that the STE is a pair consisting of an F center at a fluoride ion site and an H center oriented along the (111) direction. It was not possible to identify from ESR alone which of the four possible orientations it actually was occupying. The actual orientation was identified from analysis of the zero-field splitting parameter D.[7] This geometry is shown in Fig. 4*b*. The present MD results were obtained at 10 and 80 K. As the relaxation in the CaF_2 lattice involves both axial translation as well as rotations, it is not possible to draw the time evolution of the principal F ions as was done for KBr. Instead, we illustrate the final geometry of the centers in a schematic way in Fig. 4. At 10 and 80 K the final relaxed structure is reached in about 0.2–0.3 ps. This may be compared with the room-temperature value 0.69 ps reported in Ref. 8. The geometry shown in Fig. 4*b* is precisely the same as deduced in Ref. 7.

We also observed that at 80 K the hole center can undergo further bond changes into a larger electron–hole separation. This is shown in Fig. 4*c*. The dividing temperature seems to be around 40 K. Starting from a slightly different set of F atoms to represent the hole center, it was possible to induce migration of the hole center to a different configuration relative to the F center, shown in Fig. 5.

We have studied the effect of hole excitation on the STE relaxation in CaF_2, similar to what we did in KBr. Two

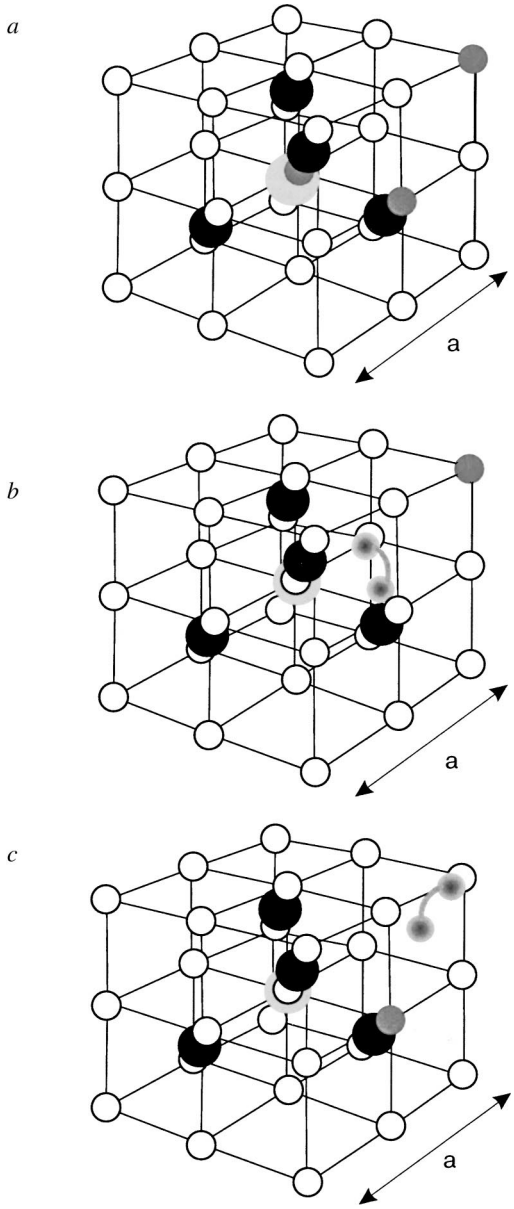

FIG. 4. A view of the CaF_2 lattice. The larger solid circles represent Ca atoms, while the smaller open circles are F atoms. A dumbbell represents the hole center. (*a*) The set of three gray F atoms are those taking part in the hole-center bonds. (*b*) The relaxed STE nearest $F-H$ pair formed after 0.2–0.3 ps at 80 and 10 K, respectively. (*c*) After further relaxation the hole center is seen to migrate to a more distant site at 80 K.

different starting states have been studied. In the first, an unrelaxed Frenkel-type exciton with a cluster of four F atoms is allowed to relax at 80 K. The MO at which the hole was kept excited was π_u (2...1222). Within about 50 fs the hole center formed away from the F center as shown in Fig. 6. The resulting system consists of an F center (an electron at (000)), an I center (F^- at (0.5,0.5,0.5)), and a V_k center formed between the F atoms at (111) and (211). In the second case, the relaxed STE shown in Fig. 4*b* served as the starting point and the hole was then brought to the same π_u (2...1222) MO. Again within about 50 fs after the hole excitation, the same set of defects as above was formed. We have studied also other sets of F atoms with several different hole excited states. Generally, a similar set of defects was created. We found that under excitation of the hole center, similar

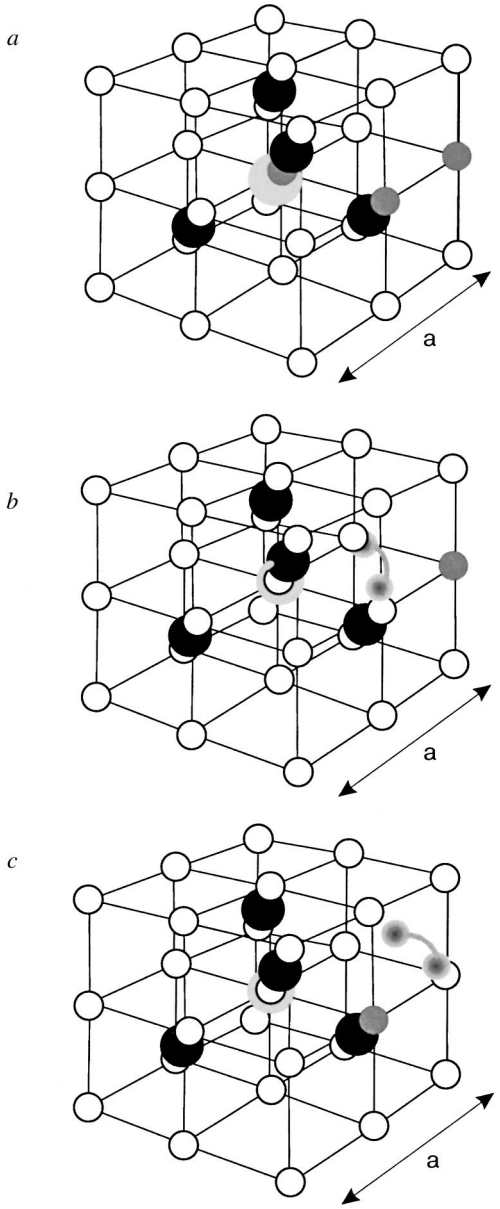

FIG. 5. Similar to Fig. 4, with a different set of F atoms taking part in the hole localization.

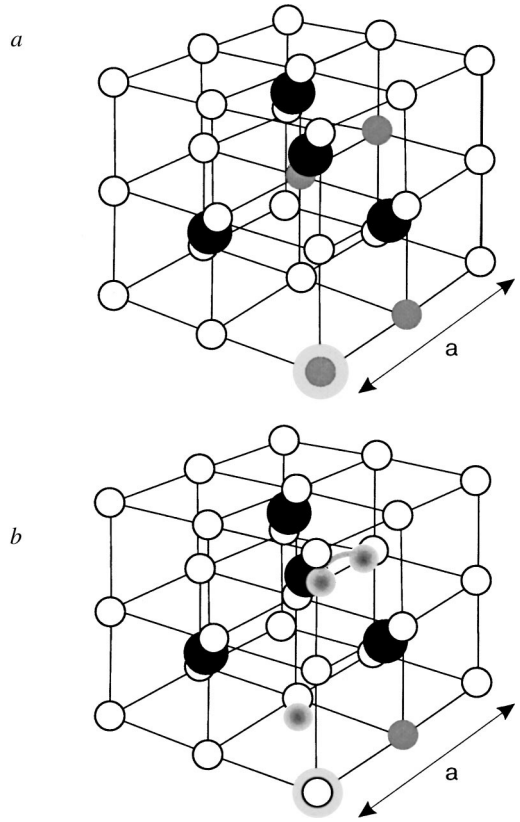

FIG. 6. Relaxation of the exciton in CaF_2 at 80 K, with the hole staying in the π_u MO state. *a*) The set of four gray F atoms are those taking part in the hole-center bonds. *b*) The final relaxed defects reached after about 50 fs. The centers are, respectively, an *F* center (large gray circle), an *I* center (inside an unoccupied cube), and a V_k center (represented by a dumbbell).

defect sets are created in both KBr and CaF_2 despite the difference in the lattice structure. In the fluorites the formation of the *I* center was clearer than in KBr, due to the presence of unoccupied body centers of the elementary cubes. The production of these centers in CaF_2 has been reported[9] and therefore lends support to our work.

4. DISCUSSION

The results of the molecular-dynamics study obtained for the lowest-energy triplet STE confirm the earlier static calculations for both KBr and CaF_2. However, it also gives the time scale for relaxation to equilibrium starting from a localized Frenkel-type exciton. The study of the relaxation of a hole-excited STE produced quite novel results in both materials. The main motivation of the present work was to examine the possible channels of $F-H$ pair creation from excited hole states, as has recently been discussed.[4] The study of higher excited states is intrinsically more complicated due to the crowding of many states, of both electron and hole excitation. Also their lifetimes are expected to be quite a bit shorter than that of the triplet state which is typically between milliseconds and microseconds. The authors of Ref. 4 argued that this excited hole-mediated channel would be faster than the dynamic channel. Indeed, according to the present study the hole excited state produces a second-nearest-neighbor hole center (a V_k center) within about 0.5 ps, compared with the dynamic channel taking about 1.25 ps (creating an *H* center). There are, however, several aspects which present difficulties. First, in the ''direct'' channel the hole center produced is not an *H* center but a V_k center. Second, the electron localized on the anion site has a Br^- very close by (refer to Figs. 2 and 3 above), and its energy is raised as a result. Both are attributable to the excited hole jumping to a distant site and forming a Br_2^- center, rather than undergoing a sequence of bond switching as does the triplet-state STE shown in Fig. 1.

It should be noted that the monitoring of fast species creation is done by observing the rise of absorption of the probe light corresponding to the *F* center or the STE. From Fig. 1 it appears that a relatively well-formed *F* center appears as soon as the first Br atom has reached the site of the next anion site, taking barely 1 ps. It is therefore possible that the primitive *F* center shows up as early as this. The off-center STE may appear at some later time. Because the

off-center STE and a well-separated $F-H$ pair are on the same adiabatic energy surface, it is not immediately clear where the two species part in Fig. 1. In the ODMR study of a correlated $F-H$ pair in KBr at 4 K, Meise *et al.*[10] have reported that stable pairs are mostly in the fourth-nearest neighbors. It is therefore reasonable to argue that the nascent F center appears earlier than the STE by maybe about 1 ps in the dynamic channel. More studies are needed. It would be interesting to conduct an experiment monitoring the onset of the hole-center absorption, thereby distinguishing the H center from the V_k center which seem to separate the dynamic channel from the ''direct'' channel. In both KBr and CaF_2 the resulting defects are rather similar under hole excitation. They can be identified as an F center, an interstitial anion (known as an I center), and a V_k center. Such a combination of defects has been reported in AEF.[9] This has not been reported in alkali halides with the NaCl lattice.

The author acknowledges helpful discussions with N. Itoh and R. T. Williams.

*E-mail: asong@physics.uottawa.ca

[1] R. T. Williams, K. S. Song, W. L. Faust, and C. H. Leung, Phys. Rev. B **33**, 7232 (1986); K. S. Song and R. T. Williams, *Self-Trapped Excitons*, Spinger, Heidelberg (1993), Chs. 5 and 6.
[2] P. J. Call, W. Hayes, and M. N. Kabler, J. Phys. C **8**, L60 (1975).
[3] T. Eshita *et al.*, Phys. Status Solidi B **22**, 489 (1984).
[4] N. Itoh and A. M. Stoneham, *Materials Modification by Electronic Excitation*, Cambridge Univ. Press (2001), Ch. 5.
[5] K. S. Song and Chun-Rong Fu, J. Phys.: Condens. Matter **13**, 2355 (2001).
[6] Chun-Rong Fu, L. F. Chen, and K. S. Song, J. Phys.: Condens. Matter **11**, 5517 (1999).
[7] K. S. Song, C. H. Leung, and A. M. Spaeth, J. Phys.: Condens. Matter **2**, 6373 (1990).
[8] R. Lindner, M. Relchling, R. T. Williams, and E. Matthias, J. Phys.: Condens. Matter **13**, 2339 (2001).
[9] W. Hayes and R. F. Lambourn, J. Phys. C **6**, 11 (1973).
[10] W. Meise, U. Rogulis, F. K. Koschnik, K. S. Song, and J. M. Spaeth, J. Phys.: Condens. Matter **6**, 1801 (1994).

This article was published in English in the original Russian journal. Reproduced here with stylistic changes by AIP.

LOW-TEMPERATURE THERMODYNAMICS AND STRUCTURE

Heat transfer by low-frequency phonons and "diffusive" modes in cryocrystal solutions: the Kr–Xe system

V. A. Konstantinov,* E. S. Orel, and V. P. Revyakin

B. Verkin Institute for Low Temperature Physics and Engineering of the Naional Academy of Sciences of Ukraine, 47 Lenin Ave., Kharkov 61103, Ukraine

Fiz. Nizk. Temp. **29**, 1007–1011 (September–October 2003)

The temperature and volume dependences of the thermal conductivity of the $Kr_{1-\xi}Xe_{\xi}$ solid solution are analyzed in a model in which heat is transferred by low-frequency phonons; above the phonon mobility edge this is done by "diffusive" modes migrating randomly from site to site. The phonon mobility edge ω_0 is determined from the condition that the phonon mean free path limited by umklapp processes and scattering on point defects cannot be smaller than one-half the phonon wavelength. The Bridgman coefficient $g=-(\partial \ln \Lambda/\partial \ln V)_T$ is the weighted mean over these modes, whose volume dependences differ strongly. It is shown that the amount of heat transferred by the "diffusive" modes above 100 K is quite large even in pure Kr and it increases with rising temperature and impurity concentration. © *2003 American Institute of Physics.* [DOI: 10.1063/1.1614186]

INTRODUCTION

The solidified inert gases Ar, Kr, and Xe are among the simplest objects in the physics of solids and are therefore used traditionally for comparison of experimental and calculated data.[1] At temperatures close to or above the Debye temperature ($T \geqslant \Theta_D$) the thermal conductivity of perfect crystals is determined solely by phonon–phonon scattering and it is expected to follow the law $\Lambda \propto 1/T$ (Ref. 2). To obey the law, the volume of the crystal should remain invariable, because the modes would otherwise change and so would the temperature dependence of the thermal conductivity.[2,3]

However, isochoric studies of the thermal conductivity of heavy solid inert gases show a considerable deviation from the above dependence due to the approach of the thermal conductivity to its lower limit.[4,5] The concept of the lower limit of the thermal conductivity proceeds from the assumption that all the excitations are weakly localized in regions whose sizes are half the wavelength, λ/2. As a result, the excitations can hop from site to site through thermal diffusion.[6] In this case the lower limit of thermal conductivity $\Lambda_{\min}$ of the lattice at $T \geqslant \Theta_D$ can be written as:

$$\Lambda_{\min}=\frac{1}{2}\left(\frac{\pi}{6}\right)^{1/3} k_B n^{2/3}(v_l+2v_t), \tag{1}$$

where v_l and v_t are the longitudinal and transverse sound velocities, $n=1/a^3$ is the number of atoms per unit volume, and k_B is Boltzmann's constant.

Further studies of heat transfer in the solid solutions $Kr_{1-\xi}(CH_4)_{\xi}$ $(0 \leqslant \xi \leqslant 1)$[7] and $Kr_{1-\xi}Xe_{\xi}$ $(0 \leqslant \xi \leqslant 0.14)$[8] have detected a gradual change from the thermal conductivity typical of a perfect crystal to the lower limit of the thermal conductivity $\Lambda_{\min}$ as the crystal becomes increasingly disordered. More recently the volume dependence of the thermal conductivity of the $Kr_{1-\xi}(CH_4)_{\xi}$ solid solution was analyzed in the framework of a model which assumes that the phonon mean free path cannot decrease infinitely.[9] In the present study, the temperature and volume dependences of the thermal conductivity of the $Kr_{1-\xi}Xe_{\xi}$ solid solution are analyzed using the model mentioned above.

MODEL

We use Debye's expression for the thermal conductivity[10,11]

$$\Lambda=\frac{k_B}{2\pi^2 v^2}\int_0^{\omega_D} l(\omega)\omega^2 d\omega, \tag{2}$$

where v is the sound velocity; ω_D is the Debye frequency $(\omega_D=(6\pi^2)^{1/3}v/a)$; $l(\omega)$ is the phonon mean free path determined by the U-processes and by scattering on point defects:

$$l(\omega)=(l_u^{-1}(\omega)+l_i^{-1}(\omega))^{-1}. \tag{3}$$

The phonon mean free paths corresponding to each mechanism of scattering are described as[2,10,11]

$$l_u(\omega)=v/A\omega^2 T,\quad A=\frac{18\pi^3}{\sqrt{2}}\frac{k_B\gamma^2}{\overline{M}\,\overline{a}^2\omega_D^3}; \tag{4}$$

$$l_i(\omega)=v/B\omega^4,\quad B=\frac{3\pi\Gamma}{2\omega_D^3}; \tag{5}$$

where the Grüneisen parameter $\gamma=-(\partial \ln \Theta_D/\partial \ln V)_T$, $\overline{M}$ is the average atomic weight of the solution:

$\overline{M}=(1-\xi)M_{Kr}+\xi M_{Xe}$; $\overline{a}=(1-\xi)a_{Kr}+\xi a_{Xe}$.

With allowance for the difference ΔM between the atomic (molecular) masses of the impurity and the matrix and the lattice dilatation, the coefficient Γ can be written as[7]

$$\Gamma = \xi(1-\xi)\left(\frac{\Delta M}{\overline{M}} + 6\gamma\frac{\Delta a}{\overline{a}}\right)^2, \tag{6}$$

where $\Delta M = \overline{M} - M_{\mathrm{Xe}}$; $\Delta a = \overline{a} - a_{\mathrm{Xe}}$.

Expression (3) is not valid if $l(\omega)$ is of the order of one-half the phonon wavelength $\lambda/2 = \pi v/\omega$ or smaller. A similar situation was considered previously for the case of U-processes alone.[11] Let us assume that in the general case

$$l(\omega) = \begin{cases} v/(A\omega^2 T + B\omega^4), & 0 \leqslant \omega \leqslant \omega_0, \\ \alpha\pi v/\omega = \alpha\lambda/2, & \omega_0 < \omega \leqslant \omega_D, \end{cases} \tag{7}$$

where α is a numerical coefficient of the order of unity. There is evidence that the Ioffe–Regel criterion, which suggests localization, is not applicable for a phonon gas.[12] Nevertheless, we will refer to the excitations whose frequencies are above the phonon mobility edge ω_0 as ''localized'' or ''diffusive.'' Since completely localized states do not contribute to the thermal conductivity, we assume that the localization is weak and the excitations can hop from site to site diffusively, as was suggested by Cahill and Pohl.[6] The frequency ω_0 can be found from the condition

$$v/(A\omega_0^2 T + B\omega_0^4) = \alpha\pi v/\omega_0, \tag{8}$$

$$\text{as} \quad \omega_0 = \frac{1}{(2\alpha\pi B)^{1/3}}\left[\sqrt[3]{1+\sqrt{1+u}} + \sqrt[3]{1-\sqrt{1+u}}\right], \tag{9}$$

where the dimensionless parameter u is

$$u = \frac{4\alpha^2\pi^2 A^3 T^3}{27B}. \tag{10}$$

If $\omega_0 > \omega_D$, the mean free path of all the modes exceeds $\lambda/2$, and at $T \geqslant \Theta_D$ we obtain the well-known expression[11]

$$\Lambda_{\mathrm{ph}} = \frac{k_B}{2\pi^2 v}\frac{1}{\sqrt{ATB}}\arctan\sqrt{\frac{B}{AT}}\,\omega_D. \tag{11}$$

At $\omega_0 \leqslant \omega_D$ the thermal conductivity integral separates into two parts, describing the contributions to heat transfer from the low-frequency phonons and the ''diffusive'' high-frequency modes:

$$\Lambda = \Lambda_{\mathrm{ph}} + \Lambda_{\mathrm{loc}}. \tag{12}$$

In the high-temperature limit ($T \geqslant \Theta_D$) these contributions are:

$$\Lambda_{\mathrm{ph}} = \frac{k_B}{2\pi^2 v}\frac{1}{\sqrt{ATB}}\arctan\sqrt{\frac{B}{AT}}\,\omega_0, \tag{13}$$

$$\Lambda_{\mathrm{loc}} = \frac{\alpha k_B}{4\pi \mathrm{v}}(\omega_D^2 - \omega_0^2). \tag{14}$$

The dependence of the thermal conductivity on the specific volume is characterized by the Bridgman coefficient:[3,13]

$$g = -(\partial \ln\Lambda/\partial \ln V)_T. \tag{15}$$

Taking into account that $(\partial \ln A/\partial \ln V)_T = 3\gamma + 2q - 2//3$, where $q = (\partial \ln\gamma/\partial \ln V)_T$, and that $(\partial \ln B/\partial \ln V)_T = 3\gamma$ [as follows from Eqs. (4), (5)] and $(\partial \ln\Gamma/\partial \ln V)_T \approx 0$, we have:

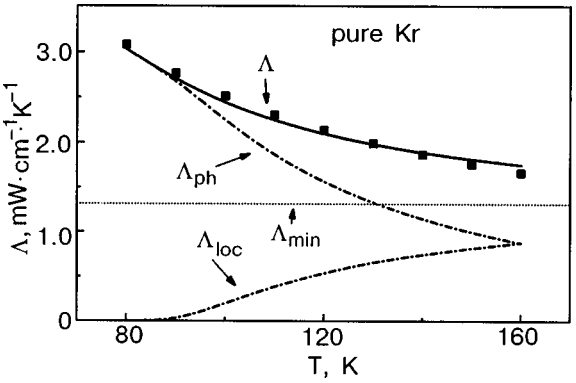

FIG. 1. Fitting results for the isochoric thermal conductivity and calculated relative contributions of low-frequency phonons and ''diffusive'' modes to the thermal conductivity of pure Kr (molar volume is 28.5 cm^3/mole).

$$g = \frac{\Lambda_{\mathrm{ph}}}{\Lambda} g_{\mathrm{ph}} + \frac{\Lambda_{\mathrm{loc}}}{\Lambda} g_{\mathrm{loc}}, \tag{16}$$

where

$$g_{\mathrm{ph}} = -\left(\frac{\partial \ln\Lambda_{\mathrm{ph}}}{\partial \ln V}\right)_T = 2\gamma + q + \frac{\sqrt{\frac{B}{AT}}\,\omega_0}{\left(1+\frac{B}{AT}\omega_0^2\right)\arctan\sqrt{\frac{B}{AT}}\,\omega_0}\left(\gamma_0 + q - \frac{1}{3}\right), \tag{17}$$

$$g_{\mathrm{loc}} = -\left(\frac{\partial \ln\Lambda_{\mathrm{loc}}}{\partial \ln V}\right)_T = -\gamma + \frac{1}{3} + \frac{2}{\omega_D^2 - \omega_0^2}(\omega_D^2\gamma - \omega_0^2\gamma_0), \tag{18}$$

$$\gamma_0 = -\left(\frac{\partial \ln\omega_0}{\partial \ln V}\right)_T = \gamma + \frac{u^{1/3}}{6\sqrt{1+u}}\left[\sqrt[3]{1+\sqrt{1+u}} - \sqrt[3]{1-\sqrt{1+u}}\right](6\gamma + 6q - 2). \tag{19}$$

RESULTS AND DISCUSSION

The isochoric thermal conductivity of the $\mathrm{Kr}_{1-\xi}\mathrm{Xe}_\xi$ ($\xi = 0.034$, 0.072, 0.14) solid solution was studied on samples of different densities in the interval of temperatures from 80 K to the onset of melting. The choice of the system, concentrations, and temperature interval was dictated by the following.

The phase diagram of the $\mathrm{Kr}_{1-\xi}\mathrm{Xe}_\xi$ solid solution is well known.[14] The liquid and solid phases have a point of equal concentrations at 114.1 K and $\xi = 0.15$. Between 75 and 114 K the components form an fcc solid solution for all $1 \geqslant \xi \geqslant 0$. When samples are grown with a temperature gradient along the measuring cell, the solid solution can become layered at $\xi > 0.15$. The highest Xe concentration was therefore limited to 14%.

The isochoric thermal conductivities of pure Kr and the $\mathrm{Kr}_{1-\xi}\,\mathrm{Xe}_\xi$ solution, for which the isochoric condition comes into play at 80 K are shown in Figs. 1–4 (black squares). The

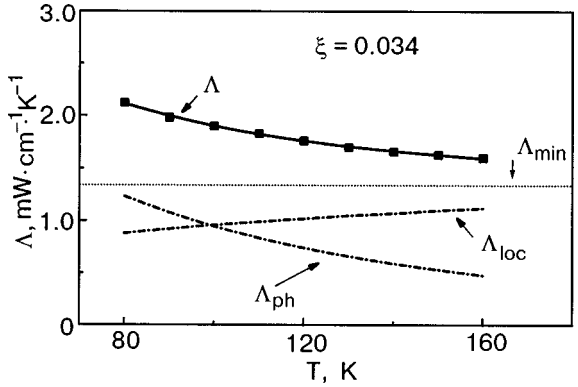

FIG. 2. Fitting results for the isochoric thermal conductivity and calculated relative contributions of low-frequency phonons and ''diffusive'' modes to the thermal conductivity of the $Kr_{1-\xi}Xe_{\xi}$ ($\xi=0.034$) solid solution (molar volume is 29.1 cm^3/mole).

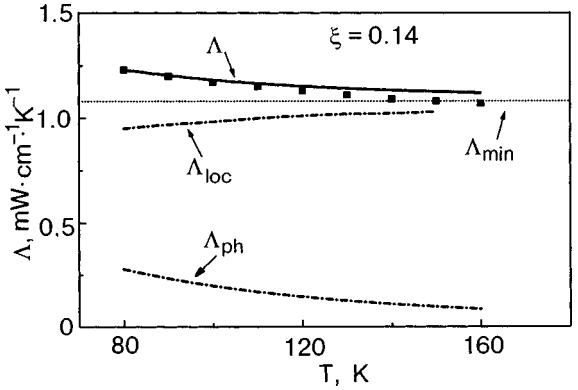

FIG. 4. Fitting results for the isochoric thermal conductivity and calculated relative contributions of mobile low-frequency phonons and ''diffusive'' modes to the thermal conductivity of the $Kr_{1-\xi}Xe_{\xi}$ ($\xi=0.14$) solid solution (molar volume is 29.8 cm^3/mole).

computer fitting of thermal conductivity using Eqs. (12)–(14) was performed by the least-squares method, varying the coefficients A and α. The parameters of the Debye model for thermal conductivity used in the fitting [a and v (Refs. 1, 14) and the coefficients Γ calculated by Eq. (6)] and the fitted values of A and α are listed in Table I along with the Bridgman coefficients obtained in the experiment and calculated by Eqs. (16)–(19). The calculation was done using the values $\gamma=2.5$ and $q=1$.[1,14]

The fitting results are shown in Figs. 1–4 (solid lines). The same figures show the contributions (dash-dot lines) to the thermal conductivity from the low-frequency phonons, Λ_{ph}, and from the ''diffusive'' modes, Λ_{loc}. The dotted line in the figures indicate the lower limits of the thermal conductivity Λ_{min}, which were obtained as asymptotes of the $\Lambda(T)$ dependence at $T\to\infty$.

It is seen in Fig. 1 that in pure Kr the ''localization'' of the high-frequency modes starts above 90 K. As the temperature rises, the amount of heat transferred by the ''diffusive'' modes increases, and at 160 K it becomes equal to the heat transferred by the low-frequency phonons. In the solution with $\xi=0.034$ (see Fig. 2) the ''localization'' of the high-frequency modes starts at 30 K, and above 100 K most of the heat is transferred by the ''diffusive'' modes. As the temperature and the impurity concentration increase, so does the amount of heat transferred by the ''diffusive'' modes. For $\xi=0.14$ (see Fig. 4) practically all the heat at $T\geqslant\Theta_D$ is transferred by the ''diffusive'' modes. The lower limit of thermal conductivity found by fitting is 1.1–1.2 times higher than Λ_{min} calculated by Eq. (1).

As is seen in Table I, the experimental and calculated Bridgman coefficients are in fairly good agreement if one notes that the value of g is estimated with large uncertainty and the model disregards phonon dispersion and the real density of states. The temperature dependence of the Bridgman coefficients $g=-(\partial\ln\Lambda/\partial\ln V)_T$ of the $Kr_{1-\xi}Xe_{\xi}$ solid solution calculated by Eqs. (16)–(19) is shown in Fig. 5. Equations (16)–(19) describe the general tendency of the Bridgman coefficient g to decrease as the crystal becomes increasingly disordered and most of the heat transferred by the ''diffusive'' modes.

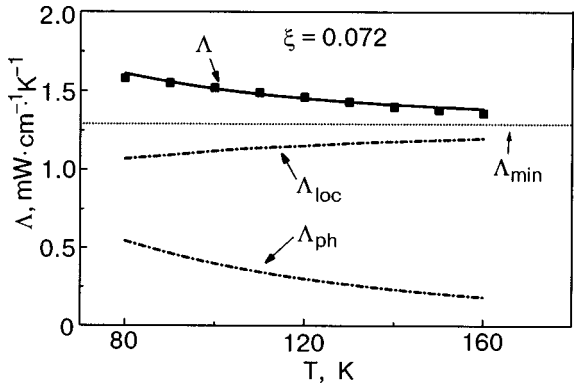

FIG. 3. Fitting results for the isochoric thermal conductivity and calculated relative contributions of mobile low-frequency phonons and ''diffusive'' modes to the thermal conductivity of the $Kr_{1-\xi}Xe_{\xi}$ ($\xi=0.072$) solid solution (molar volume is 29.4 cm^3/mole).

CONCLUSIONS

We have shown that the temperature and volume dependences of the thermal conductivity of the $Kr_{1-\xi}Xe_{\xi}$ ($\xi<0.14$) solid solution can be described in the framework of a model in which heat is transferred by low-frequency phonons; above the phonon mobility edge, heat is transferred by the ''diffusive'' modes migrating randomly from site to site. The phonon mobility edge ω_0 is found from the condition that the phonon mean free path determined by the um-

TABLE I. Parameters of the Debye model for thermal conductivity used in the fitting: a, v, and Γ, obtained through fitting A and α; the calculated g_{th} and experimental g_{exp} Bridgman coefficients.

ξ	$a\cdot10^{-8}$, cm	v, km/s	Γ	$A\cdot10^{-16}$, s/K	α	g_{exp}	g_{th}
0	3.62	0.86	0	3.1	1.2	9.4	9.2
0.034	3.64	0.86	0.1	3.8	1.2	8.0	5.7
0.072	3.65	0.87	0.19	6.4	1.2	5.5	4.6
0.14	3.67	0.87	0.29	9.8	1.1	4.0	3.8

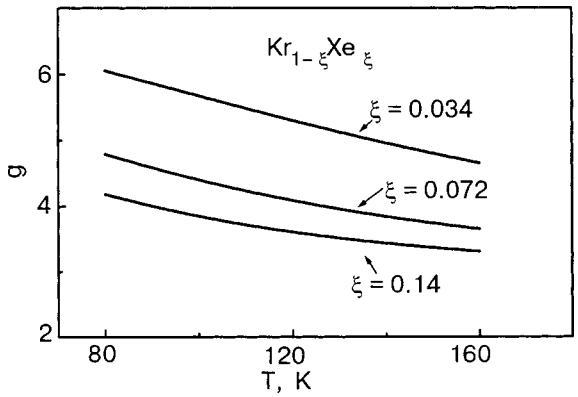

FIG. 5. Calculated temperature dependence of the Bridgman coefficient $g=-(\partial \ln \Lambda/\partial \ln V)_T$ for the $Kr_{1-\xi}Xe_{\xi}$ solid solution.

klapp processes and scattering on point defects cannot become smaller than one-half the phonon wavelength. The Bridgman coefficient $g=-(\partial \ln \Lambda/\partial \ln V)_T$ is the weighted mean over these modes, which differ strongly in their volume dependence. It is shown that the amount of heat transferred by the ''diffusive'' modes is quite large above 100 K even in pure Kr, and it increases with rising temperature and impurity concentration.

The authors are indebted to Prof. V.G. Manzhelii, Full Member of the National Academy of Sciences of Ukraine, and Prof. R. O. Pohl (Cornell University) for fruitful discussions.

This study was supported by the Ukrainian Ministry of Education and Science, Project F7/286-2001.

*E-mail: konstantinov@ilt.kharkov.ua

[1] M. L. Klein and J. A. Venables (Eds.), *Rare Gas Solids*, Vols. I–II, Academic Press, London, New York (1977).
[2] R. Berman, *Thermal Conduction in Solids*, Clarendon Press, Oxford (1976).
[3] G. A. Slack, in *Solid State Physics*, Vol. 34, H. Ehrenreich, F. Seitz, and D. Turnbull (Eds.) Academic Press, New York (1979).
[4] V. A. Konstantinov, V. G. Manzhelii, M. A. Strzhemechnyi, and S. A. Smirnov, Fiz. Nizk. Temp. **14**, 90 (1988) [Sov. J. Low Temp. Phys. **14**, 48 (1988)].
[5] V. A. Konstantinov, J. Low Temp. Phys. **122**, 459 (2001).
[6] D. G. Cahill, S. K. Watson, and R. O. Pohl, Phys. Rev. B **46**, 6131 (1992).
[7] V. A. Konstantinov, V. G. Manzhelii, R. O. Pohl, and V. P. Revyakin, Fiz. Nizk. Temp. **27**, 1159 (2001) [Low Temp. Phys. **27**, 858 (2001)].
[8] V. A. Konstantinov, R. O. Pohl, and V. P. Revyakin, Fiz. Tverd. Tela (St. Petersburg) **44**, 824 (2002) [Phys. Solid State **44**, 857 (2002)].
[9] V. A. Konstantinov, E. S. Orel, and V. P. Revyakin, Fiz. Nizk. Temp. **28**, 194 (2002) [Low Temp. Phys. **28**, 136 (2002)].
[10] P. G. Klemens, High Temp.-High Press. **5**, 249 (1983).
[11] M. C. Roufosse and P. G. Klemens, J. Geophys. Res. **79**, 703 (1974).
[12] J. L. Feldman, M. D. Kluge, P. B. Allen, and F. Wooten, Phys. Rev. B **48**, 12589 (1993).
[13] R. G. Ross, P. A. Andersson, B. Sundqvist, and G. Backstrom, Rep. Prog. Phys. **47**, 1347 (1984).
[14] V. G. Manzhelii, A. I. Prokhvatilov, I. Ya. Minchina, and L. D. Yantsevich, *Handbook of Binary Solutions of Cryocrystals*, Begell House Inc., New York (1996).

This article was published in English in the original Russian journal. Reproduced here with stylistic changes by AIP.

Quantum effects in the thermal conductivity of solid krypton–methane solutions

A. I. Krivchikov,* B. Ya. Gorodilov, V. G. Manzhelii, and V. V. Dudkin

B. Verkin Institute for Low Temperature Physics and Engineering of the National Academy of Sciences of Ukraine, 47 Lenin Ave., Kharkov 61103, Ukraine
Fiz. Nizk. Temp. **29**, 1012–1017 (September–October 2003)

The dynamic interaction of a quantum rotor with its crystalline environment has been studied by measurement of the thermal conductivity of the $Kr_{1-c}(CH_4)_c$ solid solutions at $c=0.05-0.75$ in the temperature region 2–40 K. The thermal resistance of the solutions was mainly determined by the resonance scattering of phonons on CH_4 molecules with the nuclear spin $I=1$ (the nuclear spin of the T species). The influence of the nuclear spin conversion on the temperature dependence of the thermal conductivity $\kappa(T)$ leads to a well-defined minimum on $\kappa(T)$. The temperature of the minimum depends on the CH_4 concentration. It was shown that the nonmonotonic increase of the anisotropic molecular field with the CH_4 concentration is caused by a compensation effect due to corrections in the mutual orientations of the neighboring rotors at c $\kappa>0.5$. The temperature dependence or $Kr_{1-c}(CH_4)_c$ is described within the Debye model of thermal conductivity taking into account the lower limit of the phonon mean free path. It is shown that phonon–rotation coupling is responsible for the anomalous temperature dependence of the thermal resistance at varying temperature. It increases strongly when the quantum character of the CH_4 rotation at low temperatures changes to a classical one at high temperatures. A thermal conductivity jump (a sharp increase in $\kappa(T)$ within a narrow temperature range) was also observed. The temperature position of the jump varies from 9.7 to 8.4 K when the CH_4 concentration changes from 0.25 to 0.45. © *2003 American Institute of Physics.* [DOI: 10.1063/1.1614187]

Owing to the high symmetry of the CH_4 molecule and to the arrangement of light H atoms at its periphery, the rotation of CH_4 molecules in some condensed media is nearly free even at low temperatures. In this case the energy spectrum of rotation is essentially dependent on the total nuclear spin of the rotating molecules.[1] The equilibrium concentration of the three possible nuclear spin species of CH_4, namely, the A, T, and E species with the total nuclear spins of the protons $I=2,1,0$, is determined by the temperature and by the symmetry of the potential field in which the CH_4 molecule is found in the condensed medium. The relaxation time taken to bring the spin species to the equilibrium concentration increases with decreasing temperature.[2] The experimental investigation at low temperatures should therefore take into account the real concentration of the A, T, and E species and the rate of their mutual transformation (the rate of spin conversion). The dynamics of the rotational motion and spin conversion have been studied in detail in different phases of solid CH_4 (Refs. 3 and 4) and in nonconcentrated solid solutions of CH_4 in Ar, Kr, and Xe crystals.[5–11]

A freely rotating molecule does not interact with the surroundings. In the real situation, however, even weak anisotropic interactions are important when we consider certain properties of condensed phases containing rotating molecules.[12] The rotor–lattice interaction in solids is referred to as a phonon–rotation coupling (PRC). It is precisely the PRC that is responsible for the equilibrium of the translational lattice vibrations and the rotation of the molecules. The PRC can, in particular, affect the thermal conductivity.[13–15] In turn, the thermal conductivity can be used as a tool to study the PRC.

The $Kr_{1-c}(CH_4)_c$ solid solutions are the most suitable objects on which to investigate the behavior of weakly hindered rotors in the crystal. Because of the spherical symmetry of Kr atoms and the close Lennard-Jones potential parameters of methane and krypton, the rotation of CH_4 molecules is weakly hindered; no significant dilatation occurs in the solid solution lattice, and the mutual solubility of the components in the solid phase is high ($0<c<0.8$). The high symmetry of the fcc lattice of the solution makes the interpretation of the results much easier. This system permits us to investigate both the PRC effect on the thermal conductivity and the anisotopic interaction within the rotor system, which manifests itself in the thermal conductivity.

As previous studies[15] of the thermal conductivity of nonconcentrated CH_4–Kr solutions ($c\leqslant 5\%$) have shown, the noninteracting T-species molecules are centers of strong resonance scattering of phonons. The conversion effect on the temperature dependence of the thermal conductivity of the solid solution was also examined.

The goal of this study is to investigate the PRC effect on the thermal conductivity of concentrated CH_4–Kr solid solutions in which the CH_4 subsystem can be considered as an ensemble of rotors interacting with one another and with the translational lattice vibrations.

The thermal conductivity of the $Kr_{1-c}(CH_4)_c$ solid solution ($c=0.05$, 0.10, 0.25, 0.45, 0.75) was measured in the interval 2–40 K using the steady-state technique. The measuring cell configuration and the technique of thermal conductivity measurement are described in Ref. 16. The samples were grown in a cylindrical stainless steel cell 38 mm long and 4.5 mm in inner diameter by crystallization of the liquid

solution at the equilibrium vapor pressure. The growth rate was 0.07 mm/min. The rate of cooling of the sample to the temperature $T=40$ K at which the measurement of the temperature dependence of the thermal conductivity was started was 0.15 K/min. During the cooling of the sample, a temperature gradient of 0.18 K/min along the cell was maintained. The technique of sample preparation with the smallest possible contents of structural defects (grain boundaries and dislocations) was optimized in the process of growing the polycrystalline samples and measurement of the thermal conductivity of pure krypton. The quality of the Kr sample could be judged from the value of the phonon maximum in the thermal conductivity. In our experiment we used krypton of natural isotopic composition, its purity being 99.94%. The Kr gas contained the following impurities: N_2–0.046%, Ar–0.012%, and $O_2 \leqslant 0.0005\%$. The chemical purity of the methane was 99.99%. The CH_4 contained 0.005% N_2. The O_2 impurity was below 0.0001%. The absolute error of the thermal conductivity coefficient was within 10% below 15 K and 20% above 15 K. In addition, the temperature dependence of the thermal conductivity $\kappa(T)$ at $c=0.05$ was measured to test our previously published results.[15]

The measured thermal conductivities of the $Kr_{1-c}(CH_4)_c$ solutions are shown in Fig. 1. The difference between the present results and the results of Ref. 15 at $c=0.05$ is within the experimental error. Figure 2 shows good agreement of our $\kappa(T)$ curves at $c=0.75$ and published data on the thermal conductivity of this solution[17] at $c=0.66$ and also with the theoretical dependence $\kappa(T)$ of the minimum thermal conductivity of solid krypton.[18]

The $\kappa(T)$ dependences taken at different CH_4 concentrations have two distinct features: i) a minimum in the thermal conductivity curve in the interval 4–10 K, and ii) a sharp change (jump) of the thermal conductivity to the right of the temperature minimum. The positions of the features on the temperature scale are dependent on the CH_4 concentration (see Table I). The temperatures of the minimum ($T_{\min}$) and of the jump (T_a) decrease as the concentration is increased to 0.45 and then increase on further concentration growth. The minimum in the $\kappa(T)$ curve is a manifestation of resonance phonon scattering by rotational excitations of the T-CH_4 molecules.

The results obtained show that on a further increase in the concentration, the dip of the $\kappa(T)$ curve observed in dilute solutions,[15] in particular at $c=0.05$, transforms into a minimum in concentrated solutions.

In the general case, the thermal conductivity of the $Kr_{1-c}(CH_4)_c$ solution is determined by the spin conversion and some processes of phonon scattering: i) the PRC between the translational lattice vibrations and the CH_4 rotor ensemble; ii) the Rayleigh scattering due to the different Kr and CH_4 masses; iii) phonon–phonon scattering, iv) scattering by structural defects. Among the above mechanisms, the PRC scattering is the most difficult to describe theoretically. Below we present the procedure of separating the PRC-related contribution from the total thermal resistance of the solution.

The basic mechanisms of phonon scattering in inert gas crystals of Ar, Kr, and Xe are well known, and commonly accepted expressions describing them are available. The temperature dependence of the thermal conductivity can usually be described by the Debye model for an isotropic solid, which ignores the difference between the phonon modes of different polarization:

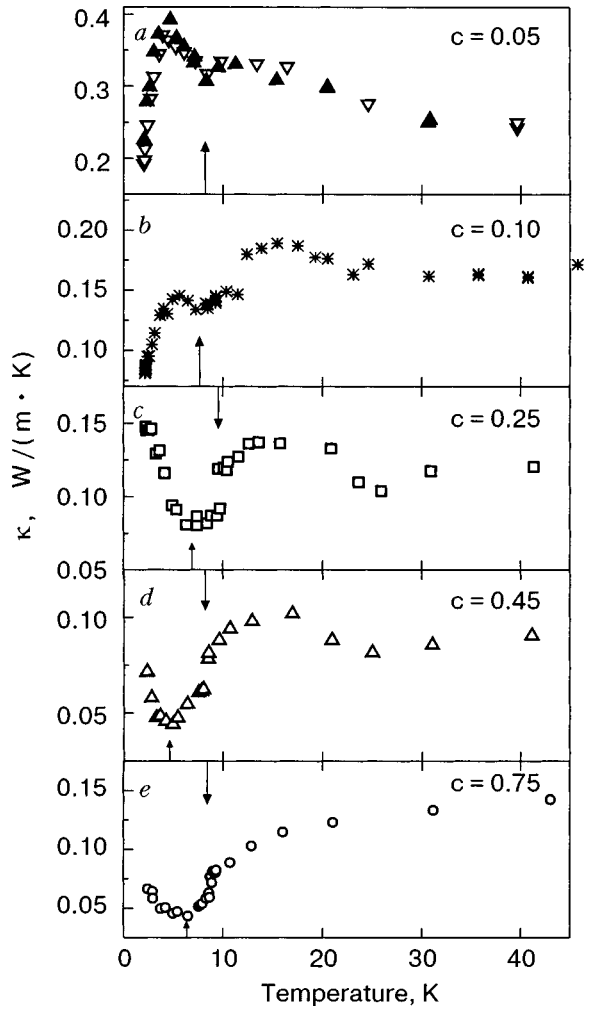

FIG. 1. The thermal conductivity of solutions $Kr_{1-c}(CH_4)_c$ as a function of temperature for various CH_4 concentrations c: 0.05 (a); 0.10 (b); 0.25 (c); 0.45 (d); 0.75 (e). The symbols ↑ and ↓, respectively, indicate the temperature values of the minimum and jump of the thermal conductivity curves.

$$\kappa(T)=\frac{k_B^4T^3}{2\pi^2\hbar^3s}\int_0^{\Theta/T}\left(\tau(x)+\frac{\pi\hbar}{k_BTx}\right)\frac{x^4e^{-x}}{(1-e^{-x})^2}dx; \quad (1)$$

where k_B is Boltzmann's constant, $\hbar$ is Planck's constant, Θ is the Debye temperature, s is the mean sound velocity, $x=\omega/k_BT$, and $\tau(x)$ is the effective relaxation time of the phonons involved in the scattering. The term $\pi\hbar/k_BTx$ is introduced into Eq. (1) to limit the thermal conductivity at high temperatures where the wavelength of the phonons becomes equal to half the lattice parameter (the limit was proposed by Cahill, Watson, and Pohl[18]). The normal phonon–phonon processes in Kr, CH_4, and their solutions are not intensive and can therefore be ignored.[15,17,19] The inverse relaxation time (relaxation rate) $\tau^{-1}(\omega,T)$ is a sum of relaxation times for all resistive processes of phonon scattering: τ_U^{-1} (three-phonon U-processes), τ_B^{-1} (by the boundaries), τ_{dis}^{-1} (by dislocations), $\tau_{\text{Rayleigh}}^{-1}$ (by point defects), and τ_{rot}^{-1} (by the rotational states of the CH_4 molecule):

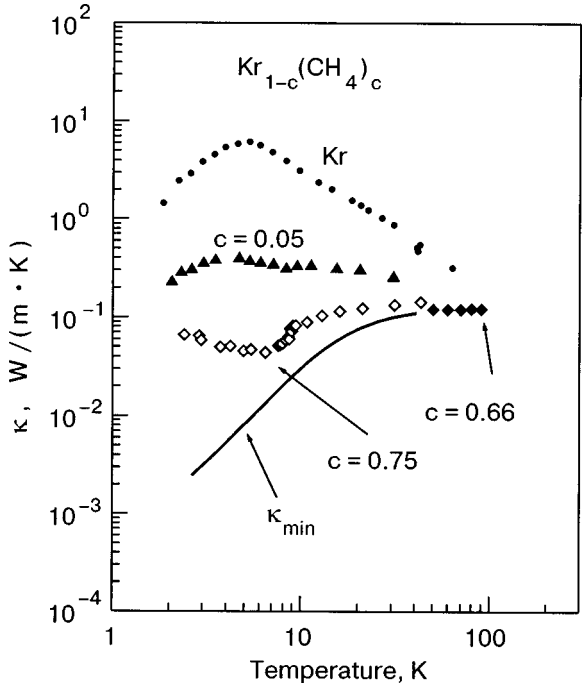

FIG. 2. Thermal conductivity $Kr_{1-c}(CH_4)_c$ for various CH_4 concentrations c: 0 (pure Kr); 0.05;[15] 0.66;[17] 0.75 (the present data). The solid curve is the calculated[18] temperature dependence of the limiting minimum value of $\kappa_{min}(T)$ for the case of pure Kr.

$$\tau^{-1}(\omega,T)=\tau_U^{-1}(\omega,T)+\tau_B^{-1}+\tau_{dis}^{-1}(\omega)+\tau_{Rayleigh}^{-1}(\omega)+\tau_{rot}^{-1}(\omega,T). \quad (2)$$

For the U-processes the relaxation rate is:

$$\tau_U^{-1}(\omega,T)=A\omega^2 T\exp(-b/T),$$

where $A\approx\hbar\gamma^2/(Ms^2\Theta)$, γ is the Grüneisen parameter, and M is the mean mass of the particles of the substance. The fitting parameters for pure Kr, $A=4.41\times10^{-16}$ s/K, $b=16$ K, were used.[15] M, s, b, and the relative variation of A as a function of the CH_4 concentration are given in Table II.

For boundary scattering the relaxation rate is:

$$\tau_B^{-1}=s/l,$$

where l is the phonon mean free path.

For scattering on dislocations the relaxation rate is:

TABLE I. Parameters characterizing the behavior of the thermal conductivity of $Kr_{1-c}(CH_4)_c$. Symbols: T_{min} and T_a are the temperatures of the minimum and jump, respectively, κ_{min} is the value of the thermal conductivity at T_{min}, $\Delta\kappa_a$ is the change of the thermal conductivity, and $\Delta W_{rot}^-/\Delta W_{rot}^+$ is the change of the relative thermal resistivity at T_a (ΔW_{rot}^- and ΔW_{rot}^+ are the values of ΔW_{rot} determined by extrapolation of $\Delta W_{rot}(T)$ from the left and right of T_a, respectively).

c, %	T_{min}, K	κ_{min}, W/(m·K)	T_a, K	$\Delta\kappa_a$, W/(m·K)	$\frac{\Delta W_{rot}^-}{\Delta W_{rot}^+}$
5	8.3 ± 0.3	0.31 ± 0.02	–	–	–
10	7.6 ± 0.3	0.133 ± 0.004	–	–	–
25	6.9 ± 0.3	0.081 ± 0.003	9.7 ± 0.2	0.025 ± 0.006	1.25
45	4.7 ± 0.2	0.043 ± 0.002	8.2 ± 0.2	0.015 ± 0.004	1.25
75	6.5 ± 0.2	0.043 ± 0.002	8.5 ± 0.2	0.016 ± 0.002	1.25

TABLE II. The values used to calculate the thermal conductivity by the Debye model. Parameters $A(c)/A(0)$ and b for the phonon–phonon mechanism and the parameter Γ for the Rayleigh scattering mechanism.

c	$\overline{M}$, g/mol	V, $\frac{cm^3}{mol}$	Θ, K	s, m/s	Γ, 10^5	$\frac{A(c)}{A(0)}$	b
0	83.8	27.13	71.7	856.9	0	1	16
0.05	80.4	27.41	72.6	870.6	0.546	0.995	16
0.10	77.0	27.69	73.5	884.4	1.084	0.990	16
0.25	66.8	28.54	76.9	934.7	2.616	0.985	16
0.45	53.3	29.66	83.4	1027	4.265	1.001	16
0.75	33.0	31.34	101	1269	4.726	1.107	16

$$\tau_{dis}^{-1}(\omega)=D\omega,$$

where D is a parameter that depends on the dislocation density. The fitting parameters for the above three mechanisms were found using measured data on the thermal conductivity of pure Kr.[15] The variation of these quantities was assumed negligible even in concentrated $Kr_{1-c}(CH_4)_c$ solutions.

Since the masses of Kr atoms and CH_4 molecules are different, the relaxation rate for scattering by point defects is expressed as

$$\tau_{Rayleigh}^{-1}(\omega)=\frac{\Gamma\Omega_0}{4\pi s^3}\omega^4,$$

where $\Gamma=c(1-c)(\Delta M/M)^2$, ΔM is the mass difference between the pure components of the solution, and Ω_0 is the unit cell volume. The values are presented in Table II. The changes in the force constants and the dilatation near the impurity center were neglected because the interaction parameters are close for Kr atoms and CH_4 molecules.[1]

There is no commonly accepted expression for the relaxation rate τ_{rot}^{-1} describing the PRC mechanism. The general PRC regularities can be established through separation from the total thermal resistance of the contributions corresponding to different mechanisms of scattering. The excess thermal resistance in $Kr_{1-c}(CH_4)_c$ can be found from the experimental thermal conductivities of the solution and pure Kr as $\Delta W(T)=W(T)-W_{Kr}(T)$, where $W(T)\equiv1/\kappa(T)$. To illustrate the separation of the thermal resistance contributions, Fig. 3 shows the temperature dependence of $\Delta W/W_{Kr}$ for $c=0.45$. There is a considerable contribution of the CH_4 molecules to the total thermal resistance. At helium temperatures ΔW is over an order of magnitude higher than W_{Kr}. The ratio $\Delta W/W_{Kr}$ decreases with increasing temperature. It is, however, impossible to separate the PRC-induced contribution ΔW_{rot} directly from the excess thermal resistance. This can be done using the expression

$$\Delta W_{rot}(T)=W(T)-W_{calc}(T),$$

where $W_{calc}(T)$ is the dependence obtained by Eq. (1) taking into account all the scattering mechanisms included in the sum of Eq. (2) except for the PRC mechanism.

The dependence $W_{calc}(T)$ was calculated taking into account that the Debye temperatures Θ of the pure components Kr and CH_4 differ considerably (see Table II). As the concentration changes from 0 to 1, the Debye temperature in-

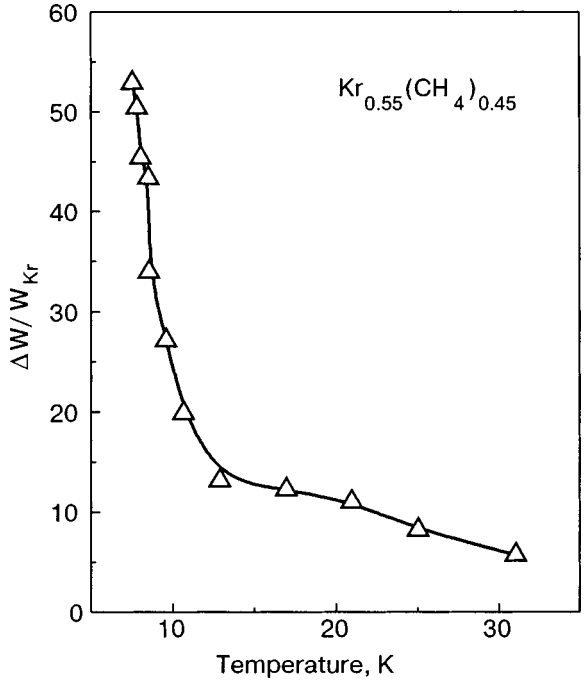

FIG. 3. The excess thermal resistance $\Delta W(T)=W(T)-W_{\mathrm{Kr}}(T)$ for $c=0.45$, divided by the thermal resistance of pure Kr, as a function of temperature.

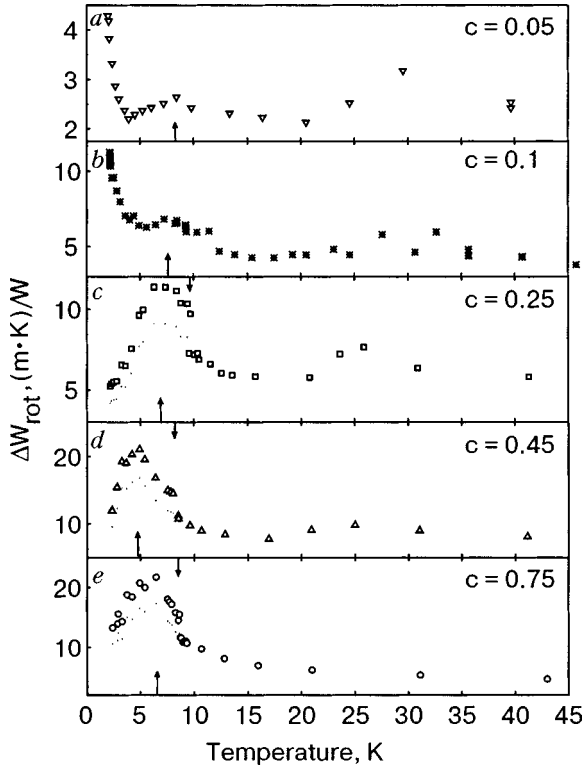

FIG. 4. The thermal resistance ΔW_{rot} due to PRC mechanism in the $\mathrm{Kr}_{1-c}(\mathrm{CH_4})_c$ solution as a function of temperature for various concentrations of CH_4, c: 0.05 (a); 0.10 (b); 0.25 (c); 0.45 (d); 0.75 (e). The arrows ↑ and ↓ indicate the temperature of the maximum and the jump of the thermal resistance.

creases from 71.7 to 140 K,[20] while the mean mass $\overline{M}$ decreases from 83.8 to 16. For a concentrated solution, Θ can be estimated roughly as a function of CH_4 concentration:[21]

$$\Theta(c)=\Theta_{\mathrm{Kr}}\left(\frac{V_{\mathrm{Kr}}}{V(c)}\right)^{d}\sqrt{\frac{M_{\mathrm{Kr}}}{M(c)}}, \tag{3}$$

where V is the molar volume, $M(c)=(1-c)M_{\mathrm{Kr}}+cM_{\mathrm{CH_4}}$, $V(c)=(1-c)V_{\mathrm{Kr}}+cV_{\mathrm{CH_4}}$, and d is a parameter equal to the Grüneisen constant for isotopic solutions. The d value for $\mathrm{Kr}_{1-c}(\mathrm{CH_4})_c$ was found by the substitution of $\Theta(c)$, $V(c)$, and $M(c)$ in Eq. (3) with the corresponding values obtained for pure solid CH_4. The sound velocity s was calculated using $\Theta(c)$ and $V(c)$:

$$s=\frac{k_B}{\hbar(6\pi^2N_A)^{1/3}}\Theta(c)V(c)^{1/3},$$

where N_A is Avogadro's number. Values of V, Θ, and s for different c are listed in Table II.

The curves $\Delta W_{\mathrm{rot}}(T)$ describing the PRC-induced thermal resistance are shown in Fig. 4 for different CH_4 concentrations.

The concentration dependence of ΔW_{rot} is nonmonotonic. A change in the concentration from 0.05 to 0.45 leads to an increase in the thermal resistance. A further increase in c from 0.45 to 0.75 has practically no effect on ΔW_{rot}. The nonmonotonic dependence $\Delta W_{\mathrm{rot}}(T)$ describes the PRC evolution in the system of interacting rotors with temperature. The dependence $\Delta W_{\mathrm{rot}}(T)$ has two maxima: a low-temperature maximum in the temperature region of the orientationally disordered phase with a frozen orientational disorder, and a maximum in the dynamic disorder phase.[6] In the whole interval of temperatures $\Delta W_{\mathrm{rot}}(T)$ is determined by resonance phonon scattering by the rotational excitations of the T-CH_4 molecules.[15] The decrease in the thermal resistance ΔW_{rot} with decreasing temperature observed to the left of the maximum occurs because the number of T molecules decreases with decreasing temperature due to the T—A spin conversion. The conversion is more intensive in the system of interacting rotors,[11] where it leads to an equilibrium distribution of the CH_4 species in the investigated temperature interval for $c>10\%$. In the system of noninteracting rotors at $c<10\%$ and $T<5$ K, the curve $\Delta W_{\mathrm{rot}}(T)$ is observed to rise as the temperature decreases. The increase can be explained by assuming that the T-CH_4 concentration exceeds the equilibrium value and does not change with temperature.

In the low-temperature interval (2–10 K) the molecules in the solutions studied have a well-structured rotational spectrum with slightly broadened energy levels for both noninteracting molecules and the interacting rotor systems.[6] The finite width of the energy levels is determined by the potential field in which the CH_4 molecules are located and by the interaction between the CH_4 rotation and the phonons. Above 10 K the energy levels broaden because the interaction of the CH_4 rotation with translational lattice vibrations becomes more intensive. In this temperature region we can observe smeared energy levels, which suggests growth of the PRC with rising temperature.

Another feature of the $\Delta W_{\mathrm{rot}}(T)$ behavior is a jump in a narrow temperature interval (a 25% increase) with decreasing temperature. The relative change in the thermal resistance at the temperature of the jump is independent of the CH_4 concentration.

A possible reason for the jump may be connected with

cooperative phenomena in the system of interacting rotors. For example, in a certain region of CH_4 concentrations and temperatures, the behavior of the system of interacting rotors can be influenced by its so-called re-entrant character:[22] when the temperature increases, the disordered system changes into the ordered state; however, on a further rise of temperature the system comes back to the disordered state. Thus the system undergoes two phase transitions with increasing temperature: a low-temperature orientational disorder–order (quantum nature) transition, and the high-temperature change of a classical nature from the ordered state into the disordered phase. The behavior of the system of interacting CH_4 molecules in $Kr_{1-c}(CH_4)_c$ is determined by the octupole—octupole interaction, which becomes more intensive with rising temperature because the number of T-CH_4 molecules increases (the T-CH_4 molecule has a larger octupole moment) and then becomes weaker as the CH_4 molecules are being partially substituted with the Kr atoms.

The authors would like to thank to Professors R. Pohl, W. Press, G. Weiss, A. Jezhowski, and B. Danilchenko for helpful discussions. This work is supported by Ukrainian Ministry of Education and Science Grant No. 2M/74.

*E-mail: krivchikov@ilt.kharkov.ua

[1] V. G. Manzhelii, Yu. A. Freiman, M. L. Klein, and A. A. Maradudin (Eds.), *The Physics of Cryocrystals*, AIP Press, New York (1996).
[2] S. Grieger, H. Friedrich, B. Asmussen, K. Guckelsberger, D. Nettling, W. Press, and R. Scherm, Z. Phys. B: Condens. Matter **87**, 203 (1992).
[3] W. Press, A. Kollmar, Solid State Commun. **17**, 405 (1975).
[4] W. Press, *Single-Particle Rotations in Molecular Crystals*, Vol. 92 of Springer Tracts in Modern Physics, Springer-Verlag, Berlin, Heidelberg (1981).
[5] B. Asmussen, M. Prager, W. Press, and H. Blank, J. Chem. Phys. **98**, 158 (1992).
[6] S. Grondey, M. Prager, W. Press, and Heidemann, J. Chem. Phys. **84**, 2204 (1986).
[7] S. Grondey, M. Prager, and W. Press, J. Chem. Phys. **86**, 6465 (1987).
[8] M. Prager, W. Langel, B. Asmussen, W. Press, C. J. Carlile, and H. Blank, J. Chem. Phys. **99**, 2052 (1993).
[9] M. Prager, B. Asmussen, W. Press, H. Blank, and C. J. Carlile, J. Chem. Phys. **95**, 569 (1991).
[10] Ya. Minchina, V. G. Manzhelii, M. I. Bagatskii, O. V. Sklyar, D. A. Mashchenko, and M. A. Pokhodenko, Fiz. Nizk. Temp. **27**, 773 (2001) [Low Temp. Phys. **27**, 568 (2001)].
[11] M. I. Bagatskii, V. G. Manzhelii, I. Ya. Minchina, D. A. Mashchenko, and I. A. Gospodarev, J. Low Temp. Phys. **130**, 459–475 (2003).
[12] R. M. Lynden-Bell and K. H. Michel, Rev. Mod. Phys. **66**, 721 (1994).
[13] A. Jezowski, H. Misiorek, V. V. Sumarokov, and B. Ya. Gorodilov, Phys. Rev. B **55**, 5578 (1997).
[14] V. G. Manzhelii and I. N. Krupskii, Fiz. Tverd. Tela (Leningrad) **10**, 284 (1968) [Phys. Solid State **10**, 221 (1968)].
[15] V. V. Dudkin, B. Ya. Gorodilov, A. I. Krivchikov, and V. G. Manzhelii, Fiz. Nizk. Temp. **26**, 1023 (2000) [Low Temp. Phys. **26**, 762 (2000)].
[16] O. A. Korolyuk, B. Ya. Gorodilov, A. I. Krivchikov, A. V. Raenko, and A. Jezowski, Fiz. Nizk. Temp. **27**, 1159 (2001) [Low Temp. Phys. **27**, 504 (2001)].
[17] V. A. Konstantinov, V. G. Manzhelii, R. O. Pohl, and V. P. Revyakin, Fiz. Nizk. Temp. **27**, 773 (2001) [Low Temp. Phys. **27**, 858 (2001)].
[18] D. G. Cahill, S. K. Watson, and R. O. Pohl, Phys. Rev. B **46**, 6131 (1992).
[19] O. A. Korolyuk, B. Ya. Gorodilov, A. I. Krivchikov, and V. V. Dudkin, Fiz. Nizk. Temp. **26**, 323 (2000) [Low Temp. Phys. **26**, 235 (2000)].
[20] E. Gregoryanz, M. J. Clouter, N. H. Rich, and R. Goulding, Phys. Rev. B **58**, 2497 (1998).
[21] M. I. Bagatskii, I. Ya. Minchina, P. I. Muromtsev, A. I. Krivchikov, and V. S. Parbuzin, Fiz. Nizk. Temp. **16**, 1009 (1990) [Low Temp. Phys. **16**, 589 (1990)].
[22] T. Yamamoto, Y. Kataoka, and K. Okada, J. Chem. Phys. **66**, 2701 (1977).

This article was published in English in the original Russian journal. Reproduced here with stylistic changes by AIP.

Role of the orientational subsystem in the expansion of pure SF_6, $CHCl_3$, C_6H_6, CCl_4, and N_2O with Kr impurity

N. N. Zholonko* and V. V. Tsibulin

Cherkasy State University of Technology, 460 Shevchenko Blvd., Cherkasy 18006, Ukraine

I. Sarwar

National Technical University of Ukraine "KPI," 37 Peremogi Ave., Kiev, Ukraine

Fiz. Nizk. Temp. **29**, 1018–1020 (September–October 2003)

The linear expansion coefficients of solid bulk samples of N_2O with 5% Kr impurity are measured by an absolute dilatometric method in comparison with pure N_2O in the temperature range 80–150 K. An additional unusual orientational effect is discussed. An analysis of the data from measurements of the linear expansion coefficients of pure solid SF_6, $CHCl_3$, C_6H_6, and CCl_4 in comparison with solid Xe in the temperature range 80–170 K is carried out in order to determine the role of molecules' orientational disordering in the thermal expansion of the given condensed systems. The results are discussed in connection with the problem of determining the contribution of orientational subsystems with different types of molecular symmetry to the total thermal expansion and its behavior in various temperature intervals of solid phase existence. © *2003 American Institute of Physics.* [DOI: 10.1063/1.1614188]

INTRODUCTION

As compared to solidified rare gases, molecular crystals have a more complicated character of the interaction between molecules on account of the existence of angular evolutions of the orientational subsystem and also fluctuational intramolecular oscillations. In the analysis of crystal lattice dynamics the last factors can rather often be neglected[1] because of the significantly larger energy of bonding in a molecule as compared to the energy of sublimation E. This allows one to simplify the analysis and to concentrate attention on the peculiarities of the interaction between the collective translational excitations (phonons) and the orientational molecular motions.

Depending on the molecular symmetry and temperature, the orientational excitations in molecular crystals can have the collective character of waves (librons) or even almost free rotation of separate molecules. In some molecular crystals (N_2O, CO_2, $CHCl_3$) the anisotropic interaction is so strong that the crystal melts before complete orientational disordering occurs. When diluted by simple atomic particles of nearly the same size, such systems often can behave in a rather unusual way. On the other hand, there still exist rather complicated problems in understanding of the temperature dependence of the thermal properties for many pure molecular crystals. This paper is devoted to further study of high-temperature behavior of the linear expansion of molecular crystals with different symmetry of the particles.

MAIN PART

The studies of the thermal expansion coefficients of solid SF_6, $CHCl_3$, CCl_4 and C_6H_6 were carried out in an interval of temperatures 85–170 K on an optical laser Michelson interferometric dilatometer. We measured the linear thermal expansion coefficients for four samples of solid SF_6, 6 mm in diameter and 10 cm long, each grown from the gas, and also two samples of CCl_4, three samples of $CHCl_3$, and two samples of C_6H_6, obtained from the liquid. The total error of determination of the linear thermal expansion is 10–15%.

The high-temperature β phase of solid SF_6 has a cubic bcc lattice of space symmetry $Im3m$ (Refs. 2–9). The existence region of the β phase is extraordinarily large: the crystallization of SF_6 occurs at 222.4 K, and the phase transition lowering the symmetry of the translational and orientational subsystems of the crystal does not occur until 94.3 K. The interaction between the nearest neighbors in the bcc phase tends to order the molecules so that their S–F bonds lie along the {100} direction, and in the interaction with the next-nearest neighbors a repulsion between the fluorine atoms predominates. The data from recent structural studies indicate a strict orientational order in SF_6 above the phase transition temperature. This makes SF_6 different from such plastic crystals as CH_4, CCl_4, adamantane, etc., in which the destruction of the long-range order occurs immediately after the phase transition. The intensive growth of processes of orientational disordering in SF_6 begins only at temperatures above 150 K and is of a dynamic nature. The SF_6 molecule has octahedral symmetry, which means a spherical rotator with three perpendicular principal axes. The CCl_4 molecule is also highly symmetric (tetrahedral) and is a spherical rotator with nonperpendicular principal axes. As opposed to this, the $CHCl_3$ and C_6H_6 molecules are less symmetrical objects. The first have an even nonzero dipole moment. They are both only symmetrical (not spherical) rotators. For this reason there will be larger barriers impeding rotation.

The contribution of rotary motion to the thermal expansion can be appraised by a comparison of the corresponding properties of molecular crystals and solidified rare gases. The properties of the latter are connected only with translational motion of the molecules, without rotations. To allocate the

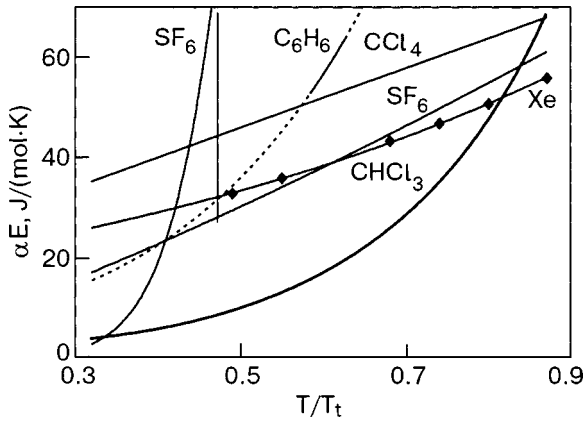

FIG. 1. Temperature dependence of the linear expansion coefficients α for solid SF_6, $CHCl_3$, C_6H_6, and CCl_4 in reduced coordinates, where E is the sublimation energy and T_t is the triple point.

contribution of the rotary subsystem to the thermal expansion of the molecular crystals studied, we used the already known temperature dependence of the volume thermal expansion coefficient of solid Xe.[10] The latter has a mass close to that of the molecular crystals studied. The experimental dependences for all the investigated substances in comparison with Xe are plotted in reduced coordinates in Fig. 1, where α is the coefficient of linear expansion, E is the sublimation energy, and T_t is the temperature of three-phase equilibrium.

In Fig. 1 we can see the known phase transition for solid SF_6 (near 94.3 K), near which a jumplike drop is observed on the temperature growth of the thermal expansion coefficient. Such anomalies of the thermodynamic properties are caused by enhancement of the correlation of rotary motion.[10] Our dilatometric SF_6 results are in good agreement with x-ray diffraction data.[11] This allows us to check our experimental equipment. Active transitions from orientational molecular oscillations to rotations of molecules in solid SF_6 give a weak additional contribution to thermal expansion in the form a somewhat larger slope of the smoothed line in comparison with Xe. In the low-temperature phase (below 94.3 K), where the free rotation is absent altogether, the above-mentioned effect appears significant. Thus the weak dependence of the thermal expansion coefficient for solid SF_6 at temperatures higher than the phase transition temperature in the given coordinates indicates the transition to rotational molecular motion. In other words, SF_6 molecule rotational correlations are weakened above the phase transition.

The low-temperature phase of solid CCl_4 is monoclinic ($C2/c-C_{2h}^6$; Ref. 13) and contains 32 molecules per unit cell. The molecular centers of interaction have tetrahedral symmetry and a slightly deformed cubic bcc lattice. The close values of the slopes of the reduced curves for solid CCl_4, Xe, and SF_6 may also indicate a transition of the motion of some of the molecules to hindered rotation in the monoclinic phase in the temperature range 80–170 K. Similar behavior of a rotary subsystem of CCl_4 crystals is caused by the high tetrahedral symmetry of their molecules.

The high-temperature phase of solid chloroform $CHCl_3$ has an orthorhombic structure of space symmetry $Pnma-D_{2h}^{16}$ with four molecules per unit cell and triple-point temperature $T_t=209.5$ K.[14] The noncentral forces in $CHCl_3$ crystals are great. The orientational order is maintained up to the melting temperature, and the rotary motion constitutes librations. The reorientation frequencies do not exceed 10^4 per second.[15,16]

As can be seen from Fig. 1, for the asymmetrical chloroform molecules, with a nonzero dipole moment in the low-temperature region, the additional effect is absent, as is indicated by the insignificant increase of the libration amplitude with the temperature. However, with further increase in temperature we have a stronger dependence of the thermal expansion of $CHCl_3$ crystals in reduced coordinates. This can be seen from a comparison with solid CCl_4, which has a central interaction of about the same value but a lower rotary barrier. This last circumstance indicates appreciable growth of the libration amplitudes.

At pressures lower than 1.2 MPa, solid benzene C_6H_6 exists in one crystalline form, corresponding to space group $Pbca-D_{2h}^{15}$ with four molecules per unit cell. A weak orientation effect is present near the transition of C_6H_6 to rotation about the sixfold symmetry axis (90–120 K). At $T>120$ K, however, the dependence of the thermal expansion in C_6H_6 in reduced coordinates is stronger even than in $CHCl_3$. This may also attest to an increase of the libration amplitudes of the benzene molecules about two other twofold symmetry axes lying in the plane of the benzene ring.

As to the $CHCl_3$ and N_2O molecules, they are far from spherical symmetry and have a dipole moment. Studies of the thermal expansion coefficients of solid bulk samples of N_2O with 5% Kr were carried out in the temperature interval 85–150 K on the same equipment. We measured the linear thermal expansion coefficients for two samples. The experimental dependence in comparison with pure N_2O is shown in Fig. 2. As we can see, dilution with atomic Kr causes a weakening of the dependence. The difference of the thermal expansion coefficients is seen to grow with increasing temperature.

This anomaly of the thermodynamic properties may be caused by easing of the free rotation due to the replacement of one-fifth of the linear atoms by spherical ones. It should be emphasized that there are unpublished data indicating that the solubility of Kr inN_2O is not less than 5%.

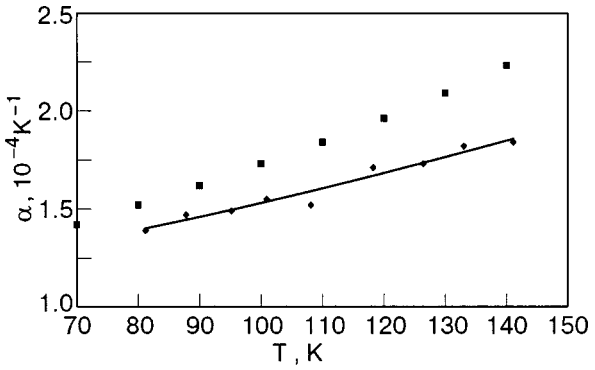

FIG. 2. Temperature dependence of the linear expansion coefficients α for solid pure N_2O (top curve) and N_2O with 5% Kr (bottom curve).

CONCLUSIONS

The thermal expansion orientational effect in reduced coordinates is weakly expressed for the more symmetric molecules SF_6 and CCl_4 in the high-temperature region investigated, while for the less symmetrical molecules $CHCl_3$ and C_6H_6 the effect is significant. This could be explained by the fact that for growth of the libration amplitudes the octahedral molecules SF_6 and tetrahedral CCl_4 require smaller additional volumes, and the transition to their hindered rotation is not accompanied by an appreciable volume increase. At the same time, $CHCl_3$ and C_6H_6 molecules do not pass to the state of hindered rotation at the temperatures of experiment (except for rotation around the sixfold axis for solid benzene), and they require significant additional volumes for increase of the libration amplitudes and jumps to adjacent equilibrium orientations with higher energy levels. Substitution of the spherically symmetric impurity Kr for the N_2O molecules leads to a weaker growth of the linear expansion with the temperature than for pure solid N_2O. This may indicate that the high-temperature volume effects in solid N_2O are influenced more strongly by the rotational states than by the translational states.

*E-mail: zholonko@yahoo.com

[1] V. G. Manzhelii and Y. A. Freiman, *Physics of Cryocrystals*, American Institute of Physics, Woodbury, New York (1997).
[2] A. Eucken and F. Schroder, Z. Phys. Chem. A **41**, 307 (1938).
[3] J. Michel, M. Drifford, and P. Rigny, J. Chem. Phys. **67**, 31 (1970).
[4] G. Dolling, B. M. Powell, and V. F. Sears, Mol. Phys. **37**, 1859 (1979).
[5] G. Raynard, G. J. Tatlock, and J. A. Venables, Acta Crystallogr., Sect. B: Struct. Crystallogr. Cryst. Chem. **38**, 1896 (1982).
[6] R. Raynard and J. A. Venables, Ultramicroscopy **23**, 433 (1987).
[7] L. S. Bartell, E. J. Valente, and J. C. Caillat, J. Phys. C **91**, 2498 (1987).
[8] B. M. Powell, M. Dove, G. S. Pawley, and L. S. Bartell, Mol. Phys. **62**, 1127 (1987).
[9] L. S. Bartell, J. C. Caillat, and B. M. Powell, Science **236**, 1463 (1987).
[10] Rare Gas Solids, M. L. Klein and L. A. Venables (eds.), Acad. Press, London (1976–1977).
[11] A. P. Isakina and A. I. Prokhvatilov, Fiz. Nizk. Temp. **19**, 201 (1993) [Low Temp. Phys. **19**, 142 (1993)].
[12] A. P. Isakina, A. I. Prokhvatilov, and J. Rodriges-Carvajal, Fiz. Nizk. Temp. **26**, 404 (2000) [Sov. J. Low Temp. Phys. **26**, 406 (2000)].
[13] R. Powers and R. Rudman, J. Chem. Phys. **3**, 1629 (1980).
[14] V. A. Konstantinov, V. G. Manzhelii, and S. A. Smirnov, Fiz. Nizk. Temp. **17**, 883 (1991) [Sov. J. Low Temp. Phys. **17**, 462 (1991)].
[15] H. S. Gutowsky and D. N. McCall, J. Chem. Phys. **2**, 548 (1966).
[16] N. G. Parsonage and A. K. Staveley, *Disorder in Crystals*, Clarendon Press, Oxford (1978).

This article was published in English in the original Russian journal. Reproduced here with stylistic changes by AIP.

Influence of rotational motion of molecules on the thermal conductivity of solid SF_6, $CHCl_3$, C_6H_6, and CCl_4

O. I. Purskii* and N. N. Zholonko

Technological State University of Cherkassy, 460 Shevchenko Blvd., Cherkassy 18006, Ukraine

V. A. Konstantinov**

B. Verkin Institute for Low Temperature Physics and Engineering of the National Academy of Sciences of Ukraine, 47 Lenin Ave., Kharkov 61103, Ukraine

Fiz. Nizk. Temp. **29**, 1021–1026 (September–October 2003)

The thermal conductivity of solid SF_6, $CHCl_3$, C_6H_6, and CCl_4 is investigated by the linear-flow method under saturated vapor pressures in the temperature range from 80 K to the respective melting temperatures, and the values obtained are then adjusted to a constant density of the samples. The contributions of the phonon–phonon and phonon–rotation interactions to the total thermal resistance are separated using the modified method of reduced coordinates. It is shown that the phonon–rotation contribution to the thermal resistance of the crystals decreases as the rotational motion of the molecules attains more freedom. © *2003 American Institute of Physics.* [DOI: 10.1063/1.1614189]

INTRODUCTION

Heat transfer in simple molecular crystals is determined by both translational and rotational motion of molecules at the lattice sites. As the temperature rises, the rotational motion of molecules in crystals can have basically the following stages: an increase in the libration amplitudes, jumplike reorientation of the molecules, increasing frequency of reorientations, hindered rotations of molecules and, finally, nearly free rotation of molecules. By choosing crystals with different parameters of the molecular interaction and varying the temperature, it is possible to change the degree of orientational ordering and thus to investigate the influence of the rotational motion of molecules on the behavior of the thermal conductivity.

The objects of this study were the molecular crystals of SF_6, $CHCl_3$, C_6H_6, and CCl_4. The SF_6 molecule has octahedral symmetry. At 222.4 K sulfur hexafluoride crystallizes into a bcc lattice of $Im3m$ (O_h^9) symmetry with two molecules per unit cell. As a result, the molecule and its surroundings have the same symmetry. On further cooling to 94.3 K a polymorphous transition occurs, which suppresses the symmetry of the translational and orientational subsystem to a monoclinic one, of space group $C2/m$ (C_{2h}^3) with $Z=6$, where Z is the coordination number. One-third of the SF_6 molecules take the high-symmetry ($2/m$) positions and two-thirds of the molecules occupy the low-symmetry (m) positions.[1,2]

Sulfur hexafluoride is often classed with substances that have a plastic crystalline phase. Indeed, the relative molar entropy of melting $\Delta S_f/R$ of SF_6 is 2.61,[3] which is close to the Timmermans criterion. Here R is the universal gas constant. However, the nature of the orientational disorder in the high-temperature phase of SF_6 is somewhat different from that of plastic phases in other molecular crystals, where the symmetries of the molecule and its surroundings do not coincide. The interaction between the nearest neighbors in the bcc phase is favorable for molecular ordering caused by the S—F bonds along the {100} direction, and the interaction with the next-nearest neighbors is dominated by repulsion between the F atoms. According to x-ray and neutron diffraction data[1,2,4] a strict order is observed in SF_6 (in phase I) just above the phase transition point. The structural dynamical factor $\mathcal{R}$ characterizing the degree of the orientational order is close to unity in the interval 95–130 K. This feature sets SF_6 apart from other plastic crystals, such as methane, carbon tetrachloride, adamantane, and so on, where the long-range orientational order becomes disturbed immediately after the phase transition. Orientational disordering in SF_6 starts to intensify only above 140 K. As follows from the analysis of the terms of the Debye—Waller factor derived from neutron-diffractometric data for the high-temperature phase of SF_6, the F atoms have large effective libration amplitudes. As the temperature rises, the amplitudes increase to 20° and higher, but the F localization is still appreciable near the {100} direction. This implies that the orientational structure of SF_6 (I) does not become completely disordered even at rather high temperatures. The disordering itself is of a dynamic nature. The increasing amplitudes of librations are not the only factor responsible for the increasing orientational disordering with rising temperature. It is, rather, connected with dynamic reorientations, which become more intensive due to frustrations of the molecular interactions.

Owing to these features, SF_6 offers a considerable possibility for investigating the influence of wide-range rotational states of the molecules on the thermal conductivity in a monophasal one-component system, where such states can vary from nearly complete orientational ordering to frozen rotation.

Chloroform ($CHCl_3$) has only one crystallographic modification in the whole interval of existence of the solid phase up to the melting temperature $T_m=209.7$ K. It has the spatial symmetry $Pnma$ (P_{2h}^{16}) and four differently oriented molecules in the orthorhombic cell.[5–7] It is known from Ra-

man and IR absorption (20 K) data[7] that the translational modes take the frequency band up to 60 cm^{-1} (86 K) and partially overlap the librational modes in the 60–100 cm^{-1} band (86–144 K). The dipole moment of the $CHCl_3$ molecule is 1.01 D. Nuclear quadrupole resonance (NQR) on the ^{35}Cl nuclei has been observed in $CHCl_3$ up to the melting temperature.[8] These data indicate that there are no molecular reorientations at frequencies above 10^4 s^{-1}. The high entropy of melting, $\Delta S_f/R=5.4$, also attests to a high degree of ordering in $CHCl_3$ (Ref. 3).

Solid benzene under the pressure of its own saturated vapor has only one crystallographic modification: it has the orthorhombic spatial symmetry $Pbca$ (D_{2h}^{15}) with four molecules per unit cell.[9,10] Benzene melts at 278.5 K and the melting-caused change in the entropy is $\Delta S_f/R=4.22$,[3] which is much higher that the Timmermans criterion for *OD* phases. The high-temperature magnitude of the Debye temperature of C_6H_6 is 120 K.[11]

In the interval 90–120 K the second NMR moment of C_6H_6 drops considerably as a result of the molecular reorientations in the plane of the ring around the sixfold axis.[12] The activation energy of the reorientational motion estimated from the spin–lattice relaxation time is 0.88 kJ/mole. The frequency of molecular reorientations at 85 K is 10^4 s^{-1}. On a further rise of the temperature it increases considerably, reaching 10^{11} s^{-1} near T_m. The fundamental frequency of the benzene molecule oscillations about the sixfold axis at 273 K is 1.05×10^{12} s^{-1} (Ref. 13).

Carbon tetrachloride has an interesting feature: on cooling to 250.3 K liquid CCl_4 crystallizes into a face-centered cubic (fcc) form (Ia) with four molecules per unit cell; at several kelvins below 250.3 K it changes spontaneously to the rhombohedral phase (Ib), whose density is slightly higher, with 21 molecules per unit cell.[14,15] On a further cooling to 225.5 K, the rhombohedral phase transforms into a monoclinic one of space symmetry group $C2/c$ (C_{2h}^6) with $Z=32$. On heating, the low-temperature monoclinic phase (II) always changes to the rhombohedral form. By virtue of the low entropy of melting, $\Delta S_f/R=1.21$,[3] the phase (Ib) of CCl_4 may be classified as plastic.

The three forms of CCl_4 are quite closely related. The centers of mass of the molecules are only slightly shifted relative to their positions in the cubic and rhombohedral phases. Besides, the molecular orientations in the phase II correlate closely with the directions of the highest-density distribution function in the phase I.

According to experimental data, the character of the molecular motion in the plastic phase of CCl_4 is closely similar to that in the liquid state. For example, for CCl_4 no discontinuities are observed in the curve of spin–spin relaxation time T_2 of ^{35}Cl on plastic phase melting[16] and in the curve of reorientational correlation time obtained from Raman line broadening.[17,18] Zuk, Kiefte, and Clouter estimated the elastic constants of CCl_4 in the phase I by the Brillouin scattering method.[19] They discovered an anomalously high (as compared to solid inert gases) ratio of sound velocities in the $\langle 110\rangle$ and $\langle 111\rangle$ directions and interpreted this as an indication of a strong translation–orientation interaction.

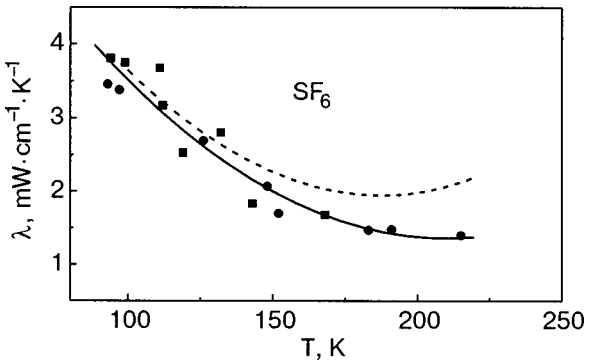

FIG. 1. The thermal conductivity (the solid line) of solid SF_6 in the high-temperature phase, measured under saturated vapor pressure. Rings and squares correspond to the two different samples. The dashed line is the thermal conductivity adjusted to a molar volume of 58.25 cm^3/mole.

EXPERIMENTAL RESULTS AND DISCUSSION

The thermal conductivity of solid SF_6, $CHCl_3$, C_6H_6, and CCl_4 was investigated by the linear-flow method under saturated vapor pressures in the temperature range from 80 K to the corresponding melting temperatures. A modified heat potentiometer was used,[20] which permitted us to minimize the error in estimation of the thermal conductivity. The uncontrollable heat flows from thermal radiation were reduced considerably with a radiation shield on which the temperature field of the measuring cell was reproduced using a set of thermocouples and precision heat controllers. The samples were grown from the liquid and gaseous phases. At the bottom of the measuring ampoule the temperature was maintained close to that liquid N_2. The measurements were made on the two samples of each substance of 99.98% purity, the random error being within 5%. The results of measurement are shown in Figs. 1–4.

The isochoric thermal conductivity of the all four substances had been measured previously in narrow temperature intervals in the vicinity of the corresponding melting points.[21–24] The isobaric thermal conductivity of C_6H_6 and CCl_4 was also measured under pressure above 100 MPa in Refs. 25, 26. Our data are in good agreement with those results for the same conditions (P,T).

To find the correlation between experimental results and theory, it is reasonable to compare the data for constant vol-

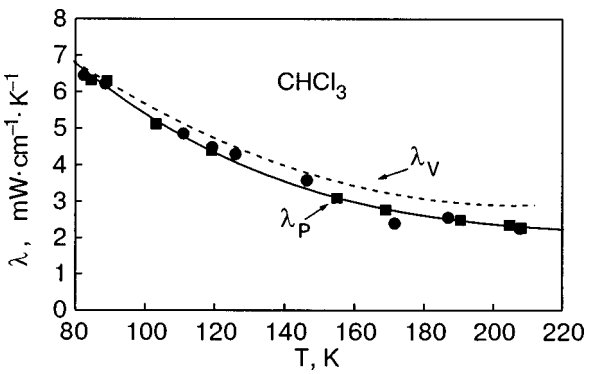

FIG. 2. The thermal conductivity (the solid line) of solid $CHCl_3$, measured under saturated vapor pressure. Rings and squares correspond to the two different samples. The dashed line is the thermal conductivity adjusted to a molar volume of 59.5 cm^3/mole.

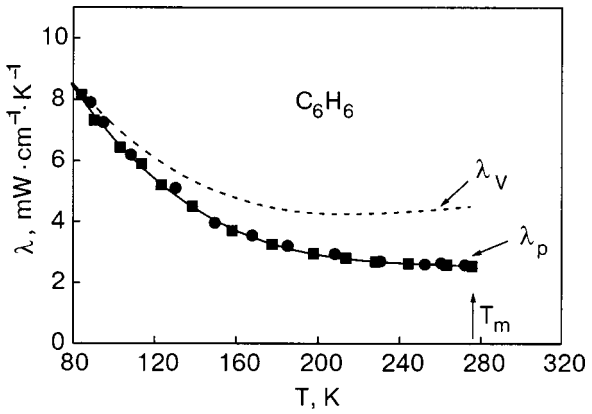

FIG. 3. The thermal conductivity (the solid line) of solid C_6H_6, measured under saturated vapor pressure. Rings and squares correspond to the two different samples. The dashed line is thermal conductivity adjusted to a molar volume of 70.5 cm^3/mole.

ume and thus to exclude the influence of thermal expansion. The results obtained were adjusted to a constant density of the samples, whose molar volumes were: V_m, cm^3/mole: 58.25 (SF_6), 59.5 ($CHCl_3$), 70.5 (C_6H_6), 76.0 (CCl_4 (II)). This was done using the data for the volume dependence of the thermal conductivity[21–24] and thermal expansion.[1,27] The crystals had these volumes at the corresponding growth temperatures. The results were adjusted by the formula

$$\lambda_v = \lambda_p (V(T)/V_m)^g, \tag{1}$$

where λ_v and λ_p are the isobaric and isochoric thermal conductivities, respectively; $V(T)$ is the current molar volume of the free sample; V_m is the volume to which the results were adjusted; $g = -(\partial \ln \lambda / \partial \ln V)_T$ is the Bridgman coefficient.

Figures 1–4 show the thermal conductivity measured under saturated vapor pressure (rings and solid lines) and the thermal conductivity adjusted to the corresponding molar volumes (broken lines). In chloroform, where the rotation of molecules is a pure librational motion and there are no reorientations, the isochoric thermal conductivity decreases as the temperature rises up to the melting point (Fig. 1). Similar behavior is observed in SF_6, C_6H_6, and CCl_4 (II) on the low-temperature side, with no intensive reorientations of the molecules. The isochoric thermal conductivity of SF_6, C_6H_6, and CCl_4 (II) passes through a minimum and then starts to grow. The minimum in the temperature dependence of the isochoric thermal conductivity occurs slightly above the temperature at which intensive molecular reorientations begin in these crystals.[1,12,16] The minimum can therefore be attributed to the reorientational motion.

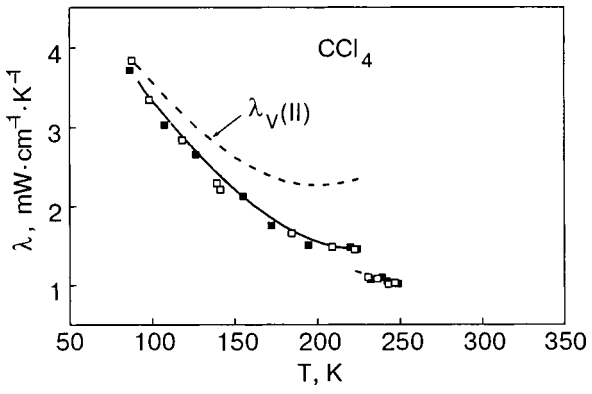

FIG. 4. The thermal conductivity (the solid line) of solid CCl_4 in the low-temperature phase, measured under saturated vapor pressure. Rings and squares correspond to the two different samples. The dashed line is the thermal conductivity adjusted to a molar volume of 76.0 cm^3/mole.

TABLE I. Reduced parameters, molar weight, and Bridgman coefficients for Kr, Xe, SF_6, $CHCl_3$, C_6H_6, and CCl_4.

Substance	T_{mol}, K	V_{mol}, cm^3/mole	μ	$W_{mol}(1/\lambda_{mol})$, m·K/W	g	References
Kr	209.4	92.01	83.8	8.06	10.2	[29]
Xe	289.7	119.4	131.3	10.0	9.6	[29]
SF_6	318.7	201.45	146.05	13.51	5.2	[22,30]
$CHCl_3$	536.6	238.8	119.4	10.9	4.0	[21,31]
C_6H_6	562.0	260.0	78.1	9.43	7.5	[23,30]
CCl_4	556.4	257.0	153.8	13.2	6.0	[24,31]

In this study the phonon–phonon and phonon–rotation contributions to the total thermal resistance were separated using a modified method of reduced coordinates.[28] It is important that with this method there is no need to involve any approximate model. As a rule, the reduction parameters are $T_{mol} = \varepsilon/k_B$, $\lambda_{mol} = k_B/\sigma^2\sqrt{\varepsilon/\mu}$, and $V_{mol} = N\sigma^3$, where σ and ε are the parameters of the Lennard-Jones potential, μ is the molar weight, and N is the total number of particles. In this study the reduction parameters T_{mol} and V_{mol} are the temperatures and molar volumes of SF_6, $CHCl_3$, C_6H_6, and CCl_4 and of the solidified inert gases krypton and xenon at the critical points T_{cr} and V_{cr} (Refs. 29–31; see also Table I).

The reason for this choice of parameters is as follows. For simple molecular substances, T_{cr} and V_{cr} are proportional to ε and σ^3, respectively. However, the accuracy of the critical parameters is much higher than that of the binomial potential parameters. Note that σ and ε are essentially dependent on the choice of binomial parameter and the method of its determination. The phonon–phonon and phonon–rotation components of the thermal resistance can be separated assuming that (i) the total thermal resistance $W = 1/\lambda$ of simple

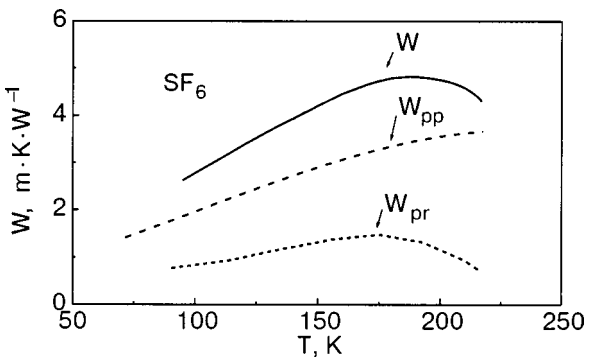

FIG. 5. Contributions of phonon–phonon scattering W_{pp} and phonon scattering caused by rotational molecular excitations W_{pr} to the total thermal resistance W of solid SF_6 with a molar volume of 58.25 cm^3/mole.

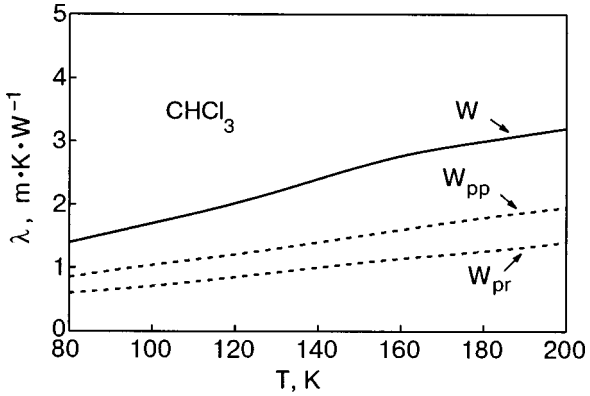

FIG. 6. Contributions of phonon–phonon scattering W_{pp} and phonon scattering caused by rotational molecular excitations W_{pr} to the total thermal resistance W of solid $CHCl_3$ with a molar volume of 59.5 cm^3/mole.

molecular crystals is a sum of phonon–phonon W_{pp} and phonon–rotation W_{pr} contributions: $W = W_{pp} + W_{pr}$, and (ii) in reduced coordinates $(W^* = W/W_{\mathrm{mol}}, T^* = T/T_{\mathrm{mol}})$ the component resulting from phonon–phonon scattering W_{pp} is identical to that in solid inert gases at equal reduced molar volumes $V^* = V/V_{\mathrm{mol}}$.

The calculation results are shown in Figs. 5–8. The phonon–phonon component of the thermal resistance W_{pp} is practically (to within 2–3%) independent of the inert gas chosen for comparison. In solid $CHCl_3$ (Fig. 6) the thermal resistance W_{pr} can be attributed to extra phonon scattering by collective rotational excitations whose density increases as the temperature rises. This is in good agreement with the data in Ref. 8 that suggests complete orientational ordering in solid $CHCl_3$ persisting up to the melting temperature. The extra contribution to the thermal resistance from the rotational degrees of freedom of the molecules is 80% of the phonon–phonon component. Unlike solid $CHCl_3$, in which the phonon–rotation component of the thermal resistance increases with growing temperature, in solid SF_6, C_6H_6, and CCl_4 the translation–rotational thermal resistance increases with temperature, passes through a maximum and then starts to decrease. The effect may be due to attenuation of phonon scattering by collective rotational excitations as the correlation of the neighboring molecular rotations decreases.

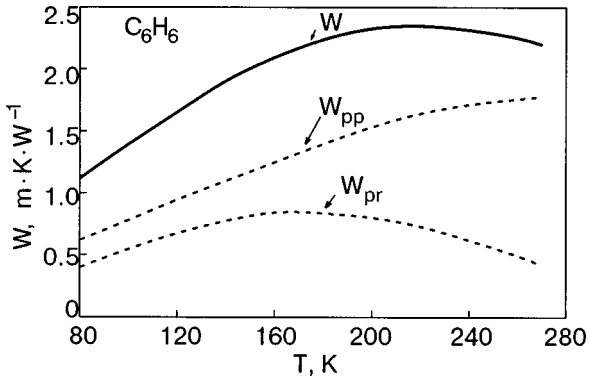

FIG. 7. Contributions of phonon–phonon scattering W_{pp} and phonon scattering caused by rotational molecular excitations W_{pr} to the total thermal resistance W of solid C_6H_6 with a molar volume of 70.5 cm^3/mole.

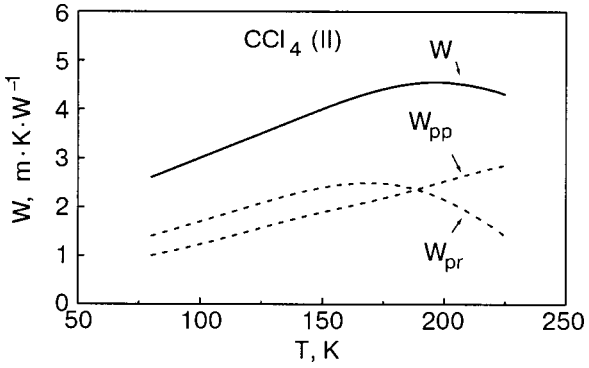

FIG. 8. Contributions of phonon–phonon scattering W_{pp} and phonon scattering caused by rotational molecular excitations W_{pr} to the total thermal resistance W of solid CCl_4 with a molar volume of 76.0 cm^3/mole.

CONCLUSIONS

The correlation between the rotational motion of molecules at the lattice sites of simple molecular crystals and the behavior of their thermal conductivity has been investigated for the examples of SF_6, $CHCl_3$, C_6H_6, and CCl_4. It is shown that the isochoric thermal conductivity increases as the frequency of reorientations grows higher with rising temperature. It is found that this effect is connected with phonon scattering by collective rotational excitations, which attenuates as the rotational correlations of the neighboring molecules become weaker.

*E-mail: pursky_O@ukr.net
**E-mail: konstantinov@ilt.kharkov.ua

[1] A. P. Isakina and A. I. Prokhvatilov, Fiz. Nizk. Temp. **19**, 201 (1993) [Low Temp. Phys. **19**, 142 (1993)].
[2] A. P. Isakina, A. I. Prokhvatilov, and J. Rodriguez-Carvajal, Fiz. Nizk. Temp. **26**, 404 (2000) [Low Temp. Phys. **26**, 296 (2000)].
[3] A. R. Ubbelohde, *Melting and Crystal Structure*, Clarendon Press, Oxford (1965).
[4] M. T. Dove, G. S. Pawley, G. Dolling, and B. M. Powell, Mol. Phys. **57**, 865 (1986).
[5] R. Fourme and M. Renaud, C. R. Acad. Sci., B **263**, 69 (1966).
[6] F. Shurvell, J. Chem. Phys. **58**, 5807 (1973).
[7] A. Anderson, B. Andrews, and B. N. Torrie, J. Chim. Phys. **82**, 99 (1985).
[8] H. S. Gutowsky and D. W. McCall, J. Chem. Phys. **32**, 548 (1960).
[9] E. G. Cox, D. W. J. Cruickshank, and J. A. Smith, Proc. R. Soc. **247**, 1 (1958).
[10] G. E. Bacon, N. A. Curry, and S. A. Wilson, Proc. R. Soc. **279**, 98 (1964).
[11] A. I. Kitaigorodskii, Mol. Cryst, Nauka, Moskow (1971) (in Russian).
[12] E. R. Andrew and R. G. Eades, Proc. R. Soc. London, Ser. A **218**, 537 (1953).
[13] N. G. Parsonage and L. A. K. Staveley, *Disorder in Crystals*, Clarendon Press, Oxford (1978).
[14] R. Rudman, Science **154**, 45 (1966).
[15] R. Powers and R. Rudman, J. Chem. Phys. **72**, 1629 (1980).
[16] D. E. O'Reilly, E. M. Peterson, and C. R. Scheie, J. Chem. Phys. **60**, 1603 (1974).
[17] F. J. Bartoli and T. A. Litovitz, J. Chem. Phys. **56**, 413 (1972).
[18] M. Djaburov, C. Levy-Mannheim, J. Leblond, and P. Papon, J. Chem. Phys. **66**, 5748 (1977).
[19] J. Zuk, H. Kiefte, and M. J. Clouter, J. Chem. Phys. **95**, 1950 (1991).
[20] T. N. Antsygina, B. Ya. Gorodilov, N. N. Zholonko, A. I. Krivchikov, V. G. Manzhelii, and V. A. Slyusarev, Fiz. Nizk. Temp. **18**, 417 (1992) [Low Temp. Phys. **18**, 283 (1992)].
[21] V. A. Konstantinov, V. G. Manzhelii, and S. A. Smirnov, Fiz. Nizk. Temp. **17**, 883 (1991) [Low Temp. Phys. **17**, 462 (1991)].
[22] V. A. Konstantinov, V. G. Manzhelii, and S. A. Smirnov, Fiz. Nizk. Temp. **18**, 1290 (1992) [Low Temp. Phys. **18**, 902 (1992)].

[23] V. A. Konstantinov, V. G. Manzhelii, and S. A. Smirnov, Ukr. Phys. J. **37**, 752 (1992).
[24] V. A. Konstantinov, V. G. Manzhelii, and S. A. Smirnov, Phys. Status Solidi B **163**, 369 (1991).
[25] R. G. Ross and P. Andersson, Mol. Phys. **36**, 39 (1978).
[26] R. G. Ross, P. Andersson, and G. Backstrom, Mol. Phys. **38**, 527 (1979).
[27] M. M. Zholonko and V. V. Tsybulin, Ukr. Phys. J. **11**, 1174 (2001).
[28] V. A. Konstantinov, V. G. Manzhelii, V. P. Revyakin, and S. A. Smirnov, Physica B **262**, 421 (1999).
[29] V. A. Rabinovich, A. A. Wassermann, V. I. Nedostup, and L. S. Weksler, *Thermophysical Properties of Ne, Ar, Kr, and Xe* [in Russian], Standarty, Moscow (1976).
[30] I. K. Kikoin (Ed.), *Table of Physical Values. Reference Book* [in Russian], Atomizdat, Moscow (1976).
[31] V. V. Altunin, V. Z. Geller, E. K. Petrov, D. C. Raskazov, and G. A. Spiridonova, *Thermophysical Properties of Freons* [in Russian], Standarty, Moscow (1980).

This article was published in English in the original Russian journal. Reproduced here with stylistic changes by AIP.

Observation of growth and structure of Kr films physisorbed on Ag(111) and Ag(100)

A. Tosaka, T. Mitake, T. Miura, and I. Arakawa*

Department of Physics, Gakushuin University, 151-8588, 1-5-1 Mejiro Toshima-ku, Tokyo, Japan
Fiz. Nizk. Temp. **29**, 1027–1031 (September–October 2003)

The structure and growth of two-dimensional crystals of Kr on Ag(111) and Ag(100) have been investigated by means of ellipsometry and eXtremely-low-current Low Energy Electron Diffraction (XLEED) under the quasi-equilibrium condition. The layered growth of a Kr film was observed up to the third layer by ellipsometry and the crystal geometry by XLEED. The Kr overlayer on Ag(100) has two types of alignment. In the predominant alignment, one of the unit vectors aligns with the ⟨001⟩ direction of the Ag substrate, while in the other it aligns with ⟨011⟩. The Kr–Kr spacing in a monolayer on Ag is 10% larger than that of the bulk. [DOI: 10.1063/1.1614190]

1. INTRODUCTION

The system of rare gas physisorbed on a metal surface has been studied since the 1970s for its interesting structure and phase transition in two dimensions. Xe/Ag(111) has been intensively investigated to reveal the structure, the isosteric heat of adsorption, and the two-dimensional phase diagram, whereas few results have been reported for Kr films on metal surfaces.

Roberts and Pritchard observed a Kr monolayer film adsorbed on Ag(111) using low energy electron diffraction (LEED) and revealed that the Kr overlayer has incommensurate hexagonal structure with the substrate.[1] Ungris *et al.* found the structure and the thermodynamic property of Kr/Ag(111): the phase diagram, the monolayer lattice constant, latent heats of adsorption, and isosteric heats.[2]

In the case of a Kr film on a metal surface, desorption of Kr atoms by the electron beam is a serious problem in a conventional LEED system, whose incident electron current is typically 1 μA. Roberts and Pritchard reported that the diffraction spots disappeared within 10–15 min.[1] Ungris *et al.* also reported that a Kr monolayer film at 40 K would be completely desorbed by an electron beam in several minutes.[2] Therefore, they either had to make experiments under a constant beam flux of Kr atoms which was sufficient to maintain the adsorbed layer or to measure the diffraction patterns before the coverage decreased due to electronic stimulated desorption (ESD).

The structure and layered growth of rare gas films on metal surfaces are determined by the balance of the adatom–adatom and adatom–surface interactions. The comparison between the same adsorbate on different substrates and between different adsorbates on the same substrate is a promising way to reveal how the subtle balance between the lateral and vertical interactions affects the growth and the structure of the overlayer. We have observed the systems of Kr and Xe on Ag(111), Ag(110) and Ag(100). In our study, the thickness of the overlayer was observed by ellipsometry and the surface geometry by LEED. Ellipsometry has no restriction on the surrounding pressure and does not destroy a physisorbed layer. Our LEED system was prepared to be free from the ESD problem, as described in Sec. 2.

We present here the results on the growth and structure of Kr films on Ag(111) and Ag(100) obtained using these two techniques and discuss how the substrate geometry affects the structure of the overlayer. A comparison of the results for the Xe/Ag(111) and Xe/Ag(100) systems with those for Kr/Ag(111) and Kr/Ag(100) is also made.

2. EXPERIMENTAL

Our experimental system makes it possible to observe simultaneously the surface geometry by XLEED and the film growth by ellipsometry.[3] The schematic diagram is shown in Fig. 1. The observation of the layer growth can be made under quasi-equilibrium conditions because ellipsometry has no restriction on the surrounding pressure.

Our XLEED system utilizes a position-sensitive detector using a microchannel-plate (MCP) electron multiplier in a pulse counting mode.[3] The detection area is 75 mm in diameter. The incident electron beam current was about 1 pA which was adjusted so that the total electron counts became 10^5-10^6 over the whole detector area for a one-minute data accumulation, which yielded a sharp diffraction pattern with adequate statistics for analysis.

The thickness of an adsorbed film was determined by the ellipsometric parameters Δ, the relative phase shift, and Ψ, the amplitude reflectance ratio. The relative change in Δ, i.e., $\delta\Delta=|\Delta-\Delta_0|$, where Δ_0 is the shift for the bare substrate, is

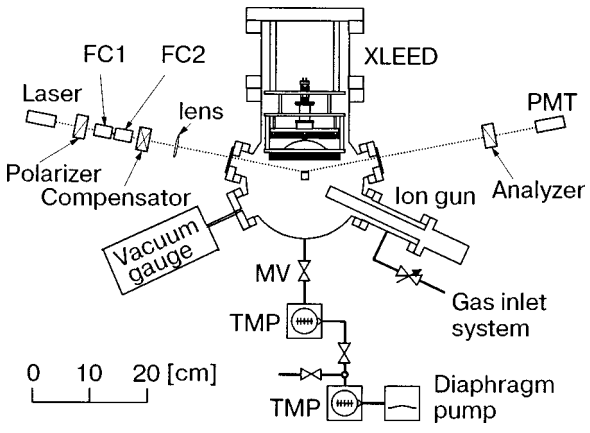

FIG. 1. Schematic diagram of our experimental system.

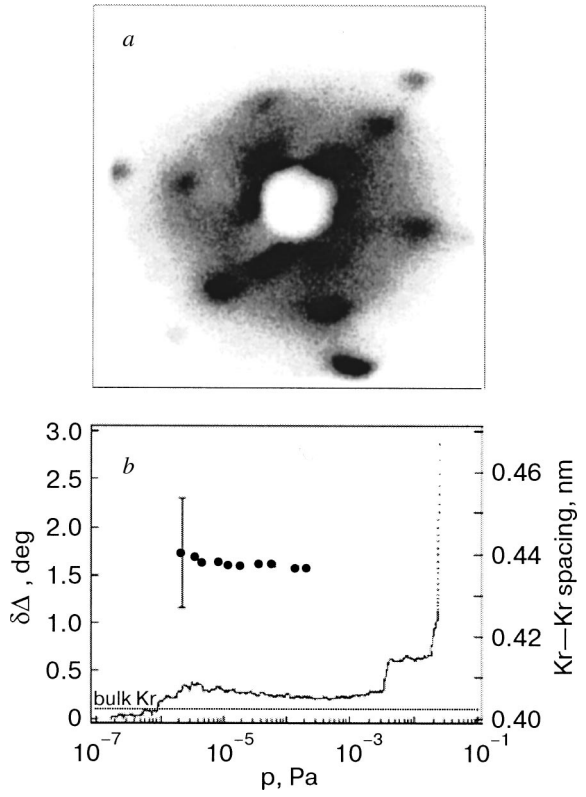

FIG. 2. *a*) XLEED pattern of a Kr monolayer on Ag(111). $E_i = 104$ eV, $P = 3\times10^{-5}$ Pa, $T = 51.3$ K. The incident electron energy was adjusted for the appearance of both Ag and Kr spots: the outer sixfold spots show Ag and the inner spots Kr. *b*) Adsorption isotherm of Kr/Ag(111) (stepwise line) and Kr–Kr spacing (solid circle) at 50.5 K.

proportional to the overlayer coverage and has been used as a measure of the amount of adsorption in ellipsometric studies of physisorbed films on metal surfaces.[4] The ellipsometer is a polarizer–compensator–sample–analyzer (PCSA) automatic null system.[3]

Silver substrates were prepared by repeated cycles of sputtering by Kr ions (1 keV, 5–8 μA, 2 min) and annealing (700 K, 3 hours). The base pressure of the main chamber was 10^{-8} Pa or lower. The Ag(111) and Ag(100) substrates were mounted side by side on the sample holder, which was cooled by cold He gas.

3. RESULTS

3.1. The growth and structure of Kr/Ag(111)

The diffraction patterns of Kr/Ag(111) are shown in Fig. 2*a*, which demonstrates a hexagonal structure of a Kr monolayer film whose unit vectors align with those of the substrate. The ellipsometric isotherm of Kr/Ag(111) at 50.5 K is shown in Fig. 2*b*, where the isotherm is represented by the change in relative phase shift $\delta\Delta$ due to adsorption as a function of Kr pressure. The isotherm for Kr on Ag(111) has several steps. Each step is due to a first-order phase condensation, where the 2D gas and solid coexist, and corresponds to the formation of one atomic layer. This isotherm for Kr—Ag(111) at 50.5 K plotted in Fig. 2*b* shows layer-by-layer growth up to three atomic layers at least. The Kr–Kr spacing in the monolayer, measured simultaneously by XLEED, is also shown in Fig. 2*b*. The interatomic distance was calculated using the spot distances in the diffraction pattern, the incident electron energy, and the distance between the sample and the MCP, which was determined by the Ag spot distance in the diffraction pattern of bare Ag surfaces. The Kr–Kr spacing is 0.440 nm just after condensation of the first layer and 0.436 nm before condensation of the second layer; the monolayer compression ratio was less than 1%. The XLEED pattern of the Kr monolayer, which has both Ag and Kr spots, as shown in Fig. 2*a*, was examined to confirm the absolute value of the Kr–Kr spacing by direct comparison with Ag interatomic distance of 0.288 nm. It was confirmed that the Kr–Kr spacing is about 8–9% larger than the Kr bulk value of 0.403 nm.[5] The experimental errors were about 1% for the Ag interatomic distance and 3% for the Kr–Kr spacing, because the Kr spots were broader than the spots of the bare Ag.

3.2. The structure of Kr/Ag(100)

The structure of Kr films on Ag(100) was observed by XLEED. It was found that the Kr film on Ag(100) has two types of alignment; the corresponding diffraction patterns are shown in Figs. 3*a* and 4*a*. The scheme of the diffraction patterns and the arrangement of the atoms in real space are shown in Figs. 3*b*,*c* and Figs. 4*b*,*c*, respectively. As shown in Fig. 3, one of the unit vectors of the Kr film aligns with the ⟨001⟩ direction of Ag. We call this type of alignment

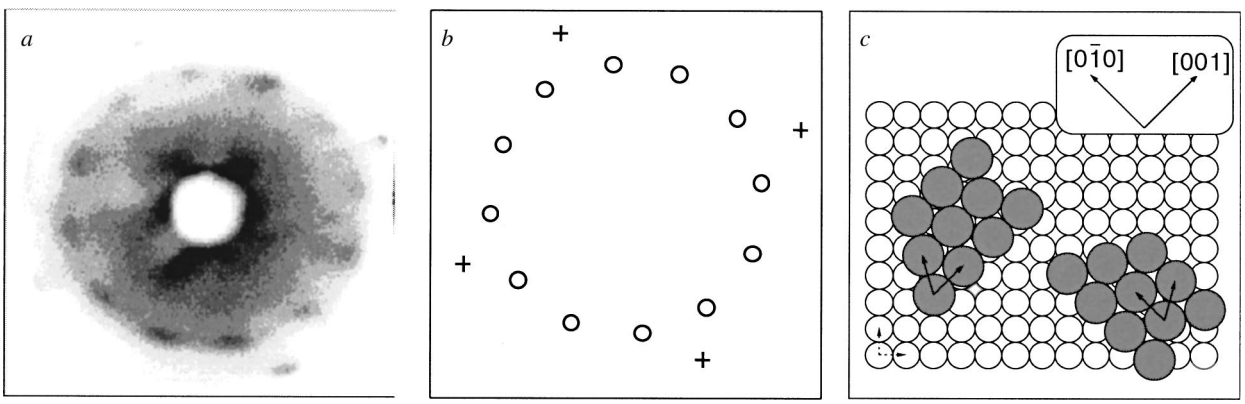

FIG. 3. *a*) XLEED pattern of Kr/Ag(100). $E_i = 66.2$ eV, $P = 3.0\times10^{-5}$ Pa, $T = 53.6$ K. *b*) Schematic of diffraction pattern shown in (*a*). Open circles show Kr spots and crosses show the substrate spots. *c*) Illustration in real space.

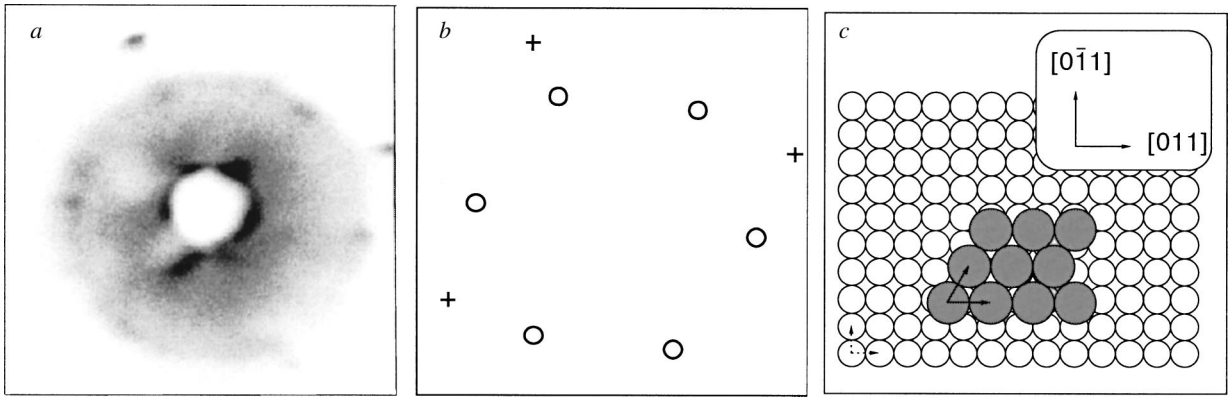

FIG. 4. *a*) XLEED pattern of Kr/Ag(100). $E_i = 66.2$ eV, $P = 3.0 \times 10^{-5}$ Pa, $T = 52.3$ K. *b*) Schematic of diffraction pattern shown in (*a*). Open circles show Kr spots and crosses show the substrate spots. *c*) Illustration in real space.

''along Ag ⟨001⟩ type.'' On the other hand, in Fig. 4 one of the unit vectors of the Kr film aligns with ⟨011⟩ of Ag: ''along Ag ⟨011⟩ type.'' The systematic observation by scanning the sample surface with an incident electron beam revealed that the Kr film has both types of alignment, but the ''along Ag⟨001⟩ type'' is predominant.

We observed that the Kr–Kr spacing in the ''along Ag ⟨001⟩ type'' monolayer was 0.450 nm, which is 11% larger than that of the bulk, as was also observed for the Kr/Ag(111) case.

4. DISCUSSION

4.1. Kr–Kr spacing of Kr/Ag(111) and Kr/Ag(100)

The fact that the Kr–Kr spacing is about 10% larger than that of the bulk must be a matter of discussion. We obtained the similar results on both Ag(111) and Ag(100). Roberts and Pritchard studied the Kr–Kr spacing on Ag(111) at 55 K and found that it was 0.419 nm.[1] Ungris *et al.* investigated Kr–Kr spacing by LEED in the temperature range between 10 and 60 K and obtained value 0.401–0.407 nm.[2] There is a considerable discrepancy in the absolute value of the Kr–Kr spacing between our results and those reported by Roberts and Pritchard and by Ungris *et al.* This discrepancy cannot be attributed only to our experimental error of about 3%.

In the case of Xe/Ag(111), it was observed that the Xe–Xe spacing just after condensation of the first layer is about 3% larger than that of the bulk. The Xe–Xe spacing in the monolayer decreases gradually with increasing pressure or decreasing temperature and reaches the bulk value before condensation of the second layer.[3] We observed that in the case of the Kr monolayer on Ag the monolayer compression ratio was no more than 1%. This result implies that the Kr film has a structure commensurate with the substrate.

It is known that rare gas films on Ag have structures incommensurate with the substrate. However, if a Kr film on Ag(111) may have the Ag(111) 1.5×1.5 commensurate structure, the Kr–Kr spacing will be 0.432 nm, which is 7% larger than that of bulk Kr. This value is between our result and that of Roberts and Pritchard.[1] However, there is no adequate commensurate structure of Kr/Ag(100).

4.2. The structure of Kr/Ag(100)

It is well known that the alignment of a rare gas film on a metal surface is affected by the substrate steps. A Xe film on Ag(111) has incommensurate structure but the unit vectors of the overlayer align with those of the substrate. The reason for this alignment is explained by the inference that the overlayer is pinned by substrate steps, and its alignment is determined by the step direction. Leatherman *et al.* have shown experimentally the effect of the surface steps on the alignment; when a small amount of CO or K is put on the surface to block the steps for rare gas adsorption, the nucleation occurs on a terrace and the overlayer grows in an orientation rotated at a nonsymmetric angle.[6]

In the present study we found that a Kr film on Ag(100) has two types of alignment and that the ''along Ag⟨001⟩ type'' is predominant. There are some possible reasons why the ''along Ag⟨001⟩ type'' is predominant.

The first possibility is that most surface steps on Ag(100) are directed along ⟨001⟩, and the Kr atoms nucleate at the step edge of the substrate. The second possibility is that the steps of Ag(100) are directed along both ⟨011⟩ and ⟨001⟩, and the step-pinning energy for the Kr film on the ⟨001⟩ Ag step edge is larger than that on the ⟨011⟩ step. The third possibility that Kr atoms nucleate on the Ag(100) terrace, and the alignment is determined by Novaco–McTague effect.[7]

It was also observed that a Xe film on Ag(100) has two types of alignment: ''along Ag ⟨001⟩ type'' and ''along Ag ⟨011⟩ type,'' but there is no preference between them.

The result that the ''along Ag ⟨011⟩ type'' was observed in the case of Xe/Ag(100) contradicts the supposition that surface steps of Ag(100) are oriented only along the ⟨001⟩ direction. The coexistence of two types of alignment can be interpreted by two possible reasons.

The first possibility is a combination of the step effect and the Novaco–McTague effect:[7] one type of alignment is determined by the step direction and the other by the Novaco–McTague effect. The second possibility is that the surface steps are along both the ⟨001⟩ and ⟨011⟩ directions on Ag(100), and its alignment within the overlayer is determined by the step-pinning energy of overlayer atoms at the step edges.

The one-dimensional structure period of Ag(100) along

⟨001⟩ direction is 0.407 nm, which is close to the Kr bulk value. This agreement should have a close relation to the preference of the ''along Ag ⟨001⟩ type'' alignment in the case of Kr/Ag(100). However, the value of 0.407 nm does not accord with our result described in Sec. 3.2. It is considered that, except for the agreement with one-dimensional periodicity, there are more complicated origins of Kr alignment.

A similar bi-structure system was found by Kiguchi *et al.*: an alkali halide monolayer film on a fcc metal surface. They reported that an overlayer on the fcc(100) surface has two types of alignment: one of them is the expected growth and the other is not.[8] They concluded that the alignment is determined by the degree of surface diffusion. When the surface diffusion constant is large, alkali halide atoms diffuse on the metal surface and nucleate at the step edges of the substrate, which cause the unexpected growth. They anticipated that most surface steps of an fcc(100) surface would be along the ⟨011⟩ direction of the substrate. However, the direct observation of the surface steps on fcc(100) has not been performed.

5. SUMMARY

The structure and layer-by-layer growth up to the third layer of Kr films were investigated simultaneously by extremely-low-current low energy electron diffraction and ellipsometry. The XLEED pattern showed that a Kr monolayer film on Ag(100) has two types of alignment: ''along Ag ⟨001⟩ type'' and ''along Ag ⟨011⟩ type.'' In the case of Kr/Ag(100), the ''along Ag ⟨001⟩ type'' is predominant. The existence of two types of alignment was explained by two possible reasons: one is the combination of the step-edge effect and the Novaco–McTague effect, and the other is the existence of surface steps along both the ⟨001⟩ and ⟨011⟩ directions.

*E-mail: ich.arakawa@gakushuin.ac.jp

[1] R. H. Roberts and J. Pritchard, Surf. Sci. **54**, 687 (1976).
[2] J. Ungris, L. W. Bruch, E. G. Moog, and M. B. Webb, Surf. Sci. **109**, 522 (1981).
[3] S. Igarashi, Y. Abe, Y. Irie, T. Hirayama, and I. Arakawa, J. Vac. Sci. Technol. A **16**, 974 (1998).
[4] A. Itakura and I. Arakawa, J. Vac. Sci. Technol. A **9**, 1779 (1991).
[5] M. L. Klein and J. A. Venables, in *Rare Gas Solids*, Vol. II, Academic Press (1977), p. 783.
[6] G. S. Leatherman, R. D. Diehl, M. Karimi, and G. Vidali, Phys. Rev. B **56**, 6970 (1977).
[7] A. D. Novaco and J. P. McTague, Phys. Rev. Lett. **38**, 1286 (1977).
[8] M. Kiguchi, S. Entani, K. Saiki, H. Inoue, and A. Koma, Phys. Rev. B (to be published).

This article was published in English in the original Russian journal. Reproduced here with stylistic changes by AIP.

Crystalline and amorphous polymeric solid nitrogen

L. N. Yakub*

Department of Thermophysics, Odessa State Refrigeration Academy, 1/3 Dvoryanskaya, Odessa 65026, Ukraine

Fiz. Nizk. Temp. **29**, 1032–1035 (September–October 2003)

The structure and thermodynamic functions of solid high-density nonmolecular nitrogen in the crystalline and amorphous phases are studied by a Monte Carlo simulation technique on the basis of the potential model proposed earlier for the cubic gauche polymeric crystal. The solid amorphous state was created by fast melting followed by instantaneous quenching of the crystalline structure. The computed atom–atom distribution functions in such solids are characteristic for amorphous structure. The simulation also reveals negativity of the thermal expansion coefficient of the amorphous solid at high density and low temperatures, as was previously found to be the case in the cubic gauche nonmolecular nitrogen crystal. Analysis of the force model shows specific anharmonicity characteristics of the crystalline vibrations responsible for this effect. © *2003 American Institute of Physics.*
[DOI: 10.1063/1.1614191]

1. INTRODUCTION

McMahan and LeSar[1] and Martin and Needs[2] first predicted the existence of a stable polymeric (nonmolecular or atomic) phase of solid nitrogen at zero temperature under pressure. They considered a number of possible threefold-coordinated structures and found the arseniclike $A7$ lattice to be the most stable one at $T=0$. Later Mailhiot, Yang, and McMahan reported new *ab initio* pseudopotential total-energy calculations.[3] They indicate that a ''cubic gauche'' (cg) distortion of the simple cubic atomic structure, in which all nitrogen atoms are threefold coordinated, has an equilibrium total energy lower than that of the arseniclike $A7$ structure mentioned above. According to Ref. 3, the diatomic form of nitrogen should transform into this hypothetical polymeric cg phase at 50 ± 15 GPa and remain the most stable nonmetallic form of nitrogen at higher densities.

This polymeric phase of solid nitrogen, long only discussed by theoreticians,[1–3] was recently discovered by experimentalists[4] at ambient temperatures and has also been investigated at elevated temperatures.[5] It was found that this phase very likely has the cg structure and is not crystalline but amorphous.

In our earlier calculations,[6–8] we predicted the thermodynamic functions of polymeric nitrogen in the $A7$ arseniclike structure at nonzero temperatures using simple atom–atom potential model. Recently[9] we proposed a new potential model representing the total energy of polymeric nitrogen as a function of both interatomic distances and angles between single chemical bonds attached to each atom. This model was used in prediction of thermodynamic behavior of solid nitrogen in its polymeric cg crystalline phase at high pressures and nonzero temperatures. The calibration of the model was based on the *ab initio* quantum mechanical calculations of Mailhiot, Yang, and McMahan[3] at $T=0$. We applied this model in Monte Carlo (MC) computer simulations of polymeric solid nitrogen at elevated temperatures.

Our simulations revealed that the polymeric *cubic gauche* crystalline structure of nitrogen would probably exhibit quite unusual high-pressure behavior at elevated temperatures. In particular, *negative* values of the thermal expansion coefficient at high pressures were predicted[9] over a wide range of temperatures. This feature may play an important role in the estimation of the relative stability of different crystalline structures and in the prediction of polymorphous transitions at elevated temperatures. Here we report the extension of the potential model proposed in Ref. 9 to simulation of amorphous polymeric solid nitrogen.

2. POTENTIAL MODEL

According to this model[9] the potential energy of N interacting nitrogen atoms consists of two contributions:

$$U_N=\sum_{\text{nonbonded atoms}}\Phi(r_{ij})+\sum_{\text{bonded atoms}}U(L_{ij},\boldsymbol{\theta}_i,\theta_j). \tag{1}$$

The first sum in Eq. (1) is taken over all nonbonded atoms, and the second contribution is a partial sum over all nearest chemically bonded atoms, $\Phi(R)=AR^{-13/2}$ is the nonvalence atomic repulsion[4] ($A/k=3.86\times 10^5$ K, and k is Boltzmann's constant). Each atom is involved in three such chemical (valence) interactions. In contrast with our older model,[4–6] here the valence potential U depends not only on the interatomic distances but also on the valence angles between the chemical bonds attached to each interacting atom.

The valence interaction of two *single-bonded* atoms U is a function of the chemical bond length L_{ij} as well as the angular variables $\boldsymbol{\theta}_i=\{\theta_i^{(1)},\theta_i^{(2)},\theta_i^{(3)}\}$ and $\boldsymbol{\theta}_j=\{\theta_j^{(1)},\theta_j^{(2)},\theta_j^{(3)}\}$ which represent the angles between the bonds attached to each atom.

Interatomic valence forces act between pairs of neighboring *single-bonded* atoms only. The corresponding interaction energy $U(L_{ij},\boldsymbol{\theta}_i,\boldsymbol{\theta}_j)$ was represented as the product of three factors:

$$U(L_{ij},\boldsymbol{\theta}_i,\boldsymbol{\theta}_j)=q(L_{ij},\boldsymbol{\theta}_i)\cdot q(L_{ij},\boldsymbol{\theta}_j)\cdot u_M(L_{ij}), \tag{2}$$

where $u_M(L_{ij})$ is the Morse potential and L_{ij} is the length of a single bond:

$$u_M(L)=D_e[\exp\{-2\beta(L-R_e)\}-2\exp\{-\beta(L-R_e)\}]. \tag{3}$$

The factors $q(L_{ij},\boldsymbol{\theta}_i)$ in Eq. (2) depend on both the bond lengths and the three plane valence angles $\boldsymbol{\theta}=\{\theta^{(1)},\theta^{(2)},\theta^{(3)}\}$ between the three bonds attached to an atom (see Fig. 1 in Ref. 9):

$$q(R,\boldsymbol{\theta})=\frac{2}{1+\exp\{-z(R,\boldsymbol{\theta})\}}. \tag{4}$$

Here

$$z(R,\boldsymbol{\theta}_i)=\alpha(R-R_e)^2+\gamma(c_i-c_e)^2+\delta(R-R_e)(c_i-c_e)+\varepsilon(1-4c_i)\Delta_i, \tag{5}$$

$$c_i=\frac{1}{3}(\cos^2\theta_i^{(1)}+\cos^2\theta_i^{(2)}+\cos^2\theta_i^{(3)}), \tag{6}$$

$$\Delta_i=[\cos^2\theta_i^{(1)}-\cos^2\theta_i^{(2)}]^2+[\cos^2\theta_i^{(1)}-\cos^2\theta_i^{(3)}]^2+[\cos^2\theta_i^{(2)}-\cos^2\theta_i^{(3)}]^2. \tag{7}$$

If the atomic configuration is near the equilibrium one, corresponding to minimum energy, all $z(R,\boldsymbol{\theta}_i)$ tend to zero and all $q(L_{ij},\boldsymbol{\theta}_j)$ approach unity. The equilibrium values of the valence angles $(\theta_i^{(j)})_{\text{eq}}=114°$ in a free cg crystal at zero temperature[3] correspond[9] to $c_e=0.165$.

The model has seven adjustable parameters: D_e, R_e, α, β, γ, δ, and ε (D_e is the depth of the potential well or equilibrium bonding energy, and R_e is the equilibrium length of the Morse potential for a single bond). We used here the same values of parameters as were found in Ref. 9: $D_e/k=35570$ K, $R_e=1.374$ Å, $\alpha=12$ Å^{-2}, $\beta=6.133$, $\gamma=-14.25$, and $\delta=-118$ Å^{-1}.

This set of parameters reproduces i) the *ab initio* total energy in the cubic gauche structure at $T=0$ as a function of volume, ii) the equilibrium bond angles, and iii) the angular dependence of the total energy within $103°<\theta^{(i)}<114°$, reported as a result of the sensitivity study by Mailhiot, Yang, and McMahan.[3]

3. MONTE CARLO SIMULATION OF AMORPHOUS SOLID

Computer simulations were carried out using the same computer MC simulation program developed for study of the cg crystal lattice[9] (512 nitrogen atoms and periodic boundary conditions). Initially, all the atoms were arranged within a main cell near the sites of a perfect cg lattice (see Ref. 9 for a more detailed description of the cg structure). The MC simulation was initiated with a high initial temperature well above the melting temperature. After some period the initial long-range order disappears and the solid melts. Note that the chemical bonds were fixed during the entirety of the computer experiment and we kept a restriction on allowable distances between bonded atoms (less than 2.5 Å).

Then the system was quenched (the temperature is suddenly reduced to room temperature) and the MC simulation process continues. It was found that after some period of relaxation (after 2000–3000 successful steps per atom) a new quasi-equilibrium state retaining amorphous structure was reached. It keeps the short-range order and threefold valence coordination in the first coordination sphere but also has some disorder in bond lengths and directions. This quasi-equilibrium state was studied as a model for the amorphous solid.

During the MC simulation process (namely after each three steps per atom) the values of pressure, internal energy, isothermal compressibility, thermal expansion, and heat capacity were calculated. All of the thermodynamic functions, along with the bond lengths and angles, were averaged over the next 40000 steps per atom to compute the mean values as well as their statistical errors. We also computed the radial atomic distribution functions. Along with the mean values of the angular variables we also monitored the minimal and maximal angles between interatomic bonds.

4. RESULTS AND DISCUSSION

The atom–atom distribution functions of polymeric crystalline and amorphous nitrogen solid at high density ($V=6$ cm^3/mol) and two temperatures are compared in Fig. 1. As one can see, the long-range order in the amorphous solid is completely lost, but the short-range first coordination peak formed by chemically bonded atoms is clearly expressed. The second coordination sphere, formed by closest nonbonded atoms, is also present but much less noticeable compared to the crystalline solid. The position of this peak is closely related (see below) to the mean valence angle between single bonds attached to each atom.

In Table I we compare calculated values of the thermal expansion α_T and isothermal compressibility β_T coefficients, as well as the isochoric heat capacity C_v and the mean valence angles $\langle\theta\rangle$ and bond lengths $\langle L\rangle$ of crystalline and amorphous polymeric nitrogen at $T=300$ and 500 K. As one can see, according to our model, negativity of the thermal expansion should persist in the amorphous state of nonmolecular nitrogen solid at high densities and lower temperatures. It is obviously related to the short-range pyramidal structure formed by neighboring nitrogen atoms. As the mean distance between closest nonbonded atoms increases (see Fig. 1 for $T=500$ K), the thermal expansion became less positive.

It is well known that anharmonicity of the crystalline vibrations is responsible for thermal expansion. The rigorous analysis of all anharmonic contributions to the energy of vibration modes is a complicated task. It requires much effort and is well beyond the scope of this work. However, we have performed an examination of symmetric longitudinal vibrations as the most important kind of crystal vibration in this regard. Our simplified analysis has been performed for the adopted force model within the cg lattice. We took into account that the chemical bonds between atoms are much stiffer than the nonvalence interatomic repulsion. Therefore a symmetric squeezing of the crystal decreases the valence angles between single bonds and correspondingly decreases

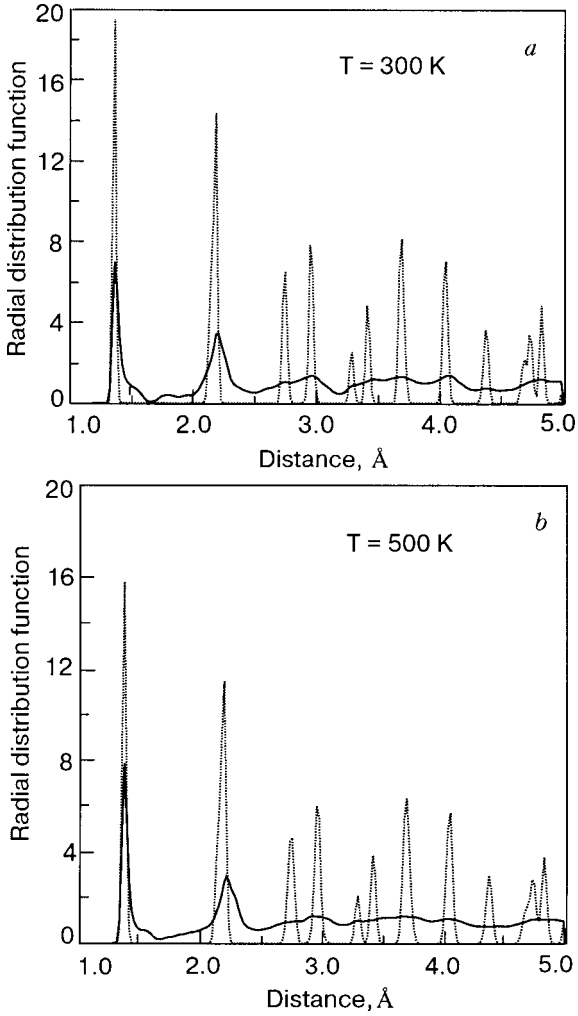

FIG. 1. Radial distribution functions of the amorphous (solid line) and crystalline (dashed line) polymeric nitrogen at 6.0 cm^3/mol and two temperatures 300 and 500 K.

the distance between nearest nonbonded atoms (see Fig. 1 for the positions of the second peaks near $R=2.3$ Å).

In Fig. 2 we compare the harmonic and anharmonic contributions to the variation of interaction energy with this distance. It is clearly seen that the anharmonic contribution to the interaction energy within our model behaves just opposite to the usual dependence of the potential energy in diatomic molecules, where anharmonicity leads to elongation of the chemical bonds with increase of temperature. In Fig. 2 the interaction energy is more negative at short interatomic distances than its harmonic counterpart. Therefore, as the temperature increases, the mean distance between nonbonded atoms should decrease. We believe that the negative thermal expansion predicted is due to this specific anharmonicity in our potential model.

TABLE I. Some properties of solid nitrogen in the crystalline and the amorphous polymeric phases at $V=6$ cm^3/mol.

Property		300 K	500 K	Δ^*
Expansivity α_T, kK^{-1}	Crystalline	−0.018	−0.014	0.002
	Amorphous	−0.011	−0.003	
Compressibility β_T, GPa^{-1}	Crystalline	0.0017	0.0018	0.0001
	Amorphous	0.0015	0.0012	
Heat capacity C_v/R	Crystalline	3.07	3.10	0.003
	Amorphous	3.11	3.08	
Mean valence angle $\langle\theta\rangle$, degrees	Crystalline	106.3	106.2	0.2
	Amorphous	103.6	105.4	
Mean bond length $\langle L\rangle$, Å	Crystalline	1.37	1.38	0.02
	Amorphous	1.52	1.42	

[a]Estimated statistical error.

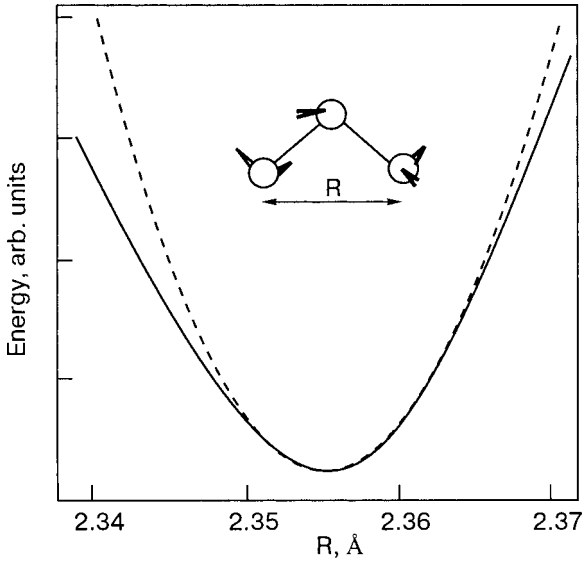

FIG. 2. Potential energy of cg crystalline nitrogen as a function of the interatomic distance between two nonbonded atoms at volume $V=6.0$ cm^3/mol (solid line). The harmonic approximation is presented by the dashed line.

5. CONCLUSIONS

Anomalous structural and thermodynamic behavior of polymeric fourfold-coordinated solids like ice, silicon, carbon etc. has been known for a long time. Negative thermal expansion has also been predicted recently in molecular-dynamic simulations of silicon both in the crystalline and amorphous states.[10] According to our simulation this peculiarity appears in threefold-coordinated structures like polymeric nitrogen only in the helical cg structure and not in the layered $A7$ structure.

The radius of the second coordination sphere in the amorphous cg solid at $T=300$ K is close to that for the crystalline (see Fig. 1). On the contrary, at $T=500$ K this radius is markedly shifted to larger distances, which leads to larger mean valence angles, and the thermal expansion at 500 K is less negative.

It should be noted that the amorphous state examined in this work as well as the real amorphous nitrogen solid studied experimentally[4,5] is actually not the real thermodynamic equilibrium state. Its properties depend on the frozen structure inherited from the high-temperature melt. Fast quenching of a high-temperature polymeric melt can produce different amorphous states having slightly different properties. We have chosen several samples at $V=8.04$ and 6 cm^3/mol and

selected two of them having no broken bonds, i.e. having lengths close to limiting 2.5 Å; see above. We have also continuously monitored the arithmetic mean as well as the maximum and minimum values of the bond lengths and angles between bonds to avoid such bond breaking after quenching. At $T=300$ K and $V=6$ cm^3/mol all the thermodynamic characteristics stabilize quickly and remain constant during the continuance of the computer simulation run. The constancy of the heat capacity computed is another strong piece of evidence of stability of the amorphous state under investigation.

This is not the case at higher temperatures and volumes. We performed several runs at $T=1000$ K which demonstrate the essential instability of the amorphous solid and gradual recovery of the crystalline structure. Probably much longer MC runs could reach the complete or partial annealing of a stable crystalline structure. But this process is very slow, and such a study is far beyond the capabilities of our facilities.

*E-mail: Lidiya@unive.odessa.ua

[1] A. K. McMahan and R. LeSar, Phys. Rev. Lett. **54**, 1929 (1985).
[2] R. M. Martin and R. J. Needs, Phys. Rev. B **34**, 5082 (1986).
[3] C. Mailhiot, L. H. Yang, and A. K. McMahan, Phys. Rev. B **46**, 14419 (1992).
[4] A. F. Goncharov, E. Grigorianz, H.-K. Mao, Z. Liu, and R. Hemley, Phys. Rev. Lett. **85**, 1262 (2000).
[5] E. Grigorianz, A. F. Goncharov, R. Hemley, and H.-K. Mao, Phys. Rev. B **64**, 052103 (2001).
[6] L. N. Yakub, Fiz. Nizk. Temp. **19**, 531 (1993) [Low Temp. Phys. **19**, 377 (1993)].
[7] L. N. Yakub, Fiz. Nizk. Temp. **21**, 1174 (1995) [Low Temp. Phys. **21**, 905 (1995)].
[8] L. N. Yakub, Fiz. Nizk. Temp. **22**, 222 (1996) [Low Temp. Phys. **22**, 174 (1996)].
[9] L. N. Yakub, J. Low Temp. Phys. **122**, 501 (2001).
[10] P. Keblinski, M. Z. Bazant, R. K. Dash, and M. M. Treacy, Phys. Rev. B **66**, 064104 (2002).

This article was published in English in the original Russian journal. Reproduced here with stylistic changes by AIP.

Properties of solid hydrogen doped by heavy atomic and molecular impurities

N. N. Galtsov,* A. I. Prokhvatilov, G. N. Shcherbakov, and M. A. Strzhemechny

B. Verkin Institute for Low Temperature Physics and Engineering of the National Academy of Sciences of Ukraine, 47 Lenin Ave., Kharkov 61103, Ukraine

Fiz. Nizk. Temp. **29**, 1036–1040 (September–October 2003)

The structural characteristics of normal and para hydrogen crystals doped with Ar, Kr, N_2, and O_2 impurities are studied by powder x-ray diffraction over the range from 5 K to the melting point of the hydrogen matrix. It is established that in spite of the very low solubility of the dopants in solid hydrogen, these impurities appreciably affect the structural characteristics. In particular, only nitrogen impurities do not change the molar volume of the matrix; the other three make the matrix expand. The Ar and Kr impurities also change the c/a ratio of the hcp matrix. The fact that both Ar and O_2 have smaller molar volumes than hydrogen may be regarded as evidence that these impurities form van der Waals complexes with the hydrogen lattice environment. © *2003 American Institute of Physics.* [DOI: 10.1063/1.1614192]

Solid mixtures of hydrogen with rare-gas and simple molecular species are interesting for several reasons. At high pressures, some of such mixtures can form stoichiometric solid-state compounds, like $Ar(H_2)_2$ (Ref. 1) or hydrogen–methane ordered alloys.[2] At low pressures, hydrogen-containing alloys with smaller molecular (atomic) species can be expected to form random binary systems that would in many aspects resemble helium–impurity gels.[3,4] Quench-condensed Ar–H_2 mixtures at sufficiently high H_2 contents in the source gas show many properties that could be treated as pertaining to gels of that kind.[5] In strongly diluted H_2-based mixtures one can expect the formation of van der Waals (VdW) complexes, loosely bound to the crystal environment due to quantum-crystal effects. Evidence of such VdW complexes has been obtained by x-ray diffraction on Ne-doped para hydrogen.[6] Similar results have been obtained for other neon-doped hydrogen matrices (normal H_2 and D_2, ortho deuterium).[7] In all those crystals, certain structural characteristics behaved in an unusual way; in particular, the reflection attributable to hcp hydrogen grew considerably in intensity, the molar volume increased upon doping against natural expectations, and the hcp lattice flattened on doping (the c/a ratio decreased). Neon impurities in solid hydrogen cause a few effects that could be explained only under the assumption that VdW complexes are present in the diluted alloys. These finding are an unusual low-temperature anomaly in the heat capacity,[8] a decrease in the thermal resistance of Ne-doped alloys (instead of an expected increase) compared to pure hydrogen,[9] an acceleration of quantum diffusion caused by Ne doping,[10] and some others.

The behavior of atoms and smaller molecules in solid hydrogen is important in view of the recent idea of using para hydrogen as an isolation matrix material.[11] On the one hand, the effect of the quantum-crystal nature of solid hydrogen on optical spectra still remains an open issue. On the other hand, the rotational dynamics of molecular impurities differs essentially in classical rare-gas and quantum (hydrogen) matrices.[12–16] Presumably, the solid hydrogen matrix is softer, interacting less with the impurity embedded there to. But in classical matrices, impurity molecules (provided they do not interact) rotate quite freely down to very low temperatures. In stark contrast to quite reasonable expectations, rotation of impurity molecules in a quantum-crystal matrix is substantially hindered and even locked into a librational state along particular crystallographic directions.[16] This fact can be easily explained by the extreme compliability. For example, it was shown[15] that an SF_6 molecule in a helium matrix has a ''coat'' of 22 to 24 He atoms, so that rotation is greatly hindered even in the superfluid phase of helium.

There is another issue in the physics of dilute impurities in various matrices, which can be directly solved with the aid of diffraction methods. This issue is the changes in the molar volume of the matrix material and the relevant displacement of the closer crystal shells, which are needed to be known for crystal-field evaluations and corrections.

Here we report effects of heavier atomic (Ar and Kr) as well as molecular (N_2 and O_2) impurities on the structural characteristics of the quantum crystals of para and normal hydrogen. To facilitate understanding of the experimental findings for H_2-based binary systems we give in Table I the basic molecular and other parameters of the species involved.

EXPERIMENTAL

These studies were done in Cu K_α radiation on a DRON-3M powder x-ray diffractometer equipped with a liquid-helium cryostat. Diffractometer control and data collection and processing were done using a PC. The samples were grown by quench condensation of gas mixtures of known composition directly to the solid phase onto a flat copper substrate at a temperature of 5 K. The polycrystalline samples were typically 0.1 mm thick with grain sizes within 10^{-4}–10^{-5} cm. The purity of all the source gases was not worse that 99.9%. The parahydrogen source had an ortho fraction of 0.23%, which is the equilibrium value at liquid-hydrogen temperature. The concentration of the impurity species in the gas mixtures was varied from 0.05% to 5% for Ar, 1% to 10% for Kr and N_2, and from 1% to 20% for O_2. The error of the impurity fraction in the gas sample was 5% of the total amount of the impurity in the gas. X-ray exami-

TABLE I. The relevant physical properties of nH_2 and pH_2 and of the impurities Ar, Kr, N_2, and O_2.

Substance	Structure at 5 K	Lattice parameters, Å	Molar volume, cm^3/mole	L-J parameters
nH_2	hcp, $P6_3/mmc$	$a = 3.770$, $c = 6.162$	22.83	$\varepsilon = 36.7$ K, $\sigma = 2.96$ Å
pH_2	hcp, $P6_3/mmc$	$a = 3.783$, $c = 6.178$	23.06	$\varepsilon = 36.7$ K, $\sigma = 2.96$ Å
Ne	fcc, $Fm3m$	$a = 4.464$	13.31	$\varepsilon = 36.7$ K, $\sigma = 2.788$ Å
Ar	fcc, $Fm3m$	$a = 5.311$	22.415	$\varepsilon = 119.8$ K, $\sigma = 3.405$ Å
Kr	fcc, $Fm3m$	$a = 5.646$	26.932	$\varepsilon = 164.0$ K, $\sigma = 3.624$ Å
N_2	fcc, $Pa3$	$a = 5.649$	27.13	$\varepsilon = 95.1$ K, $\sigma = 3.708$ Å
O_2	monoclinic, $C2/m$	$a = 5.375$, $b = 3.425$, $c = 4.242$, $\beta = 117.8°$	20.57	$\varepsilon = 117.3$ K, $\sigma = 3.817$ Å

nation was carried out from 5 K up to the melting point of the hydrogen matrix. The temperature was stabilized to within ± 0.05 K at every measurement point. Because of a partial overlap of certain reflections from the hydrogen matrix and the impurity solid, the resulting lattice parameter error was larger than for pure cryocrystals but did not exceed $\pm 0.04\%$. If should be noted that, in contrast to what we had found for neon-doped hydrogen and deuterium,[7] the condensation in small spurts (the pressure drop in the mixing chamber being 2–3 mm Hg) of mixtures with heavier impurities yielded strongly stressed samples, as expected. This was evidenced by the absence of most of the reflections, while the observed reflection (as a rule, the 002 ones) were broad. To remove stresses, such samples were annealed for 1 to 1.5 hours at a temperature 2 to 3 K below the melting point.

After annealing all the reflections appear in the x-ray patterns with intensity ratios close to normal and linewidths typical of mixtures. We think that quench condensation onto a substrate at 5 K yields samples with a large amount of lattice defects, finer-than-usual crystallites, and stresses. The high-temperature annealing not only removes stresses due to fast crystallization and cooldown but also promotes a homogenization of the impurity distribution. This argumentation is corroborated by the results of experiments with samples grown on the same 5 K substrate but at a rate twice as fast (with pressure drops of 5–7 Hg mm). Under these conditions, the condensate surface was momentarily heated up to the melting point, immediately producing an equilibrium sample, so that subsequent annealing did not change the diffraction pattern.

RESULTS AND DISCUSSIONS

As the impurity, two types of species have been chosen, considerably differing in molecular parameters from one another and from the hydrogen matrix (see Table I). This, in particular, concerns the Lennard-Jones parameters and the Debye temperatures. The molar volume differences between impurity and matrix were such that doping of the H_2 crystal would result in dilatations of opposite signs. Thus, judging from molar volumes (Table I) of the pure solids, argon and oxygen impurities were expected to contract the hydrogen lattice, and krypton and nitrogen, to expand it. It should be also taken into account that the molar volumes of both molecular solids N_2 and O_2 are to an appreciable extent controlled by rather strong anisotropic interactions, which tend to compress these solids. In addition, the paramagnetic impurities of oxygen can essentially affect the conversion process in the normal hydrogen crystals.[20–22]

Some of preliminary results of hydrogen doped with Ar, Kr, and N_2 have been reported at the 3rd Cryocrystals Conference.[23] Later we carried out a few complementing and more precise experiments on the these above-mentioned systems, in particular, using normal hydrogen as the matrix, and we repeated the entire set of measurements on oxygen-doped normal hydrogen.

When embarking on this program, we expected to find evidence of VdW complexes around the impurity particles. However, our analysis shown that there is no unambiguous confirmation of this hypothesis, at least within the content sensitivity (about 1%) of our method. The x-ray patterns contained reflections only from the hcp hydrogen-rich phases (both for normal and para H_2) and, when observable, reflections from the lattices of the respective pure substances (Fig. 1), the monoclinic lattice of O_2 and the fcc lattices of all other crystals. It should be remarked here that the determination of the least concentration at which impurity-based phases appeared was difficult, because for the krypton and nitrogen impurities the (111) reflection of the respective cubic phases partially overlapped with the first (100) reflection of H_2, and for argon and oxygen—with second (002) and third (101) reflections of the H_2 matrix, respectively (cf. Figs. 1*a*–*d*). However, in spite of these aggravations we have established that reflections of the pure phases of all the dopants are detectable in x-ray patterns when the normal fraction of the impurity in the source gas mixture exceed 0.5%.

Typical powder x-ray patterns for hydrogen-based solid mixtures with the four impurity species are shown in Fig. 1. The position and shapes of the H_2 reflections differ from those from pure normal and para hydrogen. This is might be caused by the following factors. Although the actual content (solubility) of all impurities can be substantially less than the lower concentration in gas mixtures (the equilibrium solubility of heavy gases in solid hydrogen from thermal conductivity measurements[24,25] is 10^{-4} or less), these impurities affect perceptibly the structural characteristics of doped hydrogen. Usually, when quench depositing pure hydrogen at low temperature it is difficult to avoid texture[26] with the close-packed (00l) basal layers being parallel to the substrate surface, so that one can only see multiple reflections from these planes in the patterns. In the experiments reported here, even seemingly insignificant amounts of impurities (as low as 0.05% of Ar in the gas mix) essentially suppresses preferable epitaxial crystal growth, and the intensity ratios from the hydrogen matrix are close to those from nontextured polycrystalline samples (cf., for example, Fig. 1*a*). The part

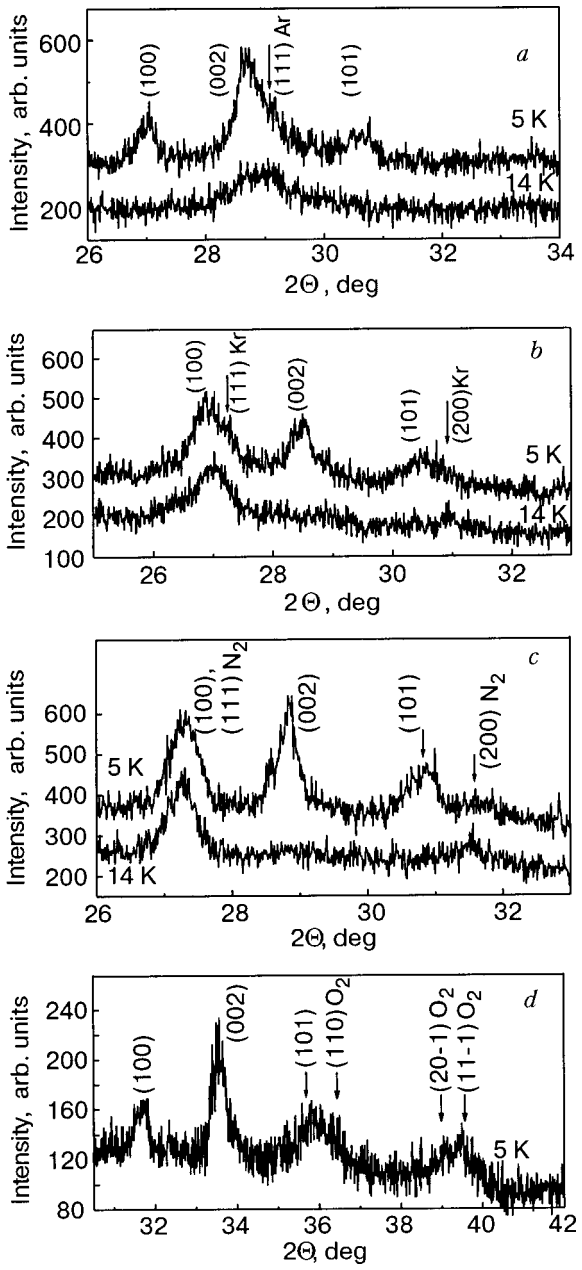

FIG. 1. Typical powder x-ray patterns for solid mixtures: $p\mathrm{H_2}+1\%$ Ar (*a*), $n\mathrm{H_2}+2\%$ Kr (*b*), $p\mathrm{H_2}+2\%$ $\mathrm{N_2}$ (*c*) for 5 K and 14 K, $n\mathrm{H_2}+2\%$ $\mathrm{O_2}$ for 5 K (*d*).

of the impurity component that was not dissolved in solid hydrogen aggregates into a separate phase producing corresponding reflections. Above the hydrogen melting temperature, only impurity-related reflections persist (Fig. 1). The integrated intensity of these reflections is noticeably higher than could be expected from the nominal concentration in the gas. The width of the reflections after annealing-related hydrogen effusion is considerably (2–2.5 times) larger than usual, which suggests a high concentration of impurities ($\mathrm{H_2}$) and/or lattice defects.

Before analyzing the structure data and giving our arguments, we note that, when considering a molecular impurity in a solid made up of spherical particles (like $\mathrm{H_2}$), one should use for scaling not the molar volume of the pure molecular solid (in which strong anisotropic forces produce a large negative contribution) but, because in an environment

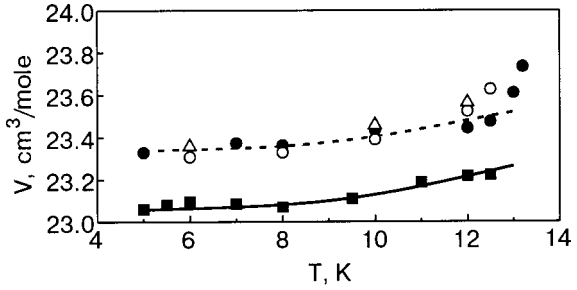

FIG. 2. Temperature dependence of the molar volume of solid para hydrogen with impurities: 0.05% Ar (●), 2% $\mathrm{N_2}$ (■), pure $p\mathrm{H_2}$ (—),[26] 5% Ar (△), 2% Ne (- - -),[6] 2% Ar (○).

of spherical particles the molecule is stripped of its anisotropic forces, σ^3, where σ is the Lennard-Jones radius.[27]

Argon impurities in para hydrogen increase the volume of the matrix by an amount comparable to those observed in $p\mathrm{H_2}-$Ne mixtures (Fig. 2) despite the slightly smaller volume in the bulk Ar compared to $p\mathrm{H_2}$. Oxygen impurities also expand the normal hydrogen lattice, approximately by the same amount as krypton. There is, however, an important difference because oxygen is known to accelerate ortho–para conversion, so that during sample preparation and measurements oxygen impurities burn out ortho states in their closest environment and thus are in fact surrounded by virtually pure para hydrogen. Therefore, the net expansion effect due to $\mathrm{O_2}$ impurities is less pronounced compared to Kr impurities. Thus the lattice expansion caused by Ar and $\mathrm{O_2}$ impurities, both of which are smaller than the size of vacant sites in hydrogen crystals, may be treated as evidence of hydrogen-based VdW complexes, similar to those presumably found in Ne-doped hydrogen.

Nitrogen apparently does not change the volume hydrogen matrix at any temperature up to melting (Fig. 2). Since the Lennard-Jones radius of the bare nitrogen molecule (3.708 Å) is close to the intermolecular distance in solid $\mathrm{H_2}$ (3.784 Å for para hydrogen), one can expect an "accurate" nesting for the $\mathrm{N_2}$ impurity in $\mathrm{H_2}$. Since the central $\mathrm{H_2}-\mathrm{H_2}$ interaction constant does not differ drastically from that for $\mathrm{H_2}-\mathrm{N_2}$, the near absence of an effect of $\mathrm{N_2}$ does not seem strange.

Krypton impurities increase the molar volume of the normal hydrogen matrix (Fig. 3). The fact that the excess volume and its temperature dependence are the same for the nominal gas fractions of 1% and 10% implies that the true Kr concentration in solid $\mathrm{H_2}$ must not exceed 1%. Our previous

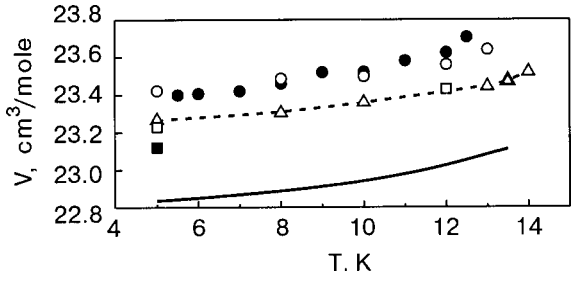

FIG. 3. Temperature dependence of molar volume of solid normal hydrogen with impurities: 1% Kr (●), 10% Kr (○), 5% Ne (-△-),[7] pure $n\mathrm{H_2}$ (—),[28] 5% $\mathrm{O_2}$ (□).

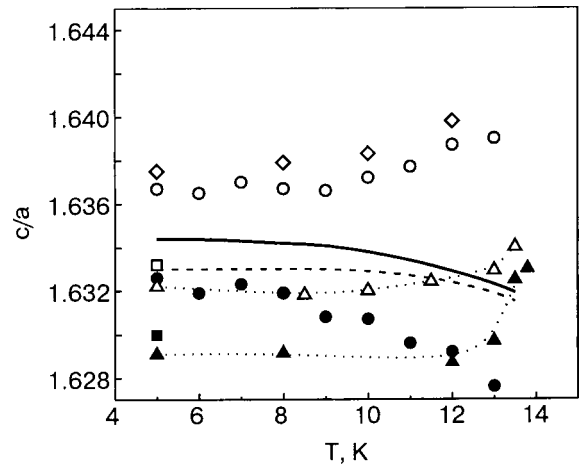

FIG. 4. Temperature dependence of the c/a ratio of solid hydrogens with impurities: $p\mathrm{H_2}+0.05\%$ Ar (●), $n\mathrm{H_2}+1\%$ Kr (○), $n\mathrm{H_2}+5\%$ Ne (△),[7] pure $n\mathrm{H_2}$ (—),[28] pure $p\mathrm{H_2}$ (- - -),[26] $n\mathrm{H_2}+1\%$ $\mathrm{O_2}$ (□); $p\mathrm{H_2}+5\%$ Ne (▲).[6]

evaluation[5] yields an upper limit value of 4%, which does not contradict the above reasoning. The very fact of the positive effect of Kr impurities seems to be quite natural because of the larger impurity size.

Although Ar and Kr bring about almost equal volume changes, they deform the hexagonal H_2 lattice in different ways (Fig. 4): Ar decreases and Kr increases the c/a ratio, and both absolute deviations increase with increasing temperature. The opposite behavior of the c/a ratio (temperature independence close to melting, then a fast buildup) in $\mathrm{Ne}-\mathrm{H_2}$ mixtures[6] may be due to a possible destruction of $\mathrm{Ne}(\mathrm{H_2})_n$ complexes at higher temperatures.

All the facts listed above imply that the doping of such a quantum crystal such as hydrogen with heavier impurities and, especially, quantum-crystal effects in the dynamics of substitutional impurities in quantum solids cannot be described by the theory of regular solid solutions. The experimental facts reported here might serve as another stimulating arguments for theorists.

This work was supported by CRDF (Grant UP2-2445-KH-02). The authors thank V.G. Manzhelii and M.I. Bagatskii for valuable discussions.

*E-mail: galtsov@ilt.kharkov.ua

[1] P. Loubeyre, R. LeToullec, and J. P. Pinceaux, Phys. Rev. Lett. **72**, 1360 (1994).
[2] M. S. Somayazulu, L. W. Finger, R. J. Hemley, and H. K. Mao, Science **271**, 1400 (1996).
[3] E. B. Gordon, L. P. Mezhov-Deglin, and O. F. Pugachev, JETP Lett. **19**, 103 (1974).
[4] V. V. Khmelenko, S. I. Kiselev, D. M. Lee, and C. Y. Lee, Phys. Scr. **102**, 118 (2003).
[5] M. A. Strzhemechny, N. N. Galtsov, and A. I. Prokhvatilov, Fiz. Nizk. Temp. **29**, 699 (2003) [Low Temp. Phys. **29**, 522 (2003)].
[6] A. S. Barylnik, A. I. Prokhvatilov, M. A. Strzhemechny, and G. N. Shcherbakov, Fiz. Nizk. Temp. **19**, 625 (1993) [Low Temp. Phys. **19**, 447 (1993)].
[7] A. S. Barylnik, A. I. Prokhvatilov, and G. N. Shcherbakov, Fiz. Nizk. Temp. **21**, 788 (1995) [Low Temp. Phys. **21**, 607 (1995)].
[8] I. Ya. Minchina, M. I. Bagatskii, V. G. Manzhelii, and P. I. Muromtsev, Fiz. Nizk. Temp. **21**, 711 (1995) [Low Temp. Phys. **21**, 530 (1995)].
[9] B. Ya. Gorodilov, A. I. Krivchikov, V. G. Manzhelii, and N. N. Zholonko, Fiz. Nizk. Temp. **20**, 78 (1994) [Low Temp. Phys. **20**, 66 (1994)].
[10] M. I. Bagatskii, I. Ya. Minchina, and V. G. Manzhelii, Fiz. Nizk. Temp. **22**, 52 (1996) [Low Temp. Phys. **22**, 37 (1996)].
[11] T. Momose and T. Shida, Bull. Chem. Soc. Jpn. **71**, 1 (1998).
[12] A. V. Danilychev, V. E. Bondybey, V. A. Apkarian, S. Tanaka, H. Kajihara, and S. Koda, J. Chem. Phys. **103**, 4292 (1995).
[13] M. E. Fajardo, S. Tam, T. L. Thompson, and M. E. Cordonnier, Chem. Phys. **189**, 351 (1994).
[14] T. Momose, M. Miki, T. Wakabayashi, T. Shida, M.-C. Chan, S. S. Lee, and T. Oka, J. Chem. Phys. **107**, 7707 (1997).
[15] M. Hartmann, R. E. Miller, J. P. Toennies, and A. Vilesov, Science **272**, 1631 (1996).
[16] J. Z. Li and V. A. Apkarian, J. Chem. Phys. **107**, 1544 (1997).
[17] B. I. Verkin and A. F. Prikhot'ko (Eds.), *Cryocrystals* [in Russian], Naukova Dumka, Kiev (1983).
[18] M. L. Klein and J. A. Venables (Eds.), *Rare Gas Solids*, Vol. 1, Academic Press, London (1976).
[19] V. G. Manzhelii, A. I. Prokhvatilov, I. Ya. Minchina, and L. D. Yantsevich, *Handbook of Binary Solutions of Cryocrystals*, Begell House, New York (1996).
[20] K. Motizuki and T. Nagamiya, J. Phys. Soc. Jpn. **11**, 93 (1956).
[21] V. Shevtsov, A. Shcherbakov, P. Malmi, E. Ylinen, and M. Punkkinen, J. Low Temp. Phys. **104**, 211 (1996).
[22] V. Shevtsov, P. Malmi, E. Ylinen, and M. Punkkinen, J. Low Temp. Phys. **114**, 431 (1999).
[23] G. N. Shcherbakov, A. I. Prokhvatilov, M. A. Strzhemechny, and A. S. Barylnik, *Abstracts of the 2nd International Conference on Cryocrystals and Quantum Crystals*, Polanica-Zdroj, Poland (1997), p. 2.
[24] B. Ya. Gorodilov, A. I. Krivchikov, V. G. Manzhelii, N. N. Zholonko, and O. A. Koroluk, Fiz. Nizk. Temp. **21**, 723 (1995) [Low Temp. Phys. **21**, 561 (1995)].
[25] V. G. Manzhelii, B. Ya. Gorodilov, and A. I. Krivchikov, Fiz. Nizk. Temp. **22**, 174 (1996) [Low Temp. Phys. **22**, 131 (1996)].
[26] I. N. Krupskii, A. I. Prokhvatilov, and G. N. Shcherbakov, Fiz. Nizk. Temp. **9**, 84 (1983) [Sov. J. Low Temp. Phys. **9**, 42 (1983)].
[27] M. A. Strzhemechny, A. I. Prokhvatilov, and L. D. Yantsevich, Physica B **198**, 267 (1994).
[28] I. N. Krupskii, A. I. Prokhvatilov, and G. N. Shcherbakov, Fiz. Nizk. Temp. **9**, 858 (1983) [Sov. J. Low Temp. Phys. **9**, 446 (1983)].

This article was published in English in the original Russian journal. Reproduced here with stylistic changes by AIP.

Structural peculiarities of quench-condensed pure and argon-doped nitrous oxide

A. A. Solodovnik* and V. V. Danchuk

B. Verkin Institute for Low Temperature Physics and Engineering of the National Academy of Sciences of Ukraine, 47 Lenin Ave., Kharkov 61103, Ukraine

Fiz. Nizk. Temp. **29**, 1041–1044 (September–October 2003)

Electron diffraction studies are carried out for condensed N_2O and N_2O–Ar films. Deposition is done at substrate temperatures of 10 and 20 K. The growth process of N_2O deposits is studied. A strong effect of argon impurities on the structure of the nitrous oxide matrix is observed. The phase separation of the solutions is studied. The equilibrium solubility of argon atoms in nitrous oxide is very low. Introduction of a small amount of argon impurity into the molecular lattice destroys the crystal structure. An effect of the size of the sample on its structure is also studied. © *2003 American Institute of Physics.* [DOI: 10.1063/1.1614193]

INTRODUCTION

Solid nitrous oxide belongs to the class of molecular cryocrystals consisting of linear molecules. At low temperature the symmetry of this crystal is described by the $Pa3$ space group in which the centers of mass of the molecules are localized at the sites of the fcc lattice and the axes of the molecules are directed along the four cube diagonals.[1,2] The strong anisotropic interaction between triatomic molecules (as both ''long'' N_2O and CO_2) stabilizes the state with orientational order up to the triple point. Doping of the ordered modification with atomic (''rotationally neutral'') impurities could lead to realization of phase transitions due to the molecule disorientation and the formation of an orientational glass state.[3,4] The number of transformations can be still greater in the case of small objects. Change in the structure of deposited particles can also be caused by the size factor. One can assume that the existence of an anisotropic interaction may also affect the character of a dimensional phase transition. The possible formation of icosahedral CO_2 clusters was considered in Ref. 5. According to the experimental data[6] the CO_2 free clusters had the structure inherent to the bulk crystal. However the authors observed an intensification of the librational motion of the CO_2 molecules in small crystalline clusters. Investigation of the initial stage of sample preparation is important for understanding the mechanism of the crystalline phase formation in pure solids and solutions.

The effect of dilution of spherically symmetric atoms in a molecular crystal matrix on the orientational order has been investigated in CO_2–Ar alloys.[3,7] It was established that the rare-gas doping lowers the potential barrier hindering the rotation of molecules. As a result, the orientational ordering factor of CO_2 molecules decreases considerably with increasing Ar concentration. The nearest analog of solid carbon dioxide is solid nitrous oxide. As a molecule, N_2O is physically very similar to CO_2, except for its dipole moment. In the case of nitrous oxide a phase transition attributed to dipole ordering may occur at $T<11$ K.[8] However according to the structure study[9] the ''head-to-tail'' order is absent in nitrous oxide condensates down to 2.2 K. A partial dipolar ordering reveales itself in peculiarities of the temperature dependence of the Grüneisen constant for solid N_2O.[10]

EXPERIMENTAL

Investigations were carried out by the transmission electron diffraction technique using a helium cryostat.[11,12] Measurements were made in the temperature range between 6 and 60 K. Samples were prepared *in situ* by depositing gaseous mixtures on a polycrystalline Al substrate film at various temperatures. CO_2 (Ref. 13) and N_2O (Ref. 14) samples quench-deposited under certain conditions may be amorphous. Our experiments also enabled us to establish conditions for the formation of a stable $Pa3$ structure. We used 99.99% pure gas to make the deposits. The concentration of the gaseous phase was determined by measuring the partial pressure of components with the help of a sensitive manometer. The Al film also served as the internal standard. The absolute error in determining the lattice parameter for high-intensity sharp peaks usually did not exceed 0.005 Å. For weak and highly blurred reflections, the error was twice as large. The samples did not reveal any noticeable signs of texture. The effective thickness of the samples ranged from 2 to 45 nm. As the procedure was capable of detecting a new phase if the dimensions of its domains were of the order of few nanometers, diffraction patterns were recorded continuously during the condensation.

RESULTS AND DISCUSSION

Pure nitrous oxide

We present a detailed study of a growth process of N_2O crystalline deposits in the temperature range 6–20 K. The structure of N_2O samples was investigated as a function of both the temperature of the substrate and the dimensional factor at the choosen conditions. The sequence of changes in the diffraction patterns during deposition at 10 K is shown in Fig. 1. The indices of the peaks are marked on top; $S=4\sin\theta/\lambda$ is the diffraction vector modulus, θ is the Bragg angle, and λ is the electron wavelength. At the initial stage of the condensation we observed the appearance aggregates having a structure with complete vanishing of reflections caused by the orientational ordering of the molecular axes [see Fig. 1*a*)]. ''Superstructural'' peaks such as (210), (320), and (321) were absent. The diffraction pattern obtained can be interpreted as that of an fcc structure. This will be dis-

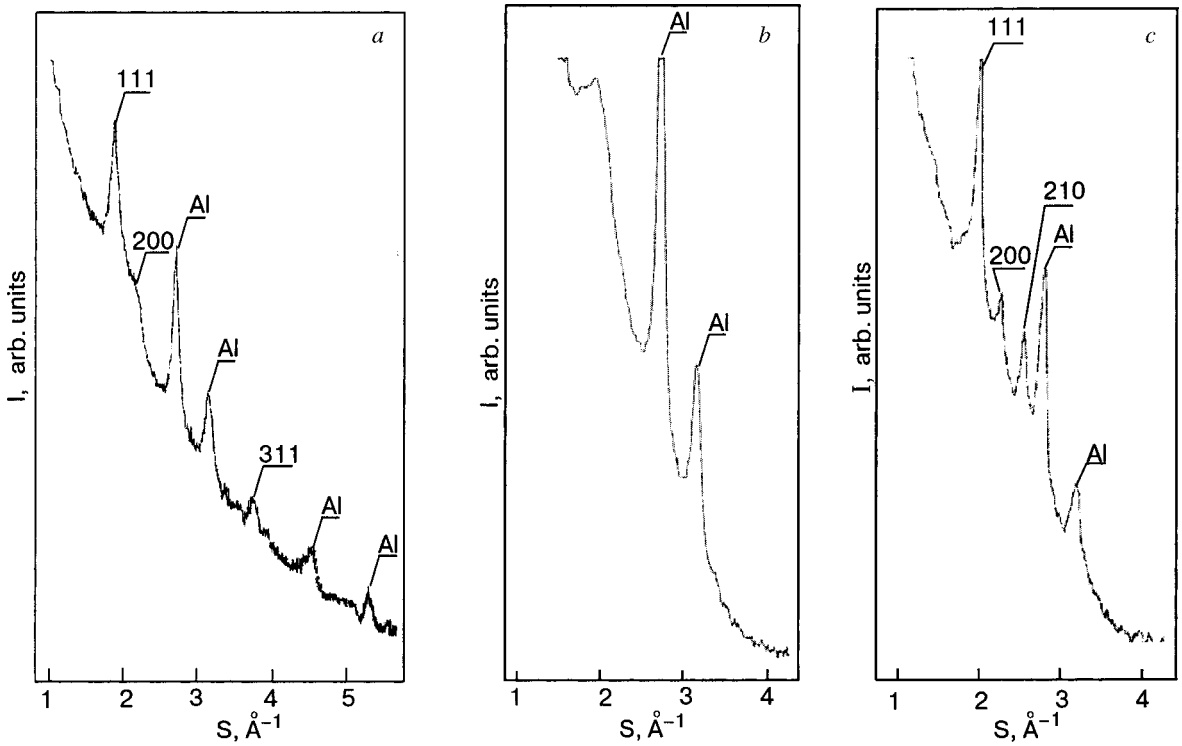

FIG. 1. Intensity distribution corresponding to the electron diffraction pattern from N_2O samples. The evolving structure during the growth process at 10 K. Time of quenching is 20 s. The initial stage of sample formation (*a*); time of quenching is 2 min, amorphous phase (*b*); time of quenching is 3.5 min, $Pa3$ structure (*c*).

cussed later. With further increase in the amount of deposited gas a transition of the crystalline phase into an amorphous one was observed (see Fig. 1*b*). The diffraction pattern of the condensate showed one broad, diffuse diffraction ring at the position where the (111) and (200) reflections are expected to occur. As the molecular aggregates became larger, the nature of the intensity distribution of the diffraction pattern changed. The amorphous modification transformed into an ordered phase (see Fig. 1*c*). All of the diffraction peaks correspond to the $Pa3$ structure. This is indicated by a sharpening of the (111) and (200) peaks and the appearance of the (210) maxima inherent to the long-range-ordered phase. No change in intensity along the diffraction rings was observed. Precise measurements of the diameters of the diffraction rings and the corresponding calculations gave the following value of the lattice parameter of the ordered phase: $a=(5.666\pm0.005)$ Å. As indicated above, the structure of the initial deposit corresponds to the fcc phase. The evidence for this conclusion is the absence of ''superstructural'' reflections and the presence of the (311) peak, which is very weak in $Pa3$ group symmetry. The value of lattice parameter of the fcc phase is $a=5.682$ Å. One can see that the difference between the values of the lattice parameter of the two phases is not big. However, it is known that disordering of the linear molecules leads to an increase of the lattice parameter. On other hand, a linear decrease in the value of the lattice parameter with decreasing cluster size was observed. The contraction from the bulk solid is about 0.35% for a small CO_2 cluster.[6] This contradiction can be explained using a simple model to account for the linear variation. The clusters have the form of isotropic spheres with compressibility and surface stress, producing an effective internal pressure. The contradiction between the lattice parameter and the character of the intensity distribution[15] (see Fig. 1*a*) permits us to suggest such an explanation. At the initial stage of growth we obtain a noncrystalline phase, as can be seen from the diffraction pattern (see Fig. 1*a*). The (111) reflection is sharp, but it

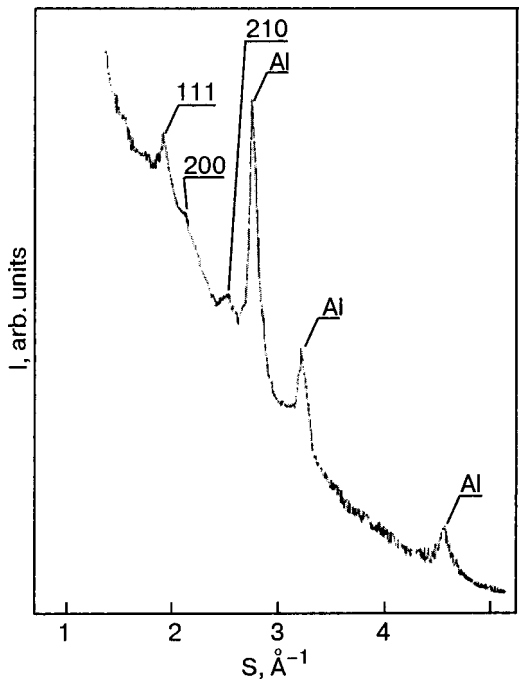

FIG. 2. Intensity distribution corresponding to the electron diffraction pattern from N_2O samples at the initial stage of formation at 20 K. Time of quenching is 20 s.

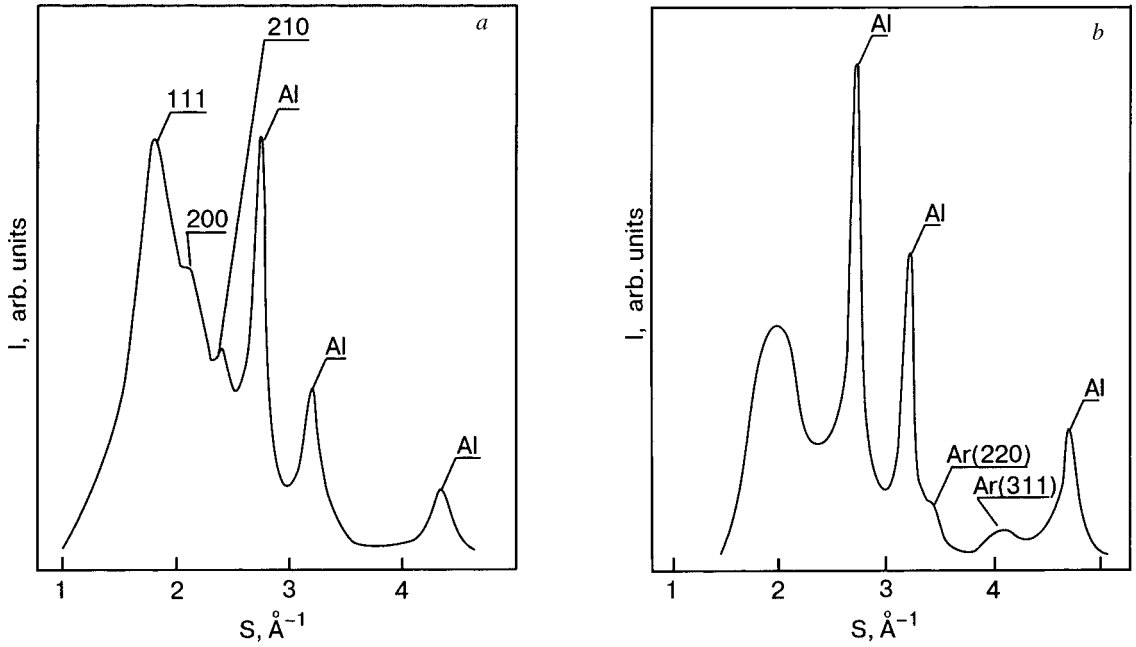

FIG. 3. The diffraction pattern of N_2O–3.5% Ar (*a*) deposited at 20 K and N_2O–10% Ar (*b*) deposited at 20 K.

differs from the line profile of ideal crystals by a strong broadening of the line base. The (200) reflection is broad and diffuse and is not distinctly separated from (111).[15] During the growth process the dimensions of the sample increase from 2 to 45 nm. The most interesting result is a nitrous oxide solid with a structure in which the ordered arrangement of N_2O molecules is absent.

At 20 K diffraction peaks appeared at the positions corresponding to the $Pa3$ structure during quenching of pure nitrous oxide (see Fig. 2). Reflections (200) and (210) were weak. However, with increasing size of a sample all the peaks of $Pa3$ symmetry were clearly manifested.

Nitrous oxide doped with argon

The choice of the N_2O–Ar system is dictated by the following circumstance. To our knowledge no data are available in the literature about the character of the phase diagram of these components. Nitrous oxide-based solutions are such systems in which the molecular component does not exhibit a transition from an orientationally ordered to a disordered phase in the solid state. The choice of argon as the dopant is motivated mainly by the considerable difference in the molar volumes. The volume difference is 7%. This fact allows us to expect interesting results. At first we present the results of the investigation of large N_2O–Ar aggregations. The aim is to obtain information about the solubility of argon in the nitrous oxide matrix and to establish the crystallographic structure of the solid solutions.

The solidified N_2O–Ar mixtures were prepared at 20 K and were recorded. We illustrate the effect of Ar doping (see Fig. 3*a*). If the argon concentration did not exceed 3.5 mol. % the electron diffraction patterns displayed the bright halo and very weak peaks of the N_2O ordered phase. The center of the halo coincides with the (111) reflection. The presence of the peaks (200) and (210) confirms the weak degree of ordered arrangement of the N_2O molecules. For argon fractions of about 10 mol., phase separation process. The character of diffraction patterns evidenced the decomposition of the solutions. In this case there are two systems of diffraction rings. One of these corresponds to the N_2O ultradisperse phase, while the other, which contains peaks of much lower intensity, corresponds to the Ar fcc modification (see Fig. 3*b*). With increasing argon content in the mixture the intensity of the Ar peaks increases. On heating the samples up to 30 K the patterns changed quickly: the halo disappeared and sharp rings appeared, the positions of which corresponded to those of the diffraction peaks from the N_2O ordered phase. Annealing above 30 K was accompanied by intense evaporation of argon. The desorption of argon made it possible to form the $Pa3$ structure of nitrous oxide. According to our measurements, the equilibrium solubility of argon atoms in the N_2O matrix is very low. The structure of the nitrous oxide lattice is very sensitive to the concentration of impurities. The introduction of a small amount of argon into the molecular lattice led to destruction of the crystal structure.

The authors wish to express thanks to M. A. Strzhemechny for stimulating discussions and substantial support.

*E-mail: solodovnik@ilt.khakov.ua

[1] L. Vegard, J. Phys. **71**, 465 (1932).
[2] W. C. Hamilton and M. Petrie, J. Phys. C **65**, 1453 (1953).
[3] M. A. Strzhemechny, A. A. Solodovnik, and S. I. Kovalenko, Fiz. Nizk. Temp. **24**, 889 (1998) [Low Temp. Phys. **24**, 669 (1998)].
[4] V. A. Hochli, K. Knor, and A. Loidl, Adv. Phys. **39**, 408 (1990).
[5] B. W. van de Waal, J. Chem. Phys. **79**, 3948 (1983).
[6] G. Torchet, H. Bouchier, J. Farges, M. F. de Feraudy, and B. Raoult, J. Chem. Phys. **81**, 2137 (1984).

[7] A. A. Solodovnik, M. A. Strzhemechny, and S. I. Kovalenko, Czech. J. Phys. **46**, 521 (1996).
[8] M. W. Melhuish and R. L. Scott, J. Phys. C **68**, 2301 (1964).
[9] S. I. Kovalenko, E. I. Indan, A. A. Khudoteplaya, and Y. N. Krupskii, Phys. Status Solidi A **20**, 629 (1973).
[10] A. M. Tolkachev, V. G. Manzhelii, V. P. Azarenkov, A. Jezowski, and E. A. Kosobutskaya, Fiz. Nizk. Temr. **6**, 1533 (1980) [Sov. J. Low Temp. Phys. **6**, 747 (1980)].
[11] S. I. Kovalenko and V. A. Godovannyi, Prib. Tekh. Eksp. **2**, 235 (1967).
[12] S. I. Kovalenko and A. A. Solodovnik, Fiz. Nizk. Temp. **18**, 889 (1992) [Sov. J. Low Temp. Phys. **18**, 626 (1992)].
[13] M. Falk, J. Chem. Phys. **86**, 560 (1987).
[14] N. V. Krainykova and M. A. Strzhemechny, Fiz. Nizk. Temp. **21**, 1254 (1995) [Low Temp. Phys. **21**, 1254 (1995)].
[15] J. W. Lee and G. D. Stein, Surf. Sci. **156**, 112 (1985).

This article was published in English in the original Russian journal. Reproduced here with stylistic changes by AIP.

The contribution of tunneling to the diffusion of protons and deuterons in rare gas solids

M. K. Beyer[a] and V. E. Bondybey[b]

Institut für Physikalische und Theoretische Chemie, Technische Universität München, 4 Lichtenbergstrasse, Garching 85747, Germany

E. V. Savchenko[c]

B. Verkin Institute for Low Temperature Physics and Engineering of the National Academy of Sciences of Ukraine, 47 Lenin Ave., Kharkov 61103, Ukraine

Fiz. Nizk. Temp. **29**, 1045–1048 (September–October 2003)

The stability and diffusion of protons and deuterons in rare gas matrices are reexamined. These are known to be stabilized in rare gas matrices in the form of linear, centrosymmetric Rg_2H^+ cations. The elementary step in their diffusion, displacement from one Rg–Rg bond to a neighboring one, can be modeled as an isomerization of the triangular Rg_3H^+ cation. Using an analytic approximation for the thermally averaged transmission coefficients for tunneling through and reflection by a truncated parabolic potential barrier [R. T. Skodje and D. G. Truhlar, J. Phys. Chem. **85**, 624 (1981)], we calculate the rate constants for this elementary diffusion step. The calculated rate constants are consistent with all experimental observations and confirm that tunneling makes the dominant contribution to the diffusion of protons and deuterons in rare gas solids. Deuteration reduces the tunneling rates by 5 to 8 orders of magnitude, which agrees with the observation that D^+ in rare gas solids is signficantly more stable than H^+. © *2003 American Institute of Physics.* [DOI: 10.1063/1.1614194]

INTRODUCTION

Infrared absorptions associated with deuterons and protons in solid rare gases have been known for more than thirty years, and in fact some of the puzzling aspects of their earliest observations were linked with their diffusion behavior. Initially, a strong infrared absorption near 644 cm^{-1} was detected, whenever argon with a small amount of deuterium was discharged and deposited on a cold substrate held at 14 K. However, no comparable absorption appeared when normal hydrogen was used instead.[1,2] The problem turned out to lie in the fact that the grating infrared spectrometers used at the time typically required some 60 minutes to scan the usual IR-range from 4000–400 cm^{-1}. When, on the other hand, the spectral scan was started directly in the expected region, the corresponding absorption due to normal hydrogen was detected near 905 cm^{-1}, shifted almost exactly by the appropriate $\sqrt{2}$ ratio. While the hydrogen absorption decreases in intensity with a half-life of a few minutes, the deuteron band is much more stable, with its rate of decrease being slower by several orders of magnitude.

Initially there also was some doubt as to the charge state of the carrier of the absorption bands, but subsequent evidence pointed increasingly towards positively charged protons.[3–7] Similar absorptions were also found in solid krypton[2] and, more recently, in xenon,[5] and it is now well established that the transitions are due to the ν_3 asymmetric stretch and $\nu_3+n\nu_1$ combination bands with the low-frequency symmetric stretching mode of the linear, centrosymmetric Rg_2H^+ cations. Already in the first investigation of these absorptions it was pointed out that the Rg_2H^+ species are isoelectronic with the well-known HX_2^- bihalide anions. From the chemical point of view, protons—or deuterons—are essentially dimensionless charges, and they therefore show a clear preference for a coordination number of two, i.e., they are strongly solvated by two and only two strongly bound rare gas ligands.[8]

As was noted above, both H^+ and D^+ are observable in solid argon, krypton, and xenon. H^+ is quite short-lived in argon and disappears on a much slower, 10^3 s, time scale in solid Kr and Xe, whereas D^+ is much longer-lived in argon and essentially stable in the heavier rare gases, the orders-of-magnitude difference in stability between protons and deuterons being suggestive of a tunneling process. Interestingly, neither protons nor deuterons have thus far been observed in solid neon. We have recently discussed these phenomena in this journal[9] and suggested that diffusion might be activated by room-temperature blackbody radiation, which exhibits a strong overlap with the ν_3 band of Rg_2H^+. At that time, we did not quantify the effect of tunneling but suggested that it might contribute to the observed differences.

A proton or a deuteron in a rare gas solid is inserted between two neighboring atoms to form the linear, centrosymmetric entitity Rg_2H^+. Interestingly, the distance between the two atoms with the proton inserted is in fact considerably shorter than the distance between two nearest-neighbor atoms in an unperturbed rare gas lattice. An elementary step of diffusion through the solid then requires displacement of the proton from one Rg–Rg bond to a neighboring one, and can be modeled as an isomerization of a triangular Rg_3H^+ cation, as shown schematically in Fig. 1. In the T-shaped, C_{2v} cation, the proton is displaced, stretching the Rg_b-H^+ and shortening the Rg_c-H^+ distance to reach the equally spaced C_{2v} transition state. We have computed the barrier heights and frequencies of this transition

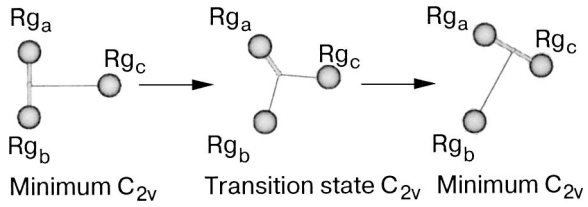

FIG. 1. Cluster model for proton diffusion in rare gas matrices. The proton changes its connectivity when it goes through the transition state of the Rg_3H^+ ion. A large number of these elementary steps lead to a random motion of the proton through the matrix. Reproduced from Ref. 8 by permission of the PCCP owner societies.

state in our recent investigation.[8,9] In the present work, we use these results to estimate the transmission rate constants for H^+ and D^+ in solid neon, argon, krypton and xenon through the diffusion barrier, with thermal activation and tunneling taken into account.

COMPUTATIONAL DETAILS

The thermally averaged transmission coefficients for truncated parabolic potential barriers are calculated using the analytic approximation of Skodje and Truhlar,[10] which resolves some problems associated with the earlier approaches by Wigner[11] and Bell.[12] As an input into this formalism, the barrier height and the imaginary frequency of the transition state are needed. The transition states of Rg_3H^+ have been calculated in our previous work[8,9] with the B3LYP functional and the 6-311++G($3df$,$3pd$) basis set on hydrogen, neon, and argon, and the Stuttgart/Dresden relativistic effective core potential basic set[13] on argon, krypton, and xenon, employing the Gaussian 94 program suite.[14] In all cases the frequencies are scaled by a factor of 0.8 to take into account the influence of the rare gas solid.[9]

RESULTS AND DISCUSSION

As argued previously,[8,9] the reaction sequence depicted in Fig. 1 for Rg_3H^+ represents one step in the diffusion of protons or deuterons in rare gas solids. The zero-point-corrected barrier heights V_0 and imaginary frequencies ν are given in Table I. The key parameter for describing tunneling is the transmission coefficient $\kappa(T)$ at temperature T,[10] which is more instructively called "the enhancement of the transfer rate due to tunneling" by Lill and Helms.[15] With

$$\alpha = -2\pi/hi\nu \tag{1}$$

and

$$\beta = 1/kT \tag{2}$$

it is easily shown that the conditions $\alpha < \beta$ and $\beta V_0 > 1$ are fulfilled for the species discussed in this work. According to Skodje and Truhlar,[10] $\kappa(T)$ is then approximated by the equation:

$$\kappa(T) = [\beta/(\beta-\alpha)]\exp[(\beta-\alpha)V_0]. \tag{3}$$

At $T = 10$ K this yields the exceedingly large numbers which are listed in Table I. They indicate that at these low temperatures, tunneling is the only contribution to the diffusion of protons as well as deuterons.

In order to get a quantitative estimate of the rate constants involved in the diffusion process, classical Arrhenius rate constants are calculated. Since the bending mode ν_2 of the protonated rare gas dimer corresponds to the imaginary mode in the transition state, its frequency is chosen as the Arrhenius A factor, i.e., the frequency with which the barrier is attempted. The Arrhenius rate constant k_A then amounts to:

$$k_A(T) = c\,\nu_2 \exp(-\beta V_0). \tag{4}$$

Calculated values for k_A are listed in Table I. They illustrate that thermal activation is in no case sufficient to overcome the diffusion barrier, and significant energy input, e.g.,

TABLE I. Matrix, dopant H^+ or D^+, barrier height V_0 in kJ·mol^{-1}, scaled imaginary frequency ν in cm^{-1}, scaled bending frequency ν_2 in cm^{-1} (scaling factor 0.8 in both cases), enhancement of the transfer rate due to tunneling κ(10 K), classical Arrhenius rate constant k_A(10 K) in s^{-1}, and semiclassical rate constant with thermal activation and tunneling taken into account, k_{SC}(10 K) in s^{-1}.

Matrix	Dopant	V_0 / kJ·mol^{-1}	$-i\nu$/cm^{-1}	ν_2/cm^{-1}	κ (10 K)	k_A(10 K)/s^{-1}	k_{SC}(10 K)/s^{-1}
Ne	H^+	11.5 [a]	609	620 [a]	$6.25\cdot10^{55}$	$1.98\cdot10^{-47}$	$1.24\cdot10^{9}$
Ne	D^+	13.8 [b]	441	444 [b]	$9.66\cdot10^{64}$	$1.37\cdot10^{-59}$	$1.33\cdot10^{6}$
Ar	H^+	29.7 [a]	506	549 [a]	$6.03\cdot10^{141}$	$1.50\cdot10^{-142}$	$9.06\cdot10^{-1}$
Ar	D^+	29.9 [b]	366	390 [b]	$3.97\cdot10^{137}$	$9.64\cdot10^{-144}$	$3.83\cdot10^{-6}$
SECP [c]							
Ar	H^+	30.7 [a]	506	518 [a]	$3.59\cdot10^{146}$	$8.48\cdot10^{-148}$	$3.05\cdot10^{-1}$
Ar	D^+	31.6 [b]	364	369 [b]	$1.97\cdot10^{145}$	$1.20\cdot10^{-152}$	$2.37\cdot10^{-7}$
Kr	H^+	32.3 [a]	471	486 [a]	$1.32\cdot10^{153}$	$3.49\cdot10^{-156}$	$4.60\cdot10^{-3}$
Kr	D^+	32.8 [b]	335	345 [b]	$1.10\cdot10^{149}$	$6.06\cdot10^{-159}$	$6.63\cdot10^{-10}$
Xe	H^+	35.5 [a]	441	444 [a]	$1.36\cdot10^{167}$	$6.15\cdot10^{-173}$	$8.35\cdot10^{-6}$
Xe	D^+	35.9 [b]	313	314 [b]	$2.70\cdot10^{161}$	$3.54\cdot10^{-175}$	$9.57\cdot10^{-14}$

Comment: [a]From Ref. 8; [b]From Ref. 9; [c]The values above the horizontal line were computed considering all electrons explicitly. The computations below the divider were carried out using the quasi-relativistic effective core potential basis sets of the Stuttgart/Dresden group.[13]

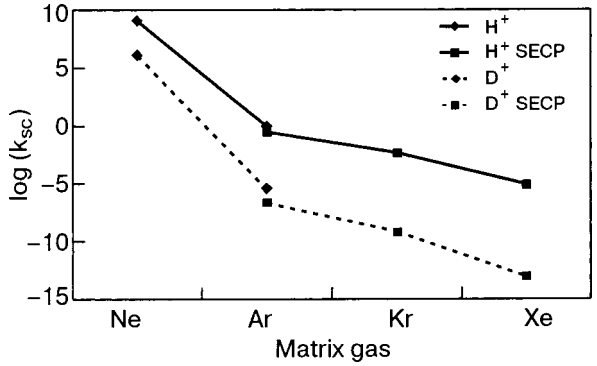

FIG. 2. Semiclassical rate constant of the elementary diffusion step for Ne, Ar, Kr, and Xe. While both H^+ and D^+ have a high mobility in a neon matrix, diffusion is considerably slowed down in argon, krypton, and xenon. Deuteration reduces the rate constants by 5 to 8 orders of magnitude, which stabilizes D^+ relative to H^+ in matrices of heavier rare gases.

from room-temperature blackbody radiation,[9] would be required to explain the diffusion. However, the enhancement of transfer rate due to tunneling described by $\kappa(T)$ is sufficiently large to balance these low Arrhenius rate constants. With the assumption that the quantum-mechanical barrier is attempted at the same frequency as the classical barrier, the semiclassical thermally averaged rate constant k_{SC} which takes thermal activation and tunneling into account amounts to:

$$k_{SC}=\kappa(T)k_A(T)=c\,\nu_2[\beta/(\beta-\alpha)]\exp(-\alpha V_0). \qquad (5)$$

These values are again given in Table I and are shown in Fig. 2. Since most parameters, like V_0 and ν, are in the argument of the exponential function, the accuracy of these results cannot be better than a few orders of magnitude. Nevertheless, the numbers clearly reflect the experimental observations: In solid neon, the deuteron changes place on a time scale of microseconds and the proton on a time scale of nanoseconds, both consistent with the fact that neither H^+ nor D^+ have been observed in solid neon. In either case, the charged particle is rapidly diffusing through the matrix and may find species like electrons, X^- impurities, neutral hydrogen atoms, H_2O, or H_2 (Ref. 16) to recombine.

The barrier V_0 is much higher for argon, krypton, and xenon than for neon. Consequently, the diffusion rate constants are reduced by 10 orders of magnitude or more. Within this group of heavier, more polarizable rare gases, there is still a significant increase in the lifetime of the charge carrier for argon via krypton to xenon, since the barriers increase slightly, and more importantly, the frequencies in the transition state decrease considerably. This is consistent with the experimental observation that H^+ is relatively short-lived in argon, and much easier to observe in krypton and xenon. Also, in the simultaneous presence of hydrogen and deuterium the rate of deuteron disappearance is increased, suggesting that the neutral sinks for the charge carrier are also diffusing in part by tunneling.

As expected, however, deuteration reduces the diffusion rate constants k_{SC} by 5 to 8 orders of magnitude, which means that in cases where H^+ is short-lived, D^+ becomes long-lived. If H^+ is long-lived, D^+ becomes essentially stable, as has been observed experimentally for xenon by Räsänen and coworkers.[5]

In the presence of two different rare gases, that is, in terms of Fig. 1, if Rg_b is different from Rg_c, then the two minima on the right- and left-hand sides will no longer be equivalent but will have substantially different energies. Under these circumstances the diffusion should stop, and the positive charge would remain localized near the heavier, more polarizable rare gas atom. Species like XeH^+ and Xe_2H^+ should therefore be observable in solid neon.

CONCLUSIONS

Calculations of the rate constants with thermal activation and tunneling taken into account show that the latter process, tunneling, dominates the diffusion of protons and deuterons in rare gas solids. At a temperature of 10 K, tunneling is faster than thermal activation by 55 orders of magnitude for H^+ in neon and by up to 167 orders of magnitude for H^+ in xenon. The values are consistent with all experimental observations. Deuteration reduces the tunneling rates by 5 to 8 orders of magnitude, which is consistent with the significantly higher stability observed for D^+ in comparison with H^+ in rare gas solids. The results also indicate that the transition states proposed earlier are indeed relevant for the diffusion of protons and deuterons in rare gas solids.

Financial support from the Deutsche Forschungsgemeinschaft through the program ''Forderung der wissenschaftlichen Beziehungen deutscher Wissenschaftler zu Wissenschaftlern in L'ándern Mittel- und Osteuropas sowie Ländern der vormaligen UdSSR'' is gratefully acknowledged.

[a)]E-mail: beyer@ch.tum.de
[b)]E-mail: bondybey@ch.tum.de
[c)]E-mail: savchenko@ilt.kharkov.ua

[1] V. E. Bondybey, G. C. Pimentel, and P. N. Noble, J. Chem. Phys. **55**, 540 (1971).
[2] V. E. Bondybey and G. C. Pimentel, J. Chem. Phys. **56**, 3832 (1972).
[3] D. E. Milligan and M. E. Jacox, J. Mol. Spectrosc. **46**, 460 (1973).
[4] C. A. Wight, B. S. Ault, and L. E. Andrews, J. Chem. Phys. **65**, 1244 (1976).
[5] H. Kunttu, J. Seetula, M. Räsänen, and V. A. Arkarian, J. Chem. Phys. **96**, 5630 (1992).
[6] H. M. Kunttu and J. A. Seetula, Chem. Phys. **189**, 273 (1994).
[7] T. D. Fridgen and J. M. Parnis, J. Chem. Phys. **109**, 2155 (1998).
[8] M. Beyer, A. Lammers, E. V. Savchenko, G. Niedner-Schatteburg, and V. E. Bondybey, Phys. Chem. Chem. Phys. **1**, 2213 (1999).
[9] M. Beyer, E. V. Savchenko, G. Niedner-Schatteburg, and V. E. Bondybey, Fiz. Nizk. Temp. **25**, 1087 (1999) [Low Temp. Phys. **25**, 814 (1999)].
[10] R. T. Skodja and D. G. Truhlar, J. Phys. Chem. **85**, 624 (1981).
[11] E. Wigner, Z. Phys. Chem. Abt. B **19**, 203 (1932).
[12] R. P. Bell, Trans. Faraday Soc. **55**, 1 (1959).
[13] A. Nicklass, M. Dolg, H. Stoll, and H. Preuss, J. Chem. Phys. **102**, 8942 (1995).
[14] *Gaussian 94, Revision D.4*, M. J. Frisch, G. W. Trucks, H. B. Schlegel, P. M. W. Gill, B. G. Johnson, M. A. Robb, J. R. Cheeseman, T. Keith, G. A. Petersson, J. A. Montgomery, K. Raghavachari, M. A. Al-Laham, V. G. Zakrzewski, J. V. Ortiz, J. B. Foresman, J. Cioslowski, B. B. Stefanov, A. Nanayakkara, M. Challacombe, C. Y. Peng, P. Y. Ayala, W. Chen, M. W. Wong, J. L. Andres, E. S. Replogle, R. Gomperts, R. L. Martin, D. J. Fox, J. S. Binkley, D. J. Defrees, J. Baker, J. P. Stewart, M. Head-Gordon, C. Gonzalez and J. A. Pople, Gaussian, Inc., Pittsburgh, PA (1995).
[15] M. A. Lill and V. Helms, J. Chem. Phys. **115**, 7985 (2001).
[16] M. Beyer, E. V. Savchenko, G. Niedner-Schatteburg, and V. E. Bondybey, J. Chem. Phys. **110**, 11950 (1999).

This article was published in English in the original Russian journal. Reproduced here with stylistic changes by AIP.

BIOLOGICAL SYSTEMS AT LOW TEMPERATURES

Structural fluctuations and aging processes in deeply frozen proteins

J. Schlichter, V. V. Ponkratov, and J. Friedrich*

Physik-Department E14 and Lehrstuhl für Physik Weihenstephan, Technische Universität, München, 40 Vöttinger Str., Freising D-85350, Germany

Fiz. Nizk. Temp. **29**, 1049–1056 (September–October 2003)

Frozen proteins are nonergodic systems and are subject to two types of structural motions, namely relaxation and fluctuation. Relaxation manifests itself in aging processes which slow the fluctuations. Within certain approximations we are able to experimentally separate the aging dynamics from the fluctuation dynamics by introducing two time parameters, namely an aging time t_a and a waiting time t_w. Both processes follow power laws in time. The fluctuation dynamics shows features of universality characterized by a rather uniform exponent of 1/4. These universality features were shown to be possible due to a random walk on a 1D random trajectory in conformational phase space. A very interesting aspect of protein dynamics concerns the influence of the host solvent on structural motions of the protein cores. We present results for sugar solvents and discuss possible mechanisms. © *2003 American Institute of Physics.* [DOI: 10.1063/1.1614196]

INTRODUCTION

Investigating structural dynamics of low-temperature proteins, it is a fair question to ask whether specific features as compared, for instance, to ordinary polymers or glasses are to be expected. Proteins are the nanomachines which keep life running. It is obvious that this cannot be accomplished by just random motions which characterize the dynamics of dead polymers. Proteins have very specific structural features which are obviously linked to specific dynamical features, even in the frozen state. They are heteropolymers built from a stock of 20 well-defined amino acids. Typical molecular weights are between 10^4 and 10^5, but there are also much larger assemblies. A characteristic feature is the rich variety of molecular interactions, most important among which are the hydrophilic and the hydrophobic interactions. These two types of interactions are mainly responsible for the fact that proteins attain well-defined structures. But, as is clear from the nature of these interactions, this is only possible if the solvent contains a sufficient amount of water. The strong interaction of proteins with water makes them sensitive to changes in their environment, which then may show up as changes in their structure and their respective dynamics.

Because of their well-defined structure, Schrödinger called proteins ''aperiodic crystals'' to stress the fact that they are structurally well defined but lack translational periodicity. However, organization and order is just one aspect of proteins. A quite specific feature is that order in proteins is accompanied by disorder. It is this in-between nature which makes them very different from dead polymers and which points to possible specific features in their dynamics.

In the following we present an overview of our spectral diffusion experiments on a series of modified heme proteins. We will show that low-temperature proteins are truely nonergodic systems which never reach equilibrium. In addition, we will show that their dynamics at low temperature differs in a characteristic fashion from that of glasses. It displays certain aspects of universal features which we believe to be due to random walks on 1D stochastic conformational trajectories.

EXPERIMENTAL

In our experiments we investigate the dynamical behavior of low-temperature proteins by measuring the absorption frequency of a dye molecule, a so-called chromophore, in the interior of the protein. Since this chromophore couples to the amino acids in its environment, dynamical processes of the protein lead to fluctuations in its absorption frequency. Hence, if the linewidth of the chromophore is small enough, one has a very sensitive tool for the measurement of protein dynamics.

All our measurements so far were done with heme proteins. The heme group, however, which is a natural constituent of this type of proteins, is not suitable as the chromophore for our experiments, since the natural widths of its optical transitions are rather broad. To circumvent this problem, we used slightly modified proteins, where the natural heme group was substituted by very similar dye molecules having linewidths of less than 1 GHz (at a temperature of 4.2 K). In this case, even dynamical processes of the proteins which are associated with small changes in the transition energy of the chromophore are—in principle—measurable.

To do this, however, another problem must be solved. Low-temperature proteins do not have a well-defined ground state but can exist in a great number of almost degenerate ''conformational substates,'' [1,2] which are characterized by small differences in the structural arrangement of their amino acids. Hence, in an ensemble of proteins every chromophore interacts with a slightly different environment. Accordingly, the absorption profile of an ensemble is inhomogeneously

broadened. Typical bandwidths of such inhomogeneous protein spectra can be of the order of 10^2 wavenumbers. As a consequence, the small frequency fluctuations associated with conformational changes are completely hidden below this inhomogeneous line. To monitor them, one needs a more sophisticated experimental technique than simple absorption spectroscopy. In our measurements, spectral hole burning was used.[3] For this kind of experiment, a narrow-line laser illuminates the protein ensemble at a certain position in the inhomogeneous band. Proteins with suitable absorption frequencies are excited and photochemically bleached. Hence, the number of absorbing molecules at the laser frequency is decreased, and a gap (a so-called spectral hole) occurs in the absorption spectrum of the protein ensemble. The width of such a hole is comparable to the linewidth of a single chromophore. In addition, it can be shown that a spectral hole behaves exactly like an ensemble of proteins with identical absorption frequencies at the time of hole burning. The problem of inhomogeneous broadening can therefore be circumvented.

In our experiments the so-called spectral diffusion, i.e., the broadening of spectral holes (due to structural fluctuations) is monitored as a function of time. Two experimental parameters are important. After cooling the sample very rapidly from room temperature to 4.2 K, we wait for a certain time, the so-called *aging time* t_a, before burning a hole. Then, after a second time period, called the *waiting time* t_w, the shape of the (broadened) hole is measured. We will show later that the broadening of spectral holes as a function of t_a can be connected with relaxational processes in the protein, whereas the dependence on t_w monitors (stationary) fluctuations of the molecule.

Mathematically the form of a spectral hole at later times is given by a convolution of the initial hole shape with a so-called spectral diffusion kernel $p(\nu_1,t_1|\nu_0,t_0)$. The width $\sigma(t_a,t_w)$ of this kernel is extracted from our experiments. Of course, since the hole-broadening is caused by structural fluctuations, the time dependence of $\sigma(t_a,t_w)$ monitors the structural dynamics of the proteins.

RESULTS

Typical experimental observations

We did a series of spectral diffusion experiments with different heme proteins (horseradish peroxidase, myoglobin, cytochrome c) containing various types of chromophores. In addition, the effect of different solvents as well as the influence of deuteration on the low-temperature dynamics of these proteins was investigated. In all these experiments we found a very similar behavior of our samples, which seems to be of a rather universal nature. As an example, measurements on horseradish peroxidase (HRP) in a water/glycerol matrix will be presented in this Section.[4] (Free-base mesoporphyrin IX served as a chromophore in this protein.)

In Fig. 1 the results of this experiment are given. The broadening of six spectral holes (burned after aging times betwen 40 min and about eleven days) is shown as a function of the waiting time t_w. Two of the main results of our measurements can be recognized immediately from this figure: obviously the broadening of the holes is governed by a power law in t_w—the data follow straight lines in a double-logarithmic representation. In addition, there are clear aging effects: the broadening of the holes which were burned at longer aging times t_a is smaller. This can be seen more clearly in the inset of the figure, which shows the dependence of the hole broadening on t_a at a fixed waiting time t_w, as obtained from a ''cut'' through the data of Fig. 1 along the dashed line. Since this is again a double-logarithmic plot, obviously this time dependence is governed by a power law, too. So what we find is:

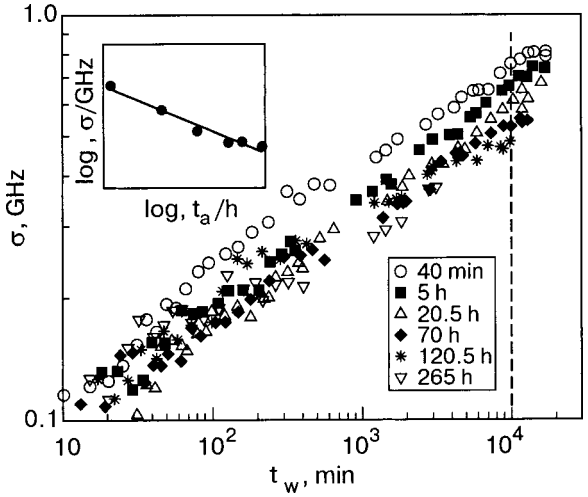

FIG. 1. Results of a spectral diffusion experiment on horseradish peroxidase at $T=4.2$ K. The broadening of six spectral holes burned after different aging times t_a (see legend) is shown as a function of the waiting time t_w. Obviously the dependence on t_w is given by a power law: $\sigma \propto t_w^{\alpha/2}$. The inset shows the hole-broadening at a fixed waiting time as a function of t_a. Again a power law is found: $\sigma \propto t_a^{-\beta}$.

$$\sigma(t_a,t_w) \propto \left(\frac{t_a}{T}\right)^{-\beta} \left(\frac{t_w}{\tau_0}\right)^{\alpha/2}. \tag{1}$$

For the exponents $\alpha/2$ and β all our experiments yielded very similar values, namely about 0.25 and 0.07, respectively. A possible explanation for this apparently universal behavior will be given below.

As can be seen from Eq. (1), it is possible to separate the influence of aging time and waiting time in the experimental results, i.e., we can scale our data with their t_a dependence to get a plot that is independent of t_a (see Fig. 2). In this so-called master plot only the stationary fluctuations of the proteins show up; in contrast, the t_a dependence monitors non-equilibrium processes in the proteins, i.e., their relaxation to an equilibrium structure.

It should be emphasized that the numerical values of the above-mentioned exponents depend on the microscopic picture which is used for the interpretation of the data (and which determines the mathematical form of the diffusion kernel); however, the power-law behavior itself is an independent experimental fact. In our earlier works we tried to analyze our spectral diffusion measurements in the framework of a two-level-system (TLS) theory, which is well known from the theory of low-temperature glasses.[5] However, when we started to pay more attention to the aging effects which can be observed in protein dynamics, it turned out that a satisfactory explanation of our data with a TLS

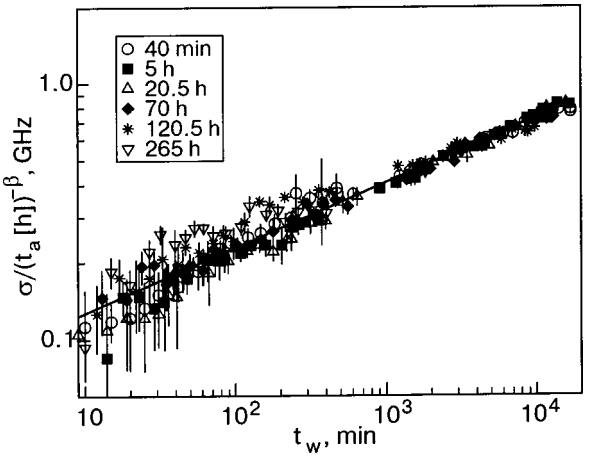

FIG. 2. Scaling the data of Fig. 1 with their aging-time dependence yields a so-called "master plot." It contains only the stationary contributions to the spectral diffusion. Again, the power-law behavior in t_w can clearly be seen.

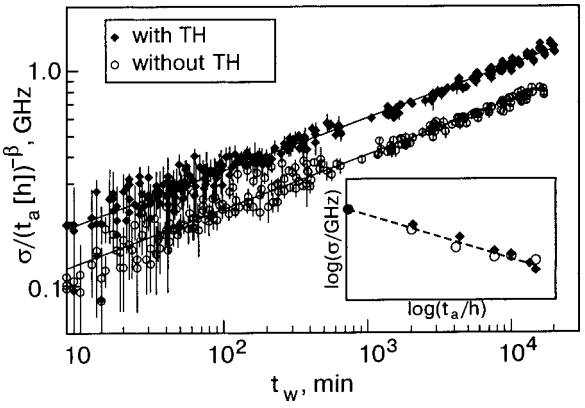

FIG. 4. Master plots of spectral diffusion experiments on HRP dissolved in a water/glycerol matrix and in a water/glycerol matrix enriched with trehalose (TH). Only the intercept of a double-logartihmic plot is affected by the trehalose. The inset shows the aging behavior of the two samples (normalized to their values at $t_a = 40$ min), which is independent of the composition of the solvent.

theory was impossible.[6] This is seen very well in Fig. 3. Here a fit of the data of Fig. 3 by a (nonequilibrium) TLS theory is attempted; obviously the agreement with the experiment is very poor.

However, this can be understood quite easily. In the TLS theory spectral diffusion is explained by coupling the chromophore to an ensemble of two-level systems with a broad range of relaxation times. At a time t_a after cooling down the sample, only TLS with time constants smaller than t_a have reached thermal equilibrium. Their influence on the broadening of a spectral hole will saturate after a waiting time $t_w > t_a$, since by then any subensemble of these TLS, which has been "marked" by hole burning, will have reached its equilibrium distribution again. If there are TLS with time constants larger than t_a, there will be spectral diffusion even for longer waiting times, but in addition there will be aging effects, since these TLS still relax to their equilibrium distribution. Behavior like that found in our protein experiments (i.e., almost no aging effects after an aging time of about a few days but still nonsaturating spectral diffusion for much longer waiting times) can thus not be explained by a TLS theory. To solve this problem, we invented a new statistical ansatz to interpret our measurements, which will be discussed below. In this new model spectral diffusion is explained by diffusionlike motions of the amino acids in the proteins; the diffusion kernel then takes the form of a Gaussian, and an analysis of our data based on this kernel leads to the exponents $\alpha/2$ and β given above.

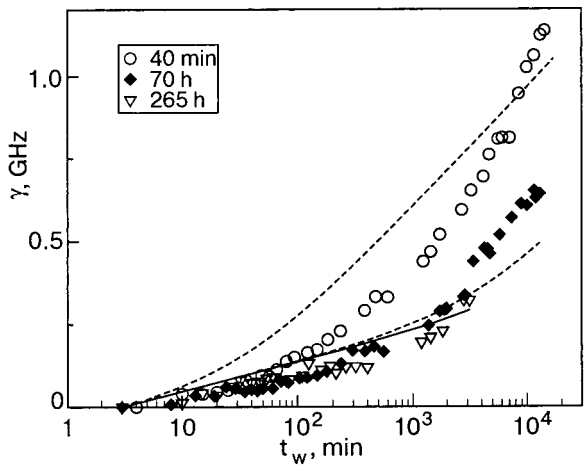

FIG. 3. An interpretation of the data of Fig. 1 according to a nonequilibrium TLS theory (dotted lines) fails completely. (Here the broadening of the holes is labeled by γ instead of σ to clarify that the data have been analyzed in a different way than in the upper figures.)

SOLVENT EFFECTS ON SPECTRAL DIFFUSION

Horseradish peroxidase in a sugar matrix

In an important part of our experiments we investigated the role of solvent effects on protein dynamics. To learn something about this interesting question, we dissolved HRP in a trehalose-enriched water/glycerol solution.[7] (In addition, as will be presented in the next Section, the behavior of cytochrome c in a dry trehalose film was investigated.) Trehalose is a disaccharide with a high affinity for the formation of hydrogen bonds[8] (and is therefore believed to replace water molecules at the surface of proteins) and with remarkably high glass-transition temperatures of its solutions.[9] It is well known that trehalose is of great importance for biological systems, helping them to survive phases of strong dehydration or low temperatures. For this reason, the influence of trehalose on protein dynamics has been investigated before. For example, Hagen *et al.*[10,11] measured the kinetics of CO rebinding in myoglobin in a trehalose environment; this reaction is dominated by the relaxational behavior of the myoglobin. Similar experiments on hemoglobin have been done by Gottfried *et al.*[12]

In Fig. 4 the results of our own HRP/trehalose experiments are given. We compared the spectral diffusion behavior of a sample wherein the proteins were dissolved in a water/glycerol mixture with the respective one in a trehalose/water/glycerol solution. (For experimental details, see Ref. 7.) Shown are master plots, i.e., the data have already been scaled with their aging time dependence as explained above. As can clearly be seen in the inset of this figure, the aging behavior of the two samples is identical, and hence the exponent β does not depend on the trehalose content of the

solvent. In addition, the exponent $\alpha/2$ (which is given by the slope of a double-logarithmic plot) is also unaffected by the solvent. Thus the only effect of the trehalose is a *decrease* of the parameter τ_0, which is a correlation time for the stationary fluctuations of the proteins. In a trehalose environment these fluctuations are faster than in a trehalose-free environment by a factor of four, i.e.:

$$\tau_0(\text{trehalose}) \approx \frac{1}{4}\,\tau_0(\text{no trehalose}). \tag{2}$$

There is divided opinion the literature as to the influence of trehalose on protein dynamics: The authors of Refs. 10 and 11 concluded from their CO-rebinding experiments that trehalose prevents relaxation processes in proteins; in contrast, Sastry *et al.*[13] believe that trehalose leads to faster *internal* fluctuations of the proteins; this is, of course, in complete agreement with the results of our own experiments, which show clear indications of faster stationary fluctuations and of the existence of relaxational processes in the presence of trehalose. As a possible microscopic reason for this faster dynamics, Sastry *et al.* propose that internal water molecules are hindered by the trehalose from leaving the protein; these water molecules bind via hydrogen bonds to amino acid residues of the protein and thus prevent the formation of further protein-internal bonds, i.e., the protein is kept in a more flexible state, which manifests itself in faster spectral diffusion.

Cytochrome c in a dry trehalose film

As mentioned above, we investigated the influence of trehalose on protein dynamics in a second series of experiments, this time with cytochrome c-type proteins, which were embedded in a dry trehalose film. (For details, see Ref. 14.) The motivation for these experiments came from an interesting neutron-scattering experiment peformed on myoglobin in pure trehalose by Cordone *et al.*[15] On the short time scales that are probed in such an experiment, the myoglobin showed at all temperatures only harmonic motions as are found in a crystal. As a rule, in crystals no spectral diffusion is observed (except in some special cases[16]). Hence, it was interesting to test whether this is true on the much longer time scales of a spectral diffusion experiment.

Our measurements were performed in complete analogy to the ones described in the previous Section, i.e., the spectral diffusion (as a function of the aging and waiting times) in a cytochrome/trehalose sample was compared with that for the sample in the water/glycerol matrix. (In this case, the chromophore was the free-base analog of the native heme group.) The main results of the experiments are given in Fig. 5, where again master plots of the data are shown. Obviously in both cases spectral diffusion can be observed (so we do not find the crystallike behavior of the neutron-scattering experiments). Again, power-law time dependences are found; however, marginal changes in the exponents $\alpha/2$ and β for the different solvents can be observed. Nevertheless, the numerical values of the exponents are close to the ones found in HRP. Most important of all, the spectral diffusion in the trehalose sample is greatly enhanced, even to a much greater extent than in our HRP experiments. We stress that the inhomogeneous band in the trehalose sample is wider by a factor of about two than in the water/glycerol sample. The reason

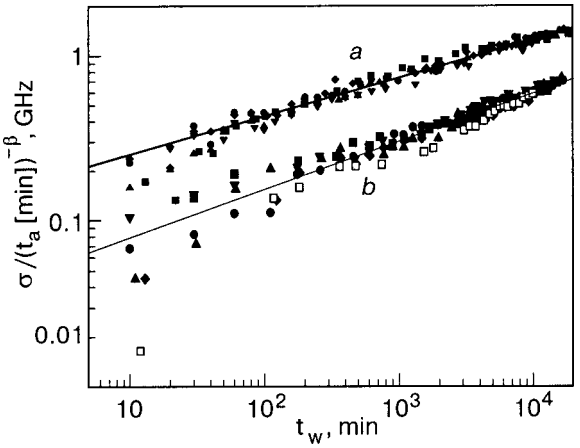

FIG. 5. Results of spectral diffusion experiments with (free-base mesoporphyrin) cytochrome c, solved in a dry trehalose film (a) and in a water/glycerol matrix (b).

for this is the rather high glass-transition temperature of the trehalose matrix (about 330 K) compared to about 200 K for the water/glycerol mixture. The inhomogeneous linewidth monitors the static disorder of the chromophore environments, i.e., the proteins. During cooling of the sample, this disorder is frozen in, when the solvent reaches its glass-transition temperature T_G, since below T_G large-amplitude motions of the amino acids are suppressed by the almost infinitely high viscosity of the solvent. Thus, in the trehalose sample the proteins are frozen in a much more ''disordered'' state, which manifests itself in the larger inhomogeneous linewidth.

Although being of a static nature the inhomogeneous linewidth σ_0 is important for an interpretation of dynamical properties as well, because spectral diffusion scales linearly with σ_0, as will be shown in detail in the next Section. However, the observed differences in the spectral diffusion cannot be explained only by the differences in σ_0. In addition, as an exact numerical analysis of the data shows, the correlation time τ_0 for the stationary fluctuations in the proteins must again be shorter by a factor four in the trehalose sample. Thus this experiment is in complete agreement with our measurements on HRP: the internal fluctuations of a protein in a trehalose environment are *faster*.

THEORETICAL FRAMEWORK: THE DIFFUSION MODEL

Inhomogeneous line broadening

It is the purpose of spectral diffusion experiments to gain insight into the structural processes that take place in a protein. To do so, one needs to know how structural rearrangements are connected with the frequency fluctuations of the chromophore. This can be achieved by a simple model:[7] we consider a chromophore inside a protein, which is separated from the various amino acid residues by distances R_i. The interaction with them gives rise to a frequency shift, which is simply the sum over the contributions of all the residues:

$$\nu = \sum_i c R_i^{-n}. \tag{3}$$

(For a van der Waals interaction, for example, $n=6$.) However, the proteins in an ensemble are not all in the same conformational substate, and the positions of the amino acids are therefore undetermined by small amounts x_i. Because of this, the absorption line of each protein in the ensemble is shifted by a small amount $\delta\nu$, which is given by

$$\nu+\delta\nu=\sum_i c(R_i+x_i)^{-n}\approx\sum_i cR_i^{-n} - nc\sum_i x_iR_i^{-(n+1)}. \quad (4)$$

The (static) distribution of the $\delta\nu$ in an ensemble of proteins is the reason for the inhomogeneous broadening observed in experiments. The width τ_0 of the inhomogeneous band is therefore given by

$$\sigma_0^2=\langle\delta\nu^2\rangle=\langle\overline{x^2}\rangle\left[n^2c^2\sum_i R_i^{-2(n+1)}\right]. \quad (5)$$

Here $\langle ...\rangle$ indicates an average over the protein ensemble, whereas averaging over the different amino acids of one protein is denoted by a bar. Obviously, the inhomogeneous linewidth and the mean square displacement of the residues in the protein are proportional to each other. Interestingly, the proportionality factor (the bracket in the upper formula) can be determined experimentally. While σ_0 is easy to measure spectroscopically, the mean square displacement $\langle\overline{x^2}\rangle$ can be obtained from a x-ray diffraction experiment, which, of course, is done with an inhomogeneous ensemble of proteins, too. A typical value for the proportionality factor is about $100\,\mathrm{cm}^{-1}/\text{Å}$, i.e., the absorption frequency of the chromophore is shifted by about $100\,\mathrm{cm}^{-1}$, if all interacting amino acid residues in the protein are moved together over a distance of 1 Å, on average.

Anomalous diffusion in conformation space

As was stated above, in our model spectral diffusion is treated as a real diffusionlike process. Though it is known from single-molecule experiments that the frequency changes of a protein are discontinuous, the diffusion picture is still a very good approximation, because the length of the frequency jumps is very small compared to the inhomogeneous linewidth. The situation is therefore in complete analogy to a classical random walk with an (almost) infinitely small step length. It is well known that this problem can be treated very well by a diffusion equation, too. As a second important assumption in our modeling, the spectral diffusion kernel is approximated by a Gaussian function. Considering that the absorption frequency of a protein is modulated by the (more or less) independent movements of several amino acids, this Gaussian shape of the spectral diffusion kernel results from the central limit theorem and is a well-justified approximation, too.

With these two assumptions it is now possible to derive an analytical expression for the spectral diffusion kernel. It is a Gaussian with the time-dependent width

$$\sigma^2(t_w)=\sigma_0^2(1-C^2(t_w)). \quad (6)$$

where $\sigma(t_w)$ is the hole-broadening, which is measured in the experiments. Its time dependence is given by the frequency correlation function $C(t_w)$. A reasonable ansatz for this correlation function is a stretched exponential:

$$C(t_w)=\exp\left[-\left(\frac{t_w}{\tau}\right)^{\alpha}\right]. \quad (7)$$

Correlation functions of this type are usually found in systems with a hierarchy of degrees of freedom[17,18] and have been observed in various experiments with proteins. Since the correlation time τ is huge compared to experimental time scales (at least at a temperature of 4.2 K), it is possible to expand Eq. (7) to the lowest order in t_w/τ. From Eq. (6) we then get

$$\sigma(t_w)=\sqrt{2}\sigma_0\left(\frac{t_w}{\tau}\right)^{\alpha/2}, \quad (8)$$

which is just the power-law behavior that is found in our measurements.

By exactly the same arguments as in the previous Section it is now possible to connect $\sigma(t_w)$ with $\langle\overline{x^2}\rangle(t_w)$, i.e., with the structural movements of the protein. Again we find a proportionality between these variables with the same proportionality factor as in Eq. (5). This means that the conformational dynamics of low-temperature proteins is governed by anomalous diffusion. The value of the exponent $\alpha/2$ in this diffusion law (about 1/4) seems to be of a rather universal nature.

Burin *et al.*[19] have proposed a simple model to explain this value of $\alpha/2$. According to them the structural changes responsible for the spectral diffusion can be seen as a random walk along a one-dimensional statistical trajectory in the complicated conformation space of the proteins. The mean separation between the initial and final point of such an trajectory after N steps scales as $N^{1/2}$. Hence, if every step shifts the transition energy of the chromophore by a certain amount, but with a random sign, the number of noncorrelated frequency shifts scales as $N^{1/2}$, too. The total frequency change then scales as $N^{1/4}$, and since the number of steps is proportional to t_w, one has a simple explanation for the time dependence that is found in our experiments.

Until now we have not included aging effects in our model. However, this can be done in a rather straightforward fashion. If a system is nonstationary, its correlation functions depend not only on the time interval t_w between hole burning and hole reading but also on the time t_a: $C=C(t_a,t_w)$. Empirically, such a time dependence can be included in Eq. (8) by looking at the experimental results once more. Obviously in our measurements the exponent $\alpha/2$ does not depend on t_a. We were never able to detect time dependence of the inhomogeneous linewidth σ_0, either. So the only parameter of our model which could be influenced by t_a is the correlation time τ. To be in agreement with our measurements (see, for example, the inset in Fig. 4), τ must have an aging-time dependence of the form

$$\tau=\tau_0\left(\frac{t_a}{T}\right)^{2\beta/\alpha}. \quad (9)$$

Here T is a typical time constant for those processes which lead to an aging-time dependence of the spectral diffusion.

As we have said, these processes are the relaxational movements of the proteins towards their equilibrium state. Equation (9) can again be interpreted as a short-time expansion of a stretched exponential. Doing this, one finds that τ_0 is the correlation time of the system, when all relaxational processes have come to an end, so it describes the *equilibrium fluctuations* of the protein. Inserting Eq. (9) into Eq. (8), one finds finally

$$\sigma(t_a,t_w)=\sqrt{2}\sigma_0\left(\frac{t_a}{T}\right)^{-\beta}\left(\frac{t_w}{\tau_0}\right)^{\alpha/2}, \tag{10}$$

which is exactly the result that has been derived from the experimental data [see Eq. (1)].

It is now possible to extract some numerical values from our experiments. One variable of interest is the correlation time τ for the structural fluctuations of the proteins. If all aging effects are neglected, τ is included in the intercept of a double-logarithmic plot of our data [see Eq. (8)]. As a typical order of magnitude for τ one finds about 10^{17} s, which is a time span comparable to the age of the universe. This clearly demonstrates the nonergodicity of low-temperature proteins: in ''reasonable times'' they can never explore their complete configuration space or reach thermal equilibrium.

One can also estimate the length scales of the structural motions responsible for the observed spectral diffusion. A typical hole-broadening that is observed after a waiting time of about two weeks is in the range of 1 GHz. Since the proportionality factor between spectral and structural disorder is known [see. Eq. (5)], the respective length scale of the structural motions can be estimated to be of the order of 10^{-4} Å. Only the high resolution of the hole-burning spectroscopy allows for the observation of such small movements.

SUMMARY

We have demonstrated how hole-burning can be used to investigate protein dynamics. The main result of these experiments is a power-law behavior for spectral diffusion, which differs completely from the time dependences found in low-temperature glasses. In addition, the exponent of this power law (which has a value of about $\alpha/2=1/4$ seems to be of a rather universal nature).

A theoretical treatment of our results is possible in the framework of the so-called diffusion model, in which diffusive movements of the amino acid residues in the protein are held to be responsible for the observed spectral diffusion. It was suggested in Ref. 19 that this diffusion takes place on one-dimensional random trajectories in the conformation space of the proteins. In this case a time dependence like the one found in our experiments is expected.

By analyzing our data according to the diffusion model it is possible to estimate a correlation time for the structural fluctuations of the proteins. This time is incredibly long, showing clearly the nonergodicity of low-temperature proteins. In addition, typical length scales for the movements of low-temperature proteins can be determined.

Besides this global behavior the influence of different solvents on protein dynamics was tested experimentally. We compared the spectral diffusion of proteins embedded in a trehalose matrix with that obtained in the case of a water/glycerol environment. Spectral diffusion, i.e., the internal motion of the proteins, was greatly enhanced by the trehalose. As a possible explanation for this behavior the presence of internal water molecules in the trehalose-solved proteins was suggested.

Though not shown here in detail, it should be mentioned that the influence of deuteration on protein dynamics has also been investigated by our group.[20,21] The results of those experiments fit perfectly in our diffusion model presented in the preceding Sections.

Support from the DFG (SFB 533, B5) and from the Fonds der Chemischen Industrie is gratefully acknowledged.

*E-mail: J.Friedrich@lrz.tu-muenchen.de

[1] H. Frauenfelder, G. A. Petsko, and D. Tsernoglou, Nature (London) **280**, 558 (1979).
[2] H. Frauenfelder, F. Parak, and R. D. Young, Annu. Rev. Biophys. Biophys. Chem. **17**, 451 (1988).
[3] S. Völker, Annu. Rev. Phys. Chem. **40**, 499 (1989).
[4] J. Schlichter, J. Friedrich, L. Herenyi, and J. Fidy, J. Chem. Phys. **112**, 3045 (2000).
[5] K. Fritsch, J. Friedrich, and B. M. Kharlamov, J. Chem. Phys. **105**, 1798 (1996).
[6] J. Schlichter and J. Friedrich, J. Chem. Phys. **114**, 8718 (2001).
[7] J. Schlichter, J. Friedrich, L. Herenyi, and J. Fidy, Biophys. J. **80**, 2011 (2001).
[8] J. Crowe, J. Carpenter, and L. Crowe, Annu. Rev. Physiol. **60**, 73 (1998).
[9] T. Chen, A. Fowler, and M. Toner, Cryobiol. **40**, 277 (2000).
[10] S. Hagen, J. Hofrichter, and W. Eaton, Science **269**, 959 (1995).
[11] S. Hagen, J. Hofrichter, and W. Eaton, J. Phys. C **100**, 12008 (1996).
[12] D. Gottfried, E. Peterson, A. Sheikh, J. Wang, M. Yang, and J. Friedman, J. Phys. C **100**, 12034 (1996).
[13] G. Sastry and N. Agmon, Biochemistry **36**, 7097 (1997).
[14] V. V. Ponkratov, J. Friedrich, and J. M. Vanderkooi, J. Chem. Phys. **117**, 4594 (2002).
[15] L. Cordone, M. Ferrand, E. Vitrano, and G. Zaccai, Biophys. J. **76**, 1043 (1999).
[16] A. Suisalu, V. Zazubovich, J. Kikas, J. Friebel, and J. Friedrich, Europhys. Lett. **44**, 613 (1998).
[17] Y. A. Berlin and A. L. Burin, Chem. Phys. Lett. **267**, 234 (1997).
[18] R. G. Palmer, D. L. Stein, E. Abrahams, and P. W. Anderson, Phys. Rev. Lett. **53**, 958 (1984).
[19] A. L. Burin, Yu. A. Berlin, A. Z. Patashinskii, M. A. Ratner, and J. Friedrich, Physica B **316**, 321 (2002).
[20] J. Schlichter, J. Friedrich, M. Parbel, and H. Scheer, J. Chem. Phys. **114**, 9638 (2001).
[21] J. Schlichter, J. Friedrich, L. Herenyi, and J. Fidy, J. Phys. C **106**, 3510 (2002).

This article was published in English in the original Russian journal. Reproduced here with stylistic changes by AIP.

Molecular probing of low-temperature incommensurate phases

J. Kikas*

Institute of Materials Science, University of Tartu, 4 Tähe, Tartu 51010, Estonia

A. Suisalu, A. Laisaar, and An. Kuznetsov

Institute of Physics, University of Tartu, 142 Riia, Tartu 51014, Estonia
Fiz. Nizk. Temp. **29**, 1057–1060 (September–October 2003)

Two-dimensional (2D) excitation–emission spectra of biphenyl doped with free-base chlorin are measured at 5 K under various pressures up to 350 MPa. Besides the features related to zero-phonon lines and their phonon sidebands, a broad spectral band amounting to 80% of the total intensity at 5 K is revealed in the 2D spectra. The inhomogeneous distribution function obtained shows drastic changes with increasing pressure—the triplet structure observable at normal pressure in the incommensurate phase ICIII of biphenyl converges to a singlet in the high-pressure commensurate phase CI. These observations are assumed to reflect a relaxation specific to incommensurate phases after optical excitation of the probe molecules and their interaction with the incommensurate modulation wave. © *2003 American Institute of Physics.*
[DOI: 10.1063/1.1614197]

INTRODUCTION

Optical spectra of impurities in solid matrices[1] contain, in principle, rich information on both static structure and dynamical processes in solids. Even for strongly disordered materials the methods of site-selection spectroscopy, such as selective excitation[2,3] and spectral hole burning,[4,5] have revealed a lot of details otherwise obscured by the inhomogeneous broadening of conventional spectra. In this paper we make use of an advanced version of site-selection spectroscopy, namely two-dimensional (2D) excitation–emission spectroscopy (also called total luminescence spectroscopy[6]), in order to study local structure and dynamics in doped incommensurate solids. Incommensurate systems[7] are a specific and interesting class of solids showing a long-range order but lacking the translational lattice periodicity of crystals. In most systems exhibiting incommensurate behavior the incommensurate phase exists in quite a narrow temperature interval between an ordinary higher-temperature commensurate phase and a low-temperature lock-in phase, which is again commensurate but generally has a larger unit cell. Incommensurate biphenyl is one of a few systems where such lock-in transition to a low-temperature commensurate structure has not been observed down to the lowest temperatures studied (60 mK,[8] 70 mK[9]). This makes it a suitable object of investigation using the methods of optical site-selection spectroscopy. (Note that some of the recent results on the temperature broadening and thermal cycling of spectral holes in doped biphenyl are presented in our papers.[8,10]) The phases of biphenyl and transitions between them have been extensively examined (see, e.g., Ref. 11 and references therein). In the cooling of a biphenyl sample it passes from the ordinary high-temperature crystalline phase CI to an incommensurate phase ICII at 40 K followed by transition to another incommensurate phase ICIII at 17 K, the spatially modulated property being the twist angle between the planes of two phenyl rings. Under pressure at liquid-helium temperature, the phase transitions ICIII→ICII and ICII→CI occur at ~20 MPa and ~180 MPa, respectively.[12] The metastability of the phase ICIII has been proposed as a possible reason for absence of the lock-in transition to a crystalline ground state at low temperatures (''incommensurate glass'' [13]).

EXPERIMENTAL

An organic dye, free-base chlorin (7,8-dihydroporphin, $H_2-C_{20}N_4H_{14}$), was used as a dopant in this study. A polycrystalline sample was obtained by slowly cooling the molten biphenyl down to room temperature. Two-dimensional excitation–emission spectra were measured on a spectrometer consisting of a CR-490 tunable linear dye laser (Coherent Inc.) and a DFS-24 double grating monochromator (LOMO) equipped with a DU420-BU CCD-camera (Andor). A small liquid-helium cryostat was used for measurements at 1 atm. For high-pressure measurements a system consisting of a 1.5-GPa helium gas compressor, optical high-pressure cell with sapphire windows and a large temperature-controlled liquid-helium cryostat was used.

RESULTS AND DISCUSSION

The two-dimensional excitation–emission spectrum (depicted as a plot of isointensity lines for emission at a constant excitation intensity) for chlorin-doped biphenyl in the incommensurate phase ICIII at 5 K and ambient pressure is shown in Fig. 1*a*. Here the excitation was scanned in 0.02-nm steps within the $(0-0)+863.4\ \mathrm{cm}^{-1}$ vibronic transition of the probe molecule while the fluorescence emission was recorded in the 0–0 region, 0–0 denoting the resonant purely electronic transition $S_0 \leftrightarrow S_1$. The high-intensity narrow ''diagonal'' features in the dashed corridor correspond to the three zero-phonon lines. By plotting the maximum emission intensity inside the corridor at each fixed excitation frequency, one obtains the static inhomogeneous distribution function (IDF) of probe transition frequencies as shown in

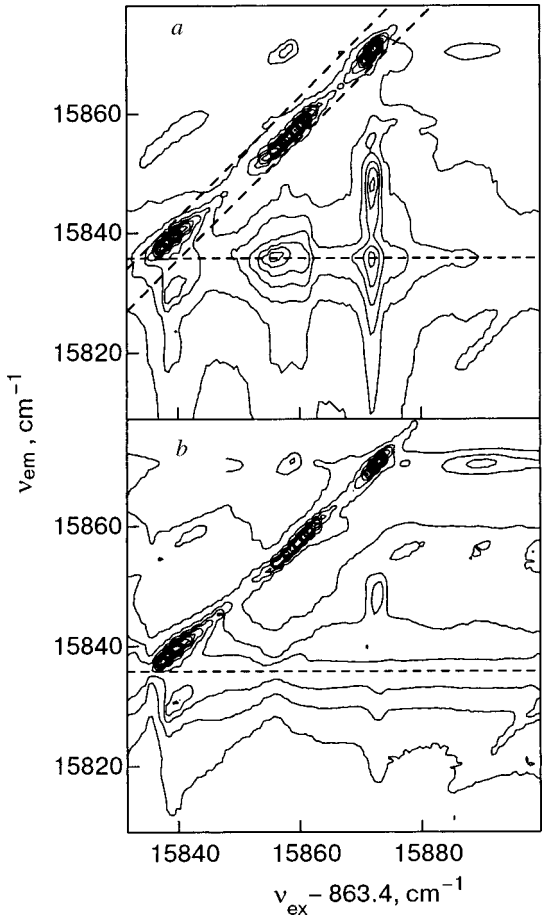

FIG. 1. Two-dimensional excitation–emission spectrum of chlorin-doped biphenyl at 5 K under normal pressure (incommensurate phase ICIII) (*a*). The same but normalized to the intensity values along the horizontal dashed line in Fig. 1*a* (*b*). The dashed diagonal corridor represents the area used to determine the inhomogeneous distribution function depicted in Fig. 2*b*.

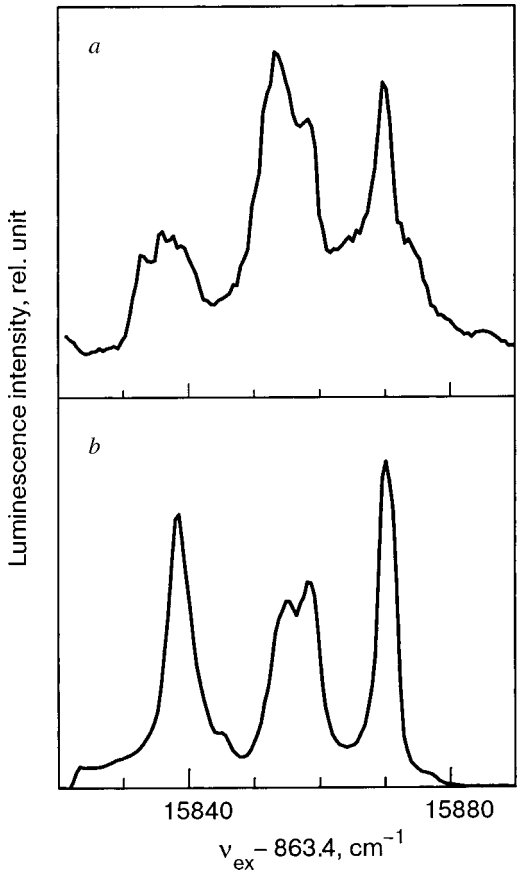

FIG. 2. Selective excitation spectrum of chlorin-doped biphenyl obtained from Fig. 1*a* by making a cut of the 2D spectrum along the horizontal dashed line at 15836 cm^{-1} (*a*). The inhomogeneous distribution function obtained by making a diagonal cut of the 2D spectrum in Fig. 1*a* (*b*).

Fig. 2*b*. The shape of the IDF reflects the distribution of static local environments around probe molecules. The triplet shape of the IDF for chlorin in the ICIII phase of biphenyl can be interpreted as arising from the interaction of a probe molecule with the static incommensurate modulation wave. While the outermost lines in the triplet can be attributed to edge singularities characteristic for such a situation,[7] the middle peak may arise from pinning of the modulation wave by probe molecules. Such a viewpoint is further supported by the results of our high-pressure measurements (Fig. 3), where one observes convergence of the low-pressure triplet to a high-pressure singlet at pressures above 180 MPa, i.e., in the crystalline phase CI (for more detailed discussion of pressure effects; see Ref. 12). This proves that we have only one substitutional site for dopant molecules in the phase CI.

A surprising and remarkable feature in Fig. 1*a*, however, is the existence of a broad 2D band located around the horizontal dashed line, which makes up more than 80% of the total intensity. As can be seen from Fig. 1*a*, the position of the maximum of the broad-band emission (as indicated by the dashed line at 15836 cm^{-1}) does not depend on the excitation frequency. Note also that this maximum is redshifted from the red peak of the IDF (see the vertical dashed line in Fig. 4), and therefore the broad band cannot be the phonon sideband of the red peak in the IDF. The excitation spectrum of the broad 2D band, recorded selectively at its emission maximum 15836 cm^{-1} (Fig. 2*a*), repeats the triplet shape of the IDF (Fig. 2*b*) but is not so clear-cut, consisting of markedly wider bands. For example, while the intensity of zero-phonon lines at 15875 cm^{-1} is about 15 times lower as compared to the peak value at 15870 cm^{-1} (see Fig. 2*b*), respective intensity reduction in the excitation spectrum of the broad 2D band is barely twofold or so (Fig. 2*a*). As we have said, the peak position of the broad-band emission is independent of the excitation frequency; however, its spectral width exhibits some frequency dependence. This can be seen from Fig. 1*b*, where the isointensity plot is given for the excitation-dependent emission spectra, normalized to the peak value of the nonresonant broad 2D band (along the dashed horizontal line in Fig. 1*a*). This band in fluorescence emission is narrowest at about 15855 cm^{-1} and broadens somewhat with increasing excitation frequency (see Fig. 1*b*). Its low-energy slope, however, does not change much at frequencies $\nu_{ex} - 863.4\ \text{cm}^{-1} > 15865\ \text{cm}^{-1}$, as follows from the parallel run of the isointensity lines. Only at the position of the blue peak in the IDF is some local structure observable.

In order to incorporate the above observations into the ''traditional'' picture of low-temperature inhomogeneously broadened impurity spectra, one has to make a number of

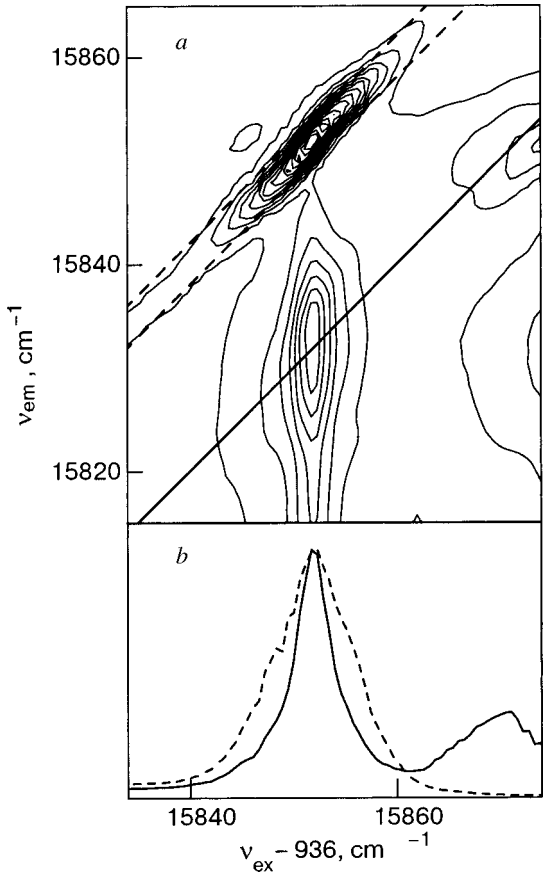

FIG. 3. Two-dimensional excitation–emission spectrum of chlorin-doped biphenyl at 5 K under pressure of 220 MPa (crystalline phase CI) (*a*). The respective inhomogeneous distribution function (dashed curve) and a diagonal cut (solid curve) along the solid line in Fig. 3*a* (*b*).

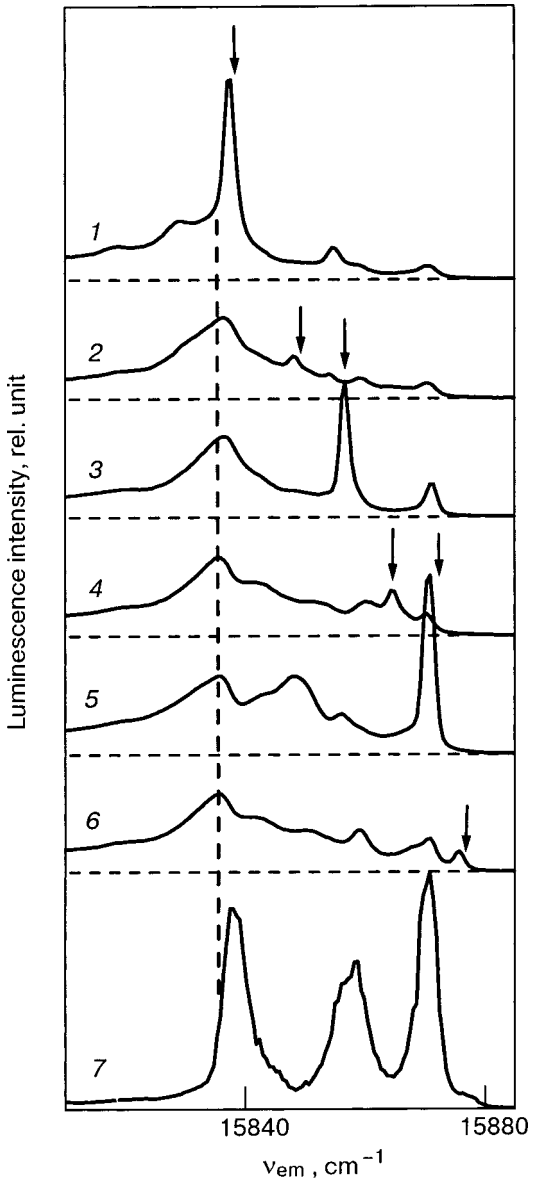

FIG. 4. Selective excitation spectra (*1*–*6*) of chlorin-doped biphenyl obtained from Fig. 1*a* by making horizontal cuts of 2D spectrum at various excitation frequencies denoted by arrows; the inhomogeneous distribution function (*7*) obtained from a diagonal cut of the 2D spectrum taken at normal pressure. The dashed vertical line indicates the broad 2D band peak position which is independent of the excitation frequency.

quite unusual assumptions, such as strong quadratic electron–phonon coupling (strong deviation from the excitation–emission mirror symmetry), strong dependence of this coupling on the electronic transition energy, etc. We recall that the chlorin probe is known to have very large Debye–Waller factors (intensive zero-phonon lines with rather weak phonon sidebands) in a number of crystalline and glassy matrices. Therefore it may be more productive to seek some novel mechanisms of relaxation which are specific to incommensurate phases. We have shown earlier[10] that in chlorin-doped biphenyl there exists an efficient mechanism of nonphotochemical spectral hole burning attributed to photo-induced depinning–repinning of the incommensurate modulation wave. Such a phase shift of the modulation wave, provided it can take place not only in the excited state but also in the course of an electronic transition, may present a possible channel for the formation of the broad spectral feature observed.

Due to softness of the torsional motion of two phenyl rings in biphenyl, even the dynamics in the high-pressure crystalline phase may still be nontrivial. Thus a simple interpretation of the nonresonant sideband as a phonon sideband of the resonant singlet, both seen in Fig. 3*a*, is rather disputable because the IDF of the resonant singlet is much broader than the diagonal cut (not to mention the narrower horizontal cut) of the nonresonant sideband in Fig. 3*b*.

CONCLUSIONS

We have demonstrated that optical spectra of probe molecules in incommensurate and commensurate phases of biphenyl exhibit uncommon features incompatible with simple models of impurity spectra. Selective hole-burning experiments, including those at elevated pressures, may shed further light on these interesting problems.

Earlier collaboration with J. Friedrich and his group has initiated these studies. Support from the Estonian Science Foundation under Grants Nos. 5544 and 3873 is greatly appreciated.

*E-mail: jaakk@physic.ut.ee

[1] K. K. Rebane, *Impurity Spectra of Solids; Elementary Theory of Vibrational Structure*, Plenum Press, New York–London (1970).
[2] A. Szabo, Phys. Rev. Lett. **25**, 924 (1970).
[3] R. I. Personov, E. I. Al'shitz, and L. A. Bykovskaya, JETP Lett. **15**, 431 (1972).
[4] A. A. Gorokhovskii, R. K. Kaarli, and L. A. Rebane, JETP Lett. **20**, 216 (1974).
[5] B. M. Kharlamov, R. I. Personov, and L. A. Bykovskaya, Opt. Commun. **12**, 191 (1974).
[6] K. Palewska, E. C. Meister, and U. P. Wild, J. Lumin. **50**, 47 (1991).
[7] R. Blinc, Phys. Rep. **79**, 331 (1981).
[8] A. Suisalu, V. Zazubovich, J. Kikas, J. Friebel, and J. Friedrich, Europhys. Lett. **44**, 613 (1998).
[9] J. Etrillard, J. E. Lasjaunias, B. Toudic, and H. Cailleau, Europhys. Lett. **38**, 347 (1997).
[10] V. Zazubovich, A. Suisalu, and J. Kikas, Phys. Rev. B **64**, 104203 (2001).
[11] J. Etrillard, B. Toudic, H. Cailleau, and G. Coddens, Phys. Rev. B **51**, 8753 (1995).
[12] V. Zazubovich, A. Suisalu, K. Leiger, A. Laisaar, An. Kuznetsov, and J. Kikas, Chem. Phys. **288**, 57 (2003).
[13] S.-B. Liu and M. S. Conradi, Phys. Rev. Lett. **54**, 1287 (1985).

This article was published in English in the original Russian journal. Reproduced here with stylistic changes by AIP.

Observation of crystallization of amorphous solid water under the conditions of secondary emission mass spectrometric experiments

M. V. Kosevich,* O. A. Boryak, V. S. Shelkovsky, and V. V. Orlov

B. Verkin Institute for Low Temperature Physics and Engineering of the National Academy of Sciences of Ukraine, 47 Lenin Ave., Kharkov 61103, Ukraine
Fiz. Nizk. Temp. **29**, 1061–1064 (September–October 2003)

A phenomenon of termination of sputtering of protonated water clusters $(H_2O)_nH^+$ in low-temperature secondary emission mass spectrometric studies of solid water is observed in the temperature range of crystallization of amorphous solid water (ASW). In this range the mass spectra contained only H_3O^+, $H_2O^{+\bullet}$, and OH^+ ions. The following explanation of the phenomenon revealed is suggested: the heat supplied to the ASW sample by the bombarding particles is spent on initiation of an amorphous–crystalline transition within the condensed sample but not for the transfer of the sample matter to the gas phase. At the same time heat released on crystallization causes a local rise in temperature of the crystallizing sample surface, which enhances the rate of sublimation of ice. The resulting increased concentration of subliming water molecules over the sample surface is reflected in a growth of the abundance of $H_2O^{+\bullet}$ molecular-ion radical, produced by gas-phase ionization mechanism. The appearance of a set of low-mass peaks in the course of crystallization observed for some types of ASW samples is explained by the release of gases trapped in the ASW film during its growth. © *2003 American Institute of Physics.* [DOI: 10.1063/1.1614198]

1. INTRODUCTION

Investigations of solid water by means of secondary emission mass spectrometry[1–14] have used either amorphous solid water (ASW) obtained by vapor deposition on some surface cooled below the temperature of the glass transition of water $T_g = 136$ K[15–17] or crystalline ice. Under bombardment by energetic particles—by neutral atoms of Ar^0 or Xe^0 in a fast atom bombardment (FAB) mode, or ions of Cs^+ or Ar^+ in secondary ion mass spectrometry (SIMS), with the energy varied in the 5–30 keV range—sets of protonated water clusters $(H_2O)_nH^+$ with n up to 30–50 are sputtered both from ASW and crystalline ice. The distribution of clusters in the secondary emission mass spectra of these two forms of water is qualitatively very similar, with a slight quantitative difference in the abundances of some clusters. The measurements have usually been conducted at some constant temperature. Secondary emission mass spectrometric experiments have not, however, been performed on gradual variation of the sample temperature in the range around the temperature of crystallization of ASW, which, according to the data of Ref. 15, can start at 140–160 K and proceed in some temperature range up to 166 K.

It was revealed in our previous works on LT FAB and SIMS of a number of organic and inorganic compounds that phase transitions in the sample matter are reflected in characteristic changes in the cluster patterns of the secondary emission mass spectra.[13,14,18–20]

The aim of the present work was to obtain secondary emission mass spectra of vapor-deposited solid water in the temperature range of crystallization of ASW with the expectation of observing and investigating changes in the mass spectral pattern resulting from this type of transition.

2. LOW-TEMPERATURE SECONDARY EMISSION MASS SPECTROMETRIC EXPERIMENTS

Mass spectrometric experiments were performed using the magnetic sector mass spectrometer MI-1201E (Sumy, Ukraine) equipped with primary FAB ion source for generating a bombarding beam of argon atoms; the energy of the primary ion beam before neutralization was 4–5 keV. The secondary ion source contained a cryogenic unit described in detail elsewhere.[12] The cryogenic unit, cooled by liquid nitrogen, had a recess for a removable copper sample holder which could be cooled either externally or directly in the ion source. A thermistor inserted into the unit served for temperature measurements. The cryogenic unit was surrounded by a toroidal cryogenic shield cooled by liquid nitrogen, which provided efficient adsorption of residual gases inside the ion source. The pressure in the FAB secondary ion source ahead of the bombarding argon inlet was about 10^{-6} Pa.

Polycrystalline ice samples were produced by freezing of deionized water in vapors of liquid nitrogen. Layers of ASW were produced in two ways. Water vapor was deposited on a substrate pre-cooled to liquid-nitrogen temperature from the residual gases in the evacuation chamber of the direct sample inlet system. During the deposition the temperature of the sample holder did not rise above the recommended one for the procedure, 140 K,[15] which was controlled by direct temperature measurement after the insertion of the sample holder to the cryogenic block. Alternatively, water vapor was deposited on the cold sample holder directly in the secondary ion source. The source of the low-pressure flux of water molecules was a crystalline hydrate $CuSO_4 \cdot 5H_2O$ kept in a heated ceramic ampoule near the sample holder. Substrates for ASW deposition were the bare copper sample holder, frozen crystalline H_2O and D_2O, and frozen solutions of inorganic salts.

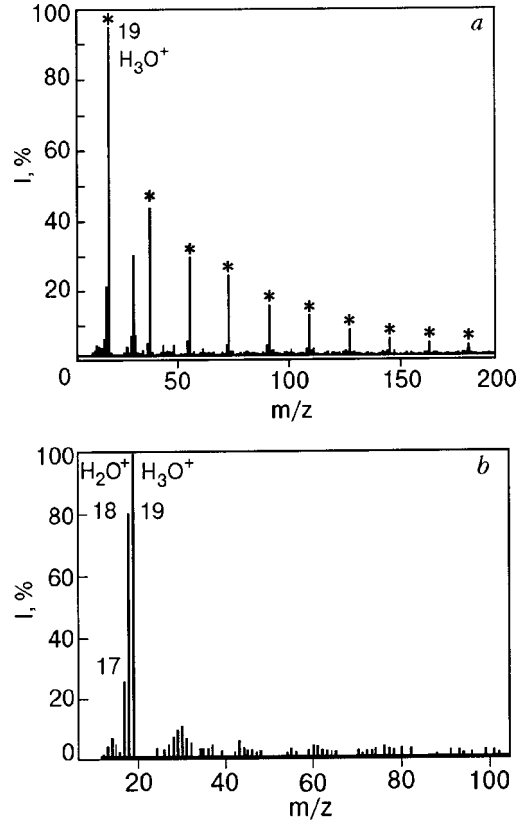

FIG. 1. FAB mass spectra of solid water: spectral pattern of ASW characteristic in the temperature range 77–110 K (*a*); peaks corresponding to protonated water clusters in the set $(H_2O)_nH^+$ ($n=1-10$) are marked by *; (the unmarked peak at m/z 30 corresponds to NO adsorbed from the residual gas at $T<110$ K); mass spectrum recorded at ~150 K (*b*).

3. RESULTS AND DISCUSSION

In the FAB mass spectra of layers of ASW deposited by various methods on various substrates, as described in the Experimental Section, a set of protonated water clusters $(H_2O)_nH^+$ ($n=1-10$) was present (Fig. 1*a*). The spectral pattern, that is the types of clusters and distribution of their abundances, did not undergo any substantial changes on temperature variation in the 77–140 K temperature range. On warming the sample up to 140–150 K a rather unexpected and pronounced effect was observed: all cluster ions of water $(H_2O)_nH^+$ except for those with $n=1$ (that is H_3O^+) decreased in abundance rather rapidly (during one spectrum scan) and disappeared from the spectrum. At the same time the absolute intensity of a peak at m/z 18 which can be attributed to water radical cation $H_2O^{+\bullet}$ increased by one to two orders of magnitude (Fig. 1*b*). The intensity of a peak of the ion at m/z 17, which is known to be an OH^+ fragment of $H_2O^{+\bullet}$, increased similarly to that of its parent ion. Thus the FAB mass spectrum contained only three intense peaks: H_3O^+, $H_2O^{+\bullet}$, and OH^+ (Fig. 1*b*). For some types of samples at somewhat higher temperatures of about 150–160 K a noisy spectrum with a peak at every mass started to interfere with the above three peaks in the low-mass range. It lasted for some time and then vanished, giving way to a recovered normal spectrum of ice containing a $(H_2O)_nH^+$ cluster set at temperatures of about 160–170K. The latter, in turn, after completion of rather rapid sublimation of the crystallized ice layer on further warming was replaced by the spectrum characteristic of the underlayer (substrate). Once they had happened on warming, the transformations described were not repeated on subsequent cyclic cooling–warming of the ice formed. The reported changes of mass spectra were qualitatively reproducible with slight quantitative variations in several tens of independent experiments.

The most remarkable feature of these changes is a temporary termination of production of all the ions except H_3O^+ and $H_2O^{+\bullet}$ when a solid water sample is still definitely present on the sample holder. Even in the case of complete exhaustion of the water layer the spectra of the exposed underlayer should appear, but they did not.

To explain the phenomena observed, the answers to at least two questions are to be searched for: what are the reasons for termination of the production of $(H_2O)_nH^+$ clusters with $n>1$ and continuation of the production of the H_3O^+ ion, and what is the origin of the abundant $H_2O^{+\bullet}$ ion. First of all, it is obvious that the temperature range of anomalous changes in the mass spectra is very close to the temperature range of spontaneous crystallization of ASW, which, according to the results of the relevant studies,[15] can start on slow warming at 140–160 K and be completed at 166 K. The action of some external factors, including energetic particle impact, initiates the so-called explosive crystallization, which can start at 15 K lower than the spontaneous crystallization.[15] This allows us to suggest that any effect observed in this temperature range may be connected with an amorphous–crystalline transition in the sample.

It is generally recognized that excitation caused by a bombarding particle in a condensed sample is ultimately converted to thermal energy.[21] It is known also that all heat deposited in a system in the phase-transition state is consumed on carrying out the transition to its completion. In this light, it may be suggested that in the present experiments practically all the energy supplied by a bombarding particle to an ASW sample at 140–166 K is spent on performing the amorphous–crystalline transition. In the zone heated by a bombarding particle, water molecules in the amorphous layer acquire some degrees of freedom which allow them to rearrange into a regular crystalline structure. Thus heat is spent on initiation and support of the crystallization process within the condensed sample but not for evaporation (sublimation) of molecules to the gas phase. This can explain the absence of ''sputtering'' of sample matter to the gas phase (the latter usually being revealed by registering charged water clusters). The effects described are valid both for spontaneous and particle-initiated scenarios of crystallization. The low flux of bombarding particles used in FAB experiments provides incidence of particles to the surface areas undamaged by preceding impacts for at least 5 minutes, which means that the probability of a new particle impact to the zone crystallized after a previous particle impact (from which cluster sputtering becomes possible) is rather low in the time frame of the experiment.

Concerning the origin of H_3O^+ ions under the above-described conditions, it is known that the very first event on contact of a bombarding particle with the condensed sample surface can consist in direct mechanical knock-out, by direct momentum transfer or by recoil, atoms of one or a few surface atoms or molecules, either in the neutral or charged

forms.[22–24] The H_3O^+ ion can be produced by this surface mechanism, which is independent of further events caused by the bombarding particle in the bulk sample.[25] The difference in the origin of the H_3O^+ ion and $(H_2O)_nH^+$ clusters with $n>1$ is supported by the results of early experiments on the determination of the kinetic energy of the sputtered species, which appeared to be higher for H_3O^+ in comparison with larger water cluster ions.[2]

This mechanism, however, could not be responsible for the appearance of the abundant molecular radical ion $H_2O^{+\bullet}$, since its abundance in ordinary secondary ion emission mass spectra of both ASW and crystalline ice is relatively small. The appearance of $H_2O^{+\bullet}$ is usually conditioned by an increase om the concentration of water in the gas phase over the sample surface,[7] since it has been proved that the $H_2O^{+\bullet}$ ion is formed by the so-called gas-phase FAB mechanism.[7,26] An increase of the absolute and relative intensity of the peak corresponding to $H_2O^{+\bullet}$ in the FAB mass spectra of ice has been observed earlier[13,14,25] under conditions of high-rate sublimation of ice samples at a temperature of about 200–220 K,[27] preceding complete rapid exhaustion of the sample. This suggests that in the experiments under discussion (Fig. 1*b*) the concentration of water molecules in the gas phase becomes relatively high apparently for the same reason, that is, due to active sublimation. Although the temperature of the sample holder and bulk sample is kept rather low (140–160 K), the temperature of the sample surface can become noticeably higher due to the known thermal effect characteristic of ASW crystallization. It was found earlier that the heat released on rapid crystallization can cause a rise in the temperature of the sample surface in the crystallizing region of about 60–80 K.[15] Assuming that the starting temperature of the sample is above 140 K, its increase by 60–80 K will raise the local temperature to a value of 200–220 K, at which the rate of sublimation is high and sufficient for recording abundant $H_2O^{+\bullet}$ ions.

As to the temporary appearance of a noisy spectrum, this effect can be explained by ionization of gaseous species trapped within the ASW on its deposition and released on its structural rearrangement during crystallization.[17,28] Some data on ASW deposition show that the amount of gases trapped by ASW can exceed by a factor of three the weight of the ASW sample.[29] The intense release of gases at a certain stage of ASW crystallization has been named the ''molecular volcano'' effect.[30]

Thus the chain of events leading to the changes in the spectra presented in Fig. 1 can be summarized as follows. In the temperature range of ASW crystallization the energy deposited by a bombarding particle contributes to carrying out the crystallization. This alternative channel of heat dissipation prevents transfer of the sample matter to the gas phase on the interaction of the bombarding particle with the sample. Only relatively simple H_3O^+ species are released by direct sputtering from the surface. Upon both spontaneous and initiated crystallization the latent heat of crystallization is released and the temperature of the sample surface rises to values at which the sublimation rate is rather high and provides a concentration of water vapor over the sample surface sufficient for abundant production of $H_2O^{+\bullet}$ by gas-phase FAB ionization. The effects described should be taken into account in the models of the interaction of accelerated particles with amorphous ices in outer space.[11]

4. CONCLUSIONS

FAB mass spectrometric studies of solid water in the temperature range of ASW crystallization have revealed a phenomenon wherein the sputtering of $(H_2O)_nH^+$ clusters, which are always the main constituents of mass spectra of both amorphous solid and crystalline water, terminates. The spectra contained only H_3O^+, $H_2O^{+\bullet}$, and OH^+ ions. An explanation of the observed phenomenon is suggested: the heat supplied to the sample by the bombarding particles is spent on carrying out the amorphous–crystalline transition but not on the transfer of the sample matter to the gas phase. At the same time, heat released on crystallization causes a rise of the sample surface temperature, which enhances ice sublimation. The increased concentration of subliming water over the sample surface is reflected in an increase of the abundance of the $H_2O^{+\bullet}$ molecular-ion radical, produced by gas-phase ionization.

This work was partially supported by the grant INTAS-99-00478.

*E-mail: mvkosevich@ilt.kharkov.ua

[1] G. D. Tantsyrev and E. N. Nikolaev, JETP Lett. **13**, 337 (1971).
[2] G. D. Tantsyrev and E. N. Nikolaev, Dokl. Akad. Nauk **206**, 151 (1972) (in Russian).
[3] E. N. Nikolaev and G. D. Tantsyrev, Zh. Tekh. Fiz. **45**, 400 (1975), [Sov. Phys. Tech. Phys. **20**, 249 (1975)].
[4] E. N. Nikolaev, G. D. Tantsyrev, and V. A. Saraev, Zh. Tekh. Fiz. **46**, 2184 (1976) [Sov. Phys. Tech. Phys. **21**, 1282 (1976)].
[5] E. N. Nikolaev and G. D. Tantsyrev, Khim. Vys. Energ. **12**, 301 (1978) (in Russian).
[6] G. M. Lancaster, F. Honda, Y. Fukuda, and J. W. Rabalais, J. Acoust. Soc. Am. **101**, 1951 (1979).
[7] R. N. Katz, T. Chaudhary, and F. H. Field, Int. J. Mass Spectrom. Ion Processes **78**, 85 (1987).
[8] K. Heckles, R. A. W. Johnstone, and A. H. Wilby, Tetrahedron Lett. **28**, 103 (1987).
[9] T. F. Magnera, D. E. David, and J. Michl, Chem. Phys. Lett. **182**, 363 (1991).
[10] J. Sunner, M. G. Ikonomou, and P. Kebarle, Int. J. Mass Spectrom. Ion Processes **82**, 221 (1988).
[11] W. L. Brown, L. J. Lanzerotti, and R. E. Johnson, Science **218**, 525 (1982).
[12] O. A. Boryak, M. V. Kosevich, and V. S. Shelkovskii, Prib. Tekh. Eksp. **6**, 935 (1993) (in Russian).
[13] O. A. Boryak, M. V. Kosevich, V. S. Shelkovsky, and Yu. P. Blagoy, Rapid Commun. Mass Spectrom. **9**, 978 (1995).
[14] O. A. Boryak, I. O. Stepanov, M. V. Kosevich, V. S. Shelkovsky, V. V. Orlov, and Yu. P. Blagoy, Eur. Mass Spectrom. **2**, 329 (1996).
[15] V. P. Scripov and V. P. Koverda, *Spontaneous Crystallization of Supercooled Liquids*, Nauka, Moscow (1984).
[16] *NIST Chemistry WebBook, NIST Standard Reference, Database*, P. J. Linstrom and W. G. Mallard (eds.), No. 69, July (2001), National Institute of Standards and Technology, Gaithersburg MD, 20899 (http://webbook.nist.gov/chemistry).
[17] V. F. Petrenko and R. W. Whitworth, *Physics of Ice*, Oxford University Press, New York (1999).
[18] M. V. Kosevich, Eur. Mass Spectrom. **3**, 320 (1997).
[19] M. V. Kosevich, G. Czira, O. A. Boryak, V. S. Shelkovsky, and K. Vekey, J. Mass Spectrom. **33**, 843 (1998).
[20] M. V. Kosevich, Eur. Mass Spectrom. **4**, 251 (1998).
[21] R. G. Cooks and K. L. Bush, Int. J. Mass Spectrom. Ion Phys. **53**, 111 (1983).
[22] J. Michl, Int. J. Mass Spectrom. Ion Phys. **53**, 255 (1983).
[23] Benninghoven, F. G. Rudenauer, and H. W. Werner, *Secondary Ion Mass*

Spectrometry: Basic Concepts, Instrumental Aspects, Applications and Trends, Wiley, New York (1987).
[24] V. Cherepin, Secondary Ion Mass Spectroscopy of Solid Surfaces, Science Press, Utrecht (1987).
[25] M. V. Kosevich, O. A. Boryak, I. O. Stepanov, and V. S. Shelkovsky, Eur. Mass Spectrom. **3**, 11 (1997).
[26] M. Takayama, Int. J. Mass Spectrom. Ion Processes **152**, 1 (1996).
[27] B. I. Verkin, V. F. Getmanets, and R. S. Mikhalchenko, *Thermophysics of Low Temperature Sublimational Cooling*, Naukova Dumka, Kiev (1980).
[28] *Water. A Comprehensive Treatise, Water and Aqueous Solutions at Subzero Temperatures*, F. Frank (ed.), Vol. 7, Plenum Press, New York (1982).
[29] F. A. Bar-Nun, J. Dror, E. Kochavi, and D. Laufer, Phys. Rev. B **35**, 2427 (1987).
[30] R. S. Smith, C. Huang, E. K. L. Wong, and B. D. Kay, Phys. Rev. Lett. **79**, 909 (1997).

This article was published in English in the original Russian journal. Reproduced here with stylistic changes by AIP.

Molecular structures of thymidine isomers isolated in low-temperature inert matrices

A. Yu. Ivanov* and G. G. Sheina

B. Verkin Institute for Low Temperature Physics and Engineering of the National Academy of Sciences of Ukraine, 47 Lenin Ave., Kharkov 61103, Ukraine

S. A. Krasnokutski

Max-Planck-Institut für Strömungsforschung, Bunsenstrasse 10, Göttingen 37073, Germany
Fiz. Nizk. Temp. **29**, 1065–1070 (September–October 2003)

The Fourier transform infrared spectra of 2′-deoxyribonucleoside–thymidine (dT) in low-temperature Ar matrices are obtained in the range 4000–1300 cm^{-1}. It is determined that anti-conformers of thymidine are dominant. The ribose rings of the main anti-conformers dT_a0, dT_a1 are in the C2′-endo conformation, but the ribose rings of minor anti-conformers dT_a2, dT_a3 have the C3′-endo conformation, stabilized by intramolecular hydrogen bonds O3′H…O5′ and O5′H…O3′, respectively. The main syn-conformer dT_s2 is stabilized by the intramolecular hydrogen bond O5′H…O2 and has C2′-endo conformation of the ribose ring. © *2003 American Institute of Physics.* [DOI: 10.1063/1.1614199]

The structural components of DNA—nucleosides and their derivatives—are important objects of investigation for the modern science of life.[1–11] The main experimental methods of investigation of nucleosides are NMR spectroscopy and crystallography.[1] But the results of investigations by these methods depend strongly on the intermolecular interactions. For example, only one form of several possible conformers can be stabilized in crystals.[1] Owing to competing interactions with the solvent, NMR spectroscopy gives no way to obtain direct data about intramolecular hydrogen bonding.[4,5] These limitations are absent in the method of matrix isolation, where molecular isomers from the gas phase are trapped in low-temperature inert matrices.[12] We previously used the Fourier transform infrared (FTIR) matrix isolation spectroscopy for the first time in the investigation of pyrimidine nucleosides isolated in low-temperature inert matrices.[10,11] The evaporation of uridine and dT without thermodestruction was demonstrated, and the intramolecular H bond O5′H…O2 was detected.[10,11] In the present research, FTIR spectra of dT in Ar matrices were obtained by using an enhanced experimental setup. The new spectral data suggest the existence of more types of isomers with intramolecular H bonds in the isolated pyrimidine nucleosides than had been considered before.[7–11]

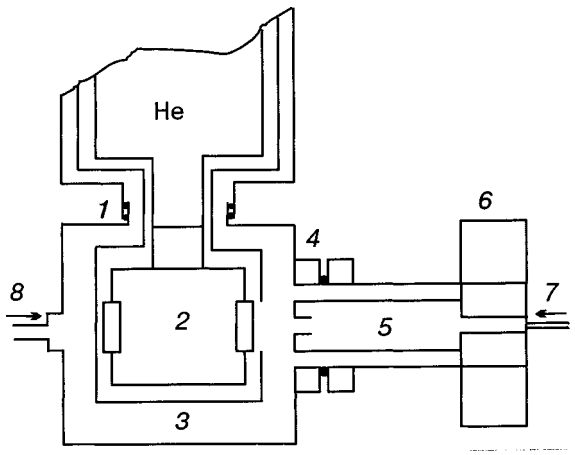

FIG. 1. The general scheme of the low-temperature setup based on liquid He cryostat: rotating vacuum seal (*1*), cryogenic block with cold mirrors and QCM (*2*), rotating nitrogen shield (*3*), flange with indium seal (*4*), Knudsen cell (*5*), electric heater of Knudsen cell (*6*), Ar flow through Knudsen cell (*7*), outside Ar flow (*8*).

EXPERIMENTAL AND COMPUTATIONAL METHODS

The basic features of the FTIR spectrometer have been described previously.[11,13–15] For this paper the FTIR spectra of thymidine and the auxiliary substance 1-methyl-thymine were obtained in the ranges 4000–1300 cm^{-1} with a CaF_2 beamsplitter at an apodized resolution of 0.4 cm^{-1}. The matrix isolation setup was based on a liquid-helium cryostat with a nitrogen shield (Fig. 1). Two low-temperature differential quartz crystal microbalances (QCM) and two metal mirrors were placed on the copper holder in the vacuum chamber (Fig. 1) and had a working temperature in the range 5–40 K. The QCM was used for the measurements of the absolute intensity of the molecular beams and the matrix-to-sample ratio (M/S).[13] Owing to the QCM, we have the capability of working not only with an Ar flux passing through the Knudsen cell but also with an outside flux of cold Ar gas (Fig. 1).

All nucleosides are very thermally labile molecules, and for their evaporation a special Knudsen cell with reduced molecular beam losses was constructed. As is shown in Fig. 2, the geometry of the Knudsen cell and its disposition to the low-temperature mirror are very important for effective operation. The data in Fig. 2 were obtained by the statistical Monte Carlo method, which is very useful for the simulation of complicated vacuum systems.[16] This evaporation cell is characterized by a working vapor pressure of around 10^{-5} Torr and Knudsen number of over 100. This evaporation cell is more effective by a factor of more than 500–1000 over one of the cells used in our previous experiments with simple compounds.[13–15] In comparison with our previous work,[11] for the present experiments the distance L (Fig. 2)

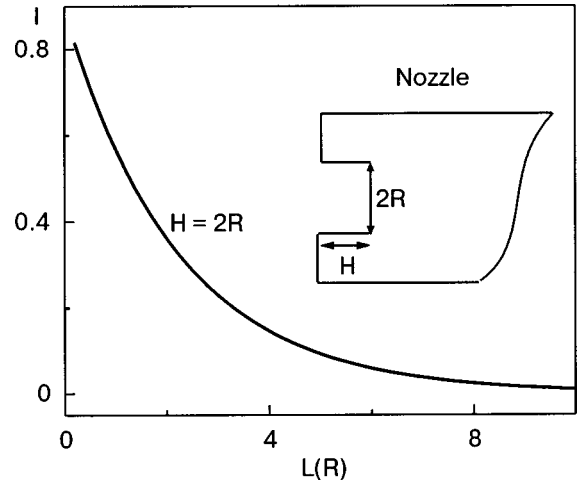

FIG. 2. The relationship of the efficiency of evaporation cell (I) as function of the distances L between the cell and cold mirror. L is in units of the radius R of the outlet nozzle of Knudsen cell.

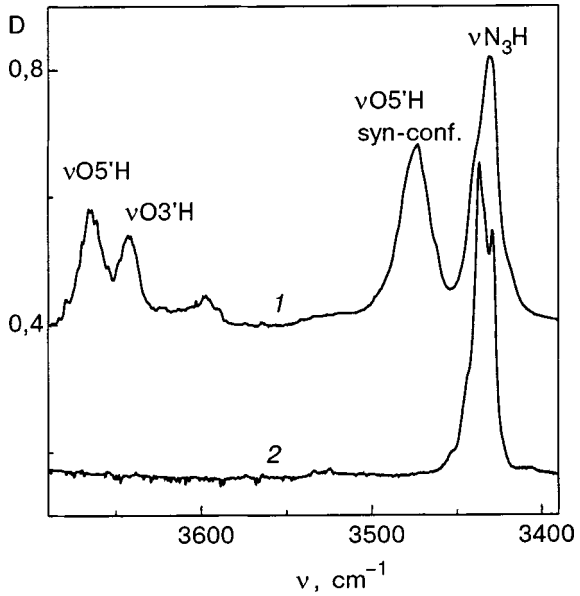

FIG. 3. The FTIR spectra of thymidine (*1*) and 1-methylthymine (*2*) isolated in Ar matrices ($T=12$ K, $M/S=700$) in the O–H, N–H stretching region ($3690-3390\ \mathrm{cm}^{-1}$).

was decreased from $4.5R$ to $2.5R$. The typical intensities of molecular beams of thymidine were about 40–70 ng/(s $\cdot$cm^2) at evaporation temperatures 410–430 K without any thermodestruction. Thymidine (commercial substance from Sigma) was used without additional purification. The auxiliary substance 1-methyl-thymine was synthesized at the Kharkov National University (Kharkov, Ukraine). All substances were annealed to remove impurities such as sorbed H_2O, CO_2, and N_2 in the initial phase of evaporation. The inert gas Ar, more than 99.99% pure, was deposited on the mirrors at 11 K. To improve the optical characteristics of the Ar matrices, before the deposition of matrix samples a thin layer of pure Ar was deposited on the mirrors over a temperature range of 35–20 K.[15] The quantum-chemical *ab initio* calculations of the relative energies and vibrational spectra of thymidine conformers were performed by the program PC GAMESS version 6.0 (Ref. 17) of the GAMESS (US) QC package.[18]

RESULTS AND DISCUSSION

Peculiarities of the vibrational spectra of dT conformers. As is evident from Fig. 3, in the region of the stretching vibrations ν(OH), ν(NH), the frequency of the ν(N3H) stretching vibration of dT coincides well with ν(N3H) of 1-methyl-thymine. Because of this, four absorption bands in this region (Fig. 3) can belong to two OH groups of 2′-deoxyribose: O3′H and O5′H only (Fig. 3). The magnification of the number of bands can be explained by intramolecular hydrogen bonds in the conformational structures, which were considered in this paper (Fig. 4). It is known that the conformational-flexible ribose rings of nucleosides has a puckered structure, and C2′-endo and C3′-endo are the main equilibrium conformations of the ribose ring in solutions.[1] As is indicated in Fig. 4, the transition C3′-endo→C2′-endo has no effect on the structure of the H bonds in the syn-conformers dT_s1, dT_s2 (Fig. 4). In the anti-conformers dT_a2, dT_a3 the transition C2′-endo →C3′-endo leads to the formation of the H bonds O3′H…O5′, O5′H…O3′ (Fig. 4). The choice of the structure dT_a1 with the orientation of hydroxymethyl group gauche$^+$ and torsion angle γ ($\angle$C3′–C4′–C5′O5′ $=+50°$ are close to the structures with hydrogen bonds C6H…O5′ in the anti-conformers of uridine and cytosine.[7,8] The structure dT_a0 with the orientation of hydroxymethyl group gauche–($\angle\gamma\approx-65°$) and the lack of any classical linear H bonds (Fig. 4) were considered also. Stabilization of the position of the pyrimidine ring in the dT_a0, dT_a2, dT_a3 conformation can be effected by the electrostatic interaction between atoms: C6H↔O4′ and C2O↔H1′. The orientation of the methyl group with respect to the carbonyl group C2O are close to the structure A from Ref. 19, where two hydrogen atoms are positioned above and below the

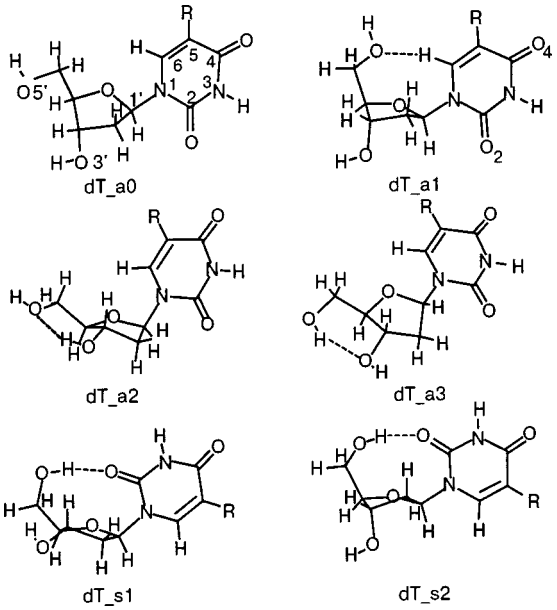

FIG. 4. The conformational structures of thymidine which are stable at the different level of calculation (HF/3–21G(p), HF/6–31G(d,p) and MP2/6–31G(d,p)). Intramolecular H bonds are represented with dashed lines. The symbol R–represents a CH3 group.

TABLE I. The parameters of the experimental FTIR spectra in Ar matrices and of the spectra calculated by the method of 6-31G(d,p) spectral bands of thymidine conformers in the 3700–3000 cm^{-1} region.

Conformer mode	Experiment		dT_a0		dT_a1		dT_a2		dT_a3		dT_s1		dT_s2	
	ν, cm^{-1}	I	ν, cm^{-1}	I^a	ν, cm^{-1}	I^a	ν, cm^{-1}	I^a	ν, cm^{-1}	I^a	ν, cm^{-1}	I^a	ν, cm^{-1}	I^a
νO5'H	3665	3.1	3673	76	3367	72	3673	84						
νO3'H	3641	1.8	3654	64	3659	54			3659	65	3681	76	3660	54
ν hb_O3'H	3620*	0.8*					3638	107						
ν hb_O5'H	3597*	0.5*							3639	86				
ν hb_O5'H	3482	6.2									3626	161	3589	351
νN3H	3428	9.2	3439	106	3441	103	3438	106	3438	106	3435	103	3436	106
νC6H	3075	0.5	3059	4	3043	14	3071	7	3070	8	3022	6	3026	5

Comment: I— relative integral intensities.
I^a—absolute integral intensities (km/mol).
νhb_OH— bands of groups involved in the intramolecular H bonds.
*— after deconvolution of the wide band 3598 cm^{-1} on the Gaussian contours.

N1–C2–O plane (Fig. 4). All conformers from Fig. 4 may be considered as local minima, since they were stable at the HF/3–21G(p), HF/6–31G(d,p), and MP2/6–31G(d,p) levels of calculation and have no imaginary frequencies in the calculated spectra.

The experimental and calculated spectra are compared in the region of ν(OH), ν(NH), ν(CH) (Table I). From this table we notice that the calculated frequencies of the free O5′H, O3′H, and N3H groups are in good agreement with the experimental frequencies for all conformers. The band 3482 cm^{-1} (Fig. 3, Table I) can be assigned to the H-bonded vibration O5′H…O2 in the syn-conformations. According to our calculations, the vibration ν(hb_O5′H) in conformer dT_s2 has a frequency about 40 cm^{-1} lower than in the dT_s1 conformer (Table I). We can see in our experimental spectra that the band at 3482 cm^{-1} does not have a high-frequency shoulder in Ar matrices (Fig. 3) and the occupancy of conformer dT_s1 can be neglected.

The calculated frequencies and intensities of the characteristic bands of the conformers dT_a2 and dT_a3 are in close agreement (Table I). This result is supported by the experiment in Ar matrices, where we can see only the one wide band 3598 cm^{-1} with a high-frequency shoulder (Fig. 3). Contrary to the calculated parameters of νC6H (Table I), only one band of νC6H vibration was detected in the experimental spectrum (Fig. 5). The influence of the intramolecular hydrogen bonds C6H…O5′ in conformer dT_a1 on the νC6H parameters was not detected experimentally, as the free C6H group in 1-methyl-thymine has Fermi resonance splitting in the spectra (Fig. 5). Consequently, it may be considered that the anti-conformers dT_a0 and dT_a1 are practically indistinguishable in the investigated region. *The populations of dT conformers in the low-temperature matrices*. It is known that the conformers' occupancies in matrices may differ widely from those in the gas phase. The effect of interconversion is observed at low barriers between conformational isomers.[12] We tested the interconversion by using the annealing of matrix samples. The annealing of matrix samples at 30 K has no influence on the conformational equilibrium. It follows that the barrier heights of dT conformers are $>2.5–3$ kcal/mole and that their conformational equilibrium in the gas phase at the evaporation temperature must be close to equilibrium in Ar matrices at 12 K. For comparison with the real experimental data the relative free Gibbs energy ΔG was estimated by the standard method:[20]

$$\Delta G_{AB}(T)=\Delta E+\Delta ZPE+\int_0^T \Delta C dT - T\Delta S(T).$$

The relative electronic energy ΔE was estimated at the MP2/6–31G(d,p) level of *ab initio* calculation, and the relative zero-point vibrational energy ΔZPE and temperature-dependent contributions of rotation and vibration were estimated at the HF/6–31G(d,p) level for temperatures of 298 and 420 K (Table II).

The association of ΔG and the experimental spectral data can be expressed by the standard equation:

$$\Delta G_{AB}(T)=-RT\ln K_{AB}=-RT\ln(\eta_A/\eta_B),$$

where $K_{A,B}$ is the equilibrium constant of conformers A and B and η_A and η_B are the populations of these conformers.

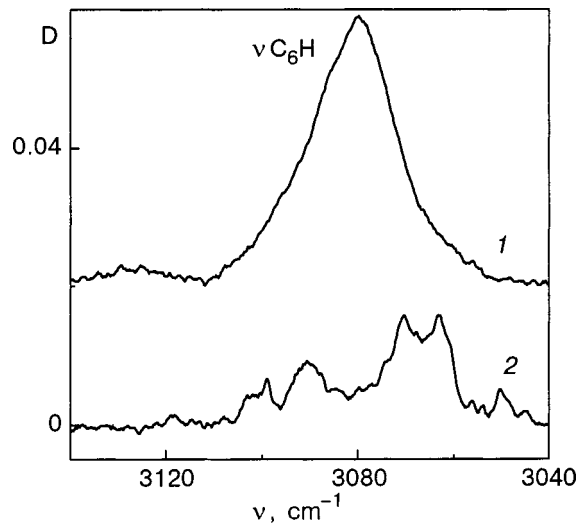

FIG. 5. The FTIR spectra of thymidine (*1*) and 1-methylthymine (*2*) isolated in Ar matrices ($T=12$ K, $M/S=700$) in the C5–H, C6–H stretching region (3140–3040 cm^{-1}).

TABLE II. Calculated and experimental relative energies (kcal/mole) of the thymidine conformers in the isolated state.

Conformer method	dT_a0	dT_a1	dT_a2	dT_a3	dT_s1	dT_s2
HF/3-21G(*p*)	5.4	2.4	2.6	4.6	3.3	0 (−865.3452)*
HF/6-31G(*d*,*p*)	2.9	1.6	1.8	3.4	1.5	0 (−870.1091)*
MP2/6-31G(*d*,*p*)	5.7	3.0	3.8	4.9	2.6	0 (−872.6776)*
ΔG (298 K)** MP2/6-31G(*d*,*p*)	3.3	1.8	2.1	3.4	1.6	0
ΔG (420 K)** MP2/6-31G(*d*,*p*)	2.4	1.4	1.6	2.9	1.2	0
ΔG (420 K) Experiment	–	0	1.8	2.2	–	1.1

*— absolute energies in a.u. are indicated in brackets.
**— vibrational–rotational contribution was estimated at the HF/g–31G(*d*, *p*) level.

To determine the equilibrium constants by using the experimental spectra it is necessary to know the molar extinction coefficients of the characteristic spectral bands or their ratios. The ratios of molar extinction coefficients of characteristic bands may be determined through the redistribution of the intensities of the characteristic bands under the influence of changing evaporation temperature or through the UV irradiation of matrix samples. If the corresponding experiments are difficult, the *ab initio* calculations of the intensities of the characteristic spectral bands may be used. *Ab initio* calculations usually overestimate the absolute infrared intensity of vibrational bands,[21,22] but the ratio of the experimental and calculated intensities I coincides much better. The equilibrium constant of isomers a and b has been presented as[23,24]

$$K_{AB}=\left(\frac{\Sigma I_a(\exp)}{\Sigma I_{a(\mathrm{calc})}}\right)\left(\frac{\Sigma I_{b(\mathrm{calc})}}{\Sigma I_{b(\exp)}}\right). \quad (1)$$

Unlike some studies,[23,24] we have used Eq. (1) with the intensities of the ν(OH), ν(NH), and ν(CH) stretching vibrations only. With our data the best agreement between the calculated and experimental results is observed for the ratio of the intensities of stretching vibrations. For determination of K_{AB} different combinations of the experimental and calculated intensities from Table I were used. As discussed above, the anti-conformers in the pairs dT_a0, dT_a1 and dT_a2, dT_a3 are practically indistinguishable in the matrix spectra. Therefore, for the sake of simplicity, the conformer dT_a0 was ignored.

According to the relative electronic energy calculations, the syn-conformer dT_s2 with the intramolecular hydrogen bond O5′H…O2 and the C2′-endo conformation of the sugar ring has the minimal energy among all conformers at all levels of optimization (Table II). The data in Table II demonstrate disagreement between the experimental and calculated occupancies of the dT_a1 and dT_s2 conformers, but the experimental and calculated data coincide well for the minor anti-conformers dT_a2 and dT_a3 (Table I). The influence of the vibrational–rotational contribution to the free energy reduces the difference of conformers' energies significantly, and this is especially noticeable with increasing evaporation temperature (Table II). Because of this, conformers dT_s2 may have an essential effect on biological processes at the relatively low physiological temperatures.

CONCLUSIONS

We have shown that FTIR matrix-isolation spectroscopy is a helpful method for investigation of the molecular structure of nucleoside conformational isomers. We have established that at evaporation temperatures of up to 430 K thymidine may be evaporated for an appreciable length of time and trapped in inert matrices without any thermodestruction. Anti-conformers of thymidine are dominant in the isolated state. The main anti-conformer, dT_a1, has the C2′-endo conformation of the ribose ring. The minor anti-conformers dT_a2 and dT_a3 have the C3′-endo conformation of the ribose ring, stabilized by intramolecular hydrogen bonds O3′H…O5′ and O5′H…O3′, respectively. The intramolecular hydrogen bonds O3′H…O5′, and O5′H…O3′ may be regarded as an indicator of the transition C2′-endo →C3′-endo between conformations of the ribose ring in the anti-conformers of thymidine. The thymidine dT_s2 syn-conformer is stabilized by the intramolecular hydrogen bond O5′H…O2, and the dominant conformation of ribose ring is C2′-endo.

This investigation was supported by the Ukrainian Academy of Sciences and in part by the INTAS-International Association under Grant No. INTAS 00–00911.

*E-mail: ivanov@ilt.kharkov.ua

[1] W. Saenger, *Principles of Nucleic Acid Structure*, Springer-Verlag, New York (1984).
[2] G. A. Jeffrey and W. Saenger, *Hydrogen Bonding in Biological Structures*, Springer-Verlag, Berlin (1991).
[3] S. N. Rao, Nucleosides and Nucleotides **14**, 1179 (1995).
[4] F. Seela, H. Debelak, H. Reuter, G. Kastner, and I. A. Mikhailopulo, Tetrahedron **55**, 1295 (1999).
[5] J. J. Barchi Jr., L.-S. Jeong, M. A. Siddiqui, V. E. Marquez, and J. Biochem, Biophys. Methods **34**, 11 (1997).
[6] J. M. Gavira, M. Campos, G. Diaz, A. Hernanz, and R. Navarro, Vib. Spectrosc. **15**, 1 (1997).
[7] N. Leulliot, M. Ghomi, G. Scalmani, and G. Berthier, J. Phys. C **103**, 8716 (1999).

[8] N. Leulliot, M. Ghomi, H. Jobic, O. Bouloussa, V. Baumruk, and C. Coulombeau, J. Phys. Chem. B **103**, 10934 (1999).
[9] O. V. Shishkin, A. Pelmenschikov, D. M. Hovorun, and J. Leszczynski, J. Mol. Struct. **526**, 329 (2000).
[10] S. A. Krasnokutski, A. Yu. Ivanov, V. Izvekov, G. G. Sheina, and Yu. P. Blagoi, *XXIV European Congress on Molecular Spectroscopy*, Prague, Czech Repablic, 470 (1998).
[11] S. A. Krasnokutski, A. Yu. Ivanov, V. Izvekov, G. G. Sheina, and Yu. P. Blagoi, J. Mol. Struct. **482–483**, 249 (1998).
[12] A. J. Barnes, J. Mol. Struct. **113**, 161 (1984).
[13] A. Yu. Ivanov, A. M. Plokhotnichenko, E. D. Radchenko, G. G. Sheina, and Yu. P. Blagoi, J. Mol. Struct. **372**, 91 (1995).
[14] A. Yu. Ivanov, A. M. Plokhotnichenko, V. Izvekov, G. G. Sheina, and Yu. P. Blagoi, J. Mol. Struct. **408–409**, 459 (1997).
[15] A. Yu. Ivanov, G. Sheina, and Yu. P. Blagoi, Spectrochim. Acta A **55**, 219 (1999).
[16] G. L. Saksagansky, *Molecular Beams in the Composite Vacuum Structures* [in Russian], Atomizdat, Moscow (1980).
[17] Alex. A. Granovsky, http://classic.chem.msu.su/gran/gamess/index.html.
[18] M. W. Schmidt, K. K. Baldridge, J. A. Boatz, S. T. Elbert, M. S. Gordon, J. J. Jensen, S. Koseki, N. Matsunaga, K. A. Nguyen, S. Su, T. L. Windus, M. Dupuis, and J. A. Montgomery, J. Comput. Chem. **14**, 1347 (1993).
[19] M. J. Nowak, L. Lapinski, D. C. Bienko, and D. Michalska, Spectrochim. Acta A **53**, 855 (1997).
[20] J. S. Kwiatkowski and J. Leszczynsky, Chem. Phys. Lett. **204**, 430 (1993).
[21] M. J. Nowak, L. Les, and L. Adamowicz, Trends Phys. Chem. **4**, 137 (1994).
[22] Y. Yamaguchi, M. Frisch, J. Gaw, H. F. Schaefer III, and J. S. Binkley, J. Chem. Phys. **84**, 2262 (1986).
[23] M. J. Nowak, L. Lapinski, and J. Fulara, Spectrochim. Acta A **45**, 229 (1989).
[24] H. Vranken, J. Smets, G. Maes, L. Lapinski, M. J. Nowak, and L. Adamovicz, Spectrochim. Acta A **50**, 875 (1994).

This article was published in English in the original Russian journal. Reproduced here with stylistic changes by AIP.

SPECTROSCOPY IN CRYOCRYSTALS AND MATRICES

Time-resolved CARS measurements of the vibrational decoherence of I_2 isolated in an Ar matrix

M. Karavitis, D. Segale, Z. Bihary, M. Pettersson, and V. A. Apkarian*

Department of Chemistry, University of California Irvine, CA 92697-2025, USA
Fiz. Nizk. Temp. **29**, 1071–1080 (September–October 2003)

Time-resolved coherent anti-Stokes Raman scattering is applied to prepare and interrogate vibrational coherences on the ground electronic surface of molecular iodine isolated in Ar matrices. The coherence decay time shows a linear dependence on vibrational quantum numbers for $v=3-15$. The temperature dependence of decoherence rates is negligible for $v<7$ in the experimental range $T=18-32$ K. For a $v=13$, 14 superposition, the temperature dependence indicates dephasing by a 66 cm^{-1} pseudo-local phonon, just outside the Debye edge of the solid. The accuracy of the data is limited due to two-photon induced dissociation of the molecule, a process which is characterized using polarized fields. The $T\rightarrow 0$ limit of dephasing is discussed. [DOI: 10.1063/1.1614200]

1. INTRODUCTION

In a recent paper we reported time-resolved coherent anti-Stokes Raman scattering (TRCARS) measurements on I_2 isolated in an Ar matrix.[1] A detailed analysis of the process was presented, based on data limited to wave packets prepared near $v=4$, and limited to $T=32$ K. We have since succeeded in making measurements on packets prepared at vibrations as high as $v=14$, and as a function of temperature, for $T=17-33$ K. TRCARS measurements are well suited for the preparation of vibrational coherences and the detailed analysis of their dephasing.[2,3] The characterization of vibrational decoherence in this model system: a diatomic impurity, in an atomic solid, with weak and relatively well understood coupling between molecule and lattice,[4] is our aim. Of particular interest is the understanding of decoherence in the $T\rightarrow 0$ limit.[5]

Studies of vibrational relaxation and dephasing dynamics in cryogenic matrices are limited for the most part to infrared active diatomics, such as CO, in which radiative relaxation or dipolar intermolecular energy transfer remains as the residual source of dephasing in the $T\rightarrow 0$ limit.[6] These mechanisms are not available to a homonuclear diatomic, which must be prepared via Raman pumping. Raman line shapes, in principle, yield overall dephasing rates; however, practical considerations do not allow studies with the required resolution.[7] TRCARS measurements allow the preparation of vibrational coherences with control and allow a detailed time domain interrogation of their evolution.

Argon matrices doped with molecular iodine prove to be difficult to scrutinize, because the signal permanently degrades during the course of measurement. We establish that the degradation is due to permanent dissociation of the molecule through multiphoton excitation, a process unavoidable at the field strengths required for the four-wave mixing measurements. Despite this limitation, important principles are established.

2. EXPERIMENTAL

A detailed description of the experimental method can be found in our earlier report.[1] Succinctly, the forward BOX-CARS geometry is adopted, using three noncollinear laser pulses at two different colors.[8] The pulses are obtained from a regeneratively amplified Ti:sapphire laser, which pumps two three-pass optical parametric amplifiers (OPA). The OPA outputs are up-converted by sum frequency generation, and compressed using prism pairs to provide independently tunable ~70 fs pulses in the range 480 nm to 2000 nm. Using a neutral density filter, the intensities of the lasers are separately attenuated to less than 1 μJ/pulse. The three horizontally polarized input beams are brought into focus on the sample through a single achromat. A pinhole is used to spatially filter the anti-Stokes (AS) output beam. Spectral filtering is provided by a combination of a bandpass filter and 1/4-m monochromator, adjusted to pass the entire band of the AS radiation. The signal is detected using a photomultiplier. Typically, 300 averages are taken at each time delay. Data were also collected with a laser system consisting of two home-built noncollinear optical parametric amplifiers, capable of generating 25 fs pulses at the sample.

The matrices are deposited at 32 K, using a pulsed valve (General Valve, Series 99) from a 5-liter glass bulb, onto a 200-μm thick sapphire substrate. The substrate is cooled using a closed-cycle cryostat, which in these experiments could only reach a base temperature of 17 K. The cryostat is mounted on an $x-y-z$ translation stage. The deposition conditions are adjusted to obtain a glassy film of high optical quality. A back pressure of ~200 Torr and long pulses of ~1 s, consistently yield films of sufficient quality for the measurements.

Using a scanning pinhole, the spot size at the overlap of the three laser beams is measured to have a typical diameter of FWHM=35 μm. This is comparable to the grain size of crystallites, as such the measurements can be expected to be

confined to single, oriented, crystalline domains. This consideration is also key to our success in carrying out temperature-dependent measurements, despite the fact that the thermal shock of cooling leads to shattering of the solid. In the shattered solids, a careful search usually allows us to find a scatter-free domain to carry out the measurements. At a given spot, the signal undergoes radiation-induced permanent decay. The signal recovers upon moving to a fresh spot. Inspection of the irradiated volume under magnification establishes that the decay is not due to physical damage of the sample. Since the TRCARS experiments are carried out with all three input beams horizontally polarized, irradiation-induced reorientation of the molecular axis could lead to signal decay. To test this hypothesis, we insert a half-wave plate in one of the pump beams to rotate its polarization by 90°. After passing the two pump beams through a cross-oriented pair of linear polarizers, we overlap the beams in space and time by optimizing the CARS signal from the sapphire substrate. We then translate the sample to the focal plane and verify that the two-photon induced molecular fluorescence at 1340 nm is proportional to the square of the sum of intensities of the beams. The sample is then irradiated on the same spot alternatively with the horizontally and vertically polarized pump beams, by blocking and unblocking beams while monitoring two-photon induced fluorescence previously assigned to $I^*I^* \rightarrow I^*I$ emission.[9]

3. RESULTS AND ANALYSIS

3.1. Photodissociation

The decay of the laser-induced molecular emission with irradiation time is shown in Fig. 1, for a sequence of irradiation periods alternating between vertically and horizontally polarized beams. The intensities of the two beams were adjusted to provide equal signal from each beam when irradiating a fresh spot. The decay curve for a given polarization is nonexponential. Upon switching from vertical to horizontal irradiation of the same spot, the fluorescence intensity jumps up; however, it starts below the pre-irradiation level. Evidently, irradiation leads to dissociation of molecules oriented both parallel and perpendicular to the polarization of the laser. After irradiation with the horizontal polarization, when we return back to the vertical polarization we observe a small increase above the limit reached in the first irradiation period. We may conclude that a small fraction of the molecules reorient, or that a small fraction of the previously dissociated molecules recombine. The same decay behavior is obtained when monitoring various molecular emissions: the ion-pair emission at 380 nm,[10–12] the I^*I^* emission in the near-IR,[9] and the $A/A' \rightarrow X$ emission near 1400 nm.[13,14] Since all molecular emissions decay in time, we may safely conclude that the molecule dissociates.

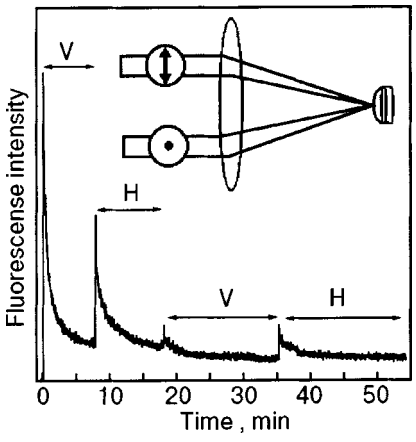

FIG. 1. Photoinduced dissociation of molecular iodine, monitored using two-photon fluoresence at 1340 nm. The experimental arrangement is shown. Two cross-polarized laser beams ($\Delta t = 50$ fs near transform-limited pulses, $\lambda = 555$ nm, 1 kHz repetition rate) are aimed at the same spot in the sample. The sample is irradiated successively with the vertical (V) and horizontal (H) polarized beams over the durations indicated by the double-sided arrows.

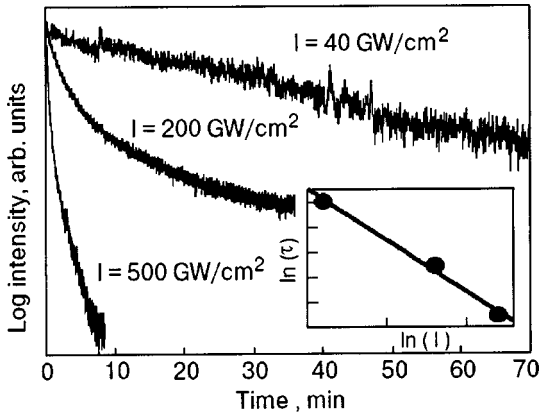

FIG. 2. Decay of I_2 fluoresence as a function of pump intensity. Experimental conditions are identical to those described in Fig. 1. Differing intensities are produced by means of a variable neutral density filter with a continuous range of optical densities between 0.02 and 3 arb. units. The inset shows a log/log plot of the decay rate versus the pump intensity. The result is a straight line of slope two, indicating that the dissociative excitation is via two-photon absorption.

The decay curves at three different irradiation intensities are shown in Fig. 2. The curves are not exponential and are not expected to be. For molecules rigidly held by the matrix, such that their orientations do not scramble during irradiation, photodissociation with polarized light leads to orientation-dependent population decay. The kinetics and observable signal will be controlled by the tensor of molecular transition matrix elements involved in the dissociative transition and probe transitions. This occurs in studies of saturation of photo-selection or induced dichroism, and many of the common cases that arise have been reviewed in the literature.[15] For the present purposes we note that the signal can be approximated by a double exponential, with decay constants at a given intensity that differ by a factor of 10. Both decay constants scale as the second power of the intensity, as illustrated for the fast component in the inset to Fig. 2. This suggests that the dissociation is due to two-photon excitation, with the two decay rates assigned to photodissociation of molecules oriented parallel and perpendicular to the linearly polarized radiation field. Thus, for irradiation with x-polarized light, denoting the two-photon excitation cross sections as $\sigma_{\parallel}^{(2)}$ and $\sigma_{\perp}^{(2)}$, and associating a quantum yield Q for dissociation upon excitation, the observable signal may be approximated as:

$$N(t)=\frac{N_0}{3}[\zeta_{\|}\exp(-\sigma_{\|}^{(2)}I_x^2Qt')+2\zeta_{\perp}\exp(-\sigma_{\perp}^{(2)}I_x^2Qt')],\quad \text{where}\quad t'=ft\Delta t \quad (1)$$

in which $\zeta_{\|}$ and $\zeta_{\perp}$ are the sensitivities of LIF detection of the parallel and perpendicular populations, I is the laser fluence in photons$\cdot$cm^{-2}s^{-1}, Δt is the laser pulse width, f is the laser repetition rate (1 kHz), and t is the duration of the irradiation.

The lower limit for the two-photon excitation cross section that leads to dissociation can be obtained by assuming $Q=1$, in which case the fits yield $\sigma_{\|}^{(2)}=2\times10^{-51}$ cm^{4}s and $\sigma_{\perp}^{(2)}=2\times10^{-52}$ cm^{4}s. The largest error in the determination of these limiting values is the uncertainty associated with the measured size of the laser spot.

The upper limit of the two-photon excitation cross section can be obtained under the assumption that beside the linear $B\leftarrow X$ absorption, this process dominates the attenuation of the pump laser, in which case the transmitted intensity I reduces to:

$$I=I_0/(1+2N\sigma^{(2)}I_0l) \quad (2)$$

in which $N=4\times10^{18}$ cm^{-3} is the dopant number density, and $l\sim50$ μm is the sample thickness. From the curvature of the transmission, for pump intensities limited to 0.5 μJ/pulse, we measure $\sigma^{(2)}=10^{-48}$ cm^{4}s. The sample thickness is the greatest uncertainty in this determination.

3.2. Time-resolved CARS

The TRCARS measurements are designed to interrogate the vibrational coherence on the ground electronic state of matrix-isolated iodine. The experiments measure a single component of the third-order polarization:

$$P^{(0,3)}_{\mathbf{k}_1-\mathbf{k}_2+\mathbf{k}_3}(t)=\langle\varphi^{(0)}(t)|\hat{\mu}|\varphi^{(3)}_{\mathbf{k}_1-\mathbf{k}_2+\mathbf{k}_3}(t)\rangle+\text{c.c.} \quad (3)$$

by detecting the AS radiation propagating in the $\mathbf{k}_1-\mathbf{k}_2+\mathbf{k}_3$ direction.[1] We detect the total AS radiation:

$$I_{CARS}(t)=\int_{-\infty}^{\infty}dt_{43}|P^{(3)}(t_{21},t_{32},t_{43})|^2 \quad (4)$$

which depends on the timing between the sequence of three pulses: t_{21} is the interval between pump and dump, t_{32} is the interval between dump and probe, and t_{43} is the radiation interval after arrival of the probe pulse. In all of the measurements to be reported, the pump and dump pulses are stationary and nearly coincident in time. Their delay t_{21} is adjusted for optimum signal. Due to fast electronic dephasing, only prompt radiation after arrival of the probe pulse contributes to the signal, $t_{43}<30$ fs. This time interval is fixed by the first arrival of $\varphi^{(3)}$ to the inner turning point of the excited electronic surface, where the energy conservation condition $\omega_{AS}=\omega_1-\omega_2+\omega_3$ can be met. Consistent with this, the AS spectrum is verified to be structureless. We adjust the spectral bandpass of the detection to accept the entire AS spectrum. The signal is then recorded as a function of t_{32}, namely, as a function of delay between the preparation of the Raman packet, $\varphi^{(2)}_{\mathbf{k}_1-\mathbf{k}_2}$ and the arrival of the probe pulse at t_3. Thus, by defining $t\equiv t_{32}$, it is made clear that the experiment measures the time correlation between the Raman packet and the zeroth-order initial state:

$$I_{CARS}(t)\propto|2\,\text{Re}\langle\varphi^{(0)}(t_{32})|\varphi^{(2)}_{\mathbf{k}_1-\mathbf{k}_2}(t_{32})\rangle|^2. \quad (5)$$

The decay of this correlation defines the vibrational decoherence (permanent dephasing).

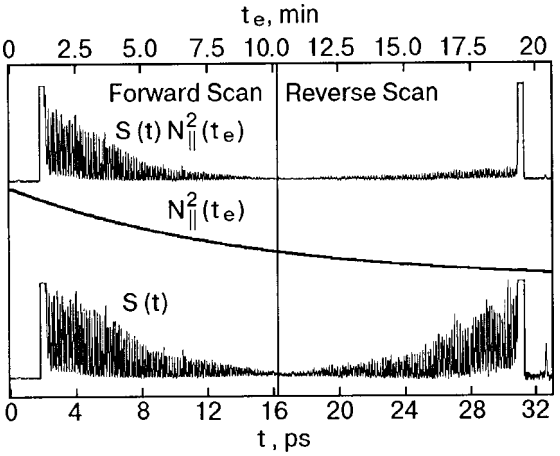

FIG. 3. Forward and reverse scans of the TRCARS signal. Overlapping $\sim$25 fs pump and Stokes pulses (at $\lambda=529$ and 575 nm) are used to generate a wave packet on the X state centered on $v=4$, 5. The lower absissa is the delay time between the Stokes and probe pulses, while the upper absissa is the data acquisition time. Around 10 percent of the original signal is recovered over the entire scan. An exponential correction $N_{\|}^2$ has been introduced in the final signal $S(t)$ to take into account the sample degradation over the course of the experimental time (t_e).

With laser intensities limited to $<$100 nJ per pulse, the sample degradation time stretches sufficiently to allow meaningful measurements. From a given spot, we record waveforms in pairs. After scanning a particular delay between pulses, we retrace the scan. An example is shown in Fig. 3. In this case, upon retracing, the signal recovers to 10% of its original amplitude over the data acquisition time of 20 minutes. This information is used to correct for signal degradation. In the TRCARS measurements, all three input beams are polarized parallel to each other, and therefore the quadrilinear signal is from the population oriented along the polarization axis, $N_{\|}(t)$. As long as the decay of this subensemble is not too extensive, it is possible to approximate it as an exponential. Accordingly, the signal, which is proportional to $N_{\|}^2(t)$, is corrected for exponential degradation with measurement time. The reconstruction of the signal is shown in Fig. 3.

In Fig. 4 we show the signal from a sample deposited at 35 K and recorded at 17 K. Both forward and corrected backward scans are shown. The good comparison between the two scans is a measure of the adequacy of the correction: the distortion of the signal due to nonexponential degradation is minor. The Fourier transforms of the two time files, which are also shown, are in good agreement. Thus, information regarding the complex amplitudes of the vibrational superposition and their beat frequencies is rather reliable, while dephasing times are subject to the uncertainty introduced by the correction for signal degradation. This data set was obtained using the short pulse NOPA setup, with pulse widths of $\sim$25 fs. The observation of the fundamental beat,

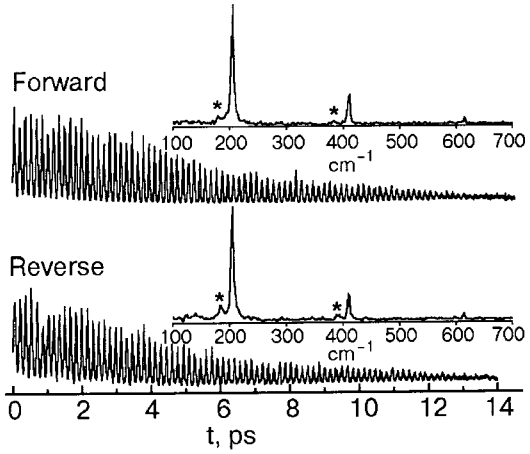

FIG. 4. Corrected CARS signal obtained using pulses described in Fig. 3. The insets are the Fourier transforms of the corresponding time files. The fundamental beat ~ 200 cm^{-1} along with two overtones is a clear indication of a four-state superposition. The Stokes shift, centered at 1475 cm^{-1}, would support a wave packet centered around a 7, 8 superposition; however, a nonlinear least-squares analysis of this signal using Eq. (7) yields frequencies corresponding to a 5, 6, 7, 8 superposition. This is not unreasonable, considering that the FWHM of the pulses used in these experiments is greater than 800 cm^{-1}.

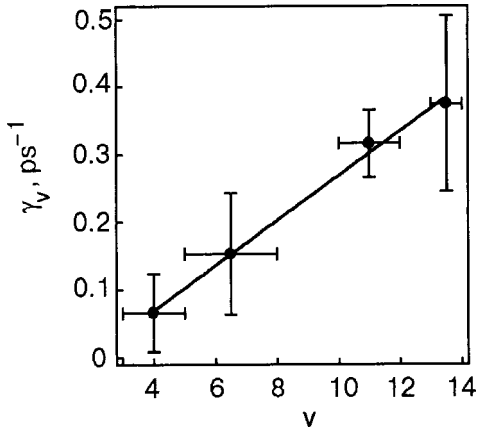

FIG. 5. Dependence of dephasing on vibrational quantum number. The four dephasing rates shown in the figure correspond to the following superpositions: (3,4,5), (5,6,7,8), (10,11,12) and (13,14). Due to the short lifetimes of these superpositions relative to the anharmonicity, the individual dephasing rates could not be decoupled from each other; therefore, only the mean dephasing rates are used. Error bars on the v axis span the superposition, while error bars on the γ_v axis correspond to the standard deviation of the mean dephasing rates obtained from a nonlinear least-squares fit to the data.

$\Delta v=1$ at 205.5 cm^{-1}, and two overtone beats, $\Delta v=2$ and $\Delta v=3$, indicates that a superposition of four vibrational levels is prepared. Given the Stokes shift of 1500 cm^{-1} between pump and dump pulses, the superposition is centered near $v=7$. Additionally, a broad sideband to the red of the molecular lines can be seen (identified by asterisks in Fig. 4). The fundamental beat of 180 cm^{-1} identifies this sideband as the dimer.[16] It is noteworthy that the dimer band is sharper during the backward scan, indicating annealing of the spot during the course of the measurement. The molecular lines do not show a discernible annealing effect. In samples deposited at $T<32$ K, the dimer is not observed.

Ignoring time convolution of the probe window with the evolving coherence and acknowledging that sum beats are outside the time resolution of the measurement, the signal is analyzed as a sum of decaying sinusoids:

$$S(t)=\sum_v c_v^2 e^{-2\gamma_v t}+\sum_{v,v'\neq v} c_v c_{v'}\cos[(\omega_v-\omega_{v'})t + (\varphi_v-\varphi_{v'})]e^{-(\gamma_v+\gamma_{v'})t} \quad (6)$$

in which γ, c, and φ represent the overall dephasing rate, amplitude, and phase of a given vibrational state of the prepared superposition. Using the Fourier analysis for initial estimates, the time files are fit through a nonlinear regression to Eq. (6). Although an excellent reproduction of the signal is retrieved, due to the relatively short time file, the individual decay constants of the constituent states are not separately determined. An equally acceptable fit of the time file is obtained by setting all decay constants to be the same, $1/\gamma=4.2$ ps in this particular case. In this regard, the use of longer pulses (narrower bandwidth) for the preparation of the Raman packet is preferable, since this allows a better discrimination of the v dependence of γ. The extracted values of γ are collected in Fig. 5, in which the horizontal error bars highlight the fact that individual dephasing rates cannot be decoupled with confidence. The dependence is linear, with $1/\gamma$ varying from 16 ps to 2.7 ps for $v=3$ to $v=13$. A representative set of waveforms from which the dephasing rates were extracted is shown in Fig. 6. Based on the Stokes shifts used, $\omega_{\text{pump}}-\omega_{\text{dump}}$, the assignment of the prepared vibrations can be made with little ambiguity. The analysis provides a rather accurate determination of vibrational frequencies and anharmonicities, as shown in Fig. 7. The extracted harmonic frequency and anharmonicity are: $\omega_e=(214.0\pm 0.17)$ cm^{-1}, $\omega_e x_e=(0.638\pm 0.009)$ cm^{-1}. These values are in good agreement with the RR measurements in solid Ar[7] and are revised somewhat from our earlier report. Note that the superposition with the lowest vibrations, assigned to $v=3$, 4, 5 in Fig. 6, lives long enough to show a weak node near $t=13$ ps, which arises from the anharmonic

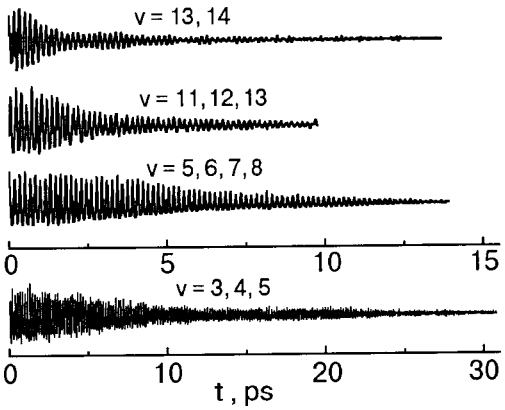

FIG. 6. Experimental waveforms corresponding to vibrational levels ranging from $v=3$ to $v=14$. These signals have their zero-frequency components subtracted out in order to make meaningful comparisons. Some important features of these signals include the nodal patterns exhibited by the 3, 4, 5 and the 13, 14 superpositions. The node in the 3, 4, 5 superposition, ~ 13 ps, corresponds to a rephasing time associated with twice the anharmonicity, indicating that at least four states must be contributing to this signal even though only three were resolvable. The slow modulation of the signal with a period of 25 ps in the $v=13$, 14 superposition is too short to be associated with anharmonicity.

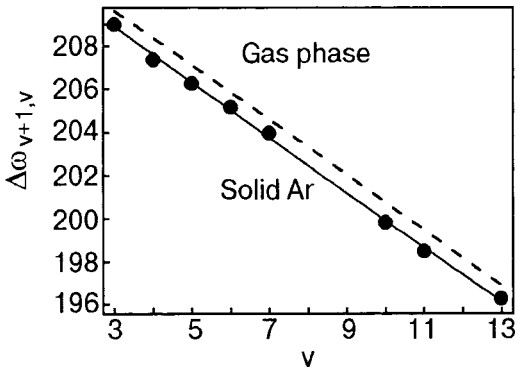

FIG. 7. Birge–Sponer plot for gas-phase I_2 (dashed line), and I_2 in solid Ar, obtained in the present TRCARS measurements (filled circles). The circles represent the experimental data points. The fundamental frequency and the first anharmonicity are slightly modified from the gas phase values and in agreement within experimental error to those obtained from resonance Raman.

beat between $\omega_{43}-\omega_{65}=4\omega_e x_e$, indicating that the superposition contains $v=6$ as well. The node between neighboring beats occurs at $t=c/2\omega_e x_e=26$ ps, by which time the signal is quite weak.

Within the accuracy of the measurements, for packets prepared below $v=10$, the decoherence rates are insensitive to temperature in the experimental range of $T=17-32$ K. Temperature has a measurable effect on the $v=13,14$ packet. This is illustrated in Fig. 8, in which the time files are shown along with the spectra of the fundamental beat. The spectra reveal sidebands at 10 cm^{-1} flanking the main peak. This in the time profile leads to the 3 ps modulation (see the 17 K signal in Fig. 8), which cannot be confused with the anharmonicity beat. The spectrum clearly shows that the lines broaden with temperature, so that in the 33 K spectrum the sidebands have completely coalesced with the central peak. The dephasing times extracted from transients through the least squares regression are: $1/\gamma=4$ ps, 3.6 ps, and 2.9 ps at $T=17$, 25, and 33 K, respectively. For the lower vibrations, in the same temperature range, the T dependence is less than 10%.

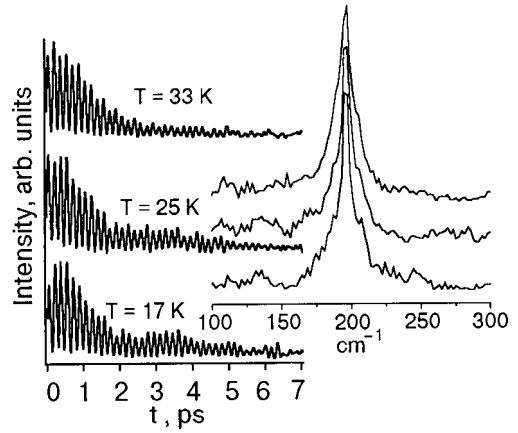

FIG. 8. Decoherence rates for different temperatures.

4. DISCUSSION

In molecular systems, with many internal degrees of freedom, the preparation and interrogation of particular coherences will be limited by competition among different channels. The dense electronic manifold of iodine leads to multiple electronic excitation channels at the intensities required to drive nonlinear processes. The time dependence of the four-wave signal is impervious to background excitation channels, except for the photodissociation of the molecule. Since the photodissociation process is two-photon driven, while the four-wave mixing process is maintained in the quadrilinear regime, it cannot be prevented through intensity control. Since the electronic resonances involved in both the TRCARS and multi-photon excitation involve repulsive walls of potentials, they are broad, and color offers little selectivity over the branching. Indeed, dissociation occurs at all colors used in the TRCARS experiments. Let us put the measured cross sections in perspective. The $B\leftarrow X$ excitation cross section is $\sigma_{BX}=10^{-18}$ cm^2 ($|\mu_{BX}|^2=1.02$ D^2 at 550 nm).[17] The cross section associated with the bilinear stimulated Raman process for preparing the vibrational coherence in the X state can be estimated as $\sigma_{SR}^{(2)}=\sigma_{XB}\sigma_{BX}\Delta\tau=2\times10^{-50}$ cm^4s, where $\Delta\tau\sim20$ fs is the residence time of the B-state packet in the Franck–Condon window. The measured two-photon induced dissociation cross section is $\sigma_{\|}^{(2)}Q=2\times10^{-51}$ cm^4s, only an order of magnitude smaller. Therefore, for a given number density of molecules transferred to the Raman packet, a tenth undergo permanent dissociation. The reduction of intensities to minimize the fraction of molecules that dissociate during the course of measurement is limited by practical signal-to-noise considerations. At intensities of 100 nJ/pulse (10^{29} photons/cm^2s), 10 ppm of the molecules are transferred to the Raman packet, and the third-order polarization consists of $\sim10^4$ molecules, leading to ~1 CARS photon detected per pulse.

The permanent photodissociation of iodine in solid argon is of interest, especially since this system has been previously studied as a prototype for the perfect cage effect.[18] A detailed analysis of the process will be taken up elsewhere. Here, we suffice by recognizing that permanent dissociation, as opposed to molecular reorientation, takes place during the measurements. The polarization dependent measurement clearly shows that early dissociation will result in orientational anisotropy and therefore dichroism in the solid.

The neglect of this consideration can have significant consequences on the interpretation of photo-selection, or photo-bleaching experiments such as have been reported recently.[12] Upon extended irradiation, the entire population is depleted. Although this would occur even if the molecule only possessed a single transition dipole, careful analysis of the decay establishes that the process is bimodal: both perpendicular and parallel molecular orientations undergo two-photon dissociation with relative yields of $\sigma_{\|}^{(2)}/\sigma_{\perp}^{(2)}=10$. Assuming quantum yields independent of orientation, the ratio must be determined by the relative excitation cross sections. There are two electronic states, $B(0_u)$ and $B'(1_u)$, that serve as intermediates for resonant two-photon excitation in the spectral range of interest. The $B\leftarrow X$ transition dipole is parallel to the molecular axis ($\Delta\Omega=0$), while that of the $B'\leftarrow X$ transition is perpendicular to the molecular axis ($\Delta\Omega$

$=\pm 1$); moreover, at the measured wavelength of 550 nm the relative absorption cross sections of these transitions have a ratio of 9:1.[17] This nicely rationalizes the observed orientation dependence of the dissociation curves, with the added implication that the two-photon cross sections are principally determined by the initial resonance.

Our main interest in the present work is the description of vibrational dephasing in the low-temperature limit. The observable vibrational coherence will decay due to dissipation and pure dephasing due to homogeneous and inhomogeneous contributions. In addition, there can be a contribution due to the preparation. We consider the signatures of each of these processes, focusing only on the most robust features of the data. Our prior theoretical analysis of the I_2/Ar system with the use of a vibrational self-consistent field (VSCF) for the analysis of anharmonic modes, their couplings, and the expected effect on TRCARS observables serves as a backdrop for this discussion.[4]

In electronically resonant CARS the preparation of the Raman packet entails evolution on the electronically excited state. Although this evolution is limited in time to the arrival of the packet into the Stokes window, 10–30 fs, depending on the Stokes shift, it will nevertheless impart momentum to lattice coordinates that are coupled through the electronic transition (electron–phonon coupling). Feedback following this impulsive drive should occur on the time scale of the characteristic local phonon periods, 0.5 ps$>\tau>$2 ps. Careful inspection of the envelopes of the time profiles of the signals reveals such modulations at early times. To uniquely assign and characterize the effect of impulsive momentum kicks, a more systematic set of accurate measurements is desirable.

Two important inhomogeneous sources of dephasing were considered explicitly in Ref. 4. The first of these recognizes that at finite temperature, the initial state, $\varphi^{(0)}=|v=0,\{n_i(T)\}\rangle$ consists of the chromophore in $v=0$, and a thermal distribution of phonon occupation numbers n_i. On the preparation time scale, save for the momentum kicks imparted to selected modes, the phonon distribution is frozen. Due to the statistical distribution of initial phases in the coupled modes, the system will dephase even if the phonons are harmonic. This will contribute a temperature-dependent inhomogeneous mechanism for dephasing, which is linear in vibrational quantum number due to the linear dependence of the anharmonic coupling on v. Although we see a linear dependence of dephasing rates on v, the only measurable temperature dependence occurs at $v=13,14$. A vibration-specific temperature dependence is not consistent for this mechanism, suggesting that this contribution is small. A second important inhomogeneous contribution can be expected from lattice defects. The explicit model considered was that of vacancy point defects. Due to the anharmonic coupling between chromophore and vacancies, this mechanism also leads to dephasing rates linear in vibrational quantum number. Moreover, due to the bimodal distribution of vacancy-induced frequency shifts, the model predicts sidebands in the spectrum and accordingly, modulation on the envelope of the signal. The predicted observable TRCARS signal for a $v=10,11$ packet (Fig. 7 of Ref. 4) is in surprisingly good agreement with the $v=13,14$ packet observed in Fig. 8. Sidebands separated by 12 cm^{-1}, which coalesce with the central peak between $T=15$ and 35 K, was predicted there, as is observed here. This is the origin of the 2.5 ps modulation of the time-domain signal. The assumed vacancy concentration in the model was 1.4%. Since the depth of modulation of the signal is also in quantitative agreement with the model, we must conclude that the defect concentration is comparable in the experiment. Small sidebands, which appear as pedestals in the Fourier spectra (see the spectra in Fig. 4) are often observed with varying amplitude, consistent with the expectation that defect concentrations may vary with preparation and with the selected spot in a given film. Although the films are polycrystalline, the measurement is carried out in selected ~ 50 μm spots that may also contain grain boundaries and, hence, unusual densities of defects.

The observation of dephasing rates linear in vibrational quantum number is consistent with the fact that the coupling between the molecular vibrations and lattice phonons is weak. Then spectral shifts and dephasing rates will be mediated through the lowest-order anharmonic couplings to the lattice modes, namely, the linear term $\alpha_{\mathbf{k}}q_{\mathbf{k}}$ and the quadratic terms $\beta_{\mathbf{kk}'}q_{\mathbf{k}}q_{\mathbf{k}'}$ (where $q_{\mathbf{k}}$ represents the normal coordinate of mode $\mathbf{k}$). The VSCF calculations considered the quadratic coupling terms $\beta_{\mathbf{kk}'}$ by evaluating the energy differences for the molecular vibrations with and without the occupation of a given lattice mode. A strictly linear dependence on v is observed for a given normal mode of the lattice, as well as for the mean over all modes. It is therefore safe to assume that the same holds for the nondiagonal couplings, $\beta_{\mathbf{kk}'}$. In essence, the observed linear dependence of dephasing with vibrational quantum numbers is consistent with expectations based on the interaction potential between iodine and argon.

Homogeneous dynamical dephasing, both dissipation $(1/T_1)$ and pure dephasing $(1/T_2)$, occurs through the scattering of phonons. Given the Debye limit of solid Ar of 65 cm^{-1}, dissipation of a quantum of molecular vibration of 200 cm^{-1} must be accompanied by the creation of at least three phonons. Pure dephasing occurs through the quasi-elastic scattering of phonons on the impurity and is most commonly diagnosed through temperature dependence studies.[19,20] Clearly, in the limit $T\to 0$ a finite dephasing rate must be reached. So, quite generally, we may expect:

$$\gamma=\gamma_0+\gamma(T), \quad \text{where} \quad \gamma_0=\gamma(T\to 0). \tag{7}$$

For pure dephasing, two important limits are widely accepted for $\gamma(T)$ in solids. The scattering of acoustic phonons, through a generalized linear coupling, $\beta_{\mathbf{kk}'}$, leads to a (T/T_D) dependence,[7] assuming a Debye density of states.[19,21,22] For solid Ar this would predict a 200-fold increase in $\gamma(T)$ for the experimental range of $T=17-35$ K. The absence of such a dramatic effect would imply that $\gamma_0 \gg \gamma(T)$ in the measured temperature range, i.e., dephasing due to scattering of acoustic phonons is negligible. Alternatively, the process may be driven through coupling to a particular coordinate, a pseudo-local mode (PLM), in which case an exponential temperature dependence given by the probability of occupation of the mode is to be expected:[23,24]

$$\gamma=\gamma_0+\frac{1}{2\tau}\exp(-E_{PL}/k_BT). \tag{8}$$

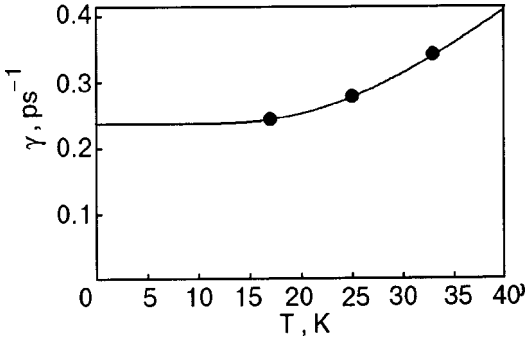

FIG. 9. The temperature dependence of measured dephasing rates (filled circles) and the curve for dephasing via a pseudo-local mode at the Debye edge [see Eq. (8)].

The limited data, the T-dependent rates for the $v=13$, 14 packet, fit this scheme, as shown in Fig. 9. The parameters for the curve are: $\gamma_0=0.237$ ps^{-1}, $\tau=0.25$ ps, $E_{PL}=98$ K (or $\omega_{PL}=68$ cm^{-1}). The implied pseudo-local mode is just outside the Debye edge, $E_D(\mathrm{Ar})=93$ K. The introduction of the impurity does generate such localized modes, modes which are intimately coupled to the molecule.[4] In this model, τ is interpreted as the local mode lifetime (the time it takes for the local mode to decay into acoustic phonons).[24] Evidently, the mode decays in half a period of its motion, which may be regarded as the fast-exchange limit where Eq. (8) is applicable.

The absence of a measurable temperature dependence for the lower vibrations, and below $T=17$ K in the case of $v=13$, 14, implies that we are in a regime where γ_0 dominates. This limit may be determined by inhomogeneous broadening due to lattice defects.

While difficult to ascertain this possibility, inhomogeneous effects can in principle be eliminated through degenerate four-wave mixing measurements (photon echo).[25] Given the elimination of inhomogeneous contributions, it is interesting to speculate as to what mechanism would control the residual dephasing, or Raman linewidth. The common assumption is that γ_0 will be determined by dissipation, since this appears to be a spontaneous process, in contrast to dephasing, which is usually defined to be stimulated via the scattering of thermal phonons. We can expect classical molecular dynamics to provide a useful estimate for vibrational relaxation, given the fairly well understood potentials of this system. To this end, we have carried out simulations using reasonable potentials: Morse for I–I; Lennard-Jones for Ar–Ar and I–Ar. In a simulation box of 250 Ar atoms and a single I_2 molecule isolated in a divacancy, we calculate the rate of energy loss from trajectories propagated for 100 ps. At the classical temperature of 20 K, we estimate a vibrational relaxation time of 200 ps for $v=5$ and 70 ps for $v=15$. Thus the classical estimates indicate rates of relaxation more than one order of magnitude smaller than what is observed experimentally for γ_0. These results may well depend on the details of the assumed potentials, a systematic analysis of which has not been done. Pump–probe experiments which follow population dynamics, should provide a more definitive assessment of dissipation rates. We find the calculated long $1/T_1$ times sensible. Moreover, since the relaxation is a multiphonon process, one would expect the classical limit to be an overestimate for the rate. It would seem to us that a spontaneous three-phonon process is less likely than pure dephasing at absolute zero, if it is recognized that in a strictly quantum world spontaneous processes are driven by quantum zero-point fluctuations.[26] If we allow for zero-point fluctuations in phonon modes, in the form of creation–annihilation events, then a natural mechanism for pure dephasing at 0 K would seem more plausible than dissipation driven by multiphonon fluctuations. We intend a more quantitative analysis of this distinction, since the issue is of relevance when control of decoherence is contemplated.

5. CONCLUSIONS

Through TRCARS experiments, we have been able to prepare and interrogate vibrational packets at vibrations as high as $v=14$ in the model system of matrix-isolated molecular iodine. This, to our knowledge, may be the first systematic study of its kind. The creation of vibrational coherences of large amplitude (up to $v=14$), which is requisite for meaningful coherent control in condensed media, has been demonstrated.

The coherences are long-lived, more than 100 vibrational periods at $v=14$, much longer than necessary for most control targets of a chemical nature. These time-domain experiments have a higher spectral resolution than has been possible in frequency-domain measurements. More importantly, the direct time-domain measurements allow detailed insights in the dephasing processes. Nevertheless, here we have focused on the more robust features of the data.

The coherence decay time decreases from 16 ps near $v=3$ to 2.5 ps near $v=13$, showing a nearly linear dependence on vibrational quantum number.

The decoherence rates are a weak function of temperature for vibrations below $v=10$, indicating that the process is controlled by the 0 K limit. We speculate on the nature of dephasing in this limit, with the conjecture that it will be driven by quantum zero-point fluctuations of the phonons.

A thermal contribution to dephasing is observed for packets prepared at $v=13$, 14. The dependence is exponential, consistent with dephasing by a pseudo-local mode just outside the Debye edge of pure Ar. This mode decays into acoustic phonons in a half-period of the motion.

Inhomogeneous dephasing due to vacancy point defects has been identified by the quantitative agreement of the observable signal with an earlier theoretical prediction.

The above conclusions are derived from limited experimental scrutiny, because the signal degrades during the measurements. The origin of this decay is shown to be due to two-photon induced photodissociation.

A more complete analysis of the breaking of the Ar cage and the kinetics and dynamics of the process will be taken up elsewhere. Under the same irradiation conditions, photodissociation rates are much smaller in solid Kr; as such, they provide a more useful medium for systematic measurements. We have initiated such measurements.

This research was made possible through a grant from the USAFOSR (F49620-01-1-0449).

*E-mail: aapkaria@uci.edu

[1] M. Karavitis, R. Zadoyan, and V. A. Apkarian, J. Chem. Phys. **114**, 4131 (2001).
[2] S. Mukamel, *Principles of Nonlinear Optical Spectroscopy*, Oxford University Press, New York (1999).
[3] J. C. Wright, Int. Rev. Phys. Chem. **21**(2), 185 (2002).
[4] Z. Bihary, M. Karavitis, R. B. Gerber, and V. A. Apkarian, J. Chem. Phys. **115**, 8006 (2001).
[5] H. Dubost, J. Low Temp. Phys. **111**, 615 (1998).
[6] M. Broquier, A. Cuisset, C. Crepin, H. Dubost, and J. P. Galaup, Phys. Rev. Lett. **94**, 575 (2001); C. Crepin, M. Broquier, H. Dubost, J. P. Galaup, J. L. Le Gouet, and J. M. Ortega, Phys. Rev. Lett. **85**, 964 (2000).
[7] W. F. Howard and L. Andrews, J. Raman Spectrosc. **2**, 442 (1974).
[8] S. Maeda, T. Kamisuki, and Y. Adachi, Adv. Nonlinear Spectrosc. **30**, 807 (1999).
[9] A. V. Benderskii, R. Zadoyan, and V. A. Apkarian, J. Chem. Phys. **107**, 8437 (1997).
[10] M. Macler and M. Heaven, Chem. Phys. **151**, 219 (1991).
[11] R. Zadoyan, Z. Li, C. Martens, P. Ashjian, and V. A. Apkarian, Chem. Phys. Lett. **218**, 504 (1994).
[12] J. Helbing and M. Chergui, J. Chem. Phys. **115**, 6158 (2001).
[13] P. B. Beeken, E. A. Hanson, and G. W. Flynn, J. Chem. Phys. **78**, 5892 (1983).
[14] R. Bohling, J. Langen, and U. Schurath, Chem. Phys. **130**, 419 (1989).
[15] D. Magde, J. Chem. Phys. **68**, 3717 (1978).
[16] J. Almy, K. Kizer, R. Zadoyan, and V. A. Apkarian, J. Phys. Chem. A **104**, 3508 (2000).
[17] J. Tellinghuisen, J. Chem. Phys. **76**, 4736 (1982).
[18] Z. Li, R. Zadoyan, V. A. Apkarian, and C. C. Martens, J. Phys. C **99**, 7453 (1995).
[19] J. L. Skinner and D. Hsu, J. Phys. C **90**, 4931 (1986); Chem. Phys. **128**, 35 (1988).
[20] M. A. Krivoglaz and V. V. Hyzhnyakov, in *Zero-Phonon Lines*, edited by O. Sild and K. Haller, Springer-Verlag, Berlin (1988).
[21] R. H. Silsbee, Phys. Rev. **128**, 1726 (1962).
[22] D. E. McCumber, J. Math. Phys. **5**, 508 (1964); D. E. McCumber and M. D. Sturge, J. Appl. Phys. **34**, 1682 (1963).
[23] C. B. Harris, J. Chem. Phys. **67**, 5607 (1977); C. B. Harris, R. M. Shelby, and P. A. Cornelius, Phys. Rev. Lett. **38**, 1415 (1977).
[24] P. deBree and D. A. Wiersma, J. Chem. Phys. **70**, 790 (1979).
[25] K. D. Rector and M. D. Fayer, Int. Rev. Phys. Chem. **17**, 261 (1998), and references therein.
[26] D. Cohen, J. Phys. A **31**, 8199 (1998).

This article was published in English in the original Russian journal. Reproduced here with stylistic changes by AIP.

Prompt and delayed secondary excitons in rare gas solids

M. Kirm, S. Vielhauer, and G. Zimmerer*

Institut für Experimentalphysik, University of Hamburg, 149 Luruper Chaussee, Hamburg D–22761, Germany

V. Kisand

Institute of Physics, University of Tartu, 142 Riia, Tartu 51014, Estonia

E. Sombrowski and B. Steeg

Deutsches Elektronensynchrotron DESY, 85 Notkestrasse, Hamburg 22607, Germany

Fiz. Nizk. Temp. **29**, 1081–1092 (September–October 2003)

Direct and indirect creation of excitons in rare gas solids has been investigated with reflectivity and luminescence spectroscopy. For the heavy rare gas solids Kr and Xe, new and more reliable exciton parameters have been deduced. With time-resolved luminescence spectroscopy, fast and delayed secondary-exciton creation has been established and separated. Thermalization of photocarriers and their delayed recombination have been analyzed, including a first attempt to investigate the influence of excitation density on the carrier dynamics. The existence of excitonic sidebands of the ionization limits E_i (either band-gap or inner-shell ionization limits) in prompt secondary exciton creation has been established. The threshold energies of these sidebands are given by $E_{\mathrm{th}} \approx E_i + nE_{\mathrm{ex}}$ (n is an integer, E_{ex} is the exciton energy). The sidebands are ascribed to the formation of electronic polaron complexes, superimposed on the inelastic scattering of photoelectrons. © *2003 American Institute of Physics.*
[DOI: 10.1063/1.1619352]

INTRODUCTION

At the onset of optical excitation of rare gas solids (RGS) in the vacuum ultraviolet spectral range, pronounced absorption lines are found. They arise from the creation of bound pairs of valence holes and conduction electrons at the center of the Brillouin zone (Γ point) and can be arranged in two series, $\Gamma(3/2)$ and $\Gamma(1/2)$, depending on the total angular momentum of the hole, $j=3/2$ or $j=1/2$. These excitations have been the subject of numerous investigations because rare gas solids are model systems for excitons in insulators.[1–4] It is not the purpose of this article to review the field, but to describe some special aspects of exciton creation which have been investigated in recent years. We have to discriminate between direct and indirect creation of excitons. Direct creation is achieved, e.g., by optical excitation with an appropriate photon energy, $E_{\mathrm{ph}}=E_{\mathrm{ex}}$ (E_{ph} is the photon energy of excitation; E_{ex} is the exciton energy). Some aspects of direct creation will be discussed in Sec. 2, because they are necessary for a better understanding of the indirect creation processes. Indirect exciton creation arises from (i) recombination of electron–hole pairs, (ii) inelastic scattering of photoelectrons, and (iii) excitonic sidebands of valence or inner-shell excitations.

All experimental results have been obtained with synchrotron radiation (SR) excitation at the Hamburger Synchrotronstrahlungslabor HASYLAB at DESY, Hamburg. Two beamlines have been used, namely beamline "I" with the set-up SUPERLUMI (normal incidence; range of excitation $\leqslant 40$ eV), and beamline "BW3" (grazing incidence; range of excitation 30 eV$\leqslant h\nu \leqslant$1000 eV). As the main part of the present paper deals with time-resolved data, some details are given here. SR at HASYLAB consists of pulses with FWHM$\cong$150 ps, at a repetition rate between 5 and 1 MHz, depending on the mode of operation. For more details, we refer to the original papers cited. If necessary, in a few cases, more details are given in the text.

1. DIRECT EXCITON CREATION

1.1. Reflectivity and new evaluation of exciton parameters

Excitons in rare gas solids are ascribed to the "intermediate " type,[5] which means that the energy positions of the lines corresponding to principal quantum numbers $n>1$ are well described by the Wannier formula,

$$E_{nj}=E_j-\frac{B_j}{n^2} \tag{1}$$

(E_{nj} is the energy of an exciton with principal quantum number n; E_j is the ionization limit of the exciton series; $E_{3/2}=E_g$, E_g is the band gap energy; B_j is the binding energy of the exciton series). According to previous measurements, however, the members with $n=1$ yield more or less pronounced deviations from the Wannier formula (see, e.g., Ref. 3). The reflectivity curves of Kr and Xe have been carefully remeasured in the excitonic range because the preparation of polycrystalline[6,7] or even monocrystalline rare gas samples[8] with high structural quality has been developed. Moreover, contrary to the early investigations, now a more precise determination of the energies of $n=1$ excitons from photoluminescence (the so-called free-exciton (FE) lines) is possible (see Sec. 1.2). As an example, the reflectivity of Kr (Ref. 9) is presented in Fig. 1 (for Xe see Ref. 10). Five members of

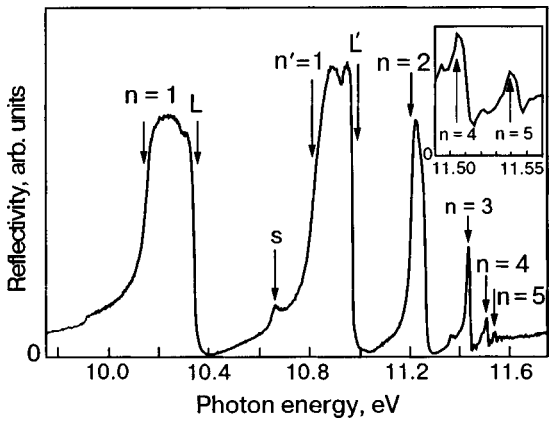

FIG. 1. Reflectivity of solid Kr, measured at $T=6$ K with a resolution interval $\Delta\lambda=0.6$ Å.[9] The inset shows the range of $n=4$ and $n=5$ excitons in an enlarged scale.

the $\Gamma(3/2)$ series are observed. The $n=1$ band clearly displays an exciton–polariton nature. In the case of Xe, a quantitative analysis has been performed in terms of the exciton–polariton model,[8] showing that the deduced energy of the transverse exciton agrees with the energy of the FE line in photoluminescence. In the case of Kr, a line-shape analysis of the reflectivity curve in terms of the exciton–polariton model has not been carried out because only the energy of the transverse exciton, which was taken from luminescence, is required for the following conclusions.

In Fig. 2, the energies of the Kr excitons are plotted as a function of $1/n^2$. All energies, including $n=1$, obey the Wannier formula with high accuracy. The same is true for Xe.[10] Thus the earlier discussion of corrections to the $n=1$ value (see, e.g., references given in Refs. 1–5) is obsolete in the case of Kr and Xe. This, however, does not mean that the model of the intermediate exciton is ruled out in general. In the case of the light rare gas solids Ar and Ne the $n=1$ value indeed deviates from the Wannier formula. Interestingly, in the light rare gas solids, the excitons are unstable against exciton–lattice interaction, whereas they are metastable in the case of the heavier rare gas solids. Consequently, no FE lines but mainly the emission of self-trapped excitons (STE) show up in the luminescence spectra of Ar and Ne, whereas both types of luminescence coexist in the case of Xe and Kr.

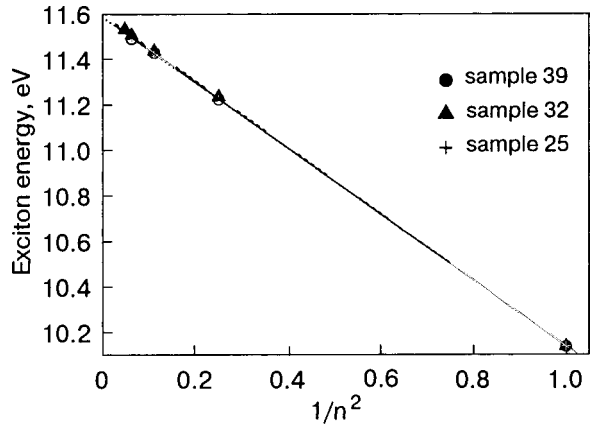

FIG. 2. Plot of exciton energies of the $\Gamma(3/2)$ series of solid Kr, measured at $T=6$ K, as a function of $1/n^2$ (n is the exciton quantum number).[9]

TABLE I. Exciton parameters of solid Kr and Xe at $T=6$ K.

Parameter	Unit	Value of the parameter	
		Kr	Xe
Binding energy	eV	(1.45±0.02)[a]	(0.903±0.036)[d]
		1.53[b]	1.02[b]
		1.73[c]	0.86[c]
Band gap	eV	(11.59±0.01)[a]	(9.298±0.005)[d]
		11.61[b]	9.33[b]
		11.67[c]	9.28[c]
Reduced mass	m_0	(0.377±0.005)[a]	(0.327±0.005)[d]
		0.40[b]	0.37[b]
		0.41 (with $\varepsilon_r=1.80$)[c]	0.31 (with $\varepsilon_r=2.23$)[c]

Comment: [a]Ref. 9;[b]Ref. 3;[c]Ref. 11;[d]Refs. 10, 30.

In Table I the exciton parameters deduced from the new reflectivity curves are presented and compared with previous results.

1.2. Radiative exciton decay

Following photon excitation of valence excitons of Kr and Xe, luminescence spectra are observed which yield (i) narrow lines originating from the free $n=1$ (transverse) exciton and (ii) broad, Stokes shifted bands originating from self-trapped excitons. Results[9,12] for Kr are given in Fig. 3 (Xe results are published, e.g., in Ref. 13). The Kr results are of special importance because the samples were nearly free from Xe impurities, which efficiently quench the Kr FE line and which also modify the STE bands as a consequence of the luminescence of heteronuclear Kr–Xe* centers.[9]

The decay curves in Fig. 3 display the decay of the FE line and the decay of the STE emission. The decay of the FE line is rather fast and nonexponential. For Xe, the details have been discussed in Ref. 13. The STE luminescence decay includes two components, one in the nanosecond range, originating from the singlet state of the STE, and another in the range of seconds, originating from the triplet state and showing up in the figure as a flat background. An analysis of the fast component shows that it displays a cascade behavior involving the decay of the FE line and the lifetime of the STE singlet state.[14]

These remarks on the radiative decay of free excitons have been included because the central part of the present paper will deal with *modifications* in the case of indirect exciton creation.

2. SECONDARY EXCITONS FOLLOWING VALENCE EXCITATIONS

2.1. Decay curves following near-band-gap excitation

2.1.1. Xenon and krypton

The decay curves of the FE line observed under direct excitation are nonexponential with an approximate decay rate of the order of some 10^8 s^{-1} and a rise time <100 ps

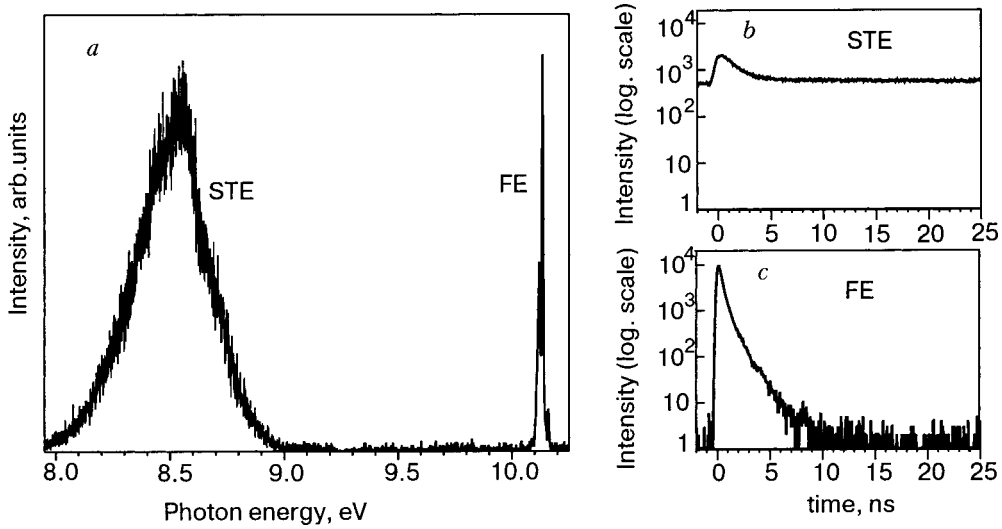

FIG. 3. *a*) Luminescence of nearly Xe-free solid Kr, excited by 10.42 eV photons at $T=6$ K and measured with a resolution interval $\Delta\lambda=12$ Å. *b*) Decay curve of STE luminescence (measured at 8.55 eV), and (*c*) decay curve of FE luminescence (measured at 10.14 eV) of the same sample. Both decay curves were obtained with a resolution interval $\Delta\lambda=9$ Å at 6 K under excitation at 10.42 eV.[12]

(experimental time resolution).[12,13] The situation changes as soon as the photon energy of excitation exceeds the band-gap energy. Then, as a result of the primary excitation, free electron–hole pairs are created. Nevertheless, the FE line still shows up with nearly the same intensity as under direct excitation of excitons. It is therefore obvious that recombination of electrons and holes into free excitons occurs. The decay curves, however, change dramatically, as is shown for Kr[12] and Xe[15] in Figs. 4 and 5. The parameter of the curves is the excess energy, $E_{\text{excess}}=E_{\text{ph}}-E_g$. It is the sum of the kinetic energies of the two carriers involved. With increasing excess energy, the cascade-type shape gets more and more pronounced. Apart from the spike near time zero, the whole luminescence intensity is delayed compared to the decay of directly excited excitons (for comparison, a directly excited curve is included in Fig. 5). This delay arises from a convolution of thermalization of the carriers and their recombina-

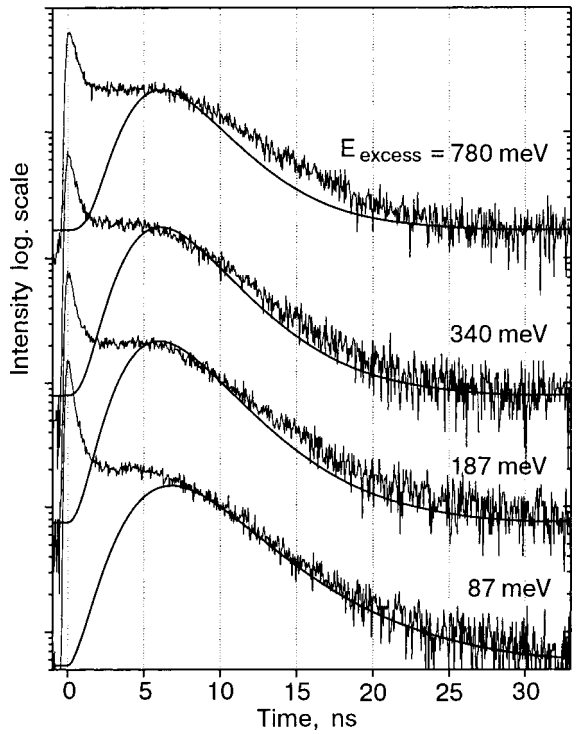

FIG. 4. FE decay curves of Kr, measured at $T=6$ K, together with fitting results (full lines) for the delayed part.[16] Resolution intervals of 35 Å in excitation and 8 Å in emission. The parameter of the curves is the excess energy.

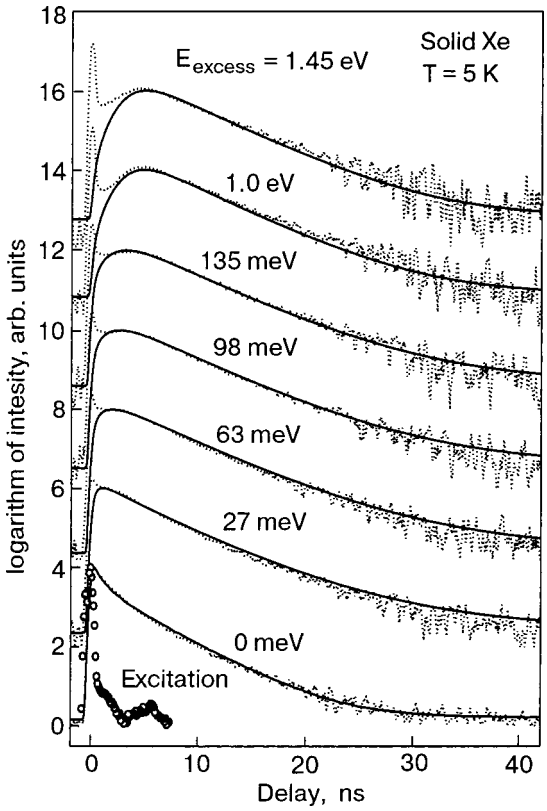

FIG. 5. FE decay curves of Xe, measured at $T=5$ K, together with fitting results (full curves) for the delayed part.[15] The parameter of the curves is the excess energy. For comparison, the instrument function (convolution of the excitation pulse with the response of the detector and the electronics) is included (open circles).

tion. Here, a special aspect of rare gas solids comes into play: the simple fcc lattice of the rare gas solids allows only for acoustical phonons, a circumstance that slows down thermalization of the carriers compared to alkali halides, for example. It turns out that the bottleneck of recombination is the thermalization process, because the recombination cross section is a sensitive function of the velocity of the carriers.[15]

The curves in Figs. 4 and 5 show also spikes at $t \approx 0$. They are ascribed to experimental artifacts. The monochromators used are single-pass instruments; therefore, a ''white'' background of VUV radiation (primary monochromator $\approx 10^{-3}$, secondary monochromator $\approx 10^{-2}$) is unavoidable. The background shows up at $t \approx 0$ as scattered light or even leads to direct excitation of excitons, although the photon energies chosen by the monochromator settings do not allow it.

The shape of the delayed FE luminescence was used to analyze the recombination dynamics of the photocarriers.[15] The full curves in Figs. 4 and 5 are results of model calculations in which the carrier dynamics have been treated in the following way.[15,16] The starting point is an initial mean kinetic energy of the carriers,

$$E_{0e,h} = \frac{m_{h,e}}{m_e + m_h} E_{\text{excess}} \tag{2}$$

(the excess energy is shared among the carriers according to the effective masses m_e and m_h), and a density of electrons and holes, $n_{e,0} = n_{h,0}$, which has been established due to the nearly δ-like photoexcitation. If it is assumed that the carriers achieve a Maxwellian distribution of temperatures T_e and T_h, the electron (e) and hole (h) energy loss due to scattering on acoustical phonons is described by[17]

$$\left\langle \frac{dE_{e,h}}{dt} \right\rangle_{\text{ac}} = -\frac{8\sqrt{2} E_d^2 m_{e,h}^{5/2}}{\pi^{3/2} \hbar^4 \rho} (kT_{e,h})^{3/2} \left(\frac{T_{e,h} - T_L}{T_{e,h}} \right) \tag{3}$$

with deformation potential E_d, effective masses m_e and m_h, mass density ρ, lattice temperature T_L, and Boltzmann's and Planck's constants k and $\hbar$. Since $m_h \gg m_e$ for RGS, the holes relax much faster than the electrons [note the factor $m_{e,h}^{5/2}$ in the numerator of Eq. (3)]. For that reason, we assume $T_h = T_L$.

For $t > 0$ the evolution of the carrier densities due to exciton formation and the exciton density n_{ex} are described by the following rate equations:

$$\frac{dn_{e,h}}{dt} = -\sigma(T_e) n_e n_h v_{\text{rel}}(T_e) - \frac{n_{e,h}}{\tau_{nr}}$$

and

$$\frac{dn_{\text{ex}}}{dt} = \sigma(T_e) n_e n_h v_{\text{rel}}(T_e) - R(t) \tag{4}$$

with a temperature-dependent cross section $\sigma(T_e)$ and relative velocity $v_{\text{rel}}(T_e)$. The termn $n_{e,h}/\tau_{nr}$ describes additional nonradiative carrier losses, e.g., at the surface. The decay of the exciton itself is described by the decay term $R(t)$, for which the *experimental FE decay curves following direct photoexcitation of the excitons*, measured on the same sample, were used. For $\sigma(T_e)$ we use the formula given by Reimand *et al.* in Ref. 15[1)]

$$\sigma(T_e) = \frac{1}{(4\pi)^3} \frac{16\sqrt{2} e^6 E_d^2 m_e^{5/2}}{3\sqrt{3\pi} \hbar^4 c_s \rho (\varepsilon_0 \varepsilon_r)^3} \sqrt{\frac{m_e}{m_h}} \frac{1}{\sqrt{kT_L} (kT_e)^2} \tag{5}$$

which is a modification of the formula given by Avakumov *et al.*[19] for $T_e \neq T_h$ (e is the electron charge, c_s is the sound velocity, and $\varepsilon_0 \varepsilon_r$ is the dielectric permittivity).

In the case of Xe the values for c_s, ρ, ε_r, m_h, and E_d were taken from the literature.[1–4] T_L was measured. Moreover, the sample quality was sufficiently good to neglect the nonradiative term in the kinetic equations. Then the only free adjustable parameter in the calculations was the initial density. A hidden approximation is the definition of an electron temperature of the relaxing system via $E = (3/2) kT_e$ (E is the mean value of the kinetic energy).

For Xe the fits are quite acceptable. Nevertheless, the result has to be taken with care for the following reason. Among the parameters taken from the literature there are some which are known to high accuracy (c_s, ρ, and ε_r) and others which are rather uncertain (m_e, m_h, and E_d). Concerning the effective masses, another difficulty has to be mentioned. In the model, isotropic parabolic bands are assumed, whereas the band structure of Xe and Kr is anisotropic. Moreover, the excess energies in the experiment extend to large values where the parabolic approximation breaks down. Therefore it is questionable to use the data for deducing more-reliable values of the mass or the deformation potential, for example.

In the case of Kr, the model was modified in the following way. The term $E_d^2 m_3^{5/2}$ in the nominator of Eq. (5) is the most important factor. It is connected with the low-field mobility according to[17,20]

$$\mu_0 = \frac{2}{3} \frac{\sqrt{2\pi} e \hbar^4 \rho v_l^2}{E_d^2 m_e^{5/2} (k_B T_L) \sqrt{k_B T_e}}. \tag{6}$$

In the case of the low-field mobility one has $T_L \approx T_e$, and ρv_l^2 is sufficiently well known (v_l is the longitudinal sound velocity). Therefore, $E_d^2 m_e^{5/2}$ was calculated from the mobility measurements of Miller *et al.*[21] In other words, by using an experimental result, the most uncertain parameters were eliminated.[2)] The Kr fits were obtained in this way. Although they are not as good as for the case of Xe, they are more satisfactory because the number of parameters has been decreased. The parameters of the fits are collected in Table II.

The values of the initial carrier densities are by far much lower than those estimated from the photon flux and from the value of the absorption coefficient at the respective photon energy of excitation[15] for the following reasons. The initial density is the density after redistribution of the carriers via Coulomb scattering. During this first stage of relaxation, carrier diffusion decreases the density. Here, the geometry of excitation comes into play. The size of the spot at the sample surface is about 0.3×4 mm. The penetration depth of light is of the order of a few hundred angstroms. On the other side, it was shown that the scattering length of excitons is of the order of 1000 Å.[13] The scattering lengths of the carriers should be similar because both are scattering on acoustic phonons. With a scattering length exceeding the thickness of

TABLE II. The values of the parameters used for the fits of the time dependence of delayed FE luminescence in solid Kr and Xe shown in Figs. 4 and 5. The values for m_e, m_h, v_l, c_s, ρ, and ε_r are taken from Refs. 1–4. E_d .was taken from Ref. 22. For $C_{\exp}$ see text.

Parameter	Unit	Value of the parameter	
		Kr	Xe
Effective electron mass, m_e	m_0	0.42	0.35
Effective hole mass, m_h	m_0	3.6	2.1
Initial carrier density, N_0*	$1/\mathrm{m}^3$	$3.6\cdot10^{14}$	$6\cdot10^{16}$
Initial excess energy, E_{excess}	meV	780	1450
Deformation potential, E_d	eV	not needed	0.79
$C_{\exp} = E_d^2 m_e^{5/2}$	$\mathrm{J}^2\cdot\mathrm{kg}^{5/2}$	$4.83\cdot10^{-114}$	not used
Longitudinal sound velocity, v_l	m/s	1370***	not needed
Averaged sound velocity, c_s	m/s		830****
Crystal temperature, T_L	K	5.5	
Nonradiative losses, $\Gamma_{nr} = 1/\tau_{nr}$	1/s	0**	0**
Density of solid Kr at 5 K, ρ	kg/m^3	3092.6	3781
Relative dielectric permeability, ε_r		1.88	2.22

*The values were obtained neglecting the correction pointed out to us by A.N. Vasil'ev (see footnote 1). Including the correction means that the values have to be multiplied by a factor of $(4\pi)^3$.

**If the value of the nonradiative losses is smaller than $\approx 5\times10^7\ \mathrm{s}^{-1}$, its influence on the fits can be neglected.

***In the case of Kr the longitudinal sound velocity was used for the whole calculation.

****For the Xe calculations the averaged sound velocity was used.

the initially excited volume by an order of magnitude, diffusion of the carriers into the bulk will rapidly decrease the carrier density.

This, however, raises the question why spatial diffusion has not been taken into account in the rate equations. Diffusion has been neglected there because the holes get self-trapped in rare gas solids. In that case the spatial diffusion of the electrons in a localized positively charged background is suppressed. It seems as if the fitting parameter characterizes the distribution after hole-trapping.

2.1.2. Argon and neon

In the light RGS, free excitons are rapidly self-trapped. Therefore, the method used in the case of Kr and Xe to study thermalization and recombination of free carriers cannot be used. In the case of Ar, we succeeded in analyzing recombination with the luminescence of self-trapped excitons. The STE emission of Ar consists of a singlet and a triplet band.[1–4] The lifetime of the singlet emission is 1.8 ns.[23] The formation should therefore be observable in the decay curves of the singlet component.

The singlet and the triplet STE bands overlap spectrally, and the singlet contribution is much weaker than the triplet one. Therefore, at first a photon energy of luminescence had to be found to get an optimal singlet/triplet ratio and sufficiently high counting rates. The chosen photon energies were 9.76 and 10.21 eV (for comparison, the maximum of the triplet STE band is 9.72 eV and that of the singlet band is 9.83 eV[24]).

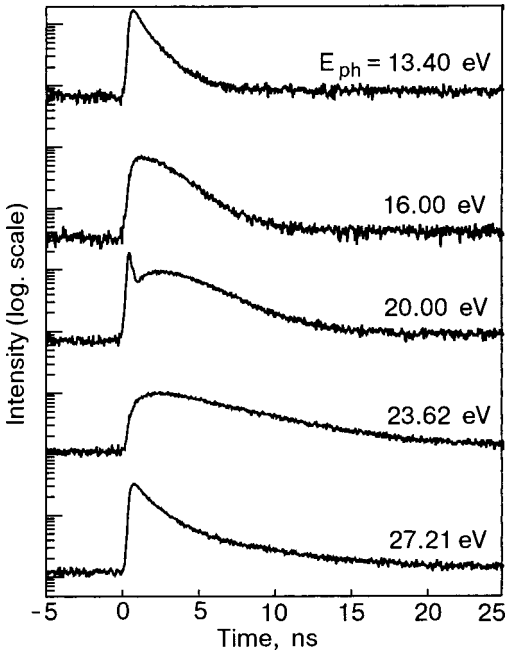

FIG. 6. Decay curves of the STE luminescence of Ar, measured at $T = 8$ K at a luminescence photon energy 10.21 eV.[24] The resolution intervals are $\Delta\lambda = 1.75$ Å in excitation and $\Delta\lambda = 11$ Å in emission. The photon energy of excitation is given at each curve.

In Fig. 6, decay curves of the singlet luminescence are shown. Most of the photon energies of excitation are above the band gap energy, $E_g = 14.16$ eV. With increasing photon energy of excitation, up to a value $E_{\text{th}} = E_g + E_{\text{ex}}$ (which will be discussed below; E_{ex} is the energy of the $n = 1$ exciton), the curves get more and more cascadelike. They were fitted with the sum of two exponentials,

$$I(t) = I_0 + A_1 \exp(-t/\tau_1) + A_2 \exp(-t/\tau_2) \tag{7}$$

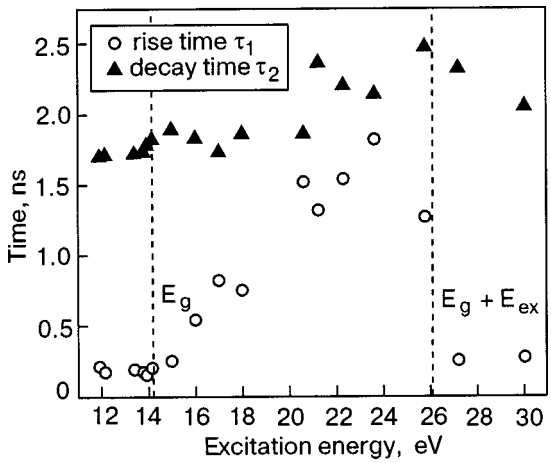

FIG. 7. Plot of the characteristic times of the cascade-type fits of decay curves of the STE singlet state of Ar as a function of photon energy of excitation.[24] The band gap at 14.15 eV and the threshold energy $E_{\text{th}} = E_g + E_{\text{ex}}$ are marked.

(A_1, A_2 with opposite sign). The results of the fits (τ_1 and τ_2) are shown in Fig. 7 as a function of photon energy of excitation.[24] Apart from the range where the values of both time constants are comparable, the decay time is independent of the photon energy of excitation.[3)] This time corresponds to the lifetime of the STE singlet, and the value is in good agreement with the one reported by Roick *et al.*[23] The rise times for excitation below the band gap correspond to the experimental time resolution. For excitation above the band gap, we observe a linear increase of the rise time until it reaches the value of the lifetime of the singlet state.[4)] Above E_{th}, the rise time drops to the value it has in the excitonic range of excitation. There the decay curves are nearly identical with those observed under excitation with a photon energy below the band-gap energy (see Fig. 6).

In view of Sec. 2.1.1, the increase of the rise time is ascribed to the thermalization of the electrons. From the slope of the linear increase of τ_2, a loss rate of approximately 5 eV/ns (slope of the straight line: 0.2 ns/eV) is obtained. With an average phonon energy 5 meV, this corresponds to a loss of one phonon energy per picosecond; in other words, an average scattering rate of 10^{12} s^{-1} has been observed.

Concerning Ne, systematic measurements like those in the case of Ar have not been possible up to now due to experimental difficulties.

2.2. Time-resolved excitation spectra and "prompt" secondary exciton formation

2.2.1. FE line of Kr and Xe

Under pulsed excitation with a sufficiently large interpulse period, the recombination-type luminescence at $t=0$ (defined by the excitation pulse) starts from zero. On the other hand, excitons created at $t=0$ start emitting at $t=0$ with maximum intensity. Based on these ideas, time-resolved excitation spectra can be used to discriminate between "prompt" (within the experimental time resolution) secondary excitons and delayed recombination-type secondary excitons. In a time-resolved excitation spectrum, following pulsed excitation, the luminescence intensity is measured within a time interval (called a time window) of length Δt with a delay δt with respect to the exciting pulse. Without a delay and with a short time window it is are sensitive to prompt secondary excitons. With a delay much larger than the lifetime of prompt excitons it is sensitive to recombination-type excitons. If the delay is zero, the time window accepts scattered light of the exciting light pulse. Therefore a slight delay is sometimes chosen to suppress scattered light, but at the expense of sensitivity for prompt luminescence. Some results have already been published.[10,12,25–27]

In Fig. 8, time-resolved excitation spectra of the FE line of Kr and Xe, measured in short time windows are presented. The details of the time windows are given in the figure caption. The special photon energy scale is well suited to illuminate the physics behind the phenomena observed. The unit of the scale is the exciton energy (Xe: 8.36 eV, Kr: 10.14 eV). As the zero point, the band-gap energy is chosen. In both curves we observe (i) low intensity until a threshold E_{th} at point 1 is reached, and (ii) a dramatic increase of intensity above E_{th}.

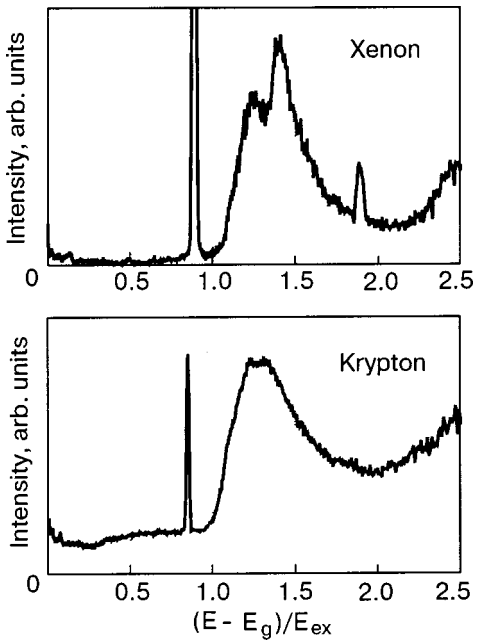

FIG. 8. Time-resolved excitation spectra of the FE luminescence of solid Kr[12] and Xe,[30] plotted on an energy scale which is described in the text. The time windows and time delays are: $\Delta t=0.94$ ns, $\delta t=0$ ns (Kr); $\Delta t=0.8$ ns, $\delta t=0.6$ ns (Xe). The sharp maxima arise from scattered light.

The low intensity underscores the slow formation of secondary excitons via recombination. The increase of the signal above the threshold underscores that in this range of excitation, "prompt" secondary excitons are created. In Kr as well as in Xe, an analysis[10,12] of the threshold energy shows that it is given within ± 0.2 eV by

$$E_{\text{th}}=E_g+E_{\text{ex}}. \tag{8}$$

This is the energy required (from the standpoint energy conservation) to obtain one electron–hole pair with negligible kinetic energy and one exciton. In both cases, the time-resolved excitation spectrum yields a broad maximum above E_{th}. It does not drop to the low value as on the low-energy side but levels off. At higher photon energies, another increase is found, starting approximately at an energy E_g+2E_{ex}.

There are two mechanisms for the prompt secondary exciton creation observed above the threshold E_{th}: (i) inelastic scattering of photoelectrons at a valence electron, resulting in an additional exciton, and (ii) *simultaneous* creation of an electron–hole pair and an exciton (electronic polaron complex[28]). Contrary to the electronic polaron complex, the scattering mechanism is a sequential process. The scattering time in the femtosecond regime cannot be resolved in our experiments, and therefore these secondary excitons are called prompt as well. On the other hand, excitons created simultaneously with an electron–hole pair could also be called "direct" because they are the result of a primary excitation process.

From an experimental point of view it is difficult to discriminate between the two mechanisms. At first, it was pointed out that discrimination should be possible via the

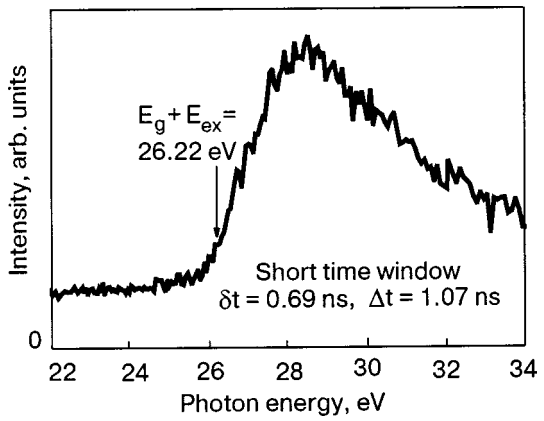

FIG. 9. Time-resolved excitation spectrum of STE luminescence of Ar.[24,31] Due to the photon energy of observation chosen (10.21 eV), the main contribution in the time window $\Delta t = 1.07$ ns and $\delta t = 0.69$ ns arises from the singlet STE. $T = 8$ K. Resolution intervals as in Fig. 6.

threshold energy because the simplest scattering model predicts a threshold considerably larger than the one predicted for the electronic polaron complex.[10] The simple model assumes parabolic bands, neglecting Bragg reflection across the Brillouin zone boundaries. With the so-called mutiple-parabolic-branch-band (MPPB) model of Vasil'ev *et al.*[29] it was shown that the threshold is practically the same for both mechanisms.[12,30] An argument in favor of the electronic polaron complex is the fact that theory predicts a resonance, as is observed, whereas the scattering process leads to a more stepwise increase of the excitation spectrum. Summing up, the curves are ascribed to inelastic scattering with a resonant enhancement near threshold due to the formation of electronic polaron complexes. In a certain sense, the time-resolved excitation spectra bring about excitonic sidebands of valence ionization, as predicted by theory: $E_{\rm res} = E_g + nE_{\rm ex}$, where n is an integer.[28]

2.2.2. The special case of argon and neon

In the light RGS, FE luminescence is missing. Time-resolved (Ar) and time-integrated (Ne) excitation spectra of the STE emission, however, yield similar results to the case of Xe and Kr. The drop of the rise time τ_2 (see Fig. 7) around $E_{\rm th}$ also shows that above $E_{\rm th}$ prompt secondary excitons are created. In Figs. 9 and 10, data are presented for Ar[24,31] and Ne.[24] In the case of Ar, the singlet component of the STE has been chosen as a fast decay channel for time-resolved excitation spectra (observation at 10.21 eV), while in the case of Ne, the emissions of the atomic-type STE at 16.75 eV and of the so-called W band at 15.5 eV were used for time-integrated measurements. Nevertheless, the threshold of prompt secondary exciton creation at $E_{\rm th} = E_g + E_{\rm ex}$ was observed. In the case of Ar, a broad resonance like in the heavy rare gases shows up, while in the case of Ne (time-integrated spectrum) a more steplike increase was found. It must be admitted that the spectral range of the Ne measurements is unfavorable for both beamlines used. The interesting features are close to the limits of the working ranges of the respective monochromators (left part of Fig. 10 for the normal-incidence monochromator; right part of Fig. 10 for the grazing-incidence monochromator), where the excitation intensity is small. The threshold itself and the creation of prompt secondary excitons is well established.

3. SECONDARY EXCITONS FOLLOWING INNER-SHELL EXCITATION

3.1. Excitonic sidebands of inner shell ionization limits

Here we start with a presentation of time-resolved excitation spectra of FE luminescence in the vicinity of the Kr $3d$ and Xe $4d$ inner-shell excitation (Fig. 11).[34] The (spin–orbit-split) ionization energies are Kr $3d_{5/2}$: 92.32 eV, Kr $3d_{3/2}$: 93.50 eV; Xe $4d_{5/2}$: 65.59 eV, Xe $4d_{3/2}$: 67.54 eV (averages of the values given by Resca *et al.*[32] and Kassühlke[33]). For comparison purposes, the spectra are aligned for the respective $d_{5/2}$ ionization limits, and the spread of the scales corresponds to the respective exciton energies (vertical lines). The numbers given at the abscissa, however, are electron-volts. Similar to the valence case, strong resonances with a threshold energy $E_{\rm th} = E_{d_{5/2}} + E_{\rm ex}$ are observed. In the case of Xe, the resonance is split. The second peak is ascribed to a resonance with a threshold $E_{d_{3/2}} + E_{\rm ex}$. Experiments with higher spectral resolution show that the Kr resonance also contains two contributions,

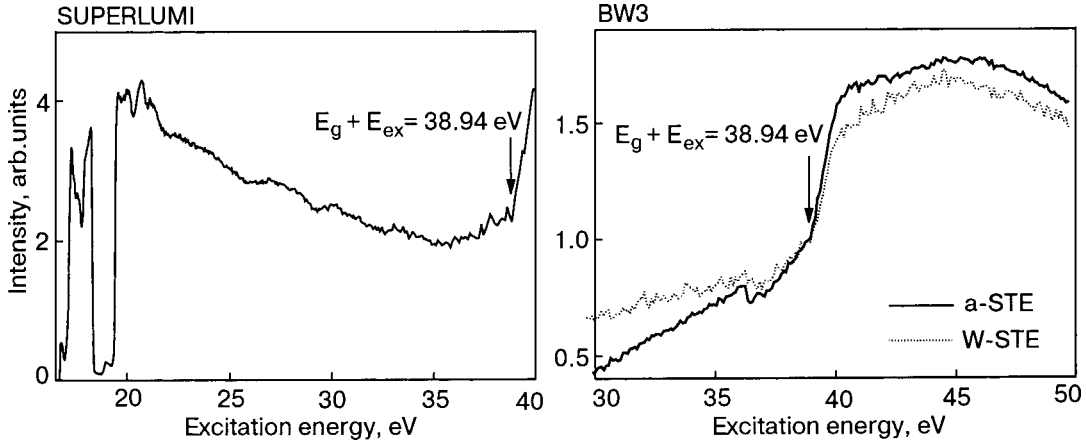

FIG. 10. Time-integrated luminescence excitation spectra of Ne.[24] Left part measured at the SUPERLUMI station (normal incidence range) at 16.75 eV (atomic-type STE). The curves in the right part were measured at the undulator beamline BW3 at 16.4 eV (a-STE) and at 15.5 eV (W-band). $T = 6$ K. The resolution interval in excitation was 0.01 eV (a-STE) and 0.02 eV (W band).

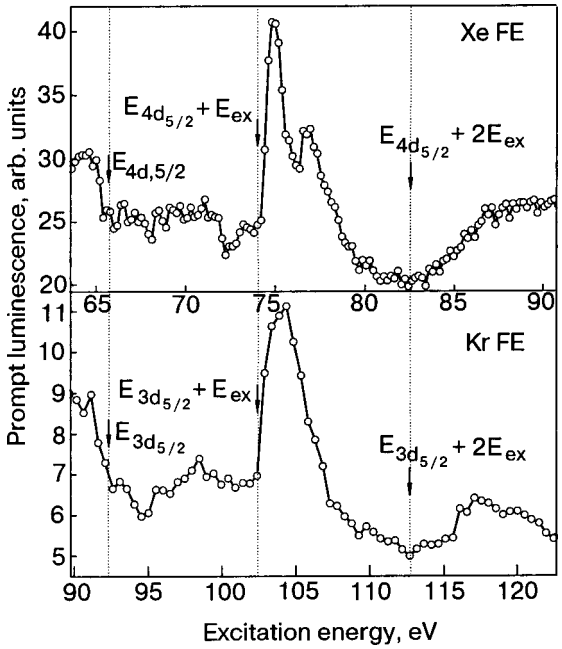

FIG. 11. Time-resolved excitation spectra of FE luminescence of Kr and Xe in the vicinity of the Kr $3d$ and the Xe $4d$ inner-shell excitations.[34] The time windows are, for Kr: $\Delta t=1.6$ ns, $\delta t=0$; for Xe: $\Delta t=1.2$ ns, $\delta t=0$. For details, especially for the scale used, see text.

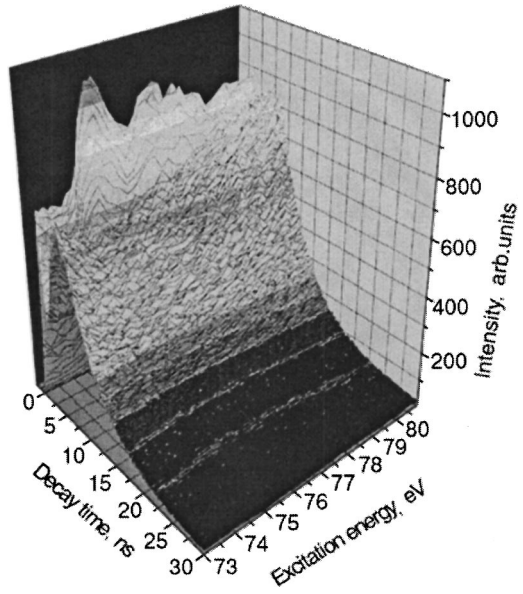

FIG. 12. Set of decay curves of the FE luminescence of Xe in the vicinity of the excitonic sideband of $5d_{5/2}$ ionization.[36] For details see text.

one of them being correlated to the $d_{3/2}$ ionization limit.[5)] Moreover, a second resonance with a threshold $E_{\rm th}=E_{d_{5/2}}+2E_{\rm ex}$ is observed. In conclusion, excitonic sidebands exist not only in the range of valence excitations but also in the range of inner-shell excitations.

In the case of light rare gas solids, up to now only the Ar $2p$ excitations have been investigated.[24,35] The results yield an excitonic sideband as well; however, degradation of the samples due to radiation damage is severe, and the excitation spectra therefore suffer from an overall decrease of intensity during the measurements.

4. CARRIER RECOMBINATION AND DENSITY EFFECTS

The influence of inner-shell excitation on the decay curves is illustrated in Fig. 12 with a set of decay curves of the FE line of Xe, presented as a function of time and photon energy of excitation around the excitonic sideband of $4d_{5/2}$ ionization. Prompt and delayed FE luminescence is observed.[36] As soon as the photon energy of excitation crosses the threshold of the excitonic sideband, the prompt part increases at the expense of the delayed part, indicating a redistribution among prompt and delayed secondary excitons. The prompt part below threshold originates from inelastic scattering of photoelectrons originating from valence excitations. The superposition of valence and inner-shell excitations makes a quantitative analysis difficult. Therefore, we restrict ourselves to presenting these qualitative results.

Excitation in the same range of excitation made feasible another type of investigation. The measurements were carried out at the undulator beamline BW3 of HASYLAB, with its high excitation intensity.[37] By tuning the undulator gap the spectral position of the first harmonic is tuned. With fixed settings of photon energy, this means that the intensity is tuned across the first harmonic. In this way, the excitation density can be varied by a factor of 50. This was used to establish density effects in the carrier dynamics. The models used to analyze the delayed FE decay predict such effects [Eq. (4)]. An excitation below the thresholds of the sidebands was chosen to avoid interference with the strong contribution of prompt secondary excitons originating from the sideband.

In Fig. 13, decay curves of the FE lines of Kr (excitation 85.3 eV) and Xe (excitation 66.1 eV) are presented.[38] The parameter of the curves is the initial carrier density at $t=0$, obtained from the fits. With increasing carrier density, the delayed part of the decay curves changes. The maximum shifts to smaller times. The full curves are fits with Eqs. (3)–(5). The variation of the excitation density by a factor of 50 leads to relatively small changes in the shape of the decay curves, although the product of the initial carrier densities in the rate Eq. (4) varies by a factor of 2500. This is explained by the fast increase of the recombination cross section $\sigma(T_e)$ [Eq. (5)] within the first nanoseconds,[15] which strongly influences the shape of the decay curves independently of the carrier densities.

Concerning the parameters, the situation is more complex than in the case of excitations into states near to the bottom of the conduction band. The initial kinetic energy of the photoelectrons (we still assume fast hole relaxation to the top of the valence band) is an open question because a broad distribution as a consequence of inelastic scattering of the *initially* created photoelectrons is expected. The time scale for this redistribution is far below the experimental time resolution. Therefore, a mean kinetic energy of the electrons after redistribution, E_0, was introduced as a fitting parameter to replace the well-defined energy for valence excitations, E_0, of Eq. (2).

It turned out that the nonradiative channel in the rate equations can not be neglected. The nonradiative rate, $1/\tau_{nr}$, has a more phenomenological character and strongly depends on sample conditions. As in the case of valence excitations, the initial carrier densities $n_{e0}=n_{h0}$ (after the fast redistributions due to elastic and inelastic scattering) have to

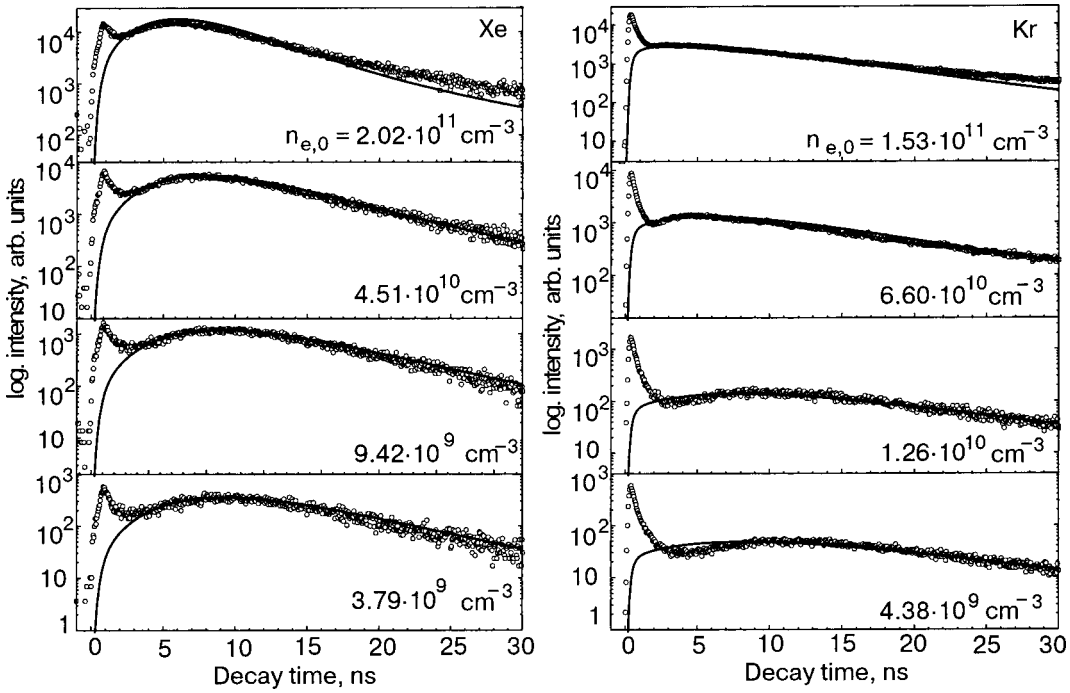

FIG. 13. Decay curves of the FE luminescence of Kr and Xe, measured with different excitation densities (circles), together with fitting results for the delayed part (full curves).[38] The initial electron densities for the calculations are given at each curve; the other fit parameters are given in Table III. The Kr curves were measured for 85.3 eV excitation at 12.5 K; the Xe curves were measured at 66.1 eV with excitation at 10.8 eV.

be included as fitting parameters. They were introduced with the constraint that they are proportional to the measured excitation density. As three fitting parameters were unavoidable, a fourth one, namely the effective mass of the electrons, was tolerated. Values are given in Table III.[36,38]

The m_e values are within reasonable limits, but cannot be taken as definite, since they are coupled to E_d in the model via $E_d^2 m_e^{5/2}$. The E_0 values seem to be in contradiction to photoemission data, which show that the bulk of the photoelectrons have kinetic energies between zero and 2 eV in the range of Xe $4d$ and Kr $3d$ excitation.[33] Note, however, that the electrons below the vacuum level are not observed in photoemission. E_0 obviously does not correspond to the mean kinetic energy after redistribution via electron–electron scattering as is observed in photoemission. It is ascribed to that range of kinetic energy in which the rates for electron–hole recombination and further phonon relaxation become comparable. An estimate for the *excitation density* based on absolute flux measurements is about two orders of magnitude higher than the results of the fits. This discrepancy corresponds to the small values of E_0 insofar as diffusion processes during the first stage of relaxation to E_0 may considerably reduce the density. Although significant simplifications have been applied, both for Kr and Xe the whole set of data can be described with a reasonable and consistent set of parameter values.

TABLE III. The values of the parameters used for the fits of delayed FE luminescence in solid Kr and Xe shown in Fig. 13. The values of m_e, $n_{e,0}$, E_0, and $\tau_n r$ and are results of fitting; m_k, v_l, c_s, ρ, and ε_r are taken from Refs. 1–4. E_d of Kr was calculated from the low-field mobility[21] with the published value of the effective electron mass given in Table II. E_d of Xe was taken from Ref. 22.

Parameter	Unit	Value of the parameter	
		Kr	Xe
Effective electron mass, m_e	m_0	0.36	0.73
Effective hole mass, m_h	m_0	3.6	2.1
Initial carrier density, $n_{e,0}$	$1/\mathrm{m}^3$	$1.53 \cdot 10^{17}$	$2.02 \cdot 10^{17}$
Mean electron energy, E_0	meV	56	24
Deformation potential, E_d	eV	1.44	0.79
Longitudinal sound velocity, v_l	m/s	1370	1300
Averaged sound velocity, c_s	m/s	845	830
Crystal temperature, T_L	K	12.5	10.8
Nonradiative losses, $\Gamma_{nr} = 1/\tau_{nr}$	1/s	$1/25.9 \cdot 10^{-9}$	$1/13.1 \cdot 10^{-9}$
Density of solid Kr at 5K, ρ	kg/m^3	3092.6	3781
Relative dielectric permeability, ε_r		1.88	2.22

CONCLUSIONS

It was shown that time-resolved luminescence spectroscopy on rare gas solids is a powerful tool for investigating the dynamics of photocarriers, namely electronic relaxation, thermalization, and recombination into secondary excitons. The temporal evolution of free excitons following primary valence excitation and, to a certain extent, also following inner-shell excitation can be explained in terms of the ''classical'' theory of the relaxation processes mentioned, with values of the various physical quantities involved as they are reported in the literature. One of the main results is the proof that there exist excitonic sidebands of the ionization limits (either band-gap or inner-shell ionization) which are ascribed

to electronic polaron complexes. Due to the fact that thermalization is slow in rare gas solids, a moderate time resolution is sufficient to carry out the experiments.

The work was supported by the Bundesministerium für Bildung und Forschung (Grants Nos. 05 650GUB and 05 ST8GUI 6) and by the Deutsche Forschungsgemeinschaft DFG (Grants Nos. DFG Zi 159/1–4). V. Kisand and G. Zimmerer acknowledge support by the EU — Project ''Regional Center of Excellence in New Functional Materials, their Design, Diagnostics and Exploitation'' (No. ICA1-1999-70086).

*E-mail: Georg.Zimmerer@desy.de

[1)]Compared to Ref. 15, a factor $1/(4\pi)^3$ was added to make this formula valid in the SI system. This was pointed out to us by A.N. Vasil'ev.[18]

[2)]This is not completely true because there is still the factor $\sqrt{m_e/m_h}$ in the equation. However, the errors introduced by this square root are much less than those introduced by $E_d^2 m_3^{5/2}$.

[3)]For mathematical reasons, the accuracy of the fits is lower for nearly equal time constants $\tau_1 \approx \tau_2$.

[4)]Of course, it is an accidental coincidence of the two values.

[5)]In Fig. 11 we preferred to present a quick scan. During high-resolution scans, which take some hours, the samples degrade due to defect formation. This leads to a continuous decrease of FE luminescence. High-resolution scans are given in Ref. 34.

[1] I. Ya. Fugol', Adv. Phys. **27**, 1 (1978); *ibid.* **37**, 1 (1988).
[2] N. Schwentner, E. E. Koch, and J. Jortner, *Electronic Excitations in Condensed Rare Gases*, Vol. 107 of Springer Tracts in Modern Physics, Springer-Verlag, Berlin, Heidelberg (1985).
[3] V. Saile, Appl. Opt. **19**, 4115 (1980).
[4] G. Zimmerer, in *Excited State Spectroscopy in Solids*, U. M. Grassano and N. Terzi (eds.), North-Holland, Amsterdam (1987), p. 37.
[5] U. Rössler, in *Rare Gas Solids*, edited by M. N. Klein and J. A. Venables, Vol. 1, Academic Press, London, New York, San Francisco (1976/77), p. 505.
[6] F. Coletti, *Thèse d'Etat*, Université Aix-Marseille II (1987).
[7] T. Kloiber, *Dissertation*, The University of Hamburg (1989).
[8] R. Kink and M. Selg, Phys. Status Solidi B **96**, 101 (1979).
[9] V. Kisand, M. Kirm, S. Vielhauer, and G. Zimmerer, J. Phys.: Condens. Matter **14**, 5529 (2002).
[10] B. Steeg, M. Kirm, V. Kisand, S. Körding, S. Vielhauer, and G. Zimmerer, J. Low Temp. Phys. **111**, 739 (1998).
[11] G. Baldini, Phys. Rev. **128**, 1562 (1962).
[12] V. Kisand, M. Kirm, E. Negodin, E. Sombrowski, B. Steeg, S. Vielhauer, and G. Zimmerer, J. Phys.: Condens. Matter **15**, 2023 (2003).
[13] D. Varding, I. Reimand, and G. Zimmerer, Phys. Status Solidi B **185**, 301 (1994).
[14] D. Varding, J. Becker, L. Frankenstein, B. Peters, M. Runner, A. Schröder, and G. Zimmerer, Fiz. Nizk. Temp. **19**, 600 (1993) [Low Temp. Phys. **19**, 427 (1993)].
[15] I. Reimand, E. Gminder, M. Kirm, V. Kisand, B. Steeg, D. Varding, and G. Zimmerer, Phys. Status Solidi B **214**, 81 (1999).
[16] V. Kisand, M. Kirm, S. Vielhauer, and G. Zimmerer, Surf. Rev. Lett. **9**, 783 (2002).
[17] E. M. Conwell, *High Field Transport in Semiconductors*, Vol. 9, Solid State Physics Academic Press, New York and London (1967).
[18] A. N. Vasil'ev, Moscow State University, Physics Department, private communication.
[19] V. N. Abakumov, V. I. Perel', and I. N. Yassievich, Zh. Éksp. Teor. Fiz. **78**, 1240 (1980) [Sov. Phys. JETP **51**, 626 (1980)].
[20] J. M. Ziman, *Electrons and Phonons: The Theory of Transport Phenomena in Solids*, Clarendon (1962).
[21] L. S. Miller, S. Howe, and W. E. Spear, Phys. Rev. **166**, 871 (1968).
[22] A. M. Ratner, Phys. Rep. **269**, 197 (1996).
[23] E. Roick, R. Gaethke, P. Gürtler, T. O. Woodruff, and G. Zimmerer, J. Phys. C **17**, 945 (1984).
[24] E. Gminder, *Dissertation*, The University of Hamburg (2000).
[25] B. Steeg, E. Gminder, M. Kirm, V. Kisand, S. Vielhauer, and G. Zimmerer, J. Electron Spectrosc. Relat. Phenom. **101–103**, 879 (1999).
[26] V. Kisand, *Proceedings of the 3rd International Conference on Excitonic Processes in Condensed Matter EXCON'98*, R. T. Williams and W. M. Yen (eds.), The Electrochem. Soc., Inc., Pennington, NJ, USA, Proceedings Volume 98–25, p. 385.
[27] V. Kisand, E. Gminder, M. Kirm, B. Steeg, S. Vielhauer and G. Zimmerer, in *Proceedings of the 5th International Conference on Inorganic Scintillators and Their Applications*, August 16–20, 1999, edited by V. V. Mikhailin, Moscow, Faculty of Physics, M. V. Lomonosov Moscow State University (2000), p. 458.
[28] J. T. Devreese, A. B. Kunz, and T. C. Collins, Solid State Commun. **11**, 673 (1972).
[29] A. N. Vasil'ev, Y. Fang, and V. V. Mikhailin, Phys. Rev. B **60**, 5340 (1999).
[30] B. Steeg, *Dissertation*, The University of Hamburg (1999).
[31] E. Gminder, M. Kirm, V. Kisand, B. Steeg, S. Vielhauer, and G. Zimmerer, J. Lumin. **87–89**, 555 (2000).
[32] L. Resca, R. Resta, and S. Rodriguez, Phys. Rev. B **18**, 702 (1978).
[33] B. Kassühlke, *Dissertation*, TU München (1998).
[34] S. Vielhauer, E. Gminder, M. Kirm, V. Kisand, E. Negodin, B. Steeg, and G. Zimmerer, Int. J. Mod. Phys. B **15**, 3695 (2001).
[35] S. Vielhauer, M. Kirm, V. Kisand, E. Negodin, E. Sombrowski, B. Steeg, and G. Zimmerer, Surf. Rev. Lett. **9**, 1333 (2002).
[36] S. Vielhauer, *Dissertation*, The University of Hamburg (2003).
[37] T. Möller, Synchr. Rad. News **6**, 16 (1993).
[38] S. Vielhauer, M. Kirm, V. Kisand, B. Steeg, A. N. Vasil'ev, and G. Zimmerer, J. Nonlinear Optics **29**, 315 (2003).

This article was published in English in the original Russian journal. Reproduced here with stylistic changes by AIP.

Quantum property of solid hydrogen as revealed by high-resolution laser spectroscopy

H. Katsuki,[a] M. Fushitani,[b] and T. Momose[c]

Department of Chemistry, Graduate School of Science, Kyoto University, Kyoto 606-8502, Japan
Fiz. Nizk. Temp. **29**, 1093–1100 (September–October 2003)

Pure vibrational overtone transitions of solid parahydrogen are studied using high-resolution laser spectroscopy. Extremely narrow spectral linewidth ($\sim$20 MHz) allows us to observe rich spectral structure that originates in subtle intermolecular interactions in the crystal. It is found that anisotropy of the distribution of zero-point lattice vibration of hydrogen molecules perturbs the energy levels of the vibrationally excited states significantly. A large amplitude of zero-point lattice vibration, an intrinsic propoerty of quantum solids, is directly observed from the present high-resolution spectroscopy. The first observation of a pure vibrational overtone transition of solid orthodeuterium is also discussed. © *2003 American Institute of Physics.*
[DOI: 10.1063/1.1619353]

1. INTRODUCTION

Optical linewidths in the condensed phase are, in general, two or three orders of magnitude broader than in the gas phase. The broadness of the linewidths wipes out most spectral information that might give us detailed information on intermolecular interactions and other properties of condensed phases. However, an exception to this generalization was recently found for solid hydrogen crystals.[1–3] Optical transitions of hydrogen crystals in the infrared spectral region are, surprisingly, as narrow as 4 MHz ($=0.00013\ \mathrm{cm}^{-1}$).[4] The exceptional sharpness of the optical transitions of hydrogen crystals allows us to observe fine spectral structures originating in subtle interactions in the condensed phase, which provides a new methodology for investigating properties of the condensed phase from a microscopic point of view.

Solid hydrogen has been attracting attention not only because it is the simplest and most fundamental molecular crystal[5,6] but also because it is a quantum crystal.[7] Since hydrogen molecules have vibrational and rotational degrees of freedom, studies of solid hydrogen will shed light on different aspects of quantum crystals that can never be obtained from studies of solid He.

One of the important properties of quantum crystals is the large amplitude of zero-point lattice vibration. Due to the small mass of a hydrogen molecule in addition to the weak intermolecular interaction between hydrogen molecules, the mean amplitude of the zero-point lattice vibration of the solid hydrogen crystal extends approximately 20% of the intermolecular distance. The delocalization of the wave function of hydrogen molecules in the lattice must affect most properties of the crystal. However, observation of such a quantum effect is difficult, and few experimental observations directly related to the quantum effect have been reported so far. High-resolution spectroscopy, then, offers a promising technique for observing the quantum effect directly, because the optical spectra give us greatly detailed microscopic information.

Here we discuss the quantum feature of solid hydrogen revealed by high-resolution spectroscopy of pure vibrational overtone transitions. We have observed and analyzed the $Q_2(0)$ $(v=2\leftarrow 0, J=0\leftarrow 0)$, and $Q_3(0)$ $(v=3\leftarrow 0, J=0\leftarrow 0)$ absorption transitions of solid parahydrogen induced by an impurity orthohydrogen molecule. Since the transitions we have studied are induced by intermolecular interactions, which are a function of the distance between molecules, the transition frequencies contain information on the effect of the large amplitude of zero-point lattice vibration. Here we focus on the quantum property of solid hydrogen obtained from analysis of the optical spectral structure.

In addition to the $Q_n(0)$ transitions of solid parahydrogen, the first observation of the high-resolution spectrum of the $Q_2(0)$ transition of solid orthodeuterium is also discussed.

2. $Q_n(0)$ TRANSITIONS OF SOLID HYDROGEN

The $Q_n(0)$ $(v=n\leftarrow 0, J=0\leftarrow 0)$ transitions of H_2 and D_2 become optically active when these molecules are placed in an electric field. Due to the polarizability α of hydrogen molecules, an electric field E induces a dipole moment $\mu=\alpha E$ on the hydrogen molecule, which interacts with radiation to cause the $Q_n(0)$ transitions.[2,8,9]

The $Q_n(0)$ transitions we have studied here are those induced by the electric field of the averaged quadrupole moment of an impurity $J=1$ hydrogen molecule in the crystal. Upon the $Q_n(0)$ transitions, the inducer $J=1$ hydrogen also changes its value of the quantum number M, which is the projection of the rotational angular momentum J. Thus the $Q_n(0)$ transitions we have observed are simultaneous transitions that should be written as $Q_n(0)+Q_0(1)$.[8] Vibrons produced by the transitions are almost localized near the inducer $J=1$ hydrogen molecule, contrary to the cases of the Raman[2] and Condon[9] transitions.

The crystal structure of solid parahydrogen and solid orthodeuterium is known to be hexagonal close packed. There are two types of nearest-neighbor pairs between two hydrogen molecules in a crystal of the hexagonal close packed structure. One is the in-plane (IP) pair and the other is the out-of-plane (OP) pair. Figure 1 depicts the 12 nearest-neighbor molecules of a $J=1$ hydrogen molecule in a crystal of the hexagonal close packed structure. Six hydrogen molecules reside on the hexagonal plane, while three hydrogen molecules are above and three molecules are below the

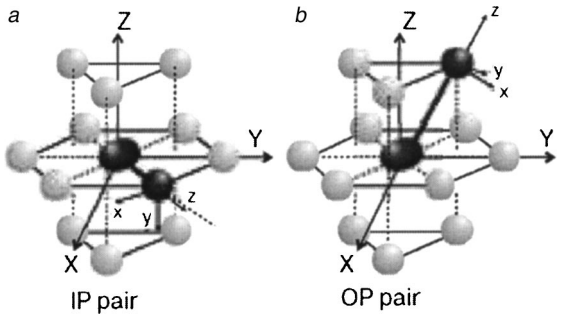

FIG. 1. A $J=1$ hydrogen molecule (displayed as ellipses) and its twelve nearest-neighbor hydrogen molecules in a crystal of the hexagonal close packed structure. *a*) In-plane (IP) pair configurations. *b*) Out-of-plane (OP) pair configurations. Molecules in the same basal plane are connected by solid lines. The IP and OP pairs are represented by a bold broken line. The crystal-fixed axes (XYZ) and the pair axes (xyz) are also shown. The crystal c axis is the same as the Z axis.

plane. The IP pair is a pair between two hydrogen molecules in the same hexagonal plane (Fig. 1a), and the OP pair is a pair between two hydrogen molecules in different planes next to each other (Fig. 1b). Since the environment around the pair is different between IP and OP pairs, we treat these pairs separately in the discussion that follows.

The $Q_1(0)$, $Q_2(0)$, and $Q_3(0)$ transitions have been observed at 4,153, 8,070 (Refs. 10 and 11) and 11,758 cm^{-1} (Ref. 12), respectively. We have studied the $Q_2(0)$ and $Q_3(0)$ transitions with higher spectral resolution than previous works to find new, fine splittings of the spectra.[13,14] It was concluded that these fine splittings we have observed contain important information on the quantum property of solid hydrogen.

3. INTERMOLECULAR INTERACTIONS IN QUANTUM CRYSTALS

Before going into the details of the experimental results, let us discuss the quantum effect on intermolecular interactions. The effect of the large amplitude of zero-point lattice vibration in solid hydrogen has to be taken into account when the interaction between hydrogen molecules is considered. Inclusion of the effect of the zero-point vibration is often referred to as the ''renormalization problem,'' and it has been discussed by Luryi and van Kranendonk in the case of hydrogen crystals.[15]

Here we consider the intermolecular interaction between $J=0$ hydrogen and $J=1$ hydrogen molecules. When the two molecules are fixed at a distance of R_0, the anisotropic interaction between these two molecules is well described as[6,13]

$$V(R_0,\omega_1)=B_0(R_0)C_{2,0}(\omega_1), \tag{1}$$

where ω_1 is the orientation of the $J=1$ hydrogen molecule with respect to the axis between two molecules (hereafter, the pair axis). The symbol $C_{l,m}(\omega)$ expresses the Racah spherical harmonics, which are related to the standard spherical harmonics $Y_{l,m}(\omega)$ as $C_{l,m}(\omega)=\sqrt{4\pi/(2l+1)}Y_{l,m}(\omega)$. The coefficient B_0 in Eq. (1) is a function of R_0. The expression in Eq. (1) is applicable only to the case when two molecules are rigidly fixed at a distance of R_0.

In solid hydrogen, however, the zero-point motion of intermolecular vibration is considerable, so that the ''instantaneous'' position of a molecule displaced from its equilibrium position needs to be explicitly taken into account. According to Luryi and van Kranendonk,[15] Eq. (1) should be modified for quantum crystal as

$$\tilde{V}(R_0,\omega_1)=\tilde{B}_0(R_0)C_{2,0}(\omega_1)+\tilde{B}_2(R_0)[C_{2,2}(\omega_1)+C_{2,-2}(\omega_1)], \tag{2}$$

where the intermolecular interaction potential is expanded in terms of R_0. The coefficients $\tilde{B}_0$ and $\tilde{B}_2$ are functions of R_0 only. The first term of the right-hand side of Eq. (2) has the same orientational dependence as the right-hand side of Eq. (1). But since the effect of zero-point vibration is renormalized, the tilde is used for the coefficient in Eq. (2) in order to distinguish it from the coefficient in Eq. (1).

The second term of the right-hand side of Eq. (2) originates in the anisotropy of the distribution of the zero-point vibration. More explicitly, when the instantaneous position of the hydrogen molecule relative to the lattice point is described by **u**, the coefficient $\tilde{B}_2(R_0)$ in Eq. (2) is approximately related to the coefficient $B_0(R_0)$ in Eq. (1) as

$$\tilde{B}_2(R_0)=\frac{\sqrt{6}}{4}\eta B_0(R_0), \tag{3}$$

where η is the nonaxiality parameter, defined as

$$\eta=\frac{1}{R_0^2}\langle u_x^2-u_y^2\rangle. \tag{4}$$

The Cartesian components u_x and u_y of the instantaneous vector **u** are those for the pair axis as shown in Fig. 1.

The physical origin of the second term of the right-hand side of Eq. (2) may become clearer when we look at the problem from the group theoretical point of view. When the distribution is axially symmetric with respect to the pair axis, the interaction potential should be described by only the first term of the right-hand side of Eq. (2), because the potential has to be totally symmetric with respect to any symmetry operation along the pair axis that belongs to the $C_{\infty v}$ point group. However, the distribution may not necessarily be axially symmetric. For example, in the case of the IP pair shown in Fig. 1a, the distribution of zero-point vibration could be deformed towards the hexagonal plane or elongated toward the c axis. Then the potential has to be totally symmetric with respect to any symmetry operation that belongs to the C_{2v} point group. It is also true for the OP pair that the potential has to be totally symmetric in C_{2v}. When we construct symmetry-adapted functions of linear combinations of the Racah spherical harmonics up to the second rank, the totally symmetric functions among them (besides $C_{0,0}(\omega)$) in the C_{2v} point group are found to be $C_{2,0}(\omega)$ and $C_{2,2}(\omega)+C_{2,-2}(\omega)$, the latter being the second term of the right-hand side of Eq. (2). Thus the second term originates in the nonaxiality of the distribution of zero-point vibration relative to the pair axis. Although both parameters $\tilde{B}_0$ and $\tilde{B}_2$ contain information on the renormalized effect, it should be emphasized that the parameter $\tilde{B}_2$ contains only the pure quantum effect of the solid.

Each hydrogen molecule in solid hydrogen is under a potential which is approximated as a sum of the pair intermolecular interaction from all the surrounding hydrogen molecules. We call this potential the ''crystal field potential.'' For the analysis of the spectra of the $Q_n(0)$ transitions, we only need to consider the interaction potential between an impurity $J=1$ hydrogen molecule and surrounding parahydrogen molecules.[13] In addition, since the quantum effect shown in Eq. (2) contributes significantly only to the nearest-neighbor pairs but not to distant pairs, Eq. (2) is used for the interaction between nearest-neighbor pairs, while Eq. (1) is used for more-distant pairs in the present analysis.

Because of the difference of the polarizability of hydrogen molecules in different vibrational states, the crystal field potential has to be considered separately between the ground state and the vibrationally excited states. When all the $J=0$ hydrogen molecules are in the ground state, the crystal field potential is found to be

$$V^{\mathrm{gr}}(\Omega,R_0)=\varepsilon_{2c}C_{2,0}(\Omega). \tag{5}$$

The coefficient ε_{2c} is called the crystal field parameter. In deriving Eq. (5) we used the relation $C_{2,m}(\omega_1)=\Sigma_n D^2_{n,m}(\mathcal{R})C_{2,n}(\Omega)$ to change the axis system from the pair axis to the crystal-fixed axis (see Fig. 1), where Ω is the orientation of the $J=1$ molecule relative to the crystal-fixed axis and $\mathcal{R}$ is the orientation of the pair axis with respect to the crystal-fixed axis. The function $D^2_{n,m}(\mathcal{R})$ is the Wigner rotation matrix.[16] In Eq. (5), only the term proportional to $C_{2,0}(\Omega)$ remains, although we used Eq. (2) for the nearest-neighbor pairs. Terms other than $C_{2,0}(\Omega)$ vanish because of the symmetry of the crystal (D_{3h}) around the central hydrogen molecule.

When one of the parahydrogen molecules is in the vibrationally excited state, the crystal field potential becomes more complicated than Eq. (5). We express the crystal field potential of the vibrationally excited states as a sum of the crystal field potential of the ground state [Eq. (5)] and the correction terms due to the excitation. When the jth hydrogen molecule is excited to its vibrationally excited state, the crystal field potential becomes

$$\begin{aligned}V^{\mathrm{ex}}(\Omega,R_0)=&\varepsilon_{2c}C_{2,0}(\Omega)\\&+\Delta\tilde{B}_0\sum_{m'=-2}^{2}D^2_{m',0}(\mathcal{R}_j)D^{2*}_{m',0}(\Omega)\\&+\Delta\tilde{B}_2\sum_{m'=-2}^{2}[D^2_{m',2}(\mathcal{R}_j)\\&+D^2_{m',-2}(\mathcal{R}_j)]D^{2*}_{m',0}(\Omega),\end{aligned} \tag{6}$$

where the first term of the right-hand side is the ground-state crystal field potential, and the second and third terms express the correction due to the vibrational excitation. The symbol $\mathcal{R}_j$ is the Euler angle of the pair axis between the jth hydrogen molecule and the central $J=1$ hydrogen molecule relative to the crystal-fixed axis. The symbol $\Delta\tilde{B}_n$ ($n=0$ or 2) represents $\tilde{B}^{\mathrm{ex}}_n-\tilde{B}_n$, where $\tilde{B}^{\mathrm{ex}}_n$ is the coefficient of the pair interaction potential in Eq. (2) between the vibrationally excited $J=0$ hydrogen molecule and the ground $J=1$ hydrogen molecule. It should be noted that the parameter $\Delta\tilde{B}_2$ related to the pure quantum effect appears explicitly in Eq. (6). In other words, determination of the parameter $\Delta\tilde{B}_2$ corresponds to direct observation of the quantum effect of solid hydrogen.

4. EXPERIMENTS

Parahydrogen crystals were grown by the same method as described previously.[13,17] Briefly, pure parahydrogen gas prepared using a ferric oxide catalyst[17] was continuously introduced in an optical cell kept at about 8 K to grow transparent crystals. The cell was made of copper with both ends sealed with BaF_2 windows with indium gaskets. The size of the cell was 5 cm long and 2 cm in diameter. The concentration of orthohydrogen in the crystal was estimated to be less than 0.01%. In order to observe the $Q_3(0)$ transition, which is about two orders of magnitude weaker than the $Q_2(0)$ transition, the concentration of orthohydrogen was increased to 0.1%.

Orthodeuterium crystals were prepared using a method similar to the one described above.[18] The conversion of paradeuterium to orthodeuterium was carried out with the ferric oxide catalyst kept at 18 K. The crystals were grown at 10.5 K as well. The concentration of paradeuterium was estimated to be around 0.25%.

The high-resolution spectra of the $Q_2(0)$ transitions of both parahydrogen and orthodeuterium crystals were observed using a difference frequency laser system developed in our laboratory.[19] The $Q_3(0)$ transition was observed using a ring type Ti:sapphire laser. The spectral purity of both laser systems was better than a few MHz ($=10^{-4}$ cm^{-1}). The tone-burst modulation technique was used for sensitive detection.[20,21] All the measurements were done at 4.8 K.

5. $Q_2(0)$ AND $Q_3(0)$ TRANSITIONS OF SOLID PARAHYDROGEN

5.1. Observed spectra

Figure 2 shows the observed spectra of the $Q_2(0)$ and $Q_3(0)$ transitions of solid parahydrogen. Panels (a) and (b) show the absorption spectra for polarization of the light parallel to and perpendicular to the c axis, respectively. Panels (c) and (d) show the $Q_3(0)$ spectra for the parallel and perpendicular polarizations, respectively. In both transitions, the spectral shapes appear as a second derivative type because of the tone-burst modulation technique. The differences in the intensities of each transition between panels (a) and (b) and between panels (c) and (d) in Fig. 2 clearly show that each transition has definite polarization dependence relative to the crystal-fixed axis.

The $Q_2(0)$ spectrum is roughly split into a doublet with a spacing of 0.30 cm^{-1}. Each component exhibits further fine splittings; the lower-frequency component shows eight lines, while the higher displays ten. On the other hand, the $Q_3(0)$ spectrum is roughly split into a doublet with a spacing of 0.45 cm^{-1}. Similar spectral structure was also observed in the $Q_3(0)$ transition, but the number of fine splittings in each component is smaller in the $Q_3(0)$ transitions than in $Q_2(0)$; the lower frequency component shows four lines, while the higher component exhibits six.

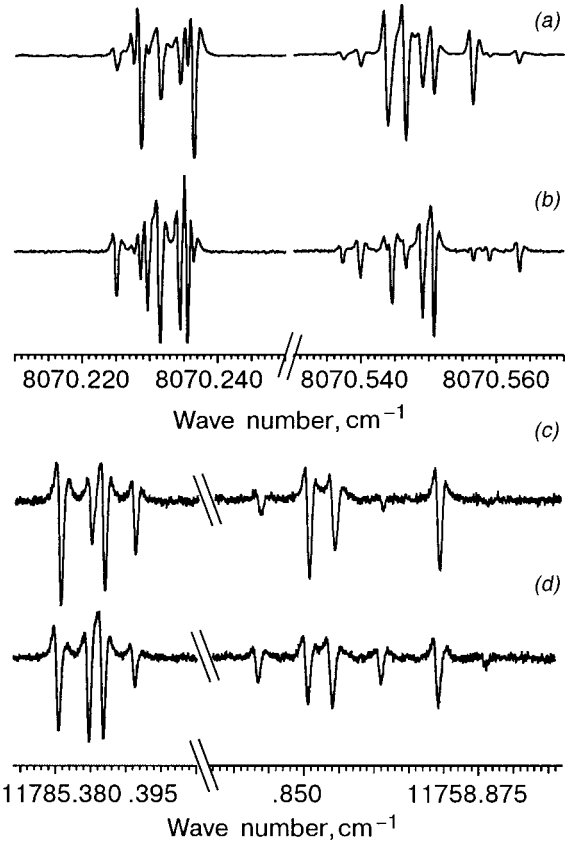

FIG. 2. a,b): The $Q_2(0)$ transition of solid parahydrogen. The polarization of light is parallel (a) and perpendicular (b), respectively. c,d): The $Q_3(0)$ transition of solid parahydrogen. The polarization of light is parallel (c) and perpendicular (d), respectively. The spectral shapes appear as a second-derivative type because of the tone-burst modulation technique.

Previously, Dickson *et al.*[12] observed roughly the same spectral structure in the $Q_3(0)$ transition as shown in panels (c) and (d) of Fig. 2. Their spectrum, however, showed a much broader linewidth than ours. The linewidth (FWHM) of each transition shown in Fig. 2 (c) and (d) is about 30 MHz, which is less than one-third of the width observed previously. The narrower spectral linewidth is due to the lower orthohydrogen concentration in our sample. The sharp linewidth allowed us to resolve all the fine splittings in the $Q_3(0)$ transition clearly.

5.2. Analysis

The theoretical framework for the analysis of the $Q_n(0)$ transition was discussed in a previous paper.[13] Briefly, the Hamiltonian H for the analysis consists of four terms; $H = H_{rv} + V_{\text{crystal}} + H_{\text{hop}} + V_{\text{Stark}}$. The first term is the standard rotation–vibration Hamiltonian of hydrogen molecules, the second term is the crystal field potential, the third term is the vibron hopping Hamiltonian, and the last term is the Stark potential of the quadrupolar field of the central $J=1$ hydrogen.

As for the crystal field potential, Eqs. (5) and (6) were used to describe the ground and vibrationally excited state, respectively. In addition, since there are two different pairs in the crystal, different parameters of both $\Delta\tilde{B}_0$ and $\Delta\tilde{B}_2$ were employed for IP and OP pairs. These are designated as $\Delta\tilde{B}_0$(IP) and $\Delta\tilde{B}_2$(IP) for the IP pair, and $\Delta\tilde{B}_0$(OP) and $\Delta\tilde{B}_2$(OP) for the OP pair.

TABLE I. Crystal field parameters and vibron hopping frequency of the $Q_2(0)$ and $Q_3(0)$ transitions (in cm^{-1}).

Parameter	$Q_2(0)$	$Q_3(0)$
ε_{2c}	−0.0116(2)	−0.0112(2)
$\Delta\tilde{B}_0$ (IP)	−0.5278(5)	−0.7879(4)
$\Delta\tilde{B}_0$ (OP)	−0.5287(5)	−0.7880(3)
$\Delta\tilde{B}_2$ (IP)	−0.0045(2)	−0.0069(3)
$\Delta\tilde{B}_2$ (OP)	0.0149(3)	0.0236(2)
σ	−0.0038(1)	0.0

The vibron hopping Hamiltonian H_{hop} is responsible for the delocalization of the vibrational excited states in the crystal. In a previous paper[13] we found that the $Q_2(0)$ spectrum could not be properly interpreted without the vibron hopping effect. The hopping frequency is designated as σ. On the other hand, the hopping in the $v=3$ vibrationally excited state is estimated to be negligibly small.

The Stark field potential V_{Stark} arises from the electric field of the $J=1$ hydrogen molecule. A quantitative discussion of the Stark energy is given in Ref. 13.

The observed transition frequencies were fitted employing the standard least-squares fitting method with the use of a total of six parameters: ε_{2c}, $\Delta\tilde{B}_0$(IP), $\Delta\tilde{B}_0$(OP), $\Delta\tilde{B}_2$(IP), $\Delta\tilde{B}_2$(OP), and σ. The fitting calculation was performed separately for the $Q_2(0)$ and $Q_3(0)$ transitions. The best-fit parameters are listed in Table I.

5.3. Crystal field potential

Although the parameters for the $Q_2(0)$ and $Q_3(0)$ transitions were calculated separately, the agreement of the crystal field parameter ε_{2c} between these two transitions is noteworthy. The parameter gives the crystal field splitting of

$$\delta_1 = E(M=\pm 1) - E(M=0) = -0.6\varepsilon_{2c} \tag{7}$$

for an orthohydrogen molecule in a pure parahydrogen crystal.

Determination of the value and sign of δ_1 has been attracting much attention because it may explain the anomalous behavior of the specific heat of solid parahydrogen.[6,22] The most accurate value of δ_1 so far reported is 0.0071 cm^{-1} by Dickson *et al.*[12] Our experimental results support their value. Since our spectral resolution was much better than the previous experiment,[12] our parameter must be more accurate than theirs. From our observations we conclude that the $M=\pm 1$ level is above the $M=0$ level, and the separation is 0.00696 ± 0.00012 cm^{-1} $= 10.01 \pm 0.17$ mK.

5.4. Quantum effect

As was discussed above, the parameter $\Delta\tilde{B}_2$ originates in the pure quantum effect. Although the absolute values of

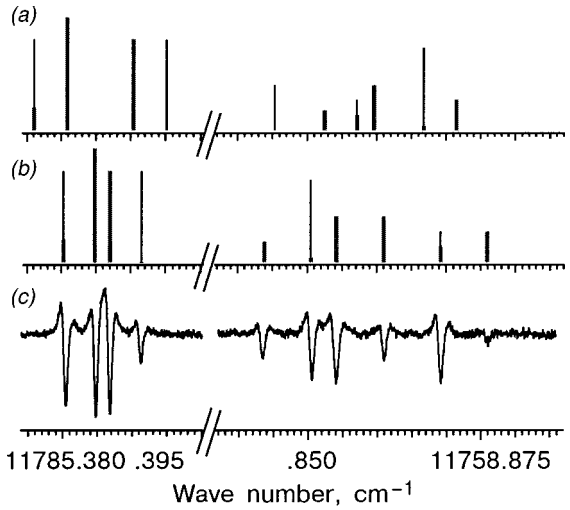

FIG. 3. *a*) Calculated $Q_3(0)$ transition frequencies obtained without using the quantum parameter ΔB_2 for the fitting. The best-fit parameters are: $\varepsilon_{2c}=-0.0238$ cm^{-1}, $\Delta\tilde{B}_0(\mathrm{IP})=-0.7980$ cm^{-1}, and $\Delta\tilde{B}_0(\mathrm{OP})=-0.7858$ cm^{-1}. The bold lines show the perpendicular transitions, while the thin lines show parallel transitions. *b*) Calculated frequencies obtained with the use of all of the five parameters. The parameters are given in Table I. *c*) Observed $Q_3(0)$ spectrum (same as Fig. 2*d*).

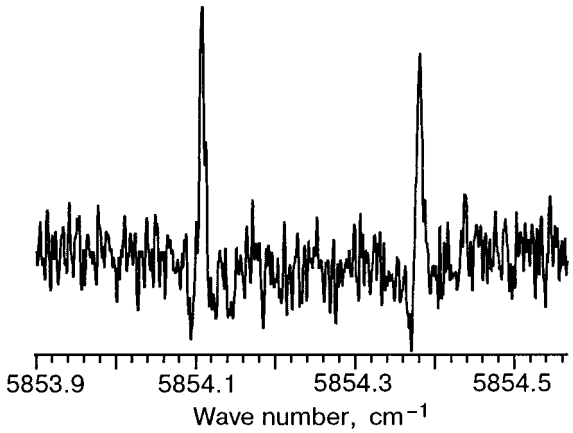

FIG. 4. The $Q_2(0)$ transition of solid orthodeuterium. The concentration of paradeuterium is estimated to be 0.25%.

the $\Delta\tilde{B}_2$ determined are small, they play a significant contribution to the energy levels of the vibrationally excited states. In order to observe the effect of the parameter $\Delta\tilde{B}_2$ in detail, we also performed the fitting calculation without the parameter $\Delta\tilde{B}_2$. Figure 3 compares the calculated results with the observed spectrum. Panel (a) shows the calculated frequencies of the $Q_3(0)$ transition using only three parameters: ε_{2c}, $\Delta\tilde{B}_0(\mathrm{IP})$, and $\Delta\tilde{B}_0(\mathrm{OP})$ for the fitting, while panel (b) shows the frequencies calculated using all five parameters: ε_{2c}, $\Delta\tilde{B}_0(\mathrm{IP})$, $\Delta\tilde{B}_0(\mathrm{OP})$, $\Delta\tilde{B}_2(\mathrm{IP})$, and $\Delta\tilde{B}_2(\mathrm{OP})$ (the vibron hopping frequency σ was fixed at zero). Panel (c) shows the observed spectrum. It is clear from panels (a) and (b) compared to panel (c) that the inclusion of the parameter $\Delta\tilde{B}_2$ is essential for quantitative analysis of the observed spectrum. In other words, the quantum effect is directly observed in the $Q_n(0)$ spectrum.

From Table I we see a significant difference of the parameter $\Delta\tilde{B}_2$ between the IP and OP pairs. This difference must be related to the difference of nonaxiality parameter η in Eq. (4). It has been discussed by Luryi and van Kranendonk[15] that the nonaxiality parameters for the IP pair, $\eta(\mathrm{IP})$, and the OP pair, $\eta(\mathrm{OP})$, are related and expressed as $\eta(\mathrm{IP})/\eta(\mathrm{OP})=1/3$. From the analysis of our spectrum, we obtained the ratio $|\Delta\tilde{B}_2(\mathrm{IP})/\Delta\tilde{B}_2(\mathrm{OP})|=0.30$. Since our ratio is not the ratio $\tilde{B}_2(\mathrm{IP})/\tilde{B}_2(\mathrm{OP})$ of the ground state but the ratio of the difference of the parameter $\tilde{B}_2$ between the vibrationally excited state and the ground state, our ratio $|\Delta\tilde{B}_2(\mathrm{IP})/\Delta\tilde{B}_2(\mathrm{OP})|=0.30$ cannot be compared directly with the ratio $\eta(\mathrm{IP})/\eta(\mathrm{OP})=-1/3$. But the similarity is worth noting.

The parameter $\Delta\tilde{B}_0$ contains a more complicated quantum effect than the parameter $\Delta\tilde{B}_2$,[13] and we do not discuss this here. We just mention that the parameter $\Delta\tilde{B}_0$ is found to be very close between the IP pairs and OP pairs. A more detailed discussion of the parameters shown in Table I is given in a separate paper.[14]

6. $Q_2(0)$ TRANSITION OF SOLID ORTHODEUTERIUM

It has been shown that there are remarkable differences in the behaviors of solid H_2 and solid D_2.[5] Some of the differences have come to be well understood—such as slower ortho–para conversion in solid D_2 than in solid H_2, and slower quantum diffusion in solid D_2. But there are still some puzzling differences between them. For example, the fact that impurity $J=1$ pairs show sharp NMR lines in solid H_2 but not in solid D_2 is yet to be understood.[23,24]

Since the high-resolution spectroscopic technique is a powerful method for investigating properties of solid hydrogen from a macroscopic point of view, application of the technique to solid orthodeuterium is worth trying. As a first step of such research, we observed the high-resolution spectrum of the $Q_2(0)$ transition of solid orthodeuterium for the first time.

Figure 4 shows the observed $Q_2(0)$ transition of solid orthodeuterium. A tone-burst modulation technique was employed herein. A doublet with a spacing of 0.27 cm^{-1} was observed. The doublet corresponds to the doublet with a spacing of 0.30 cm^{-1} of the $Q_2(0)$ transition of solid parahydrogen shown in Fig. 2a,b. The linewidth of the doublet in Fig. 4 is about 300 MHz ($=0.01$ cm^{-1}). We could not resolve any further splitting in each component, as is seen in Fig. 2, contrary to the case of the $Q_2(0)$ transition of solid parahydrogen. The broad linewidth is mostly due to a higher $J=1$ concentration in solid orthodeuterium (0.25%) than in solid parahydrogen (0.01%).

The doublet originates in the splitting between $M=0$ and $M=\pm1$ in the $v=2$ excited state. From the spacing 0.27 cm^{-1}, we estimate the crystal field parameter ΔB_0 to be 0.45 cm^{-1} for solid orthodeuterium.[4] The ratio of ΔB_0 between solid D_2 and solid H_2 for the $Q_2(0)$ transition $\Delta B_0^{D_2}/\Delta B_0^{H_2}$ is roughly 0.85.

Since the intermolecular interaction between hydrogen molecules originates in the dispersion interaction, the coefficient B_0 in Eq. (2) is, as a first order approximation, roughly proportional to $\gamma_{J=1}\alpha_{J=0,v}/R^6$, where $\gamma_{J=1}$ is the anisotropic polarizability of the $J=1$ hydrogen molecule, $\alpha_{J=0,n}$

is the isotropic polarizability of the $J=0$ hydrogen molecule in the $v=n$ vibrational state, and R is the distance between the two molecules. By referring to the theoretically calculated polarizabilities,[25] the ratio $\Delta B_0^{D_2}/\Delta B_0^{H_2}$ is calculated to be around 0.9, which is in good agreement with the observed value of 0.85.

Since no further splitting is observed in each component of the doublet, we conclude that the ground state crystal field splitting δ_1 of solid orthodeuterium is less than the width; that is, $0.01\ \mathrm{cm}^{-1}$. In order to determine the crystal field parameter accurately as in the case of solid parahydrogen, we need to reduce the concentration of paradeuterium in our crystal. Such work is now underway.

7. CONCLUSION

In this paper we have discussed the quantum property of solid hydrogen, which is obtainable from high-resolution spectroscopy of the rotation–vibration transitions of hydrogen molecules. It was demonstrated that the large amplitude of zero-point lattice vibration modifies significantly the energy levels of the vibrational excited states, which were clearly observed using high-resolution spectroscopy. Further studies with this high-resolution technique will give us more information on the nature of quantum solids, which is otherwise difficult to obtain.

The work described herein was supported in part by the Grant-in-Aid for Scientific Research of the Ministry of Education, Science, Culture, and Sports of Japan.

The authors would like to thank Prof. H. Meyer for drawing our attention to the problems of solid deuterium. Further, H. Katsuki would also like to acknowledge the support from JSPS Research Fellowships for Young Scientists.

[a]Present address: Physical Chemistry Institute, University of Zurich, Switzerland

[b]Present address: Institute für Experimentalphysik, Freie Universität Berlin, Germany

[c]E-mail: momose@kuchem.kyoto-u.ac.jp

[1] M. Okumura, M. C. Chan, and T. Oka, Phys. Rev. Lett. **62**, 32 (1989).
[2] T. Momose, D. P. Weliky, and T. Oka, J. Mol. Spectrosc. **153**, 760 (1992).
[3] T. Oka, Annu. Rev. Phys. Chem. **44**, 299 (1993).
[4] D. P. Weliky, K. E. Kerr, T. J. Byers, Y. Zhang, T. Momose, and T. Oka, J. Chem. Phys. **105**, 4461 (1996).
[5] F. Silvera, Rev. Mod. Phys. **52**, 393 (1980).
[6] J. van Kranendonk, *Solid Hydrogen. Theory of the Properties of Solid* H_2, HD, *and* D_2, Plenum, New York (1983).
[7] L. H. Nosanow, Phys. Rev. **146**, 120 (1966).
[8] V. F. Sears and J. van Kranendonk, Can. J. Phys. **42**, 980 (1964).
[9] K. E. Kerr, T. Momose, D. P. Weliky, C. M. Gabrys, and T. Oka, Phys. Rev. Lett. **72**, 3957 (1994).
[10] D. P. Weliky, T. J. Byers, K. E. Kerr, T. Momose, R. M. Dickson, and T. Oka, Appl. Phys. B: Lasers Opt. **59**, 265 (1994).
[11] M. Mengel, B. P. Winnewisser, and M. Winnewisser, Phys. Rev. B **55**, 10420 (1997).
[12] R. M. Dickson, T. Momose, T. J. Byers, and T. Oka, Phys. Rev. B **57**, 941 (1998).
[13] H. Katsuki and T. Momose, J. Chem. Phys. **116**, 8881 (2002).
[14] H. Katsuki and T. Momose, to be submitted.
[15] S. Luryi and J. van Kranendonk, Can. J. Phys. **57**, 136 (1979); 307 (1979); 933 (1979).
[16] M. E. Rose, *Elementary Theory of Angular Momentum*, Wiley, New York (1957).
[17] T. Momose and T. Shida, Bull. Chem. Soc. Jpn. **71**, 1 (1998).
[18] H. Hoshina, M. Fushitani, and T. Momose, J. Chem. Phys., to be submitted.
[19] T. Momose, T. Wakabayashi, and T. Shida, J. Opt. Soc. Am. B **13**, 1706 (1996).
[20] H. M. Pickett, Appl. Opt. **19**, 2745 (1980).
[21] C. S. Gudeman, M. H. Begemann, J. Pfaff, and R. J. Saykally, Opt. Lett. **8**, 310 (1983).
[22] T. Nakamura, Prog. Theor. Phys. **14**, 135 (1955).
[23] M. Calkins, R. Banke, X. Li, and H. Meyer, J. Low Temp. Phys. **65**, 47 (1986).
[24] A. B. Harris, H. Meyer, and X. Quin, Phys. Rev. B **49**, 3844 (1994).
[25] W. Kolos and L. Wolniewicz, J. Chem. Phys. **46**, 1426 (1967).

This article was published in English in the original Russian journal. Reproduced here with stylistic changes by AIP.

Purely electronic zero-phonon line as the foundation stone for high-resolution matrix spectroscopy, single-impurity-molecule spectroscopy, and persistent spectral hole burning. Recent developments

K. K. Rebane*

Institute of Physics, University of Tartu, 142 Riia, Tartu, 51014, Estonia
Fiz. Nizk. Temp. **29**, 1101–1108 (September–October 2003)

A few examples of recent progress in the study and applications of purely electronic zero-phonon line (ZPL) and its offshoots are briefly considered: new experimental values of the narrowest ZPL; time-and-space-domain holography in the femtosecond domain, and the realization of a femtosecond Taffoli gate by it; single-impurity-molecule spectroscopy, its relation to single-photon interference and to the realization of quantum computing; the promises of quantum computing compared to what has already been done in holography. © *2003 American Institute of Physics.* [DOI: 10.1063/1.1619354]

The purely electronic zero-phonon line (ZPL) is a remarkable feature of low-temperature spectra of the absorption and luminescence of quite a number of various impurity centers in various solid hosts (see Refs. 1–5 and references therein). ZPLs can be very narrow and have very high peak absorption cross sections. These valuable properties, as well as several other features, are in close correspondence with features of the Mössbauer γ-resonance line. Because of this correlation, originating from the symmetry of the harmonic oscillator Hamiltonian in coordinate and momenta,[6] J.F. Gross called the ZPL the optical analog of the Mössbauer line,[7] helping considerably to popularize optical ZPLs.

I must note that two main features of the optical ZPL were pointed out in Ref. 8, five years before the first publication by Mössbauer.[9] That result of this early paper, however, was not given due attention. ZPLs, as sharp and intense features in the low-temperature spectra of some impurities in solids (without detailed explanation of their properties), had been found and fruitfully studied experimentally years before the Mössbauer effect. ZPL widths of around $1\ \mathrm{cm}^{-1}$ were measured in the spectra of rare-earth impurity ions introduced in proper ionic single-crystal hosts and also ruby (see Ref. 10 and 11 and references therein). The new wave of theoretical studies brought the understanding that even the very narrow widths of around $1\ \mathrm{cm}^{-1}$ are essentially inhomogeneous widths.[1,2,5,12,13] It was predicted that for dipole-allowed transitions the homogeneous lines should be (at liquid-helium temperatures) another 3–4 orders of magnitude narrower still, i.e., the homogeneous linewidth is 10^{-3}–$10^{-4}\ \mathrm{cm}^{-1} \approx 10$–$100\ \mathrm{MHz}$ (see Refs. 5, 12–14 and references therein), and even a few orders of magnitude narrower yet for forbidden ones. The theoretical point, later confirmed experimentally,[12,14] was that the ZPL's homogeneous width, $\Gamma_{\mathrm{hom}}(T)$, tends in the limit $T \to 0$ to the value determined by the lifetime of the excited electronic state.

This theoretical prediction stimulated experimentalists to search for methods of how to eliminate or use the inhomogeneous broadening and to utilize the precious properties of ZPLs in the frequency domain.

The ZPL became the foundation stone for three novel fields of modern optics and spectroscopy:[3,4,15] (1) very high spectral resolution ZPL studies of atoms and molecules as impurities in low-temperature solids (very high spectral resolution matrix-isolation spectroscopy); (2) single impurity molecule spectroscopy (SMS) (see Ref. 16 and references therein); (3) persistent spectral hole burning (PSHB) (see Ref. 17 and references therein).

VERY HIGH RESOLUTION ZPL SPECTROSCOPY OF IMPURITY CENTERS

Recently photon echo measurements of optical dephasing of forbidden transitions in rare-earth ions have revealed low-temperature linewidths as narrow as a few tens of hertz. The narrowest feature reported up to now is $\Gamma_{\mathrm{hom}} \approx 50$ Hz for the ${}^4I_{15/2} \leftrightarrow {}^4I_{13/2}$ transition in Er^{3+}: Y_2SiO_5 with 0.001% concentration of Eu^{3+} at $T = 1.5$ K and in a magnetic field of $B = 70$ kG (to freeze the nuclear spin fluctuation, which can be considered as causing unresolved or time-dependent inhomogeneous broadening).[18,19]

In the conventional optical spectroscopy of impurity solids, we have been accustomed to routinely neglecting the effect of the recoil momentum associated with the absorption and emission of optical photons, because the recoil of the emitting/absorbing atom corresponds to a frequency shift of about 1 kHz, which is really small compared to the allowed transitions' SMS linewidths about 10–100 MHz. For the very narrow ZPLs like those mentioned above, $\Gamma_{\mathrm{hom}} < 1$ kHz, and the recoil has to be taken into account. The development of a new version of the theory of ZPLs taking into account simultaneously the Stokes shift and recoil has been started.[20]

A novel aspect is that recoil *entangles* the emitted photon and the *free* atom which had emitted it. The entanglement is utilized to build a new quantum description of the spontaneously emitted single localized photon.

The situation for an impurity in a solid is more sophisticated than for an atom in vacuum. ZPL occupies here a very specific position: for ZPL a macroscopic piece of the solid accepts and absorbs the recoil, and the recoil momentum and energy imparted is practically zero. The transitions creating the phonon sideband distribute the recoil between

phonons, and the entanglement is not clearly displayed and will be very shortly cancelled by the macroscopic piece of solid, acting as a thermostat.

Low-temperature narrow ZPLs are very sensitive to various kinds of even very small irregularities of the surrounding solid, leading for a body of impurities to large inhomogeneous broadening of the ZPL. Depending on the solid host, on the impurity, and on the features of the electronic transition, the inhomogeneous ZPL width can vary from a tenth of cm^{-1} (e.g., rare-earth ions in good single crystals) to thousands of cm^{-1} (impurity molecules in amorphous glasses, frozen solutions, and polymers). Due to inhomogeneous broadening, even the narrowest low-temperature ZPL obtained by conventional absorption–emission measurements (i.e., without special spectroscopic techniques) comprises thousands of slightly different homogeneous ZPLs.

In the early years of ZPL spectroscopy,[1,5] inhomogeneous broadening (IB) of optical spectra was considered as an annoying impediment, and the absence of IB in Mössbauer ZPLs was viewed as a great advantage of the latter. Nowadays the situation has changed.[2,3] IB of optical ZPLs has turned out to be a valuable feature for ZPL science and applications, especially in areas such as optical data storage and processing. In fact, the larger the ratio between the inhomogeneous linewidth ($\Gamma_{\rm inh}$) and the homogeneous linewidth ($\Gamma_{\rm hom}$), $\alpha_{ih}=\Gamma_{\rm inh}/\Gamma_{\rm hom}$, the larger is the potential utility of these applications.

A ratio α_{ih} as high as 10^8 has been achieved for Er^{3+}:$LiNO_3$ (Ref. 19). IB also helps to address a single molecule in SMS via spectrally selective excitation.

SINGLE IMPURITY MOLECULE SPECTROSCOPY (SMS) AND SINGLE MOLECULE DETECTION (SMD)

SMS and SMD (see Ref. 21, references therein, and Refs. 22–25) is a rapidly growing novel field of ZPL studies. The applications are especially promoting in biology and molecular biology and also in chemistry.[6] A brand new development in physics are attempts to push ahead quantum computing, quantum communication, etc. Utilization of the sharp and narrow ZPLs[1,2,16,21–23] for the implementation and transformation of qubits (N–V centers in diamond) and also studies of single impurity molecules as single-photon sources and interference phenomena in SMS should be mentioned.

Both SMS and SMD are based on multiple excitation of luminescence and collecting photons. SMD can use also markers without ZPLs. On the other hand, single impurity molecule spectroscopy, which is based on ZPLs and consequently requires low temperatures, is 3–5 orders of more sensitive than SMD (the peak absorption cross section of fluorescence excitation being up to 5×10^{-11} cm^2; Ref. 24). The shape of the ZPL and other fine features can be measured. The peak absorption cross section and the spectral selectivity of luminescence excitation in SMD without ZPLs is 4–5 orders of magnitude smaller than in SMS using good ZPLs. On the other hand, SMD also works at room temperatures, and this is a great advantage in biological studies.

A ZPL of 10 MHz width (typical for the popular SMS molecular impurities today[2–4,16]) can be shifted to a new spectral position (compared to the ZPL's width) by a change of the host structure or a change of the electronic state of a neighboring impurity even hundreds of nanometers away. Besides causing IB, this makes SMS a supersensitive method using ZPL impurities as probes. For it is sometimes too sensitive. The measurements of the widths of individual ZPLs in SMS reveal clearly the presence of various spectral diffusion processes even at liquid He temperatures.[25–27] An effective driving force at low temperatures is the nonequilibrium lattice energy stored in the cooling process. Measurements performed at various times after cooling of the sample display changes in the ZPLs' positions and shapes, which are remarkably different (individualistic) for different molecules. In most cases this is the result of the dependence of the IB on time.[26,27]

A recent development which is promising, in particular, for fundamental quantum optics is the study of interference between the exciting laser beam and the resonantly scattered light emitted by a single molecule,[28] and also the interference of the emission of a single molecule with its mirror image.[29] The novel field of single-photon sources and single-photon phenomena has been opened.

Single-photon states of light today hold an important position in quantum computation,[30] quantum cryptography,[31] and interferometric quantum nondemolition measurements.[32] Several candidates for single-photon sources has been proposed: faint laser pulses and parametric down-conversion,[33] recombination of electrons and holes in single quantum dots,[34] and optically excited single molecules.[35]

The advantage of a single molecule as a source of single photons is the clear situation that after emission of a photon, the emission of the next can take place only when the molecule gets excited again.

It takes some waiting time $T_w=T_{\rm exc}+T_{\rm rad}$, where $T_{\rm exc}$ is the time required for excitation and $T_{\rm rad}$ is the radiative lifetime, which is about 10^{-7} s for allowed transitions but can be orders of magnitude longer for forbidden ones. $T_{\rm exc}$ is longer when the excitation is weaker and the time gap between two subsequent photons longer. In interference experiments like that of Ref. 24 the excitation must match in good resonance the frequency of the ZPL, i.e., the 0–0 transition. To have the possibility for this absorption, the vibrational relaxation in the ground electronic state must be completed. We have $T_w=T_{\rm exc}+T_{\rm rad}+T_{\rm rel}$, where $T_{\rm rel}$ is the (vibrational) relaxation time, which also can be very different for different impurity centers. Thus T_w can be different by orders of magnitude and manipulated via excitation intensity.

A promising candidate for a photon gun and single-photon interference experiments is the N–V impurity center (substitutional nitrogen trapped by a vacancy) in diamond,[36,37] which is photostable even at room temperatures. First, the quality of the transition of the N–V center excited via the ZPL has been verified to be good through measurements of the interphoton time in the process of photon counting and also through the second-order correlation functions of the fluorescence intensity. Both show clearly the antibunching nature of the process of photon emission and, consequently, that the source really is a single impurity center, emitting photons one by one separated by rather long time delays. To create and measure the interference, the stream of (single, well-separated in time and space) photons was directed into a Michelson interferometric detection set,

and the change of the interference pattern of a photon with itself as a function of the delay introduced by the interferometer was detected. The measurements showed that in a system with an interferometer a single photon from a N–V center exists as a superposition of two states of the single photon using both paths of the interferometer. The coherence length of the single-photon emitter was found from the decay of the visibility of the fringes in the interferogram. Interpretation of the measurements gave values in reasonable accordance with the expected ones for wavelength, linewidth, decay time (phase relaxation time T_2), and coherence length. When only the spectral interval corresponding to the ZPL frequency was selected for detection, the coherence length was increased by more than two orders of magnitude.

SMS has been successfully applied to spin dynamics in organic molecules[38–40] and proposed for sequencing of nucleotides in the DNA molecule.[41,42] Let us point out that the task of sequencing of nucleotide in the DNA molecule is an ideal one for low-temperature SMS spectroscopy: the biological essence—the sequence—is most probably not spoiled by cooling to liquid He and applying moderate laser excitation.

Recently single molecule spectroscopy has been applied to paramagnetic single nitrogen–vacancy (N–V) defect centers in diamond[43–48] (actually the only SMS-studied inorganic impurity center up to now). They show high fluorescence emission yield, allowing optical detection of individual defects at low temperature under resonant excitation. The measured homogeneous linewidth of 150 MHz is smaller than the 2.88 GHz zero-field splitting of the triplet ground state of the center, allowing control of the single electron spin state.[8] Individual spin dynamics has been analyzed qualitatively using fluorescence correlation spectroscopy.[49] Time-resolved data show that the spin–lattice relaxation time is in the range of milliseconds.

It was shown that polarization-sensitive single-molecule fluorescence analysis provides a detailed insight into the photophysics of photosynthetic antenna complexes. The picture of excitonic interactions in the light-harvesting complex LH2 is a matter of significant perturbation at room temperature. Dynamical disorder results in the fluctuation of the emission polarization on a time scale of a few hundreds of milliseconds.[50] Strong influence of the local protein environment on the spectral characteristic of pigments has been observed for the plant antenna LHCII.[51] This photosynthetic aggregate was extensively investigated at low temperature, where the spectral jumps of individual Chls molecules reveal the dynamics of the protein matrix. Room temperature studies of LHCII show that only one emitting state is responsible for the fluorescence emission at room temperature. For the trimeric LHCII, the energy transfer between monomeric subunits is slower than the fluorescence lifetime, resulting in an unpolarized fluorescence emission. Recently the single-molecule approach was successfully applied to a reaction center containing a photosynthetic aggregate—Photosystem I from the cyanobacterium *Synechococcus elongatus*.[52,53] It was shown that the red-most pigment pool contains two subgroups of Chls molecules, which differ not only by their spectral position but also by the strength of the electron–phonon coupling. It was proposed that the red-most state is a Chl dimer, which is located near the special pair. High-resolution fluorescence emission and excitation spectra revealing the single chlorophyll structure were recorded at cryogenic temperatures. It was shown that the low fluorescence quantum yield (a few percent at room temperature) is not a severe obstacle to detection of the reaction center containing the photosynthetic species. Quenching of pigment fluorescence can be deactivated at cryogenic temperatures when the required uphill energy transfer is blocked.

The *homogeneous* width Γ_{hom} (shape) of the ZPL is important especially in the novel applications, and to have its definition seems desirable. If the measurement of the luminescence (of the secondary emission, generally speaking) is performed shortly after the act of excitation with a short pulse, then the result is a time-dependent spectrum which can differ entirely from those of conventional stationary measurements. The critical time parameters are the radiative lifetime and the nonradiative relaxation times. If the measurement period is too long, then spectral diffusion can introduce basic changes. Therefore, I would suggest the following definition of the homogeneous ZPL's line shape: ''the homogeneous ZPL spectrum is that of a *single* impurity center measured in a proper time interval.'' [54]

For sake of quantitative interpretation of experimental data, it is generally useful to consider four separate factors that can contribute to the width of homogeneous ZPL (and also the line shape):

$$\Gamma_{\mathrm{hom}}(T,t)=\Gamma_{\mathrm{rad}}(T)+\Gamma_{\mathrm{dep}}(T)+\Gamma_{\mathrm{nrad}}(T)+\Gamma_{\mathrm{inh}}(T,t), \tag{1}$$

where $\Gamma_{\mathrm{rad}}(T)$ is the linewidth caused by spontaneous emission (for allowed transitions the T dependence is not critical); $\Gamma_{\mathrm{nrad}}(T)$ is the linewidth caused by quenching of luminescence (the T dependence is critical); $\Gamma_{\mathrm{dep}}(T)$ is the line broadening caused by dephasing, in most cases by scattering of phonons on the impurity, leading to degradation of the phase coherence (optical coherence) of the excited electronic state (the T dependence is strong because the number of phonons in the solid increases rapidly with T); $\Gamma_{\mathrm{inh}}(T,t)$ arises from different rearrangements and heating/cooling processes taking place in the matrix during the measurement. For individual single molecules the time dependence of the inhomogeneous broadening is also individual and can be strong and complicated. For example, in SMS hundreds of fluorescence photons are being collected for each point of the spectrum, and the measurement process may last up to tens of seconds.

Note that every individual impurity may have its own values for each of the factors in (1). Linewidth SMS measurements of individual molecules have revealed variations of $\Gamma_{\mathrm{hom}}(T,t)$ up to tens of percent between chemically identical impurity centers and also from one measurement time to another delayed by tens of seconds (see next Section). Variations in Γ_{rad} may occur; the dependence of Γ_{rad} can be due to different densities of photon states in the crystal and in vacuum, or can depend on its position relative to the sample's surface. It is interesting to note that similar dependence on the density of the electromagnetic field states causes the well-known Casimir effect.[55]

Persistent spectral hole burning (PSHB) is actually bleaching of luminescence. What makes PSHB a remarkable and useful phenomenon is that the bleaching can be performed, owing to ZPLs, with very high spectral selectivity—with an accuracy of their width. A precious gift of Nature is that the very narrow homogeneous ZPLs form a broad inhomogeneous ZPL band. Illuminating a PSHB material by a light beam having the intensity spectrum (summed up over the excitation time) $I(\omega)$ bleaches the inhomogeneous absorption in accordance with $I(\omega)$ and forms a ''hole'' having the shape $I(\omega)$ and thus memorizing the frequency distribution of the excitation. PSHB is an effective tool of optical engineering by means of illumination: it enables one to predesign and change the profile of the inhomogeneous absorption band of impurity absorption, i.e., actually to control the coefficient of absorption and the index of refraction, which is bound to it via the Kramers—Kronig relations.

When we deal with time-dependent holographic pictures (events) (see next Section) this relation guarantees causality in the theoretical description. A novel chapter of optical engineering has opened using light as the tool. The hole structure fixed in the changes of the sample's material can have long and very long lifetimes—depending on the lifetime of the changes caused by bleaching. In Ref. 56 the lifetime of holes in deuterated organic solids has been estimated as a hundred thousand years. Thus PSHB devices can be made: broad-spectral-band and broad-apperture spectral filters, modulators and, the most remarkable application—optical memories having lifetimes lasting hours, days, and longer.

In the case of pulsed light excitation, the intensity spectrum of the bleaching pulse is stored in the broad and complicated hole structure with a high accuracy equal to the width $\Gamma_{\rm hom}$. If the approach of holography is applied—a reference pulse (shifted in time) is added to the pulse carrying the information and the two pulses are stored together—the equivalent of phases of the information pulse's Fourier components can also be stored. Thus the signal pulse can be restored completely and with high accuracy. The realization of this possibility has opened new and spectacular chapters of optical information storage and processing—frequency-and-space-domain holography[57] and time-and-space-domain holography (TSDH) (see Refs. 3, 4, 17, and 58 and references therein). If the excitation laser band is narrow compared to the homogeneous linewidth $\Delta\omega_l \ll \Gamma_{\rm hom}$ the hole width measured (in the limit of weak excitation) is $\Gamma_{\rm hol} = 2\Gamma_{\rm hom}$. The factor of 2 originates from $\Gamma_{\rm hom}$ being involved twice—first, in hole burning and, second, in the hole shape measurement.

The selectivity, given by $\Gamma_{\rm hom} \approx 10^{-3}$ cm^{-1}, shows that the profile of a picosecond pulse (with $\Delta\omega_{\rm exc} \approx 10$ cm^{-1}) can be stored with a rather high accuracy, given by the ratio

$$\Delta_{\rm exc}:\Gamma_{\rm hom} \approx 10:10^{-3} \approx 10^4.$$

Here $\Gamma_{\rm inh} \gg 10$ cm^{-1}.

The remarkable feature of PSHB holographic studies and applications is that practically everything proposed theoretically has been realized experimentally in the laboratory environment. Commercial applications are still absent because the really nice applications require large α and, consequently, also low temperatures. In fact, liquid He temperatures are nowadays quite a minor technical problem. An essential recent development is femtosecond PSHB.

Femtosecond pulses. Pulses of 10–100 fs duration and hundreds of cm^{-1} wide provide a convenient field for frequency-domain experiments and thus also PSHB technique. The first femtosecond experiment was published ten years ago.[59] In Ref. 60 it is shown how to produce arbitrary time-domain pulse shapes by using PSHB.

The Fourier amplitudes of the desired time dependence of the light pulse are calculated. The corresponding profile of the frequency dependence of the absorption coefficient of a PSHB sheet is written in through PSHB by scanning a narrow-line laser.

The PSHB sheet prepared in that way is illuminated with a broad-band pulse (a ''white pulse'') which, after passing through, is modulated in accordance with the calculated profile of the absorption coefficient (together with it the index of refraction) and will propagate having the desired shape in time.[60]

If a time-dependent *picture* (an event) is to be composed (a scene of an artificial movie) the procedure has to be performed for each spatial pixel of the PSHB sheet.

In the case of a given time-dependent picture (event) it is projected to the sheet. When the PSHB sheet prepared in that way is illuminated with a properly directed ''white'' interrogating pulse, an image of the event is created in full: color picture, time dependence, and even polarization properties are available. The same PSHB structure can be created pixel-by-pixel by means of a cw laser writing the precalculated hole structure. Note that the scenes are artificial: nothing like them ever existed (happened) in reality. The time dependence is continuous, different from our conventional movies or TV, where it is a deception created by changing static pictures with 50 Hz frequency. PSHB time-and-space-domain holography provides a means for really continuous time dependence. In principle, to make a movie, only the scenario, a team of PSHB laser-optics professionals and proper equipment and materials are necessary. No artists, no requisites, panoramic sights, etc. are needed. The present-day limitation comes from the materials—the maximum duration of a scene is limited by the material's phase relaxation time to small fractions of second.

In Ref. 61 a femtosecond interference effect created in a ultrafast two-pulse photon echo in dye-doped polymer films at low temperatures was used to demonstrate an ultrafast three-port all-optical logic ''controlled NOT'' gate (Taffoli gate).

A fascinating result of nonlinear optics is the very large slowing down of the group velocity of light in matter down to the complete ''stopping of light'' (see Refs. 62 and 63 and references therein). In fact this means that the information carried by a light pulse can be stored in the structure of $n(x)$ and later (within the limits of the coherence time of the excited state of matter) be retrieved by a suitable interrogating pulse. PSHB time-and-space domain holography has performed the same task with the following essential differences: coherence (no phase relaxation of the excited state is required only for the write-in time), and the storage time can, as mentioned above, last hours and if desired, be even longer

by orders of magnitude. Note that the light–matter interaction in PSHB is linear.[3,4,64]

An interesting brand-new attempt to indicate the possibility of increasing considerably (by a factor of ~ 100) the number of qubits involved in processing has been made via the use of spectral holes.[65]

PROMISES OF QUANTUM COMPUTING COMPARED TO WHAT IS DONE IN PSHB HOLOGRAPHY

What can be actually achieved in quantum computing (QC) is not clear yet. Current literature prefers to focus on comparing the *future* of QC to the *present* state of *conventional* digital electronic data storage and computing. The outcome of such comparison is overwhelmingly in favor of the future QC. However, it would be fair and educational if QC would be also compared to *holographic* data storage and processing, in particular, to PSHB-based time-and-space-domain holography (see Ref. 66).

Holography is based on distributed data storage and uses interference of light waves. PSHB adds to the two pillars the frequency–time dimension. In holography, owing to these features, parallelism in storage, processing, and retrieval of information is naturally present. Holography provides self-correction of errors and associative recall of information, PSHB TSDH—also in the time domain—in the sequence of events; effective data search (search for events), retrieval of the whole picture (event) by interrogating with a fragment of the picture (event). Time-and-space-domain holography comprises the time-arrow and allows manipulating temporal order of recalled signals, time-reversal, time lens, and fast time shutter (based on causality).[2–4]

As a further advantage of holography I would like to point out that it is based on read-out of *whole pictures and events*, which appears as a natural path to human comprehension. In contrast, digital computers, no matter how advanced they may get in the future, produce ''mountains of bits,'' which are digestible only for another large computer.

The strongest point of TSDH compared to QC is that phase memory has to be preserved only for the time of write-in. In the experiments performed up to now the phase memory of the excited electronic states lasts for about 1 ns in organic materials and up to 1 ms in rare-earth doped crystals. After the phase information is written in, it will be preserved through the stored pattern of intensities (amplitudes) in the modulated structure of the complex index of refraction $n(r,\omega)$. The latter is fixed by the rather stable positions of the atoms of the sample. The information can be read out at a later time (up to years) and many times over.

In contrast, QC requires that phase memory be preserved at all times during writing, storing, and readout of the information. The last completely destroys the content of the memory. It would be desirable to combine the ideas of QC with the features of holography (or to prove that such a combination is impossible).

CONCLUSION

The laser era of ZPL studies and applications started almost 40 years ago, persistent spectral hole burning is thirty years old, and single-impurity-molecule spectroscopy is ten years of age. All three are in good health, producing and promising fine new results. The most interesting results and future developments seem to lie in optical data storage and processing, including quantum informatics. We have to expect remarkable results also in SMS and SMD applications through single marker-carrying impurities as probes in biology.

The author is grateful to F. Jelezko, A. Rebane, and J. Wrachtrup for discussions (especially to F.J. for information and references on SMS studies on N–V centers in diamond and photosynthetic units); to the A. von Humboldt Foundation for making possible his work at Stuttgart University, and to the World Laboratory and Estonian Science Foundation (Grant 4003) for support.

*E-mail: rebanek@fi.tartu.ee

[1] K. Rebane, *Impurity Spectra of Solids*, Plenum Press, New York (1970).
[2] O. Sild and K. Haller (eds.), *Zero-Phonon Lines and Spectral Hole Burning in Spectroscopy and Photochemistry*, Springer, Berlin (1988).
[3] K. K. Rebane and A. Rebane, in *Molecular Electronics, Properties, Dynamics and Applications*, G. Mahler, V. May, and M. Schreiber (Eds.), Marcel Dekker, New York (1996), Chapter 13, p. 257.
[4] K. K. Rebane, in *Current Trends in Optics*, J. C. Dainty (Ed.), Academic Press, London (1994), Chapter 13, p. 177.
[5] K. K. Rebane and V. V. Hizhnyakov, Opt. Spectrosc. **14**, 362 (1963); *ibid.* **14**, 491 (1963).
[6] E. D. Trifonow, Phys. Dokl. **147**, 826 (1962).
[7] E. F. Gross, B. S. Razbirin, and S. A. Permogorov, Phys. Dokl. **147**, 338 (1962); E. F. Gross, S. A. Permogorov, and B. S. Razbirin, *ibid.* **154**, 1306 (1964).
[8] M. A. Krivoglaz and S. I. Pekar, Trudy Instituta Fiziki AN Ukr. SSR Kiev **4**, 37 (1953).
[9] R. Mössbauer, Z. Physik **151**, 124 (1958); Z. Naturforschung **14a**, 211 (1959).
[10] A. A. Kaplyanskii and R. M. Macfarlan (Eds.), *Spectroscopy of Solids Containing Rare-Earth Ions*, Vol. 21 of Modern Problems in Condensed Matter Science, North-Holland, Amsterdam (1989).
[11] A. L. Schawlow, in *Advances in Quantum Electronics*, J. R. Singer (Ed.), New York-London (1961), p. 50; G. F. Imbusch, W. M. Yen, A. L. Schawlow, D. E. McCumber, and M. D. Struge, Phys. Rev. A **133**, 1029 (1964).
[12] L. A. Rebane, A. A. Gorokhovskii, and J. V. Kikas, J. Appl. Phys. B **29**, 215 (1982).
[13] A. Szabo, Phys. Rev. Lett. **25**, 924 (1970).
[14] L. A. Rebane, Zh. Prikl. Spektrosk. **34**, 1023 (1981).
[15] Karl K. Rebane, J. Chem. Phys. **189**, 139 (1994).
[16] T. Basche, W. E. Moerner, M. Orrit, and U. P. Wild, *Single-Molecule Optical Detection, Imaging and Spectroscopy*, Weinheim, New York (1997).
[17] W. E. Moerner (Ed.), *Persistent Spectral Hole Burning, Science and Applications*, Springer, Berlin (1988).
[18] R. W. Equall, Y. Sun, R. L. Cone, and R. M. Macfarlane, Phys. Rev. Lett. **72**, 2179 (1994).
[19] Y. Sun, C. W. Thiel, R. L. Cone, R. W. Equall, and R. I. Hutcheson, J. Lumin. **98**, 281 (2002).
[20] O. Sild and K. Rebane, Opt. Spektrosk. **90**, 766 (2001) [Opt. Spectrosc. **90**, 686 (2001)].
[21] F. Güttler, *Spektroskopie Einzelner Moleküle*, Dissertation ETH nr. 10707, Zürich (1994).
[22] W. E. Moerner and L. Kador, Phys. Rev. Lett. **62**, 2535 (1989).
[23] M. Orrit and J. Bernard, Phys. Rev. Lett. **65**, 2716 (1990).
[24] K. Rebane and I. Rebane, J. Lumin. **56**, 39 (1993).
[25] V. Palm, K. Rebane, and A. Suisalu, J. Phys. C **98**, 2219 (1994).
[26] K. K. Rebane, O. Ollikainen, and V. V. Palm, Opt. Spektrosk. (USSR) **84**, 431 (1998) [Opt. Spectrosc. **84**, 374 (1989)].
[27] V. V. Palm, K. K. Rebane, and A. Zabrodskiĭ, Phys. Solid State **42**, 477 (2000).
[28] T. Plakhotkin and V. Palm, Phys. Rev. Lett. **87**, 183602 (2001).
[29] J. Escher, Ch. Raab, F. Schmidt-Kaier, and R. Blatt, Nature (London) **413**, 496 (2001).

[30] E. Knill, R. Laflamme, and G. J. Milburn, Nature (London) **409**, 46 (2001).
[31] N. Gisin, G. G. Ribordy, W. Tittel, and H. Zbinden, Rev. Mod. Phys. **74**, 145 (2002).
[32] B. Lounis and W. E. Moerner, Nature (London) **407**, 491 (2000).
[33] G. Nogues *et al.*, Nature (London) **400**, 239 (1999).
[34] P. Michler *et al.*, Science **290**, 2282 (2000); A. Peveratos, R. Brouri, T. Gacoin, J. P. Poizat, and P. Grangier, Phys. Rev. A **6406**, 061802 (2001).
[35] A. Gruber *et al.*, Science **276**, 2012 (1997).
[36] F. Jelezko, A. Volkmer, I. Popa, K. K. Rebane, and J. Wrachtrup (submitted).
[37] V. Kiisk, V. Palm, A. Suisalu, and I. Sildos, J. Lumin. **86**, 349 (2000); V. Hizhnyakov, H. Kaasik, and I. Sildos, Phys. Status Solidi B **234**, 644 (2002).
[38] J. Wrachtrup, C. von Borczyskowski, J. Bernard, M. Orrit, and R. Brown, Nature (London) **363**, 244 (1993).
[39] J. Wrachtrup, C. von Borczyskowski, J. Bernard, M. Orrit, and R. Brown, Phys. Rev. Lett. **71**, 3565 (1993).
[40] R. Brown, J. Wrachtrup, M. Orrit, J. Bernard, and C. von Borczyskowski, J. Chem. Phys. **100**, 7182 (1994).
[41] K. K. Rebane, Experimental Technique of Physics **41**, 295 (1995); Fiz. Tverd. Tela (St. Petersburg) **38**, 3487 (1996) [Phys. Solid State **38**, 1902 (1996)].
[42] K. Rebane, *A Means and Method for Sequencing Nucleotides in DNA Molecule Using Laser Spectroscopy*, Patent application of Tartu University, accepted in Estonian Patent Agency Sept. 27, 1996, No. 0134196; No. P 9600101, Apr. 15, 1998.
[43] A. Gruber, A. Drabenstedt, C. Tietz, L. Fleury, J. Wrachtrup, and C. von Borczyskowski, Science **276**, 2912 (1997).
[44] A. Drabenstedt, C. Tietz, F. Jelezko, J. Wrachtrup, S. Kilin, and A. Nizovtzev, Acta Phys. Pol. A **96**, 665 (1999).
[45] A. Drabenstedt, L. Fleury, C. Tietz, F. Jelezko, S. Kilin, A. Nizovtzev, and J. Wrachtrup, Phys. Rev. B **60**, 11503 (1999).
[46] F. Jelezko, C. Tietz, A. Gruber, I. Popa, A. Nizovtsev, S. Kilin, and J. Wrachtrup, Single Molecules **2**, 255 (2001).
[47] F. Jelezko, I. Popa, A. Gruber, C. Tietz, J. Wrachtrup, A. Nizovtsev, and S. Kilin, Appl. Phys. Lett. **81**, 2160 (2002).
[48] S. Y. Kilin, A. P. Nizovtsev, T. M. Maevskaya, A. Gruber, A. Drabenschtedt, J. Wrachtrup, and C. von Borczyskowski, Opt. Spectrosc. **87**, 624 (1999).
[49] A. P. Nizovtsev, S. Y. Kilin, C. Tietz, F. Jelezko, and J. Wrachtrup, Physica B **308**, 608 (2001).
[50] C. Tietz, O. Chekhlov, A. Drabenstedt, J. Schuster, and J. Wrachtrup, J. Phys. Chem. B **103**, 6328 (1999).
[51] C. Tietz, F. Jelezko, U. Gerken, S. Schuler, A. Schubert, H. Rogl, and J. Wrachtrup, Biophys. J. **81**, 556 (2001).
[52] F. Jelezko, C. Tietz, U. Gerken, J. Wrachtrup, and R. Bittl, J. Phys. Chem. B **104**, 8093 (2000).
[53] F. Jelezko, C. Tietz, U. Gerken, E. Thews, S. Schuler, A. Wechsler, and J. Wrachtrup, Opt. Spectrosc. **91**, 457 (2001).
[54] K. Rebane, J. Lumin. **100**, 219 (2002).
[55] H. B. G. Casimir and D. Polder, J. Phys. (Paris), Colloq. **46**, 407 (1949); H. B. G. Casimir and D. Polder, Phys. Rev. **73**, 360 (1948).
[56] J. Friedrich and D. Haarer, Angew. Chemie **23**, 113 (1984); D. Haarer, in *Persistent Spectral Hole Burning, Science and Applications*, W. E. Moerner (Ed.), Springer, Berlin (1988), p. 79.
[57] A. Renn, U. P. Wild, and A. Rebane, J. Phys. C **106**, 3045 (2002); C. D. Caro, S. Bernet, A. Renn, and U. P. Wild, in *Molecular Electronics, Properties, Dynamics and Applications*, Marcel Dekker, New York (1996), Ch. 14, p. 303.
[58] A. Rebane, Chimia **52**, 112 (1998).
[59] A. Rebane, J. Aaviksoo, and J. Kuhl, Appl. Phys. Lett. **54**, 93 (1989).
[60] A. Rebane, M. Drobizhev, and C. Sigel, Opt. Lett. **25**, 1633 (2000).
[61] M. Drobizhev, A. Karotki, and A. Rebane, Chem. Phys. Lett. **334**, 76 (2001).
[62] B. G. Levi, Physics Today, March 2001, p. 17.
[63] D. E. Phillips, A. Fleischhauer, A. Mair, R. L. Walsworth, and M. D. Lunin, Phys. Rev. Lett. **86**, 783 (2001).
[64] A. Rebane, in *Trends in Optics. Research Developments and Applications*, A. Consortini (Ed.), San Diego, Academic Press (1996), p. 165.
[65] M. S. Shahriar, P. R. Hemmer, S. Lloyd, P. S. Bathia, and A. E. Craig, Phys. Rev. A **66**, 032301 (2002).
[66] K. K. Rebane, Opt. Spektrosk. **91**, 472 (2001) [Opt. Spectrosc. **91**, 442 (2001)].

This article was published in English in the original Russian journal. Reproduced here with stylistic changes by AIP.

Kr–Cl stretching vibration of HKrCl: Matrix-isolation and anharmonic *ab initio* study

A. Lignell,* J. Lundell,† M. Pettersson, L. Khriachtchev, and M. Räsänen

Laboratory of Physical Chemistry, University of Helsinki, P.O. Box 55, FIN-00014, Finland
Fiz. Nizk. Temp. **29**, 1109–1112 (September–October 2003)

The Kr–Cl stretching vibration of HKrCl molecule is studied. The absorption shows ^{35}Cl and ^{37}Cl isotopic splitting due to natural abundance of the Cl isotopes. The observed Kr–Cl stretching vibrations of the HKrCl are at 253.1 (^{35}Cl) and 248.3 cm^{-1} (^{37}Cl). Experimentally, deuteration of the HKrCl does not cause a shift of the Kr–Cl stretching frequency. In addition to the Kr–Cl stretching mode, the bending mode of DKrCl is observed at 397.7 cm^{-1}. The vibrational analysis suggests that the Kr–Cl bond shows some covalent character in addition to the ionic. Anharmonic *ab initio* calculations are employed to verify the vibrational properties of various isotopologues of HKrCl. © *2003 American Institute of Physics.*
[DOI: 10.1063/1.1619355]

1. INTRODUCTION

A number of hydrogen-containing rare gas molecules HRgY (H is hydrogen, Rg is a rare gas atom, and Y is an electronegative fragment) have been synthesized and studied in low-temperature matrices within the last several years.[1,2] Preparation of these HRgY molecules consists of photodecomposition of the HY precursor followed by thermal mobilization of atomic hydrogen in a low-temperature rare gas matrix. Infrared absorption spectroscopy is a useful method for detecting these molecules due to the large intensity of the H–Rg stretching vibration absorption.[2] In addition to the H–Rg stretching modes, bending vibrations for many of the HRgY molecules have been observed. The heavy-atom stretching vibration modes ν(Rg–Y) have been observed only for HArF and HKrF.[3–5] The indirect observation of the Xe–I stretching frequency of HXeI, calculated as a difference between combination and fundamental vibration, has been previously reported.[6] Since there are a variety of Rg–Y bonds in these HRgY compounds, it would be very interesting to learn more about the nature of the bonding via direct observation of the Rg–Y stretching vibration. In this work, we study experimentally and computationally the Kr–Cl stretching modes of the H/D and ^{35}Cl/^{37}Cl isotopologues of HKrCl. The experimental data are compared with our previous experimental measurements for HKrF.[5]

2. EXPERIMENTAL AND COMPUTATIONAL DETAILS

In the HCl/Kr experiments, HCl (99%, CIL) and Kr (99.995%, Aga) gases were mixed in a glass bulb. The gas mixture was deposited onto a CsI window kept at 27 K in a closed-cycle helium cryostat (APD, DE 202A). The typical matrix thickness after the 30-minute deposition was 100–200 μm. Deuteration of HCl was achieved by passing premixed gas over the deuterated sulphuric acid (>99% D_2, Merck) in the deposition line. The resulting HCl/DCl ratio was typically ~1. The samples were photolysed through a MgF_2 window at 7.5 K by an 193 nm ArF excimer laser (MPB, MSX-250) using $\sim 10^4$ pulses with a pulse energy density of ~10 mJ/cm^2. The infrared (IR) spectra were measured with a Nicolet SX 60 FTIR spectrometer. In the mid-IR spectral region, the spectrometer was operated with a Ge–KBr beam splitter (BS) and a MCT detector and resolutions of 0.25 and 1 cm^{-1} were used, while in the far-IR region (<400 cm^{-1}) a 6 μm Mylar BS with a DTGS detector and 1 cm^{-1} resolution were used.

In the computational description of the potential energy surface of HKrCl, electron correlation was considered via Møller-Plesset perturbation theory to the second order (MP2), and all electrons were taken into account in the calculations (MP2=FULL). The correlation consistent double-zeta quality all-electron basis set, aug-cc-pVDZ, was employed for all atoms. The equilibrium structure and harmonic vibrational frequencies of HKrCl were also studied by the higher-level coupled cluster [CCSD(T)] approach. The anharmonic vibrational frequencies were obtained from the vibrational self-consistent field (VSCF) and its extension by corrections via second-order perturbation theory (CC-VSCF).[7–10] A pairwise coupling approximation was made to the potential in the normal mode representation.[8] Further details of CC-VSCF combined with an *ab initio* electronic structure code are given in Refs. 9 and 10. All *ab initio* calculations at the MP2 and CC-VSCF levels were performed in the framework of the GAMESS electronic structure program on dual PIII/500 MHz workstations.[11] The CCSD(T) calculations were performed on a SGI Origin 2000 computer at the CSC-Center for Scientific Computing Ltd. (Espoo, Finland) using the Gaussian 98 package of programs.[12]

3. EXPERIMENTAL RESULTS

The HCl/Kr samples were highly monomeric with respect to HCl and DCl precursors and the known absorption bands of HCl at 2872.9 and 2870.5 cm^{-1}, and DCl at 2078.6 and 2075.6 cm^{-1} dominate in the spectra.[13] A small amount of HCl and DCl was complexed with N_2 due to natural nitrogen impurity in the matrices. Interestingly, the complexation efficiency of DCl was observed to be significantly higher than that of HCl. Typically, >90% of HCl was decomposed upon 193 nm photolysis, and the decomposition of DCl was somewhat slower than that of HCl.

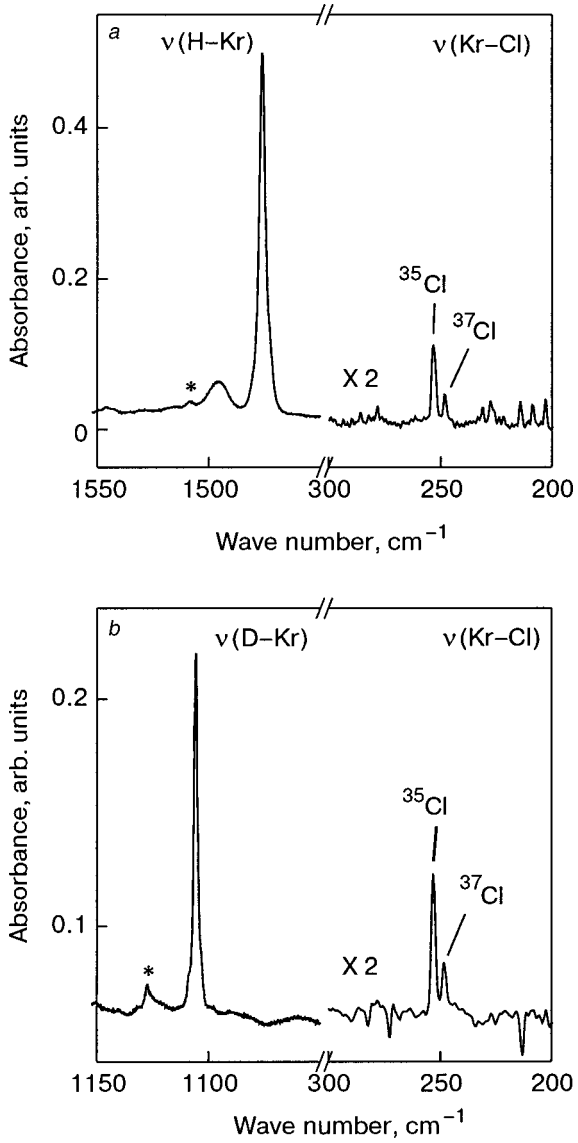

FIG. 1. FTIR spectra of HKrCl (*a*) and DKrCl (*b*) in the middle and far infrared regions. ^{35}Cl/^{37}Cl isotopes cause a splitting (4.8 cm^{-1}) of the bands in the Kr–Cl stretching vibration mode. A band marked with an asterisk belongs to the N_2 complex of HKrCl and DKrCl (see Ref. 23) induced by small nitrogen impurity present in the matrix. In plot (*b*), the bands of HKrCl are subtracted.

HKrCl and DKrCl appeared already during photolysis, as reported previously.[14] Annealing of the sample at ~30 K led to an increase of the amount of HKrCl and DKrCl due to mobilization of atomic hydrogen in a Kr matrix.[15] The observed H–Kr stretching (1476.1 cm^{-1}; see Fig. 1) and H–Kr–Cl bending vibration bands (543.7 and 542.1 cm^{-1} with the overtone at 1069.3 and 1067.9 cm^{-1}) are in good agreement with the previous experimental data.[1] The Kr–Cl stretching vibrations of HKrCl were observed at 253.1 and 248.3 cm^{-1}, the splitting (4.8 cm^{-1}) being due to the natural ^{35}Cl and ^{37}Cl isotopes (see Fig. 1). The intensity ratio between the HKr^{35}Cl and HKr^{37}Cl bands is ~3.2, in accordance with the natural isotope ratio of 3.1. In addition to the previously reported band of the D–Kr stretching mode of DKrCl at 1105.6 cm^{-1} (Ref. 1), the D–Kr–Cl bending vibration band was found at 397.7 cm^{-1}, which is the new spectroscopic data obtained here. The Kr–Cl stretching vibrations of DKrCl were practically unshifted from the corresponding HKrCl bands (see Fig. 1). The experimental assignment of the Kr–Cl stretching bands of HKrCl and DKrCl are based on the following arguments. They increase synchronously with the known HKrCl and DKrCl bands upon annealing. The photostability of the bands is similar, as was checked with the ArF excimer laser (193 nm). The ^{35}Cl/^{37}Cl isotopic shift and intensity ratio show the proper values. Finally, the computations (see below) agree with the observed experimental findings.

4. COMPUTATIONAL RESULTS AND DISCUSSIONS

The optimized H–Kr and Kr–Cl bond distances of the linear HKrCl molecule, calculated at the MP2/aug-cc-pVDZ computational level, are 1.500 and 2.563 Å, respectively. The harmonic vibrational frequencies obtained at this computational level are 1943.1, 604.2, and 275.7 cm^{-1}. The increase of electron correlation to the CCSD(T) level gives longer H–Kr and Kr–Cl distances of 1.545 and 2.580 Å, respectively, and the frequency of the H–Kr stretching mode shifts down to 1512.8 cm^{-1}, which is close to the experimentally observed H–Kr stretching frequency (1476.1 cm^{-1}). Increasing the electron correlation affects less the bending and Kr–Cl stretching modes. At the CCSD(T) level of theory the predicted frequencies are at 569.9 and 273.0 cm^{-1}, respectively, which are very similar to the values obtained using the MP2 calculations.

The high-level harmonic calculations neglect anharmonicity of the potential energy surfaces. However, there is experimental and theoretical evidence for important anharmonic effects for HRgY molecules.[6,16–18] The anharmonic MP2 vibrational frequencies of the HKrCl isotopologues are shown in Table I. The H–Kr stretching (ν_3) is predicted at 1691.0 cm^{-1}, ~250 cm^{-1} below the corresponding harmonic value. Clearly, both electron correlation and anharmonicity are important for adequate description of this molecule. The H–Kr–Cl bending (ν_2) and Kr–Cl stretching (ν_1) modes appear to be less anharmonic than the H–Kr stretching. In the anharmonic calculations, the bending vibration mode is reduced to 575.2 cm^{-1}, i.e., ~30 cm^{-1} below its harmonic value. The ν(Kr–Cl) mode is relatively insensitive to the inclusion of anharmonicity, and the vibration is predicted to be at 274.3 cm^{-1}, shifted only by +1.4 cm^{-1} from the harmonic prediction.

The computational overtone spectrum of HKrCl is rather rich, and several bands are predicted to be promising for experimental detection. The experimentally observed first overtone of the H–Kr–Cl bending mode offers a good benchmark for the anharmonic calculations. The first overtone is predicted to lie at 1149.8 cm^{-1}, while the experimentally observed[1] overtone is at 1069.4 cm^{-1}. Computationally the infrared intensity of the first overtone is 10% from its fundamental intensity, whereas the experimental value is ~30%. The first and second overtones of the H–Kr stretching mode and the first overtone of the Kr–Cl stretch are predicted to be intense enough to be experimentally searched for; however, they were not observed experimentally in this work.

The HRgY molecules have $(HRg)^+Y^-$ ion-pair character. The stronger electronegative moiety Y^- causes larger

TABLE I. Anharmonic computational (MP2/CC-VSCF) and experimental frequencies (in cm^{-1}) of HKrCl and its isotopologues. The computational IR intensities (in km/mol) calculated at the HF level are given in parentheses. The experimental IR intensities are in arbitrary units.

Level	$HKr^{35}Cl$ Computational	$HKr^{37}Cl$ Computational	Experimental	$DKr^{35}Cl$ Computational	$DKr^{37}Cl$ Computational	Experimental
$3\nu_3$	4627.2 (1.0)	4627.1 (1.0)	–	3496.9 (0.2)	3496.8 (0.2)	–
$2\nu_3$	3207.1 (3.9)	3207.0 (3.9)	–	2410.1 (1.2)	2410.0 (1.2)	–
$3\nu_2$	1723.7 (0.4)	1723.3 (0.4)	–	1267.6 (0.1)	1267.0 (0.1)	–
ν_3 ν(H–Kr)	1691.0 (680.9)	1691.0 (681.3)	1476.1 (1.00)	1250.9 (351.6)	1250.8 (352.1)	1105.6 (1.00)
$2\nu_2$	1149.8 (3.3)	1149.5 (3.3)	1069.4,1067.9 (0.01)	844.1 (1.0)	843.7 (1.0)	–
$3\nu_1$	817.3 (0.0)	801.7 (0.0)	–	817.0 (0.0)	801.4 (0.0)	–
ν_2 δ(H–Kr–Cl)	575.2 (33.1)	575.0 (33.3)	543.7, 542.1 (0.03)	421.6 (13.3)	421.4 (13.5)	397.7 (0.02)
$2\nu_1$	546.7 (1.1)	536.3 (1.1)	–	546.5 (1.1)	536.0 (1.0)	–
ν_1 ν(Kr–Cl)	274.3 (137.7)	269.0 (132.4)	253.1 (0.05) ^{35}Cl	274.2 (137.1)	268.9 (131.9)	253.1 (0.17) ^{35}Cl
			248.3 (0.05) ^{37}Cl			248.3 (0.17) ^{37}Cl

charge separation between the $(HRg)^+$ and Y^- moieties, shortening the H–Rg distance and enhancing its vibrational frequency. This leads to stronger covalent bonding of the $(HRg)^+$ entity, while the covalent character of the Rg–Y bond is reduced, lowering the activation energy of dissociation via bending motion. According to the experimental data, the quadratic force constant (f_2) for the Kr–Cl stretch of HKrCl is 0.93 N/cm, as calculated from the equation $f_2 = 4\pi^2 c^2 \omega^2 \mu$, where ω is the vibrational wavenumber, c is the velocity of light, and μ is the reduced mass. For comparison, f_2 for the Kr–F stretch of HKrF is 1.57 N/cm,[5] and the force constants for asymmetric stretches of KrF_2 and $XeCl_2$ are 2.59 N/cm and 1.32 N/cm,[19,20] respectively. These data indicate a stronger Kr–F chemical bonding than Kr–Cl bonding, in accordance with the electron localization studies of Berski and co-workers.[21] A similar trend can be seen for the H–Kr moiety when its covalent character is enhanced from HKrCl to HKrF, as judged by the increase of the H–Kr stretching frequency. As a reference, the harmonic wavenumbers for the Kr^+Cl^- and Kr^+F^- exciplexes, deduced from their electronic emission spectrum,[22] are 208 ± 20 and 284 ± 27 cm^{-1}, resulting in force constants of $f_2(Kr^+Cl^-) = 0.63$ N/cm and $f_2(Kr^+F^-) = 0.74$ N/cm. Since the exciplexes are ionic in nature, the higher frequency of the Kr–Y stretch in HKrY molecules suggest that the Kr–Y bonding in HKrY molecules is not purely ionic but contains also some covalent contribution between the Kr and Y fragments. The covalent contribution between Rg–Y fragments is essential for the existence of a bending barrier in HRgY molecules and is thus important for the intrinsic stability of HRgY molecules.

5. CONCLUSIONS

The Kr–Cl stretching vibration mode for various isotopologues of HKrCl is studied experimentally and compared with the previous measurements on the Kr–F stretching mode of HKrF. Anharmonic vibrational calculations are done on the HKrCl molecule and show good argeement with the experiments. According to the vibrational analysis, it is suggested that the Kr–Cl and Kr–F bonds of HKrCl and HKrF molecules have some covalent contributions in addition to the ionic.

The Ministry of Education, Finland supported this work. The CSC-Center for Scientific Computing Ltd. (Espoo, Finland) is thanked for providing excellent computer facilities. A.L. is a member of the graduate school LASKEMO (Academy of Finland).

*E-mail: lignell@csc.fi
†Permanent address: eChemicum (Chemistry ICT-center), University of Helsinki, P.O. Box 55, FIN-00014, Finland

[1] M. Pettersson, J. Lundell, and M. Räsänen, J. Chem. Phys. **102**, 6423 (1995).
[2] J. Lundell, L. Khriachtchev, M. Pettersson, and M. Räsänen, Fiz. Nizk. Temp. **26**, 923 (2000) [Low Temp. Phys. **26**, 680 (2000)].
[3] L. Khriachtchev, M. Pettersson, N. Runeberg, J. Lundell, and M. Räsänen, Nature (London) **406**, 874 (2000).
[4] L. Khriachtchev, M. Pettersson, A. Lignell, and M. Räsänen, J. Am. Chem. Soc. **123**, 8610 (2001).
[5] M. Pettersson, L. Khriachtchev, A. Lignell, M. Räsänen, Z. Bihary, and R. B. Gerber, J. Chem. Phys. **116**, 2508 (2002).
[6] J. Lundell, M. Pettersson, L. Khriachtchev, M. Räsänen, G. M. Chaban, and R. B. Gerber, Chem. Phys. Lett. **322**, 389 (2000).
[7] J. O. Jung and R. B. Gerber, J. Chem. Phys. **105**, 10332 (1996).
[8] J. O. Jung and R. B. Gerber, J. Chem. Phys. **105**, 10682 (1996).
[9] G. M. Chaban, J. O. Jung, and R. B. Gerber, J. Chem. Phys. **111**, 1823 (1999).
[10] G. M. Chaban, J. O. Jung, and R. B. Gerber, J. Phys. Chem. A **104**, 2772 (2000).
[11] M. W. Schmidt, K. K. Baldridge, J. A. Boatz *et al.*, J. Comput. Chem. **14**, 1347 (1993).
[12] M. J. Frisch, G. W. Trucks, H. B. Schlegel *et al.*, *Gaussian 98, Rev. A.11.4*, Gaussian Inc., Pittsburgh PA (2002).
[13] M. T. Bowers and W. H. Flygare, J. Chem. Phys. **44**, 1389 (1966); L. F. Keyser and G. W. Robinson, J. Chem. Phys. **44**, 3225 (1966); D. E. Mann,

N. Acquista, and D. White, *ibid.* **44**, 3453 (1966).
[14] L. Khriachtchev, M. Pettersson, J. Lundell, and M. Räsänen, J. Chem. Phys. **114**, 7727 (2001).
[15] K. Vaskonen, J. Eloranta, T. Kiljunen, and H. Kunttu, J. Chem. Phys. **110**, 2122 (1999).
[16] J. Lundell, G. M. Chaban, and R. B. Gerber, J. Phys. Chem. A **104**, 7944 (2000).
[17] M. Pettersson, J. Lundell, and M. Rasanen, Eur. J. Inorg. Chem. , 729 (1999).
[18] L. Khriachtchev, J. Lundell, M. Pettersson, H. Tanskanen, and M. Räsänen, J. Chem. Phys. **116**, 4758 (2002).
[19] C. Murchison, S. Reichman, D. Anderson, J. Overend, and F. Schreiner, J. Am. Chem. Soc. **90**, 5690 (1968).
[20] L. Y. Nelson and G. C. Pimentel, Inorg. Chem. **6**, 1758 (1967).
[21] S. Berski, B. Silvi, J. Lundell, S. Noury, and Z. Latajka, in *New Trends in Quantum Systems in Chemistry and Physics*, Vol. 1, J. Maruani, C. Minot, R. McWeeny, Y. G. Smeyers, and S. Wilson (Eds.), Kluwer Academic Publishers, Dordrecht (2001), p. 259.
[22] M. F. Golde, Mol. Spectrosc. (Chem. Soc., London) **58**, 261 (1975).
[23] A. Lignell, L. Khriachtchev, M. Pettersson, and M. Räsänen, J. Chem. Phys. **117**, 961 (2002).

This article was published in English in the original Russian journal. Reproduced here with stylistic changes by AIP.

Luminescence and formation of alkali-halide ionic excimers in solid Ne and Ar

G. Śliwiński* and M. Frankowski

Polish Academy of Sciences, IF-FM, Fiszera 14, PL 80-952 Gdansk, Poland

N. Schwentner

Institute of Experimental Physics, Free University, Arnimallee 14, Berlin D-14195, Germany
Fiz. Nizk. Temp. **29**, 1113–1117 (September–October 2003)

Transitions from ionic states $A^{2+}X^{-}$ of the alkali halides CsF, CsCl, and RbF isolated in solid Ne and Ar films recorded under pulsed e-beam excitation are studied. The $B(^2\Sigma_{1/2})-X(^2\Sigma_{1/2})$ and $C(^2\Pi_{3/2})-A(^2\Pi_{3/2})$ luminescence bands of $Cs^{2+}F^{-}$ (196.5 nm, 227 nm), $Cs^{2+}Cl^{-}$ (220.1 nm, 249.2 nm) and $Rb^{2+}F^{-}$ (136 nm) in Ne, and a weaker $B-X$ emission of $Cs^{2+}F^{-}$ (211.2 nm) in Ar are identified. For CsF the depopulation of the $A^{2+}X^{-}$ state is dominated by the radiative decay. The ratio of the recorded exciplex emission intensities, $I(\mathrm{CsF})/I(\mathrm{CsCl})/I(\mathrm{RbF})=20/5/1$, reflects the luminescence efficiency, and for RbF and CsCl a competitive emission channel due to predissociation in the $A^{2+}X^{-}(B^2\Sigma_{1/2})$ state is observed. For those molecules the efficient formation of the X_2^* state is confirmed through recording of the the molecular $D'(^3\Pi_{2g})-A'(^3\Pi_{2u})$ transition. A strong dependence of the luminescence intensities on the alkali-halide content reveals quenching at concentrations higher than 0.7%. © *2003 American Institute of Physics.* [DOI: 10.1063/1.1619356]

1. INTRODUCTION

Luminescence of ionic excimers covers the VUV and deep UV wavelength region and represents an interesting perspective for an extension of the gas phase excimer media towards shorter wavelengths. Since the first studies around 1985[1,2] the ionic systems have been extensively investigated. Spectroscopic studies in the gas phase provided emission from ionic states $A^{2+}X^{-}$ of alkali halides (AX) and from diatomic $(RgA)^{+}$ and triatomic $(Rg2A)^{+}$ rare gas alkali ions.[3–8] Although optical gain has been achieved,[9] recent kinetic studies indicate the presence of quenching processes that can seriously limit amplification.[10]

The electronic configurations for the family of alkali-halide ions $(AX)^{+}$ correspond to those of rare gas halides RgX in the ground state and correlate to the atomic states $A^{+}(^1S)$ and $X(^2P)$. Also the ionically bound upper states $(A^{2+}X^{-})$ due to transfer of an alkali $5p$ core electron to the halogen are isoelectronic to $Rg^{+}X^{-}$ exciplex states with similar potential surfaces and correlate to $A^{2+}(^2P)$ and $X^{-}(^1S)$ atomic states. Since the potential of the lower $(AX)^{+}$ state has a dissociative character, it is anticipated that population inversion can be obtained in these systems. The upper bound state can be directly populated by photoionization of AX. Radiative transitions with large cross section for stimulated emission and short radiative lifetimes of the order of 1 ns can be expected for $A^{2+}X^{-}$. These ions considered in the condensed phase combine the favorable properties of the short-wavelength, strong excimer emissions known from the gas phase with the high number densities of excited states attainable in the solid.

Recently, deep UV fluorescence bands of $A^{2+}X^{-}$ ions have been observed for CsF, CsCl, and RbF isolated in Ne and Ar matrices under e-beam excitation.[11,12] It was shown that the exciplex states $B^2\Sigma_{1/2}$ and $X^2\Pi_{3/2}$ are effectively populated via host excitons resulting mainly in the $B^2\Sigma_{1/2}\rightarrow X^2\Sigma_{1/2}$ emission. Also a much weaker $C^2\Pi_{3/2}\rightarrow A^2\Pi_{3/2}$ transition for the ionic states of CsF and CsCl was observed. The observed transitions were red shifted compared to the gas phase due to interaction with the dielectric host.

The first indication of the homonuclear $D'-A'$ transition of Cl_2^* and F_2^* was reported and ascribed to predissociation via the $A+X^*$ state.[13]

In this work we study the spectroscopic data and formation of the ionic states $A^{2+}X^{-}$ of alkali halides: CsF, CsCl, and RbF isolated in thin Ne and Ar films. Conclusions on the formation efficiency of X_2^* molecules due to predissociation in the $A^{2+}X^{-}(B^2\Sigma_{1/2})$ state of RbF and CsCl following from the concentration-dependent measurements are discussed.

2. TRANSITIONS FROM ALKALI-HALIDE IONIC STATES

For understanding of the excitation and decay processes it is instructive to consider the energy level scheme of the alkali-halide states involved in the observed radiative transitions. Since the problem was discussed for the CsCl elsewhere,[12] here we shall just recall the features that are valid for the general case of the $A^{+}X^{-}$ ionic states. For this purpose it is convenient to consider the energy of states in units equal to the binding potential of the AX ground state and the internuclear separation in units of the equilibrium distance r_e—see Fig. 1. The states relevant for discussion are described by potential curves; for the other states only the positions of the dissociation limits are given. The rare gas excitons formed in the host by the pulsed electron beam are responsible for the $A^{+}(^1S)$ core ionization of the $^1\Sigma$ ground state of AX molecules (the upward arrow in Fig. 1). Due to the equilibrium distance r_e in this state the higher vibrational levels ν'' of the $A^{2+}(^2P)X^{-}(^1S)$ state are populated, and a

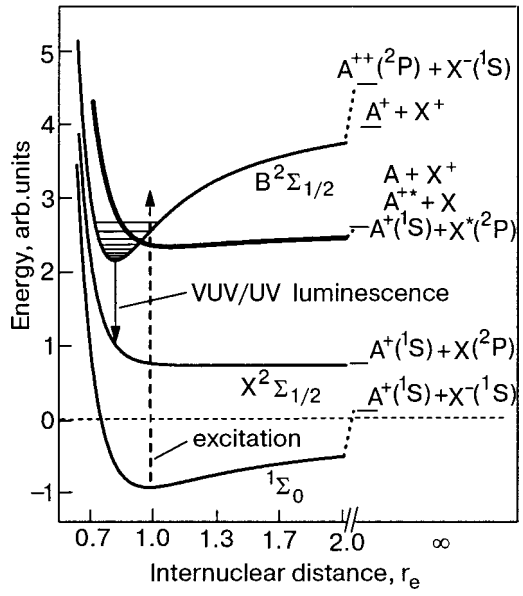

FIG. 1. The potential energy diagram of the alkali halides; energy and internuclear separation are in units of the ground-state binding potential and r_e, respectively; the relevant states are described by the shell configurations, while for the other states only the energy positions at $r=\infty$ are given; for simplicity, the states $C^2\Pi$ and $A^2\Pi$ resulting from the spin–orbit splitting of the upper and lower excimer state, respectively, are not shown. Selective excitation of the ground-state A^+X^- molecule is provided by the e-beam via rare gas excitons — dashed arrow. The radiative decay follows a fast radiationless relaxation to the $\nu'=0$ level of the $A^{2+}X^-$ ionic bound state.

fast radiationless relaxation to the $\nu''=0$ level occurs because of the low temperature, around 5 K. It is followed by the bound–free radiative transition

$$A^{2+}X^- \Rightarrow (AX)^+ + h\nu \tag{1}$$

to the repulsive part of the lower $X^2\Sigma_{1/2}$ potential and is characterized by the emission of UV photons on a time scale close to one nanosecond (the downward arrow in Fig. 1). From an energy standpoint, population of the closely spaced B and C states of $A^{2+}X^-$ is equally likely, and emissions from these states are observed, contrary to the D state, which lies higher in energy by the $^2P_{3/2}$–$^2P_{1/2}$ spin–orbit splitting of the A^{2+} ion.

The potential curves for the bound states, i.e., the ground state $^1\Sigma$, the A^+X^* state, and the ionic state $B^2\Sigma_{1/2}$ in Fig. 1 are based on the truncated Rittner potential (at $1/r^4$) with the effect of the dielectric host taken into account by introducing a factor of $1/\varepsilon$ into the Coulombic and $1/r^4$ terms. Bond lengths and polarizabilities are taken from the literature.[4,14] For the lower A^+X state the Born–Mayer potential

$$V(r)=\varepsilon_0 \exp[-\alpha_0(r-r_e)] \tag{2}$$

is used with the assumption that the consideration refers to the vicinity of the equilibrium distance r_e, with ε_0 being the energy of the lower state at $r=r_e$. The shape of $V(r)$ and also the ε_0 and α_0 values are derived from experimental data for the gas phase B–X transitions of the $A^{2+}X^-$ ions. The potential minima of the $X^2\Sigma_{1/2}$ states are taken equal to their gas phase counterparts.[4]

The transition energies observed in experiment are red shifted by ΔE relative to the gas phase. This can be explained by means of the cavity shell model for a transition dipole moment $\Delta|\mu|$ given by the relation

$$(\Delta|\mu|)^2 = C(\varepsilon)\Delta E d^3 \tag{3}$$

with $C(\varepsilon)=0.125(2\varepsilon+1)/(\varepsilon-1)$, d corresponding to the cavity diameter, and ε being the dielectric constant of the surrounding. The measured ΔE values yield the estimates for $\Delta|\mu|$ and the measured transition energies result in potential minima of the upper $A^{2+}X^-(B^2\Sigma_{1/2})$ states with the red shifts reflecting the solvation energy of the ionic states of AX molecules.

For CsCl and RbF it can be deduced from Fig. 1 that the Frank—Condon region corresponding to the excitation of the $^1\Sigma$ state falls close to the crossing point of the $A^{2+}X^-$ and A^+X^* potential surfaces. This indicates predissociation of the $A^{2+}X^-$ state as the probable depopulation channel due to the reaction

$$A^{2+}X^- \Rightarrow A^+ + X^* \tag{4}$$

which is accompanied by a partial, nonradiative energy loss. As in the gas phase results,[5] the competing predissociation effect is only observed for CsCl- and RbF-doped samples, and in both cases the X_2^* molecular emission

$$X_2^* \Rightarrow X_2 + h\nu_1, \quad h\nu_1 < h\nu \tag{5}$$

occurs. However, in the host a strong cage effect traps the excited X* atoms in the lattice. This leads to a decrease of the population of X_2 molecules finally formed in the ground state. For CsF doped samples the X_2^* emission was not observed in either the matrix or the gas phase. The difference in separations of the crossing point of $A^{2+}X^-$ and A^+X^* potentials from the bottom of the $^1\Sigma$ potential ($r_e=1$) in Fig. 1, and also the longer radiative lifetime of the C state explain the low intensity of the C–A band for CsF and CsCl in Ne obtained from experiment. The spectroscopic data of the observed ionic transitions for RbF, CsCl, and CsF are calculated following the procedure described previously;[15] they are given in Table I.

As most of the data obtained pertain to the Ne host, a comment should be added for the transition energies observed in the solid. These are shown as the matrix-dependent (Ne, Ar, or Kr) peak positions of the emission bands, together with the respective data from the gas phase measurements and those of the solid state XeF excimer for reference—Fig. 2. The peak positions are given for optimal contents of the alkali halides CsF (0.45% in Ar, and 0.7% in Ne), CsCl (0.37%), and RbF (0.6%) in solid Ar and Ne films. The variable $(\varepsilon-1)/(2\varepsilon+1)$ describes the host interaction, and the slanted lines connect data of the same dopant. In comparison to the gas phase results[5] the matrix shift of the $B\rightarrow X$ luminescence from the ionic states of RbF, CsF, and CsCl has a value of 0.43, 0.39, and 0.33 eV, respectively. This is in good agreement with the values 0.3–0.4 eV predicted from relation (3) and coincides with the results obtained for the XeF excimer in solid Ne and Ar.[15,16] Moreover, the values obtained so far from experiment (solid data

TABLE I. Spectroscopic properties of matrix-isolated, core-excited RbF, CsF, and CsCl alkali halides in the VUV and deep UV spectral range: λ_{em} is the peak position, FWHM is the half-width, σ_s is the cross section for stimulated emission, and τ_f is the radiative lifetime.

Molecule, transition	Matrix	λ_{em}, nm	FWHM, nm	σ_S, 10^{-16} cm^2	τ_r, ns
$Rb^{++}F^-$					
$B \rightarrow X$	Ne	136	4.5	1.5	0.9
$Cs^{++}F^-$					
$B \rightarrow X$	Ne	196.5	9.5	2.5	1.2
$C \rightarrow A$	Ne	227.1	15	0.22	11.3
$B \rightarrow X$	Ar	211.2	11.3	2.74	0.8
$Cs^{++}Cl^-$					
$B \rightarrow X$	Ne	220.1	10.4	2.22	1.4
$C \rightarrow A$	Ne	249.2	14.8	0.29	12.6

points) allow one to deduce estimates of the transition energies for emission bands not yet observed in the solid and in the gas phase as well (hollow data points).

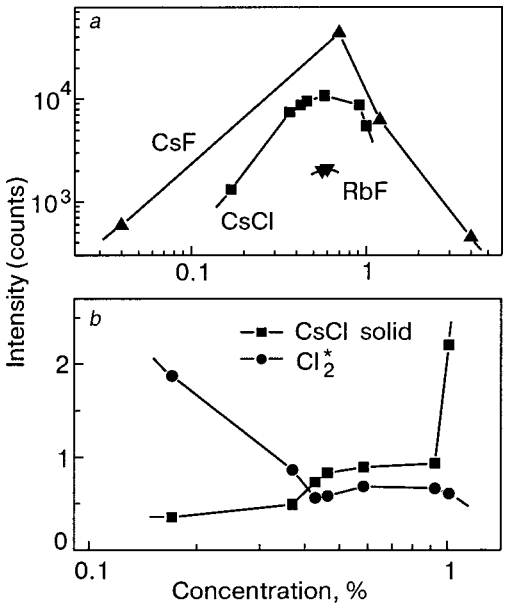

FIG. 3. Emission intensities of the $B \rightarrow X$ transition of the $A^{2+}X^-$ exciplexes versus the AX concentration in Ne solid films for CsF (▲), CsCl (■), and RbF (▼) (*a*), and the case of CsCl-doped Ne sample; luminescence intensities of the Cl_2^* molecular transition $D'(^3\Pi_{2g}) \rightarrow A'(^3\Pi_{2u})$ and of the intrinsic band of CsCl aggregates (245 nm), related to the $B^2\Sigma_{1/2} \rightarrow X^2\Sigma_{1/2}$ band intensity versus concentration (*b*); concentrations are in percent and the intensities are the peak values measured.

3. THE CONCENTRATION EFFECT

The measured intensities of the $B-X$ band are highly sensitive to changes in the original sample composition. Dependences of the peak intensity values versus the dopant concentrations in Ne films presented in the form of experimental data sets for CsF, RbF (up and down triangles), and CsCl (squares) are summarized in Fig. 3. The dependence observed for CsCl is more pronounced than for CsF, and for RbF only two data points are available due to the relatively low signal. In all cases the optimal alkali-halide content corresponding to the maximum band intensity lies around 0.6–0.8% and is in accordance with the data obtained for the gas phase[4] and also coincides with those from our previous results reported for XeF.[15,16] A comparison of the band intensities for the optimal concentrations related to the highest one (CsF) lead to a ratio of $I(\mathrm{CsF})/I(\mathrm{CsCl})/I(\mathrm{RbF}) = 20/5/1$, which reflects the energy transfer efficiency for the investigated species. In the case of CsF a change of the concentration-dependent intensity of almost two orders of magnitude is observed. The data for CsCl indicate a weaker concentration dependence for samples doped below optimum than for the more highly doped ones. The occurrence of the predissociation of molecules in the ionic state can be observed exclusively in the low doping range. This is confirmed by the detailed analysis of the CsF and CsCl spectra reported elsewhere.[11,12] The relevant decay channels of the $Cs^{2+}Cl^-(B^2\Sigma_{1/2})$ state become more evident when the $D'(^3\Pi_{2g} \rightarrow A'(^3\Pi_{2u})$ transition of the Cl_2^* molecule is taken into account. An appearance of the molecular emission can only be observed for CsCl content not exceeding values of about 0.6–0.7%. The intensity of this transition is even much larger than that of $B-X$ for lower concentrations, around 0.1–0.2%. This, together with a decrease of the Cl_2^* band intensity with increasing CsCl content in that range, reflects a strong competition between the deep UV emission and the concentration quenching process, which is due to short-range

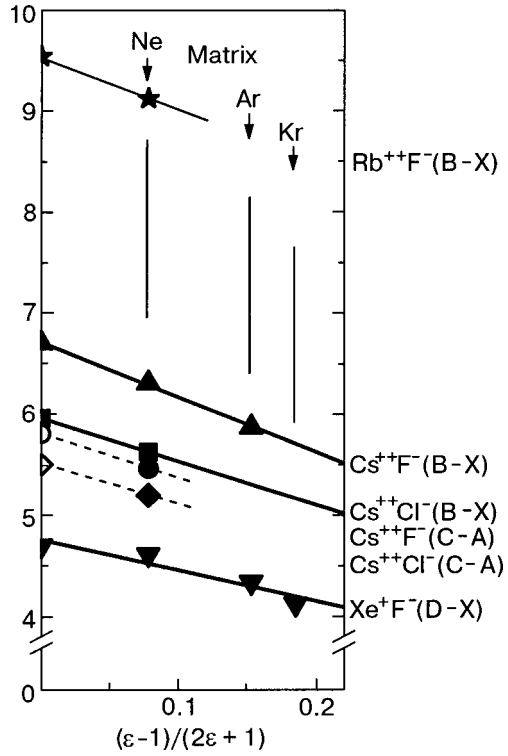

FIG. 2. The matrix-dependent transition energies of the *e*-beam excited CsF, CsCl, and RbF in Ar and Ne solid films for the optimal alkali-halide concentrations, and XeF data for reference; values for $(\varepsilon-1)/(2\varepsilon+1)=0$ correspond to the gas phase data already measured (solid data points) and postulated (hollow points).

energy migration, aggregation, and also self-absorption by the ground-state CsCl($^1\Sigma$) molecules. For a concentration increase in the range from about 0.4 to 0.9% the optimal values of the dopant content correspond to the highest band intensities. An AX content larger than 0.9% results in a decrease of the $B-X$ band intensities. Moreover, in that doping region a rapid growth of the intrinsic fluorescence bands originating from aggregates occurs. In the case of CsF the concentration quenching seems to represent the main negative contribution to the emission efficiency of the excimer band. In general, the effect observed most clearly for CsCl is representative for the decay of $(AX)^+$ states of alkali halides in general. This is supported by the similar concentration dependences of the band intensities observed for CsF and in part for RbF, too.[17,18]

4. CONCLUSION

The favorable population of the $A^{2+}X^-$ state of alkali halides by ionization of the trapped AX molecules via host excitons of solid Ne and Ar can be deduced from the energy level scheme and is confirmed experimentally. The $B(^2\Sigma_{1/2})-X(^2\Sigma_{1/2})$ radiative transition from ionic states represents the most efficient depopulation channel for e-beam excited, rare gas matrix-isolated CsF, CsCl, and RbF. Also the much weaker emission bands $C(^2\Pi)-A(^2\Pi)$ of $Cs^{2+}F^-$ and $Cs^{2+}Cl^-$ occur besides the intrinsic luminescence bands of aggregates. For RbF and CsCl the concentration dependent formation of X_2^* molecules due to predissociation in the $A^{2+}X^-(B^2\Sigma_{1/2})$ state is observed in experiment. The resulting molecular transition $D'(^3\Pi_{2g})-A'(^3\Pi)$ competes efficiently with the exciplex emissions at low doping concentrations around 0.1%. A strong dependence of the emission intensities on the alkali-halide content leads to aggregation and quenching at doping concentrations higher than the optimal range of about 0.7%. The marked difference in the $B-X$ emissions intensities observed for alkali halides CsF, CsCl, and RbF is explained by the position of the crossing point of the $A^{2+}X^-$ and A^+X^* potential surfaces relative to the equilibrium internuclear separation of the A^+X^- ground state. The condensed phase ionic excimer $Cs^{2+}F^-$ represents the best emission properties compared to $Cs^{2+}Cl^-$ and $Rb^{2+}F^-$. This is demonstrated by the $B-X$ fluorescent transition dominating the excited state decay and also the fluorescence intensity exceeding those of $Cs^{2+}Cl^-$ and $Rb^{2+}F^-$ by a factor of about 6 and 20, respectively.

*E-mail: gerards@imp.gda.pl

[1] R. Sauerbrey and H. Langhoff, IEEE J. Ocean. Eng. **QE-21**, 179 (1985).
[2] N. G. Basov, M. G. Voitik, V. S. Zuev, and V. P. Kutalchov, Sov. J. Quantum Electron. **15**, 1455 (1985).
[3] H. M. I. Bastiaens, F. T. J. L. Lankhorst, P. J. M. Peters, and W. J. Witteman, Appl. Phys. Lett. **60**, 2834 (1992).
[4] S. Kubodera, P. J. Wisoff, and R. Sauerbrey, J. Opt. Soc. Am. B **9**, 10 (1992).
[5] C. Toth, J. F. Young, and R. Sauerbrey, Opt. Lett. **18**, 2120 (1993).
[6] T. T. Yang, V. T. Gylys, and D. G. Harris, J. Opt. Soc. Am. B **6**, 1536 (1989).
[7] D. Xing, K. Ueda, and H. Takuma, Chem. Phys. Lett. **163**, 193 (1989).
[8] S. Kubodera, P. J. Wisoff, and R. Sauerbrey, J. Chem. Phys. **92**, 5867 (1990).
[9] S. Kubodera and R. Sauerbrey, Opt. Commun. **94**, 515 (1992).
[10] M. Schumann and H. Langhoff, J. Chem. Phys. **101**, 4769 (1994).
[11] G. Śliwiński, Ch. Bressler, and N. Schwentner, Phys. Status Solidi B **193**, 247 (1996).
[12] G. Śliwiński and N. Schwentner, J. Appl. Phys. D **30**, 2229 (1997).
[13] G. Śliwiński and N. Schwentner, J. Low Temp. Phys. **111**, 733 (1998).
[14] E. S. Rittner, J. Chem. Phys. **19**, 1030 (1951).
[15] G. Zerza, G. Śliwiński, and N. Schwentner, Appl. Phys. B: Photophys. Laser Chem. **55**, 331 (1992).
[16] G. Zerza, G. Śliwiński, and N. Schwentner, Appl. Phys. A: Solids Surf. **56**, 156 (1993).
[17] M. Frankowski, G. Śliwiński, and N. Schwentner, SPIE Proc. **3724**, 362 (1999).
[18] M. Frankowski, G. Śliwiński, and N. Schwentner, J. Low Temp. Phys. **122**, 443 (2001).

This article was published in English in the original Russian journal. Reproduced here with stylistic changes by AIP.

The vibration–rotation of H_2O and its complexation with CO_2 in solid argon revisited

X. Michaut,* A. M. Vasserot, and L. Abouaf-Marguin

Laboratoire de Physique Moléculaire et Applications, UMR CNRS 7092, Université Pierre et Marie Curie, boîte 76, 4 place Jussieu, 75252 Paris, Cedex 05, France
Fiz. Nizk. Temp. **29**, 1118–1124 (September–October 2003)

Fourier-transform infrared spectroscopy in the frequency range 400–4000 cm^{-1} has been used to investigate the absorption of H_2O and H_2O:CO_2 complex isolated in solid argon. Thanks to the lowest temperature reached in our experiment, temperature effects and nuclear spin conversion studies allow us to propose a new assignment of the rovibrational lines in the bending band ν_2 for the quasi-freely rotating H_2O. An additional wide structure observed in this band shows two maxima around 1657.4 and 1661.3 cm^{-1}, with nuclear spin conversion of the high-frequency part into the low-frequency one. This structure is tentatively attributed to a rotation–translation coupling of the molecule in the cage. However, the equivalent effect is not observed in the vibrational stretching bands ν_1 and ν_3. Finally, in double doping experiments with CO_2 important new structures appear, allowing us to unambiguously extract the frequencies of the lines of the H_2O:CO_2 complex. © *2003 American Institute of Physics.*
[DOI: 10.1063/1.1619357]

1. INTRODUCTION

The water molecule is of C_{2v} symmetry. In the gas phase its rovibrational spectrum is well known[1–3] up to 26000 cm^{-1}, and in the solid state the structures of the different forms of ice have been extensively studied.[4–6] Ice grains play an important role in the chemistry of the interstellar medium and of planetary atmospheres.[7,8] D'Hendecourt *et al.*[9] have shown from IRAS-LRS observations of protostars that CO_2 is a wide-spread and very common component of the interstellar medium. The complexes between H_2O and CO_2 have also been the subject of several previous studies.[10,11]

It is well known that the matrix isolation technique, combined with IR absorption spectroscopy, remains a powerful tool for studying the formation and geometry of weakly bonded complexes. Before looking at the H_2O:CO_2 complex, pure H_2O in matrices had to be studied under our experimental conditions. Since the work of Glasel,[12] all evidence indicates that H_2O trapped in inert matrices is almost freely rotating.[13–17] After some initial controversies, there is now general agreement on the assignment of the rovibrational absorptions in the ν_2 and ν_1/ν_3 regions in solid argon.[16] This assignment is also very important for all matrix isolation studies because water is a common impurity. In the same way, since CO_2 is also always present as an impurity in matrix experiments, the identification of complexes of water with CO_2 is essential.

In the present paper we will focus attention on the hindered rotational motion of water molecules in solid argon. After a brief description of the experimental conditions, we will present a calculation of the cold gas transitions. Then experimental results will be presented, including temperature and time effects. An assignment of the lines will be proposed. The last Section is devoted to identification of absorption lines of CO_2:H_2O weakly bonded complexes through double doping experiments with CO_2. The results will be discussed in the light of recent data.

2. EXPERIMENTAL

The experimental setup has already been described.[18] We only review here the main and specific features.

Ar and CO_2 (L'Air Liquide–99.995% and 99.99% respective purity) are used without purification. Water is deionized, doubly distilled, and carefully degassed. The gaseous mixture is obtained by standard manometric procedures. As water is adsorbed on the walls of the stainless steel part of the sample system, we carefully passivated the system with a pressure of water equal to its partial pressure in the gas mixture. During deposition, we checked that water absorptions were proportional to the amount of deposited gas mixture.

To study weakly bonded complexes, the relative concentrations have to be carefully chosen.[19] For molecules which do not react with each other, as is the present case,[10] more than the statistical number of mixed pairs can be obtained by premixing the two molecules with argon in the gas sample.[20]

The samples were obtained by the slow spray-on technique (10 mmol/h) of the gaseous mixture onto a gold-plated mirror held at 20 K. The solid sample is then cooled to 6 K and annealed at least up to 30 K to allow a reorganization of the polycrystalline film (narrowing of the lines) and a migration of molecular species.

Absorption spectroscopy is performed using a Bruker IFS 113V FTIR spectrometer, with a maximum resolution of 0.03 cm^{-1} and, at this resolution, an accuracy better than 0.02 cm^{-1}. The frequencies of broad lines are estimated within a 0.1 cm^{-1} precision.

3. CALCULATION OF THE "COLD" GAS TRANSITIONS

As the rotation is almost free, a comparison with the expected spectrum of the gas at 6 and 20 K is helpful for the transition assignments. The water molecule, of symmetry type C_{2v}, is an asymmetric rotor, with two magnetic species, ortho (spin degeneracy 3) and para (spin degeneracy 1). In Fig. 1, the rovibrational transitions are indicated for the three

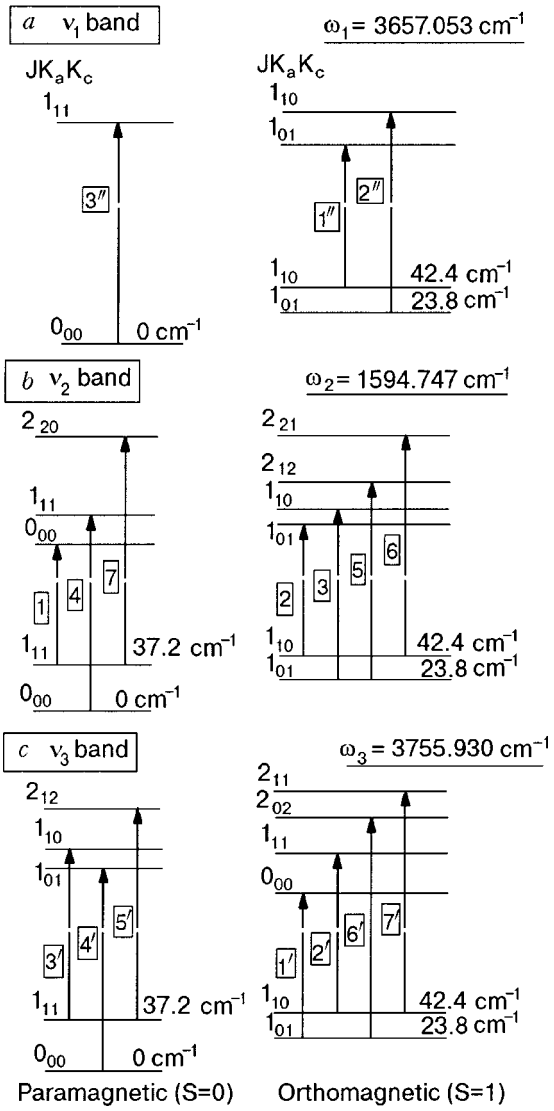

FIG. 1. Rovibrational transitions of the three modes of gaseous H_2O at 20 K: ν_1 band (*a*); ν_2 band (*b*); ν_3 band (*c*); J, K_a, and K_c are the rotational quantum numbers of the asymmetric rotator; S is the nuclear spin quantum number.

fundamental bands of H_2O, numbered in increasing frequencies of the gas phase. At 20 K, the $J=0$ and 1 energy levels are the only ones sufficiently populated to give rise to detectable absorptions. If the nuclear spin conversion were fast, only the para line *4* should appear for the ν_2 mode at 6 K. But, as is well known, the conversion is very slow in low-temperature matrices.[21] Then 2 other lines, the ortho lines *3* and *5*, remain detectable, as long as the 20-K Boltzmann population is trapped for some time on the 1_{01} ortho level. Using the intensities reported in HITRAN96 data base,[1] bar spectra can be calculated at 20 and 6 K (graphs labeled G in Figs. 2).

4. EXPERIMENTAL RESULTS IN THE ν_2 REGION OF H_2O

We will now discuss in detail the ν_2 range and then give the results obtained with similar arguments for the ν_1 and ν_3 bands. The observed frequencies, measured with 0.03 cm^{-1} maximum resolution are in Table I, and compared to the most recent data in the literature.[16]

A typical spectrum of a sample $H_2O/Ar=1/500$ is presented in Fig. 2 at 20 and 6 K.

Temperature effect

The two lines at 1556.6 and 1573.2 cm^{-1} and the broad structure around 1690 cm^{-1}, which appear at 20 K, disappear totally at 6 K. The effect is reversible. By comparison with the gas spectrum it seems obvious that those structures correspond, respectively, to lines *1*, *2*, and *6/7*. Intensity comparisons with the gas also favor this interpretation, as it is known that the matrix does not lead to dramatic changes in the relative intensities of the transitions.

At this point, we would disagree with the conclusions of previous studies in solid argon[13–16] which assign lines *6* and *7* to the double structure observed at 1660 cm^{-1}. This does not seem possible, since these lines do not start from the lowest energy level. They should disappear at 6 K, as do lines *1*, *2*, and *6/7*, whereas this 1660 cm^{-1} double structure remains. On the other hand, the 1690 cm^{-1} structure appears only when the temperature is raised. Our very recent experiments at 20 K with high-optical-density samples[22] show that in this broad structure at 1690 cm^{-1}, which clearly exhibits two maxima (1689.7 and 1697.8 cm^{-1}), the low-frequency maximum decreases much faster than the high-frequency one as the temperature is lowered. This low-frequency shoulder must therefore correspond to a transition from a level with a higher energy gap to the fundamental than the high-frequency one, and it should be assigned to line *7*. Then the line at 1697.8 cm^{-1} must correspond to transition *6*. Those lines, like the 1636.3 line, are broad compared to lines *2*, *4*, and *5* because they involve a $J=2$ level, which is more affected by the coupling to the matrix than are the levels with $J=0$ or 1.

At 6 K, the 1607.82, 1623.72, and 1636.3 cm^{-1} lines correspond to transitions *3*, *4*, and *5*, respectively, in agreement with previous assignments. Transition *5*, which involves a $J=2$ level, is also broad.

So far, there is no obvious assignment for the double structure at 1660 cm^{-1}, which remains at 6 K and does not nonvanish at 20 K, showing only a weak broadening. By changing the concentrations and considering the changes upon annealing, we have checked that its intensity is related to the concentration of the monomer absorbers.

In Fig. 2 one additional line appears at 1592.94 cm^{-1}, which corresponds to the dimer of H_2O, in agreement with previous work, as is noted in Table III below (see Sec. 6).

Furthermore, the line measured[16] at 1589.2 cm^{-1} may be assigned to nonrotating molecules.[13–16] Whatever our experimental conditions, with samples of pure H_2O, this line was always very weak. In Sec. 6 of this paper we will show that it is due to the H_2O:CO_2 complex, since CO_2 is generally present as an impurity in the samples.

Time effect

As we have said, the nuclear spin conversion from the ortho to the para form is slow in low-temperature matrices.[21] The time evolution of the spectra can confirm the assignments, since ortho lines should decrease to the benefit of para lines when starting from nonequilibrated Boltzmann populations at 6 K.

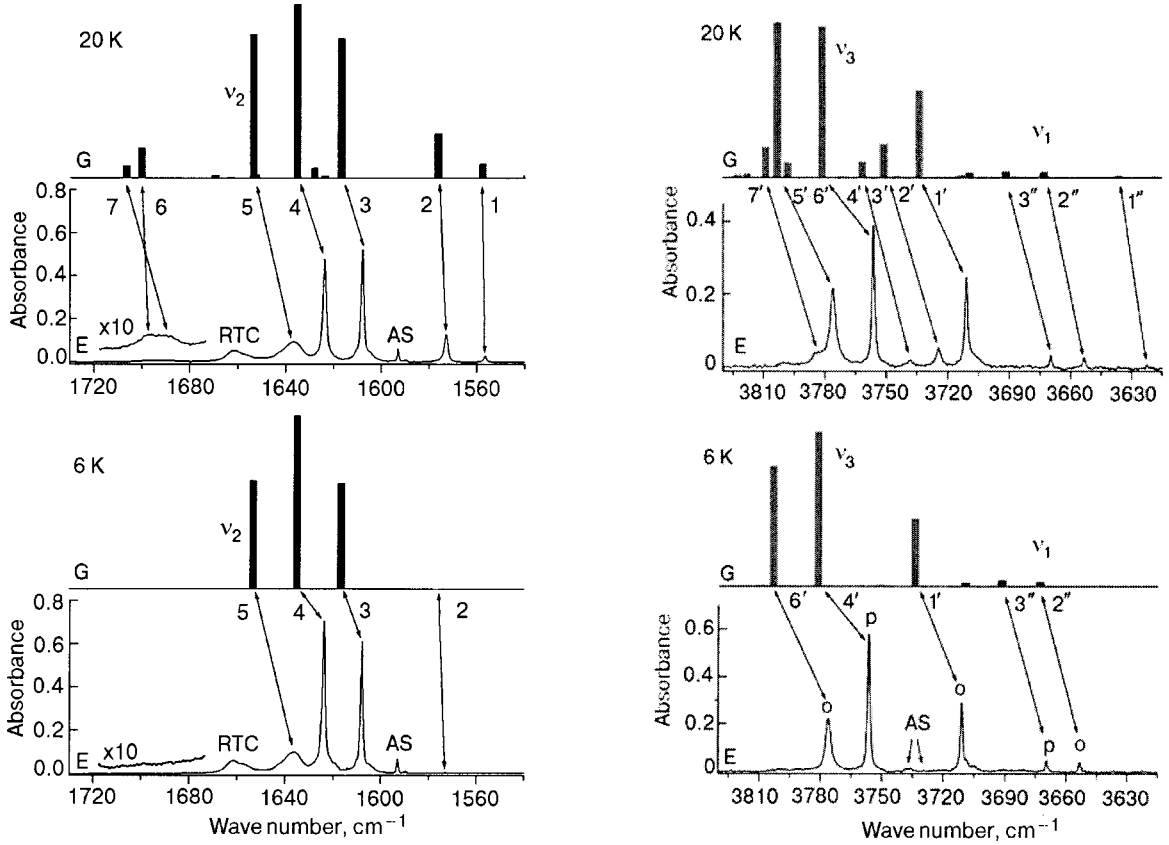

FIG. 2. Spectra at 20 and 6 K of the ν_1, ν_2, ν_3 regions of H_2O. G is the simulated bar spectrum of the gas, the numbers refer to the transitions of Fig. 1; E is the experimental spectrum (H_2O/Ar= 1/500) recorded with 0.15 cm^{-1} resolution, just after deposition at 20 K (thickness ~250 μm); the arrows indicate the present assignments, RTC is the rotation–translation coupling structure, and AS corresponds to the H_2O dimer; *o* and *p* are orthomagnetic and paramagnetic species.

Figure 3 exhibits these intensity changes after two hours. The first spectrum is taken just after a fast cooling from 30 K. Lines *3* and *5* decrease when *4* increases, which is consistent with the assignments. In the double structure near 1660 cm^{-1}, the high-frequency part (1661.3 cm^{-1}) decreases and the low-frequency part (1657.4 cm^{-1}) increases accordingly. This structure presents an ortho and a para component, is situated between 50 and 100 cm^{-1} away from the pure vibrational frequency, and remains at 6 K. It does not belong to the rovibrational structure but is related to the

TABLE I. Frequencies (cm^{-1}) and assignments of absorption lines of monomeric H_2O in the ν_2 region in solid argon.

Line	Transition	Magnetic species	Gas [1]	This work	Perchard [16]
1	$1_{11}\rightarrow 0_{00}$	para	1557.611	1556.6[a]	1556.7
2	$1_{10}\rightarrow 0_{01}$	ortho	1576.188	1573.2[a]	1573.1
					1589.2[c] (NRM)
3	$1_{01}\rightarrow 1_{10}$	ortho	1616.714	1607.82[b]	1607.9
4	$0_{00}\rightarrow 1_{11}$	para	1634.970	1623.72[b]	1623.8
5	$1_{01}\rightarrow 2_{12}$	ortho	1653.268	1636.3[b]	1636.5
RTC	Rotation translation coupling	para / ortho		1657.4[b] / 1661.3[b]	
6	$1_{10}\rightarrow 2_{21}$	ortho	1699.935	1697.8[a]	1661.4
7	$1_{11}\rightarrow 2_{20}$	para	1706.355	1689.7[a]	1657.2
					1687.6 / 1699.9 (Phonon activation)

[a] Measured at 20 K. [b] Measured at 6 K. [c] Nonrotating molecule.

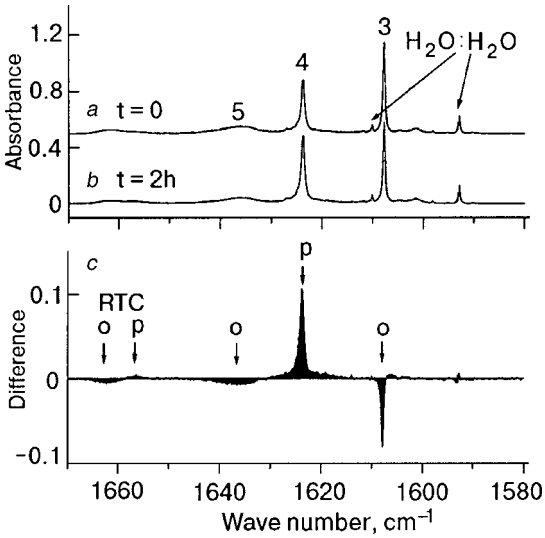

FIG. 3. Time effect in the ν_2 region of H_2O, due to nuclear spin conversion at 6 K. The spectra (H_2O/Ar= 1/1000) are recorded with 0.15 cm^{-1} resolution, after annealing at 30 K (thickness ~220 μm) after a time $t=0$ (*a*) and 2 hours (*b*); the numbers refer to the transitions of Fig. 1; (*c*) presents the difference of spectra (*a*) and (*b*); *o* and *p* are orthomagnetic and paramagnetic species.

TABLE II. Frequencies (cm^{-1}) and assignments of absorption lines of monomeric H_2O in the ν_1 and ν_3 region in solid argon.

Line	Transition	Magnetic species	Gas [1]	This work	Perchard [16]
ν_1 band					
1″	$1_{10}\rightarrow1_{01}$	ortho	3638.082	3622.4[a]	3622.7
					3638.3[c] (NRM)
2″	$1_{01}\rightarrow1_{10}$	ortho	3674.697	3653.38[b]	3653.5
3″	$0_{00}\rightarrow1_{11}$	para	3693.294	3669.85[b]	3669.7
ν_3 band					
1′	$1_{01}\rightarrow0_{00}$	ortho	3732.135	3711.2[a]	3711.3
2′	$1_{10}\rightarrow1_{11}$	ortho	3749.331	3724.7[a]	3724.9
					3736.0[c] (NRM)
3′	$1_{11}\rightarrow1_{10}$	para	3759.845	3739.4[a]	3739.0
4′	$0_{00}\rightarrow1_{01}$	para	3779.493	3756.49[b]	3756.6
6′	$1_{01}\rightarrow2_{02}$	ortho	3801.420	3776.30[b]	3776.4
7′	$1_{10}\rightarrow2_{11}$	ortho	3807.014	3784.5[a]	

[a] Measured at 20 K. [b] Measured at 6 K. [c] Nonrotating molecule.

number of rotating molecules. It may then be a manifestation of the rotation–translation coupling (RTC) involved in the movement of the molecule in its cage.[23]

The weak lines at 1592.94 and 1610.12 cm^{-1} are due to dimers (Table III). The line 1610.12 cm^{-1} is hidden in the high-frequency wing of line *3* in Fig. 2 but appears after annealing to 30 K (Fig. 3).

5. EXPERIMENTAL RESULTS IN THE ν_1 AND ν_3 REGIONS OF H_2O

The 3600–3800 cm^{-1} region is represented in Fig. 2 at 20 and 6 K (H_2O/Ar=1/500), together with the calculated gaseous bar spectra. With the same arguments as for ν_2, we present the assignments in Table II, which agree with the most recent work.[16]

TABLE III. Most intense observed lines (cm^{-1}) of H_2O dimer and H_2O:CO_2 complex isolated in solid argon.

Line	H_2O:H_2O		H_2O:CO_2	
	This work	Perchard [16]	This work	Svensson et al. [24]
H_2O (ν_1)	3574.77 3633.22	3574.0 (PD) 3633.1 (PA)	3638.0	3632.7
H_2O (ν_2)	1592.94 1610.12	1593.1 (PA) 1610.6 (PD)	1589.48 1589.86 1590.54	1593.1
H_2O (ν_3)	3708.5 3738.1	3708.0 (PD) 3715.7 (PA) 3737.8 (PA)	3732.46	3732.9
CO_2 (ν_2)			656.03 667.95 668.05	656.0 668.0
CO_2 (ν_3)			2340.20	2340.5

PA: proton acceptor; PD: proton donor.

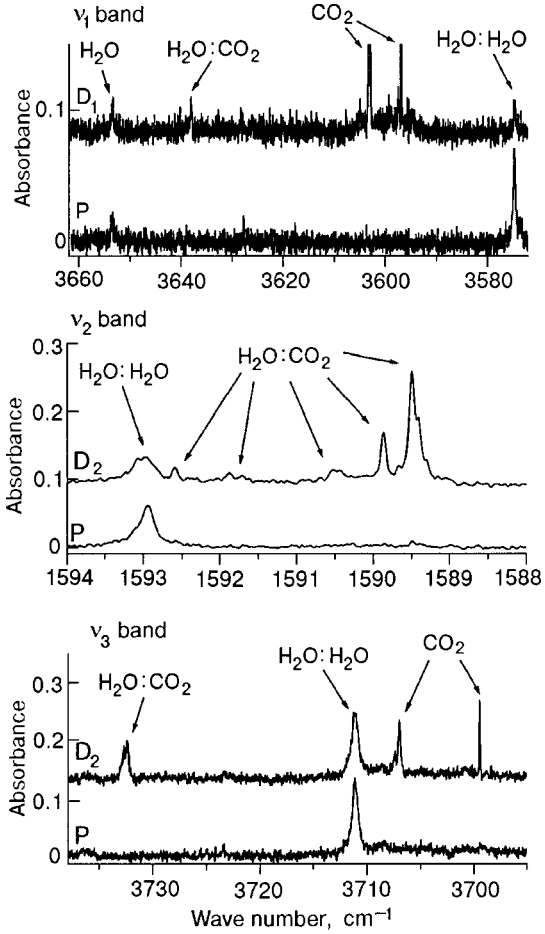

FIG. 4. Double doping with CO_2: water regions at 6 K. The spectra are recorded with 0.03 cm^{-1} resolution, after annealing at 30 K; P is a pure H_2O sample (H_2O/Ar=10/5000, thickness ~60 μm); D_1 and D_2 are the double doped samples (D_1: H_2O/CO_2/Ar=10/5/5000, thickness ~80 μm; D_2: H_2O/CO_2/Ar=10/2/5000, thickness ~60 μm).

However, two points should be noted: i) the lines involving a $J=2$ level are not as broad as in the ν_2 case; ii) there is no evidence of a RTC structure as observed for ν_2.

This could be explained by a weaker coupling of the rotation–vibration to the translation in the cage for the stretching modes ν_1 and ν_3 than for the bending mode ν_2.

Some dimeric species are also observed in this frequency range. The measured frequencies (see Table III) are in good agreement with the literature.[16]

6. DOUBLE DOPING EXPERIMENTS WITH CO_2: THE COMPLEX

H_2O frequency ranges

To look at the H_2O:CO_2 complex near H_2O absorptions, the sample should be concentrated in CO_2.[19] However, as CO_2 has a great tendency to form polymers, its concentration should be kept low enough to avoid aggregates of H_2O with more than one CO_2 molecule. In Fig. 4, we can compare typical spectra obtained with a sample of pure H_2O (spectrum P—H_2O/Ar=1/5000) to spectra of CO_2 double doped samples (spectra D_1—H_2O/CO_2/Ar=10/5/5000 and D_2—H_2O/CO_2/Ar=10/2/5000), recorded with 0.03 cm^{-1} resolution. The spectra were recorded at 6 K, after an annealing at 30 K, which enhances the complex absorptions. Some

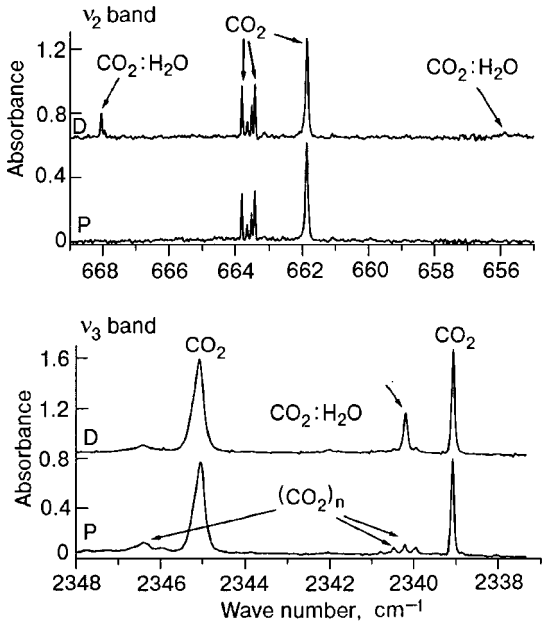

FIG. 5. Double doping with CO_2: carbon dioxide regions at 6 K. The spectra are recorded with 0.03 cm^{-1} resolution, after annealing at 30 K; P is a pure CO_2 sample ($CO_2/Ar=1/5000$, thickness $\sim 60\ \mu m$) and D is a double doped sample ($H_2O/CO_2/Ar=1/10/5000$, thickness $\sim 60\ \mu m$).

new lines appear in the double doped experiment due to the simultaneous presence of H_2O and CO_2. As the dilutions remain high enough, there is a weak probability of trimolecular species. With the H_2O dimer absorptions, for the H_2O:CO_2 complex, the most intense narrow structures which can be measured are indicated in Table III. By varying the relative concentration of CO_2, we have checked that the behavior of these lines is consistent with a 1:1 pair, as they grow proportionally with the concentration of CO_2 for a given concentration of H_2O. Our results are compared in Table III with the recent ones of Svensson *et al.*[24]

In the H_2O ν_1 range, besides the combination bands $(2\nu_2+\nu_3)$ of CO_2 reported by Schriver *et al.*[25] around 3596.9 and 3602.98 cm^{-1}, only a weak line due to the double presence of H_2O and CO_2 can be detected at 3638 cm^{-1}. Near ν_2, two clear structures appear at 1589.48 cm^{-1}, with shoulders at 1589.04 and 1589.81 cm^{-1} and a narrower line at 1589.86 cm^{-1}. The broad and weak absorptions around 1591.5 and 1591.8 cm^{-1} are also due to the presence of CO_2. The spectra, for the ν_3 mode, exhibit clearly a broader absorption at 3732.46 cm^{-1}, close to the combination bands $(\nu_1+\nu_3)$ of CO_2.[25]

The number of these absorptions, especially for the ν_2 mode of H_2O, is probably due to multiple trapping sites for the complex and different geometries, as the vibrational modes of H_2O are not degenerate. The broad structures could be due to very perturbed crystalline double cages.

CO_2 frequency ranges

In typical experiment presented in Fig. 5, the samples are more dilute in CO_2 (spectra P: $CO_2/Ar=1/5000$ and D: $CO_2/H_2O/Ar=1/10/5000$). The striking new features are: one narrow structure at 668.05 cm^{-1} (with a shoulder at 667.95 cm^{-1}), a much weaker broad one at 656.03 cm^{-1} in the ν_2 range, and one narrow line at 2340.20 cm^{-1} in the ν_3 range. These results are consistent with those reported in the literature.[24] We should mention that the line at 2340.2 cm^{-1} had already been assigned to this complex by Guasti *et al.*[26] in 1978, in an experiment on CO_2 in solid argon, for which an amount of water was present due to a leak in the system.

7. CONCLUSION

Our new experimental data have led to some new assignments of the rovibrational frequencies of H_2O on the ν_2 mode, and the absorptions of the H_2O:CO_2 complex in the H_2O regions in an argon matrix. From our refined measurements of rovibrational frequencies, the ''effective'' rotational constants of water trapped in solid argon may be determined. Furthermore, our experimental results will support calculations able to explain the RTC structure. For the complex with CO_2, some more experimental work is needed in order to understand the different trapping sites and structures. A modeling similar to that developed for the CO:CO_2 complex[27] will be attempted.

The authors acknowledge Louise Schriver-Mazzuoli for helpful discussions.

*E-mail: xmichaut@ccr.jussieu.fr

[1] L. S. Rothman, C. P. Rinsland, A. Goldman, S. T. Massie, D. P. Edwards, J. M. Flaud, A. Perrin, C. Camy-Peyret, V. Dana, J. Y. Mandin, J. Schroeder, A. McCann, R. R. Gamache, R. B. Wattson, K. Yoshino, K. V. Chance, K. W. Jucks, L. R. Brown, V. Nemtchinov, and P. Varanassi, J. Quant. Spectrosc. Radiat. Transf. **60**, 665 (1998).
[2] L. R. Brown, R. A. Toth, and M. Dulick, J. Mol. Spectrosc. **212**, 57 (2002).
[3] P. F. Coheur, S. Fally, M. Carleer, C. Clerbaux, R. Colin, A. Jenouvrier, M. F. Merienne, C. Hermans, and A. C. Vandaele, J. Quant. Spectrosc. Radiat. Transf. **74**, 493 (2002).
[4] C. Lobban and J. L. Finney, J. Mol. Spectrosc. **112**, 7169 (2000).
[5] L. Schriver-Mazzuoli, A. Schriver, and A. Hallou, J. Mol. Spectrosc. **554**, 289 (2000).
[6] V. P. Dmitriev, S. B. Rochal, and P. Toledano, Phys. Rev. Lett. **71**, 553 (1993).
[7] D. Prialnik and Y. Mekler, Astrophys. J. **366**, 318 (1991).
[8] A. Coustenis, A. Salama, E. Lellouch, Th. Encrenaz, G. L. Bjoraker, R. E. Samuelson, Th. de Graauw, H. Feuchtgruber, and M. F. Kessler, Astron. Astrophys. **336**, L85 (1998).
[9] L. B. d'Hendecourt and M. Jourdain de Muizon, Astron. Astrophys. **223**, L5 (1989).
[10] L. Fredin, B. Nelander, and G. Ribbegard, Chem. Scr. **7**, 11 (1975).
[11] P. Ehrenfreund, A. C. A. Boogert, P. A. Gerakines, A. G. G. M. Tielens, and E. F. van Dishoeck, Astron. Astrophys. **328**, 649 (1997).
[12] J. A. Glasel, J. Chem. Phys. **33**, 252 (1960).
[13] R. L. Redington and D. E. Milligan, J. Chem. Phys. **39**, 1276 (1963).
[14] R. M. Bentwood, A. J. Barnes, and W. J. Orville-Thomas, J. Mol. Spectrosc. **34**, 391 (1980).
[15] A. Engdahl and B. Nelander, J. Mol. Spectrosc. **193**, 101 (1989).
[16] J. P. Perchard, Chem. Phys. **273**, 217 (2001).
[17] D. Forney, M. E. Jacox, and W. E. Thompson, J. Mol. Spectrosc. **157**, 479 (1993).
[18] D. Jasmin, P. Brosset, R. Dahoo, B. Gautier-Roy, and L. Abouaf-Marguin, J. Mod. Opt. **108**, 2302 (1998).
[19] V. Raducu, D. Jasmin, R. Dahoo, P. Brosset, B. Gauthier-Roy, and L. Abouaf-Marguin, J. Chem. Phys. **101**, 1878 (1994).
[20] V. Raducu, D. Jasmin, R. Dahoo, P. Brosset, B. Gauthier-Roy, and L. Abouaf-Marguin, J. Chem. Phys. **102**, 9235 (1995).
[21] B. Gauthier-Roy, L. Abouaf-Marguin, and P. Boissel, J. Chem. Phys. **98**, 6827 (1993) and references therein.
[22] X. Michaut, A. M. Vasserot, and L. Abouaf-Marguin, to be published.
[23] H. Friedmann and S. Kimel, J. Chem. Phys. **47**, 3589 (1967).

[24] T. Svensson, B. Nelander, and G. Karltrom, Chem. Phys. **265**, 323 (2001).
[25] A. Schriver, L. Schriver-Mazzuoli, and A. A. Vigasin, Vib. Spectrosc. **23**, 83 (2000).
[26] R. Guasti, V. Schettino, and N. Brigot, Chem. Phys. **34**, 391 (1978).
[27] J. Langlet, J. Caillet, M. Allavena, V. Raducu, B. Gauthier-Roy, R. Dahoo, and L. Abouaf-Marguin, J. Mol. Spectrosc. **484**, 145 (1999).

This article was published in English in the original Russian journal. Reproduced here with stylistic changes by AIP.

Exciton self-trapping into diatomic and triatomic molecular complexes in xenon cryocrystals

A. N. Ogurtsov*

B. Verkin Institute for Low Temperature Physics and Engineering of the National Academy of Sciences of Ukraine, 47 Lenin Ave., Kharkov 61103, Ukraine; Department of Physics of Ukrainian Academy of Railway Transport, 7 Feuerbach Sq., Kharkov 61050, Ukraine

E. V. Savchenko

B. Verkin Institute for Low Temperature Physics and Engineering of the National Academy of Sciences of Ukraine, 47 Lenin Ave., Kharkov 61103, Ukraine

E. Sombrowski

Deutsches Elektronen-Synchrotron DESY, 85 Notkestrasse, Hamburg 22607, Germany

S. Vielhauer and G. Zimmerer

Institut für Experimentalphysik der Universität Hamburg, 149 Luruper Chausee, Hamburg 22761, Germany
Fiz. Nizk. Temp. **29**, 1125–1129 (September–October 2003)

Our recent study of molecular trapped centers in Xe cryocrystals is extended to triatomic self-trapped excitons. Time- and spectrally-resolved molecular luminescence is measured in the temperature range 5–60 K. The processes of intrinsic exciton self-trapping into diatomic and triatomic molecular complexes and extrinsic exciton trapping at lattice imperfections are separated by selective photoexcitation of Xe cryocrystals with synchrotron radiation. The temperature dependences of the triplet lifetimes of molecular exciton subbands are measured for the first time. © *2003 American Institute of Physics.* [DOI: 10.1063/1.1619358]

1. INTRODUCTION

Rare-gas cryocrystals are attractive objects for investigation of electronic excitation trapping processes in condensed matter. Because of strong coupling with phonons, free excitons (FE) in rare-gas cryocrystals are localized into quasi-atomic and quasi-excimer (excited dimer) self-trapped excitonic states (STE). Radiative decay of quasi-excimer trapped excitons produces the most prominent feature in a vacuum-ultraviolet (VUV) luminescence from solid Ar, Kr and Xe—the so-called M (molecular luminescence) band, which is formed by $^{1,3}\Sigma_u^+ \rightarrow {}^1\Sigma_g^+$ transitions in a molecular dimer R_2^* embedded in the host lattice (R stands for a rare-gas atom).[1] The hole part of the STE is self-trapped between two neighboring rare-gas atoms in the diatomic bonding configuration, and the excited electron is bound to it primarily by the Coulomb interaction.[2] The internal structure of the M band, which indicates the peculiarities of crystal lattice structure, has been studied recently.[3] Translational motion of a molecular-STE along the atomic chain by continuous redistribution of the hole part of an exciton among atoms inevitably passes a symmetric triatomic configuration, which is presumed to be metastable.[4] However, in solid Xe at elevated temperature ($T>50$ K), in addition to the M_1 and M_2 molecular luminescence subbands of the M band in the emission spectrum of molecular self-trapped excitons, a third molecular band (the M_3 band) appears at 7.6 eV. It has been suggested that the M_3 band is attributable to radiative decay of excitons self-trapped into triatomic linear molecular complexes,[5] whose electronic and geometric structure was studied recently.[6]

Such a variety of trapping channels for excitons makes solid Xe a suitable medium for modeling the processes of self-trapping of electronic excitations.[2] This paper reports the results of the analysis of the time- and spectrally-resolved luminescence from excited diatomic and triatomic intrinsic molecular complexes in Xe cryocrystals following primary selective excitation by synchrotron radiation in the temperature range 5–60 K.

2. EXPERIMENT

The photoluminescence experiments were carried out at the SUPERLUMI experimental station at HASYLAB, DESY, Hamburg. The selective photon excitation was performed with $\Delta\lambda = 0.2$ nm. The low-resolution spectral and time-resolved analysis of the molecular luminescence was performed with a high-flux VUV-monochromator equipped with a multisphere plate detector. The convolution of the temporal behavior of the excitation synchrotron pulse, the response of the detector and of the electronics used was about 430 ps. High-resolution spectra were measured with $\Delta\lambda = 0.1$ nm by a 1-m near-normal incidence VUV-monochromator equipped with a position-sensitive detector. The cathodoluminescence measurements were performed at the molecular spectroscopy laboratory of Verkin Institute, Kharkov. The electron beam excitation was performed by electrons of energy 1 keV, insufficient to form defects by elastic collisions. The luminescence analysis with $\Delta\lambda = 0.2$ nm was carried out with a 1-m near-normal incidence monochromator equipped with a solar-blind photomultiplier.

The crucial part of the luminescence experiments with rare-gas solids is the sample preparation technique. There are two most commonly used methods of Xe sample preparation from the vapor phase: (i) isothermal growth at $T=118$ K with a growth rate of about 1 μm/min, and (ii) growing of the sample under isobaric ($P\approx 1000$ Pa) conditions with the constant cooling in the temperature range 125–110 K. The isothermal growth is rather slow, but it provides the preparation of the samples with the best crystal quality.[7] The isobaric growth is much faster and it allows one to vary the quality of the crystals by changing the cooling rate from 0.01 K/s (''slow'' isobaric growth with a growth rate of about 10 μm/min) to 0.5 K/s (''fast'' isobaric growth with a growth rate of about 50 μm/min). In the present study we used the fast isobaric method of sample preparation. The samples were grown *in situ* on a copper substrate from a high-purity (99.999%) room-temperature vapor phase in special closed cells.[8] The thickness of the samples was ≈ 0.5 mm.

3. RESULTS AND DISCUSSION

The VUV-luminescence spectra of solid Xe at temperatures below and above the threshold of M_3 band appearing are shown at Fig. 1. The broad Stokes-shifted STE emission band (M band) contains contributions of radiative decay of quasi-excimer centers of two types.[3] Depending on the structure of the surrounding lattice, the molecular STE centers emit different subbands of the molecular luminescence band—high-energy subband M_2 is emitted by STE quasiexcimers in perfect lattice, whereas the low-energy subband M_1 is emitted by molecular excitons, which are trapped at lattice imperfections. Analysis of the mutual behavior of the subbands for various treatments of the samples under selective photoexcitation allows one to elucidate the complicated picture of branched relaxation of electronic excitations in rare-gas cryocrystals.[9]

The high-resolution spectra of Xe cryocrystals in the FE emission range are shown at Fig. 1*c*. The narrow line at $E_{FE}=8.36$ eV (FE line) is formed by radiative decay of free excitons from the bottom of the lowest $\Gamma(3/2)$, $n=1$ excitonic band. The energy position of the maximum of FE line exhibits a temperature shift because of thermal expansion of the lattice.[10] In addition, in the spectra of Xe cryocrystals grown by a fast isobaric method, two luminescence features appear: a narrow band at 8.15 eV in the whole temperature range, and a weak asymmetric band at 8.23 eV at high temperature (Fig. 1*c*). The 8.15 eV band (the E_2 band) has been reported earlier in cathodoluminescence[8,10] and in laser- and x-ray-excited luminescence spectra.[11] The intensity of the E_2 band grows when the crystal quality of the sample decreases.[8] The asymmetric band at 8.23 eV is attributed to luminescence from ''hot'' states of molecular self-trapped excitons in solid Xe.[11,12] Neither the E_2 band nor the 8.23 eV band was visible in the spectrum of the best sample of solid Xe[7] prepared by isothermal growth. At the same time, in the laser- and x-ray-excited luminescence there was no FE line. This suggests that formation of both the 8.15 eV and 8.23 eV

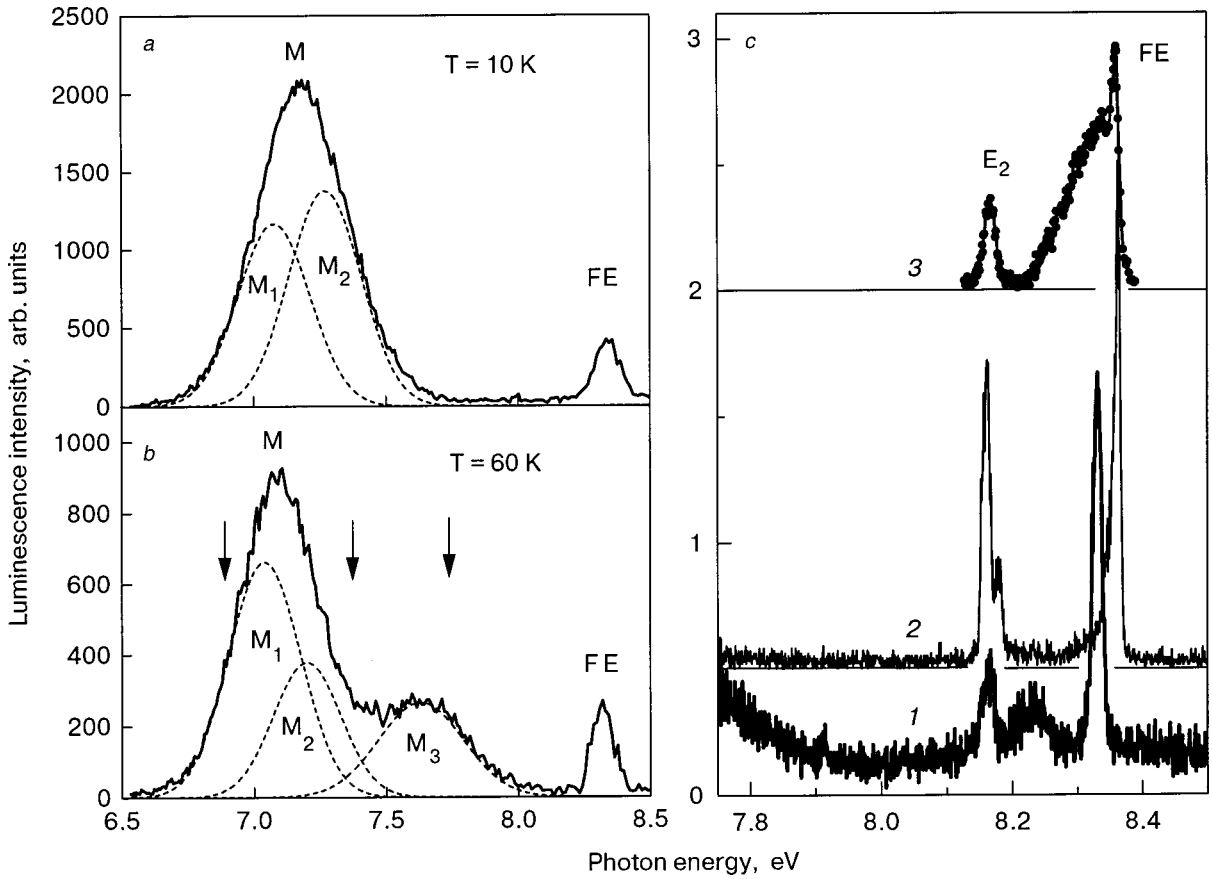

FIG. 1. Luminescence spectra of Xe cryocrystals under selective photoexcitation with $h\nu=8.86$ eV (*a* and *b*). Photoluminescence (curves *1* and *2*) and cathodoluminescence (curve *3*) spectra of solid Xe at $T=10$ K (curves *2* and *3*) and $T=60$ K (curve *1*) (*c*).

emitting centers is stimulated by crystal lattice imperfections.

Above $T=50$ K a third wide molecular-like band M_3, centered at 7.63 eV with FWHM 0.36 eV, appears in addition to the M_1 and M_2 molecular luminescence bands (Fig. 1*b*). There is as yet no final conclusion about the nature of this high-temperature molecular band in solid Xe. At the very beginning of the study of excitons in rare-gas solids it was suggested that the M_3 band is emitted by real STE in the perfect lattice, whereas the M band corresponds to excitons localized at lattice defects.[13,14] This hypothesis is in contradiction to recent studies of exciton self-trapping into molecular states in rare-gas cryocrystals[3,5,7,9,12] and excludes the exciton self trapping in solid Kr and Ar, where there is no luminescence band similar to the M_3 band of solid Xe. There have been several attempts to associate the M_3 band with the forbidden transition $^1\Sigma_g^+ \rightarrow {}^1\Sigma_g^+$ (Ref. 15), with emission from high-energy molecular states $^{1,3}\Pi_g$ (Ref. 16), and with radiative decay of the $n=2$ STE.[17] An alternative explanation for the origin of the M_3 band was proposed by Ratner *et al.*[5] Based on the concentration dependence of the M_3 band intensity in the various Xe/Rg systems (Rg denotes Kr, Ar, Ne) and comparison of this dependence with the similar dependence of the M band, it was suggested that the M_3 band is emitted by linear triatomic excited molecular centers self-trapped in a perfect lattice.[5] Each of the two resonant bindings in the linear triatomic complex Xe_3^* is weaker compared to a single binding in the quasi-excimer Xe_2^* and a correspondent elongation of the binding in the Xe_3^* results in a blue shift of the M_3 band compared to that in the diatomic molecule.[5] Such triatomic linear complexes are inevitably formed during translational motion of molecular excitons in the perfect lattice.[4] Recent accurate calculations of linear Xe_3^+ (Ref. 18) and Xe_2^+ (Ref. 19) molecular ions confirm this trend. In the linear ion Xe_3^+ the charge e is distributed over the three atoms like 0.239–0.523–0.239 (e) and the length of the bonds is 3.274 Å,[18] whereas in the Xe_2^+ ion the bond length is 3.11 Å.[19] Assuming the similarity of the hole part of STE with the corresponding molecular ions[2] we suppose a similar elongation of the bond in the Xe_3^* in comparison with Xe_2^*. In addition to linear symmetric configuration of the Xe_3^+ cation the only stable asymmetric triatomic configuration was found—a triangular structure with the positive charge localized on two atoms and the third, almost neutral atom attached in a equilateral position.[18] The length of the bond between the charged atoms in this case is 3.12 Å[18] and the emission from such triangular centers in solid Xe, if it occurs, may contribute to the M_1 subband. This is a possible reason why the M_3 band has no "defect" subband.

The excitation spectra of the luminescence bands from various trapped centers reveal the peculiarities of the different channels and of branching between them in relaxation of electronic excitations.[1,3,9] The strong overlap of the molecular components of the luminescence from solid Xe above $T=50$ K gives no way of recording the excitation spectra of subbands by scanning the photon excitation energy by the primary monochromator at a fixed detection wavelength of the secondary monochromator. To recover the excitation spectra of the M_1, M_2, and M_3 subbands we used the method of decomposition of the sequence of luminescence spectra, measured at different excitation energies.[3] Figure 2*a* shows the recovered excitation spectra at $T=60$ K. The similarity of excitation spectra of M_2 and M_3 bands under-

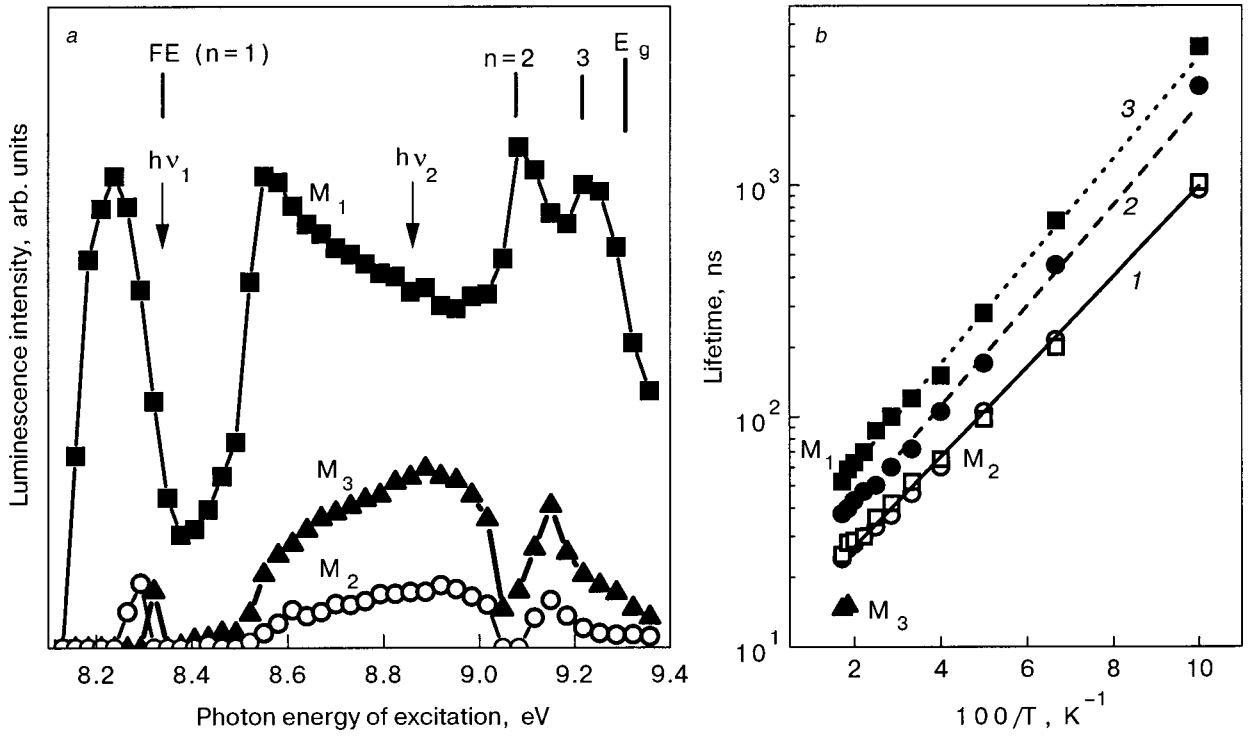

FIG. 2. Excitation spectra of molecular subbands of solid Xe at $T=60$ K (*a*). Temperature dependence of the triplet lifetime of molecular subbands of solid Xe (luminescence energy; excitation energy), detected at the photon excitation energies denoted by the arrows in Fig. 1*b* under selective photoexcitation with energies $h\nu_1=E_{FE}$ and $h\nu_2=8.86$ eV, arrows of Fig. 2*a* (*b*). M_1(6.89 eV; $h\nu_1$) (■); M_1(6.89 eV; $h\nu_2$) (●); M_2(7.38 eV; $h\nu_1$) (□); M_2(7.38 eV;$h\nu_2$) (○); M_3(7.74 eV; $h\nu_2$) (▲).

scores the common intrinsic nature of the emitting trapping centers in them—self-trapped excitons, whereas the antibatic behavior of the excitation spectrum of the ''defect'' subband M_1 reflects the competition of the processes of extrinsic exciton trapping at lattice defects and the exciton self-trapping. One of the possible processes which stimulate the high intensity of the excitation spectrum of the M_1 subband below the bottom of the lowest excitonic band is the process of trapped-center creation as a result of the formation of nucleation states responsible for localization of electronic excitation due to thermal lattice disorder in the ground state.[21] The formation of such centers intensifies near the lattice defects, and the direct photoabsorption by such centers[22] results in M_1 band emission.

Both the triplet $^3\Sigma_u^+$ and singlet $^1\Sigma_u^+$ states of the STE contribute to M band and decay curve of molecular luminescence yields a slow decay component and a fast one. The fast decay component is independent of temperature.[1] The slow decay component exhibits pronounced temperature dependence because of phonon mixing of the $^3\Sigma_u^+$ substates.[20] The lifetime obtained asymptotically at low temperature is ascribed to the totally forbidden A_u state. With increasing temperature, it can also be depleted by phonon transitions to the allowed $B_{3u,2u}$ state, which then radiates. Coexistence in solid Xe of two types of excimerlike emitting centers (intrinsic and extrinsic) implies different efficiency of the process of phonon mixing of $^3\Sigma_u^+$ substates depending on the crystal lattice environment of these centers. It should result in differences in the temperature dependence of triplet lifetimes of M_1 and M_2 subbands.

For the first time we have measured the decays of the M_1 and M_2 subbands (Fig. 2*b*) at the photon energies denoted by arrows in Fig. 1*b*, under excitation by photons with energies $h\nu_1 = E_{FE}$ and $h\nu_2 = 8.86$ eV (Fig. 2*a*). In the temperature range 10–50 K the temperature dependence of the triplet lifetime may be well approximated by a single exponent: $\tau(T) = C\exp(D/T)$, where C and D are fitting constants. Both temperature dependences for the M_2 subband may be approximated by the same exponent, with $C_1 = 11$ ns and $D_1 = 45$ K (Fig. 2*b*, curve 1) and phonon mixing of the triplet substates in the self-trapped excimerlike excitons independent of photon excitation energy. On the contrary, the decay of the ''defect'' subband M_1 yields different temperature dependences at different excitation energies: for excitation by photons with energies $E = 8.86$ eV, the fitting constants are $C_2 = 15$ ns and $D_2 = 50$ K (Fig. 2*b*, curve *2*), whereas for excitation by photons with energies equal to the energy of the lowest $\Gamma(3/2)$, $n = 1$ excitons, $E = E_{FE}$, the fitting constants are $C_3 = 22$ ns and $D_3 = 51$ K (Fig. 2*b*, curve *3*). The acceleration of the decay of the M_1 subband with increasing excitation energy is in line with our recent analysis of relaxation of electronic excitations below E_g. As the excitation energy nears E_g, the trapping cross section of excitons by lattice defects, which results in M_1 subband emission, grows proportionally to $\rho^{2/3}$ (ρ is the exciton-state radius).[9] The lifetime of the M_3 band was measured only in the temperature range 50–60 K since the high-vacuum requirements of the equipment for working with synchrotron radiation do not allow an increase of the temperature of Xe sample above 60 K. It yields $\tau(M_3) = 15$ ns at both excitation energies.

Thus the analysis of luminescence of molecular centers of Xe cryocrystals under selective photoexcitation within excitonic energy range in temperature range 5–60 K demonstrates the similar intrinsic nature of the M_2 and M_3 bands. They are emitted by diatomic and triatomic excitons self-trapped in the perfect lattice. The extrinsic exciton trapping at lattice imperfections is a competitive channel of exciton relaxation. It results in the M_1 subband emission.

The support of DFG Grant 436 UKR 113/55/0 is gratefully acknowledged.

*E-mail: ogurtsov@ilt.kharkov.ua

[1] N. Schwentner, E. E. Koch, and J. Jortner, *Electronic Excitations in Condensed Rare Gases*, Vol. 107 of Springer Tracts in Modern Physics, Springer-Verlag, Berlin (1985).
[2] K. S. Song and R. T. Williams, *Self-Trapped Excitons*, Vol. 105 of Springer Series in Solid-State Sciences, Springer-Verlag, Berlin (1993).
[3] A. N. Ogurtsov and E. V. Savchenko, J. Low Temp. Phys. **122**, 233 (2001).
[4] A. M. Ratner, Phys. Lett. A **298**, 422 (2002).
[5] A. M. Ratner, I. Ya. Fugol, A. G. Belov, and Yu. L. Steshenko, Phys. Lett. A **137**, 403 (1989).
[6] J. A. Gascon, R. W. Hall, C. Ludewigt, and H. Haberland, J. Chem. Phys. **117**, 8391 (2002).
[7] D. Varding, I. Reimand, and G. Zimmerer, Phys. Status Solidi B **185**, 301 (1994).
[8] I. Ya. Fugol, A. N. Ogurtsov, O. N. Grigorashchenko, and E. V. Savchenko, Fiz. Nizk. Temp. **18**, 44 (1992) [Low Temp. Phys. **18**, 27 (1992)].
[9] A. N. Ogurtsov, A. M. Ratner, E. V. Savchenko, V. Kisand, and S. Vielhauer, J. Phys.: Condens. Matter **12**, 2769 (2000).
[10] I. Ya. Fugol, O. N. Grigorashchenko, and E. V. Savchenko, Phys. Status Solidi B **111**, 397 (1982).
[11] M. Selg, M. Kink, R. Kink, J. Maksimov, and I. Martinson, Surf. Rev. Lett. **9**, 609 (2002).
[12] A. N. Ogurtsov, E. V. Savchenko, S. Vielhauer, and G. Zimmerer, *HASYLAB Annual Report 2001*, DESY, Hamburg (2002), p. 279.
[13] O. Cheshnovsky, A. Gedanken, B. Raz, and J. Jortner, Solid State Commun. **13**, 639 (1973).
[14] R. Kink, A. Lohmus, and M. Selg, Phys. Status Solidi B **107**, 479 (1981).
[15] R. Heumuller and M. Creuzburg, Opt. Commun. **26**, 363 (1978).
[16] I. Ya. Fugol, Adv. Phys. **37**, 1 (1988).
[17] K. M. Monahan and V. Rehn, Nucl. Instrum. Methods Phys. Res. **152**, 255 (1978).
[18] R. Kalus and D. Hrivnak, Chem. Phys. **278**, 21 (2002).
[19] I. Paidarova and F. X. Gadea, Chem. Phys. **274**, 1 (2001).
[20] R. Kink, A. Lohmus, M. Selg, and T. Soovik, Phys. Status Solidi B **84**, K61 (1977).
[21] J. L. Gavartin and A. L. Shluger, Phys. Rev. B **64**, 245111 (2002).
[22] A. N. Ogurtsov, E. V. Savchenko, E. Gminder, S. Vielhauer, and G. Zimmerer, Surf. Rev. Lett. **9**, 45 (2002).

This article was published in English in the original Russian journal. Reproduced here with stylistic changes by AIP.

Temperature dependence of hot luminescence in solid xenon: theory and experiment

M. Selg* and R. Kink

Institute of Physics of the University of Tartu, 142 Riia, Tartu 51014, Estonia
Fiz. Nizk. Temp. **29**, 1130–1134 (September–October 2003)

Vibrational relaxation of self-trapped excitons in solid xenon has been investigated both experimentally and theoretically. Hot luminescence spectra of the crystal have been measured in a wide temperature range (from liquid helium temperature to 100 K), using x-ray and two-photon excimer laser (ArF and KrF) excitation. The theoretical analysis is based on a recent nonperturbative relaxation theory and on a rigorous quantum-mechanical Franck–Condon approach. [DOI: 10.1063/1.1619359]

INTRODUCTION

Self-trapped excitons (STE) in rare gas crystals (RGC) are strong vibrational excitations very similar to free diatomic excimers R_2^* (R=Xe, Kr, Ar, Ne), whose level spacings considerably exceed the maximum phonon energies. Therefore, to adequately describe vibrational relaxation of such STE, one definitely has to use a nonperturbative quantum-mechanical approach. Such a concept has recently been elaborated,[1] and it is most suitable for the rigorous analysis in solid Xe, where two- and three-phonon relaxation processes are dominant. The theory predicts an abrupt increase of the relaxation rate around a critical level ($n_{cr}=22$ in Xe), which results in a dramatic population drop of the levels in this characteristic region.

Useful information on the relaxation processes in R_2^* centers is contained in their hot luminescence (HL) spectra, whose explicit calculation is a rather demanding task for several reasons. First, one needs to construct reasonable potential curves for the system. Second, one has to determine the relaxation rates and relative populations for all vibrational levels of interest. Third, one has to ascertain a huge set of correctly normalized Franck–Condon (FC) factors for bound–free and bound–bound transitions. Moreover, one cannot use the convenient ''reflection'' approximation of the FC principle,[2,3] which ignores the quantum structure of the final state and therefore fails to allow correctly for the transitions to the scattering states near the dissociation limit and to the bound states, which are the most important in our case. To overcome these complicated computational/technical problems, we used a rigorous quantum-mechanical method by one of the authors.[4,5]

In this paper we present new experimental data on the temperature dependence of HL in solid Xe and carry out a relevant theoretical analysis. The choice of Xe crystal for testing the reliability of the new nonperturbative relaxation theory[1] is not accidental. Compared with R_2^* centers in other RGC, a much larger range of vibrational levels (from $n=14$ to $n=40$ for the potential curve used) is involved in two-phonon relaxation processes, in which case it is expected that the acceleration effect will be most pronounced around n_{cr}.

EXPERIMENTAL RESULTS

Bulk Xe crystals of volume 2 cm^3 were grown from the liquid near the triple point in a special tube made of organic glass (see Ref. 6 for more details). Two methods of excitation were used: irradiation by a tungsten x-ray source (40 kV, 15 mA) through a Be window, and the two-photon ArF (193 nm) or KrF (248 nm) excimer laser radiation. The HL spectra were recorded with the help of a 2m double vacuum monochromator, which ensures a spectral resolution of 10–15 meV and a light dispersing factor of less than 10^{-5}.

An important specific feature of good-quality Xe crystals is the existence of two broad emission bands, as shown in Fig. 1. Here we shall not discuss the origin of these bands, since this has been already done more than 20 years ago.[7] In the present context we put emphasis on their intrinsic nature and will use the same abbreviation STE for both the 7.2 and 7.6 eV bands. Figures 2 and 3 demonstrate the high-energy wings of the luminescence spectra, where we observed several weak bands (their intensity being less than 1% compared with that at the maximum of the STE bands), which at least partially can be attributed to HL. There always persists a spectral feature with a maximum at 8.14–8.17 eV, depending on temperature and the method of excitation. This band has been reported earlier[8] and is probably related to surface excitons, in accordance with relevant absorption[9] and reflectivity[10] data. However, we cannot completely rule out its possible relationship with HL. At low temperatures and under laser excitation another weak band shows up near 8.05 eV, whose origin is unknown.

According to our earlier interpretation[11,12] the ''real'' HL band is the feature with maximum at 8.22–8.23 eV, which is most effectively induced by two-photon KrF laser excitation, while other excitation methods tend to bring forth the 8.15 eV feature (cf. Figs. 2 and 3). We will discuss the fine structure of the 8.23 eV band in more detail below. One can see that separation of the ''pure'' HL part from the various weak emission bands is rather complicated. Moreover, we observed a clear correlation between the temperature dependence of the HL and the intensity redistribution of the main STE bands (see Fig. 1), which makes an adequate theoretical analysis even more difficult.

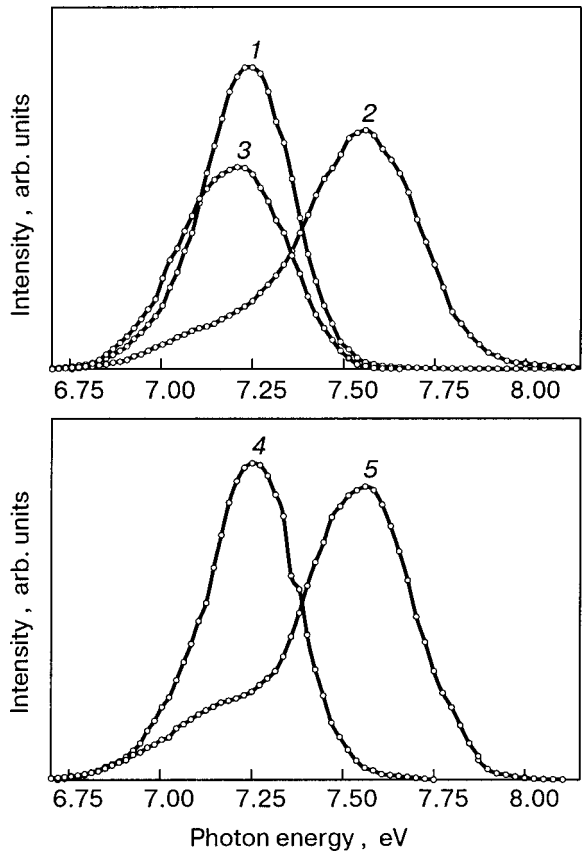

FIG. 1. Overall luminescence spectra of STE in the Xe crystal, corresponding to different excitation methods: ArF laser excitation (spectra *1* and *2*), x-ray excitation (*3*), KrF laser excitation (*4* and *5*). Curves *1, 3* and *4* have been measured at $T=10$ K, while *2* and *5* correspond to $T=90$ K.

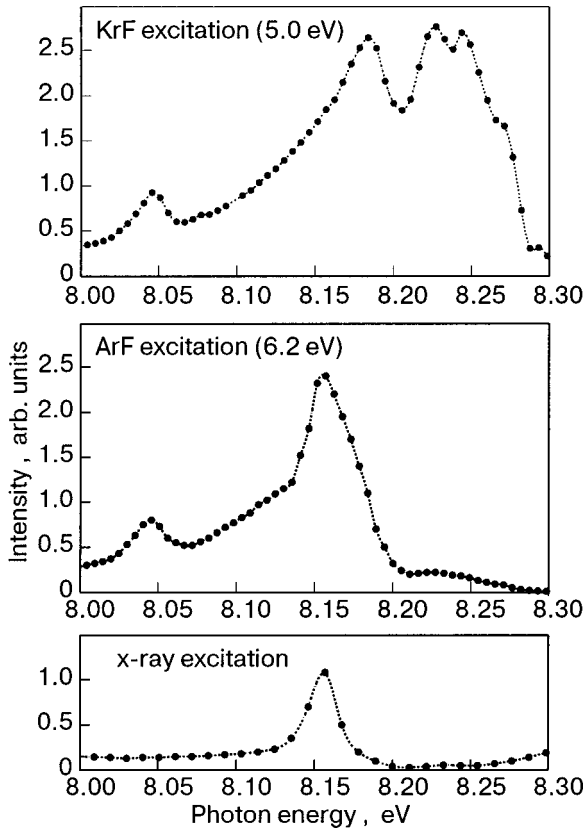

FIG. 2. Experimental emission spectra of Xe crystal in the supposed HL region at $T=10$ K under different excitation, as shown in the graphs. Intensities are given in arbitrary but comparable units.

THEORETICAL RESULTS

In a recent paper[5] a thorough FC analysis has been performed for free xenon excimers. In particular, exactly solvable multi-component reference potentials for the $0_u^+(^3P_1)$ state and for the ground state 0_g^+ of Xe_2 have been constructed and their agreement with available spectroscopic data demonstrated. As the same electronic states play the key role in the formation of the main STE emission bands in solid Xe (including HL), one would expect to receive some benefit from the results of this gas phase analysis. To this end, however, one has to adjust the free excimer's potential curves to the crystal environment.

The spectral characteristics of the 7.2 eV STE emission band are quite close to those of the well-known second continuum in the gas phase, while the free exciton peak ($E_{ex}=8.359$ eV)[13] is red-shifted by about 80 meV compared with its gas-phase analog—the $^3P_1$ atomic resonance line (8.437 eV). In view of these experimental facts we deformed the free $0_u(^3P_1)$ excimer's potential curve slightly but left the ground-state potential unchanged. We also left the equilibrium position ($R_e=3.00\pm0.001$ Å, $U(R_e)=7.885$ eV)[5] of the $0_u^+(^3P_1)$ potential well unchanged, but the overall curve was proportionally compressed to fit its dissociation limit with E_{ex}. Of course, there is no real dissociation limit for a quasimolecular center in the crystal, but this is of secondary importance for our treatment, because all of the needed FC factors nicely converge in a rather narrow distance interval. In the upper graph of Fig. 4 one can see a direct comparison between the bound–free FC factors related to free Xe_2^* excimers and their crystal analogs just described.

The normalization of the FC factors is determined by the rigorous sum rule

$$\int_0^\infty\left[\int_0^\infty \psi(E,r)\varphi_i(r)dr\right]^2 dE + \sum_j\left[\int_0^\infty \psi_j(r)\varphi_i(r)dr\right]^2=1 \quad (1)$$

which results directly from a fundamental property of the Schrödinger equation: completeness of its system of eigenfunctions. Here $\varphi_i(r)$ is the wave function of the initial (0_u^+) bound state, while $\psi_j(r)$ and $\psi(E,r)$ represent the full set of normalized bound-state ($E<0$) and scattering-state ($E=\hbar^2k^2/2m\geqslant 0$) wave functions, which are related to the final electronic state (0_g^+ in our case). Therefore, $\psi(E,r)=2\cos(kr-\delta)/F(E)$ (δ is the phase shift), where $F(E)=[4\pi\sqrt{E\hbar^2/2m}]^{1/2}$ (Ref. 14). The quantities in the square brackets are recognized as the FC overlap integrals for bound–free and bound–bound transitions. Excellent agreement with Eq. (1) is explicitly demonstrated in the middle graph of Fig. 4 for all vibrational levels ($n=0-40$) of the 0_u^+ state that have been used in our HL analysis.

The next step is to ascertain the vibrational relaxation rates for the vibrational levels of the quasimolecule Xe_2^*. For this purpose we calculated the probabilities $\Gamma_{n,n-1}$ (relaxation rates at $T=0$) of the multi-phonon transitions from level n to $n-1$ according to Ref. 1, using the value β

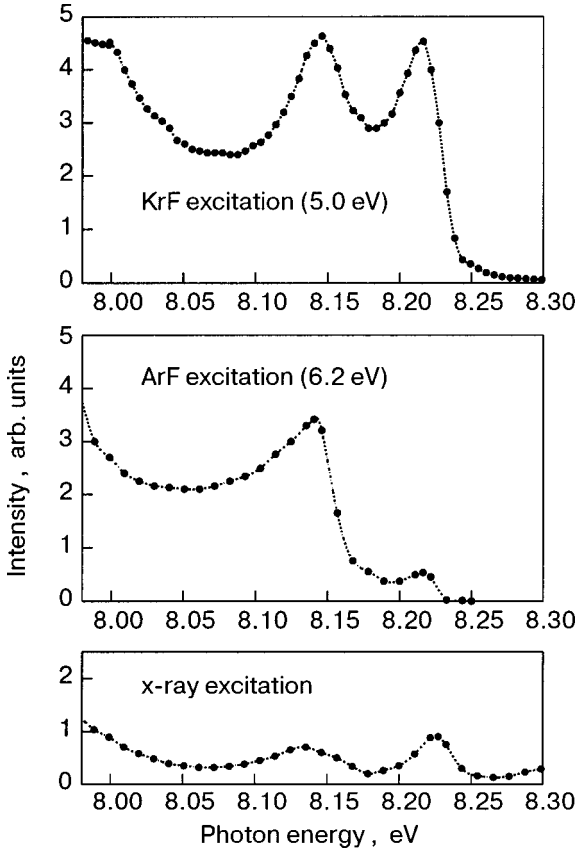

FIG. 3. The same spectra shown in Fig. 2, but measured at temperature $T=70$ K.

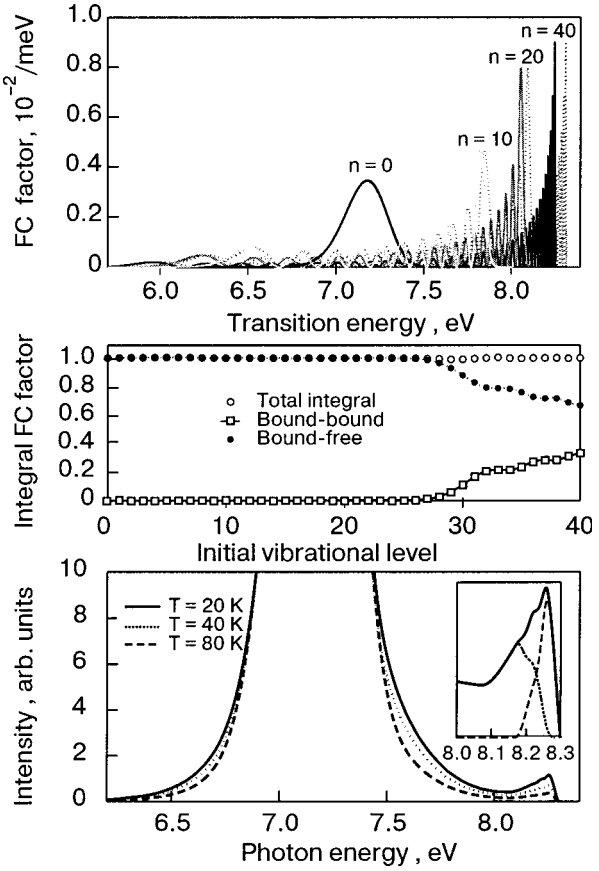

FIG. 4. Visualization of the main theoretical results of this paper. The upper graph compares two sets of calculated FC factors for bound–free transitions from the selected vibrational levels ($n=0$, 10, 20, and 40) of the $0_u^+(^3P_1)$ state. The dotted curves correspond to the potential curves constructed in Ref. 5 for free molecules Xe_2, while the solid curves show the FC factors for the same levels related to the ''deformed'' potential curve of the 0_u^+ state, whose dissociation limit coincides with $E_{ex}=8.395$ eV.[13] Note that the $n=0$ curves are indistinguishable. The middle graph demonstrates excellent agreement with the rigorous sum rule expressed by Eq. (1). Contributions from both bound–bound and bound–free transitions can be seen. The lowest graph depicts the calculated luminescence spectra for Xe_2^* in solid Xe at different temperatures. Thanks to the rigorous quantum-mechanical approach, one can elucidate the substructure of the HL band. This is shown in the inset: the dotted curve there corresponds to bound–free transitions, while the dash curve is related to bound–bound transitions. All the spectra have been averaged with a spectral resolution of 20 meV.

$=0.3$ for the characteristic displacement parameter (see Fig. 1 in Ref. 1), and taking $n_{cr}=22$. The probability $\Gamma_{n,n-1}$ of the reverse transitionn $n-1\rightarrow n$ is determined by the principle of detailed balance, i.e., $\Gamma_{n-1,n}=\exp(-\Delta_n/kT)\Gamma_{n,n-1}$, where Δ_n is the spacing between the levels. Thereafter, we solved the system of kinetic equations including the levels from 0 to 40, and assuming the radiative decay rate $\Gamma_R=2\times10^8$ s^{-1} (Ref. 15) to be constant for all levels. The quantity Δ_{40} is nearly equal to the maximum phonon energy in Xe (5.3 meV). We therefore assume that the levels $n>40$ give a very small contribution to HL, because fast one-phonon relaxation processes are allowed for them.

Finally, we summed the FC factors according to the relaxation law to get the luminescence spectrum for $Xe_2(0_u^+)$ centers in solid Xe. The results are presented in the lowest graph of Fig. 4 for three different temperatures. The calculations nicely reproduced the overall 0_u^+ component of the 7.2 eV STE band, including its HL part shown in the inset. It can be seen that the relative intensity of HL in the theoretical spectra gradually diminishes with increasing T; this is confirmed experimentally only for relatively high temperatures.

A possible reason for this partial disagreement is discussed in the next Section.

CONCLUSIONS

It is well known that the luminescence properties of RGC depend strongly on both temperature and the sample's structural quality. As has been demonstrated in this paper, the intensity of emission in the far high-energy edges of the main luminescence bands, which can be associated with HL of STE in solid Xe, depends strongly on the method of excitation as well. We have acquired some new evidence to support our earlier hypothesis that the ''real'' HL feature in Xe is the band near 8.23 eV. Indeed, this weak emission band is most effectively induced by KrF laser excitation (5.0 eV), which supports two-photon transitions from the upper subband ($j=3/2$) of the highest spin–orbit-split valence band into the lowest conduction band. Consequently, such an excitation is most effective in producing delocalized $\Gamma(3/2)$ excitons, the precursors of STE we are examining. In contrast, ArF laser excitation (6.2 eV) seems to support the formation of STE via capture of electrons by trapped holes. This may be the cause of the weakness of the ''real'' HL under ArF laser excitation at low temperatures (see Fig. 2). As regards x-ray excitation, its penetration depth in solid Xe is only about 0.5 mm.[6] This means that a lot of emission centers are created

near the surface, which could explain relatively high intensity of the surface-sensitive 8.15 eV feature compared to the 8.23 eV band.

The 8.23 eV band is also well pronounced in our calculated emission spectra based on the potential curves for the quasimolecular centers Xe_2^* in solid Xe. Both bound–bound and bound–free transitions contribute to the intensity distribution of this HL feature, the former being much more important for establishing its maximum position and substructure. The calculated spectra presented in the lowest graph of Fig. 4 represent averaged curves with resolution 20 meV, which nearly corresponds to the real experimental resolution at the moment. Our prediction is that one would see an abundant fine structure of the 8.23 eV band, if the experimental resolution could be essentially improved, because the band actually represents a line spectrum against the background of a continuum. Experimental efforts in this direction would therefore be of great importance for the verification of our HL concept.

As already reported earlier[12] the actual temperature dependence of the HL intensity is more complicated than just the monotonic decrease predicted theoretically. Independent of the excitation method we observed an abrupt drop in the intensity of the 8.23 eV band at about $T=40$ K, followed by rapid rise in the range from about 50 to 65 K (under KrF excitation), and gradual vanishing at still higher temperatures. Such behavior clearly correlates with the intensity redistribution between the 7.2 and 7.6 eV bands (see Fig. 1), which possibly means that both these STE bands have HL constituents at nearly the same spectral positions. We have not succeeded in working out a more detailed model to explain this phenomenon, but this is one of the main goals of our forthcoming research.

The authors wish to express their gratitude to the Estonian Science Foundation for support through Grants Nos. 4032 and 4508.

*E-mail: matti@fi.tartu.ee

[1] V. Hizhnyakov, Europhys. Lett. **45**, 508 (1999).
[2] N. S. Baylis, Proc. Roy. Soc. (London) A **158**, 551 (1937).
[3] M. Lax, J. Chem. Phys. **20**, 1752 (1952).
[4] M. Selg, Phys. Rev. E **64**, 056701 (2001).
[5] M. Selg, J. Mol. Spectrosc. **220**, 187 (2003).
[6] M. Kink, R. Kink, V. Kisand, J. Maksimov, and M. Selg, Nucl. Instrum. Methods Phys. Res. B **122**, 668 (1997).
[7] R. Kink, A. Lõhmus, and M. Selg, Phys. Status Solidi B **107**, 479 (1981).
[8] D. Varding, *Dissertation*, Universität Hamburg (1994).
[9] N. Schwentner, E. E. Koch, and J. Jortner, *Electronic Excitations in Condensed Rare Gases*, Vol. 107 of Springer Tracts in Modern Physics, Springer-Verlag (1985).
[10] B. Steeg, *Dissertation*, Universität Hamburg (1999).
[11] V. Hizhnyakov, M. Selg, R. Kink, M. Kink, and J. Maksimov, Physica B **263–264**, 683 (1999).
[12] M. Selg, M. Kink, R. Kink, J. Maksimov, and I. Martinson, Surf. Rev. Lett. **9**, 609 (2002).
[13] B. Steeg, M. Kirm, V. Kisand, S. K. K'ording, S. Vielhauer, and G. Zimmerer, J. Low Temp. Phys. **111**, 739 (1998).
[14] L. D. Landau and E. M. Lifshitz, *Quantum Mechanics: Nonrelativistic Theory*, Pergamon Press, Oxford (1976).
[15] T. D. Bonifield, F. H. K. Rambow, G. K. Walters, M. V. McCusker, D. C. Lorents, and R. A. Gutcheck, J. Chem. Phys. **72**, 2914 (1980).

This article was published in English in the original Russian journal. Reproduced here with stylistic changes by AIP.

The vibrational relaxation of CO_2 isolated in solid argon

A. Cenian* and G. Śliwiński

Institute of Fluid-Flow Machinery, Polish Academy of Sciences, Gdansk 80-952, Poland

G. Grigorian

Institute of Physics, St. Petersburg State University, St. Petersburg 198504, Russia
Fiz. Nizk. Temp. **29**, 1135–1139 (September–October 2003)

The vibrational relaxation of CO_2 molecules embedded in an Ar matrix is described using a model based on multiphonon transitions. Rates for the VT and VV processes are determined from a fitting of simulated and experimental data. The calculations confirmed that radiative processes influence significantly the vibrational energy relaxation of CO_2 embedded in solid Ar; e.g., the rate determined for energy transfer between the ν_3 and ν_2 modes is significantly lower than that predicted under the assumption of nonradiative relaxation. © *2003 American Institute of Physics.* [DOI: 10.1063/1.1619360]

INTRODUCTION

A large number of physical and chemical processes in the solid-state involve the vibrational energy relaxation (VER) of molecules. A study of this process for molecules isolated in noble-gas matrices has attracted considerable attention over past years. Among the systems studied, CO, NO, O_3, CO_2 or XeF* molecules in solid Ar constitute a spectacular class.[1–4] The vibrational energy transfer in $^{13}C^{16}O_2$ isolated in solid Ar has been investigated by the laser-induced fluorescence method.[2] The intense radiation observed in the 16-μm region after strong excitation of the state (00^01) was ascribed to vibrational stimulated emission. Also, for processes of the type $(11^10(2)\rightarrow\nu_1,2\nu_2)$ and $(00^01\rightarrow\nu_1+\nu_2,3\nu_2)$ the relaxation times τ_{VT} and τ_{V_3V} were estimated from decay times of stimulated emission based on the assumption that nonradiative relaxation prevails.

In this work we aim at clarifying the influence of different relaxation channels on the populations of vibrational levels using the theory of multiphonon relaxation proposed by Nitzan *et al.*[5] Also the results of an estimation of the VER rate constants for the CO_2/Ar system by comparing the experimental and calculated temporal pulseform of the radiation are discussed.

In particular, we refer to the experimental results for the $^{13}CO_2$ vibrational-energy relaxation in solid argon under conditions of a matrix-to-reagent molecular ratio M/R $=2000$.[2] The laser excitation of the ν_3 $(v=1)$ level of carbon dioxide molecules was found to induce strong emissions $(\nu_1+\nu_2, 3\nu_2)\rightarrow(\nu_1, 2\nu_2)$ and $(\nu_1, 2\nu_2)\rightarrow\nu_2$ in the spectral region around 16 μm. Their sharp threshold as a function of laser excitation density was interpreted as a signature of vibrational stimulated emission. It is known that CO_2 molecules in solid argon are trapped in two distinct sites: single substitutional, which is stable, and double substitutional, which appears to be an unstable site.[2] The first one, because of the limited free space, is characterized by a stronger vibration–phonon coupling and shorter relaxation times (one order of magnitude). The lasers used in the experiments[2] allowed for a good time resolution and a site-selective excitation. Both sites were found to be luminescent. The reported emission spectrum due to the stable site consisted of three lines (see Fig. 1). The relaxation times τ_{VT} and τ_{V_3V} for processes of the type $(11^10(2)\rightarrow\nu_1,2\nu_2)$ and $(00^01\rightarrow\nu_1+\nu_2,3\nu_2)$ were estimated in Ref. 2 from the decay times of the stimulated emission on the assumption that the radiative relaxation may be neglected. In the case of stable site the respective decay times were $\sim$700 and $\sim$100 ns.

During the final stage of preparation of this paper, we became aware of the interesting work of Chabbi *et al.*,[6] reporting the rate constants for the VER processes of isolated CO_2 determined by a radiation-pulse fitting procedure using 6 independent constants, i.e., not related by any scaling law.

MODEL DESCRIPTION

The vibrational energy relaxation following strong pulsed excitation is studied by solving the kinetic equations describing the time evolution of the populations of different vibrational levels of the CO_2 molecules:

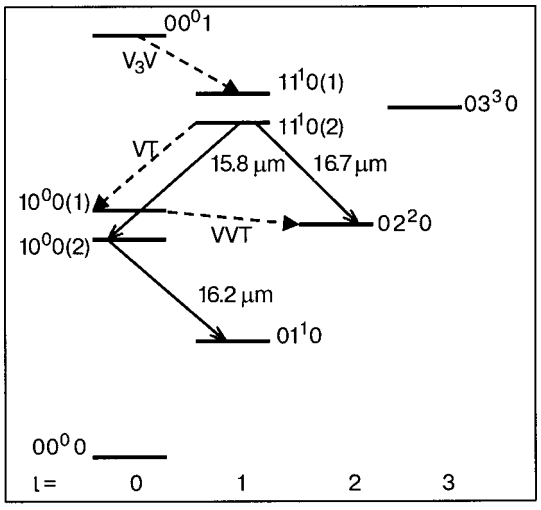

FIG. 1. Diagram of the CO_2 vibrational levels with energy lower than 3000 K; the solid arrows denote the transitions of vibrationally stimulated emission observed in Ar matrices; the dashed arrows represent exemplary nonradiative transitions of the types VT, V_3V, and VVT.

$$dn_v/dt = R^v_{\mathrm{VT}} + R^v_{\mathrm{VVT}} + R^v_{\mathrm{V_3V}} + R^v_{\mathrm{sp}} + R^v_{\mathrm{ind}}, \quad (1)$$

where n_v denotes the population of vibrational level v, and the R^v terms describe population changes due to the VT, VVT, and V_3V intramolecular processes of nonradiative relaxation as well as to spontaneous and induced radiative transitions (the notations are the same as those of Ref. 2). The intermolecular VV processes are neglected because of low concentration of CO_2 in the Ar matrix. A Boltzmann-type initial vibrational distribution is assumed. Excitation is taken into account by a sudden increase of the initial vibrational population (N_{001}) of the 00^01 state up to an arbitrary level (a fitting parameter).

The equations describing the evolution of the photon number has the form:

$$dN_i/dt = R^i_{\mathrm{sp}} + R^i_{\mathrm{ind}} + R^i_{\mathrm{loss}}, \quad (2)$$

where N_i is the number of photons of the ith transition (see Fig. 1), and R_i corresponds to photon gain (both through spontaneous and induced processes) and loss processes. The main loss channel is related to the photon leaving the excited region as described in Ref. 2.

For spontaneous emission the Einstein coefficients are applied:[7]

$$A_{v,v-1} = \frac{64\pi^4 \nu^3_{v,v-1}}{3hc^3} |\langle v|\mu|v-1\rangle|^2 n \left(\frac{n^2+2}{3}\right)^2,$$

where $\nu_{v,v-1}$ is the frequency of the $v \rightarrow v-1$ vibrational transition, $|\langle v|\mu|v-1\rangle$ is the respective matrix element of the dipole moment, and n is the refractive index. The last term describes generally the effects of solid environment.

The stimulated emission cross section are derived from the expression[8]

$$\sigma_{v,v-1} = c^2 A_{v,v-1}/8\pi\nu^2_{v,v-1} n^2 \gamma,$$

where γ is the FWHM of the spectral line associated with the $v \rightarrow v-1$ transition, assumed to have a Gaussian profile, and is estimated to be equal to 0.15 cm^{-1} (Ref. 2).

Several approaches have been proposed for discussion of the nonradiative vibrational relaxation of a guest molecule in a dense medium.[5,9–11] In the present paper the relaxation rates are described by the multiphonon relaxation model proposed by Nitzan *et al.*[5] This model has proven to provide a satisfactory description of the relaxation for the case of a matrix-isolated diatomic.[12–14] Accordingly, the rate constant of the $v \rightarrow v-1$ transition is given by[5]

$$K_{v,v-1}(T) = K_{v,v-1}(0) F(T), \quad (3)$$

where $F(T) = (1+\tilde{n})^N e^{2S\tilde{n}}$ is the temperature coefficient, S is the average vibration–phonon coupling strength (assumed here to be 1), $N = \Delta E_{v,v-1}/h\nu_{\mathrm{ph}}$ is the number of matrix phonons involved in dissipation of the vibrational energy gap $\Delta E_{v,v-1}$ in the nonradiative relaxation process, ν_{ph} is the average phonon frequency ($h\nu_{\mathrm{ph}} = 64$ K was assumed for the Ar matrix), $\tilde{n} = [\exp(h\nu_{\mathrm{ph}}/kT) - 1]^{-1}$ is the phonon occupation number. For low temperatures ($T \sim 5$ K) one has $\tilde{n} \sim 0$, $F(T) \sim 1$, and $K_{v,v-1}(T) \cong K_{v,v-1}(0)$. The expression

$$K_{v,v-1}(0) = A v \frac{e^S S^N}{N!} \frac{1}{\Delta E_{v,v-1}} \quad (4)$$

corresponds to the relaxation rate at $T = 0$ K, where A is a constant related to the value of the average phonon frequency and the variation of the interaction potential between CO_2 molecules and the surrounding matrix atoms.

Three types of processes are taken into account, and the notation corresponds to that of Ref. 2:

$$\text{VT:} \quad CO_2(\nu_1+\nu_2, 3\nu_2) + \mathrm{Ar} \rightarrow CO_2(\nu_1, 2\nu_2) + \mathrm{Ar}, \quad (5)$$

$$\text{VVT:} \quad CO_2(\nu_1, 2\nu_2) + \mathrm{Ar} \rightarrow CO_2(\nu_1, 2\nu_2)' + \mathrm{Ar}, \quad (6)$$

$$\text{V}_3\text{V:} \quad CO_2(00^01) + \mathrm{Ar} \rightarrow CO_2(\nu_1+\nu_2, 3\nu_2) + \mathrm{Ar}, \quad (7)$$

where $CO_2(\nu_1, 2\nu_2)$ and $CO_2(\nu_1, 2\nu_2)'$ denote different vibrational states of the $(\nu_1, 2\nu_2)$ multiplet at Fermi resonance—see, e.g., Ref. 15.

Due to the strong dependence of the rates (3) upon N, only VT processes of $\Delta\nu_2 = 1$ contribute significantly to energy relaxation. The other processes (V_3V and VVT) also proceed with the minimum vibrational energy gap. The VT and V_3V reverse processes responsible for energy transfer from translation to vibration are neglected. However, in the case of VVT processes some rates obtained from the principle of detailed equilibrium are not negligibly small.

RESULTS AND DISCUSSION

For the stable site emission the time evolution of the photon numbers related to radiative profiles is studied in order to get best agreement with experimental data reported in Ref. 2. Accordingly, three fitting parameters, A_{VT}, A_{VVT}, and $A_{\mathrm{V_3V}}$, related to the constant A in expression (4) for the rates of nonradiative processes, which correspond to transitions of the VT, VVT, and V_3V type [Eqs. (5)–(7)] are determined. As a result, all rates for vibrational energy exchange can be calculated. Thus this procedure replaces the determination of the seven independent rate constants as proposed in Ref. 6. In both cases, the initial excitation N_{001} is an additional fitting parameter.

The sets of equations (1) and (2) are solved using the GEAR code for numerical integration. the equations describe the populations of all nine vibrational states, which become populated during the relaxation process at a temperature $T = 5$ K, and the photon numbers of the three active radiative transitions $(\nu_1+\nu_2, 3\nu_2 \rightarrow \nu_1, 2\nu_2)$ and $(\nu_1, 2\nu_2 \rightarrow \nu_2)$—see Fig. 1. The terms related to radiation gain and losses were determined from the Einstein coefficients, the stimulated emission cross sections, and the populations of the respective levels. The nonradiative terms were determined by rates (4) scaled by the constants A_{VT}, A_{VVT} and $A_{\mathrm{V_3V}}$.

It should be stressed again that in Ref. 2 the following rates for the processes

$$\text{VT:} \quad CO_2(11^10(2)) + \mathrm{Ar} \rightarrow CO_2(10^00(1)) + \mathrm{Ar},$$

$$K_{\mathrm{VT\_exp}} = 1.4\times10^6 \ \mathrm{s}^{-1} (\tau_{\mathrm{VT}} = 700 \ \mathrm{ns}), \quad (5')$$

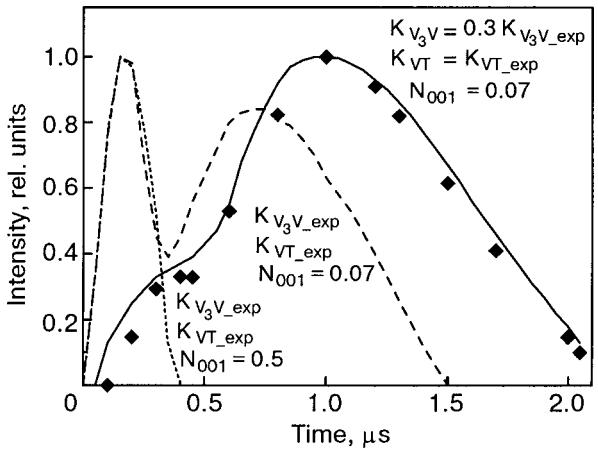

FIG. 2. Time-resolved pulse of vibrational stimulated emission from CO_2 located in a stable site of the Ar matrix; the black diamond symbols correspond to the measurements, while the curves represent simulations: solid curve–for the best-fit parameters, dotted curve–for the rates determined in Ref. 2 and the saturation condition ($N_{001}=0.5$); dashed curve—for the rates determined in Ref. 2 and $N_{001}=0.07$.

$$V_3V: \quad CO_2(00^01)+Ar\rightarrow CO_2(11^00(1))+Ar,$$

$$K_{V_3V\_exp}=10^7\ \ s^{-1}(\tau_{V_3V}=100\ \ ns) \qquad (6')$$

were proposed, based on the assumption of nonradiative relaxation. The saturation condition ($N_{001}=0.5$) for initial excitation was also assumed.

Results of the calculations are presented in Figs. 2–7. Figure 2 demonstrates the evolution of radiation intensity determined by rates scaled (by changing A_{VT} and A_{V_3V}) to the values as proposed in Ref. 2 (see dotted line). The assumed value of the excitation is evidently too high—as was also confirmed in later considerations of energy conservation.[6] It was found here that the best fit is obtained for $N_{001\_b}=0.07$, $K_{VT\_b}=K_{VT\_exp}$ and $K_{V_3V\_b}=0.3K_{V_3V\_exp}$ (see solid line in Fig. 2). A similar value 4×10^6 s^{-1} for the rate K_{V_3V} was proposed in Ref. 6. The signal profile is not very sensitive to the rates of quasiresonant processes of the

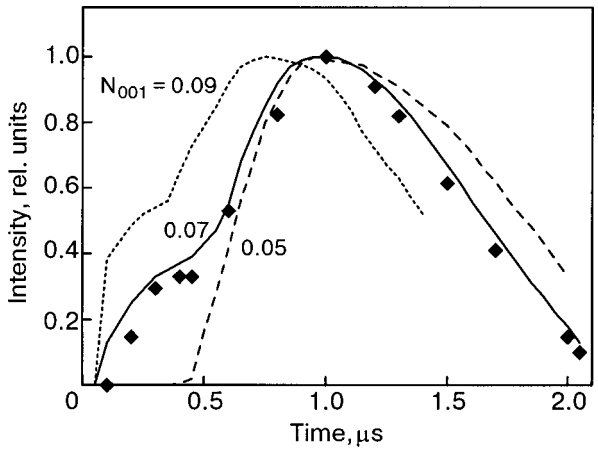

FIG. 3. Time evolution of the stimulated-emission pulse from CO_2 located in a stable site of the Ar matrix; the black diamond symbols correspond to the measurements, while the curves represent simulations: solid curve–for the best-fit parameters; dotted curve—for the optimal rates and $N_{001}=0.09$; dashed curve—for the optimal rates and $N_{001}=0.05$.

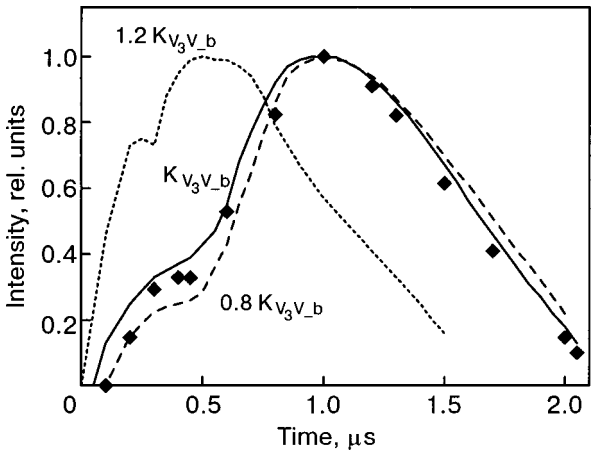

FIG. 4. Same as Fig. 3; solid curve—for the best fit parameters, dotted curve—for the best-fit parameters except $K_{V_3V}=1.2K_{V_3V\_b}$; dashed curve–for the best-fit parameters except $K_{V_3V}=0.8K_{V_3V\_b}$.

type (7) as long as they exceed the value of K_{V_3V}. The optimal value of the rate for the VVT process

$$CO_2(10^00(1))+Ar\rightarrow CO_2(02^20)+Ar, \qquad (7')$$

$K_{VVT\_b}\sim10^9$ s^{-1} was found, and this value was assumed for all curves in Fig. 2. Figure 3 presents the sensitivity of the profile ton the initial-excitation parameter.

The signal profile depends strongly on the rate K_{V_3V} (see Fig. 4). Both the position of maximum and the slope change with variation of the rate. The value $K_{V_3V\_b}$ is smaller by a factor of about 1/3 compared to $K_{V_3V\_exp}$—this should be due to radiative effects neglected in Ref. 2. It is evident that the radiative processes have a serious influence on the kinetics, e.g., they determine the temporal scale of the pulse profile. This agrees well with the data reported in Ref. 6 and stands in sharp contrast to the previous assumptions.[2] If we decrease further the rate for the V_3V process, an additional maximum on the temporal pulseform appears; this is clear evidence of the independent radiation from all 3 transitions.

The changes of the rate K_{VT} influence the investigated profile much less significantly (see Fig. 5). Increasing the

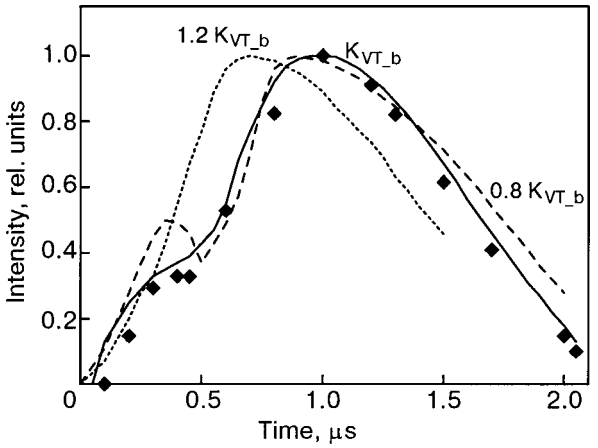

FIG. 5. Same as Fig. 3; solid curve—for the best-fit parameters; dotted curve—for the best-fit parameters except $K_{VT}=1.2K_{VT\_b}$; dashed curve—for the best-fit parameters except $K_{VT}=0.8K_{VT\_b}$.

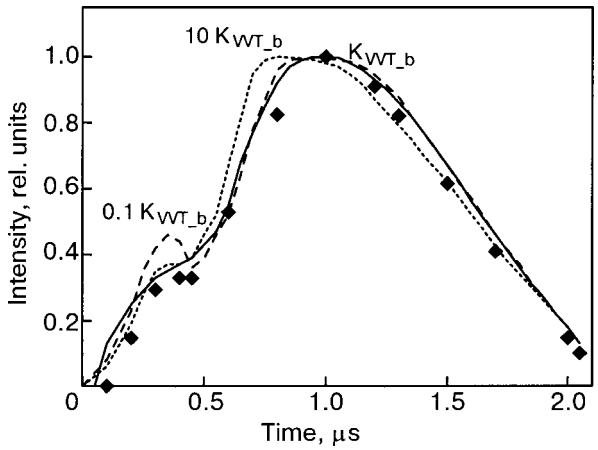

FIG. 6. Same as Fig. 3; solid curve—for the best-fit parameters; dotted curve—for the best-fit parameters except $K_{\mathrm{VVT}}=10K_{\mathrm{VVT\_}b}$; dashed curve—for the best-fit parameters except $K_{\mathrm{VVT}}=0.1K_{\mathrm{VVT\_}b}$.

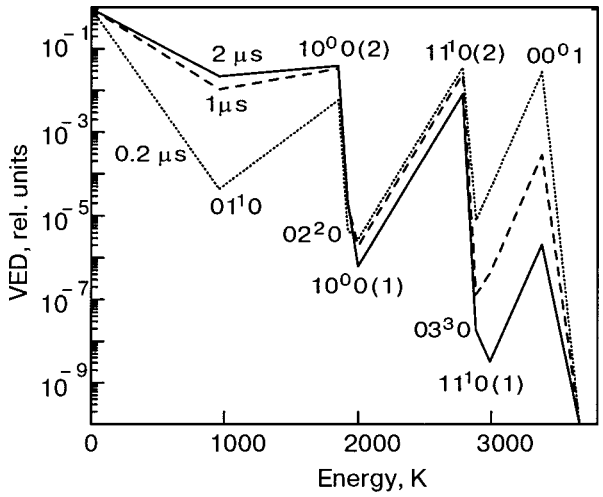

FIG. 7. The Treanor–Likal'ter type of distribution for the best-fit parameters and its time evolution; dotted curve—0.2 μs; dashed curve—1 μs; solid curve—2 μs after excitation.

rate shifts the maximum to smaller values and smoothes all structures. In contrast, decreasing K_{VT} leads to more-pronounced structures. The profile is even less sensitive to changes of the rates for near-resonant transitions (7)—in Fig. 6 we compare the results for K_{VVT} differing by two orders of magnitude. Again, decreasing the rate K_{VVT} leads to structure enforcement and also widens the maximum of the profile—compare the broken and solid lines.

Figure 7 presents the time evolution of vibrational distribution function. The characteristic saw-tooth distribution of the Treanor—Likal'ter type, as described previously in detail,[15] can be observed. The gradual saturation of the all laser-active transitions $(\nu_1+\nu_2,3\nu_2\rightarrow\nu_1,2\nu_2)$ and $(\nu_1,2\nu_2\rightarrow\nu_2)$ is evident.

CONCLUSION

We have shown that the vibrational relaxation of CO_2 molecules embedded in solid Ar matrix can be well described by the theory of multiphonon transitions. The simulations performed have confirmed that radiative processes influence significantly the vibrational energy relaxation of CO_2 embedded in solid Ar, e.g., the value determined for the rate $K_{\mathrm{V_3V}}$ is significantly lower than that predicted under the assumption of nonradiative relaxation.

*E-mail: cenian@imp.gda.pl

[1] D. Jasmin *et al.*, J. Chem. Phys. **108**, 2303 (1998).
[2] H. Chabbi and P. R. Dahoo *et al.*, Chem. Phys. Lett. **285**, 252 (1998).
[3] G. Zerza, G. Śliwińsski, and N. Schwentner, Arrl. Phys. A **56**, 156 (1993).
[4] C. Crepin and M. Broquler *et al.*, Laser Chem. **13**, 65 (1999).
[5] A. Nittzan, S. Mukamel, and J. Jontner, J. Chem. Phys. **62**, 200 (1975).
[6] H. Chabbi and B. Gautier-Roy *et al.*, J. Chem. Phys. **117**, 4436 (2002).
[7] E. U. Conder and G. E. Shortley, *Theory of Atomic Spectra*, Cambridge Univ. Press, Cambridge (1967).
[8] W. Koecher, *Solid State Laser Engineering*, Springer, Berlin (1996).
[9] D. J. Diestler, J. Chem. Phys. **60**, 2692 (1974).
[10] J. Jortner, Mol. Phys. **32**, 379 (1976).
[11] S. H. Lin, P. H. Lin, and D. Knittel, Chem. Phys. **64**, 441 (1976).
[12] I. H. Bachir, R. Charneau, and H. Dubost, Chem. Phys. **163**, 451 (1992).
[13] I. H. Bachir, R. Charneau, and H. Dubost, Chem. Phys. **177**, 675 (1993).
[14] A. Salloum and H. Dubost, Chem. Phys. **189**, 179 (1994).
[15] A. Cenian, Chem. Phys. **132**, 41 (1989).

This article was published in English in the original Russian journal. Reproduced here with stylistic changes by AIP.

Matrix-isolation FTIR study of azidoacetone and azidoacetonitrile

M. Frankowski,* B. S. Fox, A. M. Smith-Gicklhorn, M. K. Beyer, and V. E. Bondybey**

Institute of Physical and Theoretical Chemistry, Technical University of Munich, Garching 85747, Germany

M. Algarra and M. L. Costa

CEFITEC, Department of Physics, Fac. Sciences and Technology, Universidade Nova de Lisboa, Caparica P-2829-516, Portugal

P. Rodrigues and M. T. Barros

CQFB, Department of Chemistry, Fac. Sciences and Technology, Universidade Nova de Lisboa, Caparica P-2829-516, Portugal

M. N. D. S. Cordeiro

REQUIMTE, Department of Chemistry, Fac. Sciences, Universidade do Porto, Porto 4169-007, Portugal
Fiz. Nizk. Temp. **29**, 1140–1146 (September–October 2003)

Azidoacetonitrile (N_3CH_2CN) and azidoacetone ($N_3CH_2COCH_3$) are studied by matrix-isolation FTIR spectroscopy in solid neon, argon, and nitrogen. The IR spectra calculated using the density-fuctional theoretical method are discussed in comparison with the experimental data. Significant broadening of the recorded azide bands indicate an awkward fit of these compounds into the solid environment. The strongest absorption is observed for both compounds in the regions of asymmetric and symmetric stretches of the N_3 azide group. Strong band splittings in the N_3 asymmetric stretch region can be most likely explained by very strong Fermi resonances with the CN stretch and combinations and overtones of the numerous lower-frequency vibrational modes. © *2003 American Institute of Physics.* [DOI: 10.1063/1.1619361]

INTRODUCTION

Organic azides are useful reagents in many fields.[1–3] Their strongly exothermic reactions make them useful as propellants.[4] Their ability to form highly reactive nitrene intermediates that are capable of being inserted into otherwise stable chemical bonds makes them important synthetic reagents, with a number of potential uses in semiconductor technology,[5] for instance.

The compounds were studied both in solution and in solid phase, and the relative volatility of some of them, for example, azidoacetonitrile (N_3CH_2CN, abbreviated in this paper as AzN) and azidoacetone ($N_3CH_2COCH_3$, AzC), allows their studies in the gas phase.[6] The thermal decomposition of these two compounds was recently studied using ultraviolet photoelectron spectroscopy (UVPES) and matrix-isolation spectroscopy in solid nitrogen, as part of a general project on decomposition of aliphatic azides.[7,8] Theoretical calculations have been also carried out for conformers of AzC.[9]

One can often obtain more insight and additional information about the interaction of isolated compounds with the solid medium by examining and comparing the spectra in several matrices. In the present paper we report the infrared spectra in solid neon, argon, and nitrogen. We complement the experimental investigation by density-functional theoretical (DFT) computations of their properties and structures, and discuss their spectra with the help of the computed vibrational frequencies and intensities.

EXPERIMENTAL

Sample preparation

Azidoacetonitrile was synthesized from chloroacetonitrile $ClCH_2CN$ and sodium azide (NaN_3) as given in Ref. 10 Azidoacetone was prepared from chloroacetone $ClCH_2COCH_3$ and NaN_3, according to the procedure described in Ref. 7.

The pre-mixed organic azide vapors with Ne, Ar, and N_2 matrix gases were prepared at room temperature with an estimated concentration of 1:700 for all experiments. Neon samples were continuously deposited onto the copper substrate (coated with silver and MgF_2) cooled to 6 K by a Leybold RGD 580 closed-cycle helium cryostat. Argon and nitrogen samples were deposited by means of a pulsed valve at 12 K onto the KCl substrate mounted on the cryotip of an APD Cryogenics refrigerator. To improve the optical quality of the N_2 matrix, deposition was started from 60 K and then the substrate was gradually cooled down to 12 K in 10 min. In all experiments the deposition rate was kept in the range of 2.5–3 mmol/h for a deposition time of 2 hours.

Spectroscopy

The infrared spectra of both compounds, N_3CH_2CN and $N_3CH_2COCH_3$, in solid Ne, Ar, and N_2 were recorded with a resolution of 0.06 cm^{-1} on a Bruker IFS 120 HR Fourier-transform spectrometer equipped with a glowbar light source, liquid-nitrogen-cooled HgCdTe (MCT) detector, and a KBr beam splitter. Typically at least 500 scans were aver-

TABLE I. Calculated frequencies of vibrational modes of azidoacetonitrile conformers (method: B3LYP/6-31+G(d,p).

Anti: dihedral angle $\phi_{NNCC} = 180°$		Gauche: dihedral angle $\phi_{NNCC} = 67°$		Approximate assignment
frequency, cm^{-1}	intensity, km/mol	frequency, cm^{-1}	intensity, km/mol	
34.9	1.3	55.7	5.5	
145.2	9.2	193.1	7.7	
260.2	1.6	258.6	0.6	
358.6	0.6	351	0.1	C–C≡N bend
519.4	2.7	523	0.1	C–C≡N bend
544.9	6.9	556.3	8.7	NNN bend
628.1	5	687.3	15.7	NNN bend
945	20.7	884.4	13.4	C–C/C–N sym. str.
973.6	0.9	937.6	26	CH_2 rock + C–C/C–N asym. str.
979	15.7	1006.2	9	CH_2 rock + C–C/C–N asym. str.
1241.5	0.6	1253.9	1	CH_2 twist
1332.6	145.2	1314.1	163.1	NNN sym. str.
1373.7	10.9	1372	10.9	CH_2 wag.
1479.1	7.4	1476.5	8.4	CH_2 bend
2255.1	517.8	2254.3	450.9	NNN asym. str.
2376.7	0.9	2358	0.6	C≡N
3021.4	15.4	3043.9	14.3	CH_2 sym. str.
3062.3	4.3	3135.7	0.4	CH_2 asym. str.

TABLE II. Calculated frequencies of vibrational modes of azidoacetone conformers (method: B3LYP/6-31+G(d,p).

Anti: dihedral angle $\phi_{NNCC} = 180°$		Gauche: dihedral angle $\phi_{NNCC} = 64°$		Approximate assignment
frequency, cm^{-1}	intensity, km/mol	frequency, cm^{-1}	intensity, km/mol	
35.4	15.3	61.1	1.9	
46.9	1.3	81	2.5	
137.8	3.8	98.6	0.3	CH_3 torsion + ?
140.9	0	216.5	4.5	CH_3 torsion + ?
262	10.5	274	4.9	
449	1.1	381.1	5.2	
473.8	0.8	461.3	2.5	
499	18.4	556	6	NNN bend + ?
556.1	8.1	573.4	20.9	NNN bend + ?
644.2	11.7	694.3	8.2	
799.9	2.3	794.6	2.2	
839.1	0.5	858.6	17.1	
969.6	19.5	949	23.5	
1012.3	2.1	994.7	4.5	
1069.5	0.5	1077.9	1.6	
1232.5	2.2	1181.8	95.9	CH_2 twist + ?
1240.6	132.4	1251	2.9	CH_2 twist + ?
1342.8	5.8	1340.3	105.4	NNN sym. str. + CH_2 wag.
1348.9	147.5	1368.1	32.1	NNN sym. str. + CH_2 wag.
1394.6	45.2	1393.5	32	CH_3 umbrella mode
1454.5	8.3	1463.4	2.3	CH_2 bend + CH_3 umbrella
1461.4	52.3	1469.6	22.5	CH_2 bend + CH_3 umbrella
1468.3	12.8	1482.5	10.7	CH_3 str. + torsion
1794.3	207.7	1807.4	109.7	CO str. + ?
2255.3	601.8	2255.9	522.3	NNN asym. str.
3024.1	21.8	2990.8	31.9	CH_2 sym. str.
3050.2	0.3	3041.7	3.4	CH_3 sym. str.
3069.8	7.5	3104.6	8	CH_2 asym. str. + ?
3110.9	3.3	3112.3	7.8	CH_2 str + CH_3 str.
3167.2	10	3161.2	5	CH_3 asym. str.

aged. The spectra were recorded immediately after deposition and then again after annealing of the samples, and after irradiation of the matrices with a tungsten lamp, a multi-line UV Ar^+ ion laser and the fourth harmonic of a Nd:YAG laser.

RESULTS AND DISCUSSION

Calculations

The optimized structures and vibrational frequencies of azidoacetonitrile and azidoacetone were calculated using the B3LYP/6-31+G(d,p) hybrid DFT technique as implemented in the Gaussian 98 program suite.[11] To check for errors due to the incomplete basis set, calculations using the larger B3LYP/6-311(3df,3pd) basis set were performed, which yielded no substantial changes from our previous results. Tables I and II summarize the results for the two most stable conformational minima, whose geometry is characterized by different values of the ϕ_{NNCC} dihedral angle. In the case of AzC the two local minima at 64° (gauche) and 180° (anti) are nearly isoenergetic, while in AzN the 67° gauche conformer is found to be considerably lower in energy than the 180° anti isomer. The tables list the computed, unscaled vibrational frequencies of both molecules. The geometries of AzN and AzC conformers are illustrated in Fig. 1.

Experimental results

The infrared absorption spectra of both compounds in solid neon, argon, and nitrogen were recorded in the range from 400 to 5000 cm^{-1}, with selected regions being shown in Figs. 2 and 3. A comprehensive listing of the bands observed in our experiments and their tentative interpretation, as well as the previous assignments by Klaeboe *et al.*,[6] are collected in Table III.

Very often matrix isolation yields excellent-quality spectra with sharp absorption bands, which exhibit little perturbation when compared with the gas phase. In fact, one way to judge the extent of the medium effect is to compare spectra using several different matrix materials, where negligible changes from matrix to matrix usually imply an also small medium shift from the gas phase to the matrix, and this was one of the reasons for performing our current study.

Unfortunately, in the present case, most of the observed spectral bands are relatively broad, and they also exhibit appreciable, matrix-dependent changes in terms of band width, band shape, and band intensity from matrix to matrix. Also somewhat surprisingly, the observed bands are broadest in solid neon, which usually yields the best-quality spectra. One

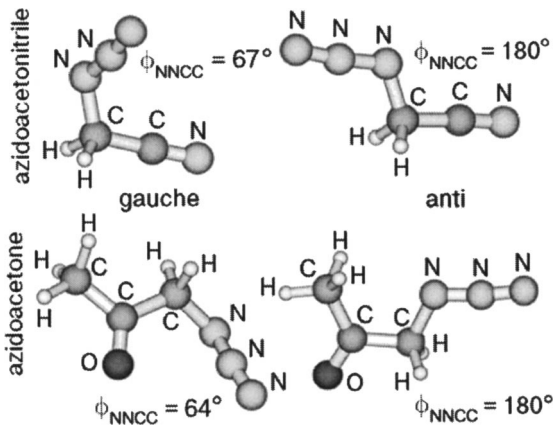

FIG. 1. Predicted structures of the gauche and anti conformers of azidoacetonitrile and azidoacetone.

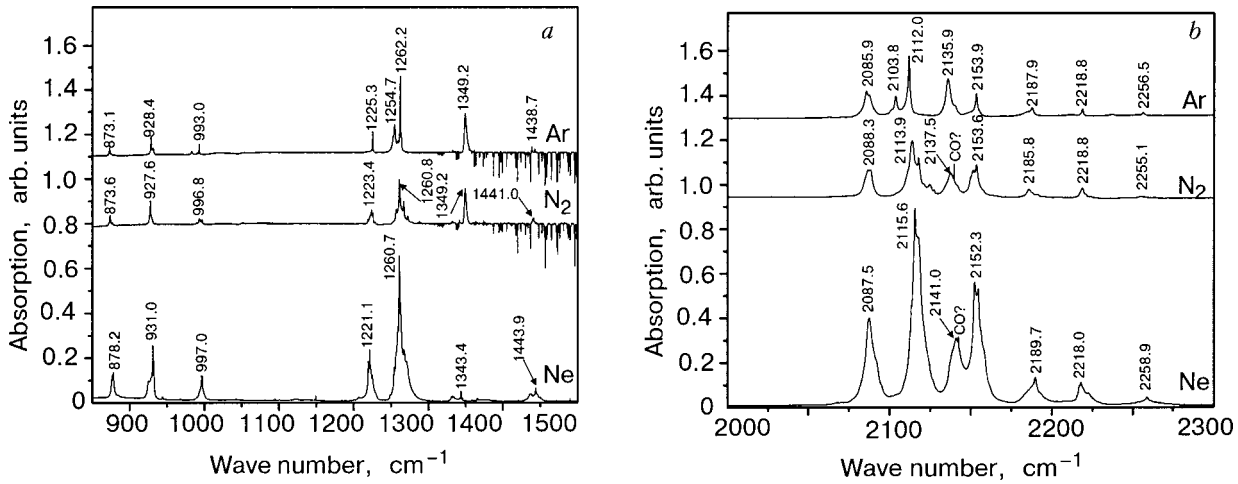

FIG. 2. Infrared spectra of azidoacetonitrile in neon, nitrogen, and argon matrices (the "negative" lines in the CH_2 bend region originate from gas phase water subtraction).

usually gets excellent-quality sharp spectra when the guest fits well into the crystalline structure of the host. Thus linear compounds and cations of the type $X-(C_2)_n-Y$, or, for instance, fluorinated benzene cations, yield very sharp, unperturbed spectra.[12–14] In fact, in both cases two spectrally shifted sites are observed, which were attributed to species isolated in relatively unperturbed closely packed crystalline fcc or hcp environment, respectively. The former, linear compounds replace a row in a plane of neon atoms, while the latter, benzenes, fit well into a site replacing seven atoms in a crystallographic plane. One interpretation of broad bands is an awkward fit of the relatively bulky, low-symmetry guest into the solid host, preventing formation of a well-developed local crystalline structure and resulting in poorly-defined sites, with a wide range of local geometries.

Also the theoretical computations are of less help than is often the case. Thus, as shown in Table I, by far the strongest band computed for AzN is the asymmetric stretching frequency of the N_3 group, predicted to lie in both conformers at about 2254 cm^{-1} (unscaled) with the only other fundamental frequency in this region being the almost three-orders-of-magnitude weaker CN stretching frequency expected at 2358 cm^{-1} (2377 cm^{-1} in the anti compound). The experimental spectrum reveals at least seven bands, several of them quite strong, extending from 2085 to 2259 cm^{-1} (Fig. 2*b*). Some of these bands exhibit asymmetric line shapes and additional splitting, and appreciable changes in their shapes, frequencies, and relative intensities from matrix to matrix. The corresponding N_3 symmetric stretch is computed to be the second strongest absorption band. It is predicted to be at 1333 and 1314 cm^{-1} in the anti and gauche conformers, respectively, with the latter value scaled by a factor of 0.96 coming very close to the observed band appearing in all three matrices between 1260 and 1262 cm^{-1} (Fig. 2*a*).

The three weak to moderately intense bands appearing in all three matrices in the relatively narrow regions around 1221–1225, 1343–1349, and 1438–1444 cm^{-1} (Fig. 2*a*) are in all probability due to the motions of the CH_2 group—twist, wagging, and bending, respectively—in acceptable agreement with the predicted values of 1254, 1372, and 1476 cm^{-1}, unscaled (gauche, Table I). These modes are computed at similar frequencies and intensities in the gauche

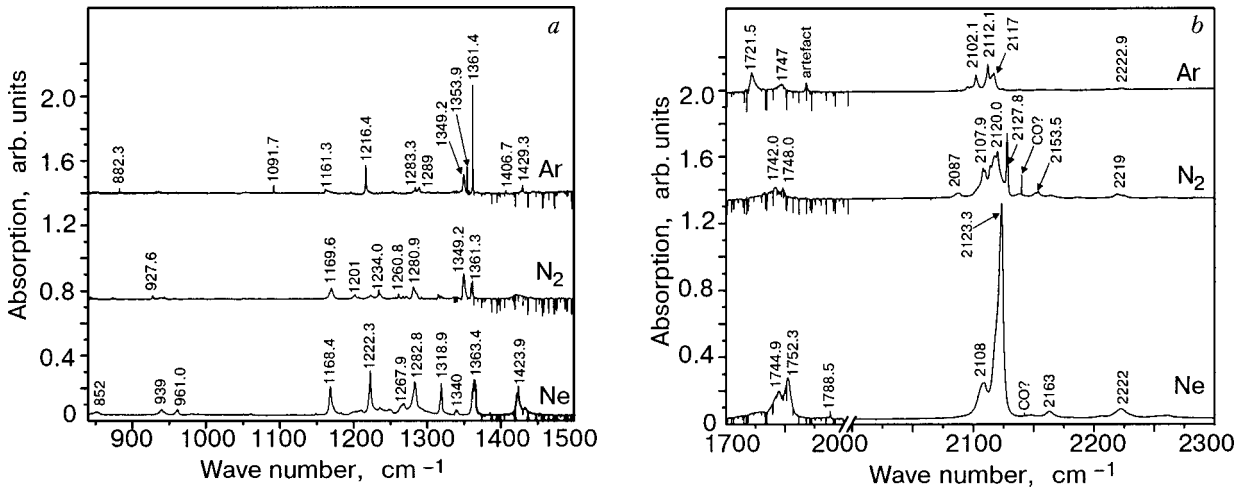

FIG. 3. Infrared spectra of azidoacetone in neon, nitrogen, and argon matrices (the "negative" lines in the CO stretch region originate from subtraction of gas phase water). No spectral features have been observed in the interval 1800–2000 cm^{-1}.

TABLE III. Experimental data for azidoacetonitrile and azidoacetone isolated in Ne, N_2, and Ar solids*.

Azidoacetonitrile					Azidoacetone			
			assignment					
Ne	N_2	Ar	prev. (N_2) #		Ne	N_2	Ar	assignment
561.8 563.3	560.0# ~561.3	560.1	NNN bop		~573.7 ~643.3	~573.9 ~641.1	~575	NNN bend
689.1 691.5	~684 ~691	686.1 698.1	NNN bend	NNN bend	~695.5	~700.2		
878.2 m	872.8 873.6 874.1 } m	873.1 m	C–C/C–N bend	C–C/C–N sym. str.	852.2		882.3	
~925.5 ~929.2 931.0 931.8 } s	927.6 929.7 } s	928.4 931.2 } s	CH_2 rock	CH_2 rock + C–C/C–N asym. str.	931.0 ~939 m,b	927.6 ~939	932.4 ~935.1	
943.7 944.6					959.7 ~961.0 m,b	943.8 ~956.6 b		
990.0 992.6 993.9 962.2 997.0 } m	~989.4 ~993 994.7 996.8 }	982.8 b 993.0 m		CH_2 rock + C–C/C–N asym. str.	~980 b			
~1123 1149.1					1050.8 1061.0 1149.1 1168.4 s	1169.6 m	1091.7 1161.3 ~1163 } sh	
~1206 1218.9 1220.0 1221.1 1222.1 1223.1 1224.9 } s	1218.5 1223.4 1225.5 1228.7 } m	1225.3 s	CH_2 tors.	CH_2 twist	~1208 } b ~1210 } 1222.3 s 1235.4	~1201 ~1223.3 1225.4 1234.0 } m ~1236.0	~1195.9 1216.4 s	CH_2 twist
1248.6 1254.0 ~1256.3 ~1258.9 1260.7 1262.7 ~1266.8 ~1270.7 ~1272.2 } vs	1256.6 1258.6 1260.8 ~1266.7 ~1272.3 } vs	~1252.5 1254.7 } m ~1258.9 1262.2 1263.5 } vs	CH_2 wag.	NNN sym. str.	~1249 b 1264 1267.8 } m 1282.8 s	1260.8 1266.7 1271.8 1280.9 1285.7 } m 1292.3	1283.3 ~1289 b	NNN sym. str.
1330.3 1332.6 1334.5 }	~1331.6	1332.5	N=N str.		1316.5 1317.8 1318.9 1319.9 } m ~1339.5 b	~1315.0 ~1318		
1343.4 1343.8 1345.5 }	1349.2 vs	1349.2 vs		CH_2 wag.	1349.2 s 1363.4 1364.4 1365.6 } s	1349.2 s 1359.2 1360.0 1361.3 } m	1353.9 s 1354.8 1356.2 1357.6 1358.1 1361.4 vs 1362.6 1363.1 1363.2 } m	CH_2 wag.
1365.5		1361.4						
1437.4 b 1443.9 1449.7 }	~1440 1440.5 1441.0 }	1438.7 1442.7 1442.8	CH_2 bend	CH_2 bend	1421.9 1423.9 } s 1432.9 m,b	~1422 b	1406.7 1429.3	CH_2 bend
					~1729 ~1744.9 } s 1752.3 s 1788.5	~1732.4 m 1742.0 1748.0	1721.5 s ~1747 m,b	CO str.?
2087.5 ~2092.2 } s	2085.8 2088.3 } s	2085.9 2087.8 } s 2103.8 s		Bands due to anharmonic resonance involving mainly NNN asym. str.		~2087		
2113.4 2115.6 2116.9 2117.7 } vs	2113.9 2117.7 } vs 2124.8 2127.6	2112.0 vs	N≡N str.		~2108 s 2123.3 vs	2107.9 2109.7 } s 2113.9 ~2117 2120.0 } vs 2127.8 vs	~2095.1 2102.1 s 2112.1 s 2115.6 2116.8 } s	Bands due to anharmonic resonance involving mainly NNN asym. str.
2141.0	2137.5 s	2135.9 ~2140.3 } s			2163 b	2151.4 2153.6		
2152.3 2154.6 } vs	2151.4 2153.6 } s	2153.5 s						
2189.7 m	2185.8 m 2191.4	2187.9 m						
2216.9 2218.0 2222.6 } m	2218.8 2221.4 } m	2218.8			~2222 m,b	~2219.0 2224.9 } m,b	2211.3 2222.9	
~2253.6 2258.9 }	~2254.7 b	2256.5	C≡N str.	C≡N str.				

*i) weak bands around 2500 cm^{-1} and in the range of 2900–4500 cm^{-1} as well as matrix-isolated water and regions of the CO_2 bands have been omitted; ii) frequencies grouped in braces show fine structure of the bands; m—medium, s—strong, vs—very strong; the others are weak or very weak; b—broad.
#Underlined frequencies for AzN/N_2 relate to a previous assignment.[6]

and anti species and therefore do not provide a useful basis for distinguishing between the two.

Most useful for discriminating between the two conformers appears to be the 700–1100 cm^{-1} region. The three moderately intense bands observed in the experimental spectrum of AzN near 993–997, 928–931, and 873–878 cm^{-1}, respectively (Fig. 2*a*), are in a distinctly better agreement with the comparably intense 1006, 938, and 884 cm^{-1} bands predicted for the gauche conformer than with the two strong and one very much weaker anti species bands, computed to lie near 979, 974, and 945 cm^{-1}.

The previously noted, complex structure in the region of the asymmetric N_3 stretch, which is insensitive to the sample deposition rate and conditions and which does not change upon sample annealing or photolysis, is unlikely to be due to the presence of multiple conformers. The more than 150 cm^{-1} range of the observed bands is way too large to be attributed to matrix sites and suggests that the appearance of the spectrum is due to an intrinsic property of AzN. The molecule has a low, C_1, symmetry, and the most likely explanation for the observed multiple strong bands seems to lie in very strong Fermi resonances between the N_3 asymmetric frequency, the CN stretching frequency, and combinations and overtones of the numerous lower-frequency vibrational modes expected in this region. It should be mentioned that a previous study[6] has also suggested a similar complexity in this region even in the gas phase spectrum. A rather weak band observed in all three matrices around 2255–2259 cm^{-1}, but absent from the spectra of azidoacetone, to be discussed below, is undoubtedly due to the CN stretching vibration (Figs. 2*b* and 3*b*).

For the more complex azidoacetone molecule, with its twelve atoms and thirty vibrational modes, more complex infrared spectra should be expected, making their interpretation correspondingly more difficult. As in AzN, by far the most intense infrared fundamental in AzC also is predicted to be the asymmetric N_3 vibration, computed to lie in both conformers near 2255 cm^{-1} (unscaled). Here several structured bands are also found in this region, the appearance, width, and splitting of which changes substantially from matrix to matrix (Fig. 3*b*). In neon a dominant band appears at 2123.3 cm^{-1} with a much weaker shoulder at 2108 cm^{-1} and two much weaker ones at 2163 and 2222 cm^{-1}. All these bands are relatively symmetric, and have widths in excess of 10 cm^{-1}. In argon and nitrogen matrices there is not one dominant band, but a more complex structure, with the strong band appearing to have split into several components with differing widths and intensities, as can be seen in Fig. 3*b*.

Three other bands of the AzC gauche conformer are predicted to have appreciable intensities: the CO stretch at 1807, and bands at 1340 and 1182 cm^{-1}, presumably the symmetric N_3 stretch and a CH_2 twist. These two latter modes are possibly strongly mixed, and they are computed to be somewhat shifted to 1349 and 1241 cm^{-1} in the higher-energy anti conformer. Experimentally, in all three matrices, two bands are found in the carbonyl region, at 1752.3 and 1744.9 cm^{-1} in neon, 1747 and 1721.5 cm^{-1} in argon, and 1748 and 1742 cm^{-1} in nitrogen (Fig. 3*b*). Besides significant changes in their frequencies from matrix to matrix, their relative intensities are also found to change, with the higher-frequency band being more intense in neon but the lowest, 1721.5 cm^{-1}, band having the highest intensity in the argon matrix.

The assignment of the numerous lower-frequency modes, which, in view of the low molecular symmetry, are probably strongly mixed, becomes more difficult. Comparison with the AzN would seem to dictate assigning the rather strong band at 1282.8 cm^{-1} in solid neon to the N_3 symmetric stretch, and the absorptions near 1222, 1363, and 1424 cm^{-1} to the twisting, wagging, and bending motions of the CH_2 group (Fig. 3*a*).

We have already commented above that many of the spectral lines of the matrix-isolated molecules investigated here are unusually broad, and suggested that one explanation might be an awkward fit into the matrix site, preventing the formation of a well-developed crystalline structure of the host matrix in the neighborhood of the guest dopant. Another remarkable observation involves the significant shifts of individual bands from matrix to matrix, and in particular the large changes in the band widths and relative intensities. A possible interpretation of this may lie in the polar nature of the azide group. In general, matrices tend to stabilize strongly ionic or polar structures, and this stabilization will be a strong function of the polarizability of the host atoms or molecules.

Another conclusion is that in a series of annealing experiments and experiments on photolysis of the matrices at various wavelengths, no appreciable spectral changes were detected. No new bands appeared following irradiation of the matrices, nor were there substantial changes in the relative band intensities, and for a given matrix the relative intensities remained consistent from experiment to experiment. Overall, the observed spectra can be interpreted in terms of the azides being isolated in the lowest-energy, gauche conformation, and no clear evidence of the simultaneous presence of several conformers was found.

SUMMARY

The infrared spectra of organic azides, azidoacetonitrile (N_3CH_2CN) and azidoacetone ($N_3CH_2COCH_3$), isolated in low-temperature solids has been measured by means of Fourier-transform technique in the range from 400 to 5000 cm^{-1}. A comparative study in neon, argon and nitrogen matrices has shown that most of the observed spectral bands are relatively broad, exhibiting appreciable changes in terms of band width, band shape, and band intensity from host to host. Significant broadening of the recorded azides bands indicate an awkward fit of the low-symmetry molecules into the solid host, resulting in a wide range of local environments. Based on DFT calculations of the IR spectra for optimized structures, the strongest absorption bands observed for both compounds were assigned to asymmetric and symmetric stretches of the N_3 azide group. Strong Fermi resonances involving the N_3 asymmetric stretch, CN stretch, and combinations and overtones of the numerous lower-frequency vibrational modes can most likely be interpreted as indicative of the strong band splittings occuring in the asymmetric stretch region of the N_3 group.

The authors gratefully acknowledge the EU for financial support within the Research Training Network ''Reactive Intermediates.''

*E-mail: frankowski@ch.tum.de
**E-mail: bondybey@ch.tum.de

[1] M. A. Bohn, Thermochim. Acta **33**, 121 (1999).
[2] C. Gauthier and Y. Ramodenec, Tetrahedron **57**, 7513 (2001).
[3] A. E. Taubl, K. Langhans, T. Kappe, and W. Stadbauer, J. Heterocycl. Chem. **39**, 1259 (2002).
[4] O. P. Korobeinichev, L. V. Kuibeida, E. N. Volkov, and A. G. Shmakov, Combust. Flame **129**, 136 (2002).
[5] G. Williams and C. Dsilva, Sens. Actuators B **30**, 151 (1996).
[6] P. Klaeboe, K. Kosa, C. J. Nielsen, H. Priebe, and S. H. Schei, J. Mol. Struct. **160**(**3-4**), 245 (1987).
[7] J. M. Dyke, A. P. Groves, A. Morris, J. S. Ogden, M. I. Catarino, A. A. Dias, A. M. S. Oliveira, M. L. Costa, M. T. Barros, M. H. Cabral, and A. M. C. Moutinho, J. Chem. Phys. **103**, 8239 (1999).
[8] M. Algarra, A. A. Dias, M. L. Costa, P. Rodrigues, M. T. Barros, V. H. C. Lopes, M. N. D. S. Cordeiro, G. Levita, J. M. Dyke, A. Morris, and J. S. Ogden (to be submitted).
[9] M. I. Catarino, B. J. Costa Cabral, and M. L. Costa, J. Mol. Struct. **397**, 223 (1997).
[10] K. Freudenberg, H. Eichel, and F. Leutert, Ber. Dtsh. Chem. Ges. **65**, 1183 (1932).
[11] *Gaussian 98*, Revision A.11, M. J. Frisch, G. W. Trucks, H. B. Schlegel, G. E. Scuseria, M. A. Robb, J. R. Cheeseman, V. G. Zakrzewski, J. A. Montgomery, Jr., R. E. Stratmann, J. C. Burant, S. Dapprich, J. M. Millam, A. D. Daniels, K. N. Kudin, M. C. Strain, O. Farkas, J. Tomasi, V. Barone, M. Cossi, R. Cammi, B. Mennucci, C. Pomelli, C. Adamo, S. Clifford, J. Ochterski, G. A. Petersson, P. Y. Ayala, Q. Cui, K. Morokuma, P. Salvador, J. J. Dannenberg, D. K. Malick, A. D. Rabuck, K. Raghavachari, J. B. Foresman, J. Cioslowski, J. V. Ortiz, A. G. Baboul, B. B. Stefanov, G. Liu, A. Liashenko, P. Piskorz, I. Komaromi, R. Gomperts, R. L. Martin, D. J. Fox, T. Keith, M. A. Al-Laham, C. Y. Peng, A. Nanayakkara, M. Challacombe, P. M. W. Gill, B. Johnson, W. Chen, M. W. Wong, J. L. Andres, C. Gonzalez, M. Head-Gordon, E. S. Replogle, and J. A. Pople, Gaussian, Inc., Pittsburgh, PA (2001).
[12] J. Agreiter, A. M. Smith, and V. E. Bondybey, Chem. Phys. Lett. **241**, 317 (1995).
[13] A. M. Smith, J. Agreiter, and V. E. Bondybey, Chem. Phys. Lett. **244**, 379 (1995).
[14] V. E. Bondybey and M. Lorenz, J. Low Temp. Phys. **122**, 509 (2001).

This article was published in English in the original Russian journal. Reproduced here with stylistic changes by AIP.

Activation spectroscopy of electronically induced defects in solid Ne

O. N. Grigorashchenko, V. V. Rudenkov, and E. V. Savchenko*

B. Verkin Institute for Low Temperature Physics and Engineering of the National Academy of Sciences of Ukraine, 47 Lenin Ave., Kharkov 61103, Ukraine

I. V. Khizhnyi

B. Verkin Institute for Low Temperature Physics and Engineering of the National Academy of Sciences of Ukraine, 47 Lenin Ave., Kharkov 61103, Ukraine; V. Karazin Kharkov National University, 4 Svobody Sq., Kharkov 61107, Ukraine

M. Frankowski

Institute of Physical and Theoretical Chemistry, TU Munich, Garching 85747, Germany; Institute of Fluid-Flow Machinery, Polish Academy of Sciences, 14 J. Fiszera, Gdansk 80-231, Poland

A. M. Smith-Gicklhorn, M. K. Beyer, and V. E. Bondybey**

Institute of Physical and Theoretical Chemistry, TU Munich, Garching 85747, Germany
Fiz. Nizk. Temp. **29**, 1147–1151 (September–October 2003)

Thermally stimulated luminescence (TSL) and thermally stimulated exoelectron emission (TSEE) methods were used in combination with cathodoluminescence to probe electronically induced defects in solid Ne. The defects were generated by a low energy electron beam. For spectroscopic study we used Ar* centers in Ne matrix as a model system. At a temperature of 10.5 K a sharp decrease in the intensity of ''defect'' components in the luminescence spectrum was observed. From the analysis of the corresponding peak in the TSL and TSEE yields, the trap depth energy was estimated and compared with available theoretical calculations. The obtained data support the model suggested by Song, that stable electronically induced defects have the configuration of second-neighbor Frenkel pairs. © *2003 American Institute of Physics.* [DOI: 10.1063/1.1619362]

1. INTRODUCTION

Activation spectroscopy is a powerful tool for the study of defects in solids.[1] Electronically induced defects represent a special class of lattice defects created

via an electronic subsystem. The basis for the physics of their formation is a concentration of the electronic excitation energy within a volume about that of a unit cell, followed by energy release. These defects have been actively studied on a variety of materials.[2–4] Atomic cryocrystals with their simple lattice and well-known electronic structure are especially suitable for these studies due to small binding energies in conjunction with a strong exciton-phonon interaction. Electronically induced stable lattice defects have been found[5] in solid Ne, Ar, Kr, and Xe using spectroscopic methods in experiments carried out with a low energy electron beam. It was suggested that the stimulating factor is the self-trapping of excitons either into molecular-type self-trapped excitons (M-STE) or atomic-type (A-STE) states. In solid Ne the main channel of the exciton self-trapping is the self-trapping into A-STE states. The recent state-selective study performed with synchrotron radiation in the range of excitonic absorption $n=2\Gamma(3/2)$ gave direct evidence of the formation and accumulation of point lattice defects via the excitonic mechanism.[6] An excited-state molecular dynamics study of the possible evolution of the self-trapped excitons into stable lattice defects has shown that the self-trapping may result in Frenkel pair creation, and a microscopic structure of the defects has been proposed.[7] However, to our best knowledge so far no experimental study of electronically induced defects structure in solid Ne exists.

We applied activation spectroscopy methods to get information on the charge traps related to electronically induced permanent lattice defects in solid Ne. The most common method in use is thermally stimulated luminescence (TSL).[1] However, interpretation of TSL data is hampered by the fact that the emission of light may be caused by recombination of both charged species and neutral species. In these cases the meaning of activation energies derived from experimental data could be quite different. In order to distinguish between the recombination processes of neutral and charged species, TSL is combined with methods of current activation spectroscopy, as demonstrated in recent experiments performed with solid Ar.[8,9] Thermally stimulated currents (TSC) have been measured along with TSL by Schrimpf *et al.*[8] The method of thermally stimulated exoelectron emission (TSEE) enabled us to prove directly that the electrons are the mobile charge carriers responsible for recombination reactions in irradiated rare gas solids.[9] In this study we also used the TSEE method in combination with TSL to probe electronically induced defects in solid Ne.

2. EXPERIMENTAL SECTION

A detailed description of the experimental procedure is given elsewhere.[9–11] High-purity Ne (99.999%) gas was

used. The samples were grown from the gas phase by pulsed deposition on a substrate cooled by a Leybold RGD 580 closed-cycle 2-stage cryostat to a temperature of 6 K. The metal substrate was coated with a thin layer of MgF_2. The gas-handling system was annealed and pumped before the experiments. The pressure in the sample chamber was 6×10^{-8} mbar. Samples were deposited with concurrent irradiation by electrons with an energy of 150 eV, which is insufficient for producing point defects via the knock-on mechanism. A typical deposition rate was 10^{-2} $\mu m \cdot s^{-1}$. We deposited Ne films of 50–100 μm thickness. The sample thickness and the deposition rate were determined by measuring the pressure decrease in a known volume of the Ne reservoir in the gas-handling system. The samples had a high optical quality and looked transparent in the visible range.

Defect levels in the energy gap were probed by measuring thermally stimulated exoelectron emission and thermally stimulated luminescence. The programmable temperature controller permitted maintaining the desired temperature during sample preparation and irradiation, as well as to control the heating rate. The temperature was measured with a calibrated silicon diode sensor, mounted at the substrate. In the TSEE and TSL experiments the samples were heated at a constant rate of $1.6\,K \cdot min^{-1}$. The measurements were performed in the temperature range 6–12 K. The emission of electrons from pre-irradiated samples was detected with a movable Au-coated Faraday plate kept at a small positive potential of $+9$ V. During the measurements it was positioned at a distance of 5 mm in front of the sample, which had been grown on a grounded substrate. The current from the Faraday plate was amplified by a FEMTO DLPCA 100 current amplifier. The signal was reversed in polarity and digitized in a PC. The total yield of TSL was detected with a photomultiplier tube (PMT). By introducing a converter of vacuum ultraviolet radiation into visible light we were able to extend the available spectral range and detect TSL from 800 nm to 10 nm.

In addition luminescence spectra from nominally pure and Ar doped solid Ne were detected in vacuum ultraviolet (VUV) range under excitation by low-energy electrons. The dose dependence and the influence of heating on the luminescence intensity and spectral distribution were examined.

3. RESULTS AND DISCUSSION

In a perfect lattice of solid Ne electrons are delocalized, and their transport exhibits free-electron behavior, as has been clearly indicated in experiments using time-of-flight[12] and muon spin rotation/relaxation (μ^+SR)[13] techniques. The second important point is a large mean free path of the conduction electrons in cryocrystals of high structural quality.[14] This makes it possible to use the TSEE method of current activation spectroscopy for trap-level studies, and one can expect to get information on the volume traps formed within the sample under irradiation. In view of the negative electron affinity $E_a = -1.3$ eV of solid Ne,[2] only such kinds of structural defects as vacancies, vacancy clusters, or pores may serve as efficient shallow traps for electrons. In addition, traces of impurities, which can be considered as ''electron scavengers'' (O_2, O, OH, etc.), form deep, thermally disconnected electron traps. The electrons from these traps can only be released optically.

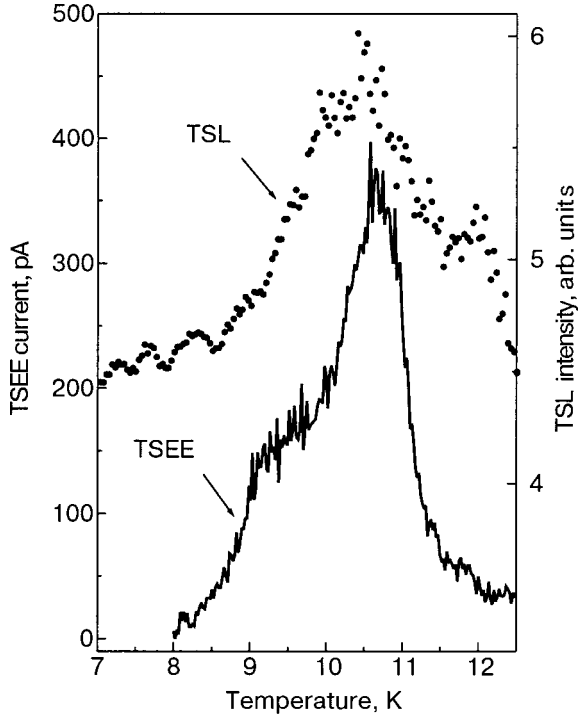

FIG. 1. Integrated yield of TSL and yield of TSEE taken from solid Ne.

At low temperature, after the irradiation was stopped, we observed a long ''afterglow'' of luminescence and ''afteremission'' of electrons from the Ne samples. The phosphorescence is due to minor traces of impurities. Such an afterglow has been observed very often in matrix isolation studies.[15,16] The afteremission of electrons is assumed to be stimulated by afterglow photons, similarly to the effect observed in nitrogen doped solid Ar.[17] TSL and TSEE yields were detected after the afteremission and afterglow had gon to completion. During annealing, if there is enough energy to release the electrons from the traps, they can either recombine with positively charged centers, with subsequent emission of light, or they can be detected as a thermally stimulated emission of electrons.

The typical yields of TSL photons and TSEE currents taken from Ne samples grown under the electron beam are shown in Fig. 1. We have found a pronounced maximum in the TSEE and TSL yields at 10.5 K. In both cases the peak is not isolated—the ''current curve'' and especially the ''glow curve'' exhibit overlapping peaks. Note that the TSEE curve has a simpler structure. Apart from the main peak at 10.5 K, a wide low-temperature shoulder was seen around 9 K. No intense peaks at the higher temperature side of the TSEE curve were detected. First of all, note the correlation in the position of the main ''thermopeak'' at 10.5 K in the yields of both photons and electrons. The observation of TSL and TSEE peaks at the same temperature is a clear indication of the common origin of recombined and emitted electrons. The absence of any shift in the peak position between TSL and TSEE is due to the negative electron affinity of solid Ne, i.e., electrons have no barrier to escaping the sample. Moreover, a

conduction electron will experience an increase of kinetic energy when it exits the surface.

To get information on the trap level related to electronically induced defects one should analyze the peak at 10.5 K, which exhibits characteristic dose behavior. One more reason to consider this peak as related to electronically induced defects comes from the experiments on Ar-doped Ne matrices. It was shown theoretically[7] and tested experimentally[5] that the processes of structural defect creation in the system ''Ar atom in Ne lattice'' (a model of the A-STE center) are quite similar to those in pure solid Ne. In other words, an Ar atom could be used as a ''probe'' to test the processes in Ne matrix. This system is more convenient for spectroscopic study because of the sharper structure of the luminescence band. The lattice expands around the excited Ar* center in response to the repulsive interaction of the excited electron and the surrounding atoms of the Ne matrix. After the formation of the primary bubble, some of the Ne atoms from the surrounding environment could be removed from the first solvation shell and fitted into second or third shell, overcoming the barrier which leads to the defect position. It was found that the second-nearest neighbor vacancy–interstitial pairs could evolve into lattice defects that0 remain stable after the electronic transition of the Ar* center to the ground state. The estimated difference in energy of the electronic transitions in the primary bubble around Ar* center and the bubble associated with the defect is reported as 105 meV.[7] The luminescence of Ar* centers in solid Ne in the range of the electronic transitions from $^1P_1$ and $^3P_1$ states was studied previously,[18] and a sharp intensity redistribution was found at 10.5 K. In connection with our current study we reinvestigated the luminescence of Ar* centers in Ne matrices and its temperature behavior. The experiments were carried out with samples of better structural quality than before.[18] The luminescence spectrum shown in Fig. 2 consists of two bands ''a'' and ''b'' of doublet structure. The ''a'' and ''b'' bands have been identified as $^1P_1 \rightarrow {}^1S_0$ and $^3P_1 \rightarrow {}^1S_0$ transitions,[18] respectively. The high-energy component ''2'' belongs to the emission from the primary bubble, the low-energy component ''1'' is related to the stable electronically induced lattice defects, as had been found before[5] by measuring the dose dependence. The luminescence band difference between ''1'' and ''2'' components in the spectrum is about 100 meV, in good agreement with theoretical data.[7] Upon heating the samples we observed some increase in the relative intensity of the defect-related component ''1'' for both transitions. As the temperature reached 10.5 K, the intensity of the defect components related to the electronically induced defects decreased drastically. A subsequent cycle of irradiation at low temperature restored the intensity distribution in the luminescence spectrum of the Ar* center. The temperature dependence of the relative intensities of the components for the singlet–singlet and the triplet–singlet transitions is shown in Fig. 2. The observed intensity redistribution could be interpreted as annealing of the electronically induced defects. Note that sharp changes in the luminescence spectra of solid Ne at 10.5 K have also been detected in experiments with x-ray irradiation.[19]

Because the peak at 10.5 K in the TSL curve taken from solid Ne is strongly influenced by overlapping peaks, we

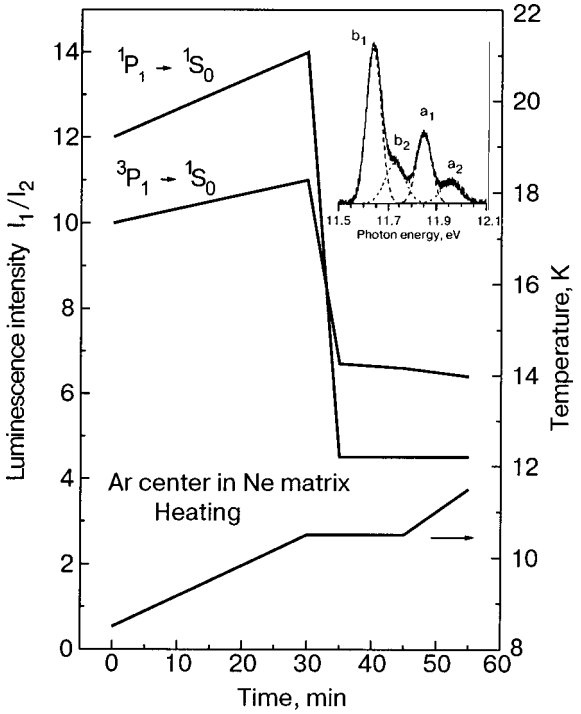

FIG. 2. Luminescence spectrum of Ar* center in Ne matrix detected under irradiation by low-energy electrons (inset). The ''a'' band corresponds to the $^1P_1 \rightarrow {}^1S_0$ transition, the ''b'' band to the transition from the $^3P_1$ state. The temperature dependence of the relative intensities of the defect (''1'') and regular (''2'') components is plotted for both transitions. The variation of the temperature with time is shown by the curve at the bottom.

used the TSEE curve for the analysis. Taking into account that the high-temperature part of the TSEE curve is practically free from overlapping, for estimation of the trap depth energy E_t we used the method suggested by Lushchik,[20] wherein only the descending part of a peak in the glow curve is used. This method is a version of the half-width method.[1] It was supposed that the experimental data could be fitted using first-order kinetics under the condition of no retrapping. In this case

$$E_t = kT_m^2/(T_2 - T_m),$$

where T_m is the temperature at the maximum of the peak and T_2 is the temperature on the high-temperature side of the peak corresponding to half the maximum intensity. The value of E_t estimated by this method from the TSEE experiment is 20 meV. This value is in good agreement with the barrier height calculated by Song[7] for the formation of the second-neighbor Frenkel pairs—the stable configuration of the electronically induced defects. This barrier prevents vacancy–interstitial pairs from annihilation at low temperatures. Upon annealing the traps disappear, and we observe emission of the electrons. The agreement of the activation energy of the intrinsic electron traps reported here with the energy of thermally activated recombination of the Frenkel pairs seems to be a strong argument in favor of the configuration of stable electronically induced defects suggested previously.[7] Note that the vacancies in the Frenkel pairs serve as the electron traps.

We thank Profs. K. S. Song and G. Zimmerer for valuable discussions. Financial support from the Deutsche Forschungsgemeinschaft through the program ''Fórderung der

wissenschaftlichen Beziehungen deutscher Wissenschaftler zu Wissenschaftlern in Ländern Mittel- und Osteuropas sowie Ländern der vormaligen UdSSR'' is gratefully acknowledged.

*E-mail: savchenko@ilt.kharkov.ua
**E-mail: bondybey@ch.tum.de

[1] D. R. Vij, in *Luminescence of Solids*, D. R. Vij (Ed.), Plenum Press, New York (1998).
[2] K. S. Song and R. T. Williams, *Self-Trapped Excitons*, Vol. 105 of Springer Series in Solid State Science, Springer-Verlag, Berlin (1996).
[3] M. A. Elango, *Elementary Inelastic Radiation-Induced Processes*, American Institute of Physics, New York (1991).
[4] N. Itoh and A. M. Stoneham, Radiat. Eff. Defects Solids **155**, 277 (2001).
[5] E. V. Savchenko, A. N. Ogurtsov, and O. N. Grigorashchenko, Phys. Solid State **40**, 831 (1998).
[6] E. V. Savchenko, A. N. Ogurtsov, and G. Zimmerer, Fiz. Nizk. Temp. **29**, 356 (2003) [Low Temp. Phys. **29**, 270 (2003)].
[7] Chun-rong Fu and K. S. Song, J. Phys.: Condens. Matter **9**, 9785 (1997).
[8] A. Schrimpf, C. Boekstiegel, H-J. Stöckman, T. Bornemann, K. Ibbeken, J. Kraft, and B. Herkert, J. Phys.: Condens. Matter **8**, 3677 (1996).
[9] E. V. Savchenko, O. N. Grigorashchenko, A. N. Ogurtsov, V. V. Rudenkov, G. B. Gumenchuk, M. Lorenz, A. Lammers, and V. E. Bondybey, J. Low Temp. Phys. **122**, 379 (2001).
[10] E. V. Savchenko, O. N. Grigorashchenko, A. N. Ogurtsov, V. V. Rudenkov, G. B. Gumenchuk, M. Lorenz, M. Frankowski, A. M. Smith-Gicklhorn, and V. E. Bondybey, Surf. Sci. **507–510**, 753 (2002).
[11] E. V. Savchenko, O. N. Grigorashchenko, A. N. Ogurtsov, V. V. Rudenkov, G. B. Gumenchuk, M. Lorenz, A. M. Smith-Gicklhorn, M. Frankowski, and V. E. Bondybey, Surf. Rev. Lett. **9**, 353 (2002).
[12] W. E. Spear and P. G. Le Comber, ''Electronic Transport Properties,'' in *Rare Gas Solids*, M. L. Klein and J. A. Venables (Eds.), Academic press, New York, (1977), p. 1120.
[13] V. G. Storchak, D. G. Eshchenko, J. H. Brewer, S. P. Cottrell, S. F. G. Cox, Karlsson, and R. W. Wappling, J. Low Temp. Phys. **122**, 527 (2001).
[14] N. Schwentner, E. E. Koch, and J. Jortner, *Electronic Excitation in Condensed Rare Gases*, Vol. 107 of Springer Tracts in Modern Physics, Springer, Berlin (1985).
[15] D. S. Tinti and G. W. Robinson, J. Chem. Phys. **49**, 3229 (1968).
[16] R. J. Sayer, R. H. Prince, and W. W. Duley, Phys. Status Solidi B **106**, 249 (1981).
[17] E. V. Savchenko, O. N. Grigorashchenko, G. B. Gumenchuk, A. N. Ogurtsov, M. Frankowski, A. M. Smith-Gicklhorn, and V. E. Bondybey, Radiat. Eff. Defects Solids **157**, 729 (2002).
[18] Yu. I. Rybalko, E. V. Savchenko, and I. Ya. Fugol', Fiz. Nizk. Temp. **11**, 637 (1985) [Sov. J. Low Temp. Phys. **11**, 349 (1985)].
[19] E. Schuberth and M. Creuzburg, Phys. Status Solidi B **71**, 797 (1975).
[20] Ch. B. Lushchik, JETP **3**, 390 (1956).

This article was published in English in the original Russian journal. Reproduced here with stylistic changes by AIP

Monte Carlo simulations of krypton adsorption in nanopores: Influence of pore-wall heterogeneity on the adsorption mechanism

B. Kuchta,* P. Llewellyn, and R. Denoyel

Laboratoire des Materiaux Divises, Revetement, Electroceramiques, Universite de Provence, Centre de Saint-Jerome, 13397 Marseille Cedex 20, France

L. Firlej

Groupe de Dynamique des Phases Condensees, Universite Montpellier II, 34095, Montpellier Cedex 5, France

Fiz. Nizk. Temp. **29**, 1152–1155 (September–October 2003)

We present molecular simulation results of the adsorption of krypton in a model of the mesoporous material MCM-41. The adsorption isotherm and adsorption enthalpies are studied at 77 K. Comparison of the experimental and simulation data allows us to analyze how the available interaction models (Kr–Kr and Kr–walls) are able to reproduce the experimental situation. The role of the heterogeneous interactions versus the homogenous model is studied and compared with the previous simulation results of nitrogen adsorption in MCM-41. The results show that a model of ideal cylindrical pores gives qualitatively and quantitatively different results. A distribution of the adsorption sites must exist to explain the loading at low pressure (below capillary condensation). Such a distribution in MCM-41 is a consequence of inhomogenous walls that contain a wide variety of attractive sites ranging from weakly attractive silica-type to highly attractive regions. In our simulations the MCM-41 structure is modeled as an amorphous array of oxygen and silicon atoms, each one interacting with an adsorptive atom via the atom–atom potential. The distribution of the adsorption sites is merely a consequence of the local atomic structure. Such a model of the wall reproduces the smooth increase in loading seen experimentally. [DOI: 10.1063/1.1619363]

1. INTRODUCTION

An application of computer modeling methods to study adsorption in pores is strongly dependent on the interaction model, in particular, the interaction of the adsorptive with the walls of the adsorbent. Much of the work has been performed using simple models with regularly shaped pores and smooth walls. However, there are relatively few real adsorbents that conform exactly to either of the regular (cylindrical and slit) shapes. A strong influence of the pore geometry on the thermodynamics of systems in confined geometry is well known.[1] It is obvious that the discrete structure of walls must play a role in the adsorption mechanism, especially in ultra-micropores, where the average diameter is few times the size of the adsorbate.

The material MCM-41, synthesized in 1992, is a model nanoporous material with a narrow pore distribution (with a mean diameter in the range 2–10 nm) and straight unconnected channels. These features are of particular interest because they make it an ideal model as well as a practical adsorbent. Adsorption isotherms have been measured for many different adsorptives.[1] They are generally of type IV in the IUPAC classification,[2] showing a strong affinity of the fluid for the pore at low pressure, followed by a gradual increase in the amount adsorbed up to a sharp capillary condensation. Except for a few cases, the desorption branch of the isotherm follows a different path from the adsorption branch.

Therefore, the MCM-41 samples are very suited to analyze the capillary condensation phenomenon and to determine the phase diagram of the confined capillary phase. However, the mechanism of the adsorption depends strongly on the detailed structure of walls on the atomic level. The amorphous structure of the pore material produces a distribution of adsorption sites and makes the interaction with the wall inhomogeneous. The recent simulations[1] of nitrogen in the pores of MCM-41 have shown that the only way to reproduce the smooth increase in loading seen experimentally is to use a model with a heterogeneous surface.

In the present paper we model the krypton adsorption in nanopores. Krypton is an example of capillary solidification at temperatures where the sorption isotherm can be measured.[3,4] Here we carry out an analysis of the influence of the krypton–wall interaction on the phenomena. It is the first step toward understanding the mechanism of krypton adsorption in the MCM-41 material. We analyze the influence of the random distribution of the adsorption sites on the adsorption isotherms. The source of the heterogeneity and adsorption sites distribution is the atomic matrix disorder of the amorphous walls of the MCM-41 material.

2. THE INTERACTION MODEL AND THE SIMULATION METHODOLOGY

The MCM-41 structure is modeled as a disordered array of oxygen and silicon atoms, each one interacting with an adsorptive atom via the potential based on the model proposed by Pellenq *et al.*[5] The skeletal density is assumed to be

the same as that proposed by Maddox *et al.*,[1] being of 27 T sites (Si atoms) per cubic nanometer for the solid MCM-41 material. Having this decided, we created disordered pseudo-hexagonal T-site bulk structure wherein we randomly inserted oxygen atoms with the constraint that the Si–O distance $d=1.61$ Å. Then we formed the pores by removing all the atoms within the assumed pore diameter D and wall thickness W. The simulation results presented in this paper correspond to a single pore with $D=40$ Å and $W=10$ Å. We have not included interpore interaction because the fluid–fluid interaction between atoms in adjacent pores proved to be negligibly small for a wall thickness of 10 Å.

The Kr–Kr and Kr–wall (Kr–O, Kr–Si) interactions include dispersion and repulsive short-range contributions. No induction energy has been used. The model based directly on the parameters taken from Pellenq and Levitz[5] turned out to give Kr–wall energies much smaller than the values reported experimentally. This fact was reflected in the adsorption behavior, which was more like of type III in the IUPAC classification.[2] Therefore, in order to reproduce the experimental enthalpies of adsorption, we have increased the strength of the interaction by a factor of 2. Such a model has given reasonable agreement with the experimental measurement, although additional ''engineering'' of the interaction parameters will be needed to reproduce Kr in the MCM-41 material.

The wall surface roughness is taken into account. We constructed a 3D grid in the Monte Carlo (MC) box (a pore of diameter $D=40$ Å, with axial length $L=25$ Å, and periodic boundary conditions). The interaction energy at each grid point has been precalculated and a linear interpolation was used during the simulation runs to calculate the off-grid energies. Our model of the MCM-41 mesopore produces a distribution of the adsorption sites strongly peaked around $E_{\min}=-1000$ K with the half-width equal to 500–700 K. This feature seems to have an important impact on the adsorption mechanism, as is illustrated below. However, currently we do not have any knowledge of experimental data to compare with our theoretical distribution.

The conventional grand canonical MC ensemble has been applied. Thus the simulation box is assumed to be in equilibrium with the bulk gas, which obeys the ideal gas law. Trial moves include translations of atoms, insertion of new atoms, and removal of existing atoms. Typical runs contained a minimum number of MC steps of the order of 10^6 (per atom). The main results are extracted from the previously equilibrated runs. The equilibration runs give information concerning the kinetics of the transformations observed in the system.

3. KRYPTON ADSORPTION AT 77 K

Our first task was to compare the adsorption of krypton in ideal cylindrical and corrugated pores. Figure 1 shows the simulated adsorption isotherm in the corrugated pore. It reproduces the experimental data in a reasonable way. However, the slope of the simulated isotherm is flatter than the experimental one below the pressure of the capillary condensation, and the capillary condensation occurs much more rapidly. The latter difference is usually explained by a distribution of the pore size in the real material that is not present in the model. The former one mirrors the differences in the Kr–wall interaction, in particular, in the distribution and energies of the adsorption sites on the MCM-41 walls. The adsorption isotherm calculated for the ideal cylindrical pore (that is with a δ-like adsorption site distribution) is totally flat below the pore condensation pressure. The pressure itself is shifted towards lower values.

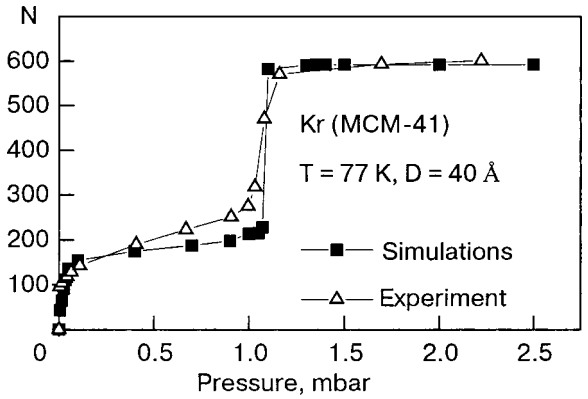

FIG. 1. Experimental and simulated adsorption isotherms. The amount adsorbed is given in units of number of atoms per volume of the Monte Carlo box.

The adsorption enthalpy as a function of the loading gives additional insight into this problem (see Fig. 2). The experimental data show energy uniformly decreasing in the range from 0 to 40% of the maximal loading. The calculated curve, however, shows a local maximum at about 25% loading. This is a consequence of our wall structure and the distribution of the adsorption sites as discussed above. The Kr–wall contribution to the total enthalpy (Fig. 2) shows different slopes above and below the energy $E\cong-1000$ K. This value corresponds to the maximum of adsorption site distribution.

The influence of the strong corrugation seems to have an effect on the microscopic states in equilibrium and on the mechanism of the transformation. During the simulation runs we have observed different metastable configurations that existed as intermediate states. As an example we present the simulated fluctuations of the number of atoms in the MC box when the system is undergoing the capillary condensation (Fig. 3). It clearly shows an intermediate, metastable state, before the pore condensation is completed. It represents the

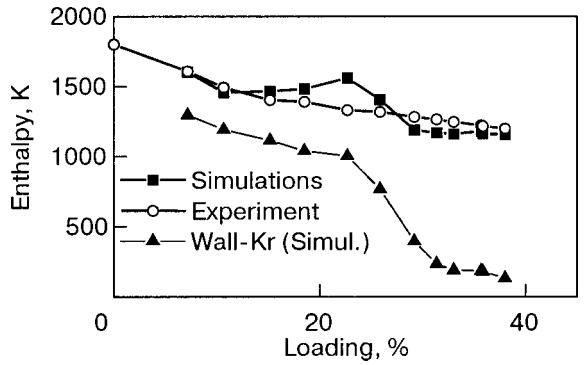

FIG. 2. Enthalpies of a adsorption as function of loading. The numerical results show the total enthalpy and, separately, the contribution from the atom–wall interaction.

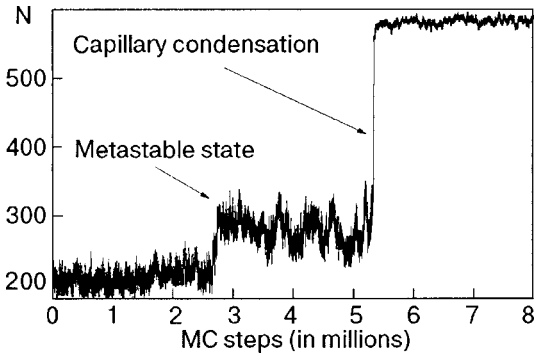

FIG. 3. The fluctuations of the number of atoms in the simulation box as a function of the Monte Carlo steps, at the capillary condensation pressure.

formation of a second layer, which exists only within a limited time of simulation. Instead of stabilizing it, the system undergoes a transformation into the condensed phase.

4. CONCLUSIONS

The results presented here show the profound influence of a corrugated wall structure on the mechanism of adsorption. The example presented here shows that it could affect the profile of an adsorption isotherm and the enthalpy of adsorption. This influence is particularly important in the range of pressures below the capillary condensation. The slope of the adsorption isotherm is determined by the distribution of the energies of the adsorption sites. This result is compatible with the conclusion reported by Maddox *et al.*,[1] where a heterogeneous interaction model was used to reproduce the experimental form of the adsorption isotherm of nitrogen in the MCM-41 system.

The existence of metastable states along the adsorption isotherm is understood and observed in many systems. The hysteresis of the adsorption–desorption curve, observed experimentally, is the most evident proof. However, our simulation shows that the inhomogeneous wall structure induces additional, short-lived metastable states that may affect the mechanism of condensation and other phase transitions. Thus we conclude that the heterogeneous interactions not only are responsible for the form of the adsorption isotherm, they also affect the mechanism of the phase transformations in the system.

The interaction model used in this paper requires additional refinement. It seems that there are no potential parameters describing the atom–wall interaction which are transferable between different pore systems, even if they are built from the same atoms and similar basis units (Si–O bonds in our case). The most probable cause is the electronic states of surface atoms modified by local imperfections of the chemical bond structure.

*E-mail: kuchta@up.univ-mrs.fr

[1] M. W. Maddox, J. P. Olivier, and K. E. Gubbins, Langmuir **13**, 1737 (1997).
[2] F. Rouquerol, J. Rouquerol, and K. Sing, *Adsorption by Powders and Porous Solids*, Academic Press, London (1999).
[3] J. P. Coulomb, Y. Grillet, P. Llewellyn, C. Martin, and G. Andre, Proc. 6th Int. Conf. Fundamen Adsorption, F. Meunier (Ed.), Elsevier (1998), p. 147.
[4] J. P. Coulomb, N. Floquet, Y. Grillet, P. Llewellyn, R. Kahn, and G. Andre, in *Studies in Surface Science and Catalysis*, K. K. Unger (Ed.), Elsevier (2000), p. 235.
[5] R. J.-M. Pellenq and P. E. Levitz, Mol. Simul (in press).

This article was published in English in the original Russian journal. Reproduced here with stylistic changes by AIP.